Records of and controls on temporal variations in activity at arc volcanoes

Stefan M. Lachowycz

University College

Thesis submitted in accordance with the requirements of the University of Oxford for the degree of Doctor of Philosophy

Hilary Term 2016

Records of and controls on temporal variations in activity at arc volcanoes

Stefan M. Lachowycz (University College)

Many attributes of volcanic activity, whether physical, geochemical/petrological, or geophysical, change over timescales from minutes to millions of years. Understanding the nature of these variations and their controls is essential both for hazard assessment and to understand volcanic and magmatic processes. Arc volcanism entails a relatively broad range of eruption styles and magma compositions, and thus wide-ranging hazards and a variety of eruption records. Despite their significance, records of activity for many arc volcanoes are inadequately characterised, so any temporal variability is poorly constrained. In this thesis, I investigate temporal variations in different styles of activity (dome-forming, Plinian-style, and effusive/glaciovolcanic) on a range of timescales (days–years, millennia, and hundreds of ky, respectively), from diverse records (seismicity, tephra deposits, and effusive eruption products), at four arc volcanoes. I analyse seismic time-series from Soufrière Hills Volcano (Montserrat) and Volcán de Colima (Mexico) using two statistical techniques, identifying temporal variation in the extent of long-range correlations and randomness in these data, which has potential to inform real-time monitoring and constrain eruptive processes. I also present new composition data for and review previous studies of tephra deposits from Volcán Hudson (Chile), revising its explosive eruption history and finding previously unrecognised shifts in the magma composition erupted through the Holocene. I also describe and analyse sequences of lithofacies from effusive eruptions of a range of magma compositions from Volcán Sollipulli (Chile), inferring varying extents of interaction with ice during their emplacement, and so changes in eruption style through time. These case studies highlight the importance of detailed characterisation of temporally varying records of volcanic activity, and some of the limitations of and uncertainties in these records and their interpretation.

Extended abstract

Records of and controls on temporal variations in activity at arc volcanoes

Stefan M. Lachowycz (University College)

Advances in monitoring and studies of the eruptive history of volcanoes in recent decades are producing an increasing amount and variety of information on the timing of volcanic activity. Temporal variations have been identified in many attributes of volcanism on a wide range of timescales, from precursory changes in seismicity only minutes to hours before eruptions, to cycles in eruption frequency or style over hundreds to thousands of years, and shifts in magma composition and vent location due to tectonic changes over millions of years. Understanding the nature of and controls on these variations is essential for hazard assessment and/or provides invaluable insight into volcanic and magmatic processes. Arc volcanism entails a relatively broad range of eruption styles and magma compositions, and thus wide-ranging hazards and a variety of eruption records. The potential for and implications of temporal variation in arc volcanism are exemplified by recent eruptions in Chile (Calbuco, Chaitén, and Cordón-Caulle volcanoes) and Indonesia (Kelud, Merapi, and Sinabung volcanoes), which included rapid escalations in activity and/or changes in eruption style. In some of these cases and at many other arc volcanoes, investigation and interpretation of their temporal variability has been hindered by limited monitoring and insufficient characterisation of eruption records. In this thesis, I explore some of the challenges and opportunities in constraining temporal variations in arc volcanism, by investigating such variations in different styles of activity (dome-forming, Plinian-style, and effusive/glaciovolcanic) on a range of timescales (days–years, millennia, and hundreds of ky, respectively), from diverse records (seismicity, tephra deposits, and effusive eruption products), at four volcanoes (Soufrière Hills Volcano (Montserrat) and Volcán de Colima (Mexico), Volcán

Hudson (Chile), and Volcán Sollipulli (Chile)). New information is obtained in each case either by statistical analysis or detailed characterisation of eruption records; in some cases this provides insight into the nature of and controls on the temporal variations in activity at these volcanoes.

Understanding the underlying structure of data from volcano monitoring is essential to identify changes in eruptive activity and their precursors and controls. However, effective analysis of longer-term trends in monitoring data is challenging as these data are not necessarily statistically stationary or linear, particularly those from lava dome-forming volcanoes, which are commonly characterised by pulsatory eruptive activity. In Chapter 2, I use detrended fluctuation analysis, a statistical technique previously applied to nonstationary data, to identify long-range (slowly decaying, e.g. power-law) correlations in a number of time-series of volcano seismicity recorded during the recent dome-forming eruptions of Volcán de Colima, Mexico, and Soufrière Hills Volcano, Montserrat. For all the time-series analysed, correlation strength varies through time and/or on different timescales; in some cases, this variation is periodic, seasonal, and/or related to activity. These results may provide new insights into eruptive processes and possibly further constrain the generation mechanisms of a number of the volcano-seismic event classes analysed. Furthermore, the correlation properties of real-time seismic measurements are shown (retrospectively) to contain information valuable to real-time volcano monitoring that is not identifiable by conventional techniques. This demonstrates that long-range correlation analysis may be useful for extracting additional information from monitoring data at dome-forming or similar volcanoes.

In Chapter 3, I examine the utility of another statistical analysis technique, Shannon entropy (a measure of the randomness of a signal), for analysis of monitoring data by its application to the same time-series of volcano seismicity analysed in Chapter 2. Entropy may be computed in real-

time by the method used even if the signal is sampled at a high frequency and/or discontinuously, so this technique is potentially widely applicable to monitoring time-series. At the two volcanoes studied, the entropy of real-time seismic measurements and the count rate of certain volcano-seismic event types is found to vary through time, generally being elevated (often close to maximal) during phases of greater volcanic activity. High entropy indicates greater uncertainty in the value taken by the variable, i.e. that the time-series is less predictable. In some instances, the entropy of a signal shifts prior to or coincident with changes in seismic or eruptive activity, some of which were not clearly recognised at that time by real-time monitoring. I examine the nature of the entropy variations by testing for uniform data distribution and comparison to the coefficient of variation. This demonstrates the sensitivity of the entropy to the data distribution, and that it is distinct from measures of data dispersion. Therefore, entropy analysis may have potential as a tool to extract additional information in real-time from volcano monitoring data streams.

Volcán Hudson, in the Andean Southern Volcanic Zone, has been identified as the source of four eruptions of >1 km^3 of tephra (volcanic ash and lapilli) and tens of smaller explosive eruptions in the past 20 ky. The resulting tephra deposits have great potential as chronological markers in studies of the palaeoenvironment of the region, and to assess any variation in eruption frequency. However, the characteristics and timing of many of the eruptions of Volcán Hudson are poorly constrained, inhibiting precise tephrochronology and hazard assessment. In Chapter 4, I present matrix glass and whole rock composition analyses of Volcán Hudson tephra units in relatively complete terrestrial sections, and catalogue occurrences of tephra previously attributed to eruptions of Volcán Hudson, in order to correlate the tephras analysed and critically evaluate previous tephra correlations. The Volcán Hudson tephras characterised generally have a narrow range in their glass composition, so in most cases can be distinguished from the other tephras of a similar age, which often have a similar composition. I find previously unrecognised shifts in

erupted magma composition during the Holocene, from silicic to mafic after the H2 eruption (~3.9 cal ka BP), and then to intermediate compositions for the last ~1 ky. The new geochemical data and tephrostratigraphy reanalysis in this study provide a framework for future tephrochronology and studies of the record of eruptions in the region. In addition, they highlight the importance of detailed tephra characterisation in developing correlations between and age models for palaeoenvironmental records, or accurate constraint of eruption frequency.

Magma-ice-meltwater interactions produce diverse landforms and lithofacies, reflecting the multitude of factors that influence glaciovolcanism, including both magmatic (e.g., composition, eruption rate) and glacial (e.g., ice thickness, thermal regime) conditions. This is exemplified by the walls of the partly ice-filled summit caldera of Volcán Sollipulli, a stratovolcano in southern Chile, which include lithofacies from eruptions of a wide range of magma compositions beneath or in contact with ice. In Chapter 5, I analyse these lithofacies and hence propose new interpretations of the eruptive and glacial history of Volcán Sollipulli. The facies include a thick, laterally extensive sequence of fragmental glaciovolcanic deposits, comprising massive, mafic lava pillow-bearing hyaloclastite overlain by sills and then hyaloclastic debris flow deposits (similar to Dalsheidi-type sequences). The distribution and thickness of these units indicate an unusual abundance of magma-meltwater interaction for an arc stratovolcano in temperate latitudes, perhaps due to eruptions beneath a thick ice cap. Coherent lava coulées, domes, lobes, and stacks of basaltic andesite–trachydacite composition are present around the top of the caldera rim; these display morphologies and fracture patterns on caldera-facing margins that indicate that the caldera was filled with ice when these lavas were erupted. The lithofacies characterised demonstrate the diversity of glaciovolcanism that is possible at arc stratovolcanoes capped by temperate ice or with ice-filled calderas, and the potential for uncertainties in inference of the palaeoenvironmental conditions of their emplacement.

The case studies presented in this thesis identify new changes or trends in distinct styles of arc volcanism on different timescales, and provide additional information on the nature of those recognised by previous work. Some of the data are suggested to further constrain (or provide evidence of previously unknown) controls on the volcanic activity studied. This work also contributes to the development of new techniques and understanding to analyse and interpret some aspects of the types of volcanism examined. Although there are many challenges and limitations to constraining temporal variations in arc volcanism from its records across the whole range of timescales, this thesis highlights the potential to better understand such variability and its controls through detailed characterisation and statistical analysis of records of volcanic activity.

Acknowledgments

My principal thanks must go to my main supervisors, David Pyle and Tamsin Mather, not only for their contributions and guidance throughout this project, but also their patience and support during a particularly tough five years for me. I am also especially indebted to Vicki Smith (Research Laboratory for Archaeology and the History of Art) for a great deal of advice and assistance, and to Ioana Cosma (Google) for her invaluable contributions to the time-series entropy analysis. In addition, Karen Fontijn and Harriet Rawson (Department of Earth Sciences) have contributed to the tephrostratigraphy aspect of this project, and Katy Mee (British Geological Survey) to the glaciovolcanism part; all have also provided much appreciated guidance.

I also thank Red Sísmica de Colima (particularly Gabriel Reyes-Dávila), Nick Varley and the volunteers at the Centro de Intercambio e Investigación en Vulcanología (Universidad de Colima), and the Montserrat Volcano Observatory (particularly Venus Bass, Christian Eligon, and Henry Odbert) for providing or processing the seismic data analysed in this project. Paul Cole (Plymouth University), Henry Odbert (University of Bristol), Mel Rodgers (Department of Earth Sciences), and Nick Varley contributed to the interpretation of the seismic data and the results of the statistical analyses. Max Little (Aston University) gave advice about detrended fluctuation analysis, and Oliver Lamb (University of Liverpool) and Emma Liu (University of Bristol) respectively assisted with and provided code and information for the associated spectral analysis. My work on Volcán Sollipulli has benefited from contributions from Jennie Gilbert and Laura Hobbs (Lancaster University), as well as Ar-Ar dates from Carolina Jara, Hugo Moreno, and José Naranjo (Servicio Nacional de Geología y Minería). José also contributed to the interpretation of the eruptive and glacial history of Volcán Sollipulli, and has generously shared his knowledge of volcanism in the wider region. Chuck Stern (University of Colorado Boulder) has also given valuable insights about

Andean volcanism and, along with Simon Haberle (Australian National University) and Guiseppe Siani (Université de Paris-Sud XI), has kindly shared tephra data. Zicheng Yu (Lehigh University) provided peatland extent data. Michael Dee (Research Laboratory for Archaeology and the History of Art) gave advice about OxCal sequence models. My fieldwork in Chile and Argentina was facilitated by the advice and/or able assistance of some of those aforementioned, as well as Alvaro Amigo (Servicio Nacional de Geología y Minería), Maria Godoi and Pedro Cid (Universidad de Magallanes), the Ñuke Mapu of Melipeuco (particularly Hendri Mora and César Sandoval), Neil Slatcher (Lancaster University), Oscar Bustamente (Universidad de Chile), and Rebecca Neely (University of Iceland). The laboratory work I have undertaken has been assisted by (in addition to some of the aforementioned) Norman Charnley, Owen Green, Phil Holdship, Jeremy Hyde, and Steve Wyatt in the Department of Earth Sciences, Christine Lane (University of Manchester), and Nick Marsh (University of Leicester).

Roberto Carniel (Università di Udine), Servando De la Cruz-Reyna (Universidad Nacional Autónoma de México), John Smellie (University of Leicester), and three anonymous reviewers provided invaluable feedback on earlier versions of the papers/manuscripts in Chapters 2–4. I also thank Seb Watt (University of Birmingham) and Conall Mac Niocaill (Department of Earth Sciences) for examining this thesis.

This work would not have been possible without the unusually large amount of financial support I have received from a variety of sources. I thank the Natural Environment Research Council for funding my DPhil (grant no. NE/I528485/1), the 'Tempo of post-glacial volcanism in southern Chile' project (NE/I013210/1, which funded some fieldwork expenses), and some additional support. In addition, the British Geological Survey provided DPhil funding (University Funding Initiative grant no. S198) and separately funded some fieldwork expenses. I am also grateful to University College

Oxford for awarding me the Senior Scholarship and, through their Old Member's Trust, funding fieldwork and conference expenses, as well as to the Department of Earth Sciences for a supplementary stipend. The Lydia Press Memorial Fund and the Burdett-Coutts Fund (Department of Earth Sciences) funded fieldwork prior to starting my DPhil that was integral to Chapters 2 and 3. For financing fieldwork, I also acknowledge International Association of Volcanology and Chemistry of the Earth's Interior project 'Ice-filled calderas in the 21st Century: consequences of volcanic unrest and environmental change', Lancaster University, Santander, Rio Tinto/the Royal Geographical Society (with IBG), and the University of Oxford A.A. Paton Fund. In addition, the Earth Observatory of Singapore, State University of New York at Buffalo, and Volcanic and Magmatic Studies Group funded my attendance at two workshops.

Finally, I thank my officemates for tolerating my sometimes unconventional studying methods, and the many health professionals who have strived to help me keep working to this end.

Contents

1. Introduction **25**

1.1. Activity at arc volcanoes 25

1.2. Records of arc volcanism 27

1.3. Scope of thesis 29

2. Long-range correlations identified in time-series of volcano seismicity during dome-forming eruptions using detrended fluctuation analysis **31**

Abstract 32

2.1. Introduction 33

2.2. Detrended fluctuation analysis (DFA) 36

2.3. Data 40

2.3.1. Volcán de Colima 40

2.3.2. Soufrière Hills Volcano 42

2.3.3. Comparison of seismicity at the volcanoes studied 46

2.4. Results 48

2.4.1. Volcán de Colima hourly RSEM, January 2004–December 2008 48

2.4.2. Soufrière Hills Volcano hourly RSAM, February 2005–June 2011 51

2.4.3. Volcán de Colima daily event counts, November 2004–December 2008 53

2.4.4. Soufrière Hills Volcano daily event counts, October 1996–July 2010 55

2.5. Discussion 62

2.6. Conclusions 67

3. Entropy analysis of time-series of volcano seismicity during dome-forming eruptions **69**

Abstract 70

3.1. Introduction 71

3.2. Methods 73

3.2.1. Shannon entropy 73

3.2.2. Entropy computation for volcano-seismic time-series 74

3.2.3. Relationship between entropy and data distribution 78

3.2.4. Applicability of entropy analysis 80

3.3. Data 81
3.3.1. Volcanoes 81
3.3.2. Seismic time-series 82
3.4. Results 84
3.4.1. Volcán de Colima hourly RSEM, January 2004–December 2008 84
3.4.2. Soufrière Hills Volcano hourly RSAM, February 2005–June 2011 88
3.4.3. Volcán de Colima daily event counts, November 2004–December 2008 91
3.4.4. Soufrière Hills Volcano daily event counts, October 1996–July 2010 94
3.5. Discussion 98
3.6. Conclusions 102

4. Late Quaternary tephrostratigraphy of Volcán Hudson, southern Chile 103
Abstract 104
4.1. Introduction 105
4.2. Volcán Hudson 108
4.2.1. Geological setting and geochemistry 108
4.2.2. Previous work on explosive eruption history 111
4.3. Methods 117
4.3.1. Field sampling 117
4.3.2. Geochemical analysis 119
4.3.3. Reanalysis of tephra unit correlations and eruption ages 122
4.4. Results and discussion 123
4.4.1. Eruptions identified in terrestrial sections 123
4.4.2. Correlation with palaeoenvironmental records 131
4.4.3. Tephrochronology and temporal variation in activity 141
4.5. Conclusions 148

5. Glaciovolcanism at Volcán Sollipulli, southern Chile: Lithofacies analysis and interpretation 149
Abstract 150
5.1. Introduction 151
5.2. Volcán Sollipulli 154
5.2.1. Geological and glaciological context 154
5.2.2. Eruptive history 157

5.2.3. Geomorphological constraints on glacial history 160
5.3. Lithofacies and sequence descriptions 161
5.3.1. Lithofacies classification 161
5.3.2. Sharkfin sequence 164
5.3.3. Chufquén valley lavas 175
5.3.4. Circum-caldera lava sequence 177
5.4. Interpretation and discussion of eruptive and glacial history 181
5.4.1. Sharkfin sequence 181
5.4.2. Chufquén valley lavas 185
5.4.3. Circum-caldera lava sequence 186
5.4.4. Discussion 188
5.5. Conclusions 194

6. Conclusions and future directions 195
6.1. Time-series from volcano monitoring 195
6.2. Records of explosive eruptions 198
6.3. Records of effusive eruptions 200

Bibliography 203

Supplementary material 233

List of figures

2.1. Location and seismometer network maps for Volcán de Colima 41
2.2. Location and seismometer network maps for Soufrière Hills Volcano 43
2.3. DFA of Volcán de Colima RSEM 49
2.4. DFA of Soufrière Hills Volcano RSAM 52
2.5. DFA of Volcán de Colima daily volcano-seismic event counts 54
2.6. DFA of Soufrière Hills Volcano daily volcano-seismic event counts 56

3.1. Comparison of entropy calculated using different window lengths 75
3.2. Comparison of entropy calculated for data discretised to different extents 77
3.3. Entropy analysis of Volcán de Colima RSEM 85
3.4. Entropy analysis of Soufrière Hills Volcano RSAM 89
3.5. Entropy analysis of Volcán de Colima daily volcano-seismic event counts 92
3.6. Entropy analysis of Soufrière Hills Volcano daily volcano-seismic event counts 95

4.1. Map of volcanoes of southern Patagonia and occurrences of Hudson tephra 109
4.2. Stratigraphy of sections sampled bearing Volcán Hudson tephra 118
4.3. Glass compositions of Volcán Hudson tephras analysed 126
4.4. Composition data for Volcán Hudson tephras from terrestrial sections 128
4.5. Composition data for Hudson tephras from palaeoenvironmental records 133
4.6. Composition data for tephras analysed by Haberle and Lumley (1998) 136
4.7. Composition data for tephras attributed to specific eruptions of Volcán Hudson 138
4.8. Summary of the inferred post-glacial explosive eruption history of Volcán Hudson 142
4.9. Cumulative tephra volume vs time plot for selected volcanoes in the SVZ 145
4.10. Schematic illustration of model of response of Andean volcanoes to deglaciation 147

5.1. Map of the volcanoes of southern Chile and Argentina and their ice cover 155
5.2. Satellite image and geological and geomorphological maps of Volcán Sollipulli 156
5.3. Total alkali-silica plot of the whole rock compositions of Sollipulli samples 158
5.4. Stratigraphy of the studied sections of the caldera rim at Volcán Sollipulli 165
5.5. Photographs showing features of the Sharkfin lava subsequence 166
5.6. Photographs showing features of the Sharkfin hyaloclastite subsequence 169

5.7. Photographs showing features of the Sharkfin debris flow subsequence 171
5.8. Photographs showing features of intrusions in the upper Sharkfin sequence 174
5.9. Photographs showing features of the Chufquén valley lavas 176
5.10. Photographs showing features of the circum-caldera lava sequence 179
5.11. Illustration of the interpreted glacial and eruptive history of Volcán Sollipulli 189

List of tables

2.1. Particulars of the volcano-seismic event types at Volcán de Colima 44

2.2. Particulars of the volcano-seismic event types at Soufrière Hills Volcano 45

4.1. Summary of the tephrostratigraphy of Volcán Hudson 112

4.2. Glass compositions of Volcán Hudson tephras analysed 124

4.3. Whole rock compositions of Volcán Hudson tephras analysed 125

5.1. Summary of the stratigraphy of the upper flanks of Volcán Sollipulli 159

5.2. Descriptions and interpretations of the lithofacies identified at Volcán Sollipulli 162

List of supplementary material

Supplementary files

SF2.1. Statistical techniques previously applied to volcano-seismic time-series 235
SF2.2. List of references in SF2.1 240

SF3.1. Normalised cumulative entropy of Volcán de Colima RSEM 244
SF3.2. Normalised cumulative entropy of Soufrière Hills Volcano RSAM 244
SF3.3. Coefficient of variation of Volcán de Colima daily volcano-seismic event counts 245
SF3.4. Coefficient of variation of Soufrière Hills daily volcano-seismic event counts 247

SF4.1. List of references in ST4.1 and ST4.2 249
SF4.2. Inter-run comparison of glass secondary standard EMP analyses 252
SF4.3. OxCal Bayesian age models for Volcán Hudson tephras 253

SF5.1. List of post-glacial volcanic centres in southern Chile and Argentina 258
SF5.2. Supporting data for Volcán Sollipulli Ar-Ar dates 260
SF5.3. Supporting data for Volcán Sollipulli radiocarbon dates and age models 262

Supplementary tables

ST4.1. Occurrences of tephra deposits attributed to Volcán Hudson 265
ST4.2. Published chemical composition data for tephra attributed to Volcán Hudson 269
ST4.3. Chemical composition data for secondary standards and blanks 291
ST4.4. Complete glass composition data for Volcán Hudson samples analysed 296

ST5.1. Whole rock composition data for samples of Volcán Sollipulli eruption deposits 306

Chapter 1 Introduction

1.1. Activity at arc volcanoes

Magmatism at subduction zones is generally expressed as a chain of volcanoes, i.e. a volcanic arc (e.g., Perfit and Davidson, 2000). Arc volcanism is characterised by a diverse range of magma compositions and eruption styles (in comparison to other tectonic settings), both between (e.g., Gill, 1981; Turner and Langmuir, 2015) and within (e.g., Stern, 2004) discrete arcs, and commonly at individual volcanoes. Many recent eruptions of arc volcanoes have entailed multiple styles of activity. For example, the eruptions of Chaitén (2008–9; e.g., Major and Lara, 2013) and Cordón Caulle (2011–12; e.g., Tuffen et al., 2013) volcanoes in Chile comprised (sub-)Plinian eruptions followed by lava dome or flow extrusion, whilst periods of lava effusion at Soufrière Hills Volcano (Montserrat) and Volcán de Colima (Mexico) have often culminated in large Vulcanian explosions (e.g., Varley et al., 2010a; Wadge et al., 2014). Understanding the nature of and controls on such temporal variability is thus essential for hazard assessment (e.g., Loughlin et al., 2015; Ogburn et al., 2015), and provides important constraints on volcanic and magmatic processes (e.g., Cashman and Sparks, 2013; Caricchi and Blundy, 2015).

Temporal variations in arc volcanism have been identified on a wide range of timescales. The explosive eruptions of Calbuco (2015), Chaitén (2008), and Cordón-Caulle (2011) volcanoes in Chile were all preceded by only hours of precursory seismicity, due to rapid magma ascent (at least in the latter cases: Castro and Dingwell, 2009; Castro et al., 2013). In longer-lived eruptive phases, cyclicity over similarly short periods is increasingly being recognised, as well as on timescales of days or months (de' Michieli Vitturi et al., 2013); for example, at Soufrière Hills Volcano, sub-daily cycles in activity have been observed together with longer cycles of ~50 days

(Odbert et al., 2014). Seasonality to volcanic activity has also been identified, both at individual volcanoes (e.g., Pavlof Volcano, Alaska: McNutt and Beavan, 1987) and at a regional scale (Mason et al., 2004). Multi-annual variations have also been reported during long-lived (usually dome-forming) eruptions, such as in lava effusion rate at Soufrière Hills Volcano (Odbert et al., 2014; Wadge et al., 2014) and Volcán de Colima (e.g., Varley et al., 2010a).

Substantial (sub-)annual variations may be superimposed on a longer-term consistent magma supply. For example, Gunung Merapi (Indonesia) is characterised by abrupt transitions in activity on a monthly to annual scale (e.g., Voight et al., 2000; Surono et al., 2012), but has been suggested to have had a constant magma supply rate for the past century (Siswowidjoyo et al., 1995), albeit since recognised to be part of a third cycle in magma composition/supply and eruption frequency over the past ~2 ky (Gertisser and Keller, 2003). However, cycles (and other variability) on a centennial timescale are apparent elsewhere, such as in eruption composition and style at Volcán de Colima (e.g., Luhr, 2002) and Mayon Volcano (The Philippines; Newhall, 1979). Variations on a millennial scale are increasingly being identified from records of explosive eruptions, for instance in eruption frequency at Gunung Agung (Indonesia; Fontijn et al., 2015) and in eruption frequency and composition at Volcán Mocho-Choshuenco (Chile; Rawson et al., 2015). The latter has been suggested to be part of a longer-term (hundreds of ky) variability in erupted magma flux due to glacial-interglacial cyclicity (Rawson et al., 2016), with volcanism increasing during deglaciation and vice versa; the extent to which this is the case for arc volcanism is unclear (e.g., Huybers and Langmuir, 2009; Kutterolf et al., 2012; Watt et al., 2013a). Glacial cycles may also generate temporal variations in eruption style by changes in the potential for magma-ice interaction (e.g., Smellie and Chapman, 2002). On longer (My) timescales, arc-scale variations include cycles in magma composition and flux (DeCelles et al., 2009) and shifts in arc location and magma composition and flux due to changes in subduction (e.g., Parada et al., 2007).

1.2. Records of arc volcanism

Investigation of the temporal variability of arc volcanism is only possible from analysis and interpretation of records of past volcanic activity. The diverse activity at arc volcanoes creates a variety of records, each with different challenges in their analysis. Volcano monitoring has generated an increasing amount and diversity of time-series of recent volcanic activity (e.g., Sparks, 2003; Loughlin et al., 2015), enabling the identification of the sub- to multi-annual variability summarised in Section 1.1. However, only ~35% of historically active volcanoes are continuously monitored (Loughlin et al., 2015), and not necessarily with a sufficient amount or diversity of equipment and techniques for comprehensive monitoring. Monitoring is even more limited for those apparently without historical activity, despite the potential of some to rapidly become active (as in the case of Volcán Chaitén: Major and Lara, 2013). Extrapolation of interpretations of activity at well-monitored volcanoes to others is not necessarily appropriate, given the apparently unique properties of many volcanic systems despite their common processes (Cashman and Biggs, 2014). Hence the potential to investigate and forecast temporal variations in activity at most volcanoes on short timescales is appreciably limited. Even at arc volcanoes that are relatively intensively monitored, precursors to activity transitions are not necessarily identifiable using conventional methods, e.g. some changes in effusion rate at Soufrière Hills Volcano (e.g., Wadge et al., 2014). In some cases, even the techniques that have been informative in previous eruptive phases have failed to identify precursors to subsequent similar activity, such as the real-time seismic energy measurement employed at Volcán de Colima (Reyes-Dávila and De la Cruz-Reyna, 2002) prior to lava effusion in 2004 (Varley et al., 2010a).

Beyond the timescale of volcano monitoring, temporal variability in activity may be apparent in historical records for volcanoes that have been frequently active (e.g., Mt Vesuvius, Italy: Arrighi

et al., 2001; Gunung Merapi: Voight et al., 2000). However, even at such volcanoes, the historical record may be incomplete (e.g., Volcán Villarrica, Chile: Van Daele et al., 2014), whilst at those with less frequent historic activity, this record is insufficient to characterise the typical activity and its variability (e.g., Fontijn et al., 2015). In these cases, and for examination of longer-term (millennial-scale) variations, analysis of the deposits of previous eruptions, typically the tephrostratigraphic record, is essential. The tephrostratigraphic record is most often constrained from terrestrial deposits, but accessible exposures are often limited and preservation may be poor, particularly of smaller (Volcanic Explosivity Index (VEI) ≤4; Newhall and Self, 1982) eruptions. This is the case, for example, in parts of the southern Andes (e.g., Fontijn et al., 2014). Furthermore, temporal bias is particularly apparent in most terrestrial records, with fewer smaller eruptions preserved with increasing age (e.g., Brown et al., 2014), and preservation of tephra from eruptions prior to deglaciation is uncommon at high latitudes (e.g., Watt et al., 2013a). Other environments, such as ice, peat, and lacustrine and marine sediments, may preserve a more continuous and/or longer record of explosive eruptions, but numerous distortions of the tephra record are possible, e.g. due to taphonomic processes and dating uncertainties (e.g., Lowe, 2011; Fontijn et al., 2014; Davies, 2015).

Records of effusive activity at arc volcanoes have been studied comparatively infrequently, due to the considerable logistical and analytical effort required to fully characterise the activity of even a single volcano. At some volcanic centres, products of effusive eruptions spanning hundreds of ky are exposed, recording variations in magma composition and eruption style (e.g., Volcán Puyehue–Cordón Caulle: Singer et al., 2008). However, these records can be considerably curtailed if effusive eruption fluxes are high enough to cover earlier deposits relatively quickly; for example, the main edifice of Volcán Llaima (Chile) has been suggested to be entirely post-glacial (Naranjo and Moreno, 1991).

1.3. Scope of thesis

This thesis comprises three studies of diverse styles of arc volcanism on different timescales, by analysis of distinct records of eruptions at four volcanoes, in order to investigate the records of and controls on temporal variations in arc volcanism. Chapters 2 and 3 analyse seismic time-series from the recent dome-forming eruptions of Soufrière Hills Volcano (Montserrat) and Volcán de Colima (Mexico) using two statistical techniques, to quantify the extent of long-range correlations and randomness in these data on timescales of days to years. Chapter 4 investigates the post-glacial explosive eruption history of Volcán Hudson (Chile) by analysing terrestrial tephra deposits and reviewing previous studies of Volcán Hudson tephra, to evaluate and better characterise its tephrostratigraphic record. Chapter 5 analyses and interprets sequences of lithofacies from effusive eruptions of a range of magma compositions from Volcán Sollipulli (Chile), to investigate the influence of ice interaction (across glacial-interglacial cycles) on eruption style and processes at arc volcanoes. The conclusions from these studies are summarised and possible future directions are discussed in Chapter 6.

Chapter 2 Long-range correlations identified in time-series of volcano seismicity during dome-forming eruptions using detrended fluctuation analysis

Majority published in: Lachowycz, S.M., Pyle, D.M., Mather, T.A., Varley, N.R., Odbert, H.M., Cole, P.D., Reyes-Dávila, G.A., 2013. Long-range correlations identified in time-series of volcano seismicity during dome-forming eruptions using detrended fluctuation analysis. J. Volcanol. Geotherm. Res. 264, 197–209.

Author contributions: Seismic time-series from Volcán de Colima and Soufrière Hills Volcano were provided by NRV/GARD and HMO/PDC respectively. All co-authors contributed to manuscript preparation.

This paper develops work included as part of my thesis submitted for a MEarthSc in Earth Sciences (University of Oxford) in 2010. Supplementary File 2.1 and part of the methods and description of Volcán de Colima and its seismicity are revised from that thesis. The data were reanalysed for this study using revised methods, so the results and interpretation have changed accordingly.

Abstract

Understanding the underlying structure of data from volcano monitoring is essential to identify precursors to changes in eruptive activity and to comprehend volcanic processes. However, effective analysis of longer-term trends (over months to years) in these signals is challenging as volcanic data are not necessarily statistically stationary or linear, particularly those from lava dome-forming volcanoes, which are commonly characterised by pulsatory eruptive activity. Here, we use detrended fluctuation analysis (DFA), a statistical technique previously applied to nonstationary data, to identify long-range (slowly decaying, e.g. power-law) correlations in a number of time-series of volcano seismicity recorded during the recent dome-forming eruptions of Volcán de Colima, Mexico, and Soufrière Hills Volcano, Montserrat. For all the time-series analysed, correlation strength varies through time and/or on different timescales; in some cases, this variation is periodic, seasonal, and/or related to activity. These results may provide new insights into eruptive processes and possibly further constrain the generation mechanisms of a number of the volcano-seismic event classes analysed. Furthermore, the correlation properties of real-time seismic measurements are shown (retrospectively) to contain information valuable to real-time volcano monitoring that is not identifiable by conventional analysis techniques. This study therefore demonstrates that long-range correlation analysis may be useful for extracting additional information from monitoring data at dome-forming or similar volcanoes.

2.1. Introduction

Long-lived lava dome-forming eruptions typically comprise non-linear episodes of extrusive and explosive activity; the eruptive style can switch rapidly, compounding the challenge of modelling and forecasting such eruptions (e.g., Wadge et al., 2014). Shifts in activity may be accompanied by major changes in hazard, as exemplified by recent eruptions of Soufrière Hills Volcano, Montserrat (e.g., in 1997: Voight et al., 1999) and Gunung Merapi, Indonesia (e.g., in 2010: Surono et al., 2012). In order to improve resilience to hazards in long-lived dome-forming eruptions, we need to develop better tools to anticipate these changes.

Analysing the signals (whether, for example, seismic, geodetic, or gas-chemical) from observation of complex eruptive behaviour often requires a statistical approach (Mader, 2006; Carniel et al., 2008). Time-series of eruption parameters and monitoring data have been analysed by a wide variety of statistical methods, as summarised in Supplementary File 2.1. However, in order to apply the majority of these techniques, one must assume that the data reflect a stochastic process and have at least weak (second-order) stationarity, defined as having time-invariant mean and variance, and autocovariance that is only dependent upon the lag time (Nason, 2006). The application of stationary models is often justified, as they make fewer assumptions about the data or volcanic behaviour, and so are more robust (an incorrect non-stationary model will result in greater bias: Marzocchi and Bebbington, 2012). However, no information about temporal variations in activity are sought or incorporated in using a stationary model (Marzocchi and Bebbington, 2012), and so such models may not be appropriate when analysing the temporal evolution of activity at volcanoes that show regime changes, periodic behaviour, or trends, which includes many dome-forming systems (Bebbington, 2010).

One group of statistical methods that can inform both forecasting and our understanding of volcanic processes are those that quantify persistence. Persistent (or correlated) behaviour, where similar values are clustered in time, may be one indicator of 'memory' in a system, when the system state at one point in time influences future conditions or events. Case studies of such behaviour by volcanic systems are described by Carniel et al. (2008): for example, Jaquet et al. (2006) use variograms to quantify memory within repose interval and amplitude time-series of a month-long sequence of Vulcanian explosions at Soufrière Hills Volcano, Montserrat. This memory has been attributed to decompression of ascending magma, from which magma ascent rates and conduit geometry could be quantitatively constrained, and later events forecast from the correlations between earlier sequential eruptions (Jaquet et al., 2006). In spite of this potential, similar correlations on longer (monthly to multi-annual) timescales have rarely been investigated quantitatively. Long-range correlations (i.e., correlations that decay slowly, such that the characteristic correlation timescale is indefinable: Kantelhardt, 2009) are commonly exhibited by non-linear dynamical systems far from equilibrium (Peng et al., 1995), so might be expected of active volcanoes.

In this study, we identify such long-range correlations in volcano-seismic time-series from two intensively monitored dome-forming volcanoes, Volcán de Colima, Mexico, and Soufrière Hills Volcano, Montserrat, by detrended fluctuation analysis (DFA) (Peng et al., 1994). This fractal scaling analysis method, which filters any local trends in the time-series, has been used to quantify the correlation properties of non-stationary data in a variety of disciplines (e.g., physiology: Peng et al., 1995, climatology: Livina and Lenton, 2007, and economics: Alvarez-Ramirez and Escarela-Perez, 2010). This technique has also been applied to volcanological data: for example, the hourly variability in geomagnetic signals recorded on Mt Etna (Italy) was (using DFA) found to show persistent behaviour that varies on different length scales and through time,

with an abrupt increase in correlation strength being associated with an eruption in October 2002 (Currenti et al., 2005a). Multifractal DFA scaling exponents (Kantelhardt et al., 2002) of these data were shown to be less variable after this eruption than before, further constraining the correlation dynamics of the signal (Currenti et al., 2005b). Similarly, DFA of the daily count of small explosions at Volcán Popocatépetl (Mexico) identified quasi-periodic temporal variation of the long-range correlations in this time-series, which varied in step with changes in eruptive activity and slow-slip events at the associated subduction zone (Alvarez-Ramirez et al., 2009, 2011). The 'log-log' plots calculated in DFA (explained in Section 2.2) have also been used, for example by Del Pin et al. (2008) to detect the presence of tectonic events in segments of noise-contaminated seismic data recorded at Pico del Teide (Tenerife, Canary Islands). Hurst rescaled range analysis (Hurst et al., 1965), which calculates an exponent comparable to that from DFA, has also been applied to volcanological data (Supplementary File 2.1), but is only appropriately calculated for stationary data.

2.2. Detrended fluctuation analysis (DFA)

DFA requires a time-series $u(i)$ of N values (where $i = 1,\ldots,N$) to first be integrated at each point, k, in the series, as follows: $y(k) = \sum_{i=1}^{k} [u(i) - \bar{u}]$, where $\bar{u}$ is the mean of the whole dataset. $y(k)$ is then divided into non-overlapping boxes (time windows) of length n, and the local trend in each box computed by a linear least-squares fit to the constituent data. Higher-order fits may be applied to calculate this trend, but are not routinely used (Little et al., 2006). The trend is removed from each box to leave locally detrended data, $y_d(k)$. The root-mean-square fluctuation $F(n) = \sqrt{\frac{1}{N}\sum_{k=1}^{N}\left[y_d(k)\right]^2}$ of the detrended data is then computed, and the whole process repeated for a range of scales of n. In this study, F is calculated for every n-value from 4 to $N/4$, a range comparable to previous applications of DFA (e.g., Currenti et al., 2005a), to give a set of fluctuation values, $F(n)$. A linear relationship between $\log[F(n)]$ and $\log(n)$ indicates self-similarity (scaling). The gradient of this line (calculated by least-squares regression) is the scaling exponent (or self-similarity parameter), $\propto$ (Peng et al., 1995). Changes in $\propto$ with increasing n reflect different scaling properties on different timescales; we identify any break points in the gradient of the $\log[F(n)]$ vs $\log(n)$ plots by inspection (although these could be determined by other means, such as change point analysis: Mulargia et al., 1987). We calculate $\propto$ using the computationally efficient 'FastDFA' algorithm (Little et al., 2006), which follows the original formulation of DFA (Peng et al., 1994, 1995) summarised above.

In a subsample of a time-series where each value is not correlated with any previous values (e.g., white noise), $\propto \cong 0.5$. Values in the range $0.5<\propto<1$ indicate long-range power-law correlation (i.e., persistence), such that a large value (relative to the mean) is more likely to be followed by large values, and vice versa. In contrast, $0<\propto<0.5$ signifies anti-persistence, where large and small

signal values are more likely to alternate. Strongly persistent, $1/f$-like ('pink') noise would have a value of $\propto \cong 1$. When $\propto > 1$, strong correlations exist, but are not of a power-law form; $\propto \cong 1.5$ would result from Brownian ('red') noise, i.e. random walk-like fluctuations in the signal through time. Thus, $\propto$ may be considered a measure of time-series 'roughness', becoming smoother with increasing $\propto$ (Peng et al., 1995). 'Critical slowing down' (a decreasing rate of recovery from small perturbations of the system) prior to a sudden change in the dynamics of a complex system (i.e., a 'tipping point') may be indicated by an increase in $\propto$ towards $\propto \geq 1$ (Livina and Lenton, 2007).

Power-law scaling can result from either long-range correlations or fat-tailed probability distributions (Mandelbrot and Wallis, 1968). These can be distinguished by removing any correlations in the time-series by randomly shuffling the data (a 'shuffling test'): this has no effect on the distribution, so any scaling identified by DFA (i.e. $\propto \neq \sim 0.5$) after shuffling will be due to a fat-tailed distribution (Alvarez-Ramirez et al., 2009). DFA of entire volcanic time-series can be informative for evaluating the general scaling behaviour (e.g., Currenti et al., 2005a); we present the results of such analysis as $\log[F(n)]$ vs $\log(n)$ ('log-log') plots, for the range of box lengths (n-values) for which well-defined scaling (a strong linear relationship between $\log[F(n)]$ and $\log(n)$) is present.

We investigate temporal variation in $\propto$ by DFA of overlapping samples (time 'windows') of the data: i.e., $\propto$ is calculated for a window of a specified constant time length, run incrementally through the time-series. Windows in which >50% of values are zero (due to a gap in recording or absence of seismicity) are not analysed. The window size would ideally be short to minimise lag effects, but longer windows reduce the potential for finite-size effects (Ivanova and Ausloos, 1999). The window lengths used were selected to balance these competing factors: small window lengths were rejected if they resulted in poorly-defined scaling relationships in a considerable

number of windows, determined by inspection of the log-log plots of a selection of windows, particularly those when the d∝/dt is comparatively high. The window lengths used are such that the n-values for calculating each exponent are within the range that show a well-defined scaling relationship in DFA of the whole time-series (specified on the log-log plots in Section 2.4), but do not necessarily capture the full range of scaling in the time-series as a whole.

The suitability of DFA as an alternative to conventional fluctuation analysis for analysing non-stationary data has been questioned by Bryce and Sprague (2012), on the basis of the impact of bias from finite-size effects. The principal effect is spurious curvature on log-log plots towards the lower limit (i.e., an increasing deviation from the expected linear trend towards the smallest n-values); this causes a bias to the resulting scaling exponent, and implies that fine-scale detrending (to properly address non-stationarities) in DFA can introduce artefacts. However, whole-dataset DFA of each time-series analysed in this study shows that this spurious deviation is only intermittently present for these data when n <5 (i.e., it affects only a couple of n-values), and so has negligible influence upon the scaling exponent(s) in each case. This effect may be more pronounced in individual time windows, but the bias in the scaling exponent would still be restricted due to the large number of n-values (∼40 or greater for overlapping-window DFA with the window lengths used) and their skewed distribution on the log-log plot; short-timescale non-stationarities may be inadequately addressed in these instances. Bryce and Sprague (2012) proposed that ∝-values greater than 1 indicate unsuccessful detrending, as such exponent values are not possible in conventional fluctuation analysis, but these values have been attributed to strong correlations of a non-power-law form (Peng et al., 1995).

Artefact periodicity is transiently present in the exponent values for some of the time-series analysed; this has a period equal to the maximum box size (n-value) used, and results from

calculating the exponents of overlapping windows. As the sampling window moves, how the data is sampled by each box (subdivisions of the window) changes cyclically: when the window has moved by a length equal to the maximum box size, ¾ of the boxes will sample exactly the same segments of the data as the initial window (as the maximum box size is ¼ of the window length); when it has moved half of this length, the boxes in the overlapping ⅞ will be completely out of phase with those in the original window (i.e., the data sampled in any one box in the initial window will be split equally between two boxes in the second window). When there is insufficient temporal variability in the data, this box/window-shift cycle effect is not masked by the influence of the new data included in the window as it is moved, and so the exponent shows a small-amplitude (typically <0.2) cycle with a period equal to the maximum box size.

In order to quantify any genuine periodicity in the correlation dynamics at other frequencies, we compute spectrograms (using the short-term Fourier transform, c.f. Nicholson et al., 2013) for the exponent time-series (from DFA of the data in overlapping windows), with the assumption that these time-series are piecewise stationary. The spectrogram function in the MATLAB signal processing toolbox is used to calculate the power spectral density of overlapping windows of a fixed length of 512 measurements, after the exponent time-series is processed using a high-pass Butterworth filter with a cut-off period of 500 measurements, and the mean subtracted. The power spectral density at frequencies equating to periods of <67 or >500 measurements is not computed, to omit frequencies where spurious cycles are likely (those equating to periods comparable to the maximum box size or greater than the spectrogram window length).

2.3. Data

Seismicity is the most widely monitored attribute of volcanoes, with well-established utility in understanding volcanic processes (Chouet and Matoza, 2013); it is therefore a particularly appropriate data type for examination of long-range correlations. Seismic monitoring has yielded the most complete and well-populated time-series available for the volcanoes studied (Volcán de Colima, Mexico, and Soufrière Hills Volcano, Montserrat), where visual observation of activity is often difficult due to persistent cloud cover.

2.3.1. Volcán de Colima

Volcán de Colima, an andesitic stratovolcano at the western end of the Mexican Volcanic Belt (Figure 2.1a), is one of the most active and hazardous volcanoes in North America (Luhr et al., 2010). Its historical eruptive activity has been characterised by ~100-year cycles of lava extrusion followed by continued extrusion with intermittent explosive activity (including large Vulcanian explosions), culminating in major Vulcanian to Plinian (Volcanic Explosivity Index (VEI) 4–5; Newhall and Self, 1982) eruptions, which last occurred in 1818 and 1913 (Luhr, 2002). The volcano has been erupting almost continuously since 1998; there have been six phases of lava dome and/or block flow extrusion, each followed by Vulcanian explosions days to months after the end of extrusion (e.g., Zobin et al., 2008; Varley et al., 2010a; Cassidy et al., 2015b). Smaller Vulcanian and transient degassing events of variable magnitude and ash content also occurred at the rate of ~2–10 per day since March 2003, except for a hiatus from June 2011 to January 2013 (Varley et al., 2006; Webb et al., 2014; Cassidy et al., 2015b). The lava extrusion rate has varied considerably between eruptive phases: for example, it was estimated to be 6–8 m^3s^{-1} at the start of the September–November 2004 phase (Varley et al., 2010a), but was only observed to reach an estimated maximum of <0.03 m^3s^{-1} during the January 2007 to June 2011 phase (Hutchison et

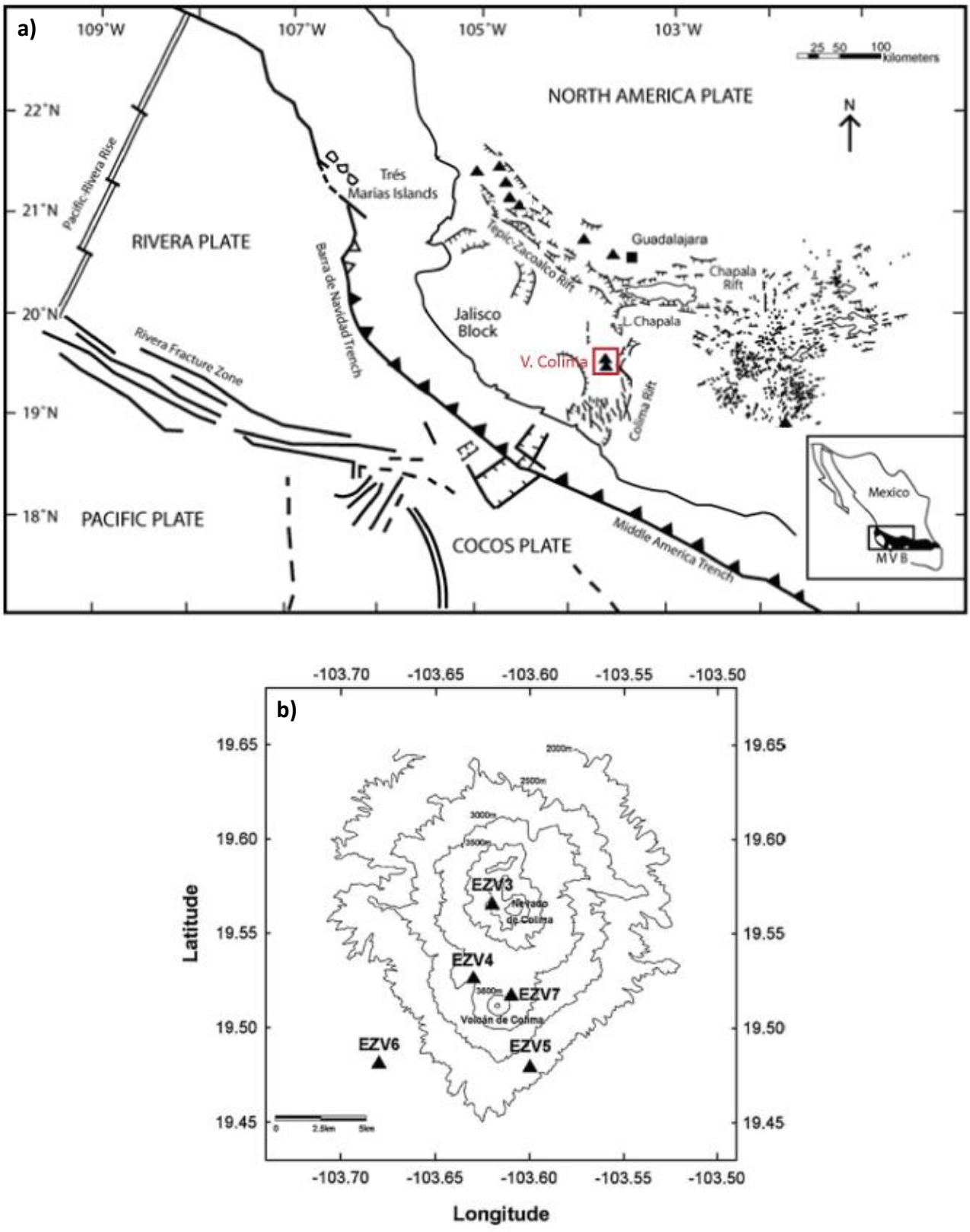

Figure 2.1 Volcán de Colima location maps. **(a)** Map of southwestern Mexico showing the volcanic centres (volcanoes (triangles) and monogenetic vents (dots)) of the western end of the Mexican Volcanic Belt (MVB), and their tectonic setting. The red box indicates the location of Nevado and Volcán de Colima. Modified from Carmichael et al. (2006), after Delgado Granados (1993). **(b)** Map of the seismometer network around Nevado and Volcán de Colima (labelled), from Vargas-Bracamontes et al. (2007).

al., 2013; Mueller et al., 2013).

We analyse two seismic time-series types from Volcán de Colima: (1) the hourly average of the real-time seismic energy measurement (RSEM) (Reyes-Dávila and De la Cruz-Reyna, 2002), which is proportional to a 2-minute running mean of the root-mean-square of the signal amplitudes recorded by a short-period seismometer (EZV4) 1.7 km from the volcano summit (Figure 2.1b); (2) the daily counts of three of the observed volcano-seismic event classes, described in Table 2.1. The other observed event types (e.g., rockfalls and larger amplitude long-period seismicity) cannot be analysed here as they occur too infrequently or erratically during most of the time period studied. Each volcano-seismic event is manually classified by the Centro de Intercambio e Investigación en Vulcanología, by inspection of the helicorder and spectrogram from the same seismometer as the RSEM is derived. Seismic data was chosen for this study as: (1) seismicity is the most commonly monitored characteristic of volcanoes (e.g., Loughlin et al., 2015) and has provided most of the main constraints on conduit processes at many volcanoes (e.g., Zobin, 2012), so statistical analysis of this data type is relatively likely to be widely informative; and (2) it is the longest, most reliable, and most complete monitoring dataset available.

2.3.2. Soufrière Hills Volcano

Soufrière Hills Volcano on Montserrat, in the Lesser Antilles island arc (Figure 2.2a), is also an andesitic stratovolcano. It has been relatively inactive historically compared to Volcán de Colima, with no eruptions for ~350 years prior to the onset of the current eruptive period in 1995 (Robertson et al., 2000). Since then, there have been five phases of activity, comprising dome extrusion at rates of 0.2–20 m^3s^{-1} (average of 3–5 m^3s^{-1}), Vulcanian explosions, and substantial dome collapses (Wadge et al., 2010, 2014). The resulting pyroclastic density currents have destroyed what were the main population centres of Montserrat prior to the eruption (e.g.,

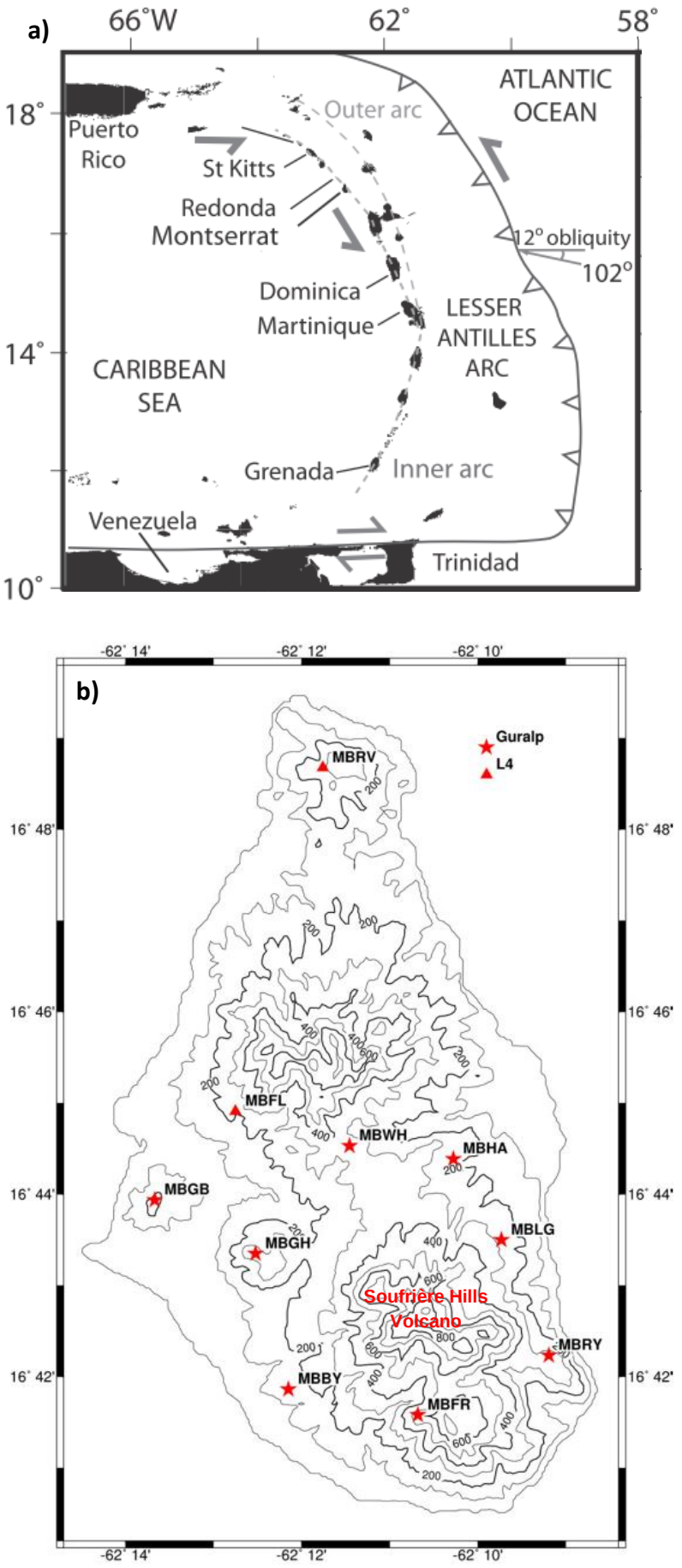

Figure 2.2 Soufrière Hills Volcano location maps. **(a)** Map of the eastern Caribbean showing the tectonic setting of Montserrat and the Lesser Antilles arc, from Cassidy et al. (2015a). **(b)** Map of Montserrat and the seismometer network around Soufrière Hills Volcano (labelled), from Luckett et al. (2008).

Table 2.1 Particulars of the principal volcano-seismic event types observed at Volcán de Colima since March 2003, after Varley et al. (2006, 2010a, 2010b) and references therein. Daily count data are for the time period analysed in this study, 1 November 2004 to 31 December 2008.

Event class	Description	Example waveform	Mechanism	Daily count		
				mean	s.d.	max.
Impulsive	Event with an impulsive onset (reaching max. amplitude <20 seconds after onset) and a wide frequency range (but spectral energy usually concentrated at 1–3 Hz). Often pulsed.		Pressure release/pathway opening, often resulting in a small explosion or transient degassing event.	5.55	5.04	49
Emergent	Event with an emergent onset (reaching max. amplitude >20 seconds after onset), often with an irregular waveform, and a frequency range similar to impulsive events. Often pulsed.	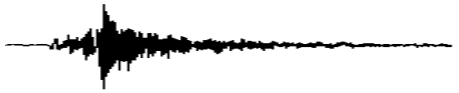	Gradual pressure release/pathway opening, often resulting in a small explosion or transient degassing event.	3.65	3.83	36
Low-amplitude long-period	Event with a low frequency (spectral energy peak at <3 Hz), an amplitude usually two orders of magnitude smaller than that of typical explosion seismicity, and of <1 minute duration. Often impulsive; commonly occurs in swarms.		Brittle failure of magma as it passes through the glass transition (at the conduit walls), and/or gas movement.	37.87	61.37	978

Table 2.2 Particulars of the principal volcano-seismic event types observed at Soufrière Hills Volcano during the current eruption, after Miller et al. (1998), Luckett et al. (2008), and references therein. Daily count data are for the time period analysed in this study, 23 October 1996 to 8 July 2010.

Event class	Description	Example waveform	Mechanism	Daily count		
				mean	s.d.	max.
Volcano-tectonic (VT)	Event with impulsive onsets, *P* and *S* waves, and most energy in the 5–10 Hz range.	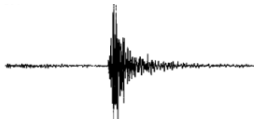	Brittle rock failure due to rock stress perturbations induced by magma motion.	1.48	3.83	142
Hybrid*	Event with an impulsive, high-frequency start and a long-period coda; i.e., shows a mix of VT and LP characteristics. Frequency changed from 1–2 Hz in Phases 1 and 2 to 3–4 Hz in later phases. Occurs mostly in swarms.	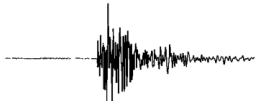	Brittle failure of magma as it passes through the glass transition at the conduit walls.	8.91	38.99	769
Long-period (LP)*	Event with an emergent, typically nearly monochromatic waveform, and a peaked spectrum at 1–2.5 Hz (some at 3–4 Hz from Phase 3 onwards). No discrete *P* and *S* phases.	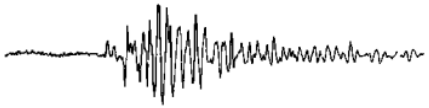	Brittle failure of magma (with high-frequency component lost from attenuation) and/or gas movement/resonance within cracks/voids in the lava dome.	5.26	17.89	621
Rockfall	Event with an emergent, symmetric waveform that has few/no distinct peaks, and a wide frequency range (e.g. 2–8 Hz; energy often concentrated at higher frequencies).		Movement of material down-slope, most commonly lava blocks/pyroclastic material being shed from a lava dome.	28.67	40.48	236
Long-period with rockfall	Rockfall event containing either a 1–2.5 Hz peak in its spectrum or a discrete LP event.		LP component attributed to gas movement and/or resonance within cracks/voids in the lava dome; gas release can trigger rockfalls, or vice versa (by localised decompression).	3.14	6.38	73

* These two classes share some properties and generation mechanisms, so some (e.g., Neuberg, 2000) consider these types end-members of a single low-frequency event class.

Kokelaar, 2002). There has been some evolution in activity between each eruption phase: for example, Phases 4 and 5 were of shorter duration with faster extrusion rates than earlier phases (Wadge et al., 2014). Some phases have ended abruptly with little warning; for example, extrusion in Phases 4b and 5 ceased after a series of Vulcanian explosions (Stewart et al., 2009) and a partial dome collapse (Cole et al., 2010a) respectively. In contrast to Volcan de Colima, explosive activity here has been minimal during most inter-eruptive phases, except as precursors to renewed extrusion (Stewart et al., 2009; Cole et al., 2010a). Cyclicity has been identified in many of the monitored parameters, during periods of a range of eruptive intensities (including inter-eruptive phases), on timescales from hours to centuries (Nicholson et al., 2013; Odbert et al., 2014).

We analyse two seismic time-series types from Soufrière Hills Volcano: (1) The hourly average of the real-time seismic amplitude measurement (RSAM) (Endo and Murray, 1991), a 1-minute running mean of the signal amplitudes recorded by a broadband seismometer (MBGH, St George's Hill; Figure 2.2b) 3.4 km from the volcano summit; (2) the daily counts of the five principal volcano-seismic event classes, which are described in Table 2.2. Each volcano-seismic event is manually classified by the Montserrat Volcano Observatory, by inspection of helicorders and spectrograms from across the seismometer network. These specific time-series were chosen as they correspond to those analysed from Volcán de Colima.

2.3.3. Comparison of seismicity at the volcanoes studied

Despite the fact that these volcanoes have similar eruptive styles, the associated seismicity differs considerably in the period of observation. Volcano-tectonic (VT) events have been unusually rare at Volcán de Colima since the 1998–1999 extrusive phase, relative to this and earlier eruptive phases (Varley et al., 2010a). This has been suggested to reflect all subsequent activity tapping the same batch of magma, stored in a shallow reservoir (Zobin et al., 2008). The absence of

detectable seismic precursors to subsequent eruptive phases and of any clear relationship between seismic tremor and eruptive activity are also attributed to this magmatic system setup (Varley et al., 2010a). In contrast, at Soufrière Hills Volcano, VT and hybrid event swarms were commonly observed prior to lava extrusion in the earlier phases of the eruption (Miller et al., 1998, 2010). Since mid-2008, these have been replaced by VT event strings (short, intense swarms of VT earthquakes, the first of which occurred in November 2007), possibly due to evolution of the stress regime (Cole et al., 2010b). Rockfalls were rare at Volcán de Colima during the study period (except late 2004) due to the usually low extrusion rate, and so seismic signals associated with explosions (impulsive and emergent types: Varley et al., 2006) and magma ascent (low-amplitude long-period seismicity: Varley et al., 2010b; Arámbula-Mendoza et al., 2011) dominate. Conversely, in the time period analysed at Soufrière Hills Volcano, rockfalls were generally much more frequent than the other event classes observed, except just prior to each phase of extrusion and between Phases 2 and 3 (Odbert et al., 2014); rockfalls are thus typically the main contributor to seismic measurements here.

The real-time seismicity measurements analysed are those made available by the corresponding observatories (Miller et al., 1998; Reyes-Dávila and De la Cruz-Reyna, 2002); both are variants of the running mean seismic amplitude (Endo and Murray, 1991). For both volcanoes, the real-time seismic measurements and event count data are from different, overlapping time periods (specified in the corresponding figure captions) because of restrictions in data availability. Sources of bias and error in the data analysed here from these networks were outlined by Lamb et al. (2014).

2.4. Results

All of the time-series analysed pass the shuffling test (see Section 2.2), so we are confident that the scaling behaviour identified in each one reflects long-range correlations in these data, instead of their distributions. Spectrograms are presented only for those exponent time-series that display any sustained periodicity; note that the cyclicity present is in these exponent time-series, not the monitoring data themselves.

2.4.1. Volcán de Colima hourly RSEM, January 2004–December 2008

The results of DFA of the hourly RSEM time-series from Volcán de Colima are shown in Figure 2.3. Figure 2.3a, a plot from DFA of these data as a whole, indicates that the time-series is moderately correlated on timescales of <40 hours ($\log(n) <\sim 3.7$), but is smoother (more predictable) on longer timescales (40–100 hours), with non-power-law scaling ($\propto >1$). This is consistent with the low occurrence of abrupt temporal variations in the RSEM (Figure 2.3b), reflecting the relatively stable low intensity eruptive activity for much of the time period analysed. However, this does not preclude considerable temporal variation in the scaling exponent, as shown in Figure 2.3b, in which $\propto$ values are calculated from the prior week's data (168 measurements). During periods of low activity (unshaded sectors and parts of the period of lava extrusion in 2007–8), $\propto$ is relatively stable at $\cong 0.45 \pm 0.15$. This is approximately that expected of random variation in the RSEM; i.e., there are no long-range correlations. Visual inspection suggests that excursions to higher $\propto$ values (indicative of persistence in the RSEM data) in late 2004, 2005, and 2007–2008 coincide with lava extrusion, the peak of Vulcanian eruptive activity, and a stage of accelerating dome growth, respectively (Varley et al., 2010a; Hutchison et al., 2013). It is also notable that there appears to be shifts in the trend of $\propto$ at the start and end of the phase of larger Vulcanian eruptions in 2005 (shaded on Figure 2.3b). Spectral analysis does not reveal any sustained periodicity in this

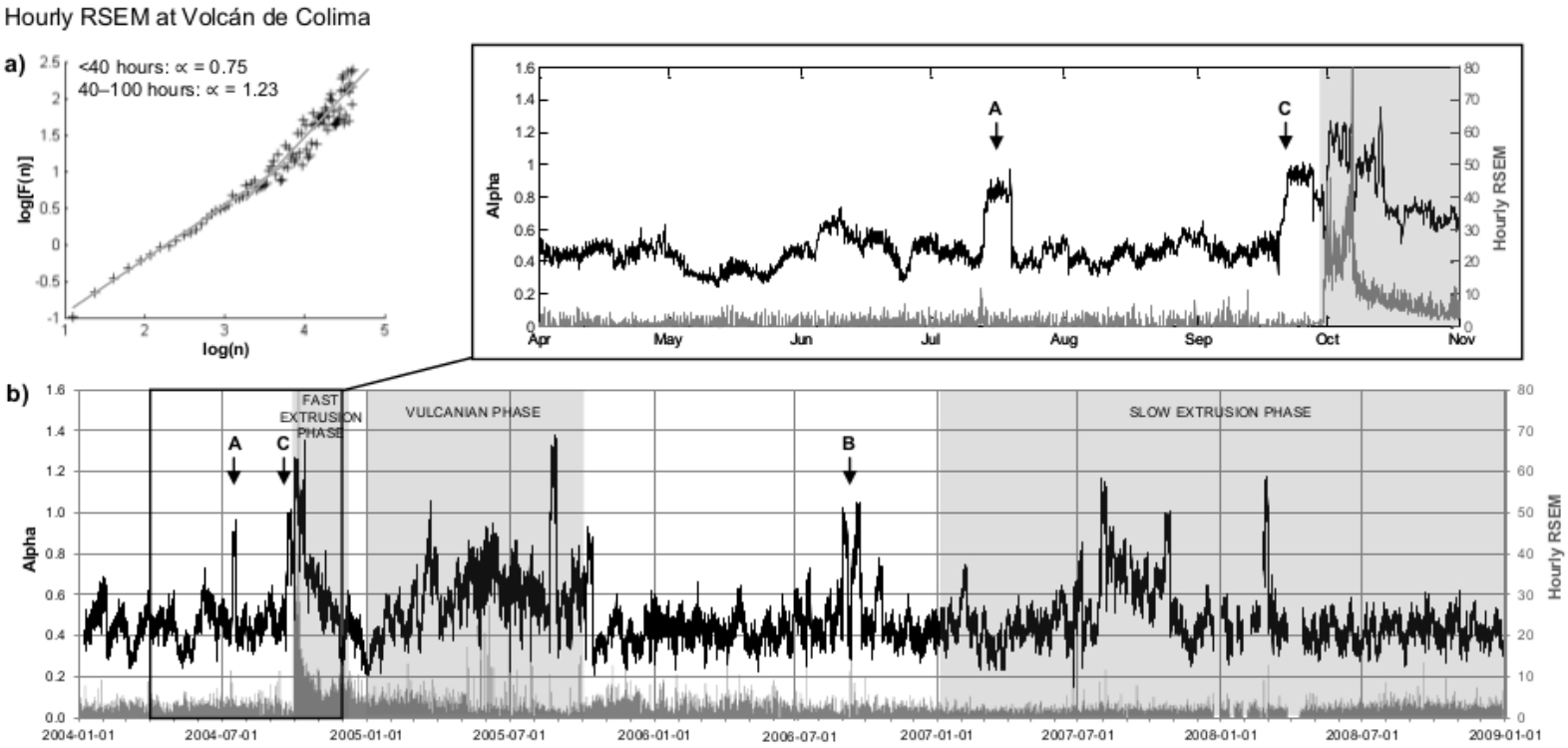

Figure 2.3 Detrended fluctuation analysis of an hourly-averaged real-time seismic energy measurement (RSEM) time-series from Volcán de Colima (data from 1 January 2004 to 31 December 2008). **(a)** Log-log plot of fluctuation function against box size for the whole time-series, with best-fit lines and their gradients. **(b)** Scaling exponents calculated for each time step using a window of the prior week of data (168 measurements) (black line), plotted with the RSEM time-series (dark grey line), with a close-up of April–October 2004. The shading highlights phases (labelled) of extrusive and/or enhanced explosive activity. The arrows indicate excursions to higher ∝ values prior to the onset of phases of extrusion (Section 2.4.1). Periods with no scaling exponent result from gaps in the raw data.

exponent time-series, and so no spectrogram is shown.

The observed association of persistent behaviour with periods of elevated activity may imply that associated factors, such as magma ascent or gas release, change the nature of the seismicity such that RSEM values become more correlated (i.e., show 'smoother' temporal variation), although further investigation is required to understand this relationship. This inference is consistent with the observation that the two occurrences of notably elevated exponent values ($\propto \geq 0.8$) outside of phases of elevated activity (shaded), indicated by arrows A and B on Figure 2.3b, coincide with transient increases in the concentration of boron in spring waters (N.R. Varley, unpublished data): Similar short-timescale increases in spring-water boron concentration have been observed prior to, or at the onset of, previous eruptive phases at Volcán de Colima (Armienta and De la Cruz-Reyna, 1995; Taran et al., 2000), as well as at Volcán Popocatépetl, where they are attributed to magma recharge/ascent (Martin-Del Pozzo et al., 2002; Armienta et al., 2008). The occurrence times of these anomalies, in late July 2004 and August–September 2006, respectively 2 and 4–5 months prior to the onset of lava extrusion, were not associated with noteworthy changes in real-time monitoring data. Another notable RSEM exponent change when there was no substantial shift recognised in monitored parameters is the rapid increase in the exponent (for the preceding week of RSEM) to $\propto > 0.75$ one week before the onset of lava extrusion in September 2004, indicated by arrow C on Figure 2.3b and shown in the close-up plot. This increase would have been identifiable on 21 September, five days before any indications of an impending eruption were recognised (Zobin et al., 2008), although alone this would clearly have been insufficient to predict the onset of extrusion. Note the low values of the RSEM during this pre-eruptive period, not atypical of the 'background' seismicity (e.g., during late April 2004): the shift in correlation dynamics may be accounted for by the approximately coincident increase in low-amplitude long-period seismic event swarm activity, retrospectively identified by Varley et al. (2010a). The

absence of similar persistence to the RSEM immediately prior to the onset of dome extrusion in January 2007, or for the first ~6 months of this eruptive phase, may reflect the extremely slow (<0.005 m^3s^{-1}) inferred initial average dome growth rate (Hutchison et al., 2013).

2.4.2. Soufrière Hills Volcano hourly RSAM, February 2005–June 2011

Figure 2.4 shows the hourly RSAM time-series from Soufrière Hills Volcano alongside the results of DFA of these data. The RSAM time-series is clipped at a threshold of 10,000 in order to moderate the disproportionate effect (on the calculated exponent values) of the short excursions to extreme values (these distort the mean and local trends computed to calculate $\propto$), without modifying the rest of the data. We find that this adjustment, affecting <0.15% of the data, removes some noise from the scaling exponent time-series without meaningfully changing the trend. The RSAM dataset as a whole is highly correlated (Figure 2.4a), which is reflected in the typically correlated behaviour ($\propto$ >0.6) of the scaling exponent through time, shown in Figure 2.4b, for which $\propto$ values are calculated from the prior two weeks' data (336 measurements). A two week window is used, rather than a one week one as with Volcán de Colima RSEM (Section 2.4.1), as inspection of selected individual windows showed that the scaling relationship was sometimes poorly defined with significantly shorter window lengths (Section 2.2). The extent of correlation is highly variable, with no clear relationship to the eruptive phases (shaded sectors in the plot), and spectral analysis does not reveal any sustained periodicity, so no spectrogram is shown. Abrupt shifts in $\propto$ (changes of >0.2 in a few days or less) are common, and are often between a stable period of moderate power-law correlation ($\propto \cong 0.7 \pm 0.1$) and a more variable phase of stronger correlation ($\propto$ >1.0). This behaviour suggests sudden transitions in which type of seismicity is the predominant control on the RSAM, and/or changes in the process that generates the principal seismicity type. An example of the former would be the occurrence of swarms of a particular event class (e.g., hybrid events: Miller et al., 1998); of the latter, events

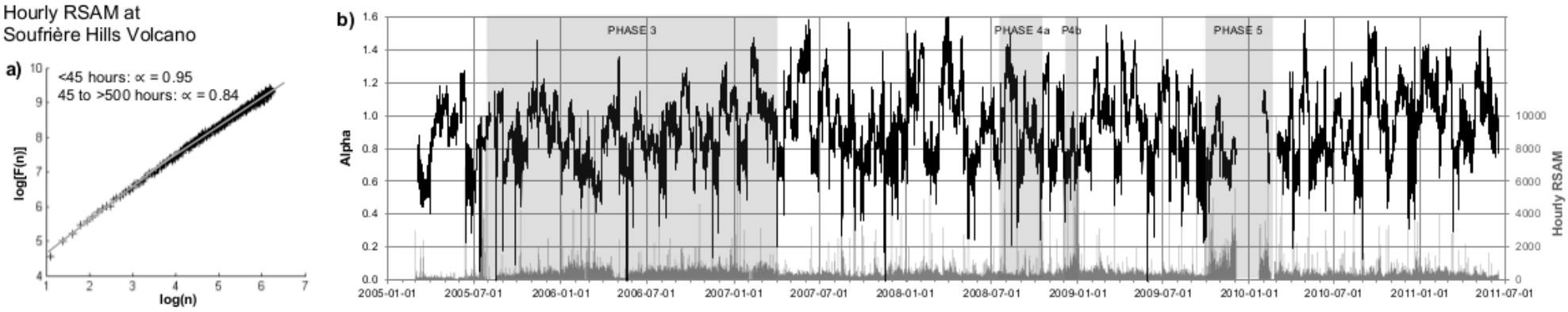

Figure 2.4 Detrended fluctuation analysis of an hourly-averaged real-time seismic amplitude measurement (RSAM) time-series from Soufrière Hills Volcano (data from 28 February 2005 to 30 June 2011). **(a)** Log-log plot of fluctuation function against box size for the whole time-series, with best-fit lines and their gradients. **(b)** Scaling exponents calculated for each time step using a window of the prior 2 weeks of data (336 measurements) (black line), plotted with the RSAM time-series (dark grey line; clipped at 10000). The shading highlights phases (labelled) of extrusive and/or explosive activity. Periods with no scaling exponent result from gaps in the raw data.

that influence the lava dome, and so the rockfall regime, such as large Vulcanian explosions or pulses of magma extrusion (Calder et al., 2002; Odbert et al., 2014). Although the RSAM signal is generally correlated, and is thus 'predictable' to an extent, these rapid switches in the correlation properties, with no clear periodicity, limit any possible inference from this.

2.4.3. Volcán de Colima daily event counts, November 2004–December 2008

The daily counts of the three event types analysed are shown in Figure 2.5, with the results of DFA of these data and spectrograms of the resulting exponent time-series (NB: $\propto$ values on the exponent-time plots are plotted at the centre of the 180-day (180-measurement) overlapping windows). Each time-series shows persistent behaviour, but with considerable temporal variation that differs for each event class. Impulsive and emergent event types (Table 2.1), collectively associated with small Vulcanian explosions and transient degassing plumes, are thought to be statistically independent (Varley et al., 2006); count rate time-series for these events and the corresponding results from DFA are presented in Figures 2.5a and 2.5b. The whole-dataset scaling behaviour of the counts of the two event types is similar, as are the broad trends in $\propto$ through time, perhaps suggesting a coupled generation mechanism for the two event types. However, the $\propto$ values of the emergent event data are generally higher and less temporally variable than the corresponding impulsive event exponents. The spectrograms of both these exponent time-series (Figures 2.5a iii and 2.5b iii) show little strong periodicity except at very low frequencies (periods of >200 days); note that the transient cyclicity of a ~45-day period in the exponent-time plots are artefacts, as explained in Section 2.2. The impulsive event count exponents appear to have a clear seasonal cycle from mid-2005 onwards, with the trend of these data alternating between random ($\propto \cong 0.5 \pm 0.1$) and correlated ($\propto \cong 0.8 \pm 0.2$) behaviour in the wet (summer) and dry (winter) seasons respectively; this is prominent on the spectrogram (Figure 2.5a iii) as high power spectral density at a period of 300–500 days. The low-frequency periodicity present in the emergent count

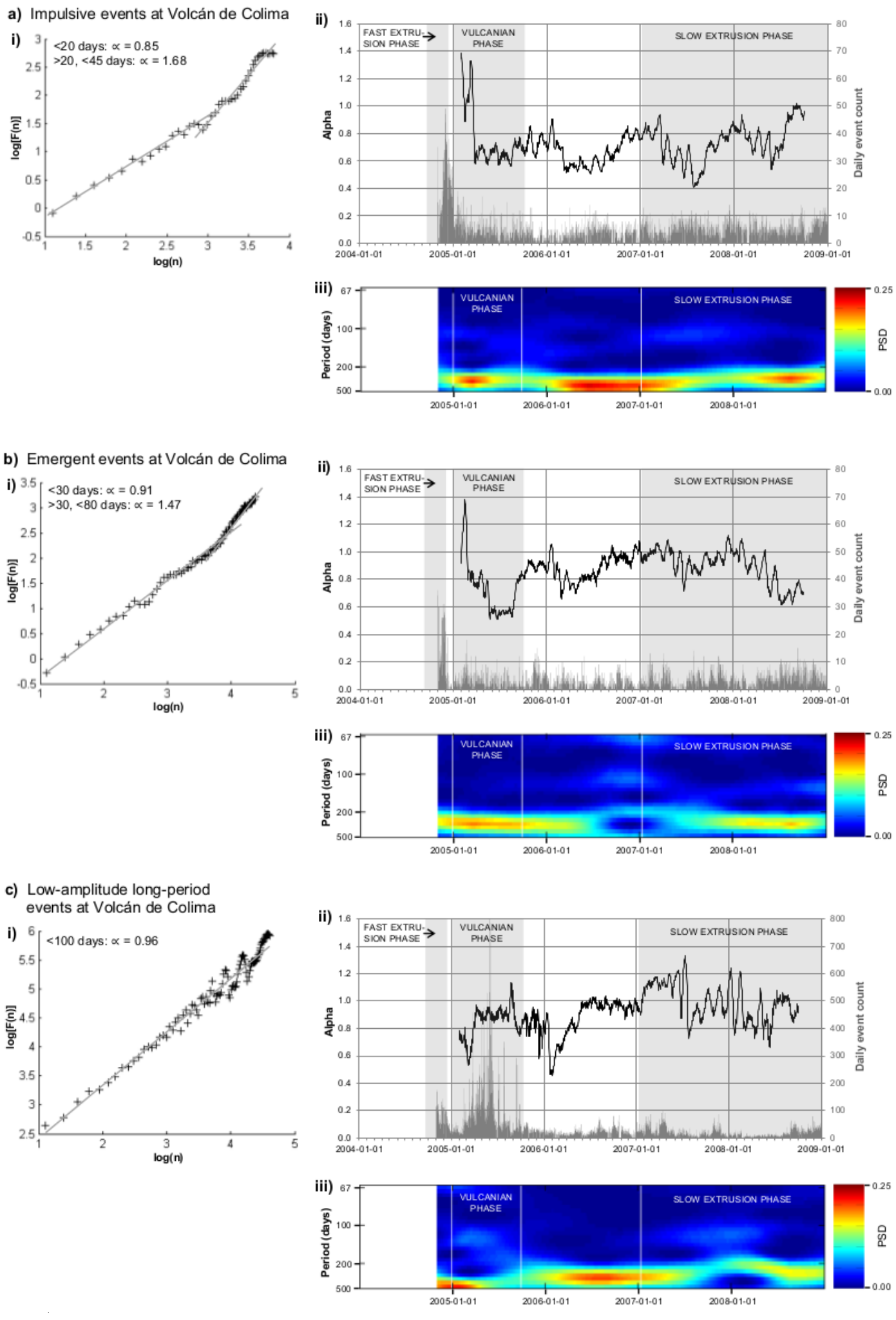

Figure 2.5 *(caption on next page)*

Figure 2.5 (previous page) Detrended fluctuation analysis of the daily count of each of the primary volcano-seismic event types at Volcán de Colima (described in Table 2.1; data from 1 November 2004 to 31 December 2008). **(i)** Log-log plot of fluctuation function against box size for the whole time-series, with best-fit line(s) and their gradient(s). **(ii)** Scaling exponents calculated for 180-day (180-measurement) overlapping windows (black line; values plotted at the centre of their windows) through the daily event count time-series (dark grey line). The shading highlights phases (labelled) of extrusive and/or enhanced explosive activity. **(iii)** ~17-month (512-measurement) overlapping-window spectrogram of the scaling exponent time-series (power spectral density plotted at the centre of the window).

---

exponents (Figure 2.5b iii) is weaker and interrupted by weak higher frequency cycles in late 2006 to early 2007; the cause of this behaviour is less clear. All these features of the data place some constraints on the generation mechanisms of the two event classes.

The scaling properties of the low-amplitude, long-period (LP) event counts, presented in Figure 2.5c, are similarly informative. These data have $\propto \cong 1.0 \pm 0.2$ during phases of elevated activity (shaded on Figure 2.5c ii) and at least three months (allowing for the lag due to the 180-day window) prior to the onset of extrusion at the start of 2007, and are less correlated ($\propto \cong 0.5$–0.8) in other periods. Superimposed on this trend are very weak cycles of a ~120-day period, present during the phases of elevated activity, when a stronger lower frequency (~200–400-day period) cycle is less apparent (Figure 2.5c iii); the latter periodicity may simply reflect the spacing of the episodes of activity. Notably, the whole-dataset analysis (Figure 2.5c i) indicates that the low-amplitude LP event count data are strongly power-law correlated across a wide range of timescales, with a similar correlation extent to those of the impulsive and emergent event types on timescales of <~20–30 days.

2.4.4. Soufrière Hills Volcano daily event counts, October 1996–July 2010

The daily counts of each event type analysed are shown in Figure 2.6, with the results of DFA of these data and spectrograms of the resulting exponent time-series (NB: $\propto$ values on the exponent-time plots are plotted at the centre of the 180-day (180-measurement) overlapping

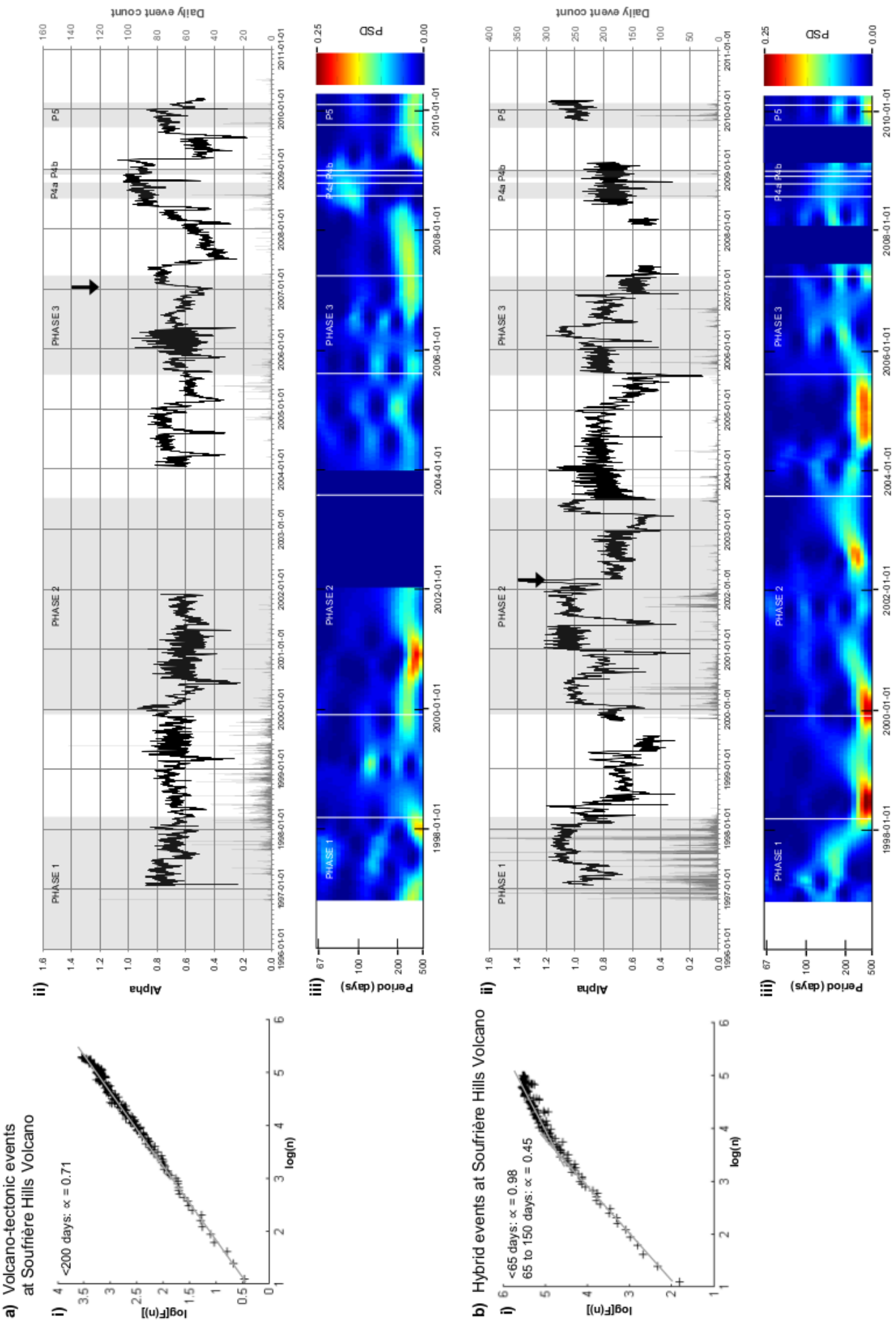

Figure 2.6 *(continued on next page)*

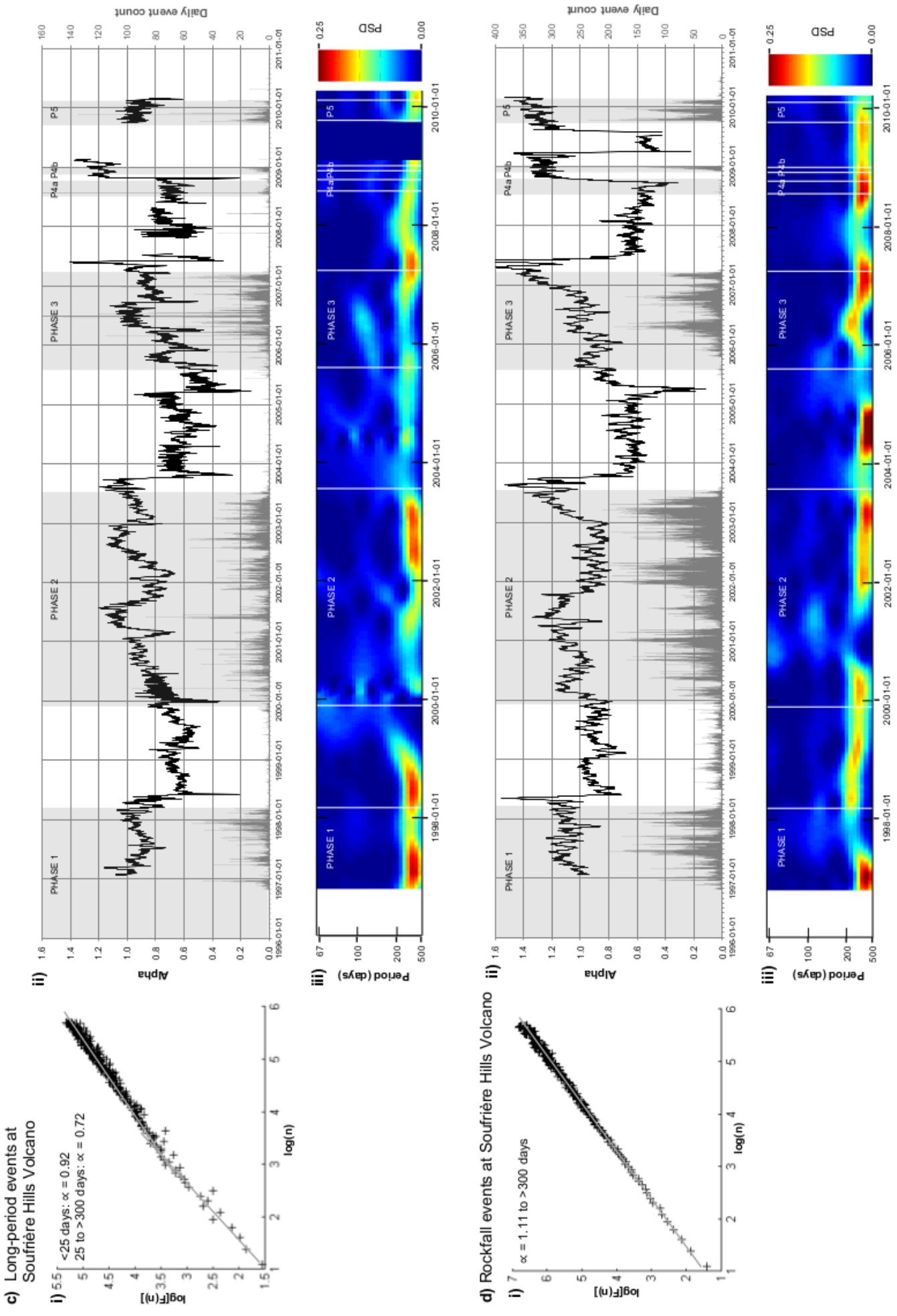

Figure 2.6 *(continued on next page)*

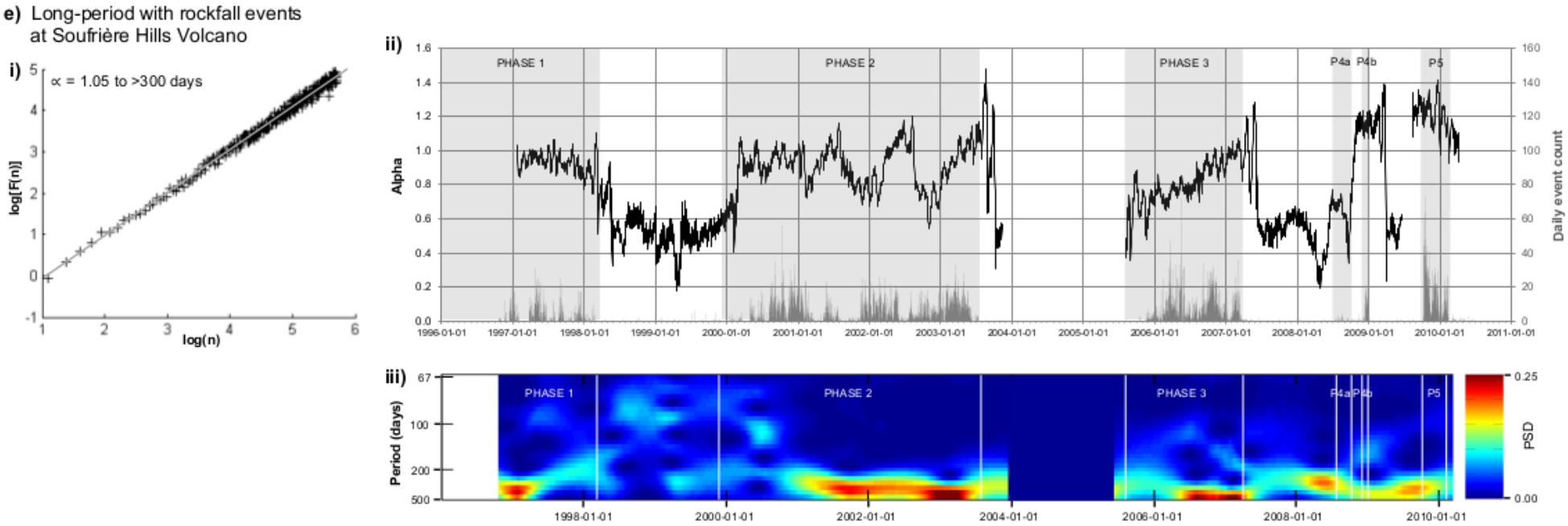

Figure 2.6 Detrended fluctuation analysis of the daily count of each of the primary volcano-seismic event types at Soufrière Hills Volcano (described in Table 2.2; data from 23 October 1996 to 8 July 2010). **(i)** Log-log plot of fluctuation function against box size for the whole time-series, with best-fit line(s) and their gradient(s). **(ii)** Scaling exponents calculated for 180-day (180-measurement) overlapping windows (black line; values plotted at the centre of their windows) through the daily event count time-series (dark grey line). The shading highlights phases (labelled) of extrusive and/or explosive activity. The arrows indicate the timing of shifts in the relationship between variations in ∝ and activity that are discussed in Section 2.4.4. **(iii)** ~17-month (512-measurement) overlapping-window spectrogram of the scaling exponent time-series (power spectral density plotted at the centre of the window). The honeycomb pattern sometimes present is an artefact of the overlapping windows. Periods with no scaling exponent or power spectral density result from extended episodes of zero counts.

windows). All the time-series analysed display correlated behaviour, although the extent of this varies with time and between event classes. Volcano-tectonic (VT) event counts (Figure 2.6a) show stable, weakly persistent behaviour through time ($\propto \cong 0.65 \pm 0.1$, similar to that of the whole time-series), independent of activity variations, until a point (identified by inspection) at the start of 2007 indicated by the arrow on Figure 2.6a ii. After this point, the event counts are generally more persistent during phases of extrusion, and random during eruptive pauses (with some lag from the use of a 180-day window). This shift in the correlation dynamics precedes the first observation of VT strings in November 2007, which were subsequently the primary seismic precursor to extrusion (Cole et al., 2010b). Figure 2.6a iii shows that the only persistent periodicity in this exponent time-series is that intermittently present at a very low frequency (period of 300–500 days; the signal does not show clear seasonality, and so the cause of this is unclear), excepting that present in late 2008, with a period of ~80 days, which may reflect the comparable duration of and repose interval between the eruptive phases at this time (Wadge et al., 2014).

The absence of VT count exponent values from December 2001 to January 2004 is due to the negligible event count in this period; the onset of this phase approximately coincides with a transition in the hybrid count correlation trend (Figure 2.6b ii). This shift is from highly persistent behaviour during extrusive phases and vice versa earlier in the eruptive episode, to stable weak to moderate correlation ($\propto \cong 0.6–0.8$) through both periods of extrusion and repose. This transition (identified by inspection), indicated by an arrow on Figure 2.6b ii, also approximately coincides with a decrease in hybrid event count, such that swarms were no longer associated with magma ascent, and possibly also with an increase in the dominant frequency of hybrid events from 1–2 Hz to 3–4 Hz (which occurred before the onset of Phase 3: Luckett et al., 2008): these changes have been attributed to a modification of the conduit geometry, inferred from a coincident

increase in the diameter of lava spines (Luckett et al., 2007; 2008). The trend in hybrid count correlation dynamics appears to revert to matching activity variations by the start of Phase 4 (at least during eruptive phases, when hybrids are recorded), shortly after the aforementioned changes in VT occurrence and correlation dynamics; after this point, VT/hybrid swarms have not been observed (Cole et al., 2010b). This also coincides with an apparent shift to shorter phases of activity with higher magmatic fluxes, consistent with some change in the eruptive mechanism (Odbert et al., 2014). Despite these changes, cyclicity of a ~150-day period appears to be present in the hybrid count exponent time-series consistently in each phase of activity except parts of Phase 2, although is often weak (Figure 2.6b iii). Higher power spectral density at periods of >~250 days is typically present when the hybrid event count is very low, so may be an artefact due to this. Note that the transient cyclicity of a ~45-day period in the exponent-time plots in this figure are also artefacts, as explained in Section 2.2.

Despite the similarities in the properties and generation mechanisms of hybrid and LP events (Table 2.2), the temporal variation in the scaling exponent of the LP event counts (Figure 2.6c) is more similar to that of rockfalls (Figure 2.6d) and rockfalls with an LP component (Figure 2.6e). These data are generally random or only weakly persistent between extrusive phases, and highly correlated ($\propto \cong 0.8$–1.4, generally) during them; peaks in $\propto$ coincide with higher event counts, which are attributed to pulses of dome growth (Loughlin et al., 2010). In all three cases, there is rather pervasive high power spectral density for periods >200 days (Figures 2.6c iii, 2.6d iii, and 2.6e iii); as each of the exponent time-series varies in step with eruptive activity, this may be an artefact of the spacing of pulses and the phases of extrusion. Higher frequency cycles are only present for relatively short durations in these exponent time-series, with different periods and at different times for each event type; the cause of this behaviour is unclear. The whole-dataset scaling properties of the LP, rockfall, and LP-rockfall event counts, except of LPs beyond ~25-day

timescales ($\log(n) > \sim 3.2$), are approximately as of pink ($1/f$-like) noise ($\propto \cong 1$), indicative of strong self-similarity. The RSAM time-series is similar in this respect (see Figure 2.4a), consistent with rockfalls (as the most commonly-occurring event type: see Table 2.2) being the most influential event class upon that parameter.

Due to the long window size required when analysing daily count time-series, the changes in correlation properties identified here could not have been recognised in near-real-time during routine monitoring, but they do indicate behaviour that may constrain models of seismicity generation/conduit processes and the temporal evolution of activity.

2.5. Discussion

The identification of temporally-varying long-range correlations in the real-time seismic measurements analysed demonstrates that statistical methods appropriate for nonstationary data can be informative for volcano monitoring. As DFA is computationally non-intensive and only requires data from a single seismometer, this specific technique is potentially widely applicable in near-real-time (at least to time-series sampled at a relatively high rate) as a tool complementary to existing techniques. Variograms could also be used as an alternative or complementary method of quantifying persistence (or 'memory') in time-series from volcano monitoring (Carniel et al., 2008). With further development, such statistical methods have the potential to highlight important changes to the structure of real-time signals that are not easily identifiable by conventional monitoring approaches, as suggested by the results presented here from Volcán de Colima. Clear changes in the correlation properties of the RSEM signal are identified by inspection both prior to some eruptive phases and at the termination of the 2005 Vulcanian phase (Section 2.4.1). This behaviour is to be expected if eruptive processes, such as magma ascent/extrusion or degassing, are associated with long-range correlated seismicity, provided that this is detectable and dominates the real-time seismic measurement. If the seismic network is unable to detect such a signal, or seismicity associated with other processes (e.g., rockfalls associated with dome degradation) are dominant, the latter of which is particularly the case for Soufrière Hills Volcano for parts of the period analysed, then, as shown in Section 2.4.2, it is unlikely that analysis of the long-range correlation properties of real-time seismic measurements would be as useful. Nonetheless, such analysis may be appropriate wherever the seismicity is predominantly due to (pre-)eruptive processes, such as at volcanoes showing signs of unrest after a long period of repose.

Progressively more persistent behaviour of a variable equates to increasingly smooth variation of this parameter through time; future values are therefore more predictable with increasing $\propto$, and vice versa (multifractal analysis is necessary to quantify the timescale(s) of the long-range correlations at any point in time: Kantelhardt et al., 2002). Real-time DFA could therefore give some indication of the susceptibility of a monitored time-series to change in the future (and be used to observe temporal variation of this susceptibility), although it is difficult to quantify the predictability of a signal from a scaling exponent time-series alone. Correlated behaviour presumably reflects fewer degrees of freedom in the system than when random, or at least dominance of specific components in determining the value of the time-series in question. Major abrupt temporal shifts in correlation extent, such as those found in the RSAM data from Soufrière Hills Volcano (Section 2.4.2), could therefore indicate important changes to the seismicity, which perhaps may reflect changes to the volcanic system that are pertinent for monitoring.

The long-range correlations identified also provide insights into the mechanisms generating the volcano-seismic event classes analysed, and so conduit processes. In the case of impulsive and emergent events at Volcán de Colima, which are collectively associated with daily-occurring small Vulcanian explosions and transient degassing plumes, any model for their generation must account for (as outlined in Section 2.4.3): (1) the similar whole-dataset scaling relationships of the two event types, which on short timescales (<~20–30 days) are also similar to that of low-amplitude LP events (Figure 2.5); (2) the coincidence of some of the temporal variations in the correlation dynamics of the two event types (e.g., with the termination of the 2004 extrusion phase; Figures 2.5a and 2.5b); (3) the seasonal variation in the impulsive event count exponent time-series (Figure 2.5a); (4) that, according to Varley et al. (2006), the occurrence rates of the event classes can best fit different survivor-type distributions, and that this can change with conduit disturbances, e.g. large explosions. Furthermore, the nature of the explosions must be

explained, specifically that: (1) both seismic event classes are associated with the full range of explosion styles and parameters (such as duration, magnitude, and ash content) (Webb et al., 2014); (2) the count rate (inferred from that of the associated seismicity) was apparently unperturbed by the phase of larger Vulcanian eruptions in 2005 (Varley et al., 2010a); (3) magma ascent up the main central conduit is believed to be inhibited by a fractured plug from earlier extrusive eruptions, but explosions have been observed originating from a variety of locations within the crater (Lavallée et al., 2012).

Based on these observations, we suggest that the two seismicity types associated with the regular explosive activity have a common source, of gas exsolving/escaping from ascending (decompressing, crystallising) relatively high-viscosity magma, perhaps by shear fracturing, as suggested for Soufrière Hills Volcano (Thomas and Neuberg, 2012) and Santiaguito (Holland et al., 2011). The differences in seismicity and eruption style may result from variations in how this gas is pressurised in and released through the partly plugged upper conduit (Webb et al., 2014). In this case, changes in upper conduit structure (e.g., due to a large explosion) would affect both seismicity types, explaining the partial coupling of their long-range correlation dynamics, and the release of the gas by shear fracturing may account for their similarity with the scaling behaviour of low-amplitude LP events. The seasonality in the correlation dynamics of the impulsive seismicity (Figure 2.5a) can also be explained within this framework: in the wet season, fractures will be opened by vaporisation of rainfall percolating into the lava dome or upper conduit (Mastin, 1994; Hicks et al., 2010), facilitating rapid pathway opening (suggested to generate impulsive events) at a random time (related to rainfall) earlier than it could otherwise occur. In contrast, during the dry season, such pathway opening will occur only when the required overpressure is reached, resulting in more regular occurrence and so persistent behaviour. The absence of clear seasonal variation in the count rate itself is probably because this is controlled by the rate of gas

supply from depth. The higher frequency transient cycles of ~120-day period present in the low-amplitude LP event exponent time-series (Figure 2.5c) have no obvious explanation; they might reflect a repeating process associated with the primary proposed LP generation mechanism, shear fracturing of magma.

As noted previously, the low-amplitude LP event count time-series at Volcán de Colima (Figure 2.5c), and those of LP (Figure 2.6c), rockfall (Figure 2.6d), and rockfall with LP (Figure 2.6e) events at Soufrière Hills Volcano, have the approximate properties of pink (or $1/f$ -like) noise, particularly during extrusive/explosive phases. This self-similar behaviour is a key characteristic of self-organised criticality, a common property of slowly-driven non-equilibrium systems with extended degrees of freedom and a high level of nonlinearity (Bak et al., 1987). We therefore suggest that the strong correlations in the counts of these event types almost exclusively during phases of elevated activity perhaps could result from self-organised critical behaviour of these event classes due to processes associated with such activity. LP seismicity associated with magma ascent has been suggested to show this behaviour (Shaw and Chouet, 1991; Piegari et al., 2011), and an unstable, growing lava dome generating rockfalls has many similarities to the original model for self-organised criticality, of the avalanche rate from a sand pile to which sand is steadily added (Bak et al., 1987; Hale et al., 2009). Between extrusive phases, other factors controlling dome stability would influence rockfall occurrence to a greater extent (Calder et al., 2005), potentially increasing the randomness of rockfalls. Similarly, in the absence of seismically detectable magma ascent, perhaps the more random process of gas movement is the primary cause of shallow LP event occurrence.

The periodicities in the exponents for each event type at Soufrière Hills Volcano (Section 2.4.4) are often transient, have time-varying frequencies, and differ between event types. These cycles

have no clear cause, and are not present in the event count time-series themselves, which when combined have a prominent 6–8-week (or 50-day) cycle almost throughout each eruptive phase; this is also observed in the extrusion rate and various monitored parameters (Nicholson et al., 2013; Odbert et al., 2014). The artefact cycles with ~45-day period intermittently present in these exponent time-series (explained in Section 2.2) inhibit assessment of periodicity in these data in this frequency range.

It is notable that the correlation dynamics of Soufrière Hills Volcano hybrid (Figure 2.6b) and LP (Figure 2.6c) event counts differ considerably (Section 2.4.4); these event types are considered idealised end-members of a single event class by some authors (e.g., Neuberg, 2000), but this result suggests that they should be considered separate classes. We find stronger indications of a relationship between hybrid (Figure 2.6b) and VT (Figure 2.6a) events: for example, in early 2002 and in 2007, there are approximately coincident transitions in the nature of these seismicity classes, the behaviour of the exponent time-series of one or both event types, and changes in eruptive style, as outlined in Section 2.4.4. The shift in the correlation dynamics of VT events, from weak correlation independent of activity to being more correlated during phases of extrusion, can be accounted for by the approximately coincident onset of strings of VT events associated with magma ascent, and so clustering in the timing of counted events. Similarly, hybrid events are only consistently strongly correlated during phases of activity (and vice versa) when they have occurred more frequently (Phases 1, 2 (in part), and 5). These particular transitions have been tentatively attributed to changes in conduit geometry and/or the stress regime (Luckett et al., 2007, 2008; Cole et al., 2010b; Odbert et al., 2014). These results provide constraints on future modelling of these processes, and, more broadly, exemplify the utility of correlation analysis in the identification of such regime shifts in the volcano-seismic system.

2.6. Conclusions

Long-range correlations are identified in each of the time-series analysed, revealing structure to these signals that is not identifiable using conventional techniques, and indicating a degree of long-term memory, and so predictability, to volcano seismicity that has not previously been recognised. The correlation dynamics of the daily counts of each of the event types are found to sometimes both highlight regime changes and provide new constraints on conduit and eruption processes, as exemplified by those of VT and hybrid event seismicity at Soufrière Hills Volcano. The potential utility of such analysis in near-real-time monitoring is also demonstrated, for example by the identification of anomalously persistent behaviour of real-time seismic measurements prior to the onset of some eruptions at Volcán de Colima, for which no clear precursors were identified using conventional monitoring approaches in real-time. These findings suggest that, with further development, statistical techniques appropriate for nonstationary data, and for analysis of long-range correlations, may have the potential to provide useful additional guidance for interpreting time-series recorded by volcano observatories.

Chapter 3 Entropy analysis of time-series of volcano seismicity during dome-forming eruptions

Manuscript in preparation: Lachowycz, S.M., Cosma, I.A., Pyle, D.M., Mather, T.A., Rodgers, M., Varley, N.R., Odbert, H.M., Cole, P.D., Reyes-Dávila, G.A.. Entropy analysis of time-series of volcano seismicity during dome-forming eruptions.

Author contributions: IAC created code for and ran the entropy and other statistical analyses. Seismic time-series from Volcán de Colima and Soufrière Hills Volcano were provided by NRV/GARD and HMO/PDC respectively. All co-authors contributed to manuscript preparation.

This manuscript develops work included as part of my thesis submitted for a MEarthSc in Earth Sciences (University of Oxford) in 2010. Part of the methods and description of Volcán de Colima and its seismicity are revised from that thesis. Different data were analysed for this study using a similar method, in addition to other techniques.

Abstract

Despite recent advances in the collection and analysis of data streams from volcano monitoring, and the consequent improvements in our understanding of volcanic processes, there are still challenges in forecasting and interpreting volcanic activity from real-time analysis of monitoring data. Additional techniques to elicit further information in real-time from these data are therefore desirable. In this study, we examine the utility of Shannon entropy (a measure of the randomness of a signal) for analysis of monitoring data, by its application to time-series of volcano seismicity from the recent lava dome-forming eruptions of Volcán de Colima (Mexico) and Soufrière Hills Volcano (Montserrat). Entropy may be computed in real-time by the method described here even if the signal is sampled at a high frequency and/or discontinuously, so this technique is potentially widely applicable to monitoring time-series. At the two volcanoes studied, the entropy of real-time seismic measurements and the count rate of certain volcano-seismic event types is found to vary through time, generally being elevated (often close to maximal) during phases of greater volcanic activity. High entropy indicates greater uncertainty in the value taken by the variable, i.e. that the time-series is less predictable. In some instances, the entropy of a signal shifts prior to or coincident with changes in seismic or eruptive activity, some of which were not clearly recognised at that time by real-time monitoring. We examine the nature of the entropy variations by testing for uniform data distribution and comparison to the coefficient of variation. This demonstrates the sensitivity of the entropy to the data distribution, and that it is distinct from measures of data dispersion. We therefore suggest that entropy analysis has potential as a tool to extract additional information in real-time from volcano monitoring data streams.

3.1. Introduction

Seismicity is the most frequently monitored characteristic of volcanoes, and the source of many insights into volcanic processes (Chouet and Matoza, 2013). Nevertheless, in some instances the established methods of real-time analysis of volcano seismicity have not provided clear prior (or sometimes even concurrent) indication of changes in volcanic activity (e.g., at Volcán de Colima, Mexico: Section 3.3.1). Statistical techniques are hence increasingly being applied to seismic and other data from volcano monitoring to elicit additional information from these data (Mader, 2006; Carniel, 2014; Supplementary File 2.1). In this study, we compute a novel statistic for volcano-seismic time-series, the Shannon entropy (Shannon and Weaver, 1949) (defined in Section 3.2.1). This is a measure of the randomness of a signal, i.e. the uncertainty in what value the signal will have; such randomness is inherent to geophysical time-series. The Shannon entropy therefore provides information that is distinct from the amplitude and frequency analysis typical of volcano-seismic monitoring (e.g., Endo and Murray, 1991; McNutt, 1996; Reyes-Dávila and De la Cruz-Reyna, 2002).

We retrospectively compute the entropy of seismic time-series to determine if application of this technique in real-time to these data would have yielded useful information. The time-series analysed are from two well-studied andesitic stratovolcanoes, Volcán de Colima (Mexico) and Soufrière Hills Volcano (Montserrat). Both are currently in long-lived episodes of dome-forming eruptions, characterised by phases of extrusive and explosive activity with abrupt changes in eruptive style (Sections 2.3.1 and 2.3.2). These abrupt changes can result in considerable shifts in hazard, exemplified by the recent eruptions of Soufrière Hills Volcano (e.g., in 1997: Voight et al., 1999). Therefore, there is an urgent need for additional means to recognise changes in activity in

real-time at such volcanic systems. Analysis of this type of volcanism also allows investigation of the entropy of seismicity through multiple phases of activity that had different characteristics.

3.2. Methods

3.2.1. Shannon entropy

Shannon entropy (Shannon and Weaver, 1949) is a measure of the uncertainty associated with a discrete random variable. Let X denote this variable, and suppose X can take any of the values $x_1,...,x_N$ with probability $p_1,...,p_N$ respectively, where $p_i > 0 \ \forall i$ and $\sum_{i=1}^{N} p_i = 1$ (N is the cardinality, i.e. the number of unique values taken by X). The Shannon entropy (hereafter 'SE' or 'entropy') is then defined as SE = $-\sum_{i=1}^{N} p_i \log(p_i)$, satisfying $0 \leq \mathrm{SE} \leq \log(N)$. Hence entropy is independent of the values of X, instead being a function of the distribution, i.e. how often each value is observed relative to all the other values. When X is constant (i.e., N = 1), SE = 0, and when the distribution of X is uniform (i.e., $p_i = 1/N \ \forall i$), SE = log(N). In the former case, there is no uncertainty associated with the value of X; in the latter, the values are equally probable, so the uncertainty is maximal. The entropy of X will decrease from the maximum if the distribution of X departs from uniformity (i.e., certain values become more probable than others, reducing the uncertainty), and vice versa.

Entropy statistics deriving from information theory have been widely applied in various disciplines, but only to a limited extent to geophysical time-series, most frequently in analysis of tectonic seismicity. For example, entropy has been calculated for the global earthquake catalogue to test for self-organised critical behaviour (e.g., Main and Al-Kindy, 2002; Al-Kindy and Main, 2003), and for earthquake sequences in Egypt to examine how their (dis)order varies with magnitude and depth (Telesca et al., 2012). It has also been applied in a time-frequency method for detecting both tectonic and volcanic events in amplitude time-series (Gabarda and Cristóbal, 2010), and in an alternate method to estimate *b* values of earthquakes at Mt Etna (Centamore et

al., 1999). However, temporal variation in the entropy of time-series from volcano monitoring (including seismicity) has not previously been investigated.

3.2.2. Entropy computation for volcano-seismic time-series

The raw seismic signal recorded on volcanoes and the occurrence rate of volcano-seismic events, and thus also the time-series we analyse in this study (described in Section 3.3.2), are time-series of observations of a discrete random variable. We compute (and hereafter refer to) the empirical Shannon entropy, calculated from the empirical distribution of the data rather than from the population distribution, which is unknown. In a time-series segment n, let N be the cardinality, i.e. the number of distinct measurements, which are denoted by $x_1,...,x_N$, and let n_i denote the number of times that x_i was observed in the segment, so $\sum_{i=1}^{N} n_i = n$. p_i, the empirical probability of observing x_i, is then given by $p_i = n_i / n$, $i = 1,...,N$, and so the entropy of the time-series segment SE = $-\sum_{i=1}^{N} p_i \log(p_i)$.

We calculate the entropy through each time-series (which are recorded at discrete, equally-spaced times $t_1, t_2, ...$) by breaking the data into 'windows' $[t_1, t_1 + n], [t_2, t_2 + n], ...$, where n is the window length. Small window lengths risk predominantly sampling short-timescale randomness due to noise in the time-series, which could mask geologically meaningful variation in the distribution (and so the entropy) of the data on longer timescales. Conversely, long windows tend to smooth the variation in the distribution of the data between windows, reducing the resolution of changes in entropy. Window lengths must therefore be selected considering on which timescales entropy changes are of interest, and the effects of varying the window size when analysing each particular dataset. Figure 3.1 shows normalised entropy time-series for one of the seismic time-series studied, each calculated using overlapping windows of different lengths, to exemplify the effects of varying the window length. In this example, the entropy time-series

a) 10-day (240 measurements) overlapping window

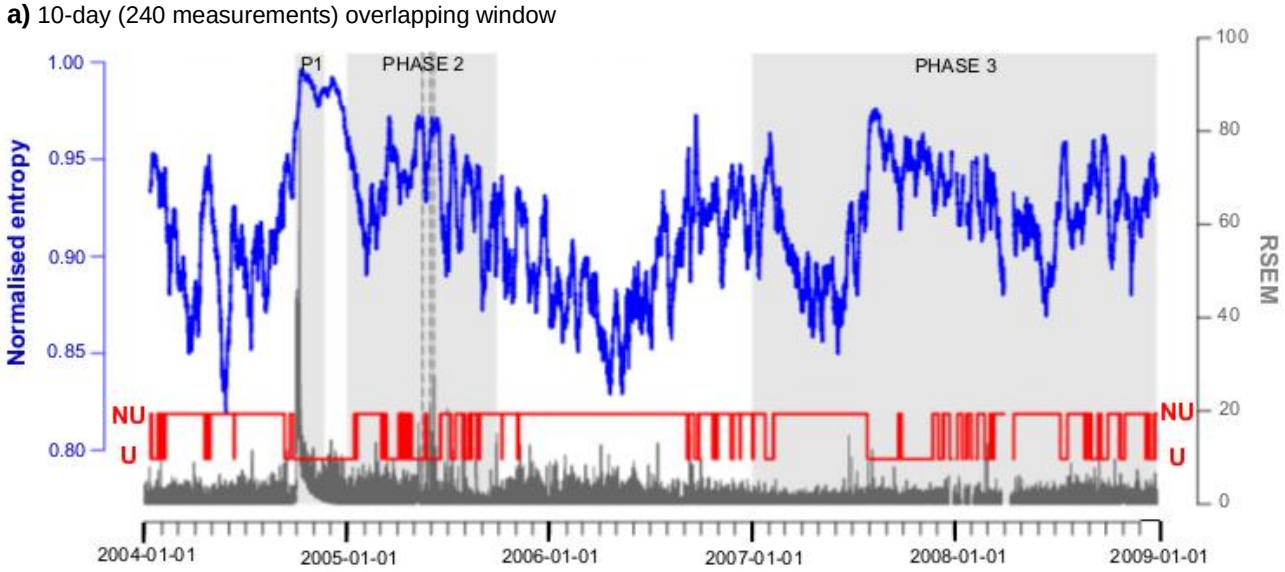

b) 20-day (480 measurements) overlapping window

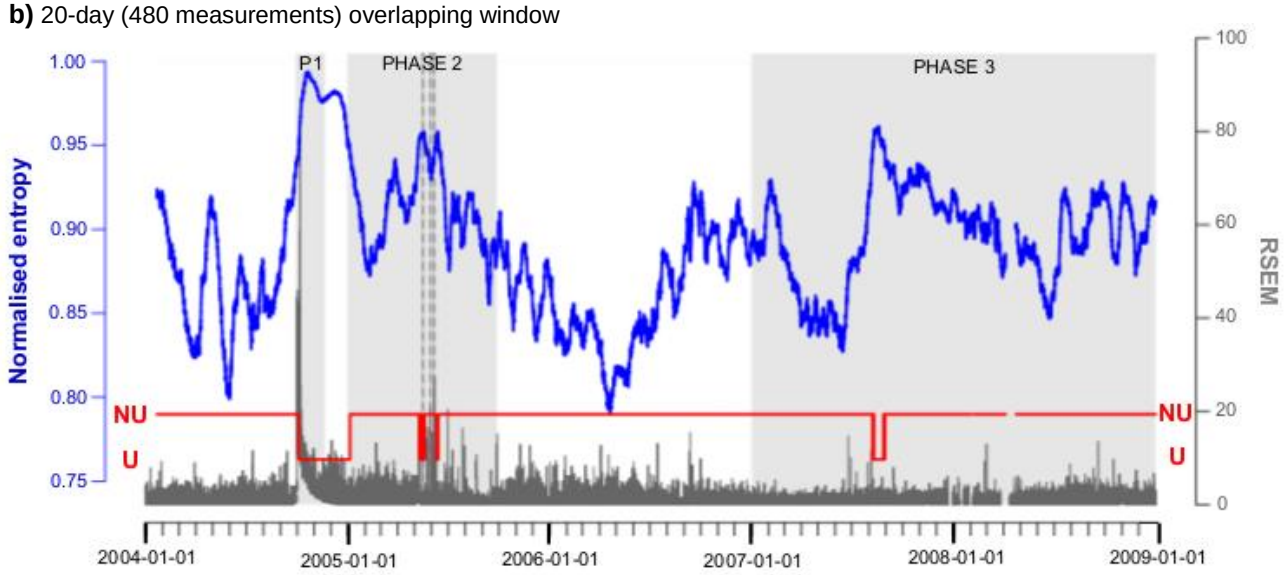

Figure 3.1 Comparison of the normalised empirical Shannon entropy (blue line) and test of hypothesis of a uniform distribution (red line; NU = not uniform, U = uniform) calculated in overlapping windows of different lengths, for an hour-averaged real-time seismic energy measurement (RSEM) time-series recorded at Volcán de Colima (dark grey line) (Section 3.3.2). As the window length increases, the entropy time-series becomes less noisy and shows less short-term variation, but there is negligible change in the medium- to long-term variability (on timescales greater than the window length). However, the occurrence and duration of periods when the data in the sampling window are uniformly distributed decrease considerably as the window length increases.

become less noisy as the window size increases, but there is no apparent change in the timing or magnitude of the prominent trends or shifts in entropy as the window length is varied.

At time t, we compute the entropy either cumulatively, in the window $[1,t]$ every k time steps, or in overlapping windows of $[t-n,t]$ (for $t \geq n$) where $t_1 = n$ and $t_2 = t_1 + 1$. The entropy is then normalised by dividing by $\log(N)$ (the maximum possible entropy), so that it satisfies $0 \leq (SE/\log(N)) \leq 1$; this reduces the sensitivity of the statistic to changes in cardinality through time, and simplifies comparison of entropy time-series. In contrast to the overlapping-window case, the normalised cumulative entropy considers all prior observations of the signal, and does not require subjective selection of a window length. However, as data accumulates in the window, the sensitivity of the entropy value to the distribution of the data added to the window is reduced. Therefore, we analyse the change in the statistic as the window is lengthened: if the normalised cumulative entropy is calculated every k time steps, i.e. in windows of $[1,k],[1,2k],[1,3k],\ldots$, resulting in a sequence of entropy values $SE_1, SE_2, SE_3, \ldots$, then the sequence of changes in normalised cumulative entropy is $SE_2 - SE_1, SE_3 - SE_2, \ldots$.

All computations are performed using the open-source statistical software R (http://www.r-project.org/). If a time-series is recorded with high precision (more than three significant figures), then the data distribution may require discretisation by rounding the measurements, so that they are not all unique; otherwise, the entropy will be consistently maximal. Such discretisation is appropriate if the variation in the time-series at the level of precision being rounded away is considered to be noise in the signal. Figure 3.2 shows the overlapping-window normalised entropy of one of the seismic time-series analysed, calculated after discretisation of the time-series to different extents, to exemplify the effects of this processing. If discretisation was required, the data were only rounded to the level at which the resulting entropy values were no

a) Rounded to 1 decimal place

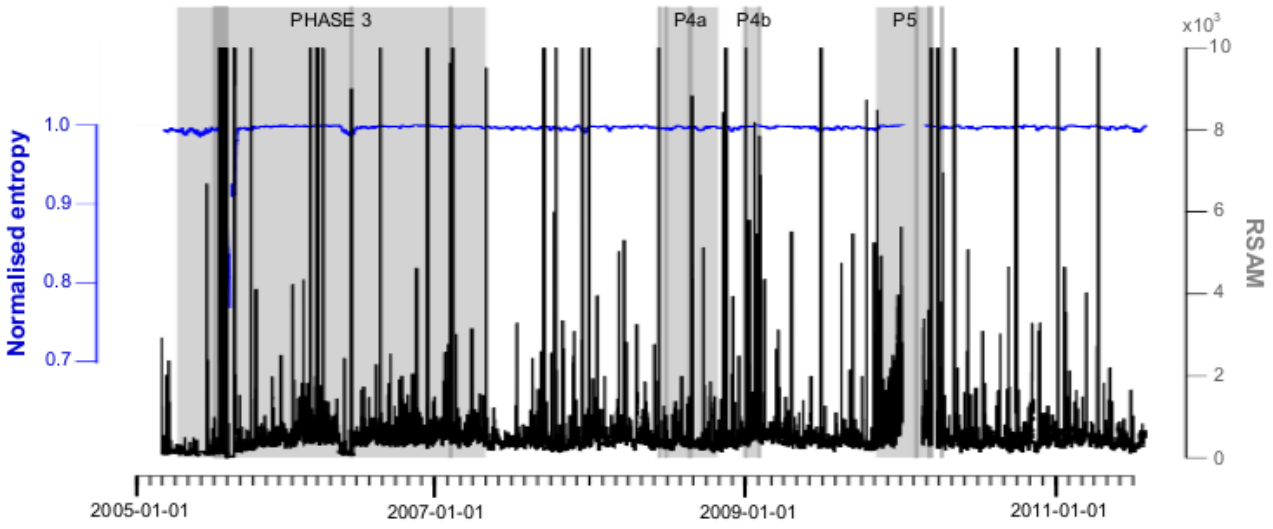

b) Rounded to 0 decimal places

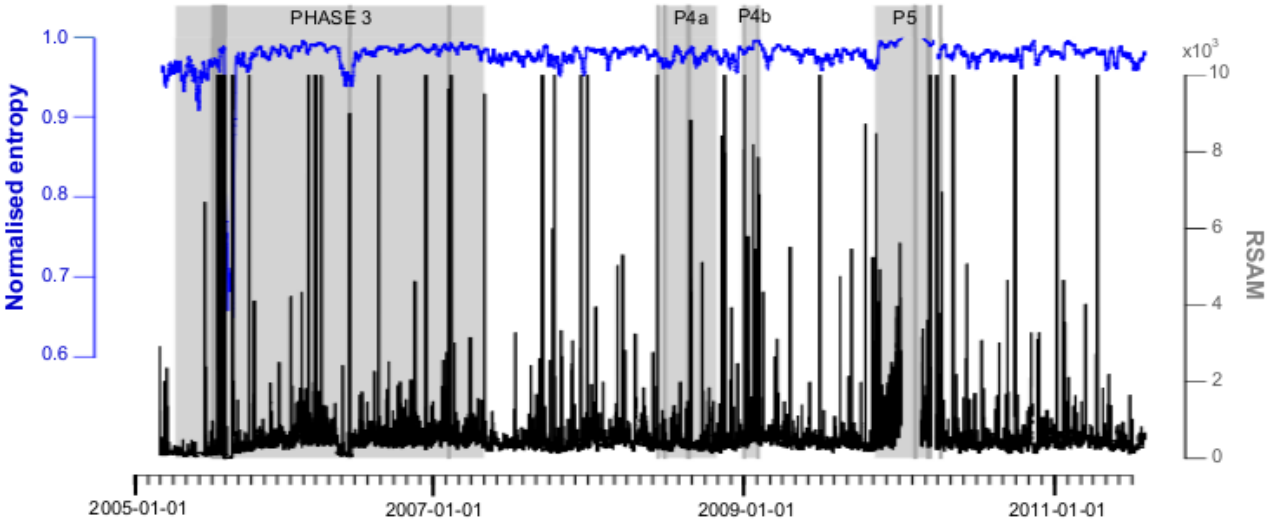

Figure 3.2 Comparison of the normalised empirical Shannon entropy calculated for 10-day (240 measurements) overlapping windows (blue line) of an hour-averaged real-time seismic amplitude measurement (RSAM) time-series recorded at Soufrière Hills Volcano (dark grey line) (Section 3.3.2), which has been discretised to different extents. As the RSAM is increasingly rounded, there is increasing temporal variation in the entropy, reflecting the reduction in the number of unique RSAM values in the time windows. With insufficient discretisation (part a), the normalised entropy is consistently ~1 (except for a period in August 2005 when there is an anomaly in the data) as the RSAM is reported to such high precision that the values in each window are almost all distinct.

longer consistently close to maximal. If a window of the data comprises >50% missing values (e.g. due to seismometer failure), we do not compute the entropy, and record it as missing; otherwise, the entropy is computed ignoring any missing values. We calculate the entropy and the cardinality exactly except when computing for a cumulative window, in which n is generally very large. In this case, exact computation of these statistics is relatively slow, so we estimate the entropy and the cardinality using the algorithms of Clifford and Cosma (2012, 2013), which maintain a lower-dimensional representation of the data from which the statistics can be estimated efficiently to the desired level of accuracy, which was evaluated with volcano-seismic data by Lachowycz (2010). Therefore, with data sampled at a higher frequency (e.g. raw seismic amplitude signals) and/or reduced computational resources, a lower-dimensional representation of the data (resulting in a less accurate estimation) can be used to maintain a computation time suitable for real-time entropy analysis.

3.2.3. Relationship between entropy and data distribution

At some volcanoes, including those studied here, the distribution of time-series of seismicity and/or activity has been found to change through time, often coincident with important eruptive events or transitions (e.g., Varley et al., 2006; Watt et al., 2007; Lamb et al., 2014). The entropy of such (non-stationary) time-series is therefore likely to also change through time, potentially notably so with shifts in activity. If a time-series is stationary, i.e. has time-invariant mean and variance (Nason, 2006), there is no temporal variation in distribution and thus also in entropy; the entropy value may still be informative, as a statistic characterising the data distribution.

(Near-)maximal entropy indicates that the data has a (close to) uniform distribution; shifts to and from this state by a monitored time-series may be of interest. It is possible to test for discrete uniformity by the following test of hypothesis (after Pardo, 2006), which incorporates entropy:

$H_0 : p_1 = ... = p_N = 1/N$: the distribution of the data is uniform, versus: $H_1 : \exists i, j \in \{1,...,N\}$ such that $p_i \neq p_j$: the distribution is not uniform. The test statistic is $T_1 = 2n(\log N - \mathrm{SE})$, asymptotically as the sample size $n \to \infty$, $T_1 \xrightarrow{D} \chi^2_{N-1}$ (this holds approximately for a fixed sample size when n is large). Thus, the null hypothesis of uniformity H_0 is rejected at level of significance $\propto$ if $T_1 > \chi^2_{N-1,\alpha}$, where $\chi^2_{N-1,\alpha}$ denotes the 100(1–$\propto$) percentile of the chi-squared distribution with $N-1$ degrees of freedom (we use $\propto$ = 0.05). The result of performing the test of hypothesis is represented by a vector of 0/1 values, where 1 indicates that $T_1 > \chi^2_{N-1,\alpha}$ (reject H_0 that the distribution is uniform) and 0 otherwise (do not reject H_0); in each figure, these are substituted for U (uniform) and NU (not uniform) for clarity. This test is only performed if $N > 1$ (testing a window containing only one distinct value does not make sense) and <50% of the values are zero or missing. The occurrence and duration of periods when the data in the sampling window are uniformly distributed decrease considerably as the window length increases (Figure 3.1), as the likelihood of variability in the distribution of the data being included in a single window increases with window length. Hence non-stationary data in a cumulative window are always non-uniform, except when the window is relatively small (e.g., Supplementary File 3.1).

When the data are non-uniformly distributed, assessment of the significance of entropy variations may be informed by comparison to other measures of the distribution of the data. We therefore also calculate and analyse the coefficient of variation (CV), the ratio of the standard deviation to the mean, which is a normalised measure of the data dispersion. The empirical CV is defined as: $\mathrm{CV} = \bar{x}^{-1}\sqrt{\frac{1}{n-1}\sum_{i=1}^{N} n_i (x_i - \bar{x})^2}$ where $\bar{x} = \sum_{i=1}^{N} \frac{x_i n_i}{n}$, the sample mean. If a window of the data comprises >50% missing values, we do not compute the CV, and record it as missing; otherwise, the CV is computed ignoring any missing values. Unlike entropy, the CV is not invariant to changes in the vector of probabilities that gives the distribution of the data. For example, consider that if

the number of times each of two values are observed (in a time window) are reversed, or another value is observed as many times instead of one of these, then the mean and CV of the data will change (except in special cases), but the entropy would be unchanged in both instances.

3.2.4. Applicability of entropy analysis

Entropy analysis by the method used here does not require the data to be (assumed) stationary or complete for long periods, and can be applied to time-series from a single monitoring instrument. It also gives normalised, dimensionless quantities, facilitating comparison of the randomness of different data streams. Furthermore, it may be employed in real-time, even when analysing a signal sampled at a high frequency, using the estimation procedure previously outlined. Therefore, this technique is potentially widely applicable and may complement existing volcanic time-series analysis methods (e.g., Odbert and Wadge, 2009). As entropy is invariant with changes in the vector of probabilities giving the data distribution, it is likely to have little sensitivity to some types of temporal variation in instrument response, e.g. drift and anomalous 'spikes', compared to some amplitude, dispersion, and frequency analysis techniques. However, this invariance also means that should a monitored time-series shift to different values (e.g., prior to a change in eruptive activity), there would be no notable change in the entropy unless there was also a substantial change in the randomness of these data.

3.3. Data

3.3.1. Volcanoes

Volcán de Colima, in the Mexican Volcanic Belt (Figure 2.1a), has been active almost continuously since 1998; there have been six phases of dome and/or block flow extrusion, each followed by Vulcanian explosions (e.g., Zobin et al., 2008; Varley et al., 2010a; Cassidy et al., 2015b). Smaller Vulcanian and transient degassing events of variable magnitude and ash content have also occurred at a rate of ~2–10 per day since March 2003, except for a hiatus from June 2011 to January 2013 (Varley et al., 2006; Webb et al., 2014; Cassidy et al., 2015b). The lava extrusion rate has varied considerably between eruptive phases; for example, it was estimated to be 6–8 m^3s^{-1} at the start of the September–November 2004 phase (Varley et al., 2010a), but was only observed to reach an estimated maximum of <0.03 m^3s^{-1} during the January 2007 to June 2011 phase (Hutchison et al., 2013; Mueller et al., 2013).

Soufrière Hills Volcano on Montserrat, in the Lesser Antilles island arc (Figure 2.2a), has had five phases of activity since the start of its current eruptive episode in 1995. These phases have typically comprised dome extrusion at rates of 0.2–20 m^3s^{-1} (average of 3–5 m^3s^{-1}), Vulcanian explosions, and substantial dome collapses (Wadge et al., 2010, 2014). In contrast to Volcán de Colima, explosive activity here has been minimal during most inter-eruptive phases, except as precursors to renewed extrusion (Stewart et al., 2009; Cole et al., 2010a). Cyclicity has been identified in many of the monitored parameters, during periods of a range of eruptive intensities (including inter-eruptive phases), on timescales from hours to centuries (Nicholson et al., 2013; Odbert et al., 2014).

Identifying transitions in (including both the start and end of phases of) eruptive activity has sometimes been difficult at both these volcanoes: for example, at Volcán de Colima since 1999, there have been no obvious precursors to the onset of phases of lava extrusion, due to the 'open' conduit (Zobin et al., 2008). Similarly, Phases 4b (2008–2009) and 5 (2009–2010) of the eruptive episode at Soufrière Hills Volcano ended abruptly with little warning, with a series of Vulcanian explosions (Stewart et al., 2009) and a partial dome collapse (Cole et al., 2010a) respectively. Changes in the seismicity have occurred during some activity shifts at these volcanoes: volcano-seismic event types associated with magma ascent (e.g., long-period events: Thomas and Neuberg, 2012) and dome extrusion (e.g., rockfalls: Calder et al., 2005) sometimes increased in magnitude and occurred more frequently before or at the onset of extrusive or explosive activity (Loughlin et al., 2010; Varley et al., 2010a). However, at present the associated changes in subaerial activity are not necessarily unambiguously identifiable in real-time.

3.3.2. Seismic time-series

Seismic data was chosen for this study as: (1) seismicity is the most commonly monitored characteristic of volcanoes (e.g., Loughlin et al., 2015) and has provided most of the main constraints on conduit processes at many volcanoes (e.g., Zobin, 2012), so statistical analysis of this data type is relatively likely to be widely informative; and (2) it is the longest, most reliable, and most complete monitoring dataset available for both volcanoes studied. We analyse two types of seismic time-series, which are also described and analysed in Lachowycz et al. (2013; Chapter 2):

(1) Real-time seismic monitoring time-series computed by the observatories. From Soufrière Hills Volcano, we use the hourly average of the real-time seismic amplitude measurement (RSAM) (Endo and Murray, 1991), a 1-minute running mean of the signal amplitude recorded by a

broadband seismometer (MBGH, St George's Hill) 3.4 km from the volcano summit (Figure 2.2b), from February 2005 to June 2011. From Volcán de Colima, we use the hourly average of the real-time seismic energy measurement (RSEM) (Reyes-Dávila and De la Cruz-Reyna, 2002), which is proportional to a 2-minute running mean of the root-mean-square of the signal amplitudes recorded by a short-period seismometer (EZV4) 1.7 km from the volcano summit (Figure 2.1b), from January 2004 to December 2008. These data are discretised prior to analysis (as explained in Section 3.2.3) by rounding the Soufrière Hills Volcano RSAM to 0 decimal places and the Volcán de Colima RSEM to 2 decimal places.

(2) The daily counts of the most commonly observed volcano-seismic event classes: during the study period at Volcán de Colima, these are impulsive and emergent events (associated with small Vulcanian explosions and transient degassing events: Varley et al., 2006; Webb et al., 2014) and low-amplitude long-period (LP) events (Varley et al., 2010a, 2010b) (Table 2.1); at Soufrière Hills Volcano, these are volcano-tectonic (VT), hybrid, LP, rockfall, and LP with rockfall events (Miller et al., 1998; Luckett et al., 2008) (Table 2.2). Other event classes (e.g., rockfalls at Volcán de Colima and explosion signals at Soufrière Hills Volcano) occur too rarely or irregularly in the time periods investigated (November 2004 to December 2008 at Volcán de Colima; October 1996 to July 2010 at Soufrière Hills Volcano) for them to be analysed. The predominant seismic event types differ between the two volcanoes because of the dissimilar shallow magmatic systems and extrusion rates during the time periods studied, as discussed in Lachowycz et al. (2013; Chapter 2). The event counts were determined manually by the observatories, by visual inspection of helicorders and spectrograms from the respective seismic networks. Sources of bias and error in the data analysed here from these networks were outlined by Lamb et al. (2014). Note that the real-time seismic measurements and event count data are from distinct, overlapping time periods in both cases, due to restricted data availability.

3.4. Results

3.4.1. Volcán de Colima hourly RSEM, January 2004–December 2008

Figure 3.3 shows the hour-averaged RSEM time-series from Volcán de Colima, with its normalised overlapping-window entropy and the uniformity test (Figure 3.3a; windows of the prior 10 days (240 measurements)), the 30-day change in normalised cumulative entropy (Figure 3.3b; normalised cumulative entropy shown in Supplementary File 3.1), and the overlapping-window coefficient of variation (Figure 3.3c; windows of the prior 10 days) for comparison. There is considerable temporal variation in the overlapping-window entropy during the period studied (Figure 3.3a); it is generally higher during phases of elevated activity (shaded on each plot in Figure 3.3). Peaks in this entropy statistic coincide with the phase of rapid lava extrusion in 2004 and the highest eruption occurrence rates and magnitudes during the phase of large Vulcanian explosions in 2005 (Varley et al., 2010a); RSEM was relatively high in both instances. Notably, the entropy increases to values greater than any observed earlier in 2004 (>0.95) for the two weeks prior to the onset of lava extrusion on 28 September 2004, coincident with a shift to uniform distribution of the RSEM (at the point indicated by arrow A on Figure 3.3a). From visual inspection, this appears to be a continuation of a trend of increasing entropy that started ∼6 weeks prior to the onset of extrusion (at the point indicated by arrow B on Figure 3.3a). Note that there is no increase in the RSEM in the run up to the onset of lava extrusion in 2004, despite increasing RSEM indicating accelerating seismic energy release prior to some earlier eruptions of Volcán de Colima (Reyes-Dávila and De la Cruz-Reyna, 2002). Similarly, the entropy increases to >0.95 (at the point indicated by arrow C on Figure 3.3a) ∼2 months prior to the start of the period of elevated RSEM associated with the peak of the Vulcanian eruptive activity in 2005. Furthermore, the entropy is persistently close to 0.95 and the RSEM intermittently uniform (from the point indicated by arrow D on Figure 3.3a) for the ∼4 months prior to the onset of lava

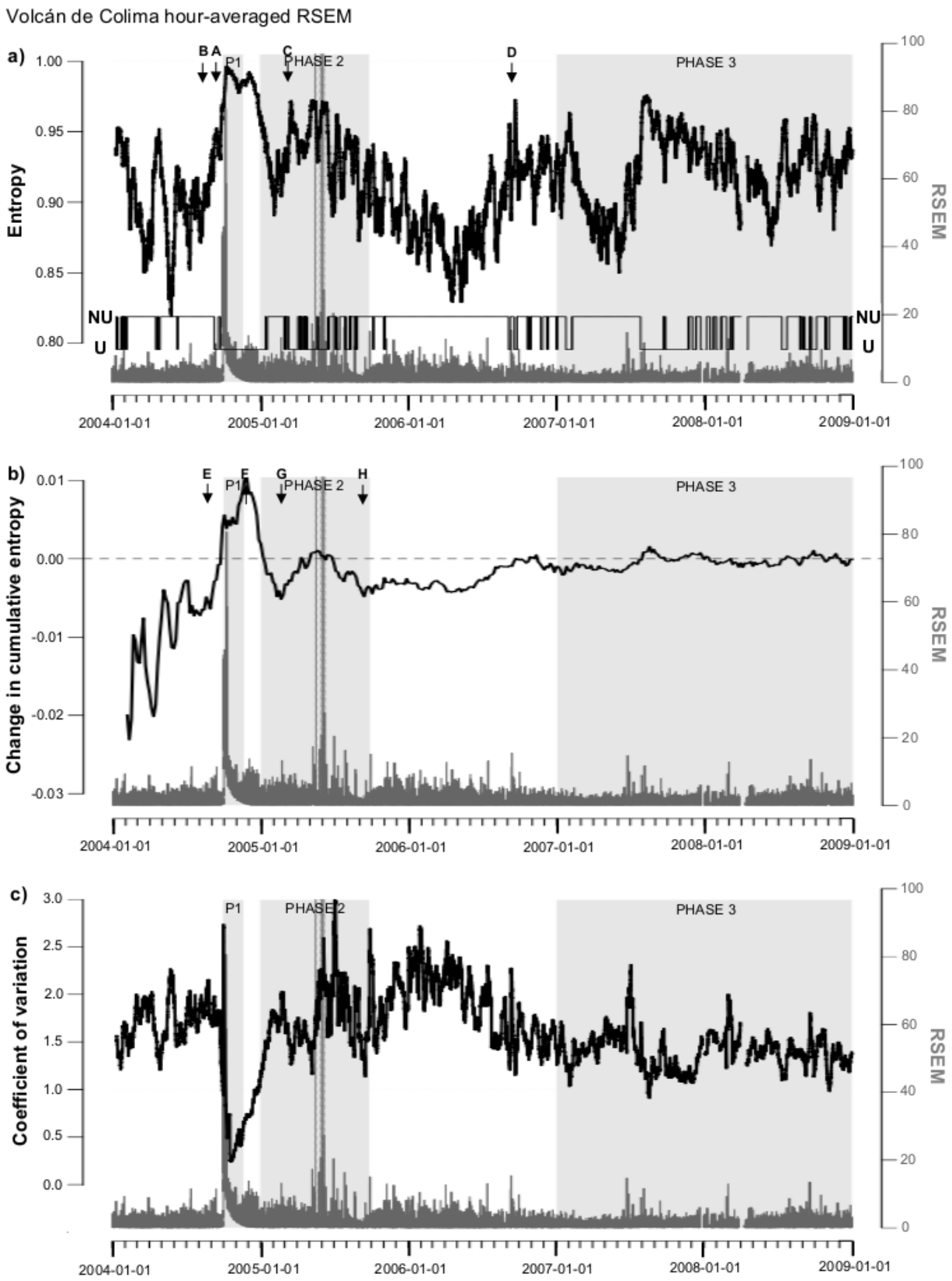

Figure 3.3 *(caption on next page)*

Figure 3.3 *(previous page)* Entropy analysis of an hour-averaged real-time seismic energy measurement (RSEM) time-series recorded at Volcán de Colima (data from 1 January 2004 to 31 December 2008; plotted in each graph (dark grey line)). **(a)** Normalised Shannon entropy (upper black line), calculated for each time-step from a window of the prior 10 days (240 measurements), and a test of hypothesis of a uniform distribution (lower black line; NU = not uniform, U = uniform), calculated for each time-step from the same window. **(b)** The 30-day change in normalised cumulative Shannon entropy (black line; the difference between the entropy of a window of all the data prior to the time-step and the same 30 days before). The horizontal dashed line indicates a threshold level of zero change in cumulative entropy. **(c)** The coefficient of variation (black line), calculated for each time-step from a window of the prior 10 days (240 measurements), for comparison. The shading in each graph indicates phases of extrusive and/or enhanced explosive activity; the vertical dashed grey lines mark major (VEI ≥ 2) Vulcanian explosions. Phase 1 is the period of relatively fast lava extrusion in late 2004, Phase 2 the period of large Vulcanian explosions in 2005, and Phase 3 is part of the period of relatively slow lava extrusion in 2007–11. The arrows indicate entropy increases prior to phases of activity, discussed in Section 3.4.1. Periods with no results are due to gaps in the RSEM time-series.

extrusion in January 2007, which again was not preceded by any increase in the RSEM.

The association of peaks in entropy just prior to and during periods of elevated activity (from visual inspection) may imply that the associated factors, such as magma ascent or gas release, change the nature of the seismicity such that there is greater uncertainty in the RSEM, and the distribution of its values (in a 10-day window) becomes more uniform. Further work is required to ascertain possible mechanisms. This inference is consistent with the observation of a peak in overlapping-window entropy prior to the start of extrusion in 2007 (at point D on Figure 3.3a) that coincides with a transient increase in spring water boron concentration (N.R. Varley, unpublished data). Similar increases in boron concentration have been observed prior to or at the onset of previous eruptive phases at Volcán de Colima (Armienta and De la Cruz-Reyna, 1995; Taran et al., 2000) and at Volcán Popocatépetl (Mexico), where they have been attributed to magma recharge/ascent (Martin-Del Pozzo et al., 2002; Armienta et al., 2008). The boron 'spike' prior to the 2004 extrusive phase occurred approximately coincident with point B, when the trend of increasing entropy prior to lava effusion began (although this would have not been recognisable in real-time). These entropy changes also, in addition to that at point C on Figure 3.3a, coincide

with transient persistence to the RSEM time-series, identified by detrended fluctuation analysis (Lachowycz et al., 2013; Chapter 2). We suggest that the variability in the overlapping-window entropy and RSEM uniformity during the 2007–8 period of the 2007–11 extrusive phase (Figure 3.3a; unlike the previous phases of elevated activity) reflects the extremely slow lava extrusion rate during this phase (e.g., <0.005 m^3s^{-1} on average for the first ~6 months (Hutchison et al., 2013), when the entropy is particularly low). The periods of high entropy (close to 0.95) in 2007–8, which coincide with those of uniform data distribution but not necessarily with high RSEM values, might indicate pulses of magma ascent that were not identified in the sporadic dome height measurements used to quantify the lava extrusion rate (Hutchison et al., 2013).

The change in cumulative entropy (Figure 3.3b) also varies through time, largely concurrent with overlapping-window entropy, but with less short-timescale variability (except in early 2004, which is anomalous due to the relatively small window size). This entropy statistic is high (close to or greater than 0) during all three phases of elevated activity (as well as just prior to the onset of extrusion in 2007, as with the overlapping-window entropy) relative to other periods. It becomes positive ~2 weeks prior to the 2004 eruptive phase, for the period of highest eruption occurrence rates and magnitudes during the phase of large Vulcanian explosions in 2005, and intermittently from ~3 months prior to the onset of extrusion in 2007–11 through to the end of 2008. From visual inspection, it appears that some of the periods of high eruptive activity are preceded and followed by the most abrupt changes in the gradient, e.g. at the end of the 2004 phase (at the point indicated by arrow F on Figure 3.3b), as well as early in and at the end of the 2005 phase (at the points indicated by arrows G and H on Figure 3.3b, respectively). These coincide with the changes in overlapping-window entropy noted previously (so also are not associated with any change in RSEM values), except that at the end of the 2005 phase, which is also marked by a decrease in the occurrence of a uniform RSEM distribution (Figure 3.3a). The negligible short-

timescale variability in the change in cumulative entropy in comparison to the overlapping-window entropy means that such shifts in the trend of the former would be more readily identifiable in real-time.

The temporal variation in the CV (Figure 3.3c), calculated using the same parameters as the overlapping-window entropy, is distinct from that of either entropy statistic. Its relationship to eruptive activity is inconsistent; CV is highest at the peak of the 2005 Vulcanian explosions and in early 2006 (a period of relative quiescence), and relatively low during the 2004 phase and in 2007–8. This appears to reflect the range in RSEM values at those times: RSEM is relatively high during both the 2004 phase and the peak of the 2005 activity, but in contrast to 2005, low values are not recorded in the 2004 phase, so the dispersion in RSEM is relatively narrow in 2004. Similarly, RSEM is more variable with higher values during early 2006 than 2007–8; the spikes in CV during the latter appear (from visual inspection) to be associated with peaks in (and so a relatively wide range of values of) RSEM. Unlike entropy, the CV does not clearly change before activity transitions; it is stable prior to the onset of both the 2004 eruptive phase and the largest Vulcanian eruptions in the 2005 phase. There are changes in the gradient of the trend in CV at the end of the 2005 phase and at the start of extrusion in 2004 and 2007, but these would only have been identifiable retrospectively. Nevertheless, these CV variations corroborate the entropy and uniformity time-series in indicating that shifts in eruptive activity are associated with changes in the distribution of the RSEM, if not its value in some instances.

3.4.2. Soufrière Hills Volcano hourly RSAM, February 2005–June 2011

Figure 3.4 shows the hour-averaged RSAM time-series from Soufrière Hills Volcano, with its normalised overlapping-window entropy and the uniformity test (Figure 3.4a; windows of the prior 10 days (240 measurements)), the 30-day change in normalised cumulative entropy (Figure

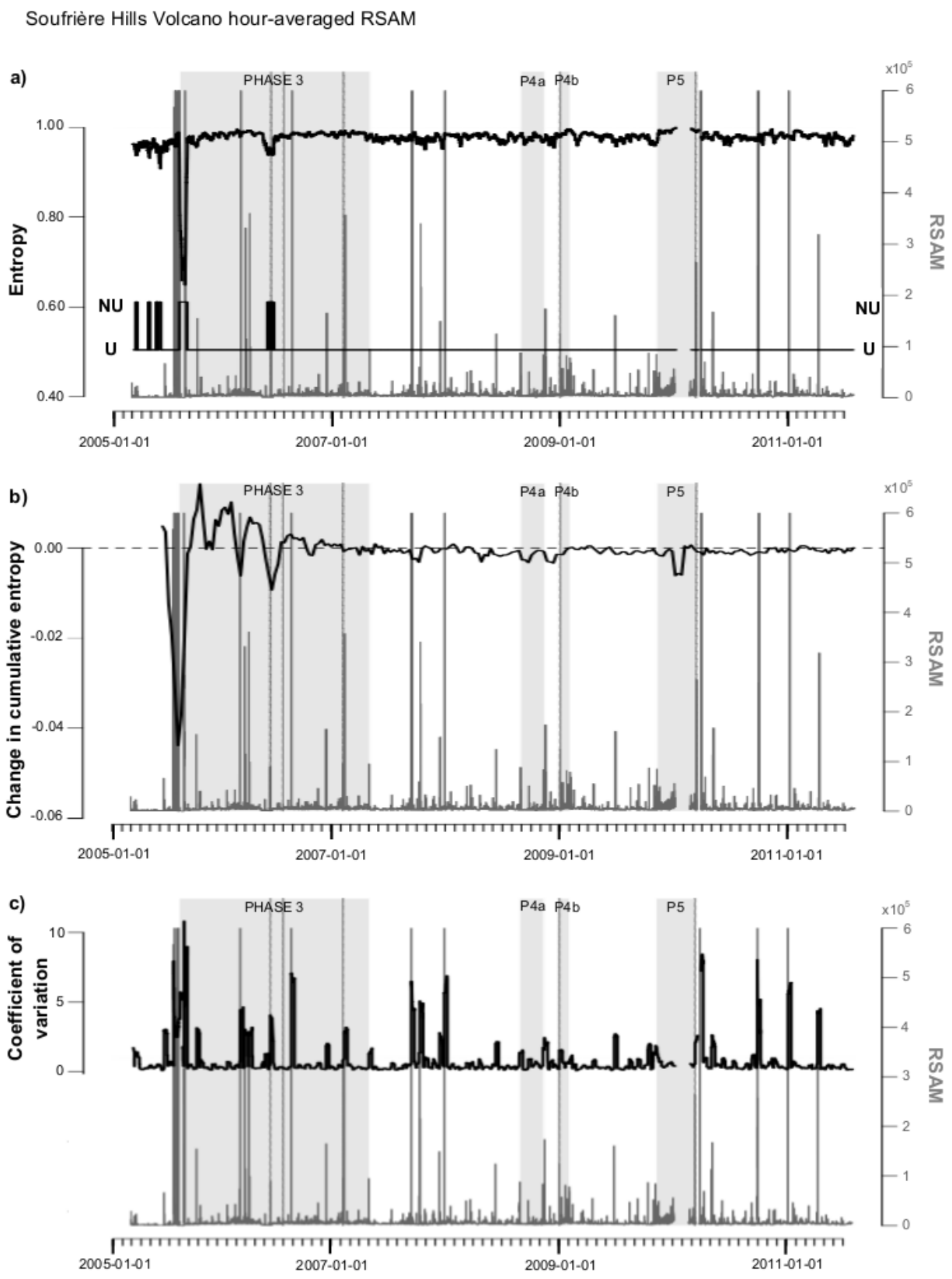

Figure 3.4 *(caption on next page)*

Figure 3.4 *(previous page)* Entropy analysis of an hour-averaged real-time seismic amplitude measurement (RSAM) time-series recorded at Soufrière Hills Volcano (data from 28 February 2005 to 30 June 2011; plotted in each graph (dark grey line)). **(a)** Normalised Shannon entropy (upper black line), calculated for each time-step from a window of the prior 10 days (240 measurements), and a test of hypothesis of a uniform distribution (lower black line; NU = not uniform, U = uniform) calculated for each time-step from the same window. **(b)** The 30-day change in normalised cumulative Shannon entropy (black line; the difference between the entropy of a window of all the data prior to the time-step and the same 30 days before). The horizontal dashed line indicates a threshold level of zero change in cumulative entropy. **(c)** The coefficient of variation (black line), calculated for each time-step from a window of the prior 10 days (240 measurements), for comparison. The shading in each graph indicates phases (labelled) of extrusive and/or explosive activity; the vertical dashed grey lines mark major dome collapse events. Periods with no results are due to gaps in the RSAM time-series.

3.4b; normalised cumulative entropy shown in Supplementary File 3.2), and the overlapping-window CV (Figure 3.4c; windows of the prior 10 days) for comparison. From visual inspection, the overlapping-window entropy (Figure 3.4a) appears to be generally slightly higher during the phases of activity (shaded on each plot in Figure 3.4) in the period analysed, except for Phase 4a, when magma ascent was associated with low levels of seismicity in comparison to the other phases (Stewart et al., 2009). Anomalous decreases in entropy (and RSAM non-uniformity) occur twice during Phase 3, coincident with anomalously low RSAM values that are most likely to be due to seismometer failure. The slight shifts to and from high entropy values appear to approximately coincide with the onset and end of Phases 3 and 5, but are not prominent enough that a threshold entropy value can be ascertained. The association of high overlapping-window entropy of RSAM with eruptive phases is consistent with that observed for RSEM at Volcán de Colima (Section 3.4.1), but more uncertain due to the relatively small difference in entropy between eruptive and inter-eruptive periods at Soufrière Hills Volcano. The magnitude of the temporal variation in this entropy statistic may be greater if the RSAM values were discretised further (the uniform distribution to the RSAM almost throughout the study period would suggest insufficient discretisation), but this may risk loss of meaningful RSAM variation during periods of low-magnitude seismicity.

The change in cumulative entropy (Figure 3.4b) is initially variable, before becoming stable (at close to zero) from late in Phase 3 onwards. It is predominantly positive during Phase 3; two of the three excursions to negative values coincide with the aforementioned anomalously low overlapping-window entropy values, and the other with a peak in RSAM. There are insufficient data prior to Phase 3 to determine if this statistic was distinct from in Phase 3 during that period. There is no clear change in this statistic associated with the subsequent eruptive phases; the decrease during Phase 5 reflects the concurrent data gap. The temporal variation in CV (Figure 3.4c), calculated using the same parameters as the overlapping-window entropy, is distinct from that of either entropy statistic, as it closely corresponds with the variation in RSAM. Despite the variance being normalised by the mean value, periods of high RSAM values have high CV due to the greater dispersion in the data compared to periods of lower magnitude seismicity.

3.4.3. Volcán de Colima daily event counts, November 2004–December 2008

The daily counts of each event type analysed are presented in Figure 3.5, with their normalised 50-day (50-measurement) overlapping-window entropy and the uniformity test; the 50-day overlapping-window CV for each time-series is provided in Supplementary File 3.3 for comparison. Variation in the impulsive (Figure 3.5a) and emergent (Figure 3.5b) event count overlapping-window entropies appears to be unrelated to eruptive activity, consistent with the observation that there was no clear association between explosion frequency and other eruptive activity during the study period (Varley et al., 2010a; Webb et al., 2014). Both entropy time-series may be weakly periodic, with a period of ~3–6 months, but are not in phase with one another; nor is there an apparent relationship between their longer-timescale variations. This periodicity is not apparent in the event counts themselves; further work would be necessary to confirm its veracity and constrain its cause. From inspection, we suggest that the times when the daily counts of these two events are uniformly distributed correspond to the phases of greater eruptive activity

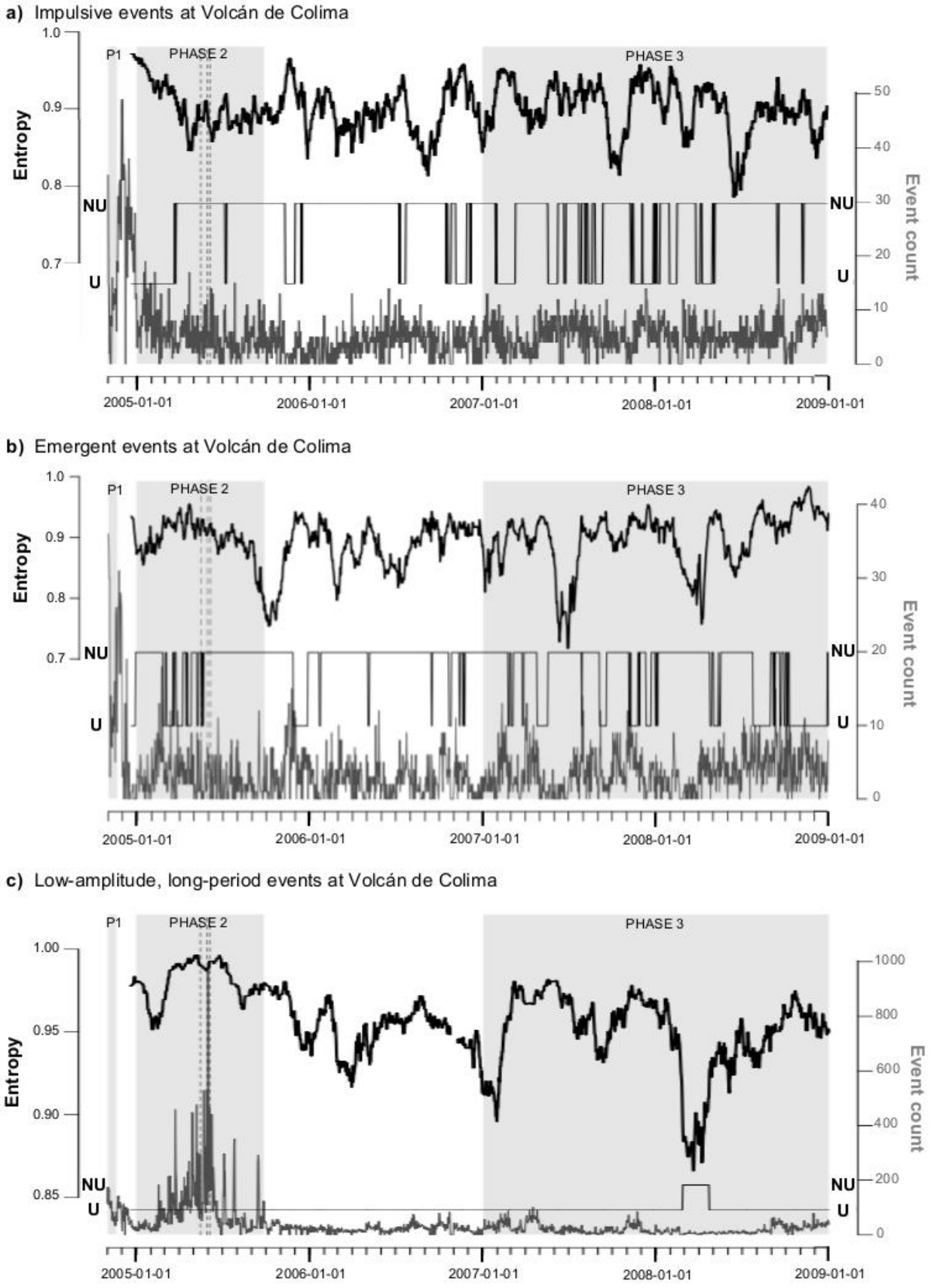

Figure 3.5 *(caption on next page)*

Figure 3.5 *(previous page)* Entropy analysis of the daily count of each of the primary volcano-seismic event types at Volcán de Colima (described in Table 2.1; data from 1 November 2004 to 31 December 2008). In each graph, the daily event count time-series is plotted (dark grey line) with the normalised Shannon entropy (upper black line), calculated for each time-step from a window of the prior 50 days (50 measurements), and a test of hypothesis of a uniform distribution (lower black line; NU = not uniform, U = uniform) calculated for each time-step from the same window. The shading in each graph indicates phases of extrusive and/or enhanced explosive activity; the vertical dashed grey lines mark major (VEI ≥ 2) Vulcanian explosions. Phase 1 is the period of relatively fast lava extrusion in late 2004, Phase 2 the period of large Vulcanian explosions in 2005, and Phase 3 is part of the period of relatively slow lava extrusion in 2007–11. The coefficient of variation for each time-series is provided for comparison in Supplementary File 3.3.

---

to some extent: almost all the periods of uniform distribution to the impulsive event counts are after or in the few months prior to the start of extrusion in 2007 (Figure 3.5a), and a uniform distribution to the emergent event counts is most sustained during part of the 2005 explosive phase and in late 2008 (Figure 3.5b), when the extrusion rate was high in comparison to earlier in 2007–8 (Hutchison et al., 2013). Variation in the CV of these time-series (Supplementary File 3.3) also shows no clear relationship to activity and possible periodicity of a similar frequency (but not in phase with that in overlapping-window entropy).

Despite the fact that the low-amplitude long-period (LP) event count is almost continuously uniform during the period analysed, there is still considerable variation in the overlapping-window entropy of these data (Figure 3.5c). The entropy is relatively high (>0.96) during the phases of elevated activity, with the highest values being concurrent with the peak of the Vulcanian eruptions in 2005 (and relatively high low-amplitude LP event counts due to the event swarms associated with these eruptions: Varley et al., 2010a, 2010b). The entropy also abruptly increases just after the onset of lava extrusion in 2007 to a value not observed since just after the 2005 Vulcanian phase (the lag relative to the start and end of activity in both cases may reflect the 50-day window length), despite the LP event count being not much greater than during late 2006. Hence we suggest that magma ascent is associated with a change in the distribution of the

occurrence of these seismic events such that the daily count becomes more uncertain. The relatively low entropy and non-uniformity of the LP event counts for two months in early 2008 is not due to the low event occurrence rate, as similar counts occur in the months after this period, so we suggest that it may be due to inconsistent manual picking of the events in that period. Variation in the CV (Supplementary File 3.3) largely corresponds to that in the event count rate.

3.4.4. Soufrière Hills Volcano daily event counts, October 1996–July 2010

The daily counts of each event type analysed are presented in Figure 3.6, with their normalised 50-day (50-measurement) overlapping-window entropy and the uniformity test; the 50-day overlapping-window CV for each time-series is provided in Supplementary File 3.4 for comparison. Note that the abrupt excursions to the maximum entropy value in these plots, indicated by the arrows, result from normalisation of the (zero) entropy of periods with no recorded events, so are disregarded. The variation in the overlapping-window entropy of the volcano-tectonic (VT) event counts (Figure 3.6a) appears to largely reflect that of the event counts themselves (high entropy generally concurrent with high event counts and vice versa), with no association with activity in Phases 1 and 2, but increasing entropy/event counts prior to the onset of subsequent phases. However, the entropy increases prior to the onset of Phase 5 and there are peaks in entropy during Phase 3, both periods of low VT event counts. The event counts are only uniformly distributed and their entropy close to maximal (>∼0.8) predominantly between Phases 1 and 2, despite a similar range of counts occurring prior to Phase 3, exemplifying that the entropy is not determined by this feature of their distribution. This is also apparent in the overlapping-window entropy of the hybrid event counts (Figure 3.6b), for example in the higher entropy between Phases 2 and 3 than during the subsequent eruptive phase. Notably, the hybrid event counts are uniformly distributed for most of Phase 1, at the start and end of Phase 2, and the start of Phase 5, although with lag in each case most likely due to the 50-day window length. The overlapping-

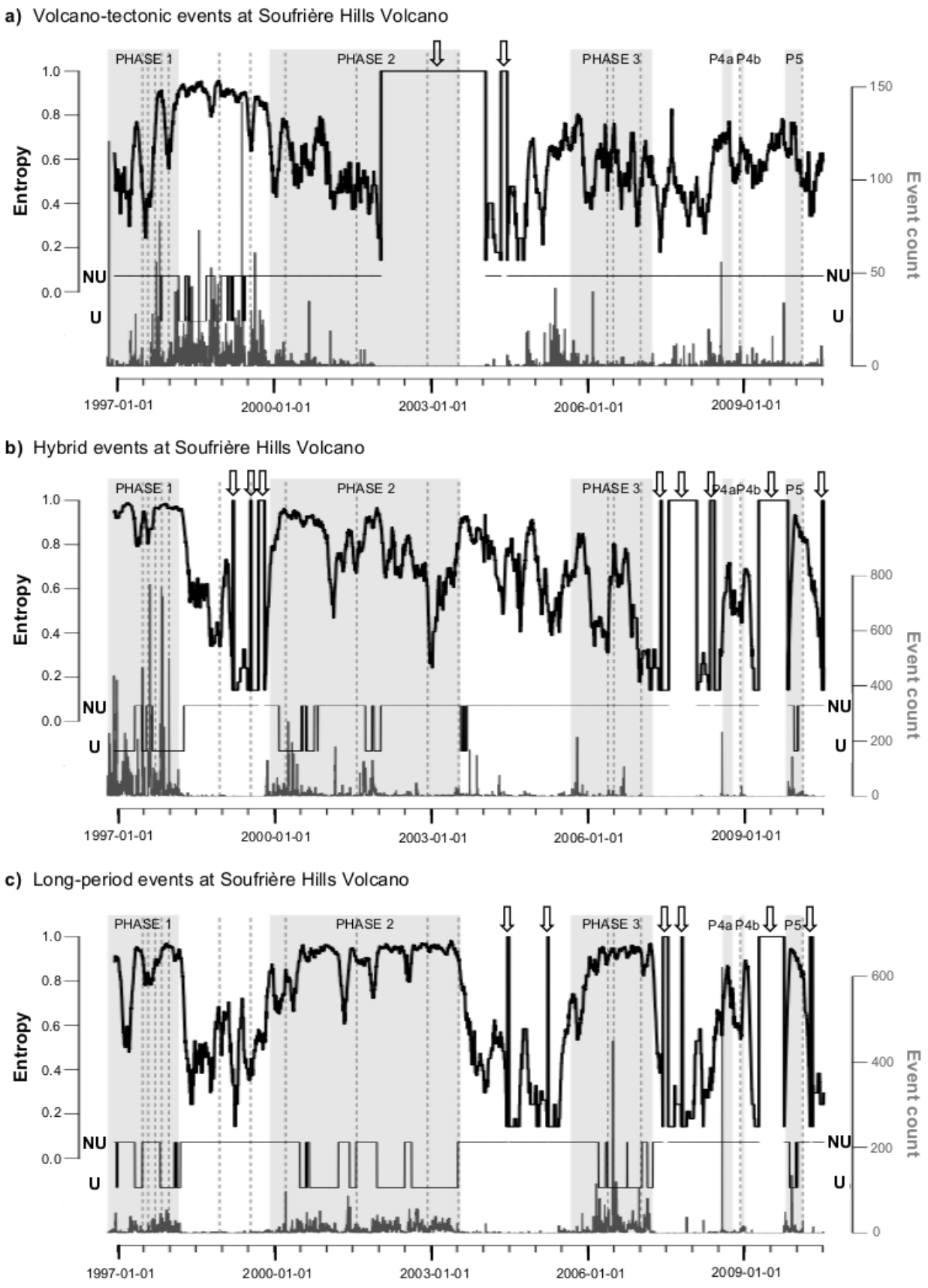

Figure 3.6 *(continued on next page)*

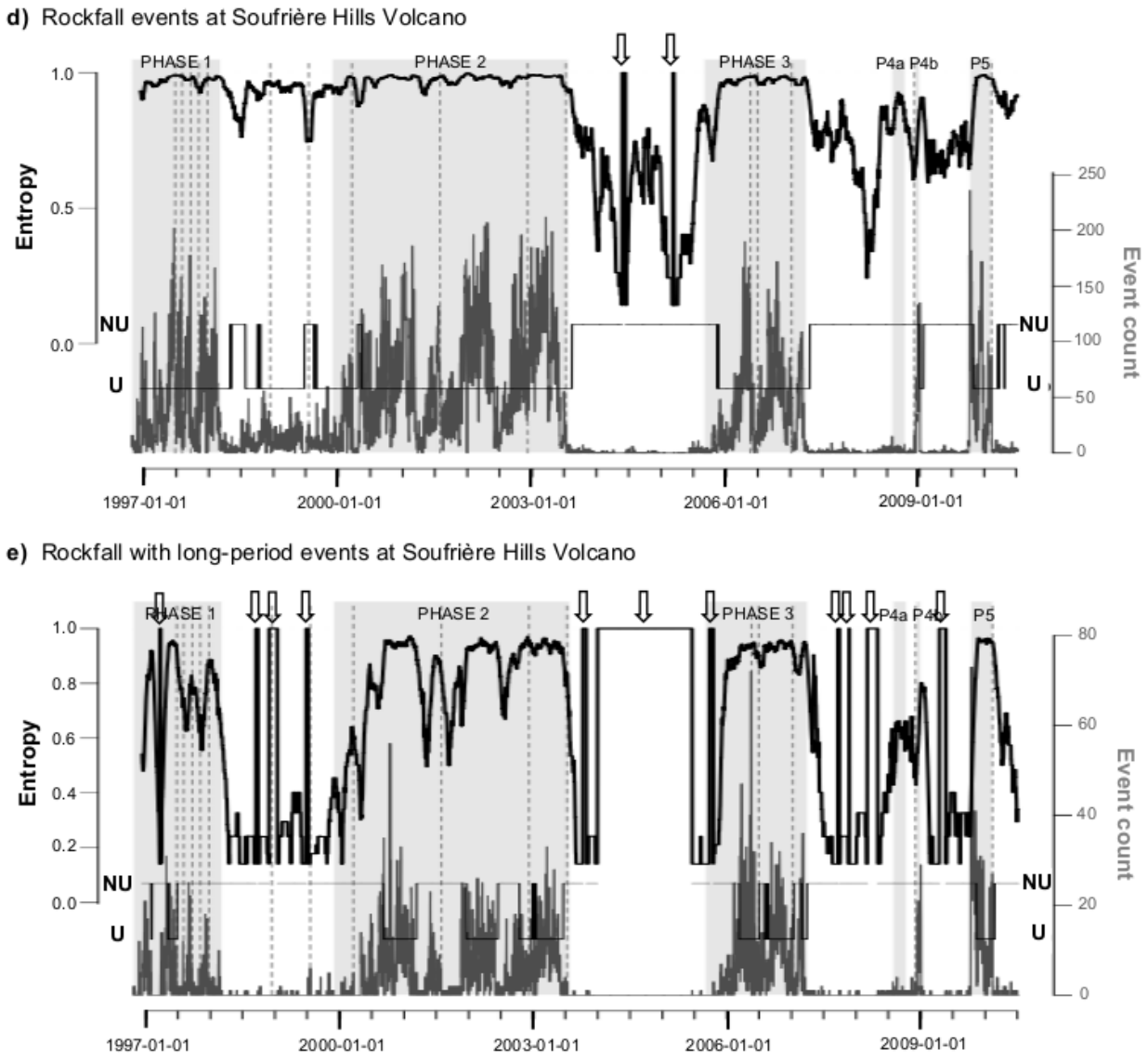

Figure 3.6 Entropy analysis of the daily count of each of the primary volcano-seismic event types at Soufrière Hills Volcano (described in Table 2.2; data from 23 October 1996 to 8 July 2010). In each graph, the daily event count time-series is plotted (dark grey line) with the normalised Shannon entropy (upper black line), calculated for each time-step from a window of the prior 50 days (50 measurements), and a test of hypothesis of a uniform distribution (lower black line; NU = not uniform, U = uniform) calculated for each time-step from the same window. The shading in each graph indicates phases (labelled) of extrusive and/or explosive activity; the vertical dashed grey lines mark major dome collapse events. The hollow arrows indicate anomalous spikes in the normalised entropy (to 1) due to periods of zero counts. The coefficient of variation for each time-series is provided for comparison in Supplementary File 3.4.

window entropy of both VT and hybrid event counts appears to be approximately in antiphase with their CV (Supplementary File 3.4), despite both statistics being expected to increase with a wider data distribution (and vice versa). During the periods when peaks in the overlapping-window entropy of these event counts do correspond to activity (e.g., Phases 3–5 for VTs, Phases 1 and 2 for hybrids), the CV does not.

The overlapping-window entropy of the long-period (LP) event counts (Figure 3.6c) is generally relatively high during phases of activity; from inspection, it exceeds ∼0.7 coincident with the onset of each phase, and decreases below this value shortly after the end of each phase. This threshold is exceeded prior to any substantial increase in LP event count in each case except Phases 4a and 5. The event counts are uniformly distributed for most of each phase except Phase 4 (and are concurrent with the highest entropy values), shifting to non-uniform coincident with the terminations of each of Phases 1–3. The same pattern of variation in overlapping-window entropy is apparent for rockfall (Figure 3.6d) and LP with rockfall (Figure 3.6e) event counts; the entropy generally exceeds ∼0.85 and ∼0.5 respectively during phases of activity, and vice versa, except between Phases 1 and 2 in the case of the rockfall event counts. From inspection, the entropy increases just prior to or at the onset of phases of activity before there is a substantial increase in event counts in some cases, e.g. Phases 3 and 4a for LP with rockfall events. The LP with rockfall event counts are less commonly uniformly distributed than those of LP and rockfall events, most likely due to their relatively infrequent occurrence rate. The CV of the counts of all three event types (Supplementary File 3.4) is generally lower during phases of activity, but not consistently so relative to eruptive phases, except for the LP with rockfall event counts.

3.5. Discussion

The identification of temporal variation in the entropy of the seismic time-series analysed suggests that quantifying the randomness of such signals can be informative for volcano monitoring. This is supported by the observation (from visual inspection) that major changes in entropy (to above or below a certain overlapping-window entropy threshold in some cases) are more typically associated with shifts in eruptive activity than the coefficient of variation, which is also dependent upon the probability distribution of the data. With further development, entropy analysis has the potential to highlight (in near-real-time) important changes to the structure of monitoring data that are not easily identifiable by conventional monitoring techniques, as exemplified by the entropy analysis of the real-time seismic measurements from Volcán de Colima presented here. The overlapping window entropy and the change in cumulative entropy of RSEM approach or exceed threshold values (not observed in the preceding periods of relative quiescence) prior to the onset of the 2004 and 2007–11 lava extrusion phases (Figure 3.3; Section 3.4.1); no unambiguous precursors to these eruptive phases were recognised in real-time monitoring data. Therefore, had it been calculated in real-time, the RSEM entropy could have been an indication of the possibility of impending lava extrusion. From inspection, the overlapping-window entropy of RSAM at Soufrière Hills Volcano may also increase at the onset and decrease at the termination of some phases of activity in the period analysed (Figure 3.4; Section 3.4.2), but the variation is relatively small. Further work is required to determine if entropy analysis has greater potential with such time-series, where rockfalls, rather than seismicity associated with magma movement, are generally the predominant contributor to the signal (discussed further below).

Although shifts in activity may not be clearly reflected in changes in the entropy of RSAM at Soufrière Hills Volcano, they are in the entropy of the event counts of individual seismic event types, particularly long-period events with or without associated rockfalls (Figure 3.6; Section 3.4.4). The entropy of these data is observed to increase above values found in inter-eruptive periods just prior to or around the onset of eruptive phases, so threshold entropy values pertinent to monitoring could be established from the entropy variations associated with earlier eruptive phases. For general application, this method requires data from prior monitoring of the expected range of eruptive activity, and the assumption that there is no change in the relationship between the probability distribution of the seismic time-series and activity with time. This assumption is not necessarily justifiable, as exemplified by the changes in the nature of volcano-tectonic and hybrid seismicity during the recent eruptive period at Soufrière Hills Volcano (Cole et al., 2010b; Lachowycz et al., 2013). Furthermore, the thresholds will differ between time-series and entropy calculation parameters (e.g., extent of discretisation and window size), so must be subjectively defined in each instance; the propensity for false positives (i.e., threshold exceedance without associated activity) will also be different in each case. The test for uniform distribution of the data applied in this study could be a less arbitrary alternative, but most of the time-series analysed here are either only intermittently uniformly distributed during eruptive phases or uniform almost throughout the period analysed.

Further work is required to understand why variations in the entropy of seismicity may relate to those in volcanic activity. Entropy is maximal when the distribution of the data is uniform, i.e. all distinct measurements are observed with equal frequency; if some values were to become more frequent than others, the entropy would decrease. The distribution of values in an event count time-series will depend upon the occurrence rate of that event type, and possibly the event magnitude (if some are close to the detection threshold, e.g. the low-amplitude LP events at

Volcán de Colima). The distribution of values constituting a real-time seismic measurement time-series will (in any given time window) be determined by the timings, durations, and magnitudes of the seismicity-generating events recorded. Both real-time seismic measurement time-series analysed appear to be predominantly determined by the properties of the most frequent volcano-seismic event type, which occurs an order of magnitude more frequently than any other event class for the majority of the time periods analysed. At Soufrière Hills Volcano from Phase 3 onwards, this is rockfall-induced seismicity, which has a quantifiable relationship to lava extrusion rate (Calder et al., 2005). Rockfalls were infrequent at Volcán de Colima during the study period, except for the lava extrusion phase in 2004; the dominant event class there is low-magnitude LP earthquakes (Varley et al., 2010a). These events, which have been attributed to brittle fracturing on the margins of an ascending magma body (Varley et al., 2010a), occurred in 'swarms' during the Vulcanian explosion phase in 2005, partly from a consistent source (Varley et al., 2010a, 2010b; Arámbula-Mendoza et al., 2011). The entropy of the daily count of these event types is generally higher, often close to maximal, during phases of activity, but does not exactly correspond to those of the real-time seismic measurements, due to the (probably subsidiary) influence of other seismicity on the latter. We suggest that the counts of LP and rockfall events have relatively high entropy during phases of activity perhaps in part because of self-organized critical behaviour (Bak et al., 1987) of these event types during magma ascent and extrusion. This was suggested by Lachowycz et al. (2013) as an explanation for the power-law correlations in these data during eruptive phases (Section 2.5), and both LP (e.g., Shaw and Chouet, 1991) and rockfall (e.g., Hale et al., 2009) seismicity during magma ascent and extrusion were suggested to show such behaviour previously. Maximal entropy (in a thermodynamic sense) has been associated with self-organised (sub-)critical behaviour of tectonic seismicity (e.g., Main and Al-Kindy, 2002; Main and Naylor, 2010).

Variation in the entropy of the seismic time-series analysed indicates temporal variability in the uncertainty associated with what value these seismic signals will have, and so their predictability; the time-series that have higher entropy during phases of activity are less predictable during those periods. The association (in some instances) of high entropy, and so low predictability, with long-range correlations (Lachowycz et al., 2013) (e.g., the peaks in Volcán de Colima RSEM entropy (Figure 3.3), and Volcán de Colima LP (Figure 3.5) and Soufrière Hills Volcano rockfall event counts (Figure 3.6) during phases of activity) and/or low coefficient of variation is not inconsistent: a relatively narrow range of values can have high entropy if these values occur with close to equal frequency. This exemplifies how computation and comparison of the entropy in addition to other data distribution parameters through time could be used to better understand how monitoring time-series vary in relation to activity, and so constrain eruption processes.

For the reasons outlined in Section 3.2.4 (e.g., not computationally intensive and appropriate for any time-series, including if non-stationary or incomplete), entropy analysis by the approach used here is potentially widely applicable in near-real-time (at least to time-series sampled at a relatively high rate) as a tool complementary to existing monitoring techniques. Further work is necessary to understand the causes and significance of temporal variation in the entropy of volcanic seismicity, and to what extent changes in other dome-forming eruptions or different styles of activity could be forecast or identified from this. Entropy variation vs other parameters, such as earthquake depth and magnitude (e.g., Telesca et al., 2012) may also be informative, as well as the entropy of a whole dataset as a measure of its disorder. Similar studies would be worthwhile to assess the utility of entropy analysis of other high-frequency volcano monitoring data, as well as other geological time-series.

3.6. Conclusions

The entropy of (and so the distribution of the values in) each of the time-series analysed is found to vary through time, revealing changes in the structure of these data that in some cases are not apparent from conventional analysis techniques, or even other statistics determined by data distribution. This implies that the uncertainty in (i.e., the predictability of) the value taken by any of these signals, and so the eruptive activity with which they are associated, is temporally variable; this can be monitored by entropy analysis. The possible utility of real-time entropy analysis is demonstrated by, for example, increases in the entropy of real-time seismic measurements prior to the onset of some eruptive phases at Volcán de Colima, for which no clear precursors were identified by conventional monitoring in real-time. Therefore with further development, entropy analysis may have the potential to provide useful additional guidance for interpreting data from volcano monitoring.

Chapter 4 Late Quaternary tephrostratigraphy of Volcán Hudson, southern Chile

Manuscript in preparation: Lachowycz, S.M., Smith, V.C., Pyle, D.M., Mather, T.A., Mee, K., Fontijn, K., Rawson, H., Naranjo, J.A.. Late Quaternary tephrostratigraphy of Volcán Hudson, southern Chile.

Author contributions: VCS and KF assisted with glass composition analysis and advised on whole rock composition analysis. HR assisted with tephra sampling and whole rock composition analysis. KM helped with map production. JAN provided information on previous studies. VCS, DMP, TAM, KF, and HR contributed to manuscript preparation.

This manuscript partly builds upon my contributions to Fontijn et al. (2014), a review of the regional tephrostratigraphy.

Abstract

Volcán Hudson, in the Andean Southern Volcanic Zone, has been identified as the source of four eruptions of >1 km^3 of tephra (volcanic ash and lapilli) and tens of smaller explosive eruptions in the past 20 ky. The resulting tephra deposits have great potential as chronological markers in studies of the palaeoenvironment of the region, which is particularly significant for investigation of Southern Hemisphere climate dynamics. However, the characteristics and timing of many of the eruptions of Volcán Hudson are poorly constrained, inhibiting precise tephrochronology as well as volcanic hazard assessment. Here we present matrix glass and whole rock composition analyses of Volcán Hudson tephra units in relatively complete terrestrial sections, and catalogue occurrences of tephra previously attributed to eruptions of Volcán Hudson in ice, peat, soils, and lake and marine sediments. We correlate the tephras analysed and critically evaluate previous tephra correlations, including those between palaeoenvironmental records. We also refine the age estimates of some of the eruptions using Bayesian analysis of published radiocarbon dates. The Volcán Hudson tephras analysed here generally have a narrow range in their glass composition, so in most cases can be distinguished from the other tephras of a similar age, which often have a similar composition. We find previously unrecognised shifts in erupted magma composition during the Holocene, from silicic to mafic after the H2 eruption (~3.9 cal ka BP), and then to intermediate compositions for the last ~1 ky. Numerous inconsistencies are identified in the prior tephrostratigraphy; most tephra units cannot be correlated using the published compositional data. The new geochemical data and tephrostratigraphy reanalysis in this study provide a framework for future tephrochronology and studies of the record of eruptions in the region, and highlight the importance of detailed tephra characterisation in developing correlations between, and age models for, palaeoenvironmental records.

4.1. Introduction

The volcanoes of the Andean Austral and Southern Volcanic Zones (AVZ and SVZ, 49–55°S and 33–47°S respectively; e.g., Stern, 2004) have produced a prolific but poorly studied post-glacial tephrostratigraphic record (Fontijn et al., 2014). Volcán Hudson, at the southern end of the SVZ (45.92°S, 72.97°W), has been postulated to be one of the most frequently active and productive of these volcanoes during the late Quaternary (Naranjo and Stern, 1998). This is supported by the identification of over 70 tephra units in post-glacial lake sediment cores from within ~100 km of the volcano, the majority of which have been attributed to Volcán Hudson (e.g., Haberle and Lumley, 1998; Weller et al., 2014). Three known prehistoric eruptions are estimated to have erupted ≥1 km^3 of tephra (corresponding to a Volcanic Explosivity Index (VEI) ≥5 (Newhall and Self, 1982)): H2 (~3.9 cal ka BP; Naranjo and Stern, 1998), H1 (~7.6 cal ka BP; Stern, 1991; Naranjo and Stern, 1998; Prieto et al., 2013), and Ho (~17.4 cal ka BP; Weller et al., 2014). Volcán Hudson has also had two major eruptions in modern times, a VEI 3 event in August 1971 (e.g., Tobar, 1973) and an eruption of ≥4 km^3 of tephra (VEI 5) in August 1991 (e.g., Naranjo et al., 1993; Scasso et al., 1994; Wilson et al., 2011), which was the second largest in the southern Andes in the 20^{th} Century (Naranjo and Stern, 1998). Constraining the history of explosive eruptions of Volcán Hudson is of particular importance for local and regional volcanic hazard assessment (e.g., Amigo, 2013), especially given the evidence of magma accumulation since 1991, causing the VEI 1–2 eruption in October–November 2011 (Global Volcanism Program, 2013; Delgado et al., 2014).

Due to its location at the northern margin of the southern westerly wind belt, and proximity to where the Antarctic Circumpolar Current is intersected by South America (Kilian and Lamy, 2012), numerous palaeoenvironmental records have been investigated in the region around Volcán

Hudson. These have been obtained from peat bogs (e.g., Markgraf et al., 2007) and lake (e.g., Haberle et al., 2000; Bertrand et al., 2012; Elbert et al., 2013) and marine (e.g., Siani et al., 2010) sediments; most of these contain multiple tephra layers (Fontijn et al., 2014). These tephras are an invaluable tool for dating and synchronising such records (e.g., Davies et al., 2012; Blockley et al., 2014). This is exemplified by Siani et al. (2013), who correlated tephras between lake and marine sediment cores to calculate marine surface radiocarbon reservoir ages, and thus infer enhanced Southern Ocean upwelling during deglaciation. Some Volcán Hudson tephra units have the potential to be used for tephrochronology on a continental scale. H1 tephra is preserved as visible layers in various environments in southernmost Patagonia (up to ~1000 km from the volcano; Stern, 1991, 2008; Fontijn et al., 2014). In addition, visible and crypto- (not visible to the naked eye) tephra horizons in ice cores from both East (e.g., Talos Dome: Narcisi et al., 2012) and West (e.g., Siple Dome: Kurbatov et al., 2006) Antarctica have been tentatively attributed to eruptions of Volcán Hudson. The high frequency of explosive eruptions from Volcán Hudson relative to other volcanoes in the southern Andes means that accurately constraining its tephrostratigraphy is particularly important for palaeoenvironmental research in this region. It is also essential to the investigation of temporal variations in eruption frequency, and of potential controls on this, such as deglaciation (Watt et al., 2013a; Rawson et al., 2016) or seismicity (Watt et al., 2009).

Fontijn et al. (2014) highlight the limitations of the tephrostratigraphic record in southern South America, and the difficulties in robustly correlating tephra units. Approximate age correspondence has been the basis of eruption attribution or tephra unit correlation in some studies, but this method is particularly unreliable for Volcán Hudson, because its high eruption frequency means there is a greater risk of miscorrelation. In most cases, the age constraints are bounding radiocarbon dates with an often poorly defined age offset from the tephra layer, rather

than dates of material associated with the tephra unit itself, which in any case may not represent the eruption age. Furthermore, lake sediments in this region are liable to contain older terrestrial organic matter, resulting in erroneously old bulk sediment radiocarbon ages: bulk sediment from three small lakes <100 km east or south of Volcán Hudson has been found to have radiocarbon ages ~300–1100 years greater than incorporated carbon (Bertrand et al., 2012). Different organic fractions of peat can also give distinct radiocarbon dates, up to 1500 years apart (e.g., Brock et al., 2011). Tephrochronology is an invaluable tool to identify and correct for such effects (e.g., Siani et al., 2001, 2013). However, there is potential for tephra units to have been remobilised by various processes in all environments in this region (e.g., Wilson et al., 2011; Wastegård et al., 2013; Bertrand et al., 2014).

Although the tephrostratigraphy of Volcán Hudson is well-constrained in comparison to that of many other southern Andean volcanoes, its accuracy and utility for tephrochronology are compromised by a paucity of thorough tephra characterisation. Robust matrix glass compositional data are particularly important, as this is the primary tool for correlating and fingerprinting, especially distal deposits (e.g., Smith et al., 2011a; Matthews et al., 2012; Fontijn et al., in review). The major element compositions of matrix glass of tephras erupted by most southern Andean volcanoes, and in some cases from individual eruptions, are distinct (e.g., Watt et al., 2011; Rawson et al., 2015; Fontijn et al., in review). Here we report analyses of matrix glass (and some of whole rock) composition of tephras preserved in important medial terrestrial sections, and compile data on occurrences of tephra previously attributed to eruptions of Volcán Hudson, to produce an updated tephrostratigraphic framework with revised age constraints and composition data for most eruptions.

4.2. Volcán Hudson

4.2.1. Geological setting and geochemistry

Volcán Hudson is the southernmost stratovolcano in the SVZ, which is a product of the subduction of the oceanic Nazca plate beneath the continental South American plate (Stern, 2004); it is the closest volcanic centre to (~300 km east of) the triple junction between these plates and the Antarctic plate (Figure 4.1). Subduction of the Chile Rise at this point has been inferred to result in a slab window, to explain the gap in arc volcanism separating the SVZ from the AVZ (e.g., Gutiérrez et al., 2005; Stern et al., 2007). The southern sector of the SVZ (SSVZ, 42–46°S; Stern, 2004) is characterised by eruption of predominantly high-Al and tholeiitic mafic magmas (e.g., Stern et al., 2007; Cembrano and Lara, 2009); more silicic magma compositions are scarce except at particular volcanic centres (e.g., Chaitén, Melimoyu, and Yanteles volcanoes: Watt et al., 2011, 2013b; Stern et al., 2015), including Hudson (e.g., Weller et al., 2014). The silicic magmas erupted generally contain hydrous minerals (hornblende and, rarely, biotite) (Stern et al., 2007), except for those from Volcán Hudson (Kratzmann et al., 2010). The extent of magma differentiation and the location of volcanism are apparently considerably influenced by tectonics: 'compressive' local regimes are associated with greater magma differentiation than 'extensional' ones, with the most primitive magmas having been erupted at monogenetic cones along the arc-parallel Liquiñe-Ofqui fault zone (LOFZ, marked on Figure 4.1) (e.g., López-Escobar et al., 1995; Cembrano and Lara, 2009). All the major volcanic centres in the SSVZ lie on or to the west of the LOFZ, except Volcán Hudson (e.g., Cembrano and Lara, 2009).

By virtue of its unique location relatively close to the slab window and to the east of the LOFZ, Volcán Hudson has an eruptive history and geochemistry distinct from the rest of the SSVZ. It is perhaps unusually long-lived in comparison to other SSVZ volcanoes, having been active for at

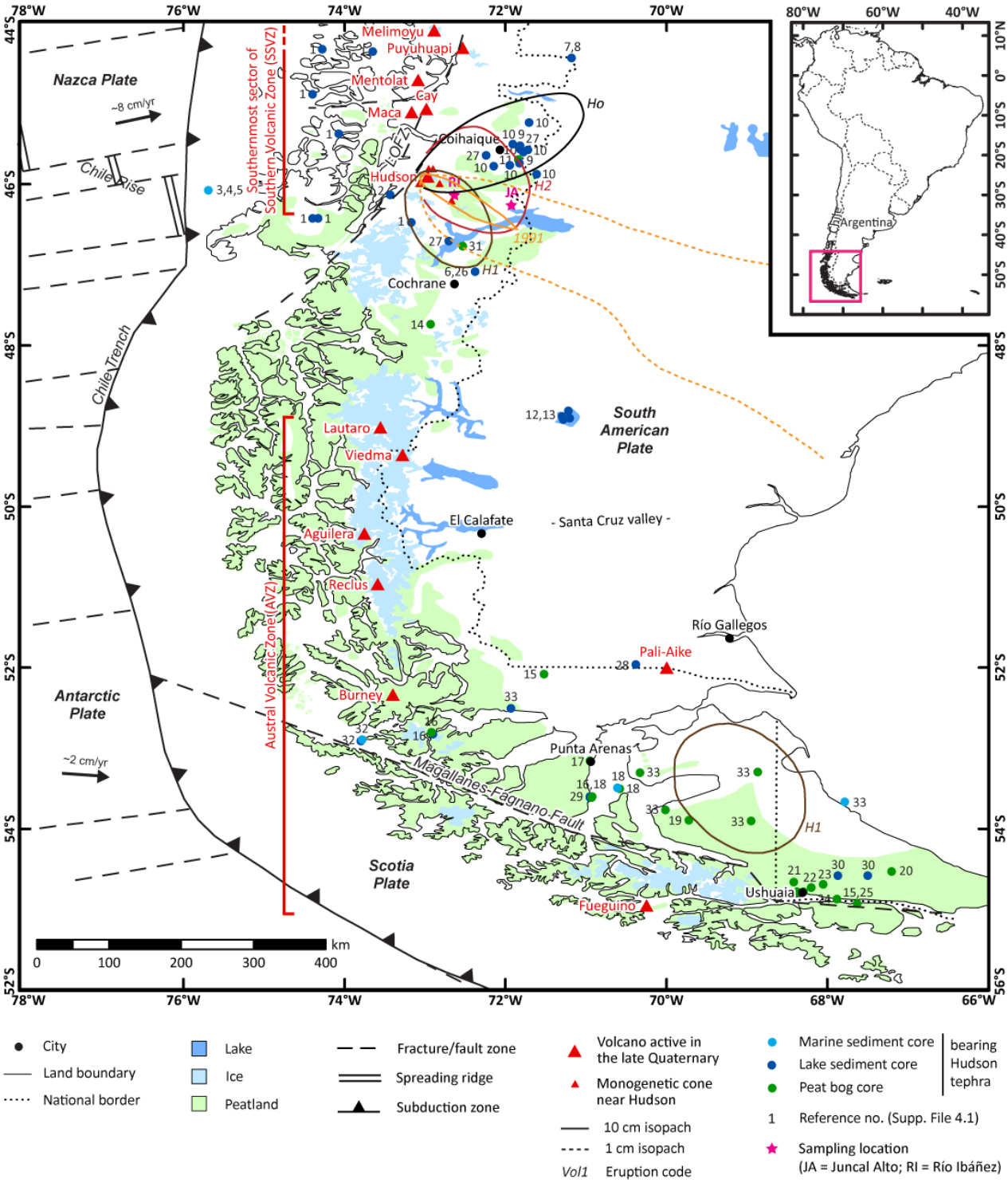

Figure 4.1 Map of southernmost Chile and Argentina (area indicated by pink box on the inset map), modified from Fontijn et al. (2014). The locations of the volcanoes in the Austral Volcanic Zone (AVZ) and southernmost part of the Southern Volcanic Zone (SVZ) for which there is evidence of activity since local deglaciation (Fontijn et al., 2014) are shown, together with some regional tectonic features (Bird, 2003; Stern, 2004; Matthews et al., 2011) and the distribution of some environments amenable to tephra preservation. Locations where tephra layers attributed to Volcán Hudson have been identified in palaeoenvironmental records are also mapped, classified by environment. The reference numbers refer to those in Supplementary File 4.1. The isopach contours shown are those published for the largest (≥1 km^3 tephra; VEI ≥5) explosive eruptions of Hudson (Scasso et al., 1994; Naranjo and Stern, 1998; Weller et al., 2014). The geographical data are from Natural Earth (www.naturalearthdata.com), except the peatland extent, which is from Yu et al. (2010).

least the past ~0.5 My (Orihashi et al., 2004). All explosive eruption deposits that have been characterised and attributed to Volcán Hudson (outlined in Section 4.2.2) date from <20 ka; the limited data available on its effusive eruption history (the products of which are largely obscured by ice or vegetation) are described by Orihashi et al. (2004) and Gutiérrez et al. (2005). The high frequency of explosive eruptions relative to those known for other SSVZ volcanoes (Naranjo and Stern, 1998, 2004) is postulated to result from higher melt production beneath Volcán Hudson due to its comparative proximity to the subducting oceanic ridge (Stern et al., 2007). The distinct geochemistry and lower eruption frequency of the stratovolcanoes that are next closest to the ridge, Cay and Maca volcanoes, is consistent with this (D'Orazio et al., 2003; Naranjo and Stern, 2004; Gutiérrez et al., 2005). Compared to other SSVZ volcanoes, Volcán Hudson has elevated TiO_2, Fe-oxide, Na_2O, K_2O, and incompatible trace element (large-ion lithophile (LILE), high field strength (HFSE), and rare earth (REE) element) concentrations at a given SiO_2 concentration, and lower LILE/HFSE (e.g., La/Nb) ratios, but retains a calc-alkaline signature (e.g., Gutiérrez et al., 2005; Kratzmann et al., 2010; Stern et al., 2015). Magmas erupted from the monogenetic centres <50 km from Volcán Hudson (marked on Figure 4.1) are generally more primitive, but with similar major and trace element compositional trends (Gutiérrez et al., 2005).

The genesis, chemistry, and petrology of the magmas erupted in the four VEI ≥5 explosive events of Volcán Hudson have been described by Kratzmann et al. (2009, 2010) and Weller et al. (2014). The deposits of two of these eruptions, Ho (Weller et al., 2014) and 1991 (Kratzmann et al., 2009), have a bimodal composition; the latter erupted chemically distinct magmas in different phases, with tephra from each phase being dispersed in different directions (Scasso et al., 1994; Kratzmann et al., 2009). This demonstrates that in some instances, a single eruption of Volcán Hudson may deposit tephra with distinct compositions in different distal locations.

4.2.2. Previous work on explosive eruption history

Figure 4.1 shows the locations (classified by environment) where tephra layers attributed to eruptions of Volcán Hudson have been reported in palaeoenvironmental records (updated from Fontijn et al., 2014), and published isopach contours for the four eruptions of VEI ≥5. Supplementary Table 4.1 lists all these tephra layers in addition to those identified in terrestrial sections, including their physical characteristics and age constraints (if these data are available). Chemical composition data for all Volcán Hudson tephras that may be used for correlation (i.e., matrix glass, mineral, and whole rock compositions) are compiled in Supplementary Table 4.2. The tephrostratigraphy derived from these data (plus new data described in Section 4.1) is summarised in Table 4.1. Tephras in this table are classified by the level of confidence with which they can be attributed to the specified eruption and/or correlated with one another, and/or whether they are primary deposits, on the basis of analysis of the previous work described in Section 4.4.2.

4.2.2.1. Historical eruptions

Volcán Hudson was not recognised as a volcano until 1970 (Fuenzalida and Espinosa, 1973); one historical eruption prior to this date, in 1886, is attributed to Volcán Hudson but incorrectly stated to have been in 1891 by Siebert et al. (2010). This derives from a citation by Salmi (1941) of an account by Burmeister (1891) of considerable ashfall in the Santa Cruz valley (Argentine Patagonia) dispersing southwards to Punta Arenas in May 1886. This account was quoted but incorrectly stated to have been in 1891 by Caldenius (1932); the southward dispersal suggests a source volcano to the north, consistent with but not definitive of Volcán Hudson being the source.

The deposits of the 1991 eruption have been characterised more thoroughly than any other Volcán Hudson tephra (e.g., Scasso et al., 1994; Kratzmann et al., 2009). The rapid rate of aeolian

Table 4.1 Summary of the tephrostratigraphy of Volcán Hudson, showing that from previous work and additions and revisions made by this study.

Eruption				Soil and peat sections[a]						
Name	Estimated magnitude	Published age (a BP; 1σ)	Revised model age (cal a BP; 1σ)	Naranjo and Stern (1998)		Stern (1991; 2008)	Markgraf et al. (2007)	Kratzmann et al. (2009)	This study	
				Various sections	Juncal Alto	Various sections	Mallín Pollux	Various sections	Río Ibáñez	Juncal Alto
1991	≥5.5*	-41		H3				1991	RI4	JA12
1971	~3	-21			T9					
[1886]	~3	64								
T8	~3	~210[1]	100 ± 95		T8					JA11
T7	~3	610 ± 90[1]	974 ± 73		T7					
HW7	~3	~1560[2]	1271 ± 268							
T3 (Elb.)		~1860[3]								
T4 (Elb.)		~2000[3]								
JA10	~3		1238 ± 207							JA10
T6	~4	2030 ± 90[1]	2081 ± 145	T6	T6					JA9
TD216	~3	2355 ± 54[4]								
HW6	~3	~2740[2]	1967 ± 300							
JA8	~3		2310 ± 133							JA8
JA7	~3		2626 ± 294							JA7
JA6	~3		3085 ± 331							JA6
JA5	~3		3454 ± 230							JA5
H2	>6.0*	3840 ± 125[1]	3877 ± 112	H2	T5	H2	H2	H2	RI3	JA4
T4	~3	4370 ± 90[1]	4284 ± 252		T4					JA3
T3	~3	7190 ± 120[1]	5958 ± 1296		T3					[JA2]
H1	>6.1*	7750 ± 95[5]	7596 ± 57	H1	T2	H1		H1	RI2	JA1
T1	~3	7780 ± 70[1]	7706 ± 75		T1					
RI1	~3		7906 ± 196						RI1	
~~TL2~~		~10750[6]								
HW3	~3	~11060[2]	9812 ± 1692							
HW2	~3	~13890[2]	13211 ± 282							
HW1		~14560[2]								
Ho	>6.2*	17370 ± 70[7]	17383 ± 122				11.3 m			
~~TL6~~		~17350[6]								
~~TL7~~		~18750[6]								
~~TL8~~		~18900[6]								
~~TL9~~		~19450[6]								
~~TL10~~		~19600[6]								
~~TL11~~		~19660[6]								
~~TL12~~		~19860[6]								

(continued on next page)

Table 4.1 *(continued from previous page)*

Eruption	Marine core[a]	Ice cores			Lake sediment cores[a,b]					
	Carel et al. (2011); Siani et al. (2013)	Narcisi et al. (2005; 2012)		Kurbatov et al. (2006)	Elbert et al. (2013)		Stern et al. (2013)			Miranda et al. (2013); Weller et al. (2014)
	Off Taito Peninsula	EPICA-Dome C	Talos Dome	Siple Dome	Escondida	Castor	Edita	Pepa	Maldonado	Various cores[c]
1991										
1971										
[1886]										
T8										
T7										
HW7	~~TL1~~									
T3 (Elb.)					*T3*	*T3*				
T4 (Elb.)					*T4*	*T4*				
JA10										
T6	[279cm]		*TD193*		*T6*	*T6*				
TD216			*TD216*							
HW6										
JA8										
JA7										
JA6										
JA5										
H2	*279 cm*					[T8]	H2			H2
T4										
T3										
H1							H1	H1	H1	
T1										
RI1										
~~TL2~~	~~TL2~~									
HW3	~~TL3~~	*339.5 m*		*SDMA-9008*						
HW2	~~TL4~~									
HW1	~~TL5~~									
Ho										Ho
~~TL6~~	~~TL6~~									
~~TL7~~	~~TL7~~									
~~TL8~~	~~TL8~~									
~~TL9~~	~~TL9~~									
~~TL10~~	~~TL10~~									
~~TL11~~	~~TL11~~									
~~TL12~~	~~TL12~~									

(continued on next page)

Table 4.1 *(continued from previous page)*

Eruption	Lake sediment cores[a,b]								
	Stern et al. (2015)	Haberle and Lumley (1998)							
	Shaman	Facil	Oprasa	Lincoln	Lofel	Miranda[c]	Marcelo	Six Minutes	Stibnite
1991									
1971									
[1886]									
T8									
T7									
HW7			*Opr-8*			*Mir-3*	[Mar-2]	*Six-4*	[Stb-4]
T3 (Elb.)									
T4 (Elb.)									
JA10									
T6									
TD216									
HW6			[Opr-7]	[Lin-4]		*Mir-2*	[Mar-1]	[Six-3]	[Stb-3]
JA8									
JA7									
JA6									
JA5									
H2						[Mir-1]			
T4									
T3									
H1			*Opr-5*						
T1									
RI1									
~~TL2~~			*Opr-4*						
HW3		*Fac-2*	*Opr-3*	*Lin-3*	[Lof-4]			[Six-2]	*Stb-2*
HW2				*Lin-2*	*Lof-2/3*			[Six-1]	[Stb-1]
HW1		*Fac-1*	*Opr-1*	*Lin-1*	*Lof-1*				
Ho	v								
~~TL6~~									
~~TL7~~									
~~TL8~~									
~~TL9~~									
~~TL10~~									
~~TL11~~									
~~TL12~~									

~~unit~~ = not a primary tephra unit; *unit* = unjustified attribution/correlation; [unit] = possible attribution/correlation.

* Estimated from published volume estimates of Scasso et al. (1994), Naranjo and Stern (1998), and Weller et al. (2014).
[1] Fontijn et al. (2014) after Naranjo and Stern (1998); [2] Haberle and Lumley (1998); [3] Elbert et al. (2013); [4] Narcisi et al. (2012); [5] Prieto et al. (2013); [6] Carel et al. (2011); [7] Weller et al. (2014).
[a] Excluding cores and sections in southern Patagonia that only contain tephra attributed to Volcán Hudson from the H1 eruption; these are included in Supplementary Table 4.1.
[b] Excluding cores that do not attribute any reported tephra layers to a specific eruption, e.g. Bertrand et al. (2012) and Blockley (2012); these are included in Supplementary Table 4.1.
[c] Additional tephra units in these cores are likely originate from Volcán Hudson, but insufficient published data are available to verify.

remobilisation and erosion of these deposits (Scasso et al., 1994; Wilson et al., 2011) demonstrates that even tephra from large eruptions of Volcán Hudson is likely to be poorly preserved beyond proximal densely vegetated areas and peat and lake sediment records. Tephra deposits from the VEI 3 eruption in 1971 were only identified years after the event in one section ~90 km from Volcán Hudson (at Juncal Alto: Naranjo and Stern, 1998), suggesting that other tephra units preserved in medial locations represent eruptions of at least comparable magnitude.

4.2.2.2. Prehistoric eruptions

The two largest Holocene eruptions of Volcán Hudson, H1 and H2, were identified by Stern (1991), who described the notably thick deposits of the former in southern Patagonia (>10 cm in Tierra del Fuego, ~900 km SSW of the volcano). These eruptions were characterised further by Naranjo and Stern (1998) from road-cuts within ~100 km from the volcano; they also found six additional prehistoric tephra layers in one section, described in Section 4.3.1. The age and physical and chemical characteristics of the H1 and H2 eruptions were further constrained by subsequent work on deposits around Volcán Hudson (Kratzmann et al., 2009, 2010), Cochrane, to the south (Stern et al., 2013), and southernmost Patagonia (Stern, 2008; Prieto et al., 2013). The earlier large Ho eruption was discovered in and characterised from sediment cores of several lakes ~100 km NE of the volcano (Weller et al., 2014), but there are no known terrestrial deposits. Many additional tephra layers have been recognised in these lake sediment cores (Miranda et al., 2013; Weller et al., 2014), and others from this region (e.g., Bertrand et al., 2012; Blockley, 2012), but published data are not yet available; many of those tephras likely originate from Volcán Hudson (e.g., Blockley, 2012; Weller et al., 2014). This is supported by whole rock composition analysis suggesting Volcán Hudson as the source of some of the several tephra units younger than H2 identified in sediment cores from two lakes in the same area (Elbert et al., 2013).

Haberle and Lumley (1998) identified five new tephra units (attributed to Volcán Hudson) in sediment cores from eight post-glacial lakes 50–200 km NW–SW of the volcano, which were each correlated between multiple lakes by the composition of their matrix glass. The sediment core from the most proximal lake contained 22 tephra layers (mostly uncharacterised), spanning the last 5.5 ky (Haberle et al., 2000). Some of the correlated units have also been correlated with tephras in a marine sediment core offshore of this area, in which several other tephra units dating from 11–20 ka were recognised (Siani et al., 2010, 2013; Carel et al., 2011). Tephras in three Antarctic ice cores have been attributed to Volcán Hudson (Narcisi et al., 2005, 2012; Kurbatov et al., 2006); one of these, in two of the cores, is correlated with one of the units identified by Haberle and Lumley (1998). These tephra occurrences and correlations are further discussed and reviewed in Section 4.4.2.

4.3. Methods

4.3.1. Field sampling

To determine the composition of the Volcán Hudson tephra deposits previously identified in terrestrial sections, we sampled those in two key sections described by Naranjo and Stern (1998) (shown in Figure 4.2): 1) a ~5 m high road-cut close to Río Ibáñez, one of the closest accessible sections to the volcano, ~40 km to the southeast (site 94T-45 in Naranjo and Stern (1998); 46.1231°S, 72.5603°W; Figure 4.1), which contains relatively thick and well-preserved deposits of H1, H2, and the 1991 eruption (Figure 4.2a); 2) a ~1.5 m deep trench in a peat bog at Juncal Alto, ~90 km ESE of the volcano (site 94T-49/59 in Naranjo and Stern (1998)). The latter was the most complete terrestrial record of Volcán Hudson eruptions known, containing 10 tephra layers younger than 9230 ± 197 cal yr BP (calibration by this study), including from the H1, H2, 1971, and 1991 eruptions (Figure 4.2b ii); it is the type section of all the other tephra layers preserved. The new section sampled for this study (at 46.2515°S, 71.9438°W; Figure 4.1) contains 12 distinct tephra units (Figure 4.2b iii), with more tephras above H2 (i.e., after ~3.9 ka) than recognised by Naranjo and Stern (1998). For both the sections, vegetation and weathered tephra were cleared before each visible tephra layer was sampled from top to bottom (to ensure a representative sample), or sub-sampled if sub-units were apparent. Samples for radiocarbon dating were not taken from either; the Juncal Alto section was pervaded by a network of young roots, inhibiting reliable carbon sampling, whilst the ages of the main units in the Río Ibáñez section have been constrained previously from numerous sites (Supplementary Table 4.1). A sample of the greenish tephra reported across southernmost Patagonia and Tierra del Fuego and attributed to the H1 eruption (no. 90-22 collected by C. Stern) (Stern, 1991, 2008) was also obtained for glass composition analysis, to verify its correlation with the proximal deposits.

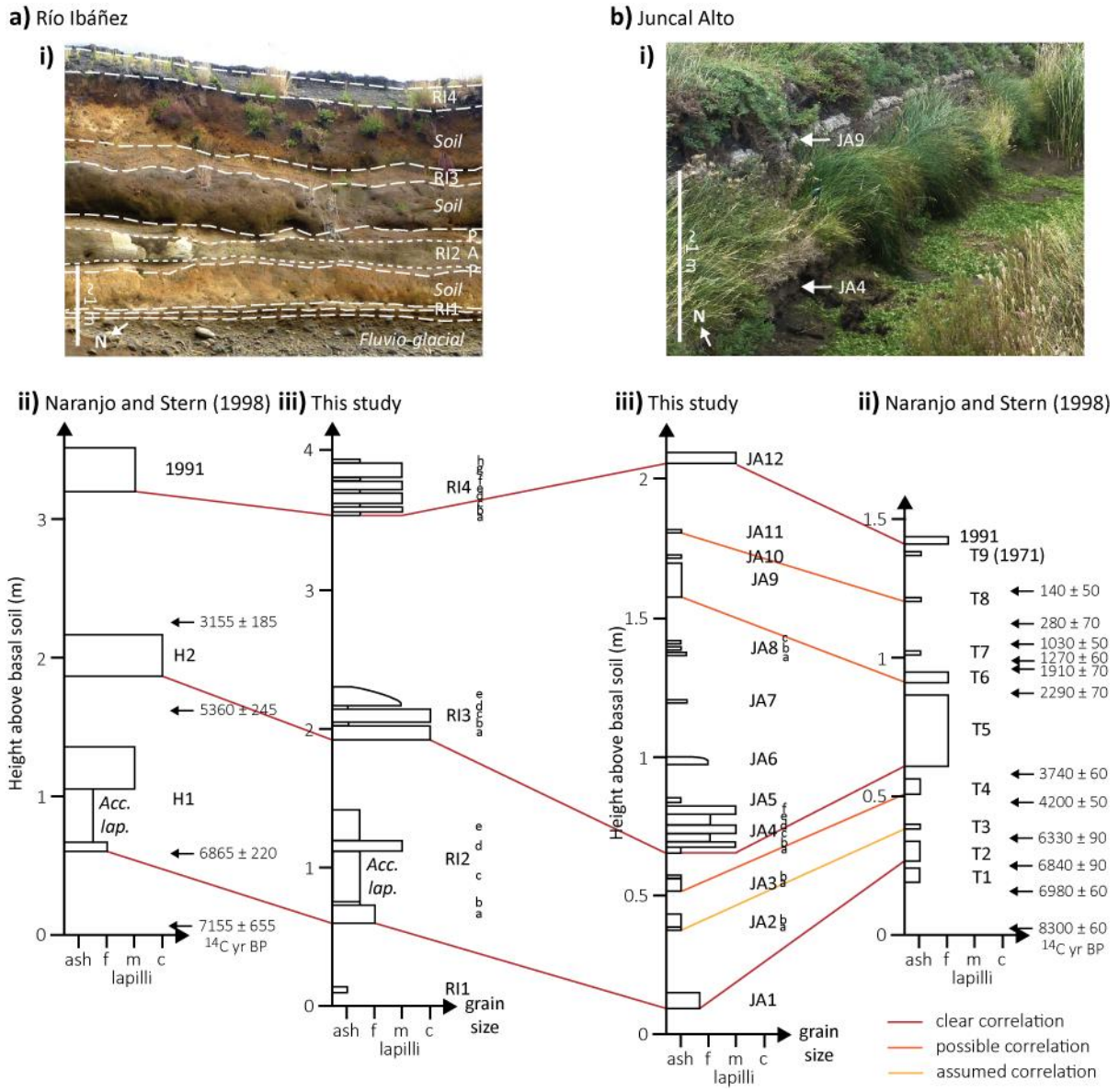

Figure 4.2 Stratigraphy of the two sections from which tephra was sampled for analysis in this study (marked by pink stars on Figure 4.1), **(a)** a road-cut near Río Ibáñez and **(b)** a partially excavated peat bog at Juncal Alto. **(i)** Photographs of parts of the sections, with major tephra units indicated (A = accretionary lapilli-rich layer; P = pumice-rich layer). **(ii)** Stratigraphy of sections from these locations in Naranjo and Stern (1998) (with uncalibrated radiocarbon dates). **(iii)** Stratigraphy of the sections sampled for this study. Correlations between sections are based upon the stratigraphy and whole rock and glass composition of the tephra units, discussed in Section 4.4.1.

4.3.2. Geochemical analysis

4.3.2.1. Matrix glass major element oxides

Tephra samples were partially crushed in an agate pestle and mortar, then wet sieved to remove the <80 μm fraction and dried at 40°C, before being mounted in epoxy resin stubs and polished to expose sectioned tephra shards. Si, Na, K, Ca, Mg, Ti, Al, Fe, Mn, and P oxide contents of the matrix glass of individual shards were measured using a wavelength-dispersive electron microprobe (WDS-EMP). Some data were collected on a JEOL JXA8600 with four spectrometers and SAMx software, at the Research Laboratory for Archaeology and the History of Art, University of Oxford, and other data on a JEOL JXA8800R with four spectrometers and JEOL software, at Begbroke Science Park, University of Oxford. A defocused 10 μm diameter beam with a 6 nA current and 15 keV accelerating voltage were used for all analyses, to minimise alkali element migration (e.g., Morgan and London, 2005; Humphreys et al., 2006) whilst maintaining an acceptable level of precision. On-peak count times were 10 s for Na, 40 s for Mn, 60 s for P, and 30 s for all other elements, and Na, Al, and Si were analysed first to maximise accuracy. Both EMPs were calibrated using a set of mineral standards, and matrix corrections were applied using the PAP model (Pouchou and Pichoir, 1984).

Basalt (GOR132-G), dacite (StHs6/80-G), and rhyolite (ATHO-G) MPI-DING reference glasses (Jochum et al., 2006) were analysed during all analytical runs as secondary standards to check accuracy, consistency, and precision. These data are presented in Supplementary Table 4.3a and Supplementary File 4.2 for the main runs; they verify that the analyses in each run on both EMPs are similarly accurate, i.e. the mean measured values for the secondary standards are within ± 2σ of the preferred values, but within ± 1σ for most elements. However, there is some variation in precision between runs, particularly for the minor oxides (MnO and P_2O_5). Less than 5% of all

analyses had oxide totals of <95 or >102 wt %; these were rejected, along with those with anomalously high CaO and low FeO_T or vice versa, which likely reflect partial analysis of plagioclase or Fe-oxide microlites or microphenocrysts respectively. The high microlite and/or (micro)phenocryst content and/or vesicularity of the majority of the tephras analysed limited the exposure of >10 μm diameter areas of matrix glass for analysis. All glass composition data are normalised to 100% (anhydrous) when presented, with their total Fe concentration reported as FeO; all the raw data are provided in Supplementary Table 4.4. 1σ relative standard deviations are shown on plots of these data, calculated from the analyses of the secondary standard of composition closest to those of the samples.

4.3.2.2. Whole rock major element oxides and trace elements

Selected pumice clasts from specific sub-units of the H1, H2, and 1991 eruption deposits in the Río Ibáñez section were cleaned in an ultrasonic bath of deionised water and dried at 40°C, before being crushed and powdered using an agate pestle and mortar and ball mill, respectively. For major element composition analysis, the powdered samples were dried at 110°C for 2 hours and then ignited at 750°C for 2 hours to determine the mass loss on ignition (LOI), before an aliquot was fused with lithium metaborate and tetraborate (ratio 5:1) flux to form glass discs using the method of Ramsey et al. (1995). The samples prepared included duplicates and a secondary standard, to verify precision and accuracy respectively. The discs were analysed by X-ray fluorescence (XRF; Fitton, 1997) using a PANalytical Axios Advanced XRF spectrometer at the Department of Geology, University of Leicester, with a variety of standards for calibration.

For minor and trace element composition analysis, known masses of ~100 mg of the powdered samples were heated at 100°C for 24 hours in 4 ml 16M HNO_3 and 2 ml HF in a Teflon vial, producing solutions that were evaporated and then re-dissolved in 2 ml 16M HNO_3 twice, before

being dissolved in 8 ml 4M HNO_3 and then diluted using MilliQ water to known masses of ~15 ml ~5% HNO_3. Aliquots of these solutions were then taken, to which 200 µl of a Rh and Re spike solution was added as an internal standard (to correct for any instrumental drift), before additional dilution in accordance with the expected concentration (minor or trace) of the elements being analysed. Standards to correct for matrix effects were prepared by taking aliquots of three samples spanning the expected compositional range, spiking them with all the elements being analysed, and then diluting to a range of known concentrations. These were all analysed using a Thermo-Finnegan Element 2 inductively coupled plasma mass spectrometer (ICP-MS) at the Department of Earth Sciences, University of Oxford. Nine scans were measured for each element to obtain average concentrations and check analytical precision. Washes between samples were periodically analysed to check for memory of prior analyses. The raw data were corrected for drift and signal suppression, and then for dilution to calculate element concentrations.

Blank, duplicate, and U.S. Geological Survey standard andesite AGV-2 (Wilson, 1998) and basalt BHVO-2 (Wilson, 1997) samples were also prepared and analysed using the same procedures, to check for contamination, precision, and accuracy respectively; these data are provided in Supplementary Table 4.3b. At least one of the secondary standard analyses are within 2σ of the preferred value for each element, except V (data rejected); the analyses outside this range are almost all within 3σ. The acid digestion blanks were found to contain orders of magnitude less of each element than the samples, except for Cu, which at <2 ppm was >20% of that in the pumice samples, so these data were discarded. Wash analyses indicated that high Zr concentrations were not consistently washed out prior to the next analysis, so these data were also rejected.

4.3.3. Reanalysis of tephra unit correlations and eruption ages

To reliably correlate the tephra layers we identify with those reported in the literature, we consider their physical characteristics and stratigraphic constraints, and compare matrix glass composition data; the same approach is taken to revise correlations made by prior work. Age estimates for some eruptions are obtained using Bayesian analysis to take the uncertainties (such as those outlined in Section 4.1) into account (e.g., Blockley et al., 2008). Published radiocarbon dates (listed in Supplementary Table 4.1) are (re)calibrated or incorporated into 'Sequence' models in OxCal v.4.2.4 (Bronk Ramsey, 2009a), using the SHCal13 atmospheric calibration curve (Hogg et al., 2013). The OxCal 'Sequence' model uses Bayesian statistics to combine stratigraphic (i.e. prior) information with radiocarbon dates and calibration (i.e. probabilistic data) using a Markov chain Monte Carlo sampling method to calculate probability density functions of the ages of the tephra units (Bronk Ramsey, 2009a; Bronk Ramsey and Lee, 2013). An outlier function was applied to all dates in each age model to identify and disregard any that are incongruous (Bronk Ramsey, 2009b), e.g. due to a reservoir effect.

4.4. Results and discussion

4.4.1. Eruptions identified in terrestrial sections

In medial terrestrial sections, only deposits of the 1991, H2, and H1 eruptions have been identified, except for at Juncal Alto and Lago Elizalde (Naranjo and Stern, 1998). Figure 4.2 presents the stratigraphies of the two sections sampled, along with the stratigraphies of the sections from the same locations from Naranjo and Stern (1998). The major element composition of matrix glass from at least one sub-unit of each visible tephra in both sections was analysed; these data are summarised in Table 4.2 and Figure 4.3. All the units in these sections are calc-alkaline, with glass compositions ranging from basaltic trachyandesite to trachydacite–rhyolite, but only two (JA8 and JA9) are of predominantly andesitic–trachyandesitic composition.

Figures 4.3c to 4.3e show matrix glass composition data for each tephra unit in stratigraphic order, to reveal more clearly the compositional range within each unit and the temporal variation. Most (sub-)units are relatively homogeneous in composition, with a standard deviation of ± <1 wt % SiO_2 (Table 4.2), not much greater than that of the secondary standard analyses (± 0.68–0.78 wt % SiO_2; Supplementary Table 4.3a). H1 and the basal ash of the H2 deposits (e.g. JA1 and JA4a, respectively) have a relatively minor more mafic component, whilst JA2a and JA9 have uniformly distributed, comparatively wide compositional ranges (1σ ± 1.77 and 1.93 wt % SiO_2 respectively; Table 4.2 and Figure 4.3). JA8b, the middle sub-unit of three thin, closely-spaced tephras (Figure 4.2b iii) has a bimodal composition very similar to a combination of those of the tephras immediately above and below (Figure 4.3). The mafic unit JA5 has a minor silicic component very similar in composition to H2 (Figure 4.3); the base of this unit is only 2 cm above the H2 deposits (Figure 4.2b iii) and bimodal magmas with a predominantly mafic component are uncommon, so it is possible that this silicic component is reworked from the H2 deposits. The mafic component

Table 4.2 Matrix glass compositions of Volcán Hudson tephra samples analysed by this study.

Eruption		1991		T8?	(undefined)	(undefined)	(undefined)				(undefined)	T6?	(undefined)
Tephra		RI4g	JA12	JA11	JA10	JA9	JA8c	JA8b pt 1	JA8b pt 2	JA8a	JA7	JA6	JA5 pt 1
n		24	24	24	23	24	20	12	11	20	20	24	16
Glass composition (wt %)	SiO_2	63.01 ± 0.49	63.98 ± 0.79	64.25 ± 0.39	52.07 ± 0.49	56.71 ± 1.93	60.64 ± 0.57	60.32 ± 0.39	55.61 ± 0.49	54.48 ± 0.49	52.39 ± 0.53	53.50 ± 0.52	52.85 ± 0.64
	TiO_2	1.27 ± 0.05	1.22 ± 0.06	1.10 ± 0.05	2.32 ± 0.12	1.70 ± 0.17	1.51 ± 0.08	1.46 ± 0.05	1.92 ± 0.19	1.91 ± 0.17	2.63 ± 0.19	1.66 ± 0.09	1.67 ± 0.15
	Al_2O_3	16.50 ± 0.14	16.57 ± 0.20	16.55 ± 0.17	15.69 ± 0.32	15.72 ± 0.65	16.18 ± 0.29	16.37 ± 0.13	14.65 ± 0.83	14.75 ± 0.65	14.05 ± 0.37	15.35 ± 0.37	15.48 ± 0.58
	FeO_T	5.25 ± 0.28	5.00 ± 0.24	4.72 ± 0.19	10.48 ± 0.34	8.73 ± 0.86	6.66 ± 0.39	6.62 ± 0.31	10.09 ± 0.68	10.26 ± 0.48	12.12 ± 0.51	9.84 ± 0.37	9.86 ± 0.60
	MnO	0.18 ± 0.04	0.17 ± 0.05	0.16 ± 0.05	0.20 ± 0.05	0.18 ± 0.05	0.16 ± 0.05	0.15 ± 0.04	0.19 ± 0.05	0.20 ± 0.05	0.22 ± 0.04	0.18 ± 0.05	0.18 ± 0.08
	MgO	1.57 ± 0.10	1.43 ± 0.06	1.30 ± 0.08	4.41 ± 0.11	3.47 ± 0.07	2.28 ± 0.13	2.32 ± 0.12	3.69 ± 0.24	4.23 ± 0.37	3.93 ± 0.39	4.92 ± 0.18	4.95 ± 0.33
	CaO	3.33 ± 0.23	3.06 ± 0.16	2.83 ± 0.12	8.25 ± 0.13	6.75 ± 1.17	4.74 ± 0.23	4.89 ± 0.22	7.37 ± 0.30	8.13 ± 0.35	8.06 ± 0.32	8.99 ± 0.22	9.23 ± 0.29
	Na_2O	5.88 ± 0.19	5.50 ± 0.91	6.07 ± 0.14	4.53 ± 0.20	4.35 ± 0.37	4.98 ± 0.40	5.05 ± 0.19	4.09 ± 0.18	3.92 ± 0.22	4.25 ± 0.23	3.83 ± 0.23	3.83 ± 0.24
	K_2O	2.58 ± 0.07	2.69 ± 0.08	2.69 ± 0.07	1.27 ± 0.07	1.70 ± 0.33	2.24 ± 0.16	2.19 ± 0.08	1.65 ± 0.15	1.42 ± 0.11	1.53 ± 0.12	1.14 ± 0.11	1.49 ± 0.16
	P_2O_5	0.42 ± 0.03	0.38 ± 0.05	0.33 ± 0.03	0.77 ± 0.09	0.69 ± 0.09	0.62 ± 0.06	0.63 ± 0.04	0.75 ± 0.11	0.71 ± 0.10	0.82 ± 0.07	0.57 ± 0.11	0.46 ± 0.05

Eruption		(undefined)	H2 (T5)			T4?	T3??		H1 (T2)				(undefined)
Tephra		JA5 pt 2	RI3a	J4d	J4a	JA3	JA2b	JA2a	RI2e	JA1 pt 1	JA1 pt 2	90-22	RI1
n		5	24	23	24	25	22	22	25	18	5	28	19
Glass composition (wt %)	SiO_2	69.00 ± 0.33	69.43 ± 0.47	69.11 ± 0.22	68.28 ± 1.55	67.88 ± 0.34	65.17 ± 0.96	66.31 ± 1.77	64.70 ± 0.52	64.81 ± 0.82	57.64 ± 2.10	64.04 ± 0.94	65.57 ± 0.37
	TiO_2	0.71 ± 0.04	0.68 ± 0.07	0.69 ± 0.04	0.77 ± 0.15	0.88 ± 0.06	1.16 ± 0.09	1.02 ± 0.18	1.20 ± 0.05	1.20 ± 0.06	1.67 ± 0.05	1.20 ± 0.08	1.00 ± 0.06
	Al_2O_3	15.42 ± 0.07	15.55 ± 0.22	15.57 ± 0.13	15.62 ± 0.22	15.69 ± 0.16	16.11 ± 0.32	15.77 ± 0.40	16.06 ± 0.22	15.95 ± 0.19	15.58 ± 0.17	15.79 ± 0.17	16.65 ± 0.14
	FeO_T	3.08 ± 0.11	2.86 ± 0.21	3.00 ± 0.15	3.38 ± 0.69	3.49 ± 0.11	4.61 ± 0.50	4.19 ± 0.73	4.77 ± 0.22	4.84 ± 0.31	8.02 ± 0.73	4.99 ± 0.44	3.81 ± 0.20
	MnO	0.09 ± 0.07	0.10 ± 0.05	0.11 ± 0.06	0.14 ± 0.04	0.12 ± 0.05	0.13 ± 0.05	0.15 ± 0.06	0.16 ± 0.05	0.15 ± 0.07	0.21 ± 0.05	0.16 ± 0.04	0.18 ± 0.05
	MgO	0.60 ± 0.03	0.59 ± 0.07	0.61 ± 0.02	0.76 ± 0.25	0.83 ± 0.05	1.30 ± 0.26	1.06 ± 0.30	1.39 ± 0.07	1.36 ± 0.12	3.48 ± 0.70	1.45 ± 0.22	1.09 ± 0.09
	CaO	1.60 ± 0.07	1.51 ± 0.13	1.58 ± 0.05	1.93 ± 0.59	1.98 ± 0.11	2.70 ± 0.47	2.31 ± 0.59	2.93 ± 0.16	2.90 ± 0.22	6.54 ± 1.17	2.98 ± 0.51	2.18 ± 0.14
	Na_2O	5.67 ± 0.23	5.55 ± 0.37	5.62 ± 0.18	5.50 ± 0.18	5.52 ± 0.34	5.52 ± 0.38	5.77 ± 0.21	5.65 ± 0.25	5.58 ± 0.35	4.49 ± 0.34	6.13 ± 0.30	6.37 ± 0.15
	K_2O	3.71 ± 0.05	3.61 ± 0.10	3.59 ± 0.07	3.46 ± 0.22	3.41 ± 0.11	2.95 ± 0.17	3.14 ± 0.37	2.80 ± 0.08	2.86 ± 0.12	1.79 ± 0.33	2.90 ± 0.16	2.90 ± 0.09
	P_2O_5	0.12 ± 0.01	0.12 ± 0.03	0.12 ± 0.02	0.16 ± 0.07	0.19 ± 0.03	0.34 ± 0.06	0.27 ± 0.10	0.35 ± 0.03	0.36 ± 0.05	0.57 ± 0.03	0.37 ± 0.05	0.25 ± 0.03

Composition data are normalised mean and standard deviation (1σ) values. Full unnormalised dataset in Supplementary Table 4.4.

Table 4.3 Whole rock compositions of Volcán Hudson tephra samples analysed by this study.

Eruption		1991	H2 (T5)	H1 (T2)
Tephra code		RI4g	RI3a	RI2e
Whole rock composition (wt %), by XRF	SiO_2	61.18	63.37	59.65
	TiO_2	1.325	0.916	1.384
	Al_2O_3	16.62	16.27	17.26
	$Fe_2O_{3\,T}$	6.17	4.30	6.65
	MnO	0.185	0.137	0.175
	MgO	1.75	0.94	1.80
	CaO	3.83	2.13	3.71
	Na_2O	6.10	5.42	5.42
	K_2O	2.395	3.052	2.246
	P_2O_5	0.462	0.221	0.507
	SO_3	0.049	0.021	0.049
	LOI	-0.03*	2.92	1.02
	Total	100.03	99.69	99.86
Whole rock composition (ppm), by solution ICP-MS	Sc	17.61	15.21	19.27
	Cr	<LDL	<LDL	<LDL
	Co	4.83	3.90	8.13
	Ni	<LDL	<LDL	<LDL
	Zn	108.86	88.00	104.85
	Ga	23.68	22.73	23.80
	Rb	63.72	85.34	56.64
	Sr	428.18	237.36	380.11
	Y	47.51	51.98	53.40
	Nb	18.17	23.48	22.36
	Mo	1.95	2.40	1.91
	Cs	1.28	1.80	1.23
	Ba	750.55	>UDL	751.00
	La	33.21	44.42	41.75
	Ce	95.72	122.33	113.07
	Pr	9.27	11.56	11.25
	Nd	36.50	45.80	43.74
	Sm	7.75	8.96	8.83
	Eu	2.22	2.00	2.34
	Gd	7.00	7.89	7.90
	Tb	1.08	1.19	1.22
	Dy	6.53	7.53	7.18
	Ho	1.26	1.52	1.45
	Er	3.75	4.47	4.30
	Tm	0.53	0.66	0.62
	Yb	3.66	4.58	4.15
	Lu	0.56	0.70	0.63
	Hf	6.98	11.13	9.15
	Ta	0.96	1.25	1.15
	Pb	12.53	20.17	15.97
	Th	6.87	11.37	8.40
	U	1.70	2.67	1.98

LDL = lower detection limit
UDL = upper detection limit
* Excluded from calculation of total

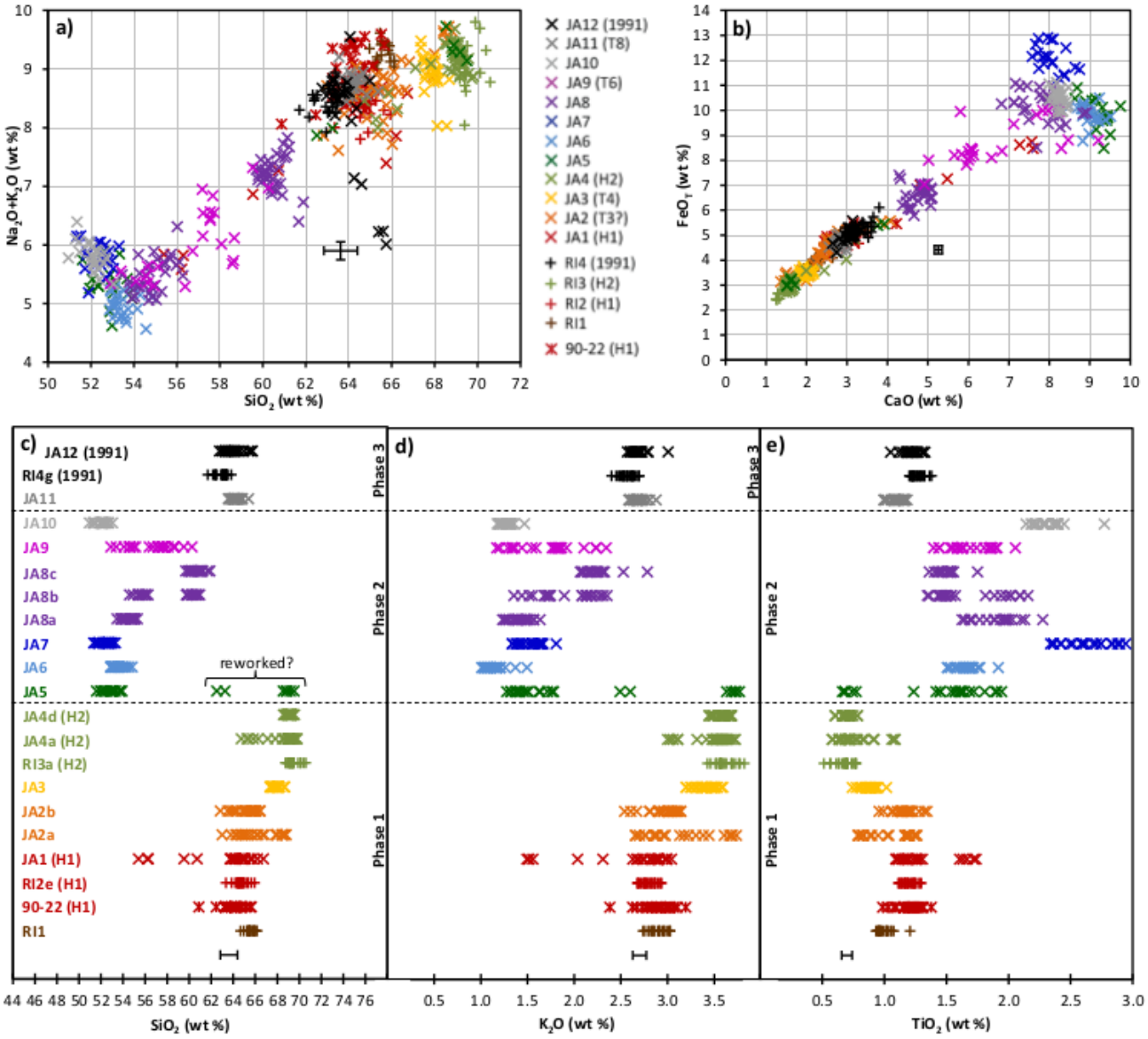

Figure 4.3 Matrix glass compositions of the tephras analysed for this study. Each colour is assigned to a distinct tephra unit or set of units thought to represent separate eruptions; the symbols indicate the different stratigraphic sections (Río Ibáñez (RI), Juncal Alto (JA), and a sample from Tierra del Fuego (90-22; Stern, 2008)). The error bar(s) on each plot indicates the mean value and 1σ r.s.d. of analyses of the secondary standard closest in composition to the tephras (Section 4.3.1; Supplementary File 4.2). **(a)** Total alkali-silica and **(b)** FeO_T vs CaO plots, showing the wide compositional range predominantly on a single calc-alkaline trend except for some of the most mafic tephras. **(c)** SiO_2, **(d)** K_2O, and **(e)** TiO_2 vs stratigraphic position (NB: units with the same colour but different symbol, i.e. tephras attributed to the same eruption sampled from different sections, are not necessarily in stratigraphic order w.r.t. one another). These plots show the similarity in composition between many neighbouring tephras, and the shifts in composition through the stratigraphy, demarcated by the dashed lines. The complete dataset is provided in Supplementary Table 4.4.

of the 1991 eruption is not found in the deposits analysed because it was erupted during the first phase, which was dispersed to the north (Kratzmann et al., 2009), away from the sections sampled. The fact that few units are bimodal or unimodal with a wide compositional range is in contrast to some glass compositions previously reported for 'Volcán Hudson' tephras (particularly Haberle and Lumley, 1998 and Carel et al., 2011; Section 4.4.2).

The wide range in the composition of Volcán Hudson tephras and the narrow compositional range of most of the individual eruption units facilitates robust correlation of the deposits using their matrix glass major element compositions. However, this is hampered by the observation that tephra units with similar glass composition are clustered in stratigraphic order within the Juncal Alto section. The compositions of the tephras shift from silicic (~63–70 wt % SiO_2) to mafic (~51–62 wt % SiO_2) after the H2 eruption, and then to intermediate compositions (~62–66 wt % SiO_2) for the most recent eruptions (Figures 4.3c to 4.3e). We number these phases 1 (silicic tephra compositions), 2 (mafic), and 3 (intermediate) respectively. Figure 4.4 shows the matrix glass and whole rock major element composition data for all tephras analysed from terrestrial sections (both for this and previous studies, provided in Tables 4.2 and 4.3 and Supplementary Table 4.2 respectively). The data are separated by the defined eruptive phases to facilitate comparison. The tephras attributed to the H2 eruption and earlier events have distinct matrix glass compositions; the distinction is generally clearest in K_2O-SiO_2 (Figure 4.4a), but RI1 is more distinguished from H1 in FeO_T-CaO (Figure 4.4b). The compositional range of JA2 overlaps with those of the other tephras, but the wide range of the basal JA2a sub-unit is diagnostic. The analysed sample of the tephra unit in southern Patagonia attributed to the H1 eruption, 90-22 (Stern 1991, 2008), has the same composition (within error) as the H1 tephra samples from the relatively proximal sections examined. The mafic tephras above H2 also all have distinct matrix glass compositions (Figures 4.4c and 4.4d). Although JA9 has a wide and (in some major element oxides) variable

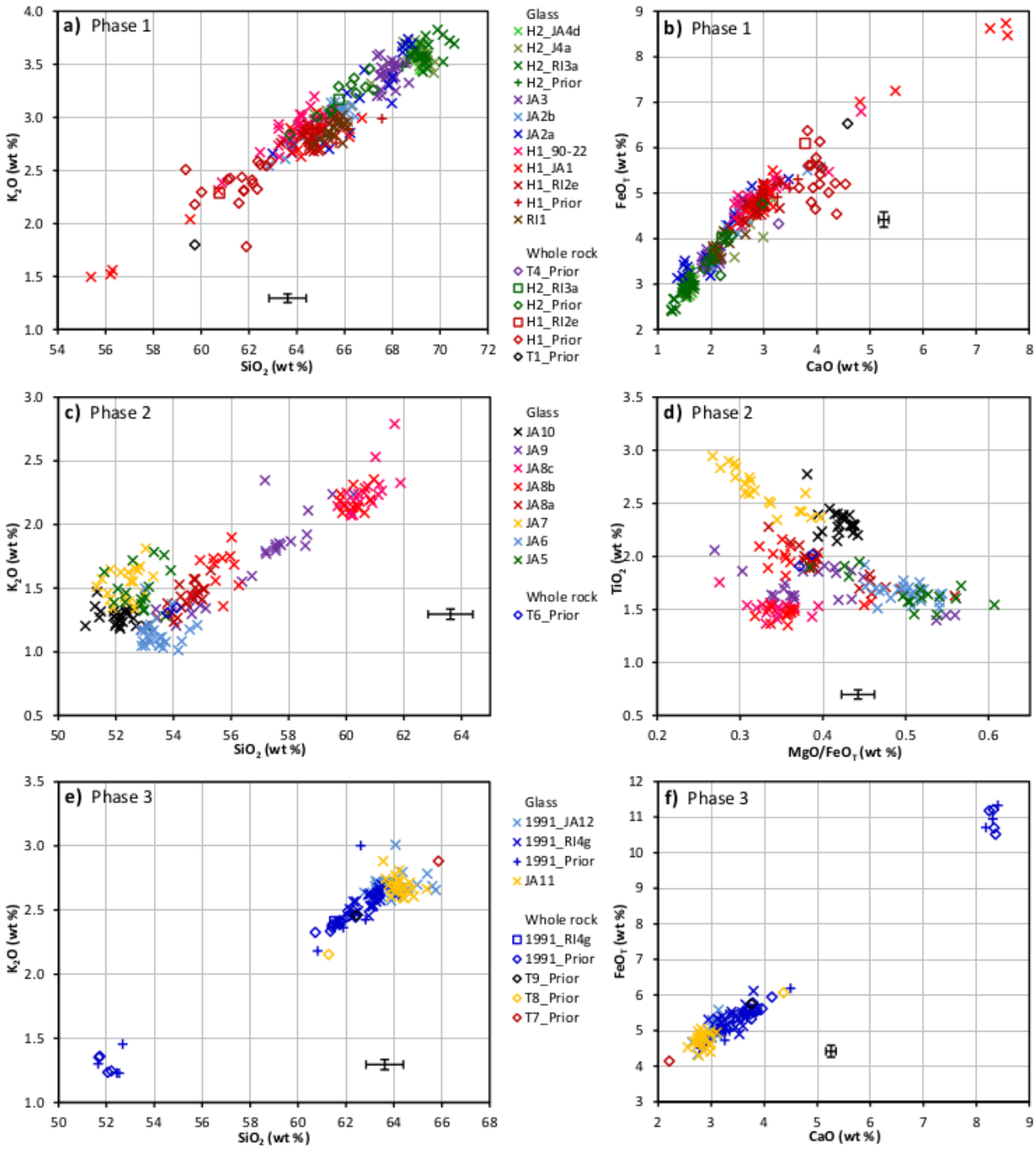

Figure 4.4 Whole rock and normalised matrix glass composition data for Volcán Hudson tephra samples from terrestrial sections. The error bars on each plot are for the new matrix glass analyses; they indicate the mean value and 1σ r.s.d. of analyses of the secondary standard closest in composition to the tephras (Section 4.3.1). In the legends, 'Prior' indicates data from previous studies, which are provided in Supplementary Table 4.2. Note that the colour assigned to each tephra does not always correspond to those in Figure 4.3. **(a)** K_2O vs SiO_2 and **(b)** FeO_T vs CaO plots of data for the early–mid-Holocene trachydacite–rhyolite glass composition eruptive phase. **(c)** K_2O vs SiO_2 and **(d)** Ti vs MgO/FeO_T plots of data for the late Holocene basalt–trachyandesite glass composition eruptive phase (excluding the assumed reworked silicic component of JA5). **(e)** K_2O vs SiO_2 and **(f)** FeO_T vs CaO plots of data for the late Holocene–historical trachydacite composition eruptive phase. The new whole rock and (complete, unnormalised) glass composition data are provided in Table 4.3 and Supplementary Table 4.4 respectively.

composition, the relative thickness of this tephra in the Juncal Alto section (Figure 4.2b iii) suggests that it is a primary fall deposit, rather than reworked. The youngest tephras, JA11 and 1991, are difficult to distinguish from each other by their matrix glass compositions (Figures 4.4e and 4.4f), and also from H1 (Figure 4.4a), in the absence of stratigraphic or age constraints.

Robust tephra correlation between the Juncal Alto sections of this study and Naranjo and Stern (1998) is difficult, because only limited whole rock composition data are available for most tephras in the latter (Figure 4.4; Supplementary Table 4.2). Our inferred correlations are shown in Figure 4.2, classified by the quality of the supporting evidence. Units JA1, JA4, and JA12 are attributed to the H1, H2, and 1991 eruptions (T2, T5, and 1991 tephras in the original section) respectively with a high degree of confidence, as their matrix glass compositions match those of these eruptions in the Río Ibáñez section (as do the whole rock composition data from the original section) (e.g., Figures 4.4a and 4.4e). T4 has a whole rock composition between that of H1 and H2 (e.g., Figure 4.4a), which is also the case for the glass composition of JA3; considering also that both these units are at similar depths below H2, it is possible that these are the same tephra. The composition of T3 was not analysed by Naranjo and Stern (1998); on the basis of its stratigraphic position (if JA3 = T4), we assume that it corresponds to JA2. T1 and RI1 (the additional tephra we identify in the Río Ibáñez section) are both stratigraphically below H1; the whole rock composition of T1 is less evolved than that of H1 (Figures 4.4a and 4.4b), so is unlikely to be the same deposit as RI1, which has a slightly more evolved glass composition than H1 (Figures 4.4a and 4.4b). Above H2, T6 is unlikely to correlate with JA5–7, as they have glass compositions lower in SiO_2 than the whole rock composition of T6 (Figure 4.4a). Considering also that T6 is the only one of the minor tephras in the section to be identified in other locations by Naranjo and Stern (1998), and is relatively thick, we correlate it with JA9. This is consistent with the fact that all the tephras in the original section above T6 have whole rock compositions >60 wt % SiO_2 (except the mafic

component of the 1991 eruption; Figure 4.4e), so are unlikely to correlate with tephras JA5–10, which have more mafic matrix glass compositions (Figure 4.4c). The implication of a considerable hiatus in deposition in the Juncal Alto section of Naranjo and Stern (1998) between T5 and T6 is supported by the ~2 kyr difference between the modelled ages of these eruptions (Figure 4.8). T7 has a more silicic whole rock composition than the glass composition of any of the units in the upper part of our section (Figure 4.4e), so appears to be absent from the latter. T8 has a whole rock composition similar to that of the silicic component of the 1991 eruption (Figure 4.4e); the glass composition of JA11 compares to that of 1991 in the same way (Figure 4.4e), and they are in a similar stratigraphic position (Figure 4.2b), so may be the same tephra. Correlation between JA11 and T9 (the 1971 eruption) is ruled out as this would require an unrealistic peat accumulation rate (Figure 4.2b); hence deposits from the 1971 eruption are inferred to be absent from the section studied.

Whole rock composition data are available for H1, H2, and 1991 eruption deposits from multiple locations, but the data for the prehistoric eruptions are scattered (e.g. H1 on Figures 4.4a and 4.4b). The major element compositions of the bulk pumice from all three eruptions analysed here (Table 4.3) closely match those of Kratzmann et al. (2009, 2010), and the trace element compositions (Table 4.3) are mostly close to the mean and almost all within the range of the previous analyses of tephra from terrestrial sections (Supplementary Table 4.2).

The tephra units characterised here all have matrix glass compositions close to or on the trends defined by those of the major eruptions of Volcán Hudson (as well as their whole rock composition data) (Figures 4.3 and 4.4), so are likely to originate from this volcano. There is a paucity of reference composition data from other potential source volcanoes in the region (e.g. Mentolat, Maca, and Melimoyu volcanoes, and the northern AVZ; Figure 4.1): published

composition ranges are typically based upon analysis of a small number of samples, in some instances with little or no age constraints or stratigraphic context, and little robust glass composition data are available. It is possible that the major element composition range of some of these volcanoes partially overlaps with that of Volcán Hudson, e.g. Volcán Melimoyu (Stern et al., 2015); hence it is difficult to rule out the possibility of an alternate source for any of the minor tephras. The mafic tephras found to have an anomalously high glass K_2O/SiO_2 ratio and TiO_2 concentration (JA7 and JA10; Figures 4.4c and 4.4d) may originate from the cones surrounding Volcán Hudson (Gutiérrez et al., 2005) rather than the main edifice. Alternatively, such magma compositions could result from melting of a mantle source separate from other magmas, or a different degree of partial melting, but still erupted from main edifice (Kratzmann et al., 2010). Gutiérrez et al. (2005) identify a gap in the whole rock composition of Hudson eruption products, between 54–59 wt % SiO_2; we also find no whole rock compositions within this range. However, eruptions with (trachy)andesitic matrix glass compositions are identified (Figure 4.3a), suggesting that the absence of intermediate whole rock compositions may be because they have not yet been sampled/analysed, rather than entirely absent.

4.4.2. Correlation with palaeoenvironmental records

Figure 4.1 shows the locations where tephra layers have been reported in palaeoenvironmental records and attributed to eruptions of Volcán Hudson. The occurrences >∼200 km from Volcán Hudson (except in Antarctica) are almost exclusively attributed to the H1 eruption, mostly on the basis of the distinctive greenish colour of the tephra or approximate age constraints rather than chemical composition, so may be uncertain. Deposits of other Volcán Hudson eruptions are likely to be preserved as cryptotephra layers, but these have only rarely been searched for in this region (Fontijn et al., 2014). The relatively proximal palaeoenvironmental records bearing visible tephra layers in addition to H1 are predominantly lake sediment cores; some preserve tephras at a high

frequency (>1 per ky) (Supplementary Table 4.1). Correlation or eruption attribution by approximate age correspondence is therefore particularly unreliable (for the reasons outlined in Section 4.1), so we only attempt to correlate the minority of these tephras for which compositional data have been published.

Elbert et al. (2013) examined cores from two lakes, Castor (CAS) and Escondida (ESC) (reference number 9 on Figure 4.1; both ~100 km NE of Volcán Hudson), which have basal ages of ~4.0 and ~2.9 ky cal BP and contain 8 and 6 tephra layers respectively. Tephras ESC-T2–6 were correlated with CAS-T2–6 (T1 being the uppermost tephra in both instances) in stratigraphic order, due to the correspondence of their model ages from ^{14}C dating. The whole rock major element compositions presented by Elbert et al. (2013) for some of these tephras are plotted in Figures 4.5a and 4.5b. Published whole rock composition data for H2 deposits (compiled in Supplementary Table 4.2) and the late Holocene tephras in the Juncal Alto section of Naranjo and Stern (1998) are also plotted for comparison. The Elbert et al. (2013) data lie in or on the trend of the Volcán Hudson glass composition field in K_2O–SiO_2 (Figure 4.5a; cf. Figure 4.5f), confirming that all these tephras are likely to be from Volcán Hudson. The tephras analysed from both lakes are all mafic except for CAS-T8, which is attributed to the H2 eruption; its whole rock K_2O and SiO_2 concentrations are consistent with this interpretation (Figure 4.5a), in addition to its age and physical characteristics. However, the whole rock TiO_2, MgO, and FeO_T concentrations (amongst other oxides) of CAS-T8 do not match those of the H2 reference data (Figure 4.5b). Similarly, CAS-T4 and ESC-T4 have near-identical concentrations of some major element oxides, but not others, particularly SiO_2 and Al_2O_3. These discrepancies suggest analytical error, considering the variable elements affected. CAS-T6 and ESC-T6 are near-identical in whole rock composition, but are distinct from the T6 tephra of Naranjo and Stern (1998) with which they were correlated (e.g., Figure 4.5a). CAS-T3 and ESC-T3 have whole rock compositions that are distinct in all major

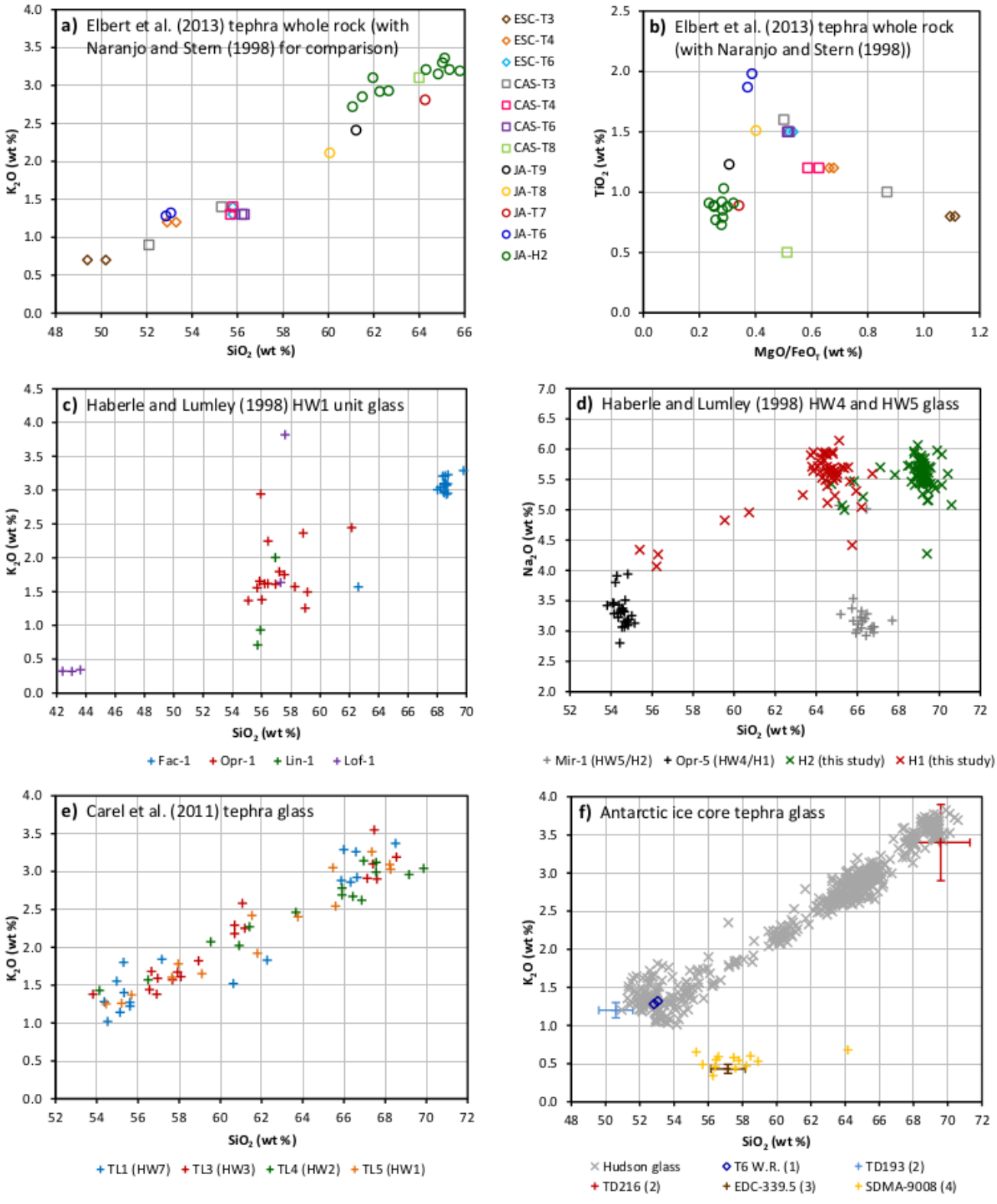

Figure 4.5 *(caption on next page)*

Figure 4.5 *(previous page)* Composition data for Volcán Hudson tephra samples from palaeoenvironmental records. Note that the colour assigned to each tephra in a specific plot does not always correspond to those in the others, or in previous figures. **(a)** K_2O vs SiO_2 and **(b)** Ti vs MgO/FeO_T plots of the whole rock composition of tephras from the Lago Castor (CAS) and Laguna Escondida (ESC) sediment cores analysed by Elbert et al. (2013), with the same data for the late Holocene tephras in the Juncal Alto (JA) peat section of Naranjo and Stern (1998) and all whole rock compositions of H2 deposits (Supplementary Table 4.2) for comparison. Note that none of the different tephras have near-identical composition on both plots (and so may be correlated), except for CAS-T6 and ESC-T6. **(c)** K_2O vs SiO_2 plot of the matrix glass composition of tephras from lake sediment cores analysed and attributed to a specific eruption of Volcán Hudson (HW1) by Haberle and Lumley (1998). Note the distinct composition of the majority of the data for each tephra, and limited number of analyses of some of the tephras; hence correlation of any of these tephras with one another is not justified. **(d)** Na_2O vs SiO_2 plot of the matrix glass composition of tephras from lake sediment cores analysed and attributed to H1 and H2 by Haberle and Lumley (1998), with the matrix glass analyses of H1 and H2 deposits by this study for comparison. This shows that the attributions by Haberle and Lumley (1998) are incorrect and/or their data are unreliable. **(e)** K_2O vs SiO_2 plot of the matrix glass composition of the four tephras in a marine sediment core analysed by Carel et al. (2011), which they correlate with eruptions identified in lake sediment cores by Haberle and Lumley (1998) (named in brackets). Note that the four tephras are indistinguishable in their composition, which in each case has an extremely wide range in comparison to most of the units analysed by this study (cf. Figure 4.3a). **(f)** K_2O vs SiO_2 plot of the matrix glass composition of the cryptotephras in Antarctic ice cores that have been analysed and suggested to originate from Volcán Hudson, with matrix glass composition data from this study and whole rock (W.R.) composition data from Naranjo and Stern (1998; (1)) for comparison. (2) = Narcisi et al. (2012), (3) = Narcisi et al. (2005), (4) = Kurbatov et al. (2006). The error bars show the mean and standard deviation of the tephra analyses for which only these data are reported.

element oxides. The observation in these cores of a sequence of mafic tephras above H2 is consistent with the Juncal Alto section analysed in this study, but correlation of the Elbert et al. (2013) tephras with this section (or other palaeoenvironmental records) is not possible due to the inconsistencies in the these compositional data.

The tephrostratigraphy of sediment cores from eight other lakes NW–SW of Volcán Hudson (reference number 1 on Figure 4.1) was studied by Haberle and Lumley (1998). They identified five tephra units (attributed to eruptions of Volcán Hudson, named HW1–3 and HW6–7) that are currently not recognised in terrestrial sections but were correlated between at least half of these lakes; in addition, tephras Opr-5 and Mir-1 are attributed to the H1 and H2 eruptions (and named HW4 and HW5) respectively (Table 4.1). These correlations were based upon ^{14}C date constraints

and statistical analysis of matrix glass compositions; however, in most cases the correlated tephras have compositions that are distinct, so are likely to in fact be associated with different eruptions, or the composition data are too scattered to be correlated robustly. The former is exemplified by the HW1 tephra, said to be preserved in four of the lakes, which has been correlated with a tephra in a marine sediment record (Siani et al., 2010; Carel et al., 2011) to show that the surface radiocarbon reservoir age was greater during deglaciation than the Holocene (Siani et al., 2013). Figure 4.5c presents glass composition data for the tephra layers (named as in Haberle and Lumley, 1998) attributed to this single eruption; each tephra has a distinct composition except for single outliers, so there is insufficient evidence to correlate any of these tephras to the same (HW1) unit. Only two of the tephras attributed to each of HW2, HW3, and HW7 can be confidently correlated. The other tephras either have distinct compositions (in the case of HW2, as with HW1; Figure 4.6a) or wide compositional ranges (HW3; Figure 4.6b), or both (HW7; Figure 4.6d). Most of attributions of tephras to HW6 are justifiable, but uncertain due to the scattered data for most of the units (Figure 4.6c). Figure 4.5d compares the Opr-4 (HW4) and Mir-1 (HW5) tephra matrix glass composition data to those of H1 and H2 tephras by this study, demonstrating that these tephras have been unjustifiably attributed to these eruptions. Mir-1 has an age and physical characteristics that suggest this is a H2 deposit, and its glass composition is similar to H2 for some elements, but its Na_2O concentration is too low and SiO_2 slightly too high (Figure 4.5d), which is indicative of alkali element migration due to inappropriate EPMA conditions. As all the tephras characterised by Haberle and Lumley (1998) were analysed using the same conditions, robust correlation of these tephras with terrestrial deposits or those in other palaeoenvironmental records is not possible.

Alkali element migration is apparent in glass composition data for tephras in other palaeoenvironmental records. The mean Na_2O concentrations in the tephras attributed to H1 in

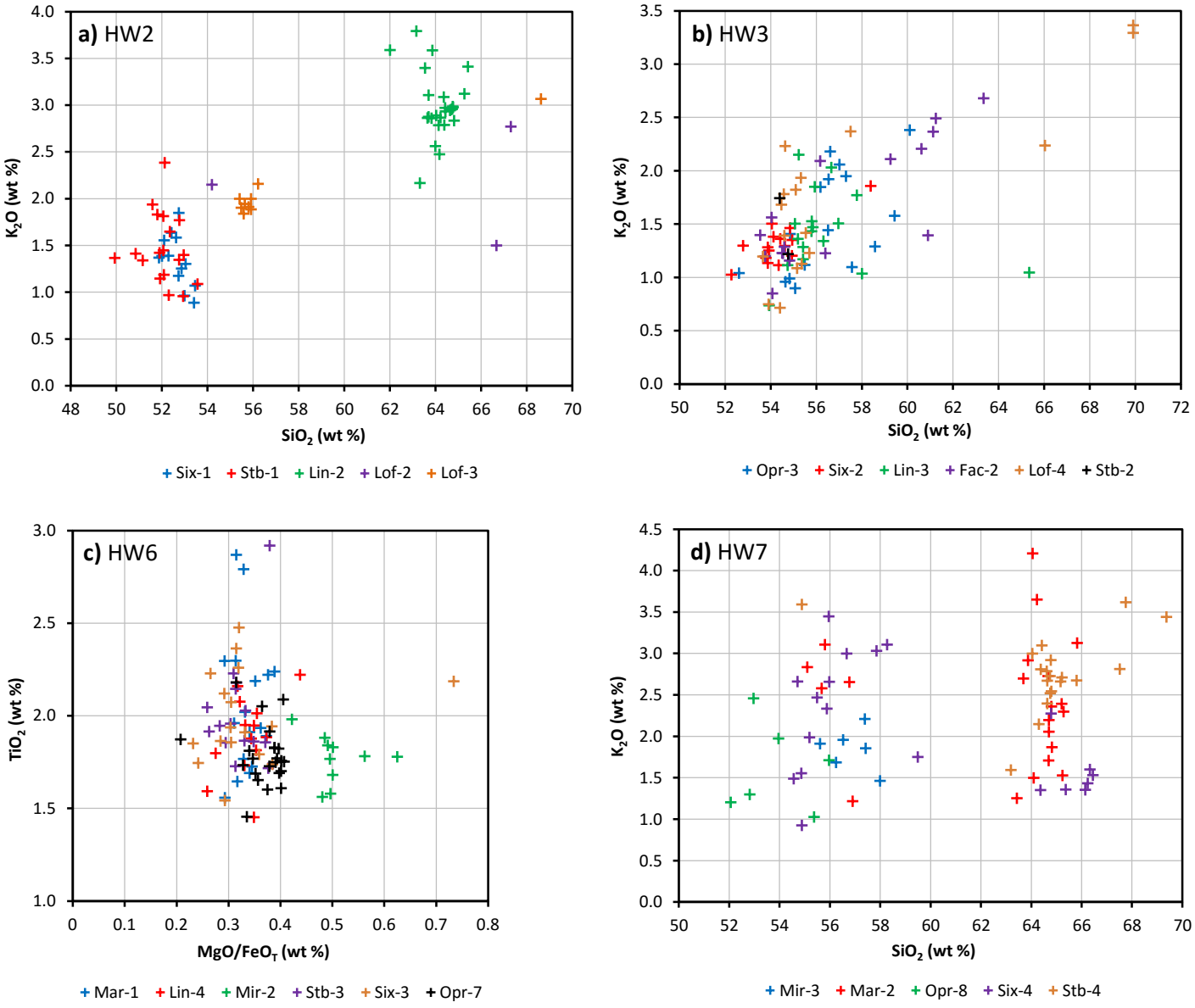

Figure 4.6 Bivariate plots of the matrix glass composition of tephras from lake sediment cores analysed and attributed to specific eruptions of Volcán Hudson by Haberle and Lumley (1998). **(a)** K_2O vs SiO_2 plot of the compositions of the tephras attributed to a single eruption, HW2. Note the distinct compositions of each tephra, except Stb-1 and Six-1. **(b)** K_2O vs SiO_2 plot of the compositions of the tephras attributed to a single eruption, HW3. The scattered data for most units, and few analyses in the case of Stb-2, mean robust correlation is not possible. Six-2 and Lof-4 have relatively clustered, overlapping composition data; thus we suggest that these tephras are most likely to correlate. **(c)** Ti vs MgO/(total Fe as FeO) plot of the compositions of the tephras attributed to a single eruption, HW6. With the exception of Mir-2, these tephras have similar compositions and are less scattered than (e.g.) those attributed to HW3, so correlation is more justifiable. **(d)** K_2O vs SiO_2 plot of the compositions of the tephras attributed to a single eruption, HW7. We consider the mafic composition data to be too scattered to correlate; Stb-4 and Mar-2 are the most likely to be from the same eruption.

Potrok-Aike lake sediment cores (reference number 28 on Figure 4.1; Haberzettl et al., 2007, 2009) and the Las Cotorras mire (reference number 22; Borromei et al., 2010) are >1 wt % (>3σ) below the mean of the analyses by this study (Figure 4.7a). Attribution to the H1 eruption is still justified in these instances due to their location in southern Patagonia, where preservation of visible tephra layers from smaller eruptions of Volcán Hudson is improbable and the composition of tephras from the other potential source volcanoes in the AVZ are very distinct (Stern, 2008). Tephras in other palaeoenvironmental records are attributed to H1 on the basis of their whole rock trace element composition (Markgraf et al., 2003; Waldmann et al., 2010; Stern et al., 2013; Vanneste et al., 2015); these data (Supplementary Table 4.2) are consistent with analyses of proximal H1 deposits, including those in Table 4.3.

Carel et al. (2011) characterised the tephrostratigraphy of a ~20 ky marine sediment record from the continental shelf ~200 km west of Volcán Hudson (reference numbers 3–5 on Figure 4.1; Siani et al., 2010, 2013). Four of the 12 tephras are correlated with eruptions identified by Haberle and Lumley (1998), but these units have indistinguishable matrix glass compositions with a wide range (~54–69 wt % SiO_2; Figure 4.4e). With the exception of TL10 and TL11, the other tephras also have this compositional range, which coincides with that of the tephras analysed from terrestrial sections (cf. Figure 4.5f), confirming Volcán Hudson as their source. The relative proportion of mafic, intermediate, and silicic analyses (and the tephra shard types described by Carel et al., 2011) does vary between units, but there are insufficient data to determine whether this reflects sampling bias or real differences in composition. The wide compositional ranges that Carel et al. (2011) report are in contrast to those of almost all tephras characterised in this study; hence we suggest that the tephras in this sediment core are reworked deposits from multiple Volcán Hudson eruptions. Correlation of these tephras with the terrestrial or other palaeoenvironmental records is therefore not justified. The core was taken ~200 km upwind from

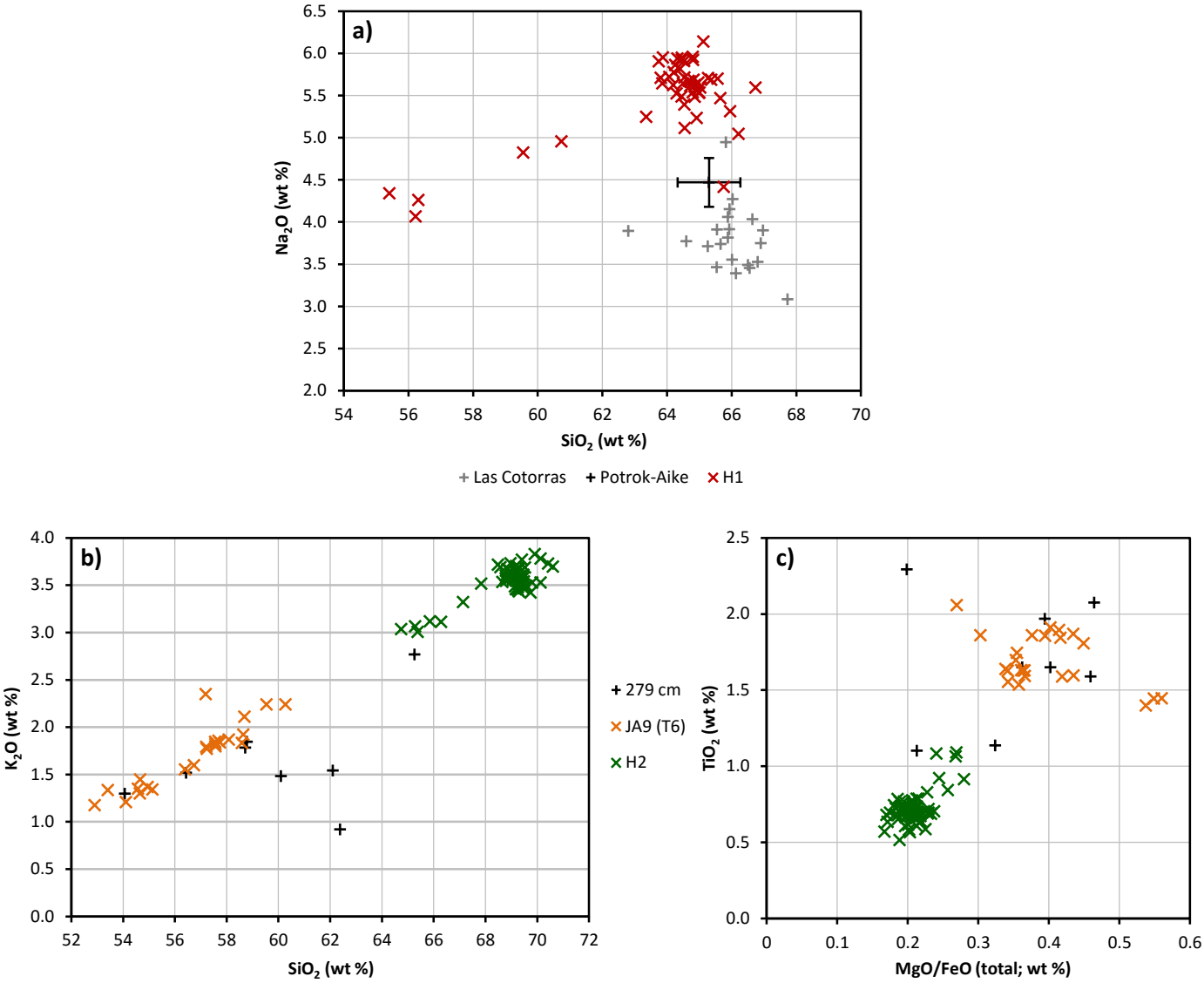

Figure 4.7 Bivariate plots of the matrix glass composition of tephras from various palaeoenvironmental records that have been attributed to specific eruptions of Volcán Hudson. **(a)** Na_2O vs SiO_2 plot of the matrix glass compositions of the tephras from Laguna Potrok-Aike and Las Cotorras that are attributed to H1 by Haberzettl et al. (2007, 2009) and Borromei et al. (2010) respectively, with H1 glass analyses by this study for comparison. The error bars show the mean and standard deviation of the tephra analyses for which only these data are reported. **(b)** K_2O vs SiO_2 and **(c)** Ti vs MgO/(total Fe as FeO) plots of the matrix glass composition of the cryptotephra at 279 cm in the marine sediment core studied by Carel et al. (2011), which Siani et al. (2013) analyse and attribute to the H2 eruption, plotted with H2 and T6 glass analyses by this study for comparison.

Volcán Hudson, but only ∼30 km from the closest outlet from the fjords into which its western drainage channels flow, so water (by the mechanisms identified by Bertrand et al., 2014) is more likely than aeolian transport. All but one of the tephra units were deposited prior to ∼11 ka, during the late glacial or glacial–interglacial transition periods, consistent with ice rafting being the transport mechanism (the likelihood of which would have considerably decreased with deglaciation), or suggestive of a change in coastal or ocean currents at the start of the Holocene. If ice rafting is the predominant transport mechanism, the fact that tephra was deposited in discrete layers may reflect intermittent glacier calving events; alternatively, intermittent lahars could have increased the flux of tephra that could be transported by ocean currents. A cryptotephra identified by Siani et al. (2013) in the same core has a relatively narrow compositional range (most analyses ∼54–62 wt % SiO_2), so could be a primary deposit. This is attributed to H2 by Siani et al. (2013), but is too mafic (Figure 4.7b). Most of the cryptotephra composition data that lie on the Volcán Hudson matrix glass composition trend are within the compositional range of JA9 (the T6 eruption of Naranjo and Stern, 1998; Figures 4.7b and 4.7c), but this correlation would imply an exceptionally high radiocarbon reservoir age of >2 ky (attributing the cryptotephra to H2 gives a reservoir age of ∼0.8 ky (Siani et al., 2013)).

Even if multiple robust tephra correlations were possible between the marine and lake sediment records of Carel et al. (2011) and Haberle and Lumley (1998), the marine surface reservoir age cannot be determined (as done by Siani et al., 2013) without correlating the lake sediments to terrestrial records, as there could be a reservoir effect or incorporation of older organic matter in the lake sediments (the latter has been found in comparable lakes in this region: Bertrand et al., 2012). Both the marine surface reservoir age and any radiocarbon offset in the lake sediments cannot be accurately constrained using the current tephrostratigraphy.

The Antarctic ice core tephras attributed to Volcán Hudson also cannot be confidently correlated with the units characterised, as shown in Figure 4.5f. The TD193 tephra in the TALDICE core (Talos Dome; Narcisi et al., 2012) has a trachybasaltic matrix glass composition, which is more mafic than the whole rock composition of the T6 tephra with which it is correlated (and more mafic than the matrix glass composition of JA9, which we correlate with T6), so this correlation cannot be correct. Its glass compositional range is mostly outside the range of glass compositions analysed in this study, so it is not clear which eruption (or volcano) the TD193 tephra is associated with. The older unit TD216 was suggested to be a deposit of a previously unknown silicic eruption of Volcán Hudson at 2.35 ka (Narcisi et al., 2012); its matrix glass composition is comparable to that of H2 (the most silicic eruption analysed), but the standard deviation of these data is large, so alternative sources cannot be ruled out. We find no silicic tephras in the terrestrial sections studied that are of a similar age to TD216; the MEL1 tephra from Volcán Melimoyu at ~1.6–2.8 ka cal BP (Naranjo and Stern, 2004; calibration by this study) is a possible alternative, considering that tephras from Volcán Melimoyu have previously been misattributed to Volcán Hudson (Stern et al., 2015), but there are insufficient compositional data for the MEL1 tephra to verify this. Volcán Hudson is also suggested to be the source of the correlated tephras EPICA Dome C 339.5 m (Narcisi et al., 2005) and Siple Dome SDMA-9008 (suggested to correlate with HW3; Kurbatov et al., 2006; Dunbar and Kurbatov, 2011) (Narcisi et al., 2012), but these units have glass K_2O concentrations below the minimum of any Hudson tephra analysed in this study, so are likely to originate from another volcano.

The difficulty of correlating the tephras characterised from terrestrial sections with those in these palaeoenvironmental records highlights the importance of robust chemical characterisation in order to determine a reliable tephrostratigraphic framework (e.g., Smith et al., 2011a; Matthews et al., 2012; Fontijn et al., 2014). Matrix glass major element composition data are sufficient to

discriminate almost all the tephras characterised by this study (Section 4.4.1). However, analytical accuracy and precision (by analysis of secondary standards and a large population of shards) is necessary for this, as demonstrated by the glass analyses by the previous studies described. Mineral (particularly Fe-Ti oxide) composition data may complement glass composition as a correlation tool, at least for proximal deposits (e.g., Fierstein, 2007; Smith et al., 2011b; Rawson et al., 2015), but only limited mineral composition data are published for Hudson tephras, and only from the largest eruptions (Kratzmann et al., 2009, 2010; Weller et al., 2014). Whole rock trace element composition may also be informative for correlating proximal deposits (Weller et al., 2014; Stern et al., 2015).

4.4.3. Tephrochronology and temporal variation in activity

We use the integrated tephrostratigraphy of the Juncal Alto and Rio Ibáñez sections of Naranjo and Stern (1998) and this study as the basis of a revised tephrochronology for Volcán Hudson. Correlation of this stratigraphy with those in palaeoenvironmental records to develop a wider tephrostratigraphic framework is not possible as the composition data available for tephras in these latter records are not reliable (Section 4.4.2). We include those eruptions identified by Haberle and Lumley (1998) where at least two of the tephras attributed to them are likely to correlate with each other (specified in Section 4.4.2 and Figure 4.6), using the age constraints only on those tephras; however, we do not correlate these with the Juncal Alto tephras due to the uncertainty in their composition. The eruptions, with their magnitude and refined age estimates, are listed in Table 4.1 and summarised in Figure 4.8. The magnitudes of the large eruptions (M >5) were estimated from published volume estimates (Scasso et al., 1994; Naranjo and Stern 1998; Weller et al., 2014) using the method of Pyle (2015), assuming a deposit density of 800 kg/m^3. The thin tephras that are only recognised in one or two locations are assumed to be from magnitude 3 eruptions, as tephra from the VEI 3 1971 eruption is only preserved as such a deposit in the Juncal

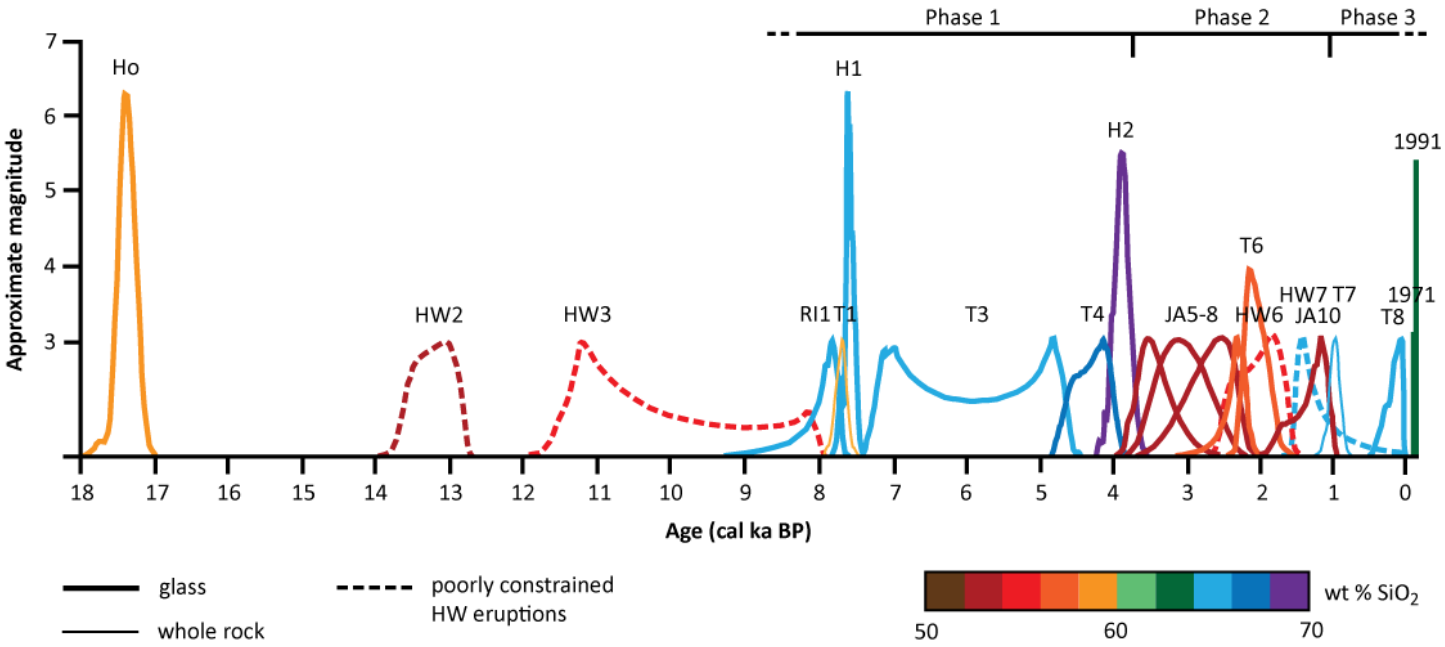

Figure 4.8 Summary of the post-glacial explosive eruption history of Volcán Hudson inferred by this study. Each eruption (also listed in Table 4.1) is represented by its age probability distribution (from Bayesian age modelling; model outputs in Supplementary File 4.3), the height of which corresponds to its estimated magnitude (Pyle, 2015). The line colour corresponds to the mean SiO_2 concentration of the matrix glass of the main component of the tephra erupted, or of the bulk tephra where data for the former are unavailable.

Alto section of Naranjo and Stern (1998), at the same location or a similar distance from Volcán Hudson as most of the other thin tephras included. T6 is estimated to be larger due to its relative thickness at Juncal Alto and identification in another terrestrial section (Naranjo and Stern, 1998). The age estimates are calculated from four OxCal 'sequence' models (Section 4.3.3): the integrated Juncal Alto tephrostratigraphy with Ho, the revised Haberle and Lumley (1998) tephrostratigraphy, and compilations of all published radiocarbon dates of the H1 (Prieto et al., 2013) and H2 (Supplementary Table 4.1) eruptions. These models are provided in Supplementary File 4.3. We use the ages for H1 and H2 from sequence models of compilations of all dates rather than from the integrated stratigraphy, as the former are better constrained. In using Bayesian analysis to incorporate the stratigraphic information, the ages of many of the eruptions have more realistic associated uncertainties, and are more accurate than pooling or taking an average of the radiocarbon dates, and/or discounting those that are arbitrarily considered to be outliers.

It has been suggested that there is temporal variation in the frequency, magnitude, and/or composition of post-glacial explosive eruptions of volcanoes in the SVZ, which has been attributed to a magmatic response to deglaciation (Watt et al., 2013a; Rawson et al., 2016). Variation in the frequency of eruptions of Volcán Hudson is particularly apparent in the marine sediment record of Carel et al. (2011), in which tephras are clustered prior to the Holocene, but here we recognise that these are likely to be reworked (Section 4.4.2) and therefore not indicative of eruption frequency. The ~17.4 cal ka Ho eruption identified by Weller et al. (2014) is inconsistent with the trend of decreasing age of onset of substantial post-glacial explosive activity with increasing latitude suggested by Watt et al. (2013a). Nevertheless, the preservation of this tephra in lakes within the Andes suggests there was little latitudinal variation in the timing of glacial retreat (Miranda et al., 2013), so a later response to deglaciation in the southern SVZ than further north may not be expected. Ho is similar in age to the ignimbrite-forming eruptions of Llaima

(Naranjo and Moreno, 1991) and Villarrica (Lohmar et al., 2007) volcanoes, which may also be of comparable magnitude. However, we note that the age and magnitude of Ho are currently poorly constrained, as they are derived from radiocarbon dates and tephra thicknesses from a small number of lakes that may have incorporated old terrestrial carbon into their sediments and are within a small geographic area.

The tephrochronology presented here indicates temporal shifts in erupted magma composition during the Holocene, from silicic to mafic after the H2 eruption (∼3.9 cal ka BP), and then to intermediate for the last ∼1 ky (Figure 4.8). The record prior to ∼9 ka is too incomplete and unreliable to assess the composition variability in that period. The presence of a mafic phase of activity after the H2 eruption is supported by the lake sediment tephra records of Elbert et al. (2013). There are insufficient major element composition data for Holocene tephras in the other palaeoenvironmental archives to compare any trends in those records to the one described here. A silicic–mafic–intermediate variation in the composition of post-glacial explosive eruptions has also been identified in the tephrostratigraphy of Volcán Mocho-Choshuenco in the central SVZ, but with earlier shifts and a ∼2 ky longer mafic phase (Rawson et al., 2015, 2016). The trend in eruptive flux at Volcán Mocho-Choshuenco, being relatively high and low during the silicic and mafic phases respectively, is also apparent in the eruption records for some other SVZ volcanoes, with different timings to the phase transitions (Rawson et al., 2016). These data are shown in Figure 4.9, together with a Holocene eruptive flux estimate for Volcán Hudson. The latter uses published tephra volume estimates for the largest eruptions (Weller et al., 2014), but assumes volumes of 0.05 and 0.5 km^3 for the eruptions that we estimate to have magnitudes of 3 and 4, respectively. Hence it should be noted that the eruption volume estimates for Volcán Hudson are relatively inaccurate (w.r.t. the others shown), and that its eruption history is also rather incomplete in comparison to that of Volcán Mocho-Choshuenco (Rawson et al., 2015)

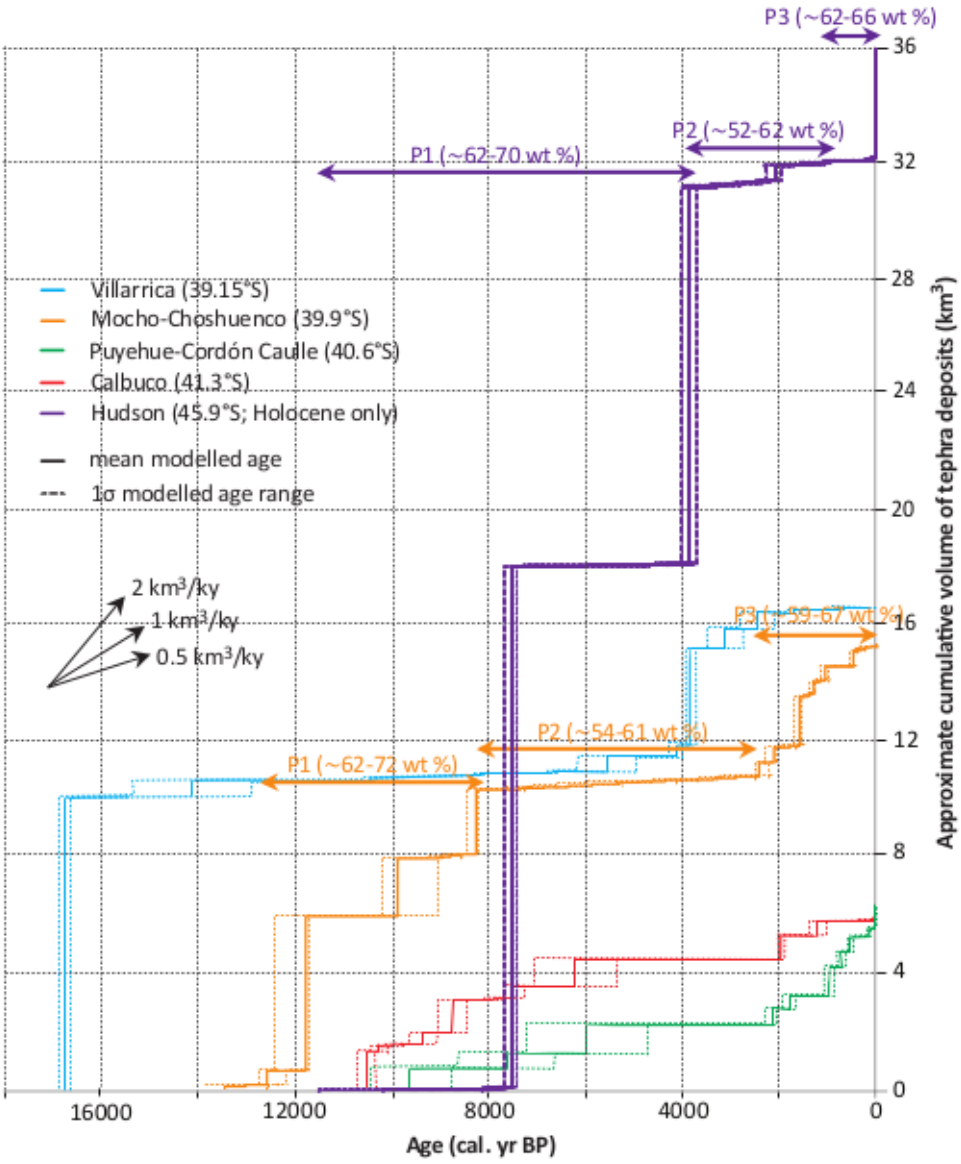

Figure 4.9 Cumulative (bulk) tephra volume estimates vs time for Volcán Hudson and other volcanoes in the Andean Southern Volcanic Zone, modified from Rawson et al. (2016). Note that for Volcán Hudson, only the Holocene record of this study is included, as volume estimates for earlier eruptions are relatively poorly constrained. The other volcanoes featured have relatively well-constrained volume estimates for their post-glacial tephra deposits, but with the exception of Volcán Mocho-Choshuenco (Rawson et al., 2015), their glass composition has not been characterised in detail. The age uncertainties are calculated by Bayesian radiocarbon age modelling (Fontijn et al., 2014; Rawson et al., 2016; Supplementary File 4.3). The records of each volcano appear to show the same three phases (labelled for Volcán Hudson and Volcán Mocho-Choshuenco with glass SiO_2 composition ranges), an early period of early eruptive flux, followed by a phase of small eruptions, and then a return to larger volume eruptions. At Volcán Hudson and Volcán Mocho-Choshuenco, these phases have similar, distinct melt compositions (silicic, mafic, and intermediate, respectively). Note that the timing and duration of the three phases varies between each volcano.

Nevertheless, the eruptive flux pattern for Volcán Hudson is consistent with the others, albeit with delayed shifts and with a considerably larger volume erupted in the first phase. Watt et al. (2013a) noted the same pattern in volume flux for the SVZ as a whole, and in Kamchatka.

Rawson et al. (2016) propose that the observed temporal variation in eruptive flux and magma composition reflects the crustal and magmatic response to glacial unloading, by the mechanism outlined in Figure 4.10. Differences in the magnitude and timing of variations between volcanoes are attributed to variance in local stress regime and magmatic plumbing (Rawson et al., 2016). We suggest that the magma composition variation observed at Volcán Hudson is consistent with this model; the relatively large eruption flux and long duration of the silicic eruptive phase and the short mafic phase at Volcán Hudson may reflect the relatively high melt supply rate at Volcán Hudson (Section 4.2.1). Further constraint of eruption volumes and the early post-glacial tephrostratigraphy are necessary to verify this.

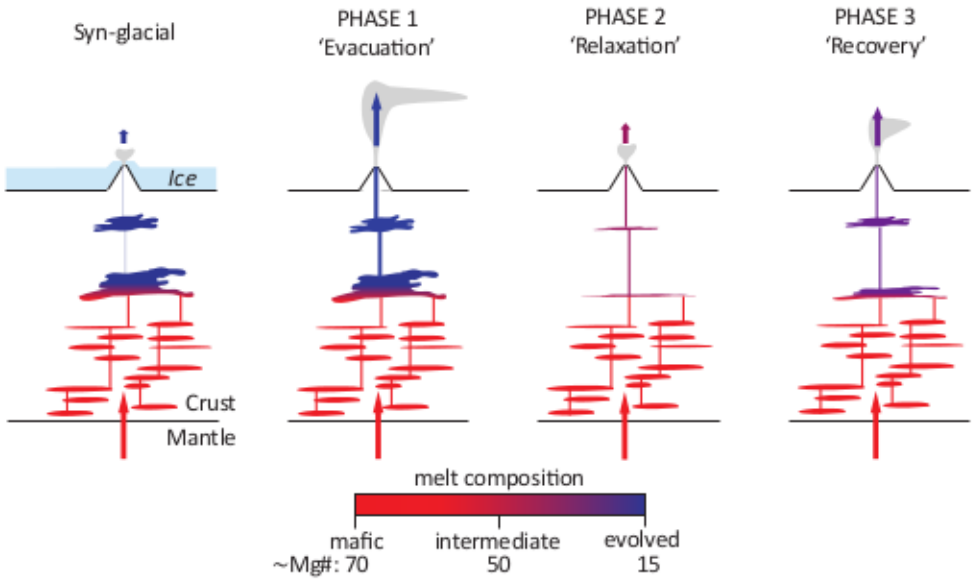

Figure 4.10 Schematic illustration of the response of the magmatic systems of Andean volcanoes to deglaciation, inferred from observations of temporal variation in post-glacial erupted magma flux and composition (Figure 4.9). During syn-glacial times, ice loading supresses dyke propagation to the surface, so the eruption flux is low and magma storage time is high. Magma accumulates in the crust, and evolves. In Phase 1, unloading of the ice enables dyke propagation, and so large eruptions that evacuate the accumulated evolved magma. During Phase 2, the magmatic system begins to be refilled by the constant mafic magma supply from the mantle. As little evolved magma has accumulated, there is only a low eruptive flux of mafic magma. During Phase 3, sufficient time has elapsed for the magmatic system to recover to steady-state, i.e. magma has evolved and continuing mafic magma input results in a moderate eruption flux of intermediate magma compositions. Magma fluxes into the crust are assumed to be (quasi-)steady throughout, due to the short timescale (order of ~10 ky) relative to mantle processes. Model proposed by and figure modified from Rawson et al. (2016).

4.5. Conclusions

The many terrestrial sections and palaeoenvironmental records identified that preserve tephra attributed to eruptions of Volcán Hudson suggest a high frequency of explosive eruptions (at least 19 during the Holocene) from this volcano relative to others in the southernmost Andes, and the great potential of their deposits for tephrochronology in Patagonia (and possibly further afield). However, their utility for tephrochronology is currently inhibited by inadequate characterisation of the tephras in regional palaeoenvironmental records in the published literature. The tephrostratigraphy of the Juncal Alto section (~90 km from Volcán Hudson) presented here is the most complete known terrestrial record of explosive eruptions of Volcán Hudson during the Holocene. Characterisation of the matrix glass major element composition of each of the eruption deposits shows that many of these tephras can be identified by their glass composition alone, if analysed precisely. In addition, this reveals a previously unrecognised temporal variation in erupted magma composition that appears to be consistent with an emerging regional trend that is attributed to the magmatic response to deglaciation. The new tephrostratigraphic framework we present can be further developed as the many other tephras identified in palaeoenvironmental records are characterised, and if new reference data from the other, poorly studied volcanoes in the southernmost Andes were to become available.

Chapter 5 Glaciovolcanism at Volcán Sollipulli, southern Chile: Lithofacies analysis and interpretation

Majority published as: Lachowycz, S.M., Pyle, D.M., Gilbert, J.S, Mather, T.A., Mee, K., Naranjo, J.A., Hobbs, L.K., 2015. Glaciovolcanism at Volcán Sollipulli, southern Chile: Lithofacies analysis and interpretation. J. Volcanol. Geotherm. Res. 303, 59–78.

Author contributions: DMP, JSG, and LKH assisted with fieldwork and preliminary lithofacies analysis. KM helped with map production and lithofacies interpretations. JAN facilitated Ar-Ar dating, created the geomorphological map, and contributed to the geological map and interpretation of the geomorphology. All co-authors contributed to manuscript preparation.

Supplementary Table 5.1, comprising whole rock compositions of samples from the sequences described in this paper, is unpublished data obtained using the methods described in Section 4.3.2.2.

Abstract

Magma-ice-meltwater interactions produce diverse landforms and lithofacies, reflecting the multitude of factors that influence glaciovolcanism, including both magmatic (e.g., composition, eruption rate) and glacial (e.g., ice thickness, thermal regime) conditions. This is exemplified by the walls of the partly ice-filled summit caldera of Volcán Sollipulli, a stratovolcano in southern Chile, which include lithofacies from eruptions of a wide range of magma compositions beneath or in contact with ice. Here we analyse these lithofacies and hence propose new interpretations of the eruptive and glacial history of Volcán Sollipulli. The facies include a thick, laterally extensive sequence of fragmental glaciovolcanic deposits, comprising massive, mafic lava pillow-bearing hyaloclastite overlain by sills and then hyaloclastic debris flow deposits (similar to Dalsheidi-type sequences). The distribution and thickness of these units indicate an unusual abundance of magma-meltwater interaction for an arc stratovolcano in temperate latitudes, perhaps due to eruptions beneath a thick ice cap. Coherent lava coulées, domes, lobes, and stacks of basaltic andesite–trachydacite composition are present around the top of the caldera rim; these display morphologies and fracture patterns on caldera-facing margins that indicate that the caldera was filled with ice when these lavas were erupted. The lithofacies characterised in this study demonstrate the diversity of glaciovolcanism that is possible at arc stratovolcanoes capped by temperate ice or with ice-filled calderas, and the potential for uncertainties in inference of the palaeoenvironmental conditions of their emplacement.

5.1. Introduction

Glaciovolcanism, the interaction between erupting magma and ice (in any form) and the resulting meltwater, is a widespread phenomenon on Earth and Mars (Smellie and Chapman, 2002), the significance of which is increasingly being recognised (Russell et al., 2014). For example, such activity can generate or exacerbate certain volcanic hazards (Tuffen, 2010), such as lahars and floods (e.g., Major and Newhall, 1989), edifice collapse (e.g., Huggel, 2009), and secondary phreatomagmatic explosions (e.g., Belousov et al., 2011). The responses of these hazards and rates of volcanism to past glacial cycles and future climate change are poorly constrained (Tuffen, 2010; Watt et al., 2013a). Furthermore, volcano-ice interactions create a distinctive and wide-ranging suite of landforms (e.g., Smellie, 2009, 2013; Russell et al., 2014) and lithofacies (e.g., Smellie et al., 1993; Loughlin, 2002; Skilling, 2009), which are an invaluable source of terrestrial palaeoenvironmental information, especially prior to the last glaciation (e.g., McGarvie et al., 2007; Smellie et al., 2011, 2014) and on Mars (e.g., Smellie, 2009). This palaeoenvironmental information may include: (1) glacier distribution, from the location of lithofacies indicative of ice interaction (e.g., Smellie, 2009); (2) ice thickness, from any lithofacies stratigraphy indicative of a subglacial to subaerial eruption (e.g., Smellie, 2009), or the magmatic volatile content of quenched glass in subglacial lithofacies (e.g., Tuffen et al., 2010); or (3) glacier thermal regime, from the presence or absence of evidence of fluvial deposits and erosion of the volcanic deposits, which suggest wet-based or cold-based glaciers respectively (e.g., Smellie et al., 2014). Detailed characterisation of the products of glaciovolcanism in each particular setting is necessary to understand their formation processes and the associated hazards, as well as their palaeoenvironmental significance.

Volcano-ice interactions have been studied most extensively in Antarctica, Iceland, and western North America. Tuyas (as defined by Russell et al., 2014), lava-fed deltas (e.g., Skilling, 2002; Smellie et al., 2013), and sheet-like sequences (e.g., Smellie et al., 1993; Smellie, 2008) are the most common glaciovolcanic landforms in these regions (Smellie, 2009, 2013), except parts of western North America (e.g., Lescinsky and Fink, 2000; Kelman et al., 2002). Glaciovolcanism at stratovolcanoes in continental arcs and/or at temperate latitudes may be distinct, as coherent lavas with fracture patterns and/or morphologies indicative of contact with and confinement by ice (e.g., Lescinsky and Fink, 2000) appear to be more typical than these landforms and fragmental glaciovolcanic lithofacies. This has been reported to be the case at volcanoes including Hoodoo Mountain (Edwards and Russell, 2002) and some in the Garibaldi Volcanic Belt (Kelman et al., 2002) in British Columbia, Nevados de Chillán in Chile (Mee et al., 2006, 2009), Ruapehu in New Zealand (Spörli and Rowland, 2006; Conway et al., 2015), and the United States Cascades (e.g., Lescinsky and Sisson, 1998; Lescinsky and Fink, 2000), although hyaloclastite has been noted locally at some volcanoes (e.g., Mee et al., 2009; Schmidt and Grunder, 2009). This difference has been attributed to the comparative rarity of considerable interaction with meltwater (e.g., producing pillow lava or hyaloclastic or phreatomagmatic breccia/tuff: e.g., Loughlin, 2002) in the latter case (Lescinsky and Fink, 2000; Kelman et al., 2002). This was suggested to reflect felsic magmas and alpine-type glacial regimes generally being common at such volcanoes (e.g., in the Andes: Stern, 2004; Rabassa, 2008; Rivera and Bown, 2013): more silicic magmas melt relatively little ice, and meltwater can drain more readily from beneath alpine-type glaciers than ice caps or sheets (Höskuldsson and Sparks, 1997; Kelman et al., 2002); meltwater retention is more likely to be the limiting factor (Stevenson et al., 2009). Nevertheless, it is unclear whether this is a genuine difference between Antarctic or Icelandic and most continental arc glaciovolcanism, or simply a reflection of the relatively few studies of the latter.

In this study, we analyse and interpret glaciovolcanic lithofacies observed on Volcán Sollipulli, a glaciated (i.e., previously glacierised) stratovolcano in southern Chile with a summit caldera that is currently partially filled with ice. In contrast to most of the few previous studies of glaciovolcanism at arc stratovolcanoes, the eruption products described result from diverse magma compositions, and include both an extensively distributed variety of fragmental glaciovolcanic lithofacies and examples of interaction between lava and intra-caldera ice.

5.2. Volcán Sollipulli

5.2.1. Geological and glaciological context

Volcán Sollipulli lies in the central sector of the Andean Southern Volcanic Zone (SVZ) of Chile and Argentina (at 38.97°S, 71.52°W), ~25 km east of the volcanic front between Llaima and Villarrica volcanoes (Figure 5.1). The geological setting of volcanism and the history of explosive eruptions in this region have been reviewed by Stern (2004) and Fontijn et al. (2014) respectively. Of the 74 volcanic centres in southern Chile and Argentina that are thought to have been active since the last glacial period (Fontijn et al., 2014), Volcán Sollipulli is one of the 43 that are at least partly ice-covered at present, and one of the (at least) 20 volcanoes known or suspected to have an ice-filled summit crater or caldera (Siebert et al., 2010; Rivera and Bown, 2013) (Figure 5.1; listed in Supplementary File 5.1). The ~4 km wide caldera at Volcán Sollipulli (Figure 5.2) contained an estimated 4.5 ± 0.5 km^3 of ice to a maximum depth of 593 ± 59 m in February 2011 (Hobbs, 2014), which has reduced in extent and depth over at least the last 50 years (Rivera and Bown, 2013; Hobbs, 2014). Permanent ice is currently almost absent from the flanks of the volcano (Figure 5.2), but there is seasonal snow cover. The volcanoes of the southern Andes were covered by ice at the Last Glacial Maximum (LGM, ~26.5–18 ka here) (Glasser et al., 2008; Clark et al., 2009; Watt et al., 2013a); the extent and timing of prior glacierisations are poorly constrained (Rabassa, 2008), despite the importance of understanding glacial variations in southern South America for palaeoclimatology (e.g., Hulton et al., 2002; Glasser et al., 2008). Glaciovolcanism could provide significant data on past glaciation, yet there are few published studies of volcano-ice interaction in this region (Gilbert et al., 1996; Mee et al., 2006, 2009).

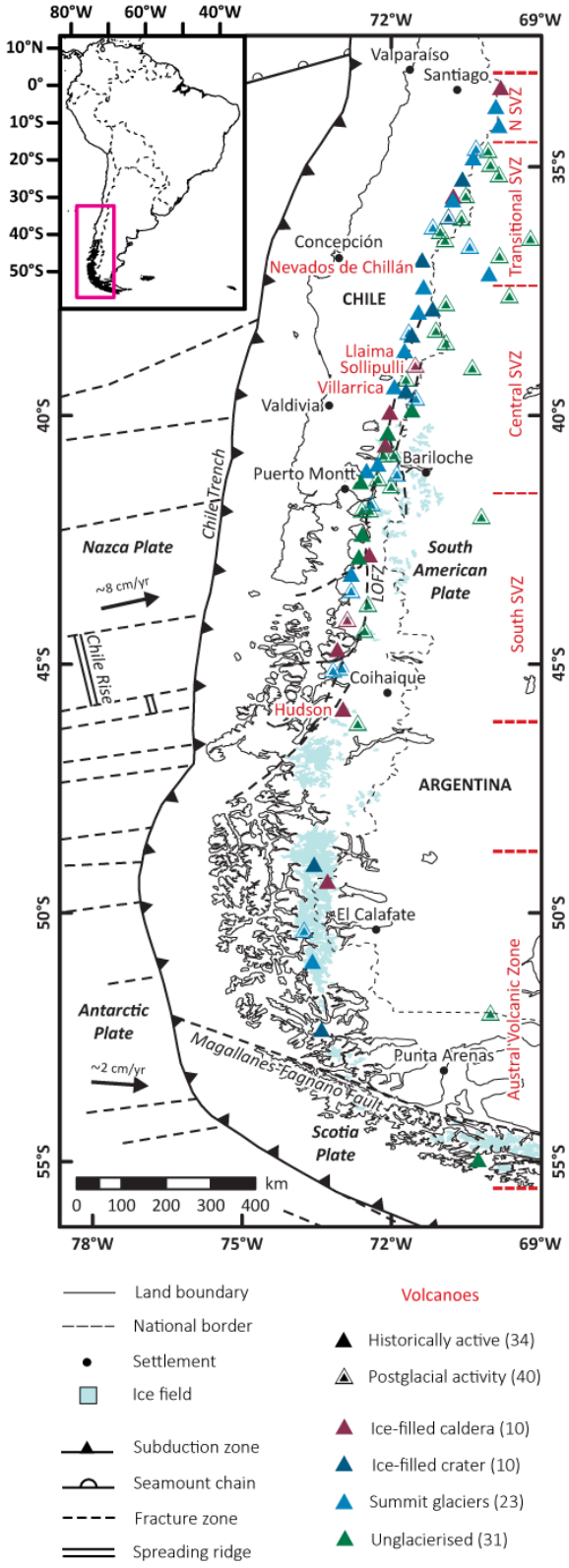

Figure 5.1 Map of southern Chile showing the volcanic centres of the Andean Southern Volcanic Zone (SVZ) and Austral Volcanic Zone (AVZ) for which there is evidence of activity since local glacial retreat (listed in Supplementary File 5.1; modified from Fontijn et al., 2014). The volcanoes are classified by the timing of their most recent known eruption and the presence of glaciers or an ice-filled crater (≤1 km diameter) or caldera (>1 km) (Siebert et al., 2010; Rivera and Bown, 2013); the abundance of glacierised volcanoes shows the considerable potential for glaciovolcanism in this region (Section 5.2.1). The labelled volcanoes are referred to in this paper. Some regional tectonic features that are potentially a significant control on the location of volcanism are also delineated (Bird, 2003; Stern, 2004; Matthews et al., 2011), e.g. the Liquiñe-Ofqui Fault Zone (LOFZ; López-Escobar et al., 1995). The geographical data are from Natural Earth (naturalearthdata.com).

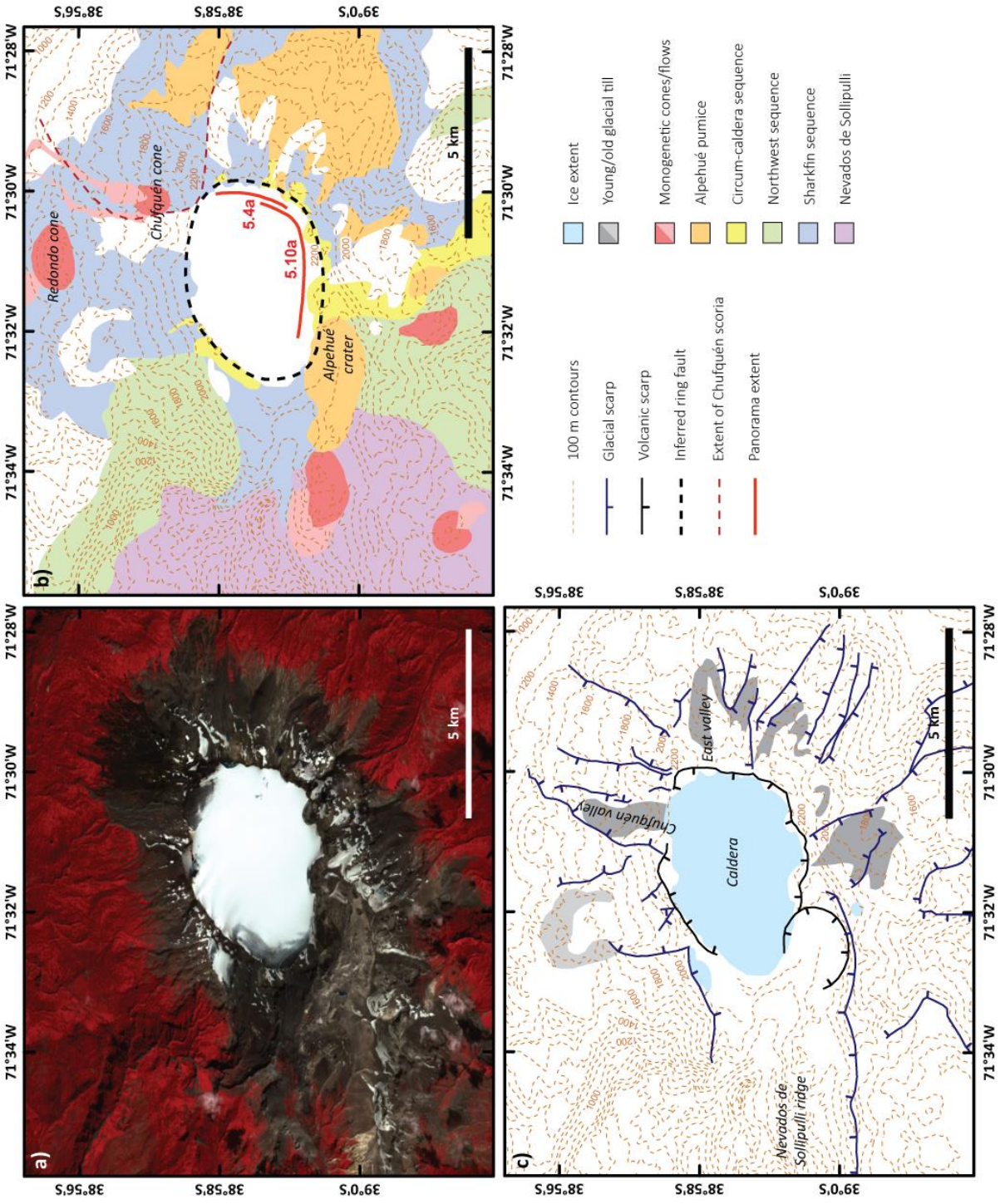

Figure 5.2 (a) Orthorectified ASTER false colour (RGB321) image (USGS and Japan ASTER program, 2012) taken in February 2005, which shows the upper flanks and summit caldera of Volcán Sollipulli. Note the ice-filled caldera and the scarcity of snow cover on the flanks (Section 5.2.1). **(b)** A topographic map of the same area, overlain by our interpretation of the geology, updated from those presented by previous studies (Naranjo et al., 1993a; Gilbert et al., 1996; Murphy, 1996) (Section 5.2.2); the mapped sequences/units are summarised in Table 5.1. The geology away from the caldera rim is largely poorly constrained. The red lines indicate the sectors of the caldera wall shown in Figures 5.4a and 5.10a. **(c)** A map of the topography and selected geomorphological features in the same area. The ice extent in the satellite image is mapped, along with glacial scarps and till deposits, from satellite and aerial imagery; the latter constrain the extent and timing of past glaciation in the summit region (Section 5.2.3). Some of the labelled locations are referred to in the text.

5.2.2. Eruptive history

Volcán Sollipulli has erupted a wide range of magma compositions, from basalt to trachydacite (Figure 5.3). The oldest volcanic rocks on Volcán Sollipulli are thought to be Pleistocene in age, and erupted due to migration of volcanism away from the Nevados de Sollipulli complex, which forms a ridge to the west of Volcán Sollipulli (Figure 5.2) (Naranjo et al., 1993a). The age of the caldera has not previously been constrained; no major pyroclastic units have been attributed to Volcán Sollipulli other than those of the post-caldera Alpehué Plinian eruption (Naranjo et al., 1993a; Fontijn et al., 2014), so the caldera is thought to have formed by a non-explosive mechanism (Gilbert et al., 1996). The main eruptive sequences that have been identified are summarised in Table 5.1, which includes new Ar-Ar and modelled radiocarbon dates for units in some of these sequences; supporting data for these are provided in Supplementary Files 5.2 and 5.3. The approximate distributions of some of the main sequences, inferred from aerial and satellite imagery with limited ground-truthing, are shown in Figure 5.2b.

Earlier work on Volcán Sollipulli (Gilbert et al., 1996; Murphy, 1996) noted evidence of glaciovolcanism, and deduced changes in ice thickness through the eruptive history. However, the stratigraphy we examine here has not previously been described and interpreted in detail. We focus on the lava and fragmental lithofacies units that are exposed on the walls of the east to south sectors of the caldera and in the uppermost Chufquén valley (Figure 5.2), which mostly comprise the 'Sharkfin', 'South', and 'Peak' units described by Gilbert et al. (1996). The pre-caldera Sharkfin sequence was previously interpreted as deposits from subglacial or subaqueous eruptions that became subaerial. The South and (overlying) Peak units, hereafter grouped as the 'circum-caldera' lava sequence (similar to Murphy, 1996), were respectively interpreted as ice-constrained and subaerial lavas emplaced on the margin of the caldera after it had formed (Gilbert et al., 1996).

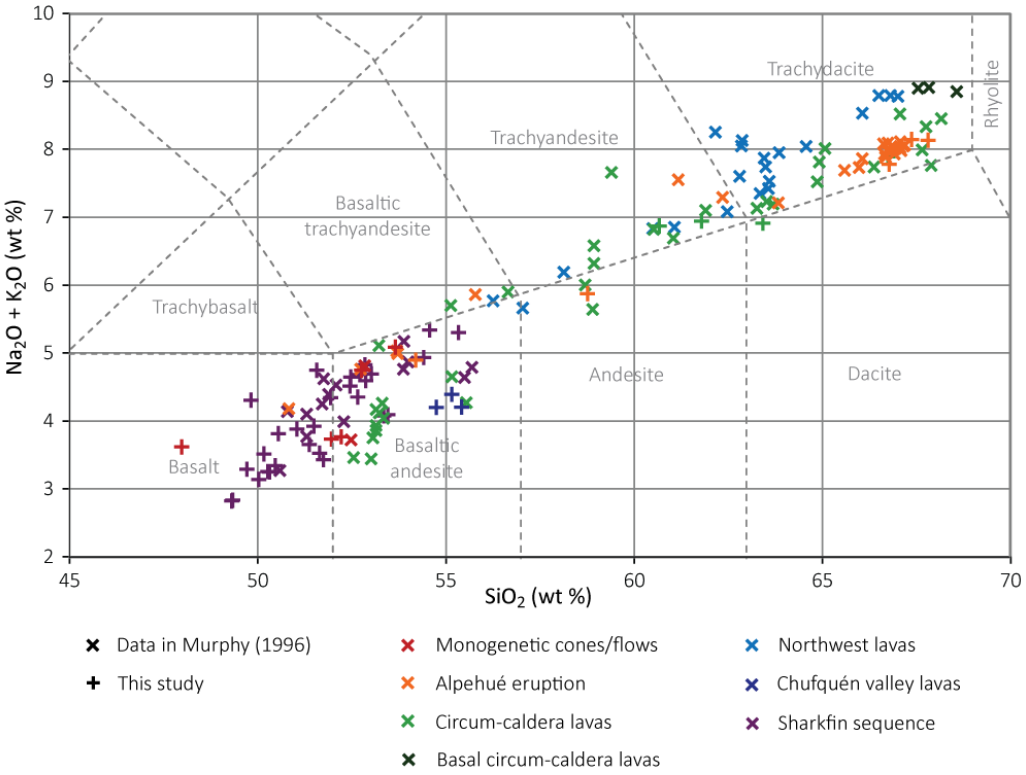

Figure 5.3 Total alkali-silica plot (Le Bas et al., 1985) of the whole rock composition of specimens from some of the sequences/units listed in Table 5.1 and described in Section 5.3. All the data are component oxide weight percentages measured by X-ray fluorescence. The new data presented are for samples prepared using the method described in Section 4.3.2.2; full composition data are provided in Supplementary Table 5.1. Note the clear trends within and mostly distinct nature of the composition of the majority of the sequences/units.

Table 5.1 Summary of the main parts of the stratigraphy of the upper flanks of Volcán Sollipulli, modified from Gilbert et al. (1996) to incorporate data from Naranjo et al. (1993a), Murphy (1996), De Vleeschouwer (2002), Fontijn et al. (in review), Jara and Moreno (in prep.), and this study.

Sequence/unit	Age constraints		Composition[g]	Description	Interpretation
	Stratigraphy	Radiometric dating			
Chufquén	Overlies all other units.	633 ± 87 cal yr BP[a,b]	Basaltic andesite	Scoria cones on the upper NE flank, with a ~6.5 km long ‘a‘ā lava; scoria fall across NE flank.	Subaerial eruption; monogenetic.
Alpehué	Post-CFE: tephra overlies circum-caldera lava sequence.	2938 ± 110 cal yr BP[a,c]	Trachydacite mixed with basaltic andesite	Pumice-rich tephra fall to the north and east of caldera, pyroclastic density current deposits to the south and NW, and lahar deposits to NW.	Plinian eruption.
Redondo	Pre-Alpehué: Alpehué tephra found on summit of scoria cone.		Basalt	Scoria cone on the north flank, with a ~3.5 km long ‘a‘ā lava.	Subaerial eruption; monogenetic.
Circum-caldera (Section 5.3.4)	Post-CFE: vents are located on the caldera rim; evidence for interaction with intra-caldera ice.	26 ± 5 ka[d], 64 ± 15 ka[f], 68 ± 14 ka[d]	Basaltic andesite to trachydacite	Fractured lava domes, coulées, lobes, and sheets on the caldera rim, often overlain by thin ‘a‘ā lavas.	Lavas extruded from a ring dyke, and either constrained by ice or erupted subaerially above the ice level.
Chufquén valley (Section 5.3.3)	Post-date the erosion of the Chufquén valley, so considerable time after the Sharkfin sequence.		Basaltic andesite	Fractured or marginally brecciated lavas in the upper Chufquén valley.	Subaerial, flooded, and ice-constrained effusive eruptions.
Northwest	Overlain by the circum-caldera lavas. Appears to overlie the Sharkfin sequence. Prior to CFE?	100 ± 30 ka[e], 110 ± 30 ka[e], 120 ± 14 ka[f], 120 ± 16 ka[f]	Dacite (and andesite?) with mafic inclusions	Thin ‘a‘ā lavas, with a few fractured lavas from a later flank eruption. The top of the sequence has glacial striae.	Subaerial effusive eruptions. Glacial advance after lava emplacement.
Sharkfin (Section 5.3.2)	Pre-CFE: forms part of the caldera walls. Overlain by the circum-caldera lava sequence.	350 ± 90 ka[d], 700 ± 140 ka[d]	Basalt to basaltic andesite	Thin ‘a‘ā lavas, pillow lava and palagonitised tuff-breccias, and palagonitised debris flow deposits with scoria units; abundant intrusions.	Predominantly subglacial/ subaqueous eruptions.
Other scoria cones	Unconstrained		Basalt to basaltic andesite?	Other scoria cones, some with lavas.	Eruptions similar to the Chufquén and Redondo cone-forming events.
Nevados de Sollipulli	Assumed Pliocene/Pleistocene.	312 ± 20 ka[e], 490 ± 30 ka[f]	Basaltic andesite to dacite?	Composite ridge of multiple sequences of lavas and tuff-breccias, possibly including hyaloclastite.	Various subaerial and/or subglacial eruptions.

CFE = caldera-forming event.

[a] ^{14}C dates calibrated in OxCal v4.2.4 (Bronk Ramsey, 2009a) using the SHCal13 atmospheric calibration curve (Hogg et al., 2013); 2σ confidence interval.
[b] Single date from Naranjo et al. (1993a) (Supplementary File 5.3).
[c] Date for eruption from Bayesian modelling (in OxCal v4.2.4) incorporating multiple dates and stratigraphic constraints (Supplementary File 5.3).
[d] Plateau Ar-Ar dates obtained from groundmass samples for this study (Supplementary File 5.2); 2σ confidence interval.
[e] Plateau and [f] isochron Ar-Ar dates from groundmass samples to be published in Jara and Moreno (in prep.); 2σ confidence interval.
[g] The whole-rock composition ranges of most of these sequences/units are shown in Figure 5.3.

5.2.3. Geomorphological constraints on glacial history

From aerial and satellite imagery, we map several till deposits and numerous scarps on the upper flanks of Volcán Sollipulli (Figure 5.2c). With the exception of those forming the walls of the caldera and the Alpehué crater, the scarps are roughly slope-parallel (i.e., mostly radiate from the caldera); we infer that these originate from glaciation. With further geological mapping and radiometric dating, the relationships between these features and the geology with which they are associated could constrain the timing and extent of glaciation of the volcano, to complement inferences from the evidence of glaciovolcanism. For example, most of the young till deposits mapped in Figure 5.2c appear to overlie pumice deposits from the Alpehué eruption, and possibly also scoria from the Chufquén eruption in the Chufquén and East valleys (Figures 5.2b and 5.2c). This suggests that these till deposits mark the maximum extent of glaciers in the past ~2.9 ky, or possibly the past ~630 years, considering the dates of those eruptions (Table 5.1). The Chufquén and East valleys themselves have eroded through the Sharkfin sequence, so must post-date its emplacement at <~350 ka (Table 5.1), and the Chufquén valley must pre-date the eruption of the (undated) Chufquén valley lavas.

5.3. Lithofacies and sequence descriptions

5.3.1. Lithofacies classification

We recognise 16 discrete volcanic lithofacies in the eruptive sequences described in this article; a summary description and interpretation and the assigned code for each lithofacies are listed in Table 5.2. No glaciogenic deposits were identified within the sequences studied. The grain size and classification terms used are as defined for primary volcaniclastic rocks by White and Houghton (2006). Discrete classification of the lithofacies in the Sharkfin sequence (Section 5.3.2) is challenging due to their diversity and complex associations, typical of some glaciovolcanic sequences (e.g., Smellie et al., 1993; Loughlin, 2002; Skilling, 2002). We distinguish lava, tuff-breccia, lapilli-tuff, and tuff; lavas are differentiated by morphology, and fragmental deposits by their componentry (including presence/absence of pillow fragments) and then sorting, association, or composition. Some of the lithofacies accompany one another (e.g., coherent lava with lava margin tuff-breccia), but not exclusively, so they are not grouped together. Most of the fragmental lithofacies are often gradational with those with which they are commonly associated. Some additional subdivisions were rejected because the resulting lithofacies would be distinguished only by characteristics that are not always present (e.g., bedforms) or can be ambiguous (e.g., stratigraphic context).

This classification scheme is similar to those of (for example) Loughlin (2002), Skilling (2009), and Watton et al. (2013). In contrast to those studies, we do not use hyaloclastite as a lithofacies descriptor (despite many of the palagonite-bearing lithofacies being interpreted as hyaloclastic), due to its genetic connotations. The term hyaloclastite has previously been ascribed to a variety of volcaniclastic rock types formed both by primary fragmentation and reworking, as outlined by Watton et al. (2013). Here it is used as prescribed by Rittman (1958), for deposits that are thought

Table 5.2 Summary descriptions and interpretations of the discrete volcanic lithofacies identified in the outcrops studied on Volcán Sollipulli.

Lithofacies		Code	Occurrence	Examples	Description	Common associations	Interpretation
Lavas	Coherent lava	*Lc*	CC, CV, SL	Fig. 5.5 Fig. 5.9c	Lava with only a low density of irregular blocky or columnar fractures, occasionally with reddened surfaces. ~0.5 to tens of m thick. Commonly grades into or is bounded by tuff-breccia or fractured lava with lava fragments of the same composition.	*BCl*, *Lf*	(Interior of) lavas emplaced subaerially or with minimal interaction with ice or water (e.g., beneath snow or a freely draining thin glacier).
	Highly fractured lava	*Lf*	CC, CV	Fig. 5.9a Fig. 5.10b	Lava that is pervasively fractured, typically in patterns indicative of rapid cooling (e.g., hackly), with negligible palagonite-bearing tuff or tuff-breccia. Present towards margins of ~1 to tens of m thick coulées, domes, lobes, and sheets.	*Lc*, *BCl*	Lava cooled rapidly by meltwater saturation/ penetration resulting from contact with ice. The orientation, distribution, and pattern of fracturing reflect the nature of the cooling front.
	Pillow lava (with minor tuff-breccia)	*Lp*	SH	Fig. 5.6b	Mostly intact lava pillows ~0.3 to a few m across, often elongate or irregular in shape, irregularly or radially fractured, and/or brecciated at their margins. <30% interstitial palagonitised fine-grained matrix with lapilli–block-sized angular lava fragments.	*BC*, *BMp*, *BM*	Lava erupted into ponded meltwater beneath ice, with only marginal quench fragmentation forming interstitial hyaloclastic tuff-breccia.
Clast-supported tuff-breccias	Clast-supported tuff-breccia	*BC*	SH	Fig. 5.6b Fig. 5.6g	Predominantly clast-supported tuff-breccia comprising poorly sorted, lapilli–block-sized angular lava fragments in a matrix of ash–fine lapilli-sized palagonitised glass and crystal fragments. Bedding rare. Can grade into and/or contain pods of matrix-supported tuff-breccia.	*Lp*, *BMp*, *BM*	Subaqueous lava (erupted into ponded meltwater beneath ice), brecciated by passive quench and mechanical fragmentation.
	Lava margin tuff-breccia	*BCl*	CC, CV	Fig. 5.9c Fig. 5.10g	Predominantly clast-supported tuff-breccia comprising poorly sorted, lapilli–block-sized angular lava fragments in a (sometimes oxidised) matrix of ash–fine lapilli-size fragments. Often bounds coherent lava.	*Lc*, *Lf*	Marginal autobreccia of subaerial ‘a‘ā or blocky lava.
	Lava margin palagonite-bearing tuff-breccia	*BClp*	SL	Fig. 5.5	Predominantly clast-supported tuff-breccia comprising poorly sorted, lapilli–block-sized angular lava fragments in a slightly oxidised matrix of ash–fine lapilli-sized fragments of crystals and partially palagonitised glass. Bounds some coherent lava units.	*Lc*	Marginal autobreccia of lavas, with some palagonitised glass from quench fragmentation and alteration due to the presence of meltwater during emplacement (beneath ice?).
Matrix-supported tuff-breccias	Matrix-supported tuff-breccia	*BM*	SD, SH	Fig. 5.6a Fig. 5.7b	Predominantly matrix-supported tuff-breccia comprising poorly-sorted, predominantly block-sized, usually angular lava fragments in a matrix of ash–fine lapilli-sized palagonitised glass and crystal fragments. Bedding rare; can form lenticular units.	*BC*, *BMp*, *TL*, *Tp*	From fragmentation of lava erupted into ponded meltwater beneath ice; sometimes remobilised by slumping and/or meltwater flow.
	Pillow lava-bearing tuff-breccia	*BMp*	SH	Fig. 5.6c Fig. 5.6e	Predominantly matrix-supported tuff-breccia comprising isolated (typically irregular) lava pillows and/or pillow fragments, together with poorly sorted, predominantly block-sized angular lava fragments in a matrix of ash–fine lapilli-sized palagonitised glass and crystal fragments. Bedding rare.	*Lp*, *BC*, *BM*	Sliding or emplacement of pillows into more fragmented primary or remobilised deposits, and/or brecciated by enhanced mechanical or quench fragmentation. Subaqueous (erupted into ponded meltwater beneath ice).

(continued on next page)

Table 5.2 *(continued from previous page)*

Matrix-supported tuff-breccias	Oxidised scoria-bearing tuff-breccia	*BMs*	SD	Fig. 5.7e	Poorly sorted, lapilli–block-sized angular scoria clasts/fragments with oxidised surfaces in a red oxidised matrix of ash–fine lapilli-sized fragments of scoria, crystals, and palagonitised glass. Clast:matrix ratio highly variable. Occasional planar bedding.	*TLp, TLw, Tb, Tp*	Subaerial spatter/explosive eruption deposits reworked in debris flows.
Lapilli-tuffs	Lapilli-tuff	*TL*	SD, SH	Fig. 5.6d	Predominantly matrix-supported lapilli-tuff comprising generally lapilli-sized, mostly angular lava fragments in a matrix of ash–fine lapilli-sized palagonitised glass and crystal fragments; variable sorting. Bedding only when associated with bedded units.	*BMp*, *BM*, *TLp*	Relatively fine-grained fraction of deposits from fragmentation of lava erupted into ponded meltwater beneath ice; likely remobilised by meltwater flow.
	Lava margin palagonite-bearing lapilli-tuff	*TLlp*	SL	Fig. 5.5	Predominantly matrix-supported lapilli-tuff comprising poorly sorted, lapilli-sized angular lava fragments in a slightly oxidised matrix of ash–fine lapilli-sized fragments of crystals and partially palagonitised glass. Grades into altered palagonite-rich tuff.	*Lc*, *TLpa*	Basal lapilli-tuff of lavas emplaced on a palagonite-rich sediment layer.
	Poorly sorted palagonite-rich lapilli-tuff	*TLp*	SD, SH	Fig. 5.6g Fig. 5.7d	Matrix-supported lapilli-tuff comprising <30% poorly sorted, typically lapilli-sized subangular lava fragments, in a matrix of ash–fine lapilli-sized palagonitised glass and crystal fragments. Massive or (less commonly) planar-bedded units.	*TLw*, *Tp*	Subglacial eruption deposits reworked in relatively high-energy debris flows (due to subglacial meltwater drainage).
	Well-sorted palagonite-rich lapilli-tuff	*TLw*	SD, SH	Fig. 5.6g Fig. 5.7d	Matrix-supported lapilli-tuff comprising <30% well-sorted, typically lapilli-sized subangular lava fragments in a matrix of ash–fine lapilli-sized palagonitised glass and crystal fragments. Massive, or planar-bedded units that sometimes extend >100 m downslope.	*TLp*, *Tp*	Finer-grained fractions of subglacial eruption deposits reworked in relatively low-energy debris flows (due to subglacial meltwater drainage); extensive deposits from outburst floods.
Tuffs	Palagonite-rich tuff	*Tp*	SD, SH, SL	Fig. 5.5 Fig. 5.7b	Well-sorted ash–fine lapilli-sized fragments of palagonitised glass and crystals, with rare lava fragment clasts. Sometimes infills cavities in underlying units; can also form massive or (usually) planar-bedded units that sometimes extend >100 m downslope.	*TLp*, *TLw*, *TLlp*, *BClp*	Fine-grained matrix fraction of subglacial eruption deposits reworked in relatively low-energy debris flows (due to subglacial meltwater drainage); extensive outburst flood deposits.
	Altered palagonite-rich tuff	*Tpa*	SL	Fig. 5.5	Well-sorted medium tuff–fine lapilli-tuff comprising fragments of palagonitised glass and crystals, increasingly altered and with increasingly abundant lapilli–block-sized lava clasts towards contacts with overlying lava margin palagonite-bearing tuff-breccia.	*Tp*, *TLlp*	Redeposited fine-grained matrix fraction of subglacial eruption deposits, which have been thermally altered and partially mixed with the basal lapilli-tuff of a lava flow emplaced on top.
	Bedded tuff	*Tb*	SD	Fig. 5.7e	Finely planar bedded/laminated (or occasionally massive), very well-sorted ash–lapilli-sized tephra. Variable palagonitisation.	*Tp*, *BMs*	Explosive subaqueous (phreatomagmatic)? eruption deposits. Potentially reworked.

CC = Circum-caldera lava sequence; CV = Chufquén valley lavas; SD = Sharkfin debris flow subsequence; SH = Sharkfin hyaloclastite subsequence; SL = Sharkfin lava subsequence.

to result from predominantly passive (quench and mechanical) magma fragmentation, with only relatively limited explosive lava-water interaction (e.g., Skilling, 2009; Watton et al., 2013), but also including those locally remobilised (Watton et al., 2013). However, some studies have argued or assumed that (phreato)magmatic fragmentation is the dominant process forming such rocks (e.g., Tuffen, 2007; Edwards and Russell, 2011; Pollock et al., 2014).

5.3.2. Sharkfin sequence

We subdivide the Sharkfin sequence into three main subsequences, lava (SL), hyaloclastite (SH), and debris flow (SD); these are described and defined below. The stratigraphy (including that of the circum-caldera lavas where overlying this sequence) in the areas studied is summarised in Figure 5.4.

5.3.2.1. Sharkfin lava subsequence (SL)

This subsequence is principally present at the bottom of the Sharkfin sequence in the SE sector of the caldera wall (Figure 5.4a), but is occasionally also above the hyaloclastite subsequence (Figure

---

Figure 5.4 *(next page)* Overview of the stratigraphy of the pre-caldera 'Sharkfin' sequence (Section 5.3.2) and part of the overlying circum-caldera lava sequence (Section 5.3.4), which shows the consistent nature of the general stratigraphy where these units are exposed around the caldera. In Parts a to f, most dashed lines approximately delineate the contacts between different subsequences (labelled), the yellow boxes and arrows indicate the extent and/or location of sections of the caldera wall shown in other figure parts, and the red arrows point to the location of dykes that have been Ar-Ar dated to the stated ages (Supplementary File 5.2; Section 5.3.2.2). **(a)** Panorama of the E to SE section of the caldera wall (marked on Figure 5.2b), showing most of the key outcrops of the Sharkfin sequence. **(b)** Outcrop of the middle to upper part of the Sharkfin sequence, overlain by circum-caldera lavas dipping both into and out of the caldera. **(c)** Alternate view of the circum-caldera lavas shown in Part b. **(d)** Outcrop of the lower to middle part of the Sharkfin sequence, including the lava subsequence capping the hyaloclastite subsequence, which is uncommon. **(e)** Outcrop of all the main parts of the stratigraphy in this section of the caldera rim. **(f)** View of the west side of the uppermost Chufquén valley (Figure 5.2c), where the middle to upper part of the Sharkfin sequence is also exposed. **(g)** Generalised and simplified vertical profiles for the sections of the caldera wall where the Sharkfin sequence is present. The (sub)sequence (bold) and lithofacies (italic) codes correspond to those in Table 5.2. Note that the clast size variations within each subsequence are representative of their range and variability, but are not based upon a specific vertical section as there is no consistent internal stratigraphy.

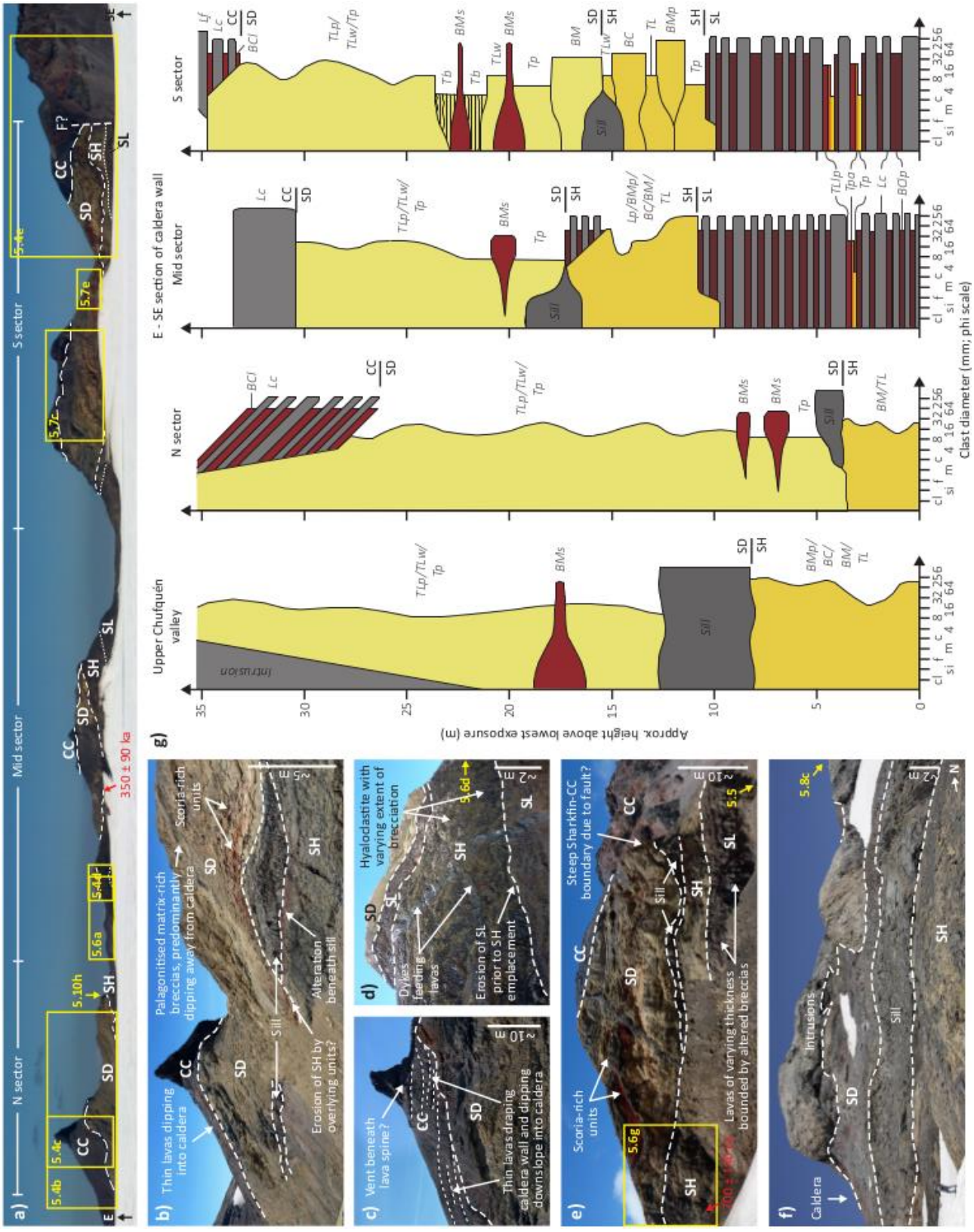

Figure 5.4 *(caption on previous page)*

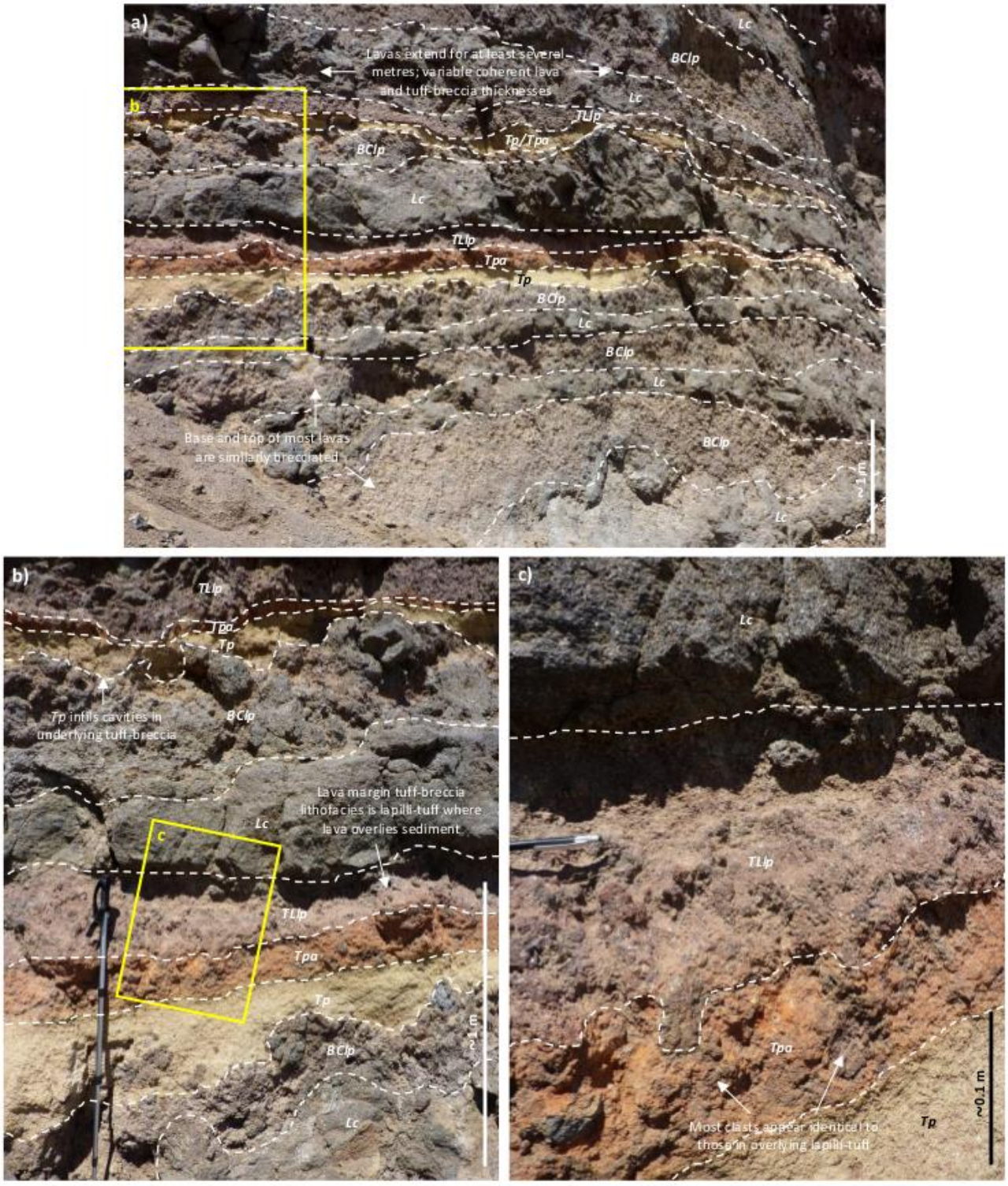

Figure 5.5 Photographs of a caldera-rim outcrop of the Sharkfin lava subsequence (located where indicated in Figure 5.4e), which show the main features of this subsequence described in Section 5.3.2.1, and the constituent lithofacies described in Table 5.2 (the lithofacies (italic) codes correspond to those in Table 5.2). The dashed lines delineate the approximate boundaries between lithofacies. The yellow boxes indicate the approximate areas magnified in other photographs. **(a)** Part of the outcrop, showing multiple tuff-breccia-enclosed lavas and two interspersed palagonitised tuff units. **(b)** and **(c)** Closer views of a section of Part a, which show the relationships between the constituent lithofacies in more detail. Note that the lava margin tuff-breccia *TLlp* shown in Part c is an atypical lithofacies that is only present where a lava unit overlies a palagonitised tuff unit.

5.4d). It predominantly comprises porphyritic basaltic ‘a‘ā lavas of varying vesicularity and (plagioclase, olivine, and minor clinopyroxene) phenocryst content; a representative exposure is presented in Figure 5.5. The coherent lava units, usually cut into sub-metre-sized blocks by irregular fractures, range in thickness from ~0.3–1.5 m, and are bounded by tuff-breccia units of a similar thickness range (Figure 5.5a). This tuff-breccia, which is generally clast-supported, is composed of poorly sorted, often scoriaceous lapilli- to block-sized angular lava fragments in a typically uniform, oxidised matrix, which comprises ash- to fine lapilli-sized glass and crystal fragments (Figure 5.5b). The majority of the finest-grained component of this matrix is palagonitised glass, which is uniformly distributed within the breccia. Some of the lava-breccia packages are separated by a <0.5 m thick layer of well-sorted medium ash- to fine lapilli-sized palagonitised glass and crystal fragments. These layers infill cavities in underlying units and appear to have been altered/oxidised where in proximity to and partly mixed with the overlying lava margin units (Figures 5.5b and 5.5c). The overlying units of lapilli-tuff have a higher proportion of smaller clasts and a lower clast:matrix ratio than the tuff-breccia elsewhere in the subsequence (Figure 5.5b).

The top of this subsequence is delineated by the first occurrence of massive palagonitised tuff-breccia or lapilli-tuff (hyaloclastite subsequence: Section 5.3.2.2), which sometimes cross-cuts the uppermost lavas (Figure 5.4d). There is no evidence of grading or apophyses of the lava into the hyaloclastite, which are often present in Mt Pinafore-type (sheet-like) sequences (Smellie et al., 1993; Smellie and Skilling, 1994). The base of the subsequence is not exposed; the largest exposure of these lavas is at least ~11 m thick (Figure 5.4g). All but the thinnest units appear to be laterally continuous in the caldera wall for at least several metres (e.g., Figure 5.4e), but it is not possible to confidently correlate individual units between the main outcrops. The downslope continuation of the subsequence was not confirmed due to the inaccessibility of the slopes. The

main outcrops in the caldera walls were not described by Gilbert et al. (1996) because they have been exposed by the intra-caldera ice retreat since this earlier study (Hobbs, 2014).

5.3.2.2. Sharkfin hyaloclastite subsequence (SH)

This subsequence mostly comprises pillow lava and massive tuff-breccia containing poorly sorted, lapilli- to block-sized monomict angular lava clasts (some discernible as pillow fragments) in a palagonitised matrix. This matrix is composed of medium ash- to fine lapilli-sized palagonitised glass and crystal fragments; matrix-dominated (i.e., palagonitised lapilli-tuff and tuff) lithofacies are present, but relatively uncommon. Example outcrops are shown in Figure 5.6. The lava components are of basalt to basaltic andesite composition, with occasional plagioclase, olivine, and minor clinopyroxene phenocrysts and, notably, variable vesicularity (from 0% to ~60%; e.g., compare Figure 5.6b and Figure 5.6f). There is considerable spatial variation (usually gradational) in pillow form (e.g., shape, fracturing, and fragmentation extent) and size, and clast size distribution and clast:matrix ratio, but no consistent stratigraphy (e.g., Figure 5.6a). The lithofacies present form a continuum from fractured irregular lava pillows (up to ~1 m tall and a few metres long; e.g., Figure 5.6b) through increasingly disaggregated lava masses (e.g., Figure 5.6c) to angular to subrounded lava fragments (e.g., Figure 5.6d), in an increasing proportion of matrix. Where they appear to be in situ, the lava pillows have highly fragmented margins, for example surrounded by tuff-breccia that is increasingly rich in palagonitised matrix away from the pillow centre (Figure 5.6b) or by fragments of chilled margin (Figure 5.6f), irrespective of the vesicularity of the lava. In places, pillows are isolated in tuff-breccia (i.e., matrix supported); a range of pillow:breccia ratios are observed (e.g., compare Figure 5.6c and Figure 5.6e). Pillow-bearing or clast-rich tuff-breccia can occasionally be found as lenses or sheets within palagonitised lapilli-tuff/tuff sorted to varying extents (Figure 5.6g). The frequent gradational spatial variations in lithofacies mean it is not possible to correlate units within this subsequence between outcrops.

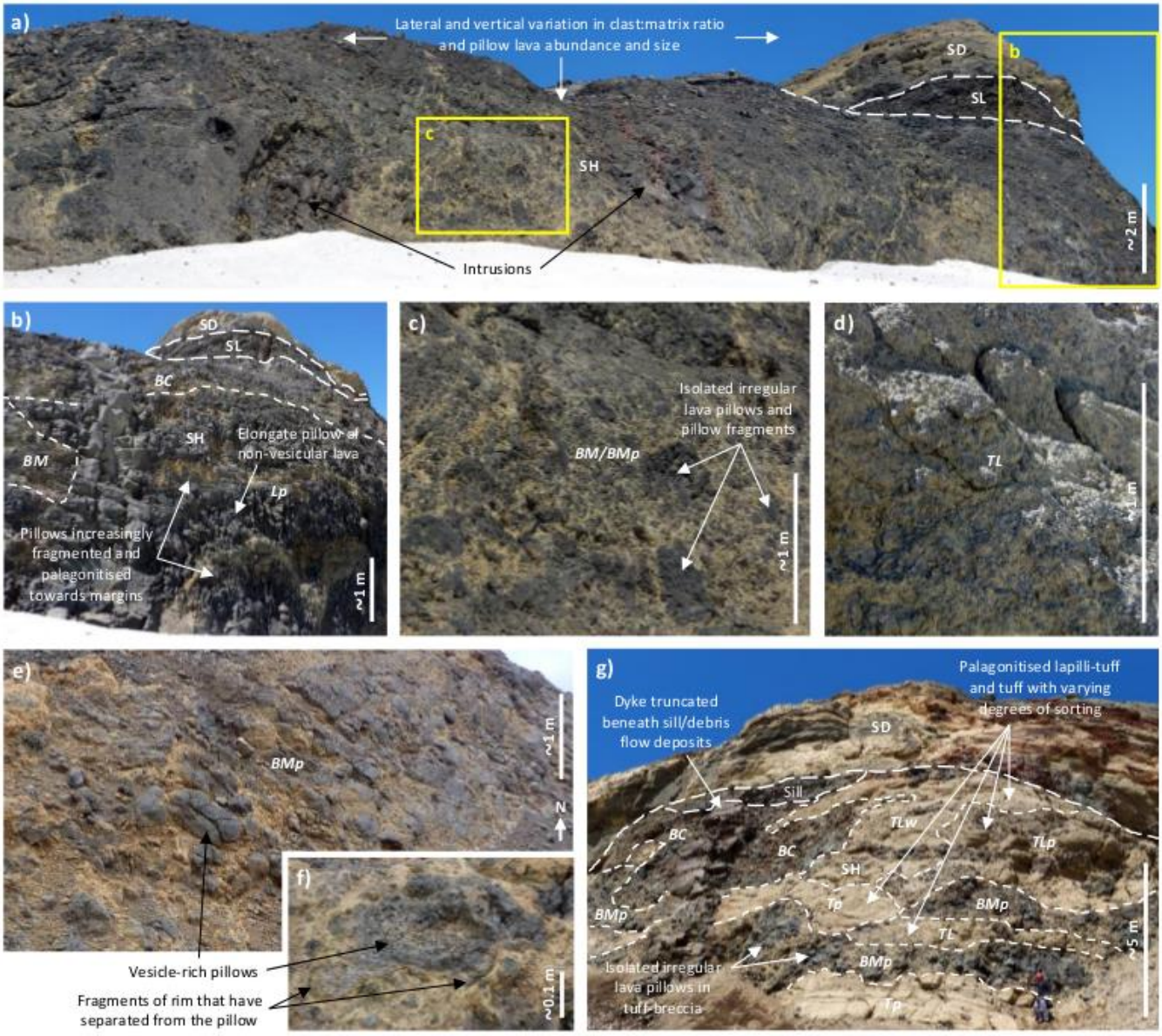

Figure 5.6 Photographs of outcrops that exemplify features of the Sharkfin hyaloclastite subsequence that are described in Section 5.3.2.2, and show the constituent lithofacies described in Table 5.2 (the (sub)sequence (bold) and lithofacies (italic) codes correspond to those in Table 5.2). The short-dashed lines approximately delineate some of the different lithofacies; the longer dashed lines approximately delineate subsequence boundaries. **(a)** A caldera-rim outcrop (approximately demarcated in Figure 5.4a), showing the metre-scale variations in pillow size/shape and content, clast size, and clast:matrix ratio (and so lithofacies) and absence of a consistent stratigraphy, which are typical of the subsequence. The yellow boxes indicate the approximate areas magnified in the subfigure specified. **(b,c,d)** Closer views of caldera-rim outcrops (Part d is located where indicated on Figure 5.4d) showing sections of the spectrum of hyaloclastite textures, from lava pillows with fragmented margins (Part b) through pillow fragment tuff-breccia (Part c) to block- and then lapillus-sized angular to subrounded lava fragment tuff-breccia and lapilli-tuff (Part d). **(e)** An outcrop in the upper Chufquén valley (Figure 5.2c) showing relatively small, vesicular, and rounded lava pillows isolated within palagonitised lapilli-tuff. **(f)** A single pillow in the same unit as the outcrop in Part e, which shows the vesicularity of the lava and a fragmented rim that has separated from the pillow. **(g)** A caldera-rim outcrop (approximately demarcated in Figure 5.4e) where this subsequence (atypically) comprises lenses/sheets of tuff-breccia (mostly pillow-bearing) within palagonitised tuff and lapilli-tuff.

Most of the studied outcrops of this subsequence are cut by dykes, the majority of which are <2 m in width and similar in composition to the lava pillows and clasts in the tuff-breccia or lapilli-tuff. Some of these dykes appear to feed lava pillows or upper parts of the subsequence (e.g., Figure 5.4d), and some are truncated at the contact with the overlying debris flow subsequence (e.g., Figure 5.6g). Groundmass samples from two of these truncated dykes (marked on Figure 5.4) have been Ar-Ar dated by the method outlined in Arancibia et al. (2006) to 350 ± 90 and 700 ± 140 ka (Supplementary File 5.2). The former of these coincides with a cool marine isotope stage during a glacial period (MIS 10, ~374–337 ka; Lisiecki and Raymo, 2005); the latter has a mean square weighted deviation (MSWD) <<1 (Supplementary File 5.2), so is unlikely to be robust. Therefore, the difference between the two dates does not necessarily indicate a long hiatus between the emplacement of the hyaloclastite and debris flow subsequences. The base of the debris flow subsequence clearly cuts into underlying units in places (e.g., Figure 5.4b), indicating erosion of parts of the hyaloclastite subsequence, which may account for its variable thickness, from ~2 to >12 m (Figure 5.4g). Outcrops of this subsequence are recognised in all sectors of the caldera wall where the Sharkfin sequence is exposed (Figures 5.2 and 5.4), rather than just some parts as reported by Gilbert et al. (1996); the additional outcrops have been exposed by the intra-caldera ice retreat since this earlier study (Hobbs, 2014). Lithofacies found in this subsequence have also been recognised on the uppermost flanks that were accessible, on the north, northeast (including at one location ~1.5 km down the Chufquén valley (Gilbert et al., 1996)), and east sides.

5.3.2.3. Sharkfin debris flow subsequence (SD)

This subsequence primarily contains massive and planar- or cross-bedded tuff and lapilli-tuff units, comprising lava clasts in a matrix of medium ash- to fine lapilli-sized palagonitised glass and crystal fragments. Examples of the lithofacies and their relationships are shown in Figure 5.7. Both

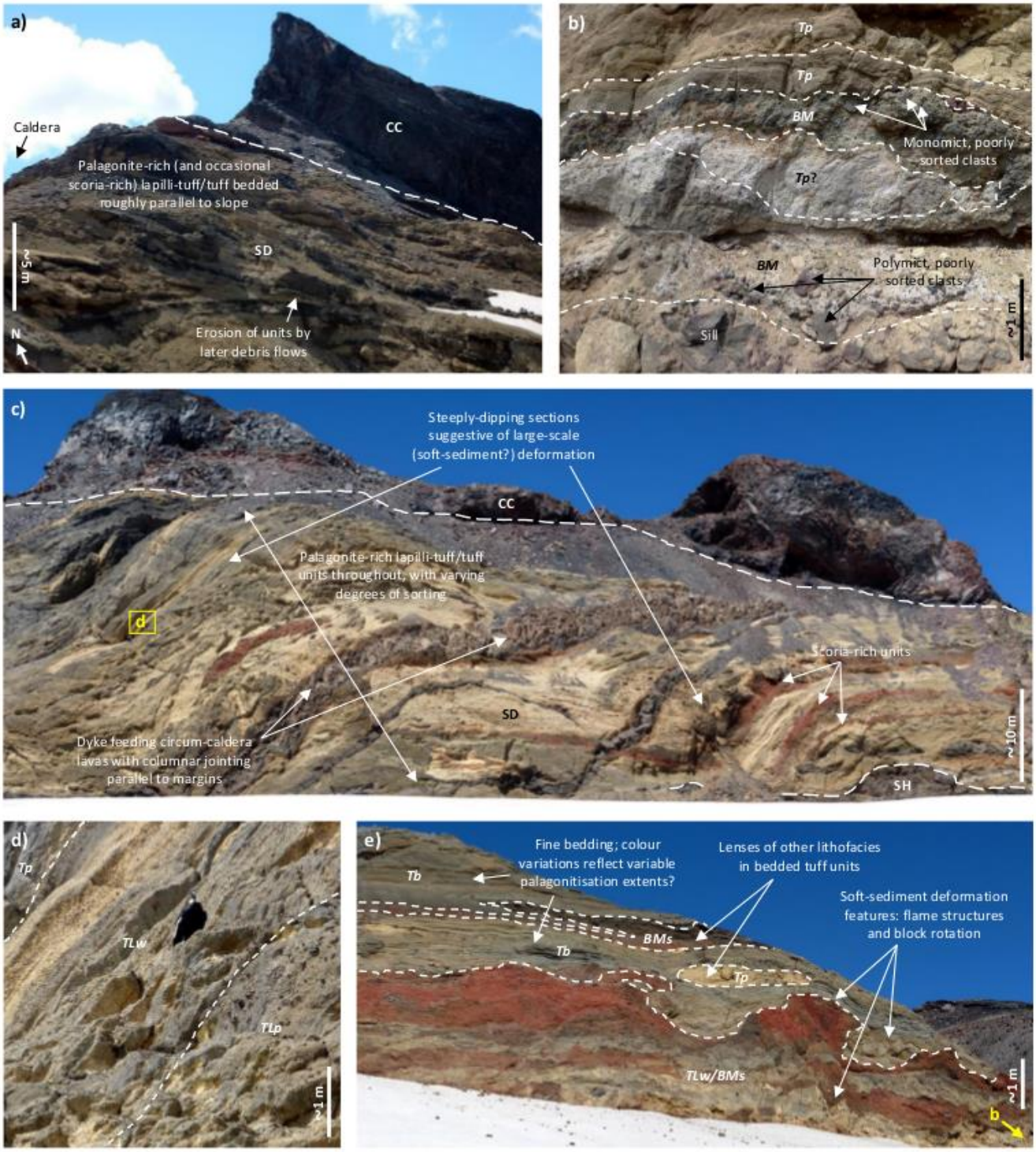

Figure 5.7 *(caption on next page)*

Figure 5.7 *(previous page)* Photographs of outcrops that exemplify features of the Sharkfin debris flow subsequence that are described in Section 5.3.2.3, and of some of the constituent lithofacies described in Table 5.2 (the (sub)sequence (bold) and lithofacies (italic) codes correspond to those in Table 5.2). The short-dashed lines approximately delineate some of the different lithofacies or units; the longer dashed lines approximately delineate subsequence boundaries. **(a)** View of the north side of the uppermost part of the East valley (Figure 5.2c), which shows the slope-parallel stratigraphy of some units of the debris flow subsequence (observed in the caldera walls in Figure 5.4b). **(b)** A caldera-rim outcrop (located where indicated on Figure 5.7e) showing examples of the tuff-breccias and palagonitised tuffs that are respectively sometimes and often present at the base of the subsequence. Note the channelised distribution of some of the units, which are defined by abrupt changes in colour and/or texture, and so even those with the same lithofacies classification are distinguishable. **(c)** A caldera-rim outcrop (approximately demarcated in Figure 5.4a) predominantly showing palagonitised tuff/lapilli-tuff lithofacies typical of the middle and upper parts of the subsequence, and examples of the large length-scale deformation present in parts of this subsequence. The yellow box indicates the approximate area shown in Part d. **(d)** View of some of the (inaccessible) units typical of the upper part of this subsequence, showing that they comprise variably sorted, palagonitised lapilli-tuff and tuff. **(e)** A caldera-rim outcrop (approximately demarcated in Figure 5.4a) showing the scoria-bearing and variably palagonitised lapilli-tuff/tuff units in this subsequence, and examples of the smallest-scale soft-sediment deformation present.

---

monomict and polymict lapilli-tuff and tuff-breccias are present (e.g., Figure 5.7b); the majority of clasts are fine to coarse lapilli-sized, angular to subrounded lava fragments of similar composition to those in the hyaloclastite subsequence. The clast:matrix ratio and extent of sorting are variable (e.g., Figures 5.7b and 5.7d); some units have inversely graded bases and/or irregular elutriation pipes (containing a higher concentration of clasts) (Gilbert et al., 1996). The matrix-supported tuff-breccias sometimes present at the base of the subsequence are distinguishable from the tuff-breccia of the hyaloclastite subsequence by their occurrence as discrete units with contrasting clast sizes and sorting (Figure 5.7b). Finely bedded, variably palagonitised/lithified, and well-sorted ash/tuff and lapilli/lapilli tuff units, which sometimes contain lenses of tuff-breccia lithofacies, are observed in some outcrops towards the middle of the subsequence (Figure 5.7e). Note that ash-lapilli units do not form the upper units of the subsequence, as thought by Gilbert et al. (1996), which are in fact palagonitised tuff/lapilli-tuff (Figures 5.7c and 5.7d).

Two (or occasionally more) distinctive scoria-bearing units, of highly variable thickness up to ~1.5 m, are present close together in the lower to middle part of this subsequence in most outcrops (see parts of Figures 5.4, 5.7, and 5.8). These comprise a variable proportion of lapilli- to block-sized oxidised scoria clasts in a matrix that is typically similar in texture to the surrounding units, but with an oxidised component. A dissected scoria cone is present in the NNE caldera wall at approximately the same stratigraphic level as the adjacent debris flow subsequence deposits, but these scoria-bearing units cannot be confidently attributed to this; other possible source scoria cones are present on the upper flanks (Figure 5.2b). These units are significant as marker horizons to correlate outcrops of this subsequence. Some other individual units are traceable for tens of metres, both in the caldera rim outcrops and downslope (e.g., Figures 5.7a and 5.7c); these sheet deposits are interspersed with some less extensive units, apparently either eroded (e.g., Figure 5.7a) or channelised (e.g., Figure 5.7b). Another distinguishing feature of this subsequence is the evidence of soft-sediment deformation on a range of length scales, exemplified in Figures 5.7c and 5.7e.

This subsequence is present in all sectors of the caldera wall where the Sharkfin sequence is exposed; defining the top as the last occurrence of palagonitised deposits, it is up to ~40 m thick (Figure 5.4g). The only substantial sills in the Sharkfin sequence are usually present along or just above the contact between this subsequence and the underlying hyaloclastite subsequence. In the caldera wall these sills, which are typically pervasively fractured (but not in a distinctive pattern), form a mostly <2 m thick discontinuous unit along this interface, with an alteration zone <1 m thick only in the underlying hyaloclastite subsequence (e.g., Figures 5.4b and 5.4d). In these outcrops there is no clear evidence of the sills having intruded the overlying debris flow subsequence (e.g., alteration or lava apophyses); one exception is alteration of these deposits around a ~6 m thick laccolith composed of multiple sills. On the accessible upper flanks (the

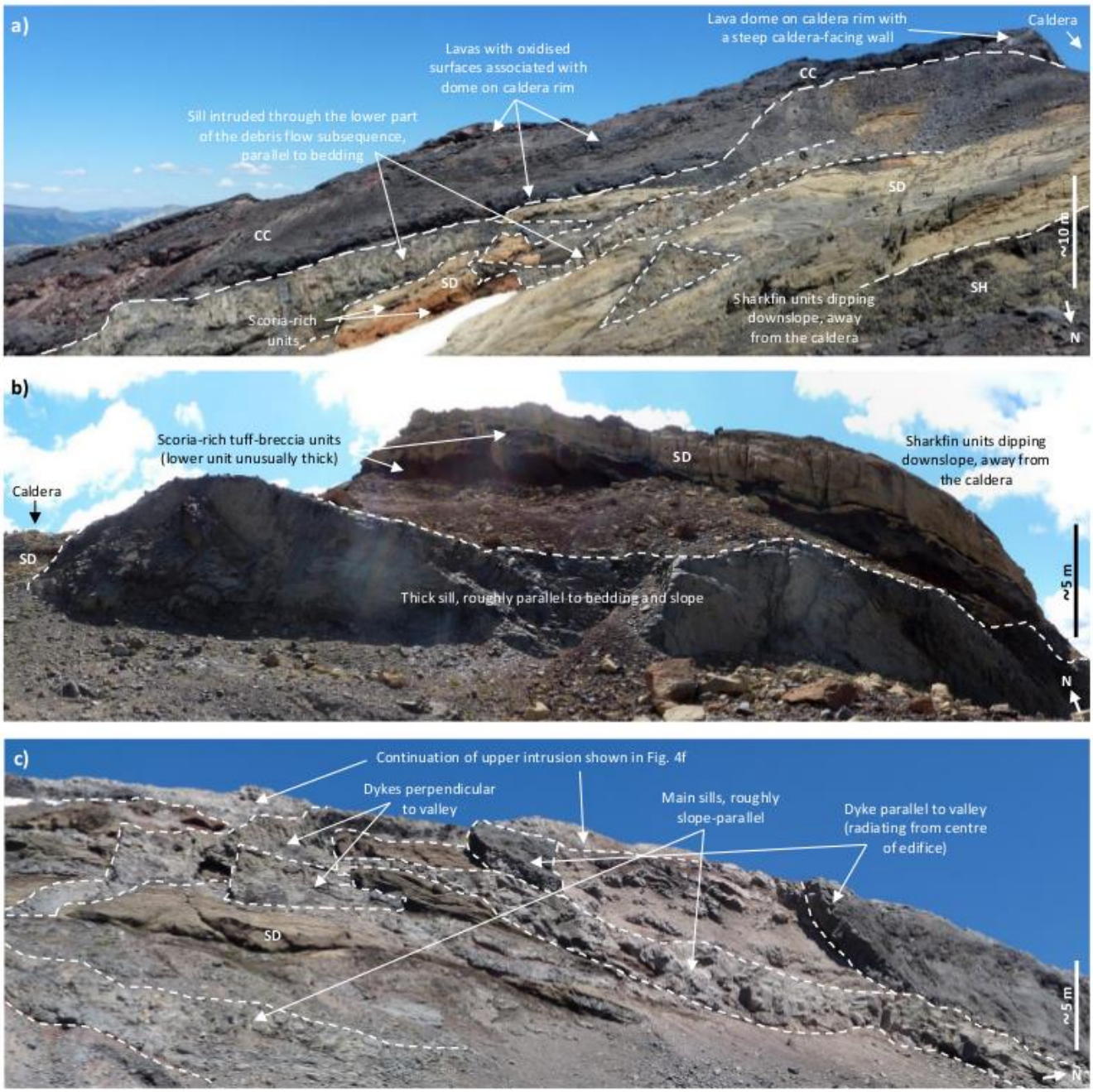

Figure 5.8 Photographs showing the extent and variety of some of the intrusions in the upper part of the Sharkfin sequence, which are discussed in Section 5.3.2.3. The short-dashed lines approximately delineate the intrusions and the longer dashed lines approximately delineate subsequence boundaries; the subsequence codes are defined in Table 5.2. **(a,b)** Views of the south (Part a) and north (Part b) sides of the uppermost East valley (Figure 5.2c), which show the downslope continuation of the stratigraphy observed in the caldera walls, including the sills at/near the base of the debris flow subsequence. Note that only the lower parts of the debris flow subsequence are present here and in the corresponding sector of the caldera wall (the mid sector in Figure 5.4a). **(c)** View of the west side of the Chufquén valley (Figure 5.2c; downslope from Figure 5.4f), showing sills at/near the base of the debris flow subsequence and additional intrusions further up the stratigraphy.

Chufquén and East valleys: Figure 5.2c), the sills are more continuous, sometimes thicker, and some intrude the lower parts of the debris flow subsequence, roughly parallel to the slope and bedding of the deposits (sometimes with alteration haloes); examples are shown in Figure 5.8. Dykes are also present in this subsequence, most notably some of distinct composition that clearly feed the circum-caldera lavas, which are surrounded by prominent alteration zones (e.g., Figure 5.7c). Groups of cross-cutting dykes with no clear association are also recognised, most clearly in the Chufquén valley (Figure 5.8c), where there is also an atypical large intrusion capping the subsequence (Figure 5.4f).

5.3.3. Chufquén valley lavas

The upper Chufquén valley (Figure 5.2c) contains several lavas, ranging from tens to hundreds of metres in length and ~3–15 m in thickness, with a variety of morphologies. Their age is currently unconstrained, except by the fact that they post-date the erosion of the Chufquén valley, and so the Sharkfin sequence. The lavas analysed chemically are all of near-identical basaltic andesite composition, but less alkalic for their silica content than almost all the samples from other units (Figure 5.3). Therefore, it is unclear how they relate to the main stratigraphy. Examples of the significant features of these lavas are shown in Figure 5.9. Some show entablature (e.g., Long and Wood, 1986; Forbes et al., 2014a) on the steep valley-facing sides of the flows; cube, curvi-columnar, chevron-like, and irregular fractures are all observed, bounded by either blocky fracturing or a colonnade of columnar jointing (Figures 5.9a and 5.9b). Hackly fractures are present at the margins of other flows (Figures 5.9d and 5.9e); these locally have curving chisel marks (striae) on their surfaces (Figures 5.9e and 5.9f). The other lavas show no pervasive fracturing, only typical marginal autobreccia (Figure 5.9c). There is no clear pattern to the distribution of lavas with each particular morphology.

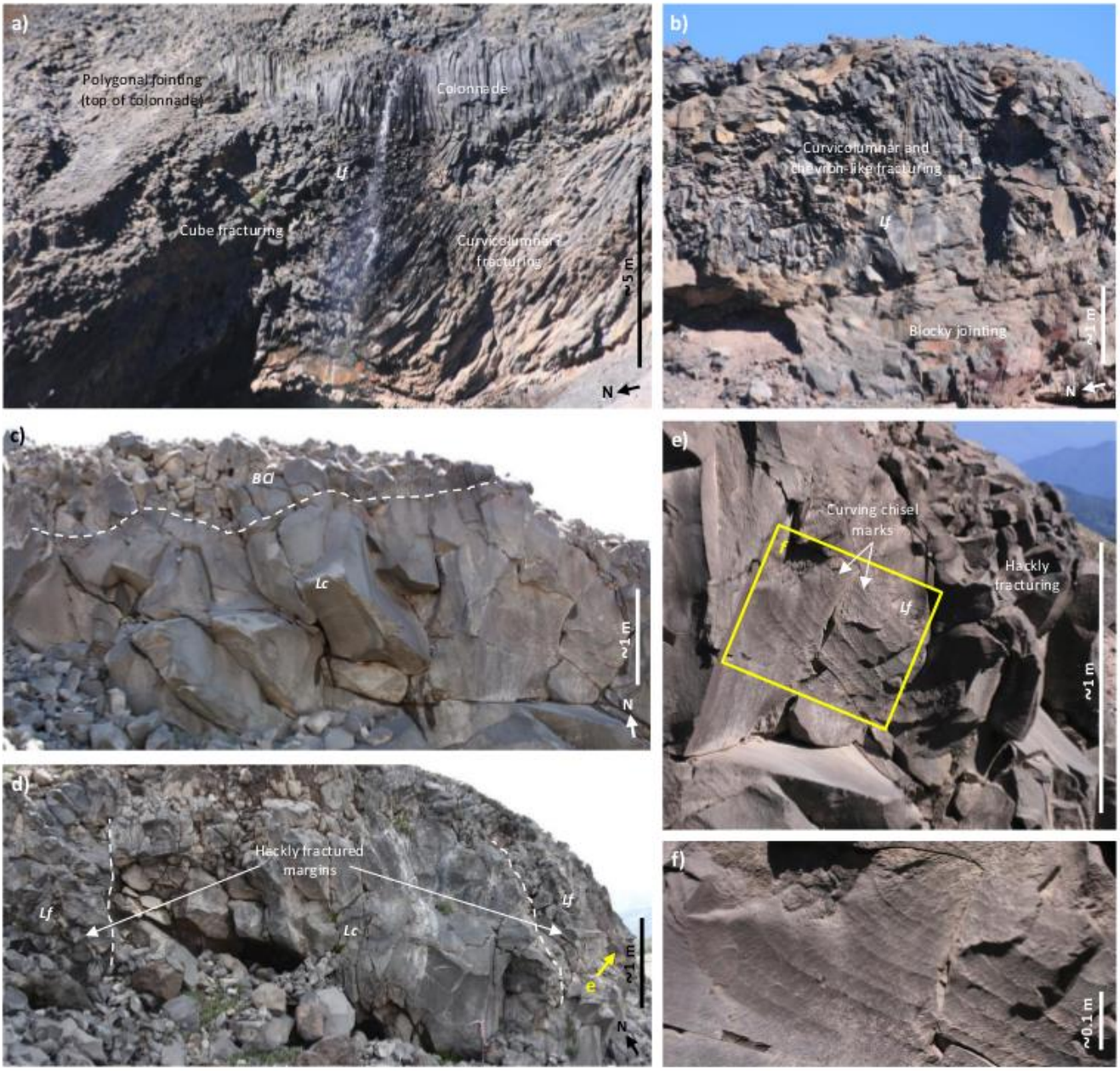

Figure 5.9 Photographs of outcrops that exemplify features of the lavas within the upper Chufquén valley, described in Section 5.3.3. The dashed lines approximately delineate the different lithofacies, the codes for which correspond to those in Table 5.2. **(a)** Outcrop of the valley-facing side of a thick lava that flowed from near the caldera rim, showing a pervasively fractured centre (entablature) capped by a colonnade. **(b)** Outcrop of a smaller lava on the valley floor, which also shows entablature-like fracturing. **(c)** Outcrop of a lava in the valley floor, in which pervasive fracturing is absent. **(d)** Outcrop of a lava in the valley floor (further downslope than the lava in Part c) with hackly fracturing at its margins. **(e,f)** Detail of part of the margin of the lava in Part d (areas indicated by the yellow arrow in Part d and approximately demarcated by the yellow box in Part e, respectively), showing the jointing and prominent curving chisel marks on some surfaces.

5.3.4. Circum-caldera lava sequence (CC)

This sequence comprises the lavas that cap the majority of the caldera walls, including those in the eastern sector that overlie the Sharkfin sequence (Figure 5.4a); it post-dates the formation of the caldera. The lavas are basaltic andesite to trachydacite in composition and contain varying concentrations of phenocrysts (plagioclase, one or two pyroxenes, olivine, and/or Fe-Ti oxides). The sequence includes the Peak and South units of Gilbert et al. (1996), which are grouped together in this study due to their very similar geochemistry (Murphy, 1996). At a few locations on the eastern caldera wall, at the base of this sequence there are thin (<2 m thick) 'a'ā lavas (Figure 5.4), which have been inferred to be subaerial (Gilbert et al., 1996). Previous work (Gilbert et al., 1996; Murphy, 1996) considered these lavas to be the uppermost part of the pre-caldera Sharkfin sequence. However, this is inconsistent with the orientation of some of the lavas, dipping both to the north and into the caldera (Figures 5.4b and 5.4c), and the trachydacite composition of those sampled (Murphy, 1996), given that the Sharkfin sequence is otherwise exclusively mafic (Figure 5.3). Hence we consider these part of the circum-caldera lavas, despite being morphologically distinct from the lavas that otherwise form the lower part of this sequence.

The bulk of the sequence comprises lava domes/coulées and stacks of flows, ~10–100 m in height and width on the caldera rim; examples are shown in Figure 5.10. There is a transition in the morphology of the lavas at approximately the same elevation around the eastern and southern caldera rim (Figure 5.10a). Below this level there are steep caldera-facing cliffs of lava, comprising both thick (>10 m) flows (e.g., Figure 5.10f) and sides of domes/coulées (e.g., Figure 5.10c). These cliffs are pervasively fractured in one or more patterns such as columnar, hackly, and pseudopillow (summary definitions in Lescinsky and Fink, 2000) (e.g., Figures 5.10b and 5.10g), or occasionally radial (Figure 5.10e). All these lava cliffs were not accessible for detailed characterisation. There are occasional lavas that flowed into the caldera from the cliffs; these

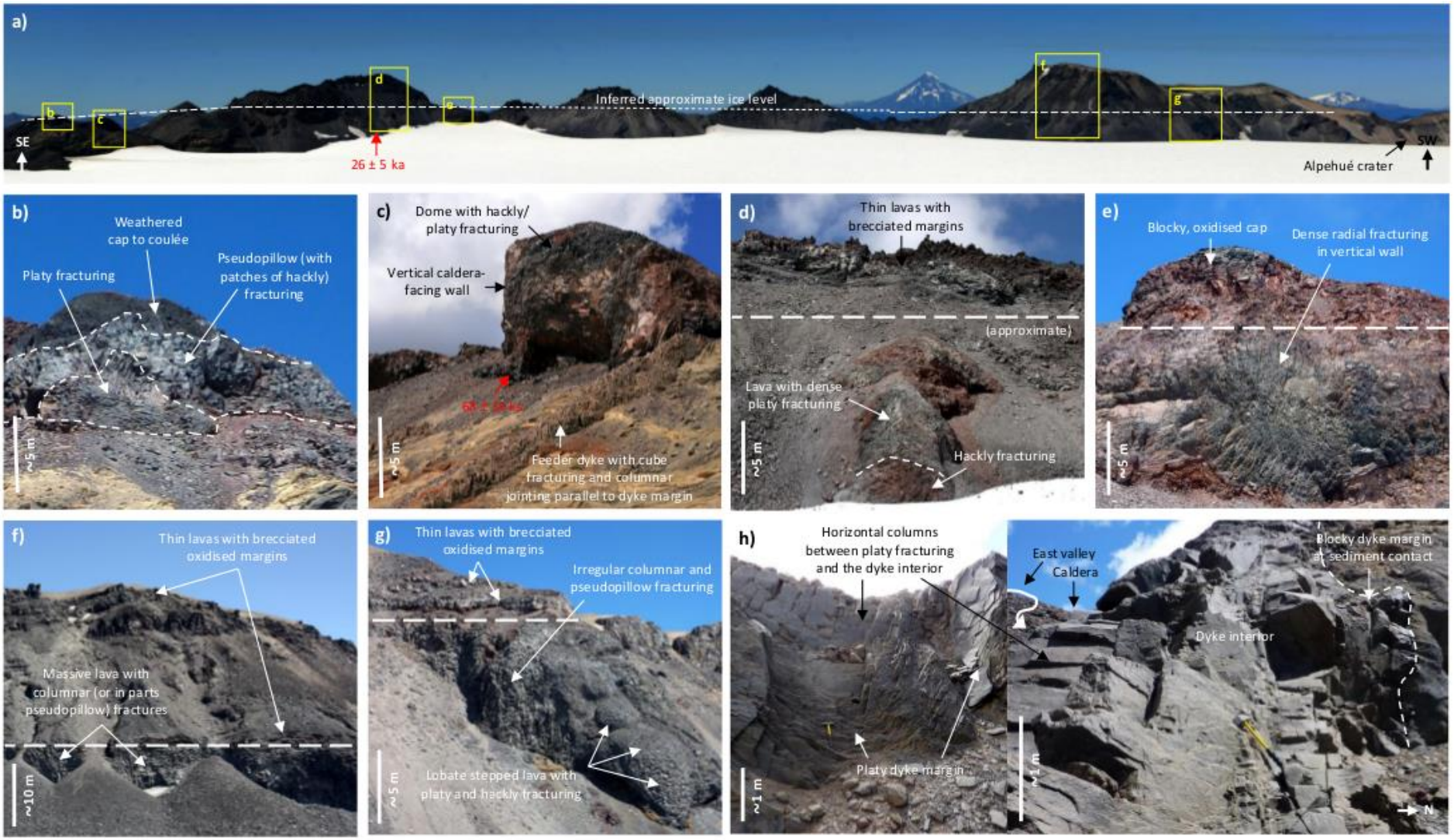

Figure 5.10 *(caption on next page)*

Figure 5.10 *(previous page)* Examples of the morphologies observed in the circum-caldera lava sequence and intrusions discussed in Section 5.3.4, and the consequent inference of syn-eruptive ice extent or thickness. The red arrows point to the sampling locations of lavas that have been Ar-Ar dated to the stated ages (Supplementary File 5.2; Section 5.3.4). **(a)** Panorama of the SE to SW sector of the caldera wall (marked on Figure 5.2), which predominantly comprises lavas of the circum-caldera lava sequence. The dashed line indicates the approximate level below which there are morphological features interpreted as evidence of interaction with ice/meltwater, and so is the inferred ice level during lava emplacement; longer dashes denote where this is better constrained. The yellow boxes indicate the parts of the caldera wall shown in Parts b to g, which, together with Part h (the location of which is indicated on Figure 5.4a) are examples of the morphological features and how the palaeoice level has been delineated. **(b)** Near-vertical caldera-facing wall to a lava coulée on the caldera rim, which displays a variety of fracturing types (labelled) that are perhaps indicative of rapid cooling due to ice contact (e.g., hackly and pseudopillow fracturing: Lescinsky and Fink, 2000), suggesting that the coulée was buttressed by intra-caldera ice on emplacement. **(c)** A lava dome on the caldera rim with a near-vertical caldera-facing wall, displaying similar fracturing types. Columnar jointing of the exposed feeder dyke parallel to its margins indicates cooling from the surface rather than the dyke margins, suggesting attempted intrusion into intra-caldera ice. **(d)** Lava that flowed down the caldera wall from near the top, with pervasive platy fracturing that might reflect emplacement along the ice-rock interface (cf. Part h), overlain by typical (subaerial) ‘a‘ā lavas. **(e)** Lava with a vertical, radially fractured caldera-facing wall, capped by a more oxidised, blocky carapace, perhaps either a cross-section of a lava tube or a small coulée that was constrained by intra-caldera ice (cf. Edwards and Russell, 2002). **(f)** A steep caldera-facing wall of columnar-jointed lavas, perhaps emplaced against intra-caldera ice, overlain by a thick sequence of typical (subaerial) ‘a‘ā lavas. **(g)** Lava lobes with hackly and platy fracturing from a steep-sided lava with irregular columnar fractures, which is overlain by typical (subaerial) ‘a‘ā lavas. The lobes are interpreted to have flowed into cavities melted in the intra-caldera ice that confined the lava cliff. **(h)** Dyke with blocky fracturing on its northern margin, where in contact with debris flow units of the Sharkfin sequence, and pervasive platy and polygonal fracturing along the south margin (shown in the left-hand photograph), where facing the dyke-parallel East valley (Figure 5.2b) that intersects the caldera rim. The different fracture patterns on the two sides are interpreted to have formed by the dyke intruding along the interface between the sidewall and ice infilling the valley.

lavas are particularly densely fractured (Figures 5.10d and 5.10g). In some instances this fracturing is platy, i.e., sub-parallel and spaced <10 cm apart, and sometimes curving (e.g., Figure 5.10b) or sub-parallel to flow direction (inferred from flow banding and/or morphology, e.g. Figure 5.10d). We also find platy fracturing on one margin of the dyke forming one side of the head of the East valley (Figure 5.2c): as shown in Figure 5.10h, the valley-facing margin of the dyke has a strong curved platy fabric, with horizontal columnar jointing (i.e., polygonal in a plane parallel to the dyke margin) just behind, whilst the other margin, in contact with Sharkfin palagonitised lapilli-tuff, is fractured into large blocks. Some of the dykes feeding the circum-

caldera lavas (in the Sharkfin sequence exposed at the caldera walls) show cube-like fracturing, and columns oriented parallel to the dyke margins (rather than perpendicular, which is expected as a dyke cools from its margins) (Figures 5.7c and 5.10c).

Above the aforementioned level on the caldera rim, there are stacks of thinner (<5 m thick), less fractured ‘a‘ā lavas, sometimes with oxidised margins (e.g., Figures 5.10f and 5.10g). These lavas form the Peak unit described by Gilbert et al. (1996), who report that they dip both into and out of the caldera, and include an unusually large, ~2 km long fractured lava (geochemically distinct according to Murphy, 1996) that flowed into and across the northwest part of the caldera. The flank-facing sides and top of the lava domes/coulées in the sequence are blocky or weathered (e.g., Figures 5.10b and 5.10e), less steep than the caldera-facing sides, and sometimes oxidised; some of the coulées have associated lavas that extend up to hundreds of metres down the flanks (e.g., Figure 5.8a). The brecciated, oxidised carapaces suggest that the domes/coulées have not been substantially eroded, and thus that the exposed faces are the actual dome margins (Gilbert et al., 1996). The largest stacks of lavas (on the southern caldera rim; Figure 5.10a) are morphologically very similar to lava-dominated flat-topped or conical tuyas (Russell et al., 2014), at least on their caldera-facing sides.

Groundmass samples of two of the aphyric lava domes on the eastern caldera rim (marked on Figure 5.10) have been Ar-Ar dated by the method outlined in Arancibia et al. (2006) to 26 ± 5 and 68 ± 14 ka (Supplementary File 5.2), coinciding with the LGM and a proposed Southern Hemisphere glacial maximum (~65 ka; Schaefer et al., 2015) respectively. The younger date is probably not robust as it is close to the limit of the dating method; the elder is consistent with the Ar-Ar date of 64 ± 15 ka obtained for a circum-caldera sequence lava on the NW caldera rim by Jara and Moreno (in prep.) (Table 5.1).

5.4. Interpretation and discussion of eruptive and glacial history

5.4.1. Sharkfin sequence

5.4.1.1. Sharkfin lava subsequence

The environmental conditions in which this subsequence was emplaced are unclear. The lavas are more brecciated than typical subaerial basaltic ‘a‘ā flows, and the matrix of the tuff-breccia units shows uniform partial palagonitisation, suggesting meltwater was present during their emplacement. We suggest that the well-sorted palagonitised tuff units interbedded with the lavas result from reworking of subaqueous/subglacial eruption deposits, and so indicate at least intermittent water flow. Nevertheless, the extent of fragmentation and palagonitisation of the lavas is much less than that in typical subaqueous or subglacial fragmental lithofacies (cf. the hyaloclastite subsequence), and the fracturing within the coherent lava is irregular, rather than of a pattern indicative of snow (e.g., Mee et al., 2006) or ice (e.g., Lescinsky and Fink, 2000) contact. Glacial evidence for coeval ice is not observed, although it is not possible to rule out the presence of striations on the lavas or basal diamict from the outcrops studied. The occasional presence of this subsequence overlying the hyaloclastite subsequence could be interpreted as an indication that these lavas can result from eruption into drained subglacial cavities. Given this association, we suggest that this subsequence results from a succession of lava flows beneath snow or ice from which the meltwater generated was able to drain rapidly; the snow/ice thickness required is impossible to constrain beyond that it must exceed that of the subsequence (>11 m). However, subaerial emplacement cannot be ruled out.

5.4.1.2. Sharkfin hyaloclastite subsequence

The lithofacies in this subsequence are similar to some of those inferred to result from mafic eruptions beneath ice (e.g., Loughlin, 2002; Schopka et al., 2006) or water (e.g., Porębski and Gradziński, 1990; Watton et al., 2013); the ubiquitous palagonitisation of the fine-grained glass component of each lithofacies is consistent with a hyaloclastic origin (e.g., Fisher and Schmincke, 1984). Topographic features such as craters and moraines can reduce the local slope and/or enable local thickening of ice cover, and so encourage meltwater ponding even on the slopes of a stratovolcano; substantial meltwater accumulation has been reported within large craters or calderas (e.g., the 1991 eruption of Volcán Hudson, Chile: Naranjo et al., 1993b) (Lescinsky and Fink, 2000). However, this subsequence is probably too extensively distributed in a consistent stratigraphic position to be accounted for by such localised ponding. We consider the most plausible formation mechanism for this subsequence to be effusive mafic eruptions beneath ice of sufficient thickness that it has surface topography independent of that of the land surface (the former being a more effective control on meltwater flow: Björnsson, 2002), and so able to create a 'hydraulic seal' that hinders drainage of meltwater generated by the eruption (Björnsson, 2002; Stevenson et al., 2009). Under such conditions, meltwater would have ponded in subglacial cavities and so been available to interact with the lava; water retention is only required for the duration of the eruptive phase. Stevenson et al. (2009) suggested that ice in excess of 300 m thick may be required to pond meltwater subglacially on steep topography. However, it is not possible to definitively constrain the absolute ice thickness range under which this subsequence could have formed without the preservation of any clear transition to subaerial activity (as identified where the emplacement conditions of similar deposits have been constrained, e.g. Brown Bluff volcano (Smellie and Skilling, 1994)). Although the ice must have been at least as thick as the deposits, at a maximum of ~12 m, this is at least an order of magnitude too thin to be a reasonable lower bound on the ice thickness.

The spectrum and spatial relationships of the lithofacies identified in this subsequence could be generated in various ways in this subaqueous/subglacial regime. If explosive fragmentation was the predominant mechanism of brecciation of the erupted lava, then spatiotemporal variation in the subglacial cavity pressure, determined by the rates of meltwater generation and discharge, would likely be the main control (lower cavity pressure allowing greater explosive fragmentation, and vice versa) (Tuffen, 2007). However, we suggest that this is inconsistent with the absence of systematic trends in fragmentation extent through the subsequence, or any relationship between fragmentation extent and the vesicularity of the lava component. Passive quench and mechanical fragmentation, to which hyaloclastite formation is attributed by studies such as Skilling (2002; 2009) and Watton et al. (2013), is suggested to be the predominant mechanism by: (1) the increasing fragmentation of lava pillows towards their margins, (2) the clast-rich, sometimes isolated pillow-bearing, and poorly sorted nature of many of the tuff-breccias, and (3) indications of slumping and/or remobilisation (e.g., the occasional lenses or sheets of one tuff-breccia or tuff/lapilli-tuff lithofacies within another), which can induce mechanical fragmentation (Skilling, 2002). Such fragmentation may have been driven by long-lived extrusion on a steep slope, encouraging slumping downslope, analogous to the formation of poorly bedded hyaloclastite foresets in ‘a‘ā lava deltas (Smellie et al., 2013, 2014). The formation of a particular hyaloclastite lithofacies will therefore depend on factors including the eruption/lava flow rate, magma-water interaction efficiency, timing and rate of meltwater discharge, and topography, all of which are likely to be highly spatially and temporally variable, consistent with the observed stratigraphy.

5.4.1.3. Sharkfin debris flow subsequence

The mix of channelised and sheet deposits (sorted to varying extents, some polymictic) in this subsequence indicates that it was formed by a series of debris flows of varying energy. Most of the subsequence comprises rocks very similar to those in the hyaloclastite subsequence (but with

textural differences, e.g. bedding and clast:matrix ratio), suggesting that these flows likely reworked deposits from subglacial eruptions. The scoria-bearing and bedded tuff units are also probably remobilised (from subaerial or subaqueous explosive eruption deposits), because they are typically found mixed with or containing lenses of breccia and are highly variable in thickness. The consistent stratigraphic position of the widely distributed pair of oxidised scoria-bearing units suggests that at least the lower units of this subsequence were emplaced approximately contemporaneously. The extensive distribution of this part of the subsequence therefore implies that it was formed by discharge of a large volume of water. It is unlikely that such a volume could have been generated by local meltwater ponding, so we suggest that it may have originated from eruptions beneath a thick ice sheet (for the reasons discussed in Section 5.4.1.2).

The association of sills and a thick sequence of debris flows is similar to the Dalsheidi-type subglacial volcanic sequences in southern Iceland described by Smellie (2008). These comprise a semi-continuous lava sheet (sometimes underlain by diamict) with columnar jointing and/or entablature, which partially intrudes into overlying massive sheet-hyaloclastite (sometimes capped by mudstone) (Smellie, 2008). These sequences can range from <5 m to hundreds of metres in thickness (where multiple sequences are present in succession) and extend many kilometres from their source. One interpretation is that they are produced by a sill intruding along the bedrock-ice interface beneath a thick ice sheet, which generates sufficient meltwater to eventually float the ice, causing a debris flow of hyaloclastite (erupted at the vent) beneath it (Smellie, 2008). Alternatively, Banik et al. (2014) argue that these sequences are the result of eruptions beneath thin or negligible ice (supported by measurements of the volatile content of glass), with the 'sills' being lava flows that either preceded the debris flows or intruded down into and along the base of pre-existing deposits. We suggest that the sills and debris flow deposits described here were emplaced beneath thick ice, in a similar way to the model of Smellie (2008).

This is because the sills appear to have intruded both along the base of the ice prior to and during the debris flows (as they are present both beneath the subsequence, with no alteration of the overlying deposits, and in its lower parts, mostly parallel to the bedding), contradicting the models of Banik et al. (2014). Furthermore, it is difficult to reconcile the apparently contemporaneous deposition of the sequence of debris flows as extensively as they are present on Volcán Sollipulli with the amount of meltwater that could be generated beneath thin glaciers. Analysis of the volatile content of the sills (Dixon et al., 2002; Tuffen et al., 2010) would be necessary to verify this interpretation. Constraint of the absolute ice thickness range under which this subsequence could have formed is not possible, due to the absence of a contemporaneous subaerial cap, but it is likely to be greater than that which resulted in the hyaloclastite subsequence, considering the greater meltwater volume required in this instance.

5.4.2. Chufquén valley lavas

We interpret these lavas to have been emplaced in a variety of environmental conditions. Entablature is diagnostic of rapid cooling due to water infiltration (e.g., Long and Wood, 1986; Forbes et al., 2014a); the (sub-)vertical fracturing orientation in the lavas with this feature suggests that this cooling resulted from flooding during emplacement, rather than ice interaction at their margins. However, the hackly fracturing (also symptomatic of rapid cooling: Lescinsky and Fink, 2000) at the margins of other lavas suggests that such ice contact occurred in the case of these other units. With further examination, the chisel marks on the fracture planes would have the potential to constrain the cooling front and rate (e.g., DeGraff and Aydin, 1987; Goehring and Morris, 2008; Forbes et al., 2012). Other lavas lack such features, and are hence inferred to be subaerial; some of these are upslope of those with fracturing indicative of ice interaction, so the glaciation extent when the suite of lavas was emplaced is unclear. We propose that they erupted over a protracted period during which the glacier size changed. Note that none of these lavas are

pervasively fragmented, nor is there evidence of palagonitisation, in contrast to the Sharkfin sequence despite also being of mafic composition; this most likely reflects a difference in the amount of meltwater interaction due to ice thickness.

5.4.3. Circum-caldera lava sequence

The morphologies and fracture patterns observed on the caldera-facing sides of these lavas suggest that when the bulk of this sequence was erupted at the top of the caldera wall, the lavas were constrained on this side by intra-caldera ice, similar to, for example, the perched lavas at Mt Rainier (Lescinsky and Sisson, 1998) and ice-dammed lava cliffs at Hoodoo Mountain (Edwards and Russell, 2002). Some lava breached out of this dammed lava and flowed into the caldera along the ice-rock interface (i.e., subglacially); we interpret their densely fractured surfaces as a reflection of the resulting enhanced meltwater interaction. Some of the lavas display multiple fracture patterns, which previous studies have attributed to cooling rate variation with distance from the ice contact (e.g., Lodge and Lescinsky, 2009). When the lavas built up to ice level, extrusion continued subaerially (forming the caps of the domes and the thin ‘a‘ā lavas); lava may have flowed over the intra-caldera ice, but only the parts of lavas on the caldera rim have been preserved.

Two of the types of fracturing observed in the lower-level lavas are not commonly associated with ice interaction. Radial fracturing is one of these; the example shown in Figure 5.10e could be interpreted as a cross-section of a lava tube rather than the ice-constrained margin of a thick flow, although the fractures are closely spaced, consistent with rapid cooling, and radial fracturing has also been interpreted as indicative of lava-ice contact at some other stratovolcanoes (e.g., Hoodoo Mountain: Edwards and Russell, 2002). The other, platy fracturing, is found in lavas erupted under various conditions, but typically only in the slowly cooled interior of lavas

(Lescinsky and Fink, 2000), whether they are subaerial (e.g., Tuffen et al., 2013), ice-contact (e.g., Mee et al., 2006), or subglacial (e.g., Forbes et al., 2014b). Conversely, in this sequence platy fracturing is present on the surface of lavas (Figure 5.10d) and the same caldera-facing lava cliffs as patterns indicative of rapid cooling, such as hackly fracturing (Figures 5.10b and 5.10g). We suggest that the platy fracturing on one surface of the dyke shown in Figure 5.10h arises from its intrusion along the contact between a glacier in the valley and the valley side, causing rapid cooling of the dyke margin in contact with the ice. Therefore, we propose that platy fracturing can result from ice interaction (e.g., in the case of the lava shown in Figure 5.10d); it perhaps forms when the lava or dyke margin is rapidly cooled into the brittle regime but the interior is still undergoing ductile flow, causing a shear fabric to form in the margin. Formation mechanisms for platy fractures in the interior of lavas proposed by previous studies include late-stage shear (Bonnichsen and Kauffman, 1987; Conway et al., 2015) and detachment of the outer parts of the lava body, possibly due to deflation (Spörli and Rowland, 2006) or inflation (Tuffen et al., 2013). However, the presence of undeformed master fractures cross-cutting the curved platy interior fractures in the subglacial lava studied by Forbes et al. (2014b) was interpreted to indicate that such fracturing is unlikely to form by inflation, deflation, or late stage shear, and so perhaps by cooling contraction instead. Conversely, modelling of the cooling of an andesite lava by Spörli and Rowland (2006) suggested that chilling alone could not reasonably account for the longitudinal strain across platy fractures, suggesting a mechanical component.

The approximately consistent elevation (~2100 m) of the ice-interaction to subaerial transition in the caldera-facing lavas indicates that the bulk of this sequence was emplaced during a period when the caldera was filled with ice. There are several hanging valleys in the caldera rim below the inferred ice level (Figures 5.4a and 5.10a), so an ice accumulation rate in excess of that of drainage by outlet glaciers would have been necessary to reach this level. The subaerial lavas

flowing into the caldera that are locally present at the base of the sequence suggests that at least part of this ice accumulation may have occurred only shortly prior to this main eruptive phase. Although the ring faulting associated with caldera formation is likely to be the primary control on the location of these lavas at the top of the caldera wall, there is potential evidence for the intra-caldera ice also having some influence. The columnar jointing parallel to the margins of the feeder dykes (e.g. Figure 5.10c) indicates rapid cooling at the caldera wall face, suggesting that these dykes were inhibited and cooled by the ice at the surface. Hence extrusion may have been focussed near the top of the caldera wall where the ice was thin, rather than into the caldera. However, the geophysical survey of the caldera by Gilbert et al. (1996) suggests that there are lavas at the base of the caldera wall, particularly on the eastern and southern sides, which these authors inferred were erupted subglacially in association with the circum-caldera lavas; thus extrusion may not have been entirely confined to the top of the caldera margin.

5.4.4. Discussion

Figure 5.11 summarises our preferred interpretation of part of the coupled glacial and eruptive history of Volcán Sollipulli that is recorded on its upper flanks. The absolute ice thickness under which some of the eruptions are inferred to have occurred is difficult to constrain without indicative lithofacies associations (e.g., passage zones: e.g., Skilling, 2002; Smellie, 2006) or analysis of the degassing of volatiles from glass or lava samples (Dixon et al., 2002; Tuffen et al., 2010). Even the relative ice extent is ambiguous in some cases, due to the many additional potential controls on eruption style and thus the resultant lithofacies. For example, it is not certain that the Sharkfin lava subsequence interacted with snow or ice during its emplacement, as discussed in Section 5.4.1.1. The local occurrence of the lava subsequence above the hyaloclastite suggests that these lavas could have been erupted under ice, but their presence beneath the hyaloclastite subsequence in all locations where its base is exposed indicates that there was a

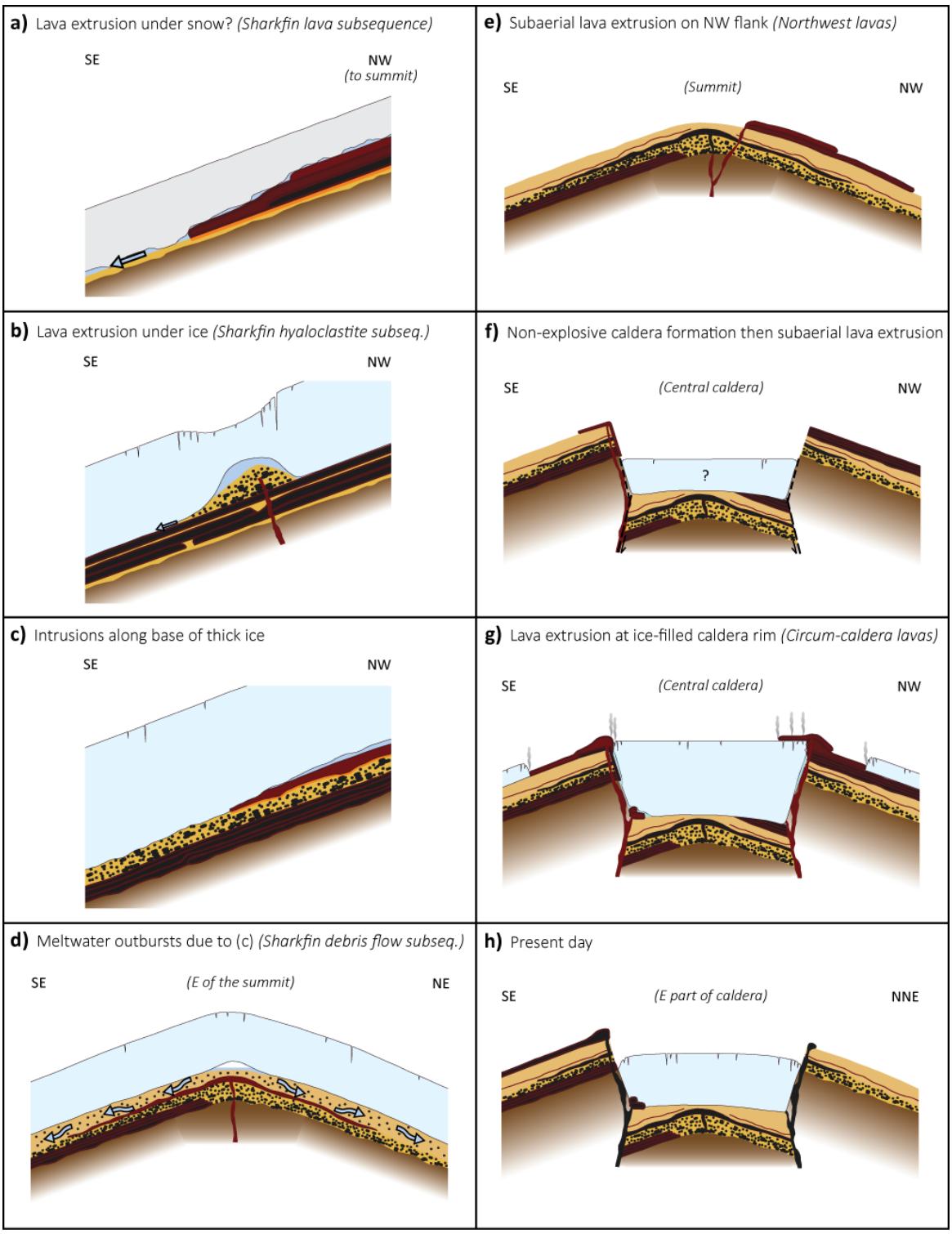

Figure 5.11 *(caption on next page)*

Figure 5.11 *(previous page)* Schematic illustration of part of the glacial and eruptive history of Volcán Sollipulli based upon the interpretations presented here and in Gilbert et al. (1996). Note the variations in the approximate orientation and extent of the schematic cross-sections, and that they are not to scale. **(a)** Emplacement of the Sharkfin lava subsequence (Section 5.4.1.1): summit or upper flank effusive eruption of mafic lava, which flows downslope, perhaps below thin ice or snow cover. Any meltwater generated rapidly drains away from the lava, so only the surfaces of the lavas are fragmented. Pauses in effusion are marked by deposition of thin layers of fine-grained palagonitised material, likely remobilised from hyaloclastic deposits upslope. **(b)** Emplacement of the Sharkfin hyaloclastite subsequence (Section 5.4.1.2): upper flank effusive eruption of mafic lava, generating meltwater that ponds at the source, probably due to a thick ice overburden restricting drainage. As a result, pillow lava is erupted, and tuff-breccia forms by in-situ quench fragmentation and palagonitisation of the lava; this is partly remobilised downslope, causing mechanical fragmentation. **(c)** Mafic lava is emplaced as sills along the interface between the bedrock and a thick ice cap, due to the ice overburden (Section 5.4.1.3). **(d)** Emplacement of the Sharkfin debris flow subsequence (Section 5.4.1.3): the meltwater generated by the emplacement of these sills escapes in periodic meltwater outbursts, eroding and redepositing hyaloclastic lithofacies. Sill propagation continues through the lower part of these deposits. **(e)** Emplacement of the subaerial Northwest lava sequence (Table 5.1; Gilbert et al., 1996) after melting of the ice cap. **(f)** Formation of the caldera by a non-explosive mechanism, followed by emplacement of subaerial lavas of intermediate composition on parts of the top of the caldera wall (Section 5.3.4). **(g)** Emplacement of the bulk of the circum-caldera lava sequence (Section 5.4.3): after the caldera has filled with ice, further effusive eruption of intermediate-composition lava occurs around the caldera wall (fed from dykes along the ring fault). Domes on and flows from the top of the caldera wall are buttressed by the intra-caldera ice, but become subaerial above the ice level. Some lava extrusion at the base of the caldera rim is suggested by geophysical data (Gilbert et al., 1996). **(h)** A schematic section through the caldera at the present day. This follows the Alpehué and Chufquén eruptions and ice advance and retreat into/from the Chufquén valley and Alpehué crater (all not shown), which are described by Gilbert et al. (1996).

widespread shift to conditions favourable to meltwater ponding, which we consider to be most plausibly explained by increased ice cover. Additionally, the ice thickness associated with Dalsheidi-type sequences, which we consider analogous to the Sharkfin debris flow subsequence, has been disputed (Smellie, 2008; Banik et al., 2014). This is discussed in Section 5.4.1.3, where we suggest that the field evidence is more consistent with the model of emplacement under thick ice. Palaeoclimate/glaciology studies have inferred an ice thickness (albeit poorly constrained) of ≥1 km on this part of the Andes at the LGM (e.g., Hulton et al., 2002), so the thick ice model is plausible in this case. Further study of similar sequences is necessary to better understand their formation.

The interpretation presented here differs from that of Gilbert et al. (1996) in that we infer an increase in ice thickness with time during the emplacement of the Sharkfin sequence, rather than an evolution from subglacial to subaerial eruptions. This is due to our observations (described further in Sections 5.3.2 and 5.3.4) that: (1) there are lavas with features suggestive of relatively limited meltwater influence at the base of the sequence (which were not described by Gilbert et al. (1996)); (2) the hyaloclastite subsequence is widely distributed, suggestive of emplacement under an ice cap (as opposed to in localised ponds of meltwater); (3) the debris flow subsequence has sills at its base, perhaps intruded beneath thick ice, and upper units comprising tuff-breccia, rather than tephra as thought by Gilbert et al. (1996); and (4) the subaerial lavas considered to be the top part of this sequence by Gilbert et al. (1996) appear to have erupted after formation of the caldera. Conversely, we concur with the interpretation of the circum-caldera lavas in Gilbert et al. (1996). They noted that there are relatively few calderas recognised to have ring vents, and that it is rare for eruptions from these to substantially build up the caldera walls, as at Volcán Sollipulli; they also hypothesised that the intra-caldera ice may have restrained eruptions from the caldera floor. The morphological features of the lava cliffs described in Section 5.3.4 indicate that the intra-caldera ice was responsible for their formation. In addition, we find some evidence that the ice also could have been a contributing factor to the focussing of the vents on the caldera rim. There are a considerable number of poorly studied ice-filled calderas in the southern Andes (Figure 5.1) and other high-latitude continental arcs that could be investigated to assess if there is an association between ring vents and intra-caldera ice loading.

The glacial conditions at the time of the caldera-forming event are uncertain: the time period bounded by the youngest unambiguously pre-caldera (350 ± 90 ka) and oldest unequivocally post-caldera (68 ± 14 ka) Ar-Ar dates (Table 5.1) spans three glacial cycles. However, the predominantly subaerial Northwest lava sequence, Ar-Ar dates for which indicate an age of ~110

ka (Table 5.1; Jara and Moreno, in prep.), during or following the last interglacial (MIS 5e, ~123–109 ka; Lisiecki and Raymo, 2005), is thought to have been erupted after the subglacial Sharkfin sequence but prior to caldera formation (Gilbert et al., 1996). If correct, the caldera-forming event must have occurred early in the last glacial period; the extent of glaciation at this time would have been less than at the LGM, but is otherwise poorly constrained (Rabassa, 2008). There is some evidence from Kamchatka (Bindeman et al., 2010) and numerical modelling (Geyer and Bindeman, 2011) that suggested that caldera-forming large explosive eruptions are more likely during glacial periods. However, the timing of the assumed caldera-forming eruptions relative to glaciations is poorly constrained for the majority of those events studied by Bindeman et al. (2010). Although tephra is less likely to be preserved when deposited supraglacially (Hobbs, 2014), the subsequent glacial advance (leading up to the LGM) alone would be sufficient to account for the absence of evidence for an explosive origin of the caldera, considering that no tephras deposited prior to local deglaciation have been found in the region (Fontijn et al., 2014). Nevertheless, the ~60 m maximum subsidence of the Bárðarbunga caldera in Iceland associated with the 2014–15 Holuhraun eruption (Riel et al., 2015; Sigmundsson et al., 2015) highlights the potential for subglacial caldera formation without an explosive eruption. Additional dating of the eruptive sequences is critical to better constrain the climate at the time (and thus to inform speculation about the mechanism) of formation of the caldera at Volcán Sollipulli.

As outlined in Section 5.1, most glaciovolcanism described at other arc stratovolcanoes at temperate latitudes comprises coherent lavas, similar to the Chufquén valley lavas and circum-caldera lava sequence. Nevertheless, the Sharkfin sequence indicates that it is possible, although perhaps difficult, for extensive (i.e., not topographically confined) fragmental lithofacies to be produced by subglacial eruptions on such volcanoes. It is unclear why these lithofacies are relatively uncommon, including elsewhere in the Andean Southern Volcanic Zone (SVZ) (although

hyaloclastite has been reported locally at Nevados de Chillán and more widely at Volcán Hudson: Gutiérrez et al., 2005; Mee et al., 2006). It is not necessarily because the magma is typically of an evolved composition, as there are examples in Iceland of fragmental deposits from subglacial eruptions of intermediate magmas (e.g., Stevenson et al., 2009) and rhyolite (e.g., McGarvie et al., 2007), although often they are only associated with mafic eruptions (e.g., Kelman et al., 2002). In any case, mafic volcanism is thought to be predominant in the central and southern sectors of the SVZ (Stern, 2004; Fontijn et al., 2014). There could be preservation bias; fragmental lithofacies are more easily eroded than lavas, and they could have been covered by the large volume of post-glacial lavas thought to have been erupted at some volcanoes (e.g., Llaima and Villarrica: Naranjo and Moreno, 1991). Alternatively, their absence could suggest a reduction in the frequency and/or volume of eruptions during glacial maxima, for which there is some evidence in the regional record of explosive eruptions (Watt et al., 2013a; Rawson et al., 2016). Further detailed mapping of the volcanoes of the SVZ and in similar arcs is essential to quantify the prevalence of subglacial eruptions at such volcanoes.

5.5. Conclusions

The glaciovolcanic eruption products preserved at Volcán Sollipulli provide new insight into the range of volcano-ice interactions that can occur on ice-capped stratovolcanoes. Widespread hyaloclastic tuff-breccia, sometimes containing lava pillows, suggests that considerable lava-meltwater interaction can occur beneath ice on such edifices apparently without topographic confinement. Furthermore, an extensive sequence of sills and debris flow deposits is recognised for the first time on a temperate-latitude stratovolcano, which, considering its similarity to Dalsheidi-type sequences, also suggests ubiquitous syn-eruptive subglacial meltwater generation and ponding. Nevertheless, the ice thickness during the emplacement of these units is not possible to constrain robustly from the lithofacies relationships. The lavas emplaced around the caldera rim and on the upper flanks exemplify the variety of interactions (and morphologies resulting from) lava flowing beneath or into ice, including that platy fracturing of the lava margin can occur, which has not been widely recognised in such lavas. Features of the circum-caldera lava sequence constrain the thickness of the intra-caldera ice during its emplacement, and also suggest that the ice might have considerably influenced the evolution of the caldera itself. Constraining the prevalence and nature of subglacial and other glaciovolcanic activity at similar volcanoes will be essential to further understanding of the influence of ice on arc volcanism.

Chapter 6 Conclusions and future directions

6.1. Time-series from volcano monitoring

The recent dome-forming eruptions of Soufrière Hills Volcano and Volcán de Colima exemplify some of the challenges in forecasting and understanding activity at arc volcanoes from monitoring time-series, such as abrupt shifts in activity with limited precursors and temporal changes in the relationship between monitored attributes and eruptive activity. The two (potentially widely applicable) statistical techniques applied here to volcano-seismic time-series from these eruptions highlight the potential of such methods to provide additional information on volcanic activity and processes from monitoring data. Detrended fluctuation analysis reveals long-range correlations in each of the time-series analysed, and therefore a degree of long-term memory and predictability to volcano seismicity that has not previously been recognised. The correlation dynamics of the daily counts of some of the event types highlights regime changes and/or provides new constraints on conduit and eruption processes. Furthermore, real-time seismic measurements are found to have anomalously persistent behaviour prior to the onset of some eruptive phases at Colima, including those in the study period for which no clear precursors were identified by conventional real-time monitoring. The entropy (i.e., randomness) of each of the time-series analysed is also found to vary through time, revealing changes in the structure of these data that are not typically apparent from other statistics determined by data distribution. In some instances, the entropy of the seismicity shifts prior to or coincident with changes in seismic or eruptive activity, some of which were not clearly recognised by real-time monitoring. These findings suggest that with further development, statistical techniques, particularly those quantifying the predictability or randomness of monitoring time-series, may have the potential to provide useful additional guidance for interpreting temporal variations in volcanic activity on sub-

decadal timescales. However, the results of this study highlight that the challenges in interpreting monitoring data also apply to statistic time-series calculated from them, such as the uniqueness of the behaviour of many volcanoes inhibiting generalised interpretation, and the potential for the relationship between a monitored or statistical attribute and volcanic activity to change with time.

The utility of the statistical techniques applied in this thesis could be further evaluated in the following ways: (1) application to longer real-time datasets (such as RSAM) from periods with more activity shifts, so the correlation between changes in the statistics and activity shifts could be statistically tested and/or to evaluate the efficacy of statistic thresholds for forecasting; (2) application to seismic time-series from other volcanoes with different styles of eruptive activity and/or seismicity, to better constrain the conditions required for and so processes that cause persistence or randomness in volcano seismicity; (3) application to time-series from different types of monitoring, to assess their utility for analysis of these other data, and to compare the temporal variability of the statistical properties of different monitoring data. This approach could also be taken to better evaluate the utility of the many other statistical methods that have been applied to volcanological time-series (Supplementary Table 2.1), but studied only to a similar or lesser degree as those investigated here. Using other techniques to quantify similar properties of the same data may further constrain the interpretation of variations in the persistence and randomness of monitoring time-series. For DFA, complementary statistical methods include multifractal DFA (e.g., Kantelhardt et al., 2002; Alvarez-Ramirez et al., 2009) and other measures of persistence, such as variograms (e.g., Jaquet et al., 2006; Carniel et al., 2008); for Shannon entropy, other entropy functions (e.g., renormalized entropy (Saparin et al., 1994) or time-dependent pattern entropy (Ishizaki and Inoue, 2013)) or information measures (e.g., Fisher information: Telesca et al., 2012) could be informative.

The results of both statistical techniques applied here imply that there are temporal variations in the predictability of the time-series analysed; this suggests that development of means to quantify the predictability of future volcanic activity from monitoring data in a way that could be included in hazard assessments (e.g., in a Bayesian framework: e.g., Aspinall et al., 2003) would be valuable. In addition, the observation of persistence and high entropy of some of the seismic time-series during phases of activity suggests that consideration of volcanoes as chaotic-deterministic systems is worth exploring. Such behaviour could be analysed in monitoring data by a number of statistical techniques, for instance calculating the Lyapunov exponent or correlation dimension (e.g., Correig et al., 1997). More generally, there is considerable potential for other statistical techniques (such as many of those in Supplementary File SF2.1) to be more widely utilised for analysis of temporal variation in monitoring data and comprehensive eruption records.

6.2. Records of explosive eruptions

Analysis of the tephrostratigraphy of Volcán Hudson exemplifies some of the challenges in constraining the history of explosive eruptions from tephrostratigraphic records. Most of the Volcán Hudson tephras analysed here, from terrestrial sections, are found to have a narrow range in their glass composition, which in almost all cases is distinct from the other Volcán Hudson tephras of a similar age, enabling a robust tephrostratigraphic framework to be presented. This contrasts with most of the previous work on ascertaining the tephrostratigraphy from palaeoenvironmental records; reanalysis here demonstrates that these tephras have often been inadequately characterised, resulting in erroneous or unjustified correlations. Further constraint of the explosive eruption history is unlikely to be achievable from additional study of the accessible tephra-bearing soil sequences, so these palaeoenvironmental records have an important role. A much more complete post-glacial tephrostratigraphy could be developed if sufficient composition data were obtained to correlate the many Volcán Hudson tephra deposits identified in lake sediments, as collectively they constitute a more continuous record over a longer period with less spatial bias than the terrestrial record.

Such composition data would also be valuable to better determine the nature of the previously unrecognised shifts we find in the magma composition erupted from Hudson, from silicic to mafic after the H2 eruption (~3.9 cal ka BP), and then to intermediate compositions for the last ~1 ky. This appears to be consistent with an emerging regional trend that is attributed to the magmatic response to deglaciation (Rawson et al., 2016), which also entails temporal variations in eruption flux. Although the estimated eruption flux variability for Hudson is consistent with the regional trend, it is relatively poorly constrained, along with those for many other volcanoes in the Andean Southern Volcanic Zone (SVZ). Most studies have focussed on determining eruption frequency

rather than accurate magnitudes, in part because of the difficulties in finding and correlating tephra records. Robust quantification of eruption flux through time would be invaluable to constrain the controls on temporal variability in eruption frequency.

Some hypotheses on the controls of millennial-scale temporal variability, including the influence of deglaciation (e.g., Watt et al., 2013a; Rawson et al., 2016), are difficult to test in detail without regional context. Recent studies have developed a detailed tephrostratigraphy for the sector of the SVZ from Volcán Llaima to Volcán Chaitén (Watt et al., 2011, 2013b; Rawson et al., 2015; Fontijn et al., in review), but acquiring an eruption record for the volcanoes to the south (including the Austral Volcanic Zone (AVZ): Stern, 2008) is more difficult due to the relative absence of accessible terrestrial sections. The tephrostratigraphy of the AVZ may be refined by the same approach used here for that of Hudson, i.e. new composition analyses of the tephras from major eruptions identified in terrestrial sections, in combination with compilation and reanalysis of the tephra record in palaeoenvironmental archives. This is work in progress, along with an attempt to extract a detailed tephrostratigraphy from a late Holocene peat core ~35 km east of Volcán Yanteles (in the poorly studied sector of the SVZ), which preserves at least several tephra units from volcanoes between Volcán Minchinmávida and Volcán Melimoyu, but with a high background tephra concentration.

6.3. Records of effusive eruptions

The characteristics and interpretation of subaerial effusive eruptions of arc volcanoes are well-constrained in comparison to those involving interaction with ice, which generate relatively diverse landforms and lithofacies. The glaciovolcanic eruption products at Volcán Sollipulli analysed here provide new insight into the range of volcano-ice interactions that can occur on ice-capped stratovolcanoes, and how the eruption style may consequently vary through time. Widespread hyaloclastic tuff-breccia, sometimes containing lava pillows, suggests that considerable lava-meltwater interaction can occur beneath ice on such edifices apparently without topographic confinement. Furthermore, an extensive sequence of sills and debris flow deposits is recognised for the first time on a temperate-latitude stratovolcano, which considering its similarity to Dalsheidi-type sequences, also suggests ubiquitous syn-eruptive subglacial meltwater generation and ponding. Nevertheless, the ice thicknesses during the emplacement of these units (and so the conditions required for such eruptions to occur on such volcanoes) are not possible to constrain robustly from the lithofacies relationships. The lavas emplaced around the caldera rim and on the upper flanks exemplify the variety of interactions (and morphologies) resulting from lava flowing beneath or into ice, including that platy fracturing of the lava margin can occur, which has not been widely recognised in such lavas. Features of the circum-caldera lava sequence constrain the thickness of the intra-caldera ice during its emplacement, and also suggest that the ice might have considerably influenced the evolution of the caldera itself. Nevertheless, the uncertainties in the interpretation of the palaeoenvironmental conditions of the emplacement of some of the sequences analysed demonstrate the necessity of detailed characterisation on an edifice scale, with comparison to other volcanoes, to further understand such effusive eruption records.

Analysis of the record of effusive eruptions in the southern Andes would also be necessary (in addition to the explosive eruption history) to constrain any long-term temporal variation in volcanism with the greatest possible accuracy, but would be an even greater challenge. Further studies of glaciovolcanism would be particularly valuable, given the potential to also ascertain a coupled glacial history. Uncertainties remain about the glacial conditions during the emplacement of the lithofacies described on Volcán Sollipulli, and in our understanding of the prevalence of different styles of glaciovolcanism (and the processes they entail) on temperate arc stratovolcanoes generally. These might be resolved by further detailed mapping, both on Volcán Sollipulli and elsewhere; in the southern Andes, the volcanoes most likely to have considerable exposures of glaciovolcanic eruption products are those with distributed vents (e.g., Antillanca and Quetrupillán volcanoes) or relatively low post-glacial eruption rates (e.g., Sollipulli and Tolhuaca volcanoes), particularly those that have been extensively dissected (e.g., Puntiagudo and Yate volcanoes). Field studies could be complemented by mapping palagonitised glaciovolcanic deposits by remote sensing (e.g., Graettinger et al., 2013), to assess their regional prevalence and distribution. The geochemistry and petrology of the sequences and lithofacies described at Volcán Sollipulli will be examined from the composition data of Murphy (1996) and in Supplementary Table 5.1, and petrographic analysis; comparison to the major element composition of similar deposits in the region could be attempted by composition mapping using remote sensing (e.g., Kobayashi et al., 2010).

Bibliography

Al-Kindy, F.H., Main, I.G., 2003. Testing self-organized criticality in the crust using entropy: A regionalized study of the CMT global earthquake catalogue. J. Geophys. Res. 108, 2521. doi:10.1029/2002JB002230

Alvarez-Ramirez, J., Escarela-Perez, R., 2010. Time-dependent correlations in electricity markets. Energy Economics 32, 269–277. doi:10.1016/j.eneco.2009.05.008

Alvarez-Ramirez, J., Sosa, E., Rodriguez, E., 2009. Assessing temporal-dependent correlations in the 2000-2008 Popocatépetl exhalation sequence by using detrended fluctuation analysis. J. Volcanol. Geotherm. Res. 186, 426–431. doi:10.1016/j.jvolgeores.2009.05.022

Alvarez-Ramirez, J., Sosa, E., Hernandez-Martinez, E., 2011. In-phase dynamics of the exhalation sequence of Popocatépetl volcano and slow-slip events in the Cocos-North American plate boundary. J. Volcanol. Geotherm. Res. 200, 83–90. doi:10.1016/j.jvolgeores.2010.12.001

Amigo, A., 2013. Estimation of tephra-fall and lahar hazards at Hudson Volcano, southern Chile: Insights from numerical models. Geol. Soc. Am. Spec. Papers 498, 177–199. doi:10.1130/2013.2498(11)

Arámbula-Mendoza, R., Lesage, P., Valdés-González, C., Varley, N.R., Reyes-Dávila, G., Navarro, C., 2011. Seismic activity that accompanied the effusive and explosive eruptions during the 2004–2005 period at Volcán de Colima, Mexico. J. Volcanol. Geotherm. Res. 205, 30–46. doi:10.1016/j.jvolgeores.2011.02.009

Arancibia, G., Matthews, S.J., Perez de Arce, C., 2006. K-Ar and $^{40}Ar/^{39}Ar$ geochronology of supergene processes in the Atacama Desert, Northern Chile: tectonic and climatic relations. J. Geol. Soc. Lond. 163, 107–118. doi:10.1144/0016-764904-161

Armienta, M.A., De la Cruz-Reyna, S., 1995. Some hydro-geochemical fluctuations observed in Mexico related to volcanic activity. Appl. Geochem. 10, 215–227. doi:10.1016/0883-2927(94)00044-7

Armienta, M.A., De la Cruz-Reyna, S., Gómez, A., Ramos, E., Ceniceros, N., Cruz, O., Aguayo, A., Martínez, A., 2008. Hydrogeochemical indicators of the Popocatépetl volcano activity. J. Volcanol. Geotherm. Res. 170, 35–50. doi:10.1016/j.jvolgeores.2007.09.006

Arrighi, S., Principe, C., Rosi, M., 2001. Violent strombolian and subplinian eruptions at Vesuvius during post-1631 activity. Bull. Volcanol. 63, 126–150. doi:10.1007/s004450100130

Aspinall, W.P., Woo, G., Voight, B., Baxter, P.J., 2003. Evidence-based volcanology: application to eruption crises. J. Volcanol. Geotherm. Res. 128, 273–285. doi:10.1016/S0377-0273(03)00260-9

Bak, P., Tang, C., Wiesenfeld, K., 1987. Self-organized criticality: An explanation of the 1/f noise. Phys. Rev. Lett. 59, 381–384. doi:10.1103/PhysRevLett.59.381

Banik, T.J., Wallace, P.J., Höskuldsson, Á., Miller, C.F., Bacon, C.R., Furbish, D.J., 2014. Magma-ice-sediment interactions and the origin of lava/hyaloclastite sequences in the Síða formation, South Iceland. Bull. Volcanol. 76, 785. doi:10.1007/s00445-013-0785-3

Bebbington, M.S., 2010. Trends and clustering in the onsets of volcanic eruptions. J. Geophys. Res. 115, B01203. doi:10.1029/2009JB006581

Belousov, A., Behncke, B., Belousova, M., 2011. Generation of pyroclastic flows by explosive interaction of lava flows with ice/water-saturated substrate. J. Volcanol. Geotherm. Res. 202, 60–72. doi:10.1016/j.jvolgeores.2011.01.004

Bertrand, S., Araneda, A., Vargas, P., Jana, P., Fagel, N., Urrutia, R., 2012. Using the N/C ratio to correct bulk radiocarbon ages from lake sediments: Insights from Chilean Patagonia. Quat. Geochron. 12, 23–29. doi:10.1016/j.quageo.2012.06.003

Bertrand, S., Daga, R., Bedert, R., Fontijn, K., 2014. Deposition of the 2011–2012 Cordón Caulle tephra (Chile, 40°S) in lake sediments: Implications for tephrochronology and volcanology. J. Geophys. Res. Earth Surf. 119, 2555–2573. doi:10.1002/2014JF003321

Bindeman, I.N., Leonov, V.L., Izbekov, P.E., Ponomareva, V.V., Watts, K.E., Shipley, N.K., Perepelov, A.B., Bazanova, L.I., Jicha, B.R., Singer, B.S., Schmitt, A.K., Portnyagin, M.V., Chen, C.H., 2010. Large-volume silicic volcanism in Kamchatka: Ar–Ar and U–Pb ages, isotopic, and geochemical characteristics of major pre-Holocene caldera-forming eruptions. J. Volcanol. Geotherm. Res. 189, 57–80. doi:10.1016/j.jvolgeores.2009.10.009

Bird, P., 2003. An updated digital model of plate boundaries. Geochem. Geophys. Geosys. 4, 1027–1079. http://dx.doi.org/10.1029/2001GC000252

Björnsson, H., 2002. Subglacial lakes and jökulhlaups in Iceland. Glob. Planet. Change 25, 255–271. doi:10.1016/S0921-8181(02)00130-3

Blockley, S., 2012. Developing distal tephrochronology for palaeoenvironmental reconstruction in Patagonia. Quat. Int. 279–280, 54. doi:10.1016/j.quaint.2012.07.239

Blockley, S.P., Ramsey, C.B., Pyle, D.M., 2008. Improved age modelling and high-precision age estimates of late Quaternary tephras, for accurate palaeoclimate reconstruction. J. Volcanol. Geotherm. Res. 177, 251–262. doi:10.1016/j.jvolgeores.2007.10.015

Blockley, S.P.E., Bourne, A.J., Brauer, A., Davies, S.M., Hardiman, M., Harding, P.R., Lane, C.S., MacLeod, A., Matthews, I.P., Pyne-O'Donnell, S.D.F., Rasmussen, S.O., Wulf, S., Zanchetta, G., 2014. Tephrochronology and the extended intimate (integration of ice-core, marine and terrestrial records) event stratigraphy 8–128 ka b2k. Quat. Sci. Rev. 106, 88–100. doi:10.1016/j.quascirev.2014.11.002

Bonnichsen, B., Kauffmann, D.F., 1987. Physical features of rhyolite lava flows in the Snake River Plain volcanic province, southwestern Idaho. In: Fink, J.H. (Ed.), The emplacement of silicic domes and lava flows. Spec. Pap. Geol. Soc. Am. 212. Geological Society of America, pp. 119–145. doi:10.1130/SPE212-p119

Borromei, A.M., Coronato, A., Franzén, L.G., Ponce, J.F., López Sáez, J.A., Maidan, N., Rabassa, J., Soledad Candel, M., 2010. Multiproxy record of Holocene paleoenvironmental change, Tierra del Fuego, Argentina. Palaeogeog., Palaeoclim., Palaeoecol. 286, 1–16. doi:10.1016/j.palaeo.2009.11.033

Brock, F., Lee, S., Housley, R.A., Bronk Ramsey, C., 2011. Variation in the radiocarbon age of different fractions of peat: A case study from Ahrenshöft, northern Germany. Quat. Geochron. 6, 550–555. doi:10.1016/j.quageo.2011.08.003

Bronk Ramsey, C., 2009a. Bayesian Analysis of Radiocarbon Dates. Radiocarbon, 51, 337–360. doi:10.2458/azu_js_rc.v.3494

Bronk Ramsey, C., 2009b. Dealing with outliers and offsets in radiocarbon dating. Radiocarbon 51, 1023–1045. http://journals.uair.arizona.edu/index.php/radiocarbon/article/view/3561

Bronk Ramsey, C., Lee, S., 2013. Recent and planned developments of the program OxCal. Radiocarbon 55, 720–730. doi:10.2458/azu_js_rc.55.16215

Brown, S.K., Crosweller, H.S., Sparks, R.S.J., Cottrell, E., Deligne, N.I., Ortiz Guerrero, N., Hobbs, L.K., Kiyosugi, K., Loughlin, S.C., Siebert, L., Takarada, S., 2014. Characterisation of the Quaternary eruption record: analysis of the Large Magnitude Explosive Volcanic Eruptions (LaMEVE) database. J. Appl. Volcanol. 3, 5. doi:10.1186/2191-5040-3-5

Bryce, R.M., Sprague, K.B., 2012. Revisiting detrended fluctuation analysis. Scientific Reports 2, 315. doi:10.1038/srep00315

Burmeister, C., 1891. Breves datos sobre una excursión a Patagonia. Revista del Museo de La Plata 2, 275–287.

Caldenius, C.C., 1932. Las Glaciaciones Cuaternarias en la Patagonia y Tierra del Fuego. Geograf. Annaler 14, 1–164. http://www.jstor.org/stable/519583

Calder, E.S., Luckett, R., Sparks, R.S.J., Voight, B., 2002. Mechanisms of lava dome instability and generation of rockfalls and pyroclastic flows at Soufrière Hills Volcano, Montserrat. In: Druitt, T.H., Kokelaar, B.P. (Eds.), The eruption of Soufrière Hills Volcano, Montserrat, from 1995 to 1999. Geological Society Memoir 21, Geological Society, London, pp. 173–190. doi:10.1144/GSL.MEM.2002.021.01.08

Calder, E.S., Cortés, J.A., Palma, J.L., Luckett, R., 2005. Probabilistic analysis of rockfall frequencies during an andesite lava dome eruption: The Soufrière Hills Volcano, Montserrat. Geophys. Res. Lett. 32, L16309. doi:10.1029/2005GL023594

Carel, M., Siani, G., Delpech, G., 2011. Tephrostratigraphy of a deep-sea sediment sequence off the south Chilean margin: New insight into the Hudson volcanic activity since the last glacial period. J. Volcanol. Geotherm. Res. 208, 99–111. doi:10.1016/j.jvolgeores.2011.09.011

Caricchi, L., Blundy, J., 2015. The temporal evolution of chemical and physical properties of magmatic systems. In: Caricchi, L., Blundy, J. (Eds.), Chemical, physical and temporal evolution of magmatic systems, Geol. Soc. Spec. Pub. 422. Geological Society, London, p. 1 – 15. doi:10.1144/SP422.11

Carmichael, I.S.E., Frey, H.M., Lange, R.A., Hall, C.M., 2006. The Pleistocene cinder cones surrounding Volcán Colima, Mexico re-visited: eruption ages and volumes, oxidation states, and sulfur content. Bull. Volcanol. 68, 407–419. doi:10.1007/s00445-005-0015-8

Carniel, R., 2014. Characterization of volcanic regimes and identification of significant transitions using geophysical data: a review. Bull. Volcanol. 76, 848. doi:10.1007/s00445-014-0848-0

Carniel R., Jaquet, O., Tárraga M., 2008. Perspectives on the application of the geostatistical approach to volcano forecasting at different time scales. In: Gottsmann, J., Martí, J. (Eds.), Caldera volcanism: Analysis, modelling and response. Developments in Volcanology 10, Elsevier, pp. 471–487. doi:10.1016/S1871-644X(07)00014-9

Cashman, K.V., Sparks, R.S.J., 2013. How volcanoes work: A 25 year perspective. Geol. Soc. Am. Bull. 125, 664–690. doi:10.1130/B30720.1

Cashman, K.V., Biggs, J., 2014. Common processes at unique volcanoes–a volcanological conundrum. Front. Earth Sci. 2, 28. doi:10.3389/feart.2014.00028

Cassidy, M., Edmonds, M., Watt, S.F.L., Palmer, M.R., Gernon, T.M., 2015a. Origin of basalts by hybridization in andesite-dominated arcs. J. Petrology 56, 325–346. doi:10.1093/petrology/egv002

Cassidy, M., Cole, P.D., Hicks, K.E., Varley, N.R., Peters, N., Lerner, A.H., 2015b. Rapid and slow: Varying magma ascent rates as a mechanism for Vulcanian explosions. Earth Plan. Sci. Lett. 420, 73–84. doi:10.1016/j.epsl.2015.03.025

Castro, J.M., Dingwell, D.B., 2009. Rapid ascent of rhyolitic magma at Chaitén volcano, Chile. Nature 461, 780–783. doi:10.1038/nature08458

Castro, J.M., Schipper, C.M., Mueller, S.P., Militzer, A.S., Amigo, A., Silva Parejas, C., Jacob, D., 2013. Storage and eruption of near-liquidus rhyolite magma at Cordón Caulle, Chile. Bull. Volcanol. 75, 702. doi:10.1007/s00445-013-0702-9

Cembrano, J., Lara, L., 2009. The link between volcanism and tectonics in the southern volcanic zone of the Chilean Andes: A review. Tectonophys. 471, 96–113. doi:10.1016/j.tecto.2009.02.038

Centamore, C., Patanè, G., Tuvè, T., 1999. Maximum entropy estimation of b values at Mt Etna: comparison with conventional least squares and maximum likelihood results and correlation with volcanic activity. Ann. Geofis. 42, 515–528. doi:10.4401/ag-3734

Chouet, B.A., Matoza, R.S., 2013. A multi-decadal view of seismic methods for detecting precursors of magma movement and eruption. J. Volcanol. Geotherm. Res., 252, 108–175. doi:10.1016/j.jvolgeores.2012.11.013

Clark, P.U., Dyke, A.S., Shakun, J.D., Carlson, A.E., Clark, J., Wohlfarth, B., Mitrovica, J.X., Hostetler, S.W., McCabe, A.M., 2009. The Last Glacial Maximum. Science 325, 710–714. doi:10.1126/science.1172873

Clifford, P., Cosma, I.A., 2012. A statistical analysis of probabilistic counting algorithms. Scandinavian Journal of Statistics 39, 1–14. doi:10.1111/j.1467-9469.2010.00727.x

Clifford, P., Cosma, I.A., 2013. A simple sketching algorithm for entropy estimation. Journal of Machine Learning Research: Proceedings of the Sixteenth International Conference on Artificial Intelligence and Statistics 31, 196–206. http://jmlr.org/proceedings/papers/v31/clifford13a.html

Cole, P.D., Bass, V., Christopher, T., Eligon, C., Fergus, M., Odbert, H.M., Simpson, R., Stewart, R.C., Stinton, A., Stone, J., Syers, R., Robertson, R., Watts, R., Williams, P., 2010a. MVO report to the Scientific Advisory Committee: report on activity between 15 August 2009 and 28 February 2010. Montserrat Volcano Observatory.

Cole, P.D., Bass, V., Christopher, T., Eligon, C., Murrell, C., Odbert, H.M., Smith, P., Stewart, R.C., Stinton, A., Syers, R., Robertson, R., Williams, P., 2010b. Report to the Scientific Advisory Committee on volcanic activity at Soufrière Hills Volcano, Montserrat: report on activity between 28 February 2010 and 31 October 2010. Montserrat Volcano Observatory, Open File Report 10-02a. http://www.mvo.ms/science/reports/1592-mvo-reports-to-sac-15 (last accessed 1 July 2013).

Conway, C.E., Townsend, D.B., Leonard, G.S., Wilson, C.J.N., Calvert, A.T., Gamble, J.A., 2015. Lava-ice interaction on a large composite volcano: a case study from Ruapehu, New Zealand. Bull. Volcanol. 77, 21. doi:10.1007/s00445-015-0906-2

Correig, A.M., Urquizu, M., Vila, J., Marti, J., 1997. Analysis of the temporal occurrence of seismicity at Deception Island (Antarctica): A nonlinear approach. Pure Appl. Geophys. 149, 553–574. doi:10.1007/s000240050041

Currenti, G., del Negro, C., Lapenna, V., Telesca, L., 2005a. Fluctuation analysis of the hourly time variability of volcano-magnetic signals recorded at Mt. Etna Volcano, Sicily (Italy). Chaos, Solitons, and Fractals 23, 1921–1929. doi:10.1016/j.chaos.2004.07.035

Currenti, G., del Negro, C., Lapenna, V., Telesca, L., 2005b. Multifractality in local geomagnetic field at Etna volcano, Sicily (southern Italy). Nat. Hazards Earth Syst. Sci. 5, 555–559. doi:10.5194/nhess-5-555-2005

Davies, S.M., 2015. Cryptotephras: the revolution in correlation and precision dating. J. Quat. Sci. 30, 114–130. doi:10.1002/jqs.2766

Davies, S.M., Abbott, P.M., Pearce, N.J.G., Wastegård, S., Blockley, S.P.E., 2012. Integrating the INTIMATE records using tephrochronology: rising to the challenge. Quat. Sci. Rev. 36, 11–27. doi:10.1016/j.quascirev.2011.04.005

DeCelles, P.G., Ducea, M.N., Kapp, P., Zandt, G., 2009. Cyclicity in Cordilleran orogenic systems. Nat. Geosci. 2, 251–257. doi:10.1038/ngeo469

DeGraff, J.M., Aydin, A., 1987. Surface morphology of columnar joints and its significance to mechanics and direction of joint growth. Geol. Soc. Am. Bull. 99, 605–617. doi:10.1130/0016-7606(1987)99<605:SMOCJA>2.0.CO;2

Delgado-Granados, H., 1993. Late Cenozoic tectonics offshore western Mexico and its relation to the structure and volcanic activity in the western Trans-Mexican Volcanic Belt. Geofís. Int. 32, 543–559.

Del Pin, E., Carniel, R., Tárraga, M., 2008. Event recognition by detrended fluctuation analysis: An application to Teide-Pico Viejo volcanic complex, Tenerife, Spain. Chaos, Solitons, and Fractals 36, 1173–1180. doi:10.1016/j.chaos.2006.07.044

Delgado, F., Pritchard, M., Lohman, R., Naranjo, J.A., 2014. The 2011 Hudson volcano eruption (Southern Andes, Chile): Pre-eruptive inflation and hotspots observed with InSAR and thermal imagery. Bull. Volcanol. 76, 815. doi:10.1007/s00445-014-0815-9

De Vleeschouwer, F., 2002. Etude tephrostratigraphique de depôts Holocènes des bassins versants de deux lacs Chiliens - Exemple del lacs Icalma et Galletue (Chili - 38°S, 71°W). Thesis, Université de Liège, Belgium.

Dixon, J.E., Filiberto, J.R., Moore, J.G., Hickson, C.J., 2002. Volatiles in basaltic glasses from a subglacial volcano in northern British Columbia (Canada): implications for ice sheet thickness and mantle volatiles. In: Smellie, J.L., Chapman, M.G. (Eds.), Volcano-ice interactions on Earth and Mars. Geol. Soc. Spec. Publ. 202, Geological Society, London, pp. 255–271. doi:10.1144/GSL.SP.2002.202.01.13.

D'Orazio, M., Innocenti, F., Manetti P., Tamponi, M., Tonarini, S., González-Ferrán, O., Lahsen, A., Omarini, R., 2003. The Quaternary calc-alkaline volcanism of the Patagonian Andes close to the Chile triple junction: geochemistry and petrogenesis of volcanic rocks from the Cay and Maca volcanoes (~45°S, Chile). J. South Am. Earth Sci. 16, 219–242. doi:10.1016/S0895-9811(03)00063-4

Dunbar, N.W., Kurbatov, A.V., 2011. Tephrochronology of the Siple Dome ice core, West Antarctica: correlations and sources. Quat. Sci. Rev. 30, 1602–1614. doi:10.1016/j.quascirev.2011.03.015

Edwards, B.R., Russell, J.K., 2002. Glacial influences on morphology and eruptive products of Hoodoo Mountain volcano, Canada. In: Smellie, J.L., Chapman, M.G. (Eds.), Volcano-ice interactions on Earth and Mars. Geol. Soc. Spec. Publ. 202, Geological Society, London, pp. 179–194. http://dx.doi.org/10.1144/GSL.SP.2002.202.01.09.

Edwards, B.R., Russell, J.K., 2011. Thermodynamic constraints on explosive vs. effusive onset of glaciovolcanic eruptions. American Geophysical Union Fall Meeting 2011, Abstract #V31E-2578.

Elbert, J., Wartenburger, R., von Gunten, L., Urrutia, R., Fischer, D., Fujak, M., Hamann, Y., Greber, N.D., Grosjean, M., 2013. Late Holocene air temperature variability reconstructed from the sediments of Laguna Escondida, Patagonia, Chile (45°30'S). Palaeogeogr., Palaeoclimatol., Palaeoecol. 369, 482–492. doi:10.1016/j.palaeo.2012.11.013

Endo, E.T., Murray, T., 1991. Real-time Seismic Amplitude Measurement (RSAM): a volcano monitoring and prediction tool. Bull. Volcanol. 53, 533–545. doi:10.1007/BF00298154

Fierstein, J., 2007. Explosive eruptive record in the Katmai region, Alaska Peninsula: an overview. Bull. Volcanol. 69, 469–509. doi:10.1007/s00445-006-0097-y

Fisher, R.V., Schmincke, H.-U., 1984. Alteration of volcanic glass. In: Fisher, R.V., Schmincke, H.-U., Pyroclastic Rocks. Springer, New York, pp. 312–345. doi:10.1007/978-3-642-74864-6_12

Fitton, G., 1997. X-Ray fluorescence spectrometry. In: Gill, R. (ed.), Modern Analytical Geochemistry: An Introduction to Quantitative Chemical Analysis for Earth, Environmental and Material Scientists: Addison Wesley Longman, UK.

Fontijn, K., Lachowycz, S.M., Rawson, H., Pyle, D.M., Mather, T.A., Naranjo, J.A., Moreno-Roa, H., 2014. Late Quaternary tephrostratigraphy of southern Chile and Argentina. Quat. Sci. Rev. 89, 70–84. doi:10.1016/j.quascirev.2014.02.007

Fontijn, K., Costa, F., Sutawidjaja, I., Newhall, C.G., Herrin, J.S., 2015. A 5000-year record of multiple highly explosive mafic eruptions from Gunung Agung (Bali, Indonesia): implications for eruption frequency and volcanic hazards. Bull. Volcanol. 77, 59. doi:10.1007/s00445-015-0943-x

Fontijn, K., Rawson, H., Van Daele, M., Moernaut, J., Abarzúa, A.M., Heirman, K., Bertrand, S., Pyle, D.M., Mather, T.A., De Batist, M., Naranjo, J.A., Moreno, H., in review. Synchronisation of sedimentary records using tephra: A post-glacial tephrochronological model for the Chilean Lake District.

Forbes, A.E.S., Blake, S., McGarvie, D.W., Tuffen, H., 2012. Pseudopillow fracture systems in lavas: Insights into cooling mechanisms and environments from lava flow fractures. J. Volcanol. Geotherm. Res. 245–246, 68–80. doi:10.1016/j.jvolgeores.2012.07.007

Forbes, A.E.S., Blake, S., Tuffen, H., 2014a. Entablature: fracture types and mechanisms. Bull. Volcanol. 76, 820–833. doi:10.1007/s00445-014-0820-z

Forbes, A.E.S., Blake, S., Tuffen, H., Wilson, A. 2014b. Fractures in a trachyandesitic lava at Öræfajökull, Iceland, used to infer subglacial emplacement in 1727–8 eruption. J. Volcanol. Geotherm. Res. 288, 8–18. doi:10.1016/j.jvolgeores.2014.10.004

Fuenzalida, R., Espinosa, W., 1973. Hallazgo de una caldera volcanica en la provincia de Aisen. Revista Geol. de Chile 1, 64–66. doi:10.5027/andgeoV1n1-a04

Gabarda, S., Cristóbal, G., 2010. Detection of events in seismic time series by time-frequency methods. IET Signal Process. 4, 413–420. doi:10.1049/iet-spr.2009.0125

Geyer, A., Bindeman, I., 2011. Glacial influence on caldera-forming eruptions. J. Volcanol. Geotherm. Res. 202, 127–142. doi:10.1016/j.jvolgeores.2011.02.001

Gilbert, J.S., Stasiuk, M.V., Lane, S.J., Adam, C.R., Murphy, M.D., Sparks, R.S.J., Naranjo, J.A., 1996. Non-explosive, constructional evolution of the ice-filled caldera at Volcán Sollipulli, Chile. Bull. Volcanol. 58, 67–83. doi:10.1007/s004450050127

Gill, J.B., 1981. Orogenic andesites and plate tectonics. Springer, New York.

Glasser, N.F., Jansson, K.N., Harrison, S., Kleman, J., 2008. The glacial geomorphology and Pleistocene history of South America between 38°S and 56°S. Quat. Sci. Rev. 27, 365–390. doi:10.1016/j.quascirev.2007.11.011

Global Volcanism Program, 2013. Report on Cerro Hudson (Chile). In: Wunderman, R. (Ed.), Bulletin of the Global Volcanism Network 38, 12, Smithsonian Institution. doi:10.5479/si.GVP.BGVN201312-358057

Goehring, L., Morris, S.W., 2008. Scaling of columnar joints in basalt. J. Geophys. Res. 113, B10203. doi:10.1029/2007JB005018

Graettinger, A.H., Ellis, M.K., Skilling, I.P., Reath, K., Ramsey, M.S., Lee, R.J., Hughes, C.G., McGarvie, D.W., 2013. Remote sensing and geologic mapping of glaciovolcanic deposits in the region surrounding Askja (Dyngjufjöll) volcano, Iceland. Int. J. Remote Sensing 34, 7178–7198. doi:10.1080/01431161.2013.817716

Gertisser, R., Keller, J., 2003. Temporal variations in magma composition at Merapi Volcano (Central Java, Indonesia): magmatic cycles during the past 2000 years of explosive activity. J. Volcanol. Geotherm. Res. 123, 1–23. doi:10.1016/S0377-0273(03)00025-8

Gutiérrez, F., Gioncada, A., González Ferran, O., Lahsen, A., Mazzuoli, R., 2005. The Hudson Volcano and surrounding monogenetic centres (Chilean Patagonia): An example of volcanism associated with ridge–trench collision environment. J. Volcanol. Geotherm. Res. 145, 207–233. doi:10.1016/j.jvolgeores.2005.01.014

Haberle, S.G., Lumley, S.H., 1998. Age and origin of tephras recorded in postglacial lake sediments to the west of the southern Andes, 44°S to 47°S. J. Volcanol. Geotherm. Res. 84, 239–256. doi:10.1016/S0377-0273(98)00037-7

Haberle, S.G., Szeicz, J.M., Bennett, K.D., 2000. Late Holocene vegetation dynamics and lake geochemistry at Laguna Miranda, XI Region, Chile. Rev. Chil. Hist. Nat. 73, 655–669. doi:10.4067/S0716-078X2000000400010

Haberzettl, T., Corbella, H., Fey, M., Janssen, S., Lücke, A., Mayr, C., Ohlendorf, C., Schäbitz, F., Schleser, G.H., Wille, M., Wulf, S., Zolitschka, B., 2007. Lateglacial and Holocene wet–dry cycles in southern Patagonia: chronology, sedimentology and geochemistry of a lacustrine record from Laguna Potrok Aike, Argentina. The Holocene 17, 297–310. doi:10.1177/0959683607076437

Haberzettl, T., Anselmetti, F.S., Bowen, S.W., Fey, M., Mayr, C., Zolitschka, B., Ariztegui, D., Mauz, B., Ohlendorf, C., Kastner, S., Lücke, A., Schäbitz, F., Wille, M., 2009. Late Pleistocene dust deposition in the Patagonian steppe - extending and refining the paleoenvironmental and tephrochronological record from Laguna Potrok Aike back to 55 ka. Quat. Sci. Rev. 28, 2927–2939. doi:10.1016/j.quascirev.2009.07.021

Hale, A.J., Calder, E.S., Loughlin, S.C., Wadge, G., Ryan, G.A., 2009. Modelling the lava dome extruded at Soufrière Hills Volcano, Montserrat, August 2005–May 2006. Part II: Rockfall activity and talus deformation. J. Volcanol. Geotherm. Res. 187, 69–84. doi:10.1016/j.jvolgeores.2009.08.014

Hicks, P.D., Matthews, A. J., Cooker, M. J., 2010. Triggering of a volcanic dome collapse by rainwater infiltration. J. Geophys. Res. 115, B09212. doi:10.1029/2009JB006831

Hobbs, L.K., 2014. The role of cold supraglacial volcanic deposits in influencing glacial ablation. PhD thesis, Lancaster University, United Kingdom.

Hogg, A.G., Hua, Q., Blackwell, P.G., Niu, M., Buck, C.E., Guilderson, T.P., Heaton, T.J., Palmer, J.G., Reimer, P.J., Reimer, R.W., Turney, C.S.M., Zimmerman, S.R.H., 2013. SHCal13 Southern Hemisphere calibration, 0–50,000 years cal BP. Radiocarbon 55, 1889–1903. doi:10.2458/azu_js_rc.55.16783

Holland, A.S.P., Watson, I.M., Phillips, J.C., Caricchi, L., Dalton, M.P., 2011. Degassing processes during lava dome growth: Insights from Santiaguito lava dome, Guatemala. J. Volcanol. Geotherm. Res. 202, 153–166. doi:10.1016/j.jvolgeores.2011.02.004

Höskuldsson, A., Sparks, R.S.J., 1997. Thermodynamics and fluid dynamics of effusive subglacial eruptions. Bull. Volcanol. 59, 219–230. doi:10.1007/s004450050187

Huggel, C., 2009. Recent extreme slope failures in glacial environments: effects of thermal perturbation. Quat. Sci. Rev. 28, 1119–1130. doi:10.1016/j.quascirev.2008.06.007

Hulton, N.R.J., Purves, R.S., McCulloch, R.D., Sugden, D.E., Bentley, M.J., 2002. The Last Glacial Maximum and deglaciation in southern South America. Quat. Sci. Rev. 21, 233–241. doi:10.1016/S0277-3791(01)00103-2

Humphreys, M.C.S., Kearns, S.L., Blundy, J.D., 2006. SIMS investigation of electron-beam damage to hydrous, rhyolitic glasses: Implications for melt inclusion analysis. American Mineralogist 91, 667–679. doi:10.2138/am.2006.1936

Hurst, H.E., Black, R.P., Simaika, Y.M., 1965. Long-term storage: an experimental study. Constable, London.

Hutchison, W., Varley, N.R., Pyle, D.M., Mather, T.A., Stevenson, J.A., 2013. Airborne thermal remote sensing of the Volcán de Colima (Mexico) lava dome from 2007 to 2010. In: Pyle, D.M., Biggs, J.B., Mather, T.A. (Eds.), Remote sensing of volcanoes and volcanic processes: integrating observation and modelling. Geological Society Spec. Pub. 320, Geological Society, London, pp. 203–228. doi:10.1144/SP380.8

Huybers, P., Langmuir, C., 2009. Feedback between deglaciation, volcanism, and atmospheric CO_2. Earth Plan. Sci. Lett. 286, 479–491. doi:10.1016/j.epsl.2009.07.014

Ishizaki, R., Inoue, M., 2013. Time-series analysis of foreign exchange rates using time-dependent pattern entropy. Physica A 392, 3344–3350. doi:10.1016/j.physa.2013.03.041

Ivanova, K., Ausloos, M., 1999. Application of the detrended fluctuation analysis (DFA) method for describing cloud breaking. Physica A 274, 349–354. doi:10.1016/S0378-4371(99)00312-X

Jaquet, O., Sparks, R.S.J., Carniel, R., 2006. Magma memory recorded by statistics of volcanic explosions at the Soufrière Hills volcano, Montserrat. In: Mader, H., Coles, S., Connor, C., Connor, L. (Eds.), Statistics in Volcanology. IAVCEI Spec. Pub. 1, Geological Society, London, pp. 175–184.

Jara, C., Moreno, H., in preparation. Geología del Volcán Sollipulli, Región de la Araucanía. Carta Geológica de Chile, Servicio Nacional de Geología y Minería.

Jochum, K.P., Stoll, B., Herwig, K., Willbold, M., Hofmann, A.W., Amini, M., Aarburg, S., Abouchami, W., Hellebrand, E., Mocek, B., Raczek, I., Stracke, A., Alard, O., Bouman, C., Becker, S., Dücking, M., Brätz, H., Klemd, R., de Bruin, D., Canil, D., Cornell, D., de Hoog, C.-J., Dalpé, C., Danyushevsky, L., Eisenhauer, A., Gao, Y., Snow, J.E., Groschopf, N., Günther, D., Latkoczy, C., Guillong, M., Hauri, E.H., Höfer, H.E., Lahaye, Y., Horz, K., Jacob, D.E., Kasemann, S.A., Kent, A.J.R., Ludwig, T., Zack, T., Mason, P.R.D., Meixner, A., Rosner, M., Misawa, K., Nash, B.P., Pfänder, J., Premo, W.R., Sun, W.D., Tiepolo, M., Vannucci, R., Vennemann, T., Wayne, D., Woodhead, J.D., 2006. MPI-DING reference glasses for in situ microanalysis: New reference values for element concentrations and isotope ratios. Geochem. Geophys. Geosyst. 7, Q02008. doi:10.1029/2005GC001060

Kantelhardt, J.W., Zschiegner, S.A., Koscielny-Bunde, E., Havlin, S., Bunde, A., Stanley, H.E., 2002. Multifractal detrended fluctuation analysis of nonstationary time series. Physica A 316, 87–114. doi:10.1016/S0378-4371(02)01383-3

Kantelhardt, J.W., 2009. Fractal and mulitfractal time series. In: Meyers, R.A. (Ed.), Springer encyclopaedia of complexity and system science. Springer, pp. 3754–3779. Pre-print on arXiv: 0804.0747v1.

Kelman, M.C., Russell, J.K., Hickson, C.J., 2002. Effusive intermediate volcanism in the Garibaldi Volcanic Belt, southwestern British Columbia, Canada. In: Smellie, J.L., Chapman, M.G. (Eds.), Volcano-ice interactions on Earth and Mars. Geol. Soc. Spec. Publ. 202, Geological Society, London, pp. 195–211. doi:10.1144/GSL.SP.2002.202.01.10

Kilian, R., Lamy, F., 2012. A review of Glacial and Holocene paleoclimate records from southernmost Patagonia (49–55°S). Quat. Sci. Rev. 53, 1–23. doi:10.1016/j.quascirev.2012.07.017

Kilian, R., Hohner, M., Biester, H., Wallrabe-Adams, H.J., Stern, C.R., 2003. Holocene peat and lake sediment tephra record from the southernmost Chilean Andes (53–55°S). Revista Geológica de Chile 30, 23–27. doi:10.4067/S0716-02082003000100002

Kobayashi, C., Orihashi, Y., Hiarata, D., Naranjo, J.A., Kobayashi, M., Anma, R., 2010. Compositional variations revealed by ASTER image analysis of the Viedma Volcano, southern Andes Volcanic Zone. Andean Geol. 37, 433–441. doi:10.5027/andgeoV37n2-a09

Kokelaar, P., 2002. Setting, chronology and consequences of the eruption of Soufrière Hills Volcano, Montserrat (1995–1999). In: Druitt, T.H., Kokelaar, B.P. (Eds.), The eruption of Soufrière Hills Volcano, Montserrat, from 1995 to 1999. Geol. Soc. Memoirs 21, Geological Society, London, pp. 1–43.

Kratzmann, D.J., Carey, S., Scasso, R., Naranjo, J.-A., 2009. Compositional variations and magma mixing in the 1991 eruptions of Hudson volcano, Chile. Bull. Volcanol. 71, 419–439. doi:10.1007/s00445-008-0234-x

Kratzmann, D.J., Carey, S., Scasso, R., Naranjo, J.-A., 2010. Role of cryptic amphibole crystallization in magma differentiation at Hudson volcano, Southern Volcanic Zone, Chile. Cont. Min. Pet. 159, 237–264. doi:10.1007/s00410-009-0426-1

Kurbatov, A.V., Zielinski, G.A., Dunbar, N.W., Mayewski, P.A., Meyerson, E.A., Sneed, S.B., Taylor, K.C., 2006. A 12,000 year record of explosive volcanism in the Siple Dome Ice Core, West Antarctica. J. Geophys. Res. 111, D12307. doi:10.1029/2005JD006072

Kutterolf, S., Jegen, M., Mitrovica, J.X., Kwasnitschka, T., Freundt, A., Huybers, P.J., 2012. A detection of Milankovitch frequencies in global volcanic activity. Geology 41, 227–230. doi:10.1130/G33419.1

Lachowycz, S.M., 2010. Statistical analysis of seismicity at Volcán de Colima, Mexico. MEarthSc thesis, University of Oxford.

Lachowycz, S.M., Pyle, D.M., Mather, T.A., Varley, N.R., Odbert, H.M., Cole, P.D., Reyes-Dávila, G.A., 2013. Long-range correlations identified in time-series of volcano seismicity during dome-forming eruptions using detrended fluctuation analysis. J. Volcanol. Geotherm. Res. 264, 197–209. doi:10.1016/j.jvolgeores.2013.07.009

Lamb, O.D., Varley, N.R., Mather, T.A., Pyle, D.M., Smith, P.J., Liu, E.J., 2014. Multiple timescales of cyclical behaviour observed at two dome-forming eruptions. J. Volcanol. Geotherm. Res. 284, 106–121. doi:10.1016/j.jvolgeores.2014.07.013

Lavallée, Y., Varley, N.R., Alatorre-Ibargüengoitia, M.A., Hess, K.-U., Kueppers, U., Mueller, S., Richard, D., Scheu, B., Spieler, O., Dingwell, D.B., 2012. Magmatic architecture of dome-building eruptions at Volcán de Colima, Mexico. Bull. Volcanol. 74, 249–260. doi:10.1007/s00445-011-0518-4

Le Bas, M.J., Le Maitre, R.W., Streckeisen, A., Zanettin, B., 1985. A Chemical Classification of Volcanic Rocks Based on the Total Alkali-Silica Diagram. J. Petrology 27, 745–750. doi:10.1093/petrology/27.3.745

Lescinsky, D.T., Fink, J.H., 2000. Lava and ice interaction at stratovolcanoes: Use of characteristic features to determine past glacial extents and future volcanic hazards. J. Geophys. Res. 105, 23711–23726. doi:10.1029/2000JB900214

Lescinsky, D.T., Sisson, T.W., 1998. Ridge-forming, ice-bounded lava flows at Mount Rainier, Washington. Geology 26, 351–354. doi:10.1130/0091-7613(1998)026<0351:RFIBLF>2.3.CO;2

Lisiecki, L.E., Raymo, M.E., 2005. A Pliocene-Pleistocene stack of 57 globally distributed benthic δ18O records. Paleoceanography 20, PA1003. doi:10.1029/2004PA001071

Little, M., McSharry, P., Moroz, I., Roberts, S., 2006. Nonlinear, Biophysically-Informed Speech Pathology Detection. In: 2006 IEEE International Conference on Acoustics, Speech and Signal Processing, ICASSP 2006 Proceedings, Toulouse, France, 2, pp. II-1080–II-1083. doi:10.1109/ICASSP.2006.1660534

Livina, V.N., Lenton, T.M., 2007. A modified method for detecting incipient bifurcations in a dynamical system. Geophys. Res. Lett. 34, L03712. doi:10.1029/2006GL028672

Lodge, R.W.D., Lescinsky, D.T., 2009. Fracture patterns at lava-ice contacts on Kokostick Butte, OR, and Mazama Ridge, Mount Rainier, WA: Implications for flow emplacement and cooling histories. J. Volcanol. Geotherm. Res. 185, 298–310. doi:10.1016/j.jvolgeores.2008.10.010

Lohmar, S., Robin, C., Gourgaud, A., Clavero, J., Parada, M.A., Moreno, H., Ersoy, O., Lopez-Escobar, L., Naranjo, J.A., 2007. Evidence of magma-water interaction during the 13,800 years BP explosive cycle of the Licán Ignimbrite, Villarrica volcano (southern Chile). Revista Geol. de Chile 34, 233–247. doi:10.5027/andgeoV34n2-a04

Long, P.E., Wood, B.J., 1986. Structures, textures, and cooling histories of Columbia River basalt flows. Geol. Soc. Am. Bull. 97, 1144–1155. doi:10.1130/0016-7606(1986)97<1144:STACHO>2.0.CO;2

López-Escobar, L., Cembrano, J., Moreno, H., 1995. Geochemistry and tectonics of the Chilean Southern Andes basaltic Quaternary volcanism (37–46°S). Revista Geol. de Chile 22, 219–234. doi:10.5027/andgeoV22n2-a06

Loughlin, S.C., 2002. Facies analysis of proximal subglacial and proglacial volcaniclastic successions at the Eyjafjallajökull central volcano, southern Iceland. In: Smellie, J.L., Chapman, M.G. (Eds.), Volcano-ice interactions on Earth and Mars. Geol. Soc. Spec. Publ. 202, Geological Society, London, pp. 149–178. doi:10.1144/GSL.SP.2002.202.01.08

Loughlin, S.C., Luckett, R., Ryan, G., Christopher, T., Hards, V., De Angelis, S., Jones, L., Strutt, M., 2010. An overview of lava dome evolution, dome collapse and cyclicity at Soufrière Hills Volcano, Montserrat, 2005–2007. Geophys. Res. Lett. 37, L00E16. doi:10.1029/2010GL042547

Loughlin, S.C., Vye-Brown, C., Sparks, R.S.J., Brown, S.K., Barclay, J., Calder, E., Cottrell, E., Jolly, G., Komorowski, J-C., Mandeville, C., Newhall, C., Palma, J., Potter, S., Valentine, G., 2015. An introduction to global volcanic hazard and risk. In: Loughlin, S.C., Sparks, R.S.J., Brown, S.K., Jenkins, S.F., Vye-Brown, C. (Eds.), Global volcanic hazards and risk. Cambridge University Press, pp. 1–80. doi:10.1017/CBO9781316276273.003

Lowe, D.J., 2011. Tephrochronology and its application: A review. Quat. Geochron. 6, 107–153. doi:10.1016/j.quageo.2010.08.003

Luckett, R., Baptie, B., Ottemoller, L., Thompson, G., 2007. Seismic monitoring of the Soufrière Hills volcano, Montserrat. Seis. Res. Lett. 78, 192–200. doi:10.1785/gssrl.78.2.192

Luckett, R., Loughlin, S., De Angelis, S., Ryan, G., 2008. Volcanic seismicity at Montserrat, a comparison between the 2005 dome growth episode and earlier dome growth. J. Volcanol. Geotherm. Res. 177, 894–902. doi:10.1016/j.jvolgeores.2008.07.006

Luhr, J.F., 2002. Petrology and geochemistry of the 1991 and 1998-1999 lava flows from Volcán de Colima, México: implications for the end of the current eruptive cycle. J. Volcanol. Geotherm. Res. 117, 169–194. doi:10.1016/S0377-0273(02)00243-3

Luhr, J.F., Navarro-Ochoa, C., Savov, I.P., 2002. Tephrochronology, petrology and geochemistry of Late-Holocene pyroclastic deposits from Volcán de Colima, Mexico. J. Volcanol. Geotherm. Res. 197, 1–32. doi:10.1016/j.jvolgeores.2009.11.007

Mader, H., 2006. Volcanic processes as a source of statistical data. In: Mader, H., Coles, S., Connor, C., Connor, L. (Eds.), Statistics in Volcanology. IAVCEI Spec. Pub. 1, Geological Society, London, pp. 1-14.

Main, I.G., Al-Kindy, F.H., 2002. Entropy, energy, and proximity to criticality in global earthquake populations. Geophys. Res. Lett. 29, 1121. doi:10.1029/2001GL014078

Main, I.G., Naylor, M., 2010. Entropy production and self-organised (sub)criticality in earthquake dynamics. Phil. Trans. R. Soc. Lond. A 368, 131–144. doi:10.1098/rsta.2009.0206

Major, J.J., Newhall, C.G., 1989. Snow and ice perturbation during historical volcanic eruptions and the formation of lahars and floods: a global review. Bull. Volcanol. 52, 1–27. doi:10.1007/BF00641384

Major, J.J., Lara, L.E., 2013. Overview of Chaitén Volcano, Chile, and its 2008-2009 eruption. Andean Geol. 40, 196–215. doi:10.5027/andgeoV40n2-a01

Mandelbrot, B.B., Wallis, J.R., 1968. Noah, Joseph, and operational hydrology. Water Resources Res. 4, 909–918. doi:10.1029/WR004i005p00909

Markgraf, V., Bradbury, J.P., Schwalb, A., Burns, S.J., Stern, C., Ariztegui, D., Gilli, A., Anselmetti, F.S., Stine, S., Maidana, N., 2003. Holocene palaeoclimates of southern Patagonia: limnological and environmental history of Lago Cardiel, Argentina. The Holocene 13, 581–591. doi:10.1191/0959683603hl648rp

Markgraf, V., Whitlock, C., Haberle, S., 2007. Vegetation and fire history during the last 18,000 cal yr B.P. in Southern Patagonia: Mallín Pollux, Coyhaique, Province Aisén (45°41′30″ S, 71°50′30″ W, 640 m elevation). Palaeogeog., Palaeoclimatol., Palaeoecol. 254, 492–507. doi:10.1016/j.palaeo.2007.07.008

Martin-Del Pozzo, A.L., Aceves, F., Espinasa, R., Aguayo, A. Inguaggiato, S., Morales, P., Cienfuegos, E., 2002. Influence of volcanic activity on spring water chemistry at Popocatepetl Volcano, Mexico. Chem. Geol. 190, 207–229. doi:10.1016/S0009-2541(02)00117-1

Marzocchi, W., Bebbington, M.S., 2012. Probabilistic eruption forecasting at short and long time scales. Bull. Volcanol. 74, 1777–1805. doi:10.1007/s00445-012-0633-x

Mason, B.G., Pyle, D.M., Dade, W.B., Jupp, T., 2004. Seasonality of volcanic eruptions. J. Geophys. Res. 109, B04206. doi:10.1029/2002JB002293

Mastin, L.G., 1994. Explosive tephra emissions at Mount St. Helens, 1989–1991: The violent escape of magmatic gas following storms? Geol. Soc. Am. Bull. 106, 175–185. doi:10.1130/0016-7606(1994)106<0175:ETEAMS>2.3.CO;2

Matthews, K.J., Muller, R.D., Wessel, P., Whittaker, J.M., 2011. The tectonic fabric of the ocean basins. J. Geophys. Res. 116, B12109. doi:10.1029/2011JB008413

Matthews, N.E., Smith, V.C., Costa, A., Durant, A.J., Pyle, D.M., Pearce, N.J.G., 2012. Ultra-distal tephra deposits from super-eruptions: Examples from Toba, Indonesia and Taupo Volcanic Zone, New Zealand. Quat. Int. 258, 54–79. doi:10.1016/j.quaint.2011.07.010

McGarvie, D.W., Stevenson, J.A., Burgess, R., Tuffen, H., Tindle, A.G., 2007. Volcano-ice interactions at Prestahnúkur, Iceland: rhyolite eruption during the last interglacial–glacial transition. Ann. Glaciol. 45, 38–47. doi:10.3189/172756407782282453

McNutt, S.R., 1996. Seismic monitoring and eruption forecasting of volcanoes: A review of the state of the art and case histories. In: Scarpa, R., Tilling, R. (Eds.), Monitoring and mitigation of volcano hazards. Springer, pp. 99–147.

McNutt, S.R., Beavan, R.J., 1987. Eruptions of Pavlof Volcano and their possible modulation by ocean load and tectonic stresses. J. Geophys. Res. 92, 11509–11523. doi:10.1029/JB092iB11p11509

Mee, K., Tuffen, H., Gilbert, J.S., 2006. Snow-contact volcanic facies and their use in determining past eruptive environments at Nevados de Chillán volcano, Chile. Bull. Volcanol. 68, 363–376. doi:10.1007/s00445-005-0017-6

Mee, K., Gilbert, J.S., McGarvie, D.W., Naranjo, J.A., Pringle, M.S., 2009. Palaeoenvironment reconstruction, volcanic evolution and geochronology of the Cerro Blanco subcomplex, Nevados de Chillán volcanic complex, central Chile. Bull. Volcanol. 71, 933–952. doi:10.1007/s00445-009-0277-7

de' Michieli Vitturi, M., Clarke, A.B., Neri, A., Voight, B., 2013. Extrusion cycles during dome-building eruptions. Earth Plan. Sci. Lett. 371–372, 37–48. doi:10.1016/j.epsl.2013.03.037

Miller, A.D., Stewart, R.C., White, R.A., Luckett, R., Baptie, B.J., Aspinall, W.P., Latchman J.L., Lynch, L.L., Voight, B., 1998. Seismicity associated with dome growth and collapse at the Soufrière Hills Volcano, Montserrat. Geophys. Res. Lett. 25, 3401–3404. doi:10.1029/98GL01778

Miller, V., Voight, B., Ammon, C.J., Shalev, E., Thompson, G., 2010. Seismic expression of magma-induced crustal strains and localized fluid pressures during initial eruptive stages, Soufrière Hills Volcano, Montserrat. Geophys. Res. Lett. 37, L00E21. doi:10.1029/2010GL043997

Miranda, C.G., Moreno, P.I., Vilanova, I., Villa-Martínez, R.P., 2013. Glacial fluctuations in the Coyhaique-Balmaceda sector of central Patagonia (45°S–46°S) during the last glacial termination. Boll. Geofis. 54 (Suppl. 2), 268–271.

Morgan, G.B., London, D., 2005. Effect of current density on the electron microprobe analysis of alkali aluminosilicate glasses. Am. Mineralogist 90, 1131–1138. doi:10.2138/am.2005.1769

Mueller, S.B., Varley, N.R., Kueppers, U., Lesage, P., Reyes Davila, G.A., Dingwell, D.B., 2013. Quantification of magma ascent rate through rockfall monitoring at the growing/collapsing lava dome of Volcán de Colima, Mexico. Solid Earth 4, 201–213. doi:10.5194/se-4-201-2013

Mulargia, F., Gasperini, P., Tinti, S., 1987. Identifying different regimes in eruptive activity: an application to Etna volcano. J. Volcanol. Geotherm. Res. 34, 89–106. doi:10.1016/0377-0273(87)90095-3

Murphy, M.D., 1996. Magmatic evolution at Volcán Sollipulli, southern Andes of Chile. PhD thesis, University of Bristol, United Kingdom.

Naranjo, J.A., Moreno, H., 1991. Actividad explosive postglacial en el Volcan Llaima, Andes del Sur (38°45'S). Rev. Geol. Chile 18, 69–80. doi:10.5027/andgeoV18n1-a06

Naranjo, J.A., Stern, C.R., 1998. Holocene explosive activity of Hudson Volcano, southern Andes. Bull. Volcanol. 59, 291–306. doi:10.1007/s004450050193

Naranjo, J.A., Stern, C.R., 2004. Holocene tephrochronology of the southernmost part (42°30'-45°S) of the Andean Southern Volcanic Zone. Revista Geol. de Chile 31, 225–240. doi:10.5027/andgeoV31n2-a03

Naranjo, J.A., Moreno, H., Emparan, C., Murphy, M.D., 1993a. Volcanismo explosivo reciente en la caldera del volcán Sollipulli, Andes del Sur (39°S). Rev. Geol. Chile 20, 167–191. doi:10.5027/andgeoV20n2-a03

Naranjo, J.A., Moreno, H., Banks, N.G., 1993b. La erupción del Volcán Hudson en 1991 (46°S), Región XI, Aisén, Chile. Serv. Nac. Geol. Min. Bol. 44, pp. 1–50.

Narcisi, B., Petit, J.R., Delmonte, B., Basile-Doelsch, I., Maggi, V., 2005. Characteristics and sources of tephra layers in the EPICA-Dome C ice record (East Antarctica): Implications for past atmospheric circulation and ice core stratigraphic correlations. Earth Planet. Sci. Lett. 239, 253–265. doi:10.1016/j.epsl.2005.09.005

Narcisi, B., Petit, J.R., Delmonte, B., Scarchilli, C., Stenni, B., 2012. A 16,000-yr tephra framework for the Antarctic ice sheet: a contribution from the new Talos Dome core. Quat. Sci. Rev. 49, 52–63. doi:10.1016/j.quascirev.2012.06.011

Nason, G., 2006. Stationary and non-stationary time series. In: Mader, H., Coles, S., Connor, C., Connor, L. (Eds.), Statistics in Volcanology. IAVCEI Spec. Pub. 1, Geological Society, London, pp. 129–142.

Neuberg, 2000. Characteristics and causes of shallow seismicity in andesite volcanoes. Phil. Trans. R. Soc. Lond. A, 358, 1533–1546. doi:10.1098/rsta.2000.0602

Newhall, C.G., 1979. Temporal variation in the lavas of Mayon volcano, Philippines. J. Volcanol. Geotherm. Res. 6, 61–83. doi:10.1016/0377-0273(79)90047-7

Newhall, C.G., Self, S., 1982. The Volcanic Explosivity Index (VEI) – an estimate of explosive magnitude for historical volcanism. J. Geophys. Res. 87, 1231–1238. doi:10.1029/JC087iC02p01231

Nicholson, E.J., Mather, T.A., Pyle, D.M., Odbert, H.M., Christopher, T., 2013. Cyclical patterns in volcanic degassing revealed by SO2 flux timeseries analysis: an application to Soufrière Hills Volcano, Montserrat. Earth Plan. Sci. Lett. 375, 209–221. doi:10.1016/j.epsl.2013.05.032

Odbert, H.M., Wadge, G., 2009. Time series analysis of lava flux. J. Volc. Geotherm. Res. 188, 305–314. doi:10.1016/j.jvolgeores.2009.09.005

Odbert, H.M., Stewart, R.C., Wadge, G., 2014. Cyclic phenomena at the Soufrière Hills Volcano, Montserrat. In: Wadge, G., Robertson, R.E.A, Voight, B. (Eds.), The Eruption of Soufrière Hills Volcano, Montserrat from 2000 to 2010. Geological Society Memoirs 39, Geological Society, London, pp. 41–60. doi:10.1144/M39.2

Ogburn, S.E., Loughlin, S.C., Calder, E.S., 2015. The association of lava dome growth with major explosive activity (VEI ≥4): DomeHaz, a global dataset. Bull. Volcanol. 77, 40. doi:10.1007/s00445-015-0919-x

Orihashi, Y., Naranjo, J.A., Motoki, A., Sumino, H., Hirata, D., Anma, R., Nagao, K., 2004. Quaternary volcanic activity of Hudson and Lautaro volcanoes, Chilean Patagonia: New constraints from K-Ar ages. Revista Geol. de Chile 31, 207–224. doi:10.5027/andgeoV31n2-a02

Parada, M.A., López-Escobar, L., Oliveros, V., Fuentes, F., Morata, D., Calderón, M., Aguirre, L., Féraud, G., Espinoza, F., Moreno, H., Figueroa, O., Muñoz Bravo, J., Troncoso Vásquez, R., Stern, C.R., 2007. Andean magmatism. In: Moreno, T., Gibbons, W. (Eds.), Geology of Chile, The Geological Society, London, pp. 115–146.

Pardo, L., 2006. Statistical inference based on divergence measures. Chapman & Hall/CRC, London.

Peng, C.-K., Buldyrev, S., Havlin, S., Simons, M., Stanley, H., Goldberger, A., 1994. Mosaic organization of DNA nucleotides. Phys. Rev. E 49, 1685–1689. doi:10.1103/PhysRevE.49.1685

Peng, C.-K., Havlin, S., Stanley, H., Goldberger, A., 1995. Quantification of scaling exponents and crossover phenomena in nonstationary heartbeat time series. Chaos 5, 82–87. doi:10.1063/1.166141

Perfit, M.R., Davidson, J.P., 2000. Plate tectonics and volcanism. In: Sigurdsson, H., Houghton, B.F., McNutt, S.R., Rymer, H., Stix, J. (Eds.), The Encyclopedia of Volcanoes (first edition). Academic Press, London, pp. 89–113.

Piegari, E., Di Maio, R., Scandone, R., Milano, L., 2011. A cellular automaton model for magma ascent: Degassing and styles of volcanic eruptions. J. Volcanol. Geotherm. Res. 202, 22–28. doi:10.1016/j.jvolgeores.2011.01.007

Pollock, M., Edwards, B., Hauksdóttir, S., Alcorn, R., Bowman, L., 2014. Geochemical and Lithostratigraphic Constraints on the Formation of Pillow-dominated Tindars from Undirhlíðar Quarry, Reykjanes Peninsula, Southwest Iceland. Lithos 200–201, 317–333. doi:10.1016/j.lithos.2014.04.023

Porębski, S.J., Gradziński, R., 1990. Lava-fed Gilbert-type delta in the Polonez Cove Formation (Lower Oligocene), King George Island, West Antarctica. In: Colella, A., Prior, D.B. (Eds.), Coarse-Grained Deltas. Spec. Pub. Int. Ass. Sediment. 10, 335–351. doi:10.1002/9781444303858.ch19

Pouchou, L.J., Pichoir, F., 1984. New model quantitative x-ray microanalysis, 1. Application to the analysis of homogeneous samples. Rech. Aerosp. 3, 13–38.

Prieto, A., Stern, C.R., Estévez, J.E., 2013. The peopling of the Fuego-Patagonian fjords by littoral hunter-gatherers after the mid-Holocene H1 eruption of Hudson Volcano. Quat. Int. 317, 3–13. doi:10.1016/j.quaint.2013.06.024

Pyle, D.M., 2015. Sizes of volcanic eruptions. In: Sigurdsson, H., Houghton, B.F., McNutt, S.R., Rymer, H., Stix, J. (Eds.), The Encyclopedia of Volcanoes (second edition). Academic Press, London, pp. 257–264. doi:10.1016/B978-0-12-385938-9.00013-4

Rabassa, J., 2008. Late Cenozoic glaciations in Patagonia and Tierra del Fuego. In: Rabassa, J., (Ed.), The Late Cenozoic of Patagonia and Tierra del Fuego. Developments in Quaternary Science 11. Elsevier, pp. 151–204. doi:10.1016/S1571-0866(07)10008-7

Ramsey, M.H., Potts, P.J., Webb, P.C., Watkins, P., Watson, J.S., Coles, B.J., 1995. An objective assessment of analytical method precision: comparison of ICP-AES and XRF for the analysis of silicate rocks. Chem. Geol. 124, 1–19. doi:10.1016/0009-2541(95)00020-M

Rawson, H., Naranjo, J.A., Smith, V.C., Fontijn, K., Pyle, D.M., Mather, T.A., Moreno, H., 2015. The frequency and magnitude of post-glacial explosive eruptions at Volcán Mocho-Choshuenco, southern Chile. J. Volcanol. Geotherm. Res. 299, 103–129. doi:10.1016/j.jvolgeores.2015.04.003

Rawson, H., Pyle, D.M., Mather, T.A., Smith, V.C., Fontijn, K., Lachowycz, S.M., Naranjo, J.A., 2016. The magmatic and eruptive response of arc volcanoes to deglaciation: temporal variability driven by changing crustal stresses. Geology, in press. doi:10.1130/G37504.1

Reyes-Dávila, G.A., De la Cruz-Reyna, S., 2002. Experience in the short-term eruption forecasting at Volcán de Colima, México, and public response to forecasts. J. Volcanol. Geotherm. Res. 117, 121–127. doi:10.1016/S0377-0273(02)00240-8

Riel, B., Milillo, P., Simons, M., Lundgren, P., Kanamori, H., Samsonov, S., 2015. The collapse of Bárðarbunga caldera, Iceland. Geophys. J. Int. 202, 446–453. doi:10.1093/gji/ggv157

Rittman, A., 1958. Il meccanismo di formazione delle lave a pillows e dei cosidelti tufi palagonitici. Att. Acad. Gioenia 4, 310–317.

Rivera, A., Bown, F., 2013. Recent glacier variations on active ice capped volcanoes in the Southern Volcanic Zone (37–46°S), Chilean Andes. J. South Am. Earth Sci. 45, 345–356. doi:10.1016/j.jsames.2013.02.004

Robertson, R.E.A., Aspinall, W.P., Herd, R.A., Norton, G.E., Sparks, R.S.J., Young, S.R., 2000. The 1995–1998 eruption of the Soufriére Hills volcano, Montserrat, WI. Phil. Trans. Roy. Soc. Lond. A 358, 1619–1637. doi:10.1098/rsta.2000.0607

Russell, J.K., Edwards, B.R., Porritt, L., Ryane, C., 2014. Tuyas: a descriptive genetic classification. Quat. Sci. Rev. 87, 70–81. doi:10.1016/j.quascirev.2014.01.001

Salmi, M., 1941. Die postglazialen Eruptionsschichten Patagoniens und Feuerlands. Annales Academiae Scientiarum Fennicae A3 2, Suomalainen Tiedeakatemia, Helsinki.

Saparin, P., Witt, A., Kurths, J., Anishchenko, V., 1994. The renormalized entropy–an appropriate complexity measure? Chaos, Solitons and Fractals 4, 1907–1916. doi:10.1016/0960-0779(94)90006-X

Scasso, R.A., Corbella, H., Tiberi, P., 1994. Sedimentological analysis of the tephra from the 12–15 August 1991 eruption of Hudson volcano. Bull. Volcanol. 56, 121–132. doi:10.1007/BF00304107

Schaefer, J.M., Putnam, A.E., Denton, G.H., Kaplan, M.R., Birkel, S., Doughty, A.M., Kelley, S., Barrell, D.J.A., Finkel, R.C., Winckler, G., Anderson, R.F., Ninneman, U.S., Barker, S., Schwartz, R., Andersen, B.J., Schluechter, C., 2015. The Southern Glacial Maximum 65,000 years ago and its unfinished termination. Quatern. Sci. Rev. 114, 52–60. doi:10.1016/j.quascirev.2015.02.009

Schmidt, M.E., Grunder, A.L., 2009. The evolution of North Sister: A volcano shaped by extension and ice in the central Oregon Cascade Arc. Geol. Soc. Am. Bull. 121, 643–662. doi:10.1016/10.1130/B26442.1

Schopka, H.H., Gudmundsson, M.T., Tuffen, H., 2006. The formation of Helgafell, southwest Iceland, a monogenetic subglacial hyaloclastite ridge: Sedimentology, hydrology and volcano–ice interaction. J. Volcanol. Geotherm. Res. 152, 359–377. doi:10.1016/j.jvolgeores.2005.11.010

Shannon, C., Weaver, W., 1949. The mathematical theory of communication. University of Illinois Press, Urbana.

Shaw, H.R., Chouet, B., 1991. Fractal hierarchies of magma transport in Hawaii and critical self-organization of tremor. J. Geophys. Res. 96, 10191–10207. doi:10.1029/91JB00771

Siani, G., Paterne, M., Michel, E., Sulpizio, R., Sbrana, A., Arnold, M., Haddad, G., 2001. Mediterranean Sea surface radiocarbon reservoir age changes since the Last Glacial Maximum. Science 294, 1917–1920. doi:10.1126/science.1063649

Siani, G., Colin, C., Michel, E., Carel, M., Richter, T., Kissel, C., Dewilde, F., 2010. Late Glacial to Holocene terrigenous sediment record in the Northern Patagonian margin: Paleoclimate implications. Palaeogeogr., Palaeoclimatol., Palaeoecol. 297, 26–36. doi:10.1016/j.palaeo.2010.07.011

Siani, G., Michel, E., De Pol-Holz, R., DeVries, T., Lamy, F., Carel, M., Isguder, G., Dewilde, F., Lourantou, A., 2013. Carbon isotope records reveal precise timing of enhanced Southern Ocean upwelling during the last deglaciation. Nat. Commun. 4, 2758. doi:10.1038/ncomms3758

Siebert, L., Simkin, T., Kimberly, P., 2010. Volcanoes of the World - Third Edition. University of California Press, Berkeley.

Sigmundsson, F., Hooper, A., Hreinsdóttir, S., Vogfjörd, K.S., Ófeigsson, B.G., Heimisson, E.R., Dumont, S., Parks, M., Spaans, K., Gudmundsson, G.B., Drouin, V., Árnadóttir, T., Jónsdóttir, K., Gudmundsson, M.T., Högnadóttir, T., Fridriksdóttir, H.M., Hensch, M., Einarsson, P., Magnússon, E., Samsonov, S., Brandsdóttir, B., White, R.S., Ágústsdóttir, T., Greenfield, T., Green, R.G., Hjartardóttir, A.R., Pedersen, R., Bennett, R.A., Geirsson, H., La Femina, P.C., Björnsson, H., Pálsson, F., Sturkell, E., Bean, C.J., Möllhoff, M., Braiden, A.K., Eibl, E.P.S., 2015. Segmented lateral dyke growth in a rifting event at Bárðarbunga volcanic system, Iceland. Nature, 517, 191–195. doi:10.1038/nature14111

Singer, B.S., Jicha, B.R., Harper, M.A., Naranjo, J.A., Lara, L.E., Moreno-Roa, H., 2008. Eruptive history, geochronology, and magmatic evolution of the Puyehue-Cordón Caulle volcanic complex, Chile. Geol. Soc. Am. Bull. 120, 599–618. doi:10.1130/B26276.1

Siswowidjoyo, S., Suryo, I., Yokohama, I., 1995. Magma eruption rates of Merapi volcano, Central Java, Indonesia during one century (1890–1992). Bull. Volcanol. 57, 111–116. doi:10.1007/BF00301401

Skilling, I., 2002. Basaltic pahoehoe lava-fed deltas: large-scale characteristics, clast generation, emplacement processes and environmental discrimination. In: Smellie, J.L., Chapman, M.G. (Eds.), Volcano-ice interactions on Earth and Mars. Geol. Soc. Spec. Publ. 202, Geological Society, London, pp. 91–113. doi:10.1144/GSL.SP.2002.202.01.06

Skilling, I., 2009. Subglacial to emergent basaltic volcanism at Hlöðufell, south-west Iceland: A history of ice-confinement. J. Volcanol. Geotherm. Res. 185, 276–289. doi:10.1016/j.jvolgeores.2009.05.023

Smellie, J.L., 2006. The relative importance of supraglacial versus subglacial meltwater escape in basaltic subglacial tuya eruptions: An important unresolved conundrum. Earth-Sci. Rev. 74, 241–268. doi:10.1016/j.earscirev.2005.09.004

Smellie, J.L., 2008. Basaltic subglacial sheet-like sequences: Evidence for two types with different implications for the inferred thickness of associated ice. Earth-Sci. Rev. 88, 60–88. doi:10.1016/j.earscirev.2008.01.004

Smellie, J.L., 2009. Terrestrial sub-ice volcanism: Landform morphology, sequence characteristics, environmental influences, and implications for candidate Mars examples. In: Chapman, M.G., Keszthelyi, L.P. (Eds.), Preservation of random megascale events on Mars and Earth: Influence on geologic history. Geological Society of America Special Paper 453, pp. 55–76. doi:10.1130/2009.453(05)

Smellie, J.L., 2013. Quaternary Vulcanism: Subglacial Landforms. In: Elias, S.A. (Ed.), Encyclopedia of Quaternary Science, second edition, pp. 780–802. doi:10.1016/B978-0-444-53643-3.00074-1

Smellie, J.L., Skilling, I.P., 1994. Products of subglacial volcanic eruptions under different ice thicknesses: two examples from Antarctica. Sediment. Geol. 91, 115–129. doi:10.1016/0037-0738(94)90125-2

Smellie, J.L., Chapman, M.G., 2002. Volcano-ice interaction on Earth and Mars. Geological Society, London, Special Publication 202.

Smellie, J.L., Hole, M.J., Nell, P.A.R., 1993. Late Miocene valley-confined subglacial volcanism in northern Alexander Island, Antarctic Peninsula. Bull. Volcanol. 55, 273–288. doi:10.1007/BF00624355

Smellie, J.L., Rocchi, S., Gemelli, M., Di Vincenzo, G., Armienti, P., 2011. A thin predominantly cold-based Late Miocene East Antarctic ice sheet inferred from glaciovolcanic sequences in northern Victoria Land, Antarctica. Palaeogeogr., Palaeoclimatol., Palaeoecol. 307, 129–149. doi:10.1016/j.palaeo.2011.05.008

Smellie, J.L., Wilch, T.I., Rocchi, S., 2013. 'A'ā lava-fed deltas: A new reference tool in paleoenvironmental studies. Geology 41, 403–406. doi:10.1130/G33631.1

Smellie, J.L., Rocchi, S., Wilch, T.I., Gemelli, M., Di Vincenzo, G., McIntosh, W., Dunbar, N., Panter, K., Fargo, A., 2014. Glaciovolcanic evidence for a polythermal Neogene East Antarctic Ice Sheet. Geology 42, 39–41. doi:10.1130/G34787.1

Smith, V.C., Isaia, R., Pearce, N.J.G., 2011a. Tephrostratigraphy and glass compositions of post-15 kyr Campi Flegrei eruptions: implications for eruption history and chronostratigraphic markers. Quat. Sci. Rev. 30, 3638–3660. doi:10.1016/j.quascirev.2011.07.012

Smith, V.C., Pearce, N.J.G., Matthews, N.E., Westgate, J.A., Petraglia, M.D., Haslam, M., Lane, C.S., Korisettar, R., Pal, J.N., 2011b. Geochemical fingerprinting of the widespread Toba tephra using biotite compositions. Quat. Int. 246, 97–104. doi:10.1016/j.quaint.2011.05.012

Sparks, R.S.J., 2003. Forecasting volcanic eruptions. Earth Plan. Sci. Lett., 210, 1–15. doi:10.1016/S0012-821X(03)00124-9

Spörli, K.B., Rowland, J.V., 2006. 'Column on column' structures as indicators of lava/ice interaction, Ruapehu andesite volcano, New Zealand. J. Volcanol. Geotherm. Res. 157, 294–310. doi:10.1016/j.jvolgeores.2006.04.004

Stern, C.R., 1991. Mid-Holocene tephra on Tierra del Fuego (54°S) derived from the Hudson volcano (46°S): evidence for a large explosive eruption. Revista Geol. de Chile 18, 139–146. doi:10.5027/andgeoV18n2-a04

Stern, C.R., 2004. Active Andean volcanism: its geologic and tectonic setting. Rev. Geol. Chile 31, 161–206. doi:10.4067/S0716-02082004000200001

Stern, C.R., 2008. Holocene tephrochronology record of large explosive eruptions in the southernmost Patagonian Andes. Bull. Volcanol. 70, 435–454. doi:10.1007/s00445-007-0148-z

Stern, C.R., Moreno, H., Lopez-Escobar, L., Clavero, J., Lara, L., Naranjo, J.A., Parada, M.A., Skewes, M.A., 2007. Chilean volcanoes. In: Moreno, T., Gibbons, W. (Eds.), Geology of Chile, The Geological Society, London, pp. 147–178.

Stern, C.R., Moreno, P.I., Henríquez, W.I., Villa-Martínez, R., Sagredo, E., Aravena, J.C., 2013. Tephrochronology in the area around Cochrane, southern Chile. Boll. Geofis. 54 (Suppl. 2), 199–202.

Stern, C.R., Eugenia de Porras, M., Maldonado, A., 2015. Tephrochronology of the upper Río Cisnes valley (44°S), southern Chile. Andean Geol. 42, 173–189. doi:10.5027/andgeoV42n2-a02

Stevenson, J.A., Smellie, J.L., McGarvie, D.W., Gilbert, J.S., Cameron, B.I., 2009. Subglacial intermediate volcanism at Kerlingarfjöll, Iceland: Magma-water interactions beneath thick ice. J. Volcanol. Geotherm. Res. 185, 337–351. doi:10.1016/j.jvolgeores.2008.12.016

Stewart, R.C., Bass, V., Christopher, T., Dondin, F., Finizola, A., Fournier, N., Joseph, E., Komorowski, J.-C., Legendre, Y., Robertson, R., Syers, R., Williams, P., 2009. Report for the Scientific Advisory Committee on Montserrat volcanic activity: report on activity between 01 October 2008 and 01 March 2009. Montserrat Volcano Observatory, Open File Report 09/01.

Surono, Jousset, P., Pallister, J., Boichu, M., Buongiorno, M.F., Budisantoso, A., Costa, F., Andreastuti, S., Prata, F., Schneider, D., Clarisse, L., Humaida, H., Sumarti, S., Bignami, C., Griswold, J., Carn, S., Oppenheimer, C., Lavigne, F., 2012. The 2010 explosive eruption of Java's Merapi volcano: a '100 year' event. J. Volcanol. Geotherm. Res. 241–242, 121–135. doi:10.1016/j.jvolgeores.2012.06.018

Taran, Y., Gavilanes, J.C., Cortés, A., Armienta, M.A., 2000. Chemical precursors to the 1998-1999 eruption of Colima volcano, Mexico. Revista Mexicana de Ciencias Geológicas, 17, 111–124.

Telesca, L., Lovallo, M., Mohamed, A.E.-E.A., ElGabry, M., El-Hady, S., Elenean, K.M.A., ElBary, R.E.F., 2012. Informational analysis of seismic sequences by applying the Fisher Information Measure and the Shannon entropy: An application to the 2004–2010 seismicity of Aswan area (Egypt). Physica A 391, 2889–2897. doi:10.1016/j.physa.2011.12.047

Thomas, M.E., Neuberg, J., 2012. What makes a volcano tick – A first explanation of deep multiple seismic sources in ascending magma. Geology 40, 351–354. doi:10.1130/G32868.1

Tobar, A., 1973. Report on the eruption of Mt Hudson. Bull. Volc. Erupt. 11, 43.

Tuffen, H., 2007. Models of ice melting and edifice growth at the onset of subglacial basaltic eruptions. J. Geophys. Res. 112, B03203. doi:10.1029/2006JB004523

Tuffen, H., 2010. How will melting of ice affect volcanic hazards in the twenty-first century? Phil. Trans. R. Soc. Lond. A 368, 2535–2558. doi:10.1098/rsta.2010.0063

Tuffen, H., Owen, J., Denton, J., 2010. Magma degassing during subglacial eruptions and its use to reconstruct palaeo-ice thicknesses. Earth-Sci Rev. 99, 1–18. doi:10.1016/j.earscirev.2010.01.001

Tuffen, H., James, M.R., Castro, J.M., Schipper, C.I., 2013. Exceptional mobility of an advancing rhyolitic obsidian flow at Cordón Caulle volcano in Chile. Nat. Commun. 4, 2709. doi:10.1038/ncomms3709

Turner, S.J., Langmuir, C.H., 2015. The global chemical systematics of arc front stratovolcanoes: Evaluating the role of crustal processes. Earth Plan. Sci. Lett. 422, 182–193. doi:10.1016/j.epsl.2015.03.056

USGS and Japan ASTER program, 2012. ASTER scene AST_14DMO_003_02182005144538, 3, USGS, Sioux Falls, 18 February 2005.

Vargas-Bracamontes, D.M., Nava, F.A., Reyes-Dávila, G.A., 2009. Time-scale wavelet patterns related to the 1998–1999 eruptions of the Colima volcano, and their possible implications for eruption forecasting. J. Volcanol. Geotherm. Res. 184, 271–284. doi:10.1016/j.jvolgeores.2009.01.025

Van Daele, M., Moernaut, J., Silversmit, G., Schmidt, S., Fontijn, K., Heirman, K., Vandoorne, W., De Clercq, M., Van Acker, J., Wolff, C., Pino, M., Urrutia, R., Roberts, S.J., Vincze, L., De Batist, M., 2014. The 600 yr eruptive history of Villarrica Volcano (Chile) revealed by annually laminated lake sediments. Geol. Soc. Am. Bull. 126, 481–498. doi:10.1130/B30798.1

Vanneste, H., De Vleeschouwer, F., Martínez-Cortizas, A., von Scheffer, C., Piotrowska, N., Coronato, A., Le Roux, G., 2015. Late-glacial elevated dust deposition linked to westerly wind shifts in southern South America. Sci. Rep. 5, 11670. doi:10.1038/srep11670

Varley, N., Johnson, J., Ruiz, M., Reyes, G., Martin, K., 2006. Applying statistical analysis to understanding the dynamics of volcanic explosions. In: Mader, H., Coles, S., Connor, C., Connor, L. (Eds.), Statistics in Volcanology. IAVCEI Spec. Pub. 1, Geological Society, London, pp. 57–76.

Varley, N.R., Arámbula-Mendoza, R., Reyes-Dávila, G., Stevenson, J., Harwood, R., 2010a. Long-period seismicity during magma movement at Volcán de Colima. Bull. Volcanol. 72, 1093–1107. doi:10.1007/s00445-010-0390-7

Varley, N.R., Arámbula-Mendoza, R., Reyes-Dávila, G., Sanderson, S., Stevenson, J., 2010b. Generation of Vulcanian activity and long-period seismicity at Volcán de Colima, Mexico. J. Volcanol. Geotherm. Res. 198, 45–56. doi:10.1016/j.jvolgeores.2010.08.009

Voight, B., Sparks, R.S.J., Miller, A.D., Stewart, R.C., Hoblitt, R.P., Clarke, A., Ewart, J., Aspinall, W.P., Baptie, B., Calder, E.S., Cole, P.D., Druitt, T.H., Hartford, C., Herd, R.A., Jackson, P., Lejeune, A.M., Lockhart, A.B., Loughlin, S.C., Luckett, R., Lynch, L., Norton, G.E., Robertson, R., Watson, I.M., Watts, R., Young, S.R., 1999. Magma flow instability and cyclic activity at Soufrière Hills Volcano, Montserrat, British West Indies. Science 283, 1138–1142. doi:10.1126/science.283.5405.1138

Voight, B., Constantine, E.K., Siswowidjoyo, S., Torley, R., 2000. Historical eruptions of Merapi Volcano, Central Java, Indonesia, 1768–1998. J. Volcanol. Geotherm. Res. 100, 69–138. doi:10.1016/S0377-0273(00)00134-7

Wadge, G., Herd, R., Ryan, G., Calder, E.S., Komorowski, J.-C., 2010. Lava production at Soufrière Hills Volcano, Montserrat: 1995–2009. Geophys. Res. Lett. 37, L00E03. doi:10.1029/2009GL041466

Wadge, G., Voight, B., Sparks, R.S.J., Cole, P.D., Loughlin, S.C., 2014. An overview of the eruption of the Soufrière Hills Volcano, Montserrat, 2000-2010. In: Wadge, G., Robertson, R.E.A, Voight, B. (Eds.), The Eruption of Soufrière Hills Volcano, Montserrat from 2000 to 2010. Geological Society Memoirs 39, Geological Society, London, pp. 1–40. doi:10.1144/M39.1

Waldmann, N., Ariztegui, D., Anselmetti, F.S., Austin Jr, J.A., Moy, C.M., Stern, C., Recasens, C., Dunbar, R.B., 2010. Holocene climatic fluctuations and positioning of the Southern Hemisphere westerlies in Tierra del Fuego (54°S), Patagonia. J. Quat. Sci. 25, 1063–1075. doi:10.1002/jqs.1263

Wastegård, S., Veres, D., Kliem, P., Hahn, A., Ohlendorf, C., Zolitschka, B., The PASADO Science Team, 2013. Towards a late Quaternary tephrochronological framework for the southernmost part of South America – the Laguna Potrok Aike tephra record. Quat. Sci. Rev. 71, 81–90. doi:10.1016/j.quascirev.2012.10.019

Watt, S.F.L., Mather, T.A., Pyle, D.M., 2007. Vulcanian explosion cycles: Patterns and predictability. Geology 35, 839–842. doi:10.1130/G23562A.1

Watt, S.F.L., Pyle, D.M., Mather, T.A., 2009. The influence of great earthquakes on volcanic eruption rate along the Chilean subduction zone. Earth Planet Sci. Lett. 277, 399–407. doi:10.1016/j.epsl.2008.11.005

Watt, S.F.L., Pyle, D.M., Naranjo, J.A., Rosqvist, G., Mella, M., Mather, T.A., Moreno, H., 2011. Holocene tephrochronology of the Hualaihue region (Andean southern volcanic zone, ~42° S), southern Chile. Quat. Int. 246, 324–343. doi:10.1016/j.quaint.2011.05.029

Watt, S.F.L., Pyle, D.M., Mather, T.A., 2013a. The volcanic response to glaciation: evidence from glaciated arcs and a reassessment of global eruption records. Earth-Sci. Rev. 122, 77–102. doi:10.1016/j.earscirev.2013.03.007

Watt, S.F.L., Pyle, D.M., Mather, T.A., 2013b. Evidence of mid- to late-Holocene explosive rhyolitic eruptions from Chaitén Volcano, Chile. Andean Geol. 40, 216–226. doi:10.5027/andgeoV40n2-a02

Watton, T.J., Jerram, D.A., Thordarson, T., Davies, R.J., 2013. Three-dimensional lithofacies variations in hyaloclastite deposits. J. Volcanol. Geotherm. Res. 250, 19–33. doi:10.1016/j.jvolgeores.2012.10.011

Webb, E., Varley, N.R., Pyle, D.M., Mather, T.A., 2014. Characterisation of short-lived Vulcanian explosions at Volcán de Colima, Mexico by analysis of thermal imagery. J. Volcanol. Geotherm. Res. 278–279, 132–145. doi:10.1016/j.jvolgeores.2014.03.013

Weller, D., Miranda, C.G., Moreno, P.I., Villa-Martínez, R., Stern, C.R., 2014. The large late-glacial Ho eruption of the Hudson volcano, southern Chile. Bull. Volcanol. 76, 831–848. doi:10.1007/s00445-014-0831-9

White, J.D.L., Houghton, B.F., 2006. Primary volcaniclastic rocks. Geology 34(8), 677–680. doi:10.1130/G22346.1

Wilson, S.A., 1997. Data compilation for USGS reference material BHVO-2, Hawaiian Basalt. U.S. Geological Survey Open-File Report.

Wilson, S.A., 1998. Data compilation and statistical analysis of intralaboratory results for AGV-2. U.S. Geological Survey Open-File Report.

Wilson, T.M., Cole, J.W., Stewart, C., Cronin, S.J., Johnston, D.M., 2011. Ash storms: impacts of wind-remobilised volcanic ash on rural communities and agriculture following the 1991 Hudson eruption, southern Patagonia, Chile. Bull. Volcanol. 73, 223–239. doi:10.1007/s00445-010-0396-1

Yu, Z., Loisel, J., Brosseau, D.P., Beilman, D.W., Hunt, S.J., 2010. Global peatland dynamics since the Last Glacial Maximum. Geophys. Res. Lett. 37, L13402. doi:10.1029/2010GL043584

Zobin, V.M., Varley, N.R., González, M., Orozco, J., Reyes, G.A., Navarro, C., Bretón, M., 2008. Monitoring the 2004 andesitic block-lava extrusion at Volcán de Colima, México from seismic activity and SO2 emission. J. Volcanol. Geotherm. Res. 177, 367–377. doi:10.1016/j.jvolgeores.2008.05.015

Zobin, V.M., 2012. Introduction to Volcanic Seismology (2nd edition). Elsevier, Amsterdam.

Supplementary material

Supplementary File 2.1 Outline of some of the various statistical techniques applied to volcanological time-series in previous work.

Analysis type	Statistical technique	Description of technique			Examples of recent applications of the technique to volcanic time-series	
		Article(s)	Summary	Advantages and/or limitations	Article(s)	Summary
Clustering, fractal, or persistence analysis	Allan and Fano factors (AF; FF)	Allan, 1966; Fano, 1947; Telesca et al., 2002a	AF: measure of the variability of successive counts in a dataset. FF: measure of the dispersion of a distribution/correlation over various timescales.	FF is sensitive to nonstationarity; AF is an appropriate alternative. Both are preferable to the coefficient of variation, which does not identify the timescales on which clustering occurs.	Telesca et al., 2002b	Examine historical eruption datasets from 35 volcanoes; find clustering (fractal behaviour) on at least some timescales at all but five of the volcanoes studied.
	Autocorrelation (and partial autocorrelation)	Chatfield, 2003	Cross-correlation of a signal with a lagged version of itself, highlighting clustering, periodicity, and/or short-timescale persistence.	Only appropriate for stationary data. Interpretation of the autocorrelation coefficients/correlograms can be ambiguous.	Privitera et al., 2003	Analyse Etna tremor associated with lava fountaining; identify periodicity to tremor, and forecast future fountaining events.
					Varley et al., 2006	Analyse inter-event times of explosions at Volcán de Colima and Tungurahua; find that the extent of clustering varies between event types and through time.
	Chaotic-deterministic analysis	Correig & Urquizu, 1996	Quantifies the chaoticity of a dynamical system by calculating the correlation dimension, Kolmogorov entropy (measure of the rate of loss of information about the system state), and Lyapunov exponent (measure of the sensitivity to initial conditions).	Appropriate for characterising data that is noisy and/or from potentially chaotic or non-linear processes or systems. Only appropriate for stationary data.	Correig et al., 1997	Analyse Deception Island seismicity inter-event times; find that this time-series is chaotic-deterministic, and that the underlying mechanism must be a non-linear system with at least three degrees of freedom.
	(Multifractal) detrended fluctuation analysis ((MF)DFA) and detrended moving average (DMA)	Alessio et al., 2002; Kantelhardt et al., 2002; Peng et al., 1994; 1995	Calculates a measure of the self-affinity or correlation dynamics (persistence; memory) to a dataset. The exponent is derived from the log ratio of the fluctuation of the detrended, integrated signal on a given length scale, against that length scale.	Suitable for non-stationary data; particularly appropriate for quantifying long-range correlations. Not fitting for small datasets.	Alvarez-Ramirez et al., 2009	Examine the daily exhalation rate at Popocatépetl; the extent of persistence to the data is found to vary with a clear periodicity (multiple cycle frequencies), with sharp changes prior to activity shifts.
					Del Pin et al., 2008	Distinguish noise from volcanic/tectonic events in seismicity recorded at Teide, by a threshold level of scaling strength. Achieve higher accuracy in event recognition than manual methods.
					Currenti et al., 2005a; 2005b	Analyse magnetic data recorded on Etna; find different correlation dynamics on different timescales, and a sharp increase in persistence coincident with an eruption.
	Fractal dimension	Feder, 1988; Smalley et al., 1987	Quantifies the degree of clustering or complexity of a dataset (a smaller fractal dimension reflects increasingly isolated clusters).	Sensitive to noise and dataset size; only appropriate for stationary, scale-invariant data.	Dubois & Cheminée, 1991	Quantify clustering in the inter-event times of historical activity at various basaltic volcanoes. At hotspot volcanoes, find strong clustering for short intervals and regular activity on longer timescales, but Etna is Poissonian on all timescales.
					Vinciguerra et al., 2001	Examine the time evolution of the fractal dimension of seismic event data from Etna; find variations in clustering relating to EQ swarms associated with flank eruptions.

	Frequency-magnitude relationship (*b*-value)	Gutenberg & Richter, 1944; Palacios et al., 2006	A coefficient related to the range of event magnitudes in an earthquake dataset.	Experimental data constrain physical interpretation of changes in *b*-value. Only suitable for analysis of high-quality seismic data; must be able to evaluate the minimum sensitivity of the network.	Palacios et al., 2006	Identify temporal variation in the *b*-value of the distribution of seismicity recorded at four Ecuadorean volcanoes.
					Ibáñez et al., 2012	Identify three phases to the seismic swarm associated with 2011-12 El Hierro eruption, each with differing *b*-values, reflecting different stages of magma ascent and storage.
	Hurst rescaled range analysis (HRAA)	Feder, 1988; Hurst, 1951	Calculates a measure of the self-affinity or correlation dynamics (persistence; memory) to a dataset. The exponent is derived from an empirical relationship relating the standard deviation to a rescaled accumulated departure of the time-series from the average.	Only appropriate for stationary data.	Correig et al., 1997	Analyse Deception Island seismicity inter-event times; find clustering in the data, implying memory to the system.
					Telesca & Lapenna, 2005	Analyse inter-event times of eruptions at 14 volcanoes; find persistent behaviour at seven of these, whilst uncorrelated dynamics are observed at the others.
	Variograms	Jaquet & Carniel, 2006; Matheron, 1962	Quantifies the degree of clustering/ similarity in a time-series on various timescales, and quantifies the continuity and regularity of the data. Based on modelling data using the Cox process.	Only assumes stationarity of the increments of the stochastic process analysed.	Carniel et al., 2008	Analyse seismic data from Teide, finding that natural and anthropogenic seismic noise sources can be distinguished by their persistence; identify changes in correlation strength coinciding with tectonic events.
					Jaquet et al., 2006	Analyse RSAM data from Soufrière Hills, Montserrat; identify persistence to a series of Vulcanian eruptions indicative of 'magma memory' on a timescale of 60-80 hrs, constraining magma ascent rate.
Information measure analysis	Fisher information measure (FIM)	Fisher, 1925; Telesca et al., 2012	Measurement of the order of a signal, derived from estimating the hidden parameters from (information content of) observed random variables.	Suitable for non-linear systems and nonstationary data.	Telesca et al., 2010	Analyse tremor data from Stromboli; temporal variation of the FIM indicates the data becomes more ordered at least 42 hrs before the start of one paroxysmal event.
	Shannon entropy	Shannon & Weaver, 1949; Telesca et al., 2012	Measure of the disorder in, or the uncertainty of, a random variable.	Suitable for non-linear systems and nonstationary data. Can be estimated to reduce computational complexity.	Chapter 3	Analyse various seismic data types from Volcán de Colima and Soufrière Hills Volcano, Montserrat; find changes in disorder associated with shifts in activity.
Pattern recognition	Artificial neural networks (ANNs; usually multilayer perceptron)	Rumelhart et al., 1986; Van der Baan & Jutten, 2000	Non-linear statistical data modelling tool; computational approach using an interconnected network of artificial neurons that can change in structure during 'training'.	Computationally complex and demanding; requires high-quality data, extensive training, and a detailed understanding of the patterns to be recognised. An individual model is only appropriate if the data are stationary.	Langer et al., 2003; 2006	Applied in an automated routine to classify seismic events at Soufrière Hills, Montserrat. Achieved 70% accuracy in classification; with reanalysis, achieve 80% accuracy, or higher for certain event types.
	Hidden Markov models (HMMs)	Baum & Petrie, 1966; Rabiner, 1989	Statistical models in which the system is assumed to be a Markov process (time-varying random phenomenon with specific conditions) with hidden (unobservable) states, which can be patterns that may be associated with the defined class of highest likelihood.		Alasonati et al., 2006; Bebbington, 2007	Applied in an automated routine to classify seismic events at various volcanoes; achieved accuracy of >90% for certain event types, but poor for some other types.
					Benítez et al., 2009	Explore applying HMMs in probabilistic analysis of volcanic data; suggest that incorporating HMMs is valuable.
	(Kohonen) self-organising maps (SOMs)	Köhler et al., 2009; Kohonen, 1982	Type of ANN capable of unsupervised learning, utilising a neighbourhood function to preserve the topological properties of the input space.	Computationally complex and demanding; requires high-quality data. Does not involve supervised learning.	Langer et al., 2009	Analyse tremor data from Etna without supervision; method identifies changes in tremor characteristics, highlighting transitions between volcanic regimes.

					Di Salvo et al., 2012	Analyse features extracted from multiple monitoring time-series from Etna; successfully cluster the data in spite of their differing temporal variability.
	Pattern recognition for forecasting	Jain et al., 2000; Marzocchi et al., 2003	Set of multivariate analysis techniques used to identify patterns within a dataset (the statistical methods used will depend upon the data and the aims of recognition), such as patterns in activity prior to new phases of volcanism.	The techniques employed can be selected to suit the data; training and/or a good understanding of the data or system may be necessary.	Sandri et al., 2004	Analyse 217 seismic swarms associated with various magnitudes of unrest or eruption; find patterns in the duration and repose time of swarms associated with eruption occurrence and magnitude.
					Novelo-Casanova & Valdés-González, 2008	Analyse seismic data from Popocatépetl; find that all the large eruptions can be predicted retrospectively from the pattern of precursory seismicity, but with some easily filterable false alarms.
Probabilistic analysis	Determining the best-fitting probabilistic distribution	Lee, 2003; Wickman, 1966	The goodness of fit of the data to a particular probabilistic distribution (with optimised shape parameters) is determined to find the distribution that best represents the dataset. Different distributions (e.g. Brownian passage-time, exponential, [generalised] gamma, linear, log-logistic, lognormal, Markov-modulated Poisson process, mixture of exponentials or Weibulls, Pareto, power law, trend renewal process, Weibull [renewal]) imply different physical processes.	Some of the distributions utilised are not appropriate for certain types of activity, and/or have specific drawbacks: for example, the Weibull distribution does not allow for periodic behaviour and is sensitive to single observations (Bebbington & Lai, 1996).	Bebbington, 2010	Model eruption onsets using a trend renewal process, and relate this to more conventional methods of clustering and probabilistic analysis.
					Bebbington, 2007 plus many others, as listed in Bebbington, 2012; Marzocchi & Bebbington, 2012	Examine inter-event times or event rates of various volcanoes; find that the best-fitting distribution varies between volcanoes, indicating differences in eruption dynamics. In a number of cases, the best-fitting shape parameters or distribution varies through time, coincident with changes in the system.
					Varley et al., 2006	Analyse the repose times of specific volcano-seismic event types at a few volcanoes; find that the best-fitting distribution can be different for each event type, and change after a large eruption.
	Extreme value theory	Coles, 2001; Leadbetter et al., 1983	Used to estimate the extreme levels of a process that may be expected in the future on the basis of past observations.	Results sensitive to threshold selection; estimates will not necessarily converge. Only appropriate for stationary data.	Coles & Sparks, 2006	Review use of such methods in modelling the occurrence of large eruptions. Results are inconclusive due to the issue of appropriate threshold selection, but not inconsistent with global eruption record.
					Furlan, 2010	Build upon Coles & Sparks (2006), using a step function/change-point model to deal with recording bias, and Bayesian inference to improve the forecasting.
	Time- and size-predictable statistical distribution modelling	Marzocchi & Zaccarelli, 2006; Shimazaki & Nakata, 1980	Determines if the data fits either a time-predictable (e.g. the repose time after the previous event is dependent upon the duration of the previous event) or size-predictable (e.g. eruption duration is dependent upon the repose time since the previous event) model.	Must assume that the data are stationary and result from a homogenous Poisson process.	Bebbington, 2007	Analyse Etna flank eruption duration data, allowing for hidden states. Identify a shift between time-predictability and Poissonian behaviour relating to change in conduit state (‘open’ vs ‘closed’).
					Marzocchi & Zaccarelli, 2006	Analyse eruption inter-event times from many volcanoes; find that ‘open’ & ‘closed’ systems generally fit time-predictable and Poissonian models respectively.

					Passarelli et al., 2010	Analyse eruption data from Kilauea and Etna; find that the volcanoes show time-predictable behaviour, and that a Bayesian model using this can make better forecasts.
Change point recognition	Structural change tests	Zeileis et al., 2002; 2010	Identification of the change points in a time-series using structural change algorithms (based on linear regression models or maximum likelihood).	Various options of testing for structural change, only some of which are appropriate for specific datasets (potential for parameter instability).	Fattori-Speranza & Carniel, 2008	Investigate tremor data from Stromboli; identify at least one structural change associated with each regional tectonic event in the period analysed.
	Two-sample distribution test, such as the Kolmogorov-Smirnov (K-S) statistic	Ebdon, 1985; Mulargia et al., 1987	Identification of change points by partitioning a dataset into two groups and applying a distribution similarity test, which is repeated to find the partitioning that gives the most dissimilar groups out of all possible groupings (e.g., indicated by the most significant K-S test statistic).	Must assume stationarity except where a change point is identified.	Burt et al., 1994	Identify two regime change points in eruption volume, duration, and inter-event time data from Nyamuragira; examine fit of data to simple models of magma supply.
					Mulargia et al., 1987	Analyse erupted volume and inter-event time data from historical eruptions of Etna; identify a number of change points in both datasets but these do not coincide, suggesting control by different factors.
Signal processing/ modelling	Autoregressive integrated moving average (ARIMA) models	Chatfield, 2003; Nason, 2006	Time-series models integrating autoregressive processes (in which the future is dependent upon the past signal) and moving average processes (which combines elements of randomness from the past signal).	Appropriate model(s) must be selected (and tested for reasonableness and predictive ability, if appropriate).	Ho, 2008	Develops an ARIMA method for modelling the recurrence rate of volcanism, using the eruption record of Avachinsky as a case study. Asserts that this technique is capable of modelling simple Poissonian through to cyclic activity.
	Cross-correlation	Chatfield, 2003; Neuberg, 2006	Measurement of the association between different components of time-series at different time lags. Various methods are routinely used with seismic and volcano-seismic data.	Typical methods are only appropriate for stationary data.	Cardaci et al., 1993	Cross-correlate Etna seismic and eruption data by correlogram analysis of all possible seismic and volcanic event pairs. Find significant correlations between flank eruptions and certain seismic event types, and between summit activity and tremor.
Signal de-composition	Independent component analysis	De Lauro et al., 2005; Hyvärinen et al., 2001	Method of separating mutually statistically independent components of a multivariate signal by minimising mutual information content and maximising non-Gaussianity.	Only appropriate for non-Gaussian data. Cannot determine the absolute amplitudes of the components that are identified.	Bottiglieri et al., 2007	Analyse ground deformation in Neapolitan region; identify five independent periodic signals and residual local signals, showing the ability to identify volcanic deformation.
					De Lauro et al., 2012	Analyse long-period seismic events at Volcán de Colima; extract oscillation modes and identify two polarisation types.
	Spectral/ spectrogram analysis (e.g. by Fourier or Hilbert transforms)	Duhamel & Vetterli, 1990; Ghil et al., 2002; Huang et al., 1998; Smith-Boughner & Constable, 2012	Decompose a time-series into its components of different frequencies, i.e. its spectral characteristics. Fast Fourier transform most widely applied due to ease of use.	Fourier transform analysis is only appropriate for linear systems and strictly periodic or stationary data. Spectrograms assume that the data are piecewise stationary. Hilbert transforms are a suitable alternative for non-linear and/or nonstationary time-series. Such analysis generally requires high-quality data (although there are methods of spectral estimation for data with gaps).	Bozzo et al., 2010	Show that singular spectrum analysis and Fourier analysis are related, and that the former can highlight precursors to a paroxysmal eruption at Stromboli.
					Odbert & Wadge, 2009	Analyse tilt data from Soufrière Hills Volcano, Montserrat; identify a clear change in spectral power that coincides with a shift in eruptive activity.
					Neuberg, 2006 (many other examples)	Create FFTs and spectrograms for various seismic data from a number of volcanoes, demonstrating utility in understanding external triggering and conduit dynamics.

	Sub-band decomposition/ reconstruction	Jones et al., 2012a	Use maximal-overlap wavelet packet transforms to filter, decompose, and recover signals from continuous multichannel tremor data.	Capable of detecting small changes in time-frequency content. Less appropriate where significant attenuation and scattering, or with an anisotropic source.	Jones et al., 2012b	Analyse continuous tremor recorded at Erta 'Ale; identify signals corresponding to source processes active in several different areas.
	Wavelet analysis	Ghil et al., 2002; Percival & Walden, 2000	Describe signal by convolution with wavelet function to describe variability distribution over a range of time and frequency scales.	Large number of wavelet options, to satisfy conflicting requirements of completeness, orthogonality, and localization in time and frequency.	Bartosch & Seidl, 1999	Analyse non-stationary tremor signals from a number of volcanoes; demonstrate utility particularly for signals containing information on a wide range of timescales.
					Odbert & Wadge, 2009	Analyse tilt data (proxy for lava flux) from Soufrière Hills Volcano, Montserrat; identify a previously unknown cycle of frequency modulation in a specific period.
Validation of data	Benford's Law	Benford, 1938; Sambridge et al., 2010	Law states that lower digits occur more frequently than higher ones in real-world data, irrespective of the unit of measurement. Nonconformity could indicate data incompleteness, errors, anomalies, or excessive round-off.	Empirical observation that is only applicable to some data.	Geyer & Marti, 2012	Test global eruption duration data (Smithsonian database), and find a good fit with Benford's Law. Find a poorer (but still reasonable) fit for data from the (less complete) global caldera database.

Supplementary File 2.2 List of references in Supplementary File 2.1.

Alasonati, P., Wassermann, J., Ohrnberger, M., 2006. Signal classification by wavelet-based hidden Markov models: application to seismic signals of volcanic origin. In: Mader, H., Coles, S., Connor, C., Connor, L. (Eds.), Statistics in Volcanology. IAVCEI Spec. Pub. 1, Geological Society, London, pp. 161–173.

Alessio, E., Carbone, A., Castelli, G., Frappietro, V., 2002. Second-order moving average and scaling of stochastic time series. Eur. Phys. J. B 27, 197–200. doi:10.1140/epjb/e20020150

Allan, D.W., 1966. Statistics of atomic frequency standards. Proc. IEEE 54, 221–230. doi:10.1109/PROC.1966.4634

Alvarez-Ramirez, J., Sosa, E., Rodriguez, E., 2009. Assessing temporal-dependent correlations in the 2000-2008 Popocatépetl exhalation sequence by using detrended fluctuation analysis. J. Volcanol. Geotherm. Res. 186, 426–431. doi:10.1016/j.jvolgeores.2009.05.022

Bartosch, T., Seidl, D., 1999. Spectrogram analysis of selected tremor signals using short-time Fourier transform and continuous wavelet transform. Annali di Geofisica 42, 497–506. doi:10.4401/ag-3733

Baum, L.E., Petrie, T., 1966. Statistical Inference for Probabilistic Functions of Finite State Markov Chains. Anns. Math. Stats. 37, 1554–1563. doi:10.1214/aoms/1177699147

Bebbington, M.S., 2007. Identifying volcanic regimes using hidden Markov models. Geophys. J. Int. 171, 921–942. doi:10.1111/j.1365-246X.2007.03559.x

Bebbington, M.S., 2010. Trends and clustering in the onsets of volcanic eruptions. J. Geophys. Res. 115, B01203. doi:10.1029/2009JB006581

Bebbington, M.S., 2012. Models for temporal volcanic hazard. Statistics in Volcanology 1, 1–24. doi:10.5038/2163-338X.1.1

Bebbington, M.S., Lai, C.D., 1996. On nonhomogeneous models for volcanic eruptions. Mathematical Geology 28, 585–600. doi:10.1007/BF02066102

Benítez, M.C., Lesage, P., Cortés, G., Segura, J.C., Ibáñez, J.M., de la Torre, A., 2009. Automatic recognition of volcanic-seismic events base on Continuous Hidden Markov Models. In: Bean, C.J., Braiden, A.K., Lokmer, I., Martini, F., O'Brien, G.S., VOLUME project, EU PF6 (No. 018471). VOLUME Project Consortium, Dublin, pp. 130–139.

Benford, F., 1938. The law of anomalous numbers. Proc. Am. Phil. Soc. 78, 551–572.

Bottiglieri, M., Falanga, M., Tammaro, U., Obrizzo, F., De Martino, P., Godano, C., Pingue, F., 2007. Independent component analysis as a tool for ground deformation analysis. Geophys. J. Int. 168, 1305–1310. doi:10.1111/j.1365-246X.2006.03264.x

Bozzo, E., Carniel, R., Fasino, D., 2010. Relationship between Singular Spectrum Analysis and Fourier analysis: Theory and application to the monitoring of volcanic activity. Computers and Mathematics with Applications 60, 812–820. doi:10.1016/j.camwa.2010.05.028

Burt, M.L., Wadge, G., Scott, W.A., 1994. Simple stochastic modelling of the eruption history of a basaltic volcano: Nyamuragira, Zaïre. Bull. Volcanol. 56, 87–97. doi:10.1007/BF00304104

Cardaci, C., Falsaperla, S., Gasperini, P., Lombardo, G., Marzocchi, W., Mulargia, F., 1993. Cross-correlation analysis of seismic and volcanic data at Mt. Etna volcano, Italy. Bull. Volcanol. 55, 596–603. doi:10.1007/BF00301812

Carniel, R., Tárraga, M., Jaquet, O., Ortiz, R., García, A., 2008. The seismic noise at Las Cañadas volcanic caldera, Tenerife, Spain: Persistence characterization, and possible relationship with regional tectonic events. J. Volcanol. Geotherm. Res. 173, 157–164. doi:10.1016/j.jvolgeores.2007.12.044

Chatfield, C., 2003. The analysis of time-series: an introduction, 6th edition. Chapman & Hall/CRC.

Coles, S.G., 2001. An Introduction to statistical modelling of extreme values (Springer series in statistics). Springer, London.

Coles, S.G., Sparks, R.S.J., 2006. Extreme value methods for modelling historical series of large volcanic magnitudes. In: Mader, H., Coles, S., Connor, C., Connor, L. (Eds.), Statistics in Volcanology. IAVCEI Spec. Pub. 1, Geological Society, London, pp. 47–56.

Correig, A.M., Urquizu, M., 1996. Chaotic behaviour of coda waves in the eastern Pyrenees. Geophys. J. Int. 126, 113–122. doi:10.1111/j.1365-246X.1996.tb05271.x

Correig, A.M., Urquizu, M., Vila, J., Martí, J., 1997. Analysis of the temporal occurrence of seismicity at Deception Island (Antarctica): A nonlinear approach. Pure Appl. Geophys. 149, 553–574. doi:10.1007/s000240050041

Currenti, G., del Negro, C., Lapenna, V., Telesca, L., 2005. Fluctuation analysis of the hourly time variability of volcano-magnetic signals recorded at Mt. Etna Volcano, Sicily (Italy). Chaos, Solitons, and Fractals 23, 1921–1929. doi:10.1016/j.chaos.2004.07.035

Del Pin, E., Carniel, R., Tárraga, M., 2008. Event recognition by detrended fluctuation analysis: An application to Teide-Pico Viejo volcanic complex, Tenerife, Spain. Chaos, Solitons, and Fractals 36, 1173–1180. doi:10.1016/j.chaos.2006.07.044

De Lauro, E., de Martino, S., Falanga, M., Ciaramella, A., Tagliaferri, R., 2005. Complexity of time-series associated to dynamical systems inferred from independent principal component analysis. Phys. Rev. E 72, 46712–46725. doi:10.1103/PhysRevE.72.046712

De Lauro, E., de Martino, S., Palo, M., Ibañez, J.M., 2012. Self-sustained oscillations at Volcán de Colima (México) inferred by independent component analysis. Bull. Volcanol. 74, 279–292. doi:10.1007/s00445-011-0520-x

Di Salvo, R., Montalto, P., Nunnari, G., Neri, M., Puglisi, G., 2012. Multivariate time series clustering on geophysical data recorded from Mt. Etna from 1996 to 2003. J. Volcanol. Geotherm. Res. 251, 65–74. doi:10.1016/j.jvolgeores.2012.02.007

Dubois, J., Cheminée, D.L., 1991. Fractal analysis of eruptive activity of some basaltic volcanoes. J. Volcanol. Geotherm. Res. 45, 197–208. doi:10.1016/0377-0273(91)90059-9

Duhamel, P., Vetterli, M., 1990. Fast fourier transforms: A tutorial review and a state of the art. Signal Processing 19, 259–299. doi:10.1016/0165-1684(90)90158-U

Ebdon, D., 1985. Statistics in geography. Blackwell, London.

Fano, U., 1947. Ionization Yield of Radiations – II: The Fluctuations of the Number of Ions. Phys. Rev. 72, 26–29. doi:10.1103/PhysRev.72.26

Fattori-Speranza, F., Carniel, R., 2008. Structural changes of volcanic tremor at Stromboli volcano. J. Volcanol. Geotherm. Res., 171, 103–117. doi:10.1016/j.jvolgeores.2007.11.003

Feder, J., 1988. Fractals (Physics of solids and liquids series). Plenum Press.

Fisher, R.A., 1925. Theory of statistical estimation. Proc. Cambridge Phil. Soc. 22, 700–725. doi:10.1017/S0305004100009580

Furlan, C., 2010. Extreme value methods for modelling historical series of large volcanic magnitudes. Statistical Modelling 10, 113–132. doi:10.1177/1471082X0801000201

Geyer, A., Martí, J., 2012. Applying Benford's Law to volcanology. Geology 40, 327–330. doi:10.1130/G32787.1

Ghil, M., Allen, M.R., Dettinger, M.D., Ide, K., Kondrashov, D., Mann, M.E., Robertson, A.W., Saunders, A., Tian, Y., Varadi, F., Yiou, P., 2002. Advanced spectral methods for climatic time series. Rev. Geophys. 40, 1003. doi:10.1029/2000RG000092

Gutenberg, B., Richter, C., 1944. Frequency of earthquakes in California. Bull. Seis. Soc. Am. 34, 185–188.

Ho, C.-H., 2008. Empirical recurrence rate time series for volcanism: Application to Avachinsky volcano, Russia. J. Volcanol. Geotherm. Res. 173, 15–25. doi:10.1016/j.jvolgeores.2007.12.003

Huang, N.E., Shen, Z., Long, S.R., Wu, M.C., Shih, H.H., Zheng, Q., Yen, N.-C., Tung, C.C., Liu, H.H., 1998. The empirical mode decomposition and the Hilbert spectrum for nonlinear and non-stationary time series analysis. Proc. Roy. Soc. A 454, 903–995. doi:10.1098/rspa.1998.0193

Hurst, H., 1951. Long term storage capacity of reservoirs. Trans. Am. Soc. Eng. 116, 770–799.

Hyvärinen, A., Karhunen, J., Oja, E., 2001. Independent component analysis. Wiley, New York.

Ibáñez, J.M., De Angelis, S., Díaz-Moreno, A., Hernández, P., Alguacil, G., Posadas, A., Pérez, N., 2012. Insights into the 2011–2012 submarine eruption off the coast of El Hierro (Canary Islands, Spain) from statistical analyses of earthquake activity. Geophys. J. Int. 191, 659-670. doi:10.1111/j.1365-246X.2012.05629.x

Jain, A.K., Duin, R.P.W., Mao, J., 2000. Statistical pattern recognition: a review. IEEE transactions on pattern analysis and machine intelligence 22, 4–37. doi:10.1109/34.824819

Jaquet, O., Carniel, R. 2006. Estimation of volcanic hazards using geostatistical models. In: Mader, H., Coles, S., Connor, C., Connor, L. (Eds.), Statistics in Volcanology. IAVCEI Spec. Pub. 1, Geological Society, London, pp. 89–103.

Jaquet, O., Sparks, R.S.J., Carniel, R., 2006. Magma memory recorded by statistics of volcanic explosions at the Soufrière Hills volcano, Montserrat. In: Mader, H., Coles, S., Connor, C., Connor, L. (Eds.), Statistics in Volcanology. IAVCEI Spec. Pub. 1, Geological Society, London, pp. 175–184.

Jones, J.P., Carniel, R., Malone, S.D., 2012a. Subband decomposition and reconstruction of continuous volcanic tremor. J. Volc. Geotherm. Res. 213-214, 98-115. doi:10.1016/j.jvolgeores.2011.07.006

Jones, J.P., Carniel, R., Malone, S.D., 2012b. Decomposition, location, and persistence of seismic signals recovered from continuous tremor at Erta 'Ale, Ethiopia. J. Volc. Geotherm. Res. 213-214, 116-129. doi:10.1016/j.jvolgeores.2011.07.007

Köhler, A., Ohrnberger, M., Scherbaum, F., 2009. Unsupervised feature selection and general pattern discovery using self-organizing maps for gaining insights into the nature of seismic wavefields, Comp. Geosci. 35, 1757–1767. doi:10.1016/j.cageo.2009.02.004

Kohonen, T., 1982. Self-organized formation of topologically correct feature maps. Biological Cybernetics 43, 59–69. doi:10.1007/BF00337288

Langer, H., Falsaperla, S., Masotti, M., Campanini, R., Spampinato, S., Messina, A., 2009. Synopsis of supervised and unsupervised pattern classification techniques applied to volcanic tremor data at Mt. Etna, Italy. Geophys. J. Int. 178, 1132–1144. doi:10.1111/j.1365-246X.2009.04179.x

Langer, H., Falsaperla, S., Powell, T., Thompson, G., 2006. Automatic classification and a-posteriori analysis of seismic event identification at Soufrière Hills volcano, Montserrat. J. Volcanol. Geotherm. Res. 153, 1–10. doi:10.1016/j.jvolgeores.2005.08.012

Langer, H., Falsaperla, S., Thompson, G., 2003. Application of artificial neural networks for the classification of the seismic transients at Soufrière Hills volcano, Montserrat. Geophys. Res. Lett. 30, 2090. doi:10.1029/2003GL018082

Leadbetter, M., Lindgren, G., Rootzén, H., 1983. Extremes and related properties of stationary sequences and processes. Springer, New York.

Lee, E., 2003. Statistical Methods for Survival Data Analysis, 3rd edition. Wiley-Interscience, Hoboken.

Marzocchi, W., Bebbington, M.S., 2012. Probabilistic eruption forecasting at short and long time scales. Bull. Volcanol. 74, 1777–1805. doi:10.1007/s00445-012-0633-x

Marzocchi, W., Sandri, L., Boschi, E., 2003. On the validation of earthquake-forecasting models: the case of pattern recognition algorithms. Bull. Seis. Soc. Am. 93, 1994–2004. doi:10.1785/0120020186

Marzocchi, W., Zaccarelli, L., 2006. A quantitative model for the time-size distribution of eruptions. J. Geophys. Res. 111, B04204. doi:10.1029/2005JB003709

Matheron, G., 1962. Traité de Géostatistique apliquée; Tome 1. Technip, Paris.

Mulargia, F., Gasperini, P., Tinti, S., 1987. Identifying different regimes in eruptive activity: an application to Etna volcano. J. Volcanol. Geotherm. Res. 34, 89–106. doi:10.1016/0377-0273(87)90095-3

Nason, G.P., 2006. Stationary and non-stationary time series. In: Mader, H., Coles, S., Connor, C., Connor, L. (Eds.), Statistics in Volcanology. IAVCEI Spec. Pub. 1, Geological Society, London, pp. 129–142.

Neuberg, J., 2006. Multi-parameter monitoring and modelling of volcanic processes. In: Mader, H., Coles, S., Connor, C., Connor, L. (Eds.), Statistics in Volcanology. IAVCEI Spec. Pub. 1, Geological Society, London, pp. 215–230.

Novelo-Casanova, D.A., Valdés-González, C. 2008. Seismic pattern recognition techniques to predict large eruptions at the Popocatépetl volcano, Mexico. J. Volcanol. Geotherm. Res. 176, 583–590. doi:10.1016/j.jvolgeores.2008.05.005

Odbert, H.M., Wadge, G., 2009. Time series analysis of lava flux. J. Volcanol. Geotherm. Res. 188, 305–314. doi:10.1016/j.jvolgeores.2009.09.005

Palacios, P., Molina, I., Segovia, M., 2006. The Gutenberg-Richter Law: assumptions, limitations and interpretations. In: Mader, H., Coles, S., Connor, C., Connor, L. (Eds.), Statistics in Volcanology. IAVCEI Spec. Pub. 1, Geological Society, London, pp. 115–127.

Passarelli, L., Sansò, B., Sandri, L., Marzocchi, W., 2010. Testing forecasts of a new Bayesian time-predictable model of eruption occurrence. J. Volcanol. Geotherm. Res. 198, 57–75. doi:10.1016/j.jvolgeores.2010.08.011

Peng, C.-K., Buldyrev, S.V., Havlin, S., Simons, M., Stanley, H.E., Goldberger, A.L., 1994. Mosaic organization of DNA nucleotides. Phys. Rev. E 49, 1685–1689. doi:10.1103/PhysRevE.49.1685

Peng, C.-K., Havlin, S., Stanley, H.E., Goldberger, A.L., 1995. Quantification of scaling exponents and crossover phenomena in nonstationary heartbeat time series. Chaos 5, 82–87. doi:10.1063/1.166141

Percival, D., Walden, A., 2000. Wavelet methods for time series analysis. Cambridge University Press.

Privitera, E., Sgroi, T., Gresta, S., 2003. Statistical analysis of intermittent volcanic tremor associated with the September 1989 summit explosive eruptions at Mount Etna, Sicily. J. Volcanol. Geotherm. Res. 120, 235–247. doi:10.1016/S0377-0273(02)00400-6

Rabiner, L., 1989. A tutorial on hidden Markov models and selected applications in speech recognition. Proceedings of the IEEE 77, 257–286.

Rumelhart, D., Hinton, G., Williams, R., 1986. Learning internal representation by error propagation. In: Rumelhart, D., McClelland, J. (Eds.), Parallel distributed processing: explorations in the microstructures of cognitions. MIT Press, pp. 318–362.

Sambridge, M., Tkalcic, H., Jackson, A., 2010. Benford's Law in the natural sciences. Geophys. Res. Lett. 37, L22301. doi:10.1029/2010GL044830

Sandri, L., Marzocchi, W., Zaccarelli, L., 2004. A new perspective in identifying the precursory patterns of eruptions. Bull. Volcanol. 66, 263–275. doi:10.1007/s00445-003-0309-7

Shannon, C., Weaver, W., 1949. The mathematical theory of communication. University of Illinois Press, Urbana.

Shimazaki, K., Nakata, T., 1980. Time-predictable recurrence model for large earthquakes. Geophys. Res. Lett. 7, 279–282. doi:10.1029/GL007i004p00279

Smalley, R.F., Chatelain, J.-L., Turcotte, D.L., Prevot, R., 1987. A fractal approach to the clustering of earthquakes: Applications to the seismicity of the New Hebrides. Bull. Seis. Soc. Am. 77, pp. 1368–1381.

Smith- Boughner, L.T., Constable, C.G., 2012. Spectral estimation for geophysical time-series with inconvenient gaps. Geophys. J. Int. 190, 1404–1422. doi:10.1111/j.1365-246X.2012.05594.x

Telesca, L., Cuomo, V., Lapenna, V., Macchiato, M., 2002a. On the methods to identify clustering properties in sequences of seismic time-occurrences. J. Seismol. 6, 125–134. doi:10.1023/A:1014275509447

Telesca, L., Cuomo, V., Lapenna, V., Macchiato, M., 2002b. Time-clustering analysis of volcanic occurrence sequences. Phys. Earth Plan. Int. 131, 47–62. doi:10.1016/S0031-9201(02)00015-8

Telesca, L., Lapenna, V., 2005. Identifying features in time-occurrence sequences of volcanic eruptions. Environmetrics 16, 181–190. doi:10.1002/env.694

Telesca, L., Lovallo, M., Carniel, R., 2010. Time-dependent Fisher information measure of volcanic tremor before the 5 April 2003 paroxysm at Stromboli volcano, Italy. J. Volcanol. Geotherm. Res. 195, 78–82. doi:10.1016/j.jvolgeores.2010.06.010

Telesca, L., Lovallo, M., El-Ela Amin Mohamed, A., ElGabry, M., El-hady, S., Abou Elenean, K.M., ElShafey Fat ElBary, R., 2012. Informational analysis of seismic sequences by applying the Fisher information measure and the Shannon entropy: An application to the 2004–2010 seismicity of Aswan area (Egypt). Physica A 391, 2889–2897. doi:10.1016/j.physa.2011.12.047

Van der Baan, M., Jutten, C., 2000. Neural networks in geophysical applications. Geophysics 4, 1032–1047. doi:10.1190/1.1444797

Varley, N.R., Johnson, J., Ruiz, M., Reyes, G., Martin, K., 2006. Applying statistical analysis to understanding the dynamics of volcanic explosions. In: Mader, H., Coles, S., Connor, C., Connor, L. (Eds.), Statistics in Volcanology. IAVCEI Spec. Pub. 1, Geological Society, London, pp. 57–76.

Vinciguerra, S., Gresta, S., Barbano, M.S., Distefano, G., 2001. The two behaviours of Mt. Etna volcano before and after a large intrusive episode: Evidences from b value and fractal dimension of seismicity. Geophys. Res. Lett. 28, 2257–2260. doi:10.1029/2000GL012434

Wickman, F., 1966. Repose-period patterns of volcanoes. Arkiv för Mineralogi och Geologi 4, 291–367.

Zeileis, A., Leisch, F., Homik, K., Kleiber, C., 2002. Strucchange: An R package for testing for structural change in linear regression models. J. Stat. Softw., 7, 1–38.

Zeileis, A., Shah, A., Patnaik, I., 2010. Testing, monitoring, and dating structural changes in exchange rate regimes. Computational Statistics & Data Analysis 54, 1696–1706. doi: 10.1016/j.csda.2009.12.005

Supplementary File 3.1 Normalised cumulative entropy of Volcán de Colima RSEM.

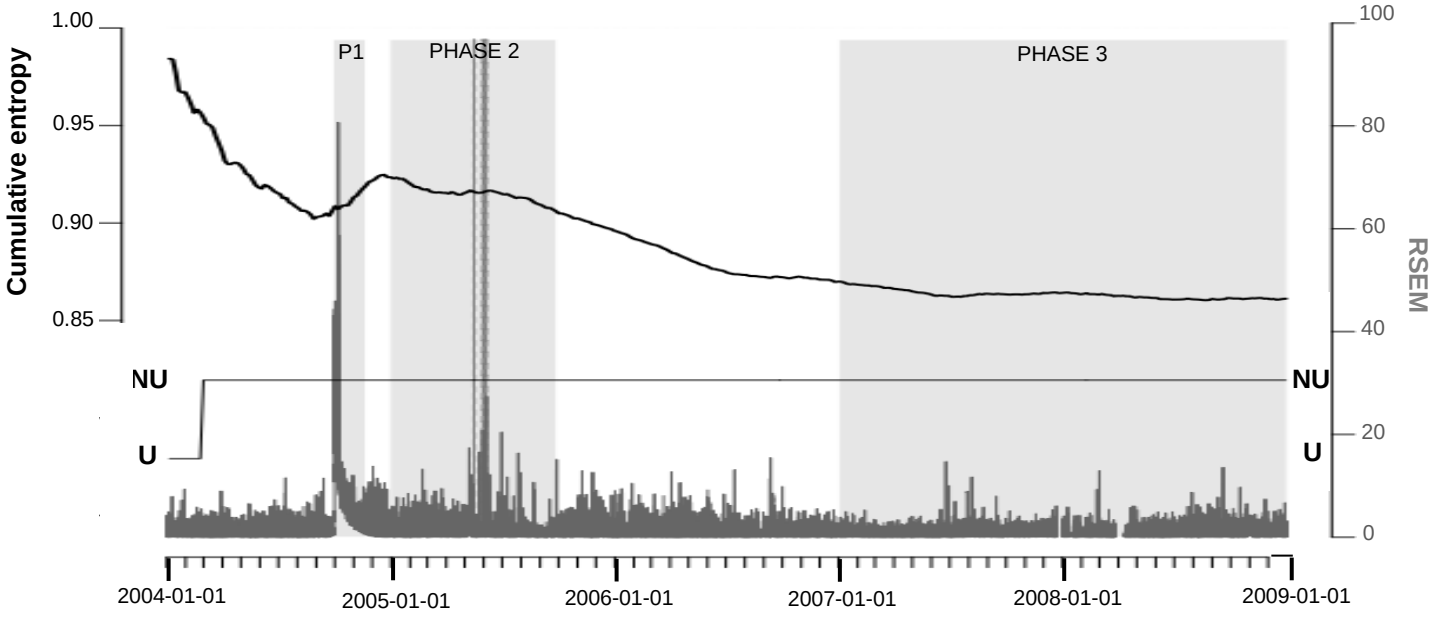

SF3.1 The normalised cumulative empirical Shannon entropy (upper black line) of an hour-averaged real-time seismic energy measurement (RSEM) time-series recorded at Volcán de Colima (dark grey line; data from 1 January 2004 to 31 December 2008), with a test of hypothesis of a uniform distribution (lower black line; NU = not uniform, U = uniform; Section 3.2.3) calculated using the same cumulative window. The shading indicates phases (labelled) of extrusive and/or enhanced explosive activity; the vertical dashed grey lines mark major (VEI ≥2) Vulcanian explosions. Phase 1 is the period of relatively fast lava extrusion in late 2004, Phase 2 the period of large Vulcanian explosions in 2005, and Phase 3 the period of relatively slow lava extrusion in 2007–11. The distribution of the data in the window quickly becomes consistently non-uniform (and so the cumulative entropy decreases relatively rapidly) due to the non-stationary nature of the RSEM time-series (i.e., because the distribution of the data changes through time).

Supplementary File 3.2 Normalised cumulative entropy of Soufrière Hills Volcano RSAM.

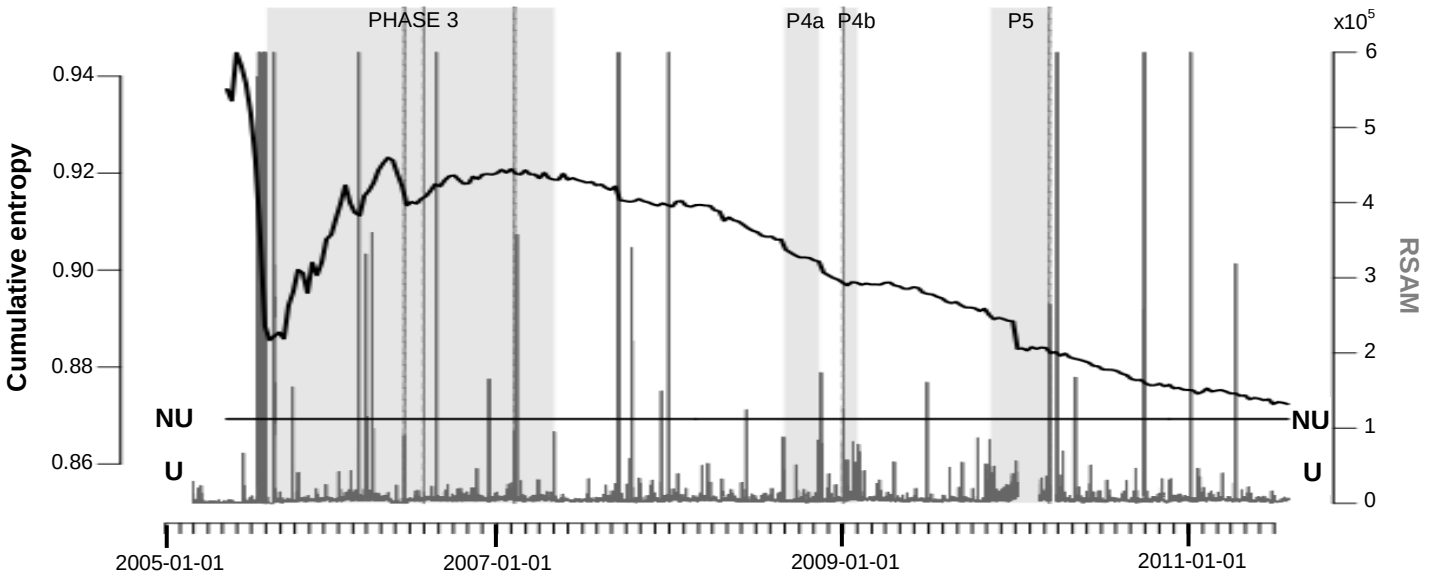

SF3.2 The normalised cumulative empirical Shannon entropy (upper black line) of an hour-averaged real-time seismic amplitude measurement (RSAM) time-series recorded at Soufrière Hills Volcano (dark grey line; data from 28 February 2005 to 30 June 2011), with a test of hypothesis of a uniform distribution (lower black line; NU = not uniform, U = uniform) calculated using the same cumulative window. The shading indicates phases (labelled) of extrusive and/or explosive activity; the vertical dashed grey lines mark major dome collapse events.

Supplementary File 3.3 Coefficient of variation of Volcán de Colima daily volcano-seismic event counts.

SF3.3a) Impulsive events

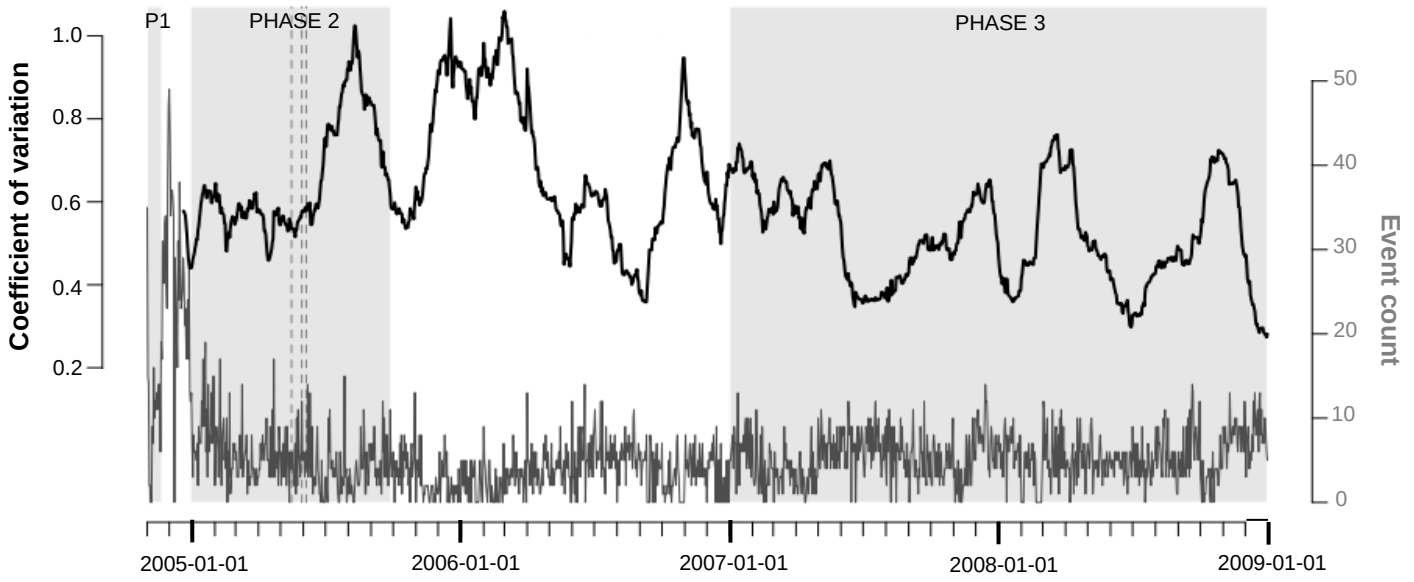

SF3.3b) Emergent events

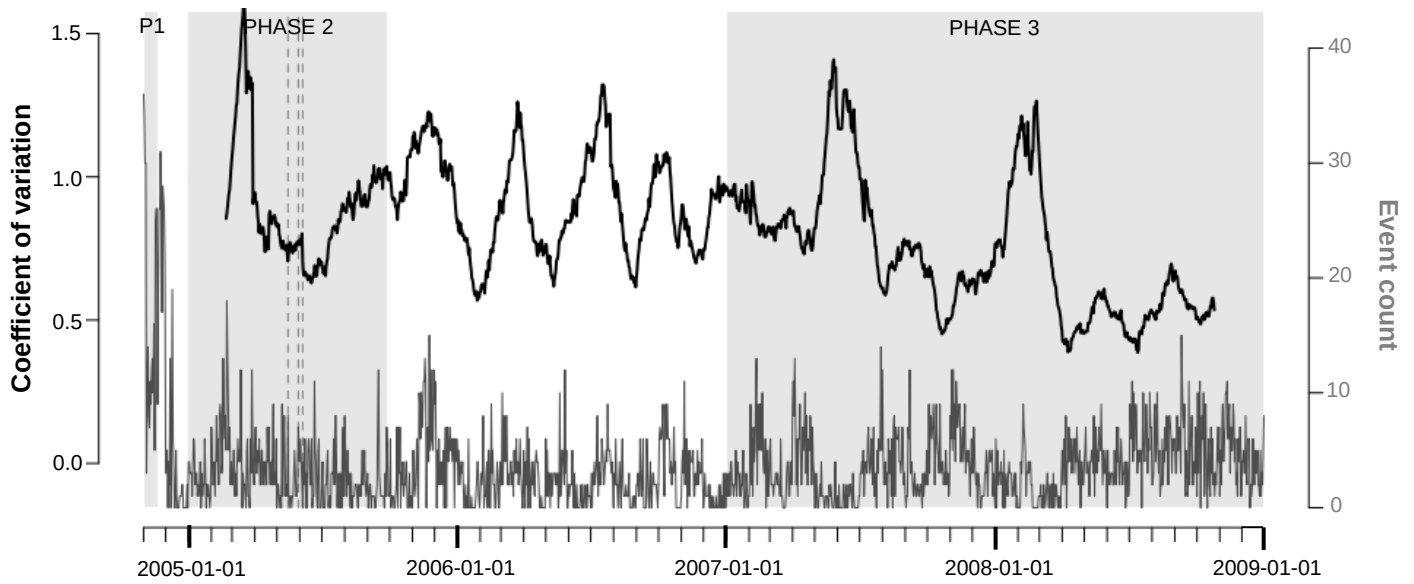

SF3.3c) Low-amplitude long-period events

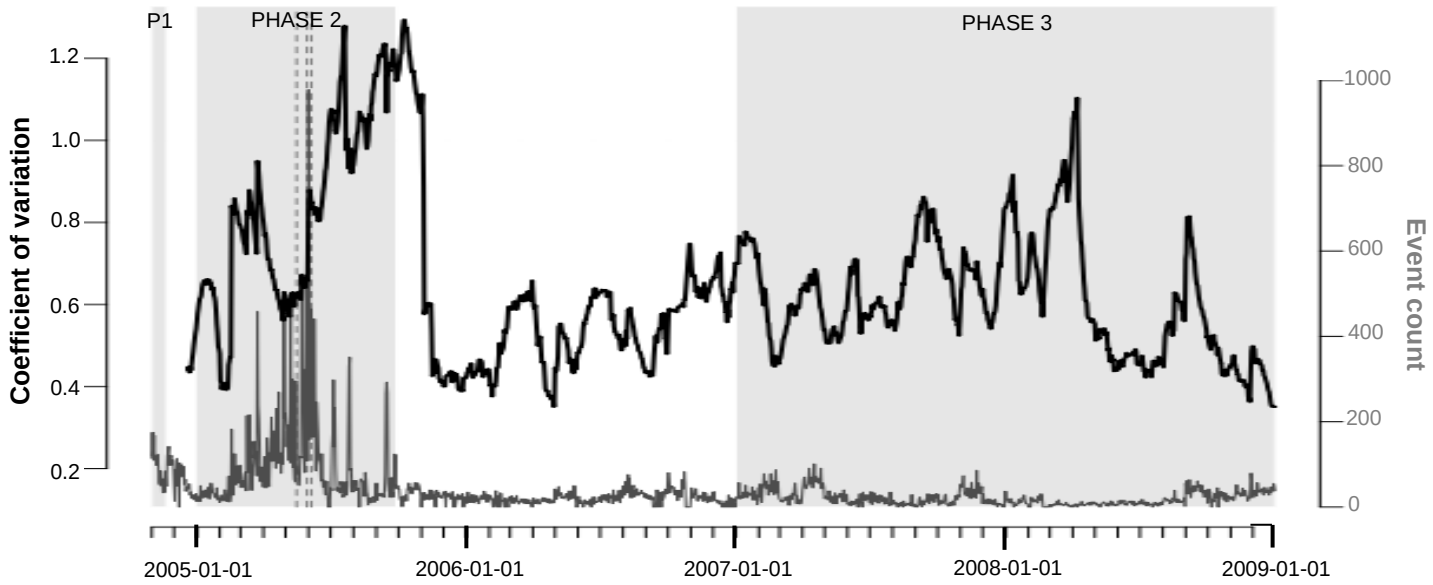

Previous page **SF3.3** The coefficient of variation (black line) of the daily count of each of the primary volcano-seismic event types at Volcán de Colima (described in Table 2.1; dark grey line; data from 1 November 2004 to 31 December 2008), calculated for each time-step from a window of the prior 50 days (50 measurements). The shading in each graph indicates phases (labelled) of extrusive and/or enhanced explosive activity; the vertical dashed grey lines mark major (VEI ≥2) Vulcanian explosions. Phase 1 is the period of relatively fast lava extrusion in late 2004, Phase 2 the period of large Vulcanian explosions in 2005, and Phase 3 the period of relatively slow lava extrusion in 2007–11.

Supplementary File 3.4 Coefficient of variation of Soufrière Hills Volcano daily volcano-seismic event counts.

SF3.4a) Volcano-tectonic events

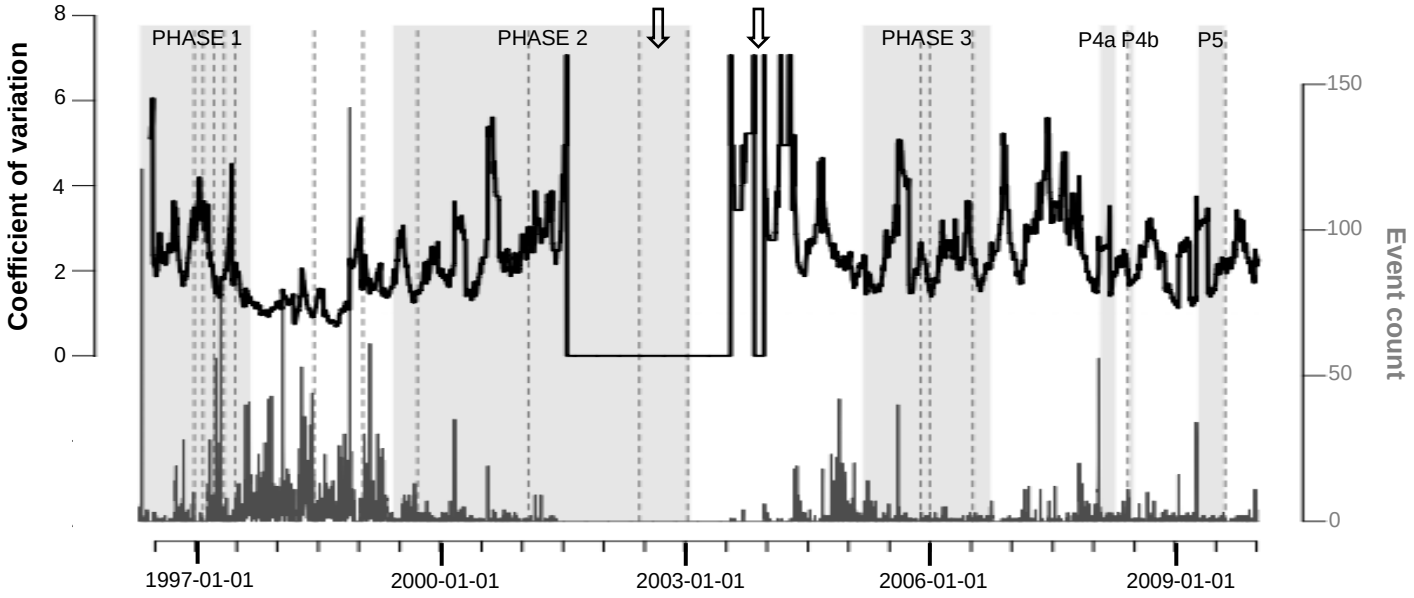

SF3.4b) Hybrid events

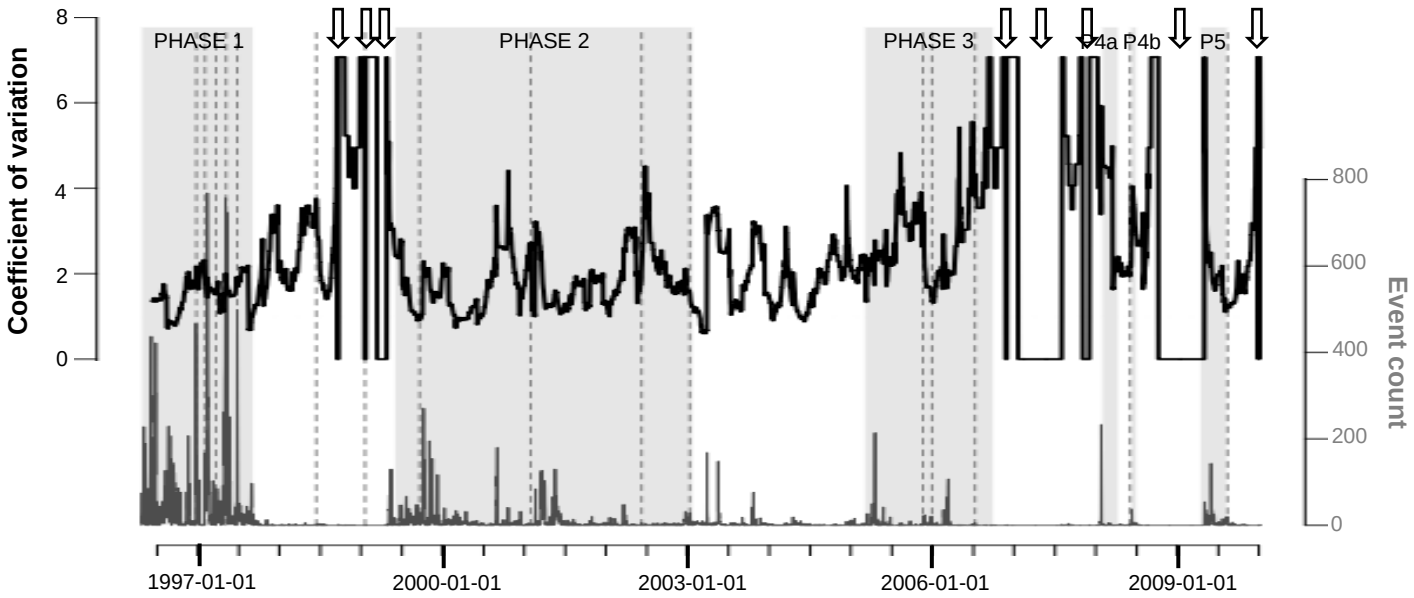

SF3.4c) Long-period events

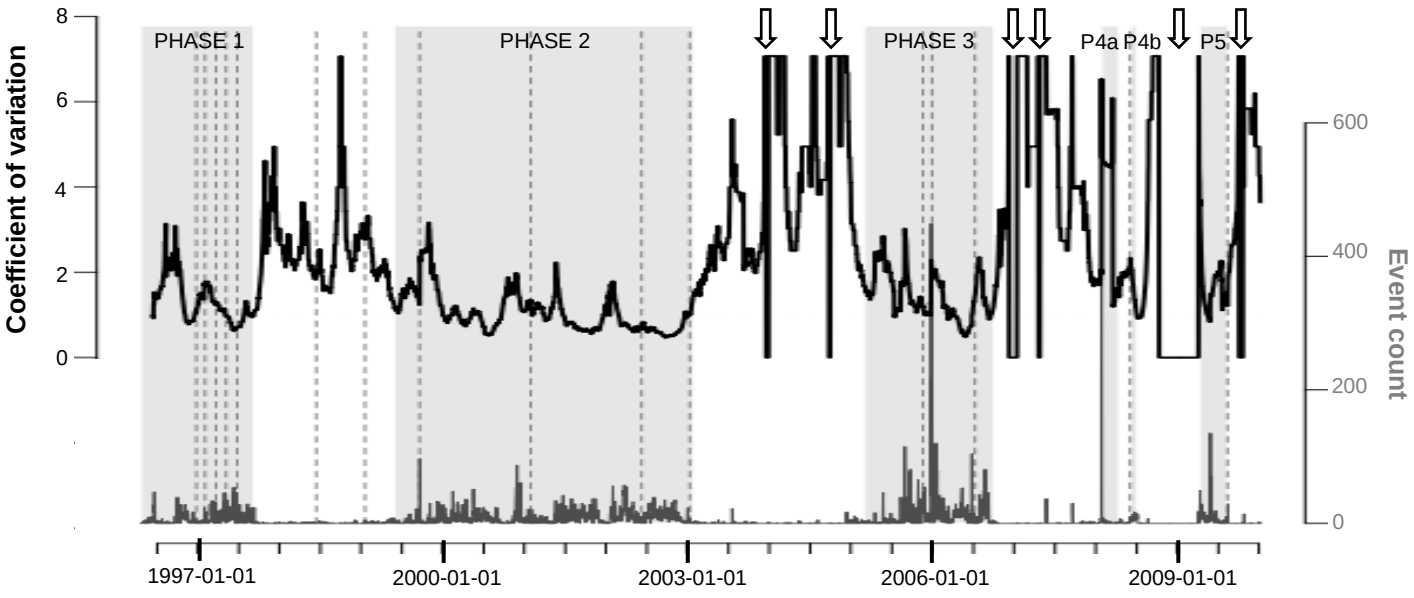

SF3.4d) Rockfall events

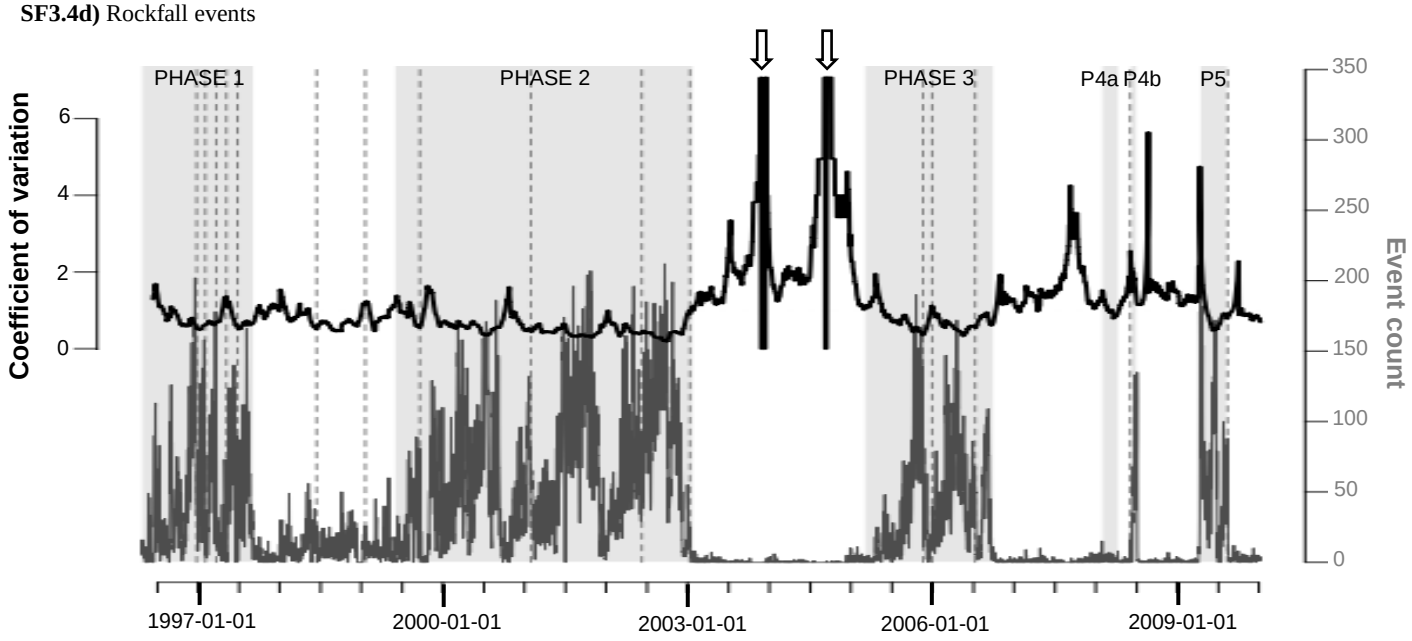

SF3.4e) Rockfall with long-period events

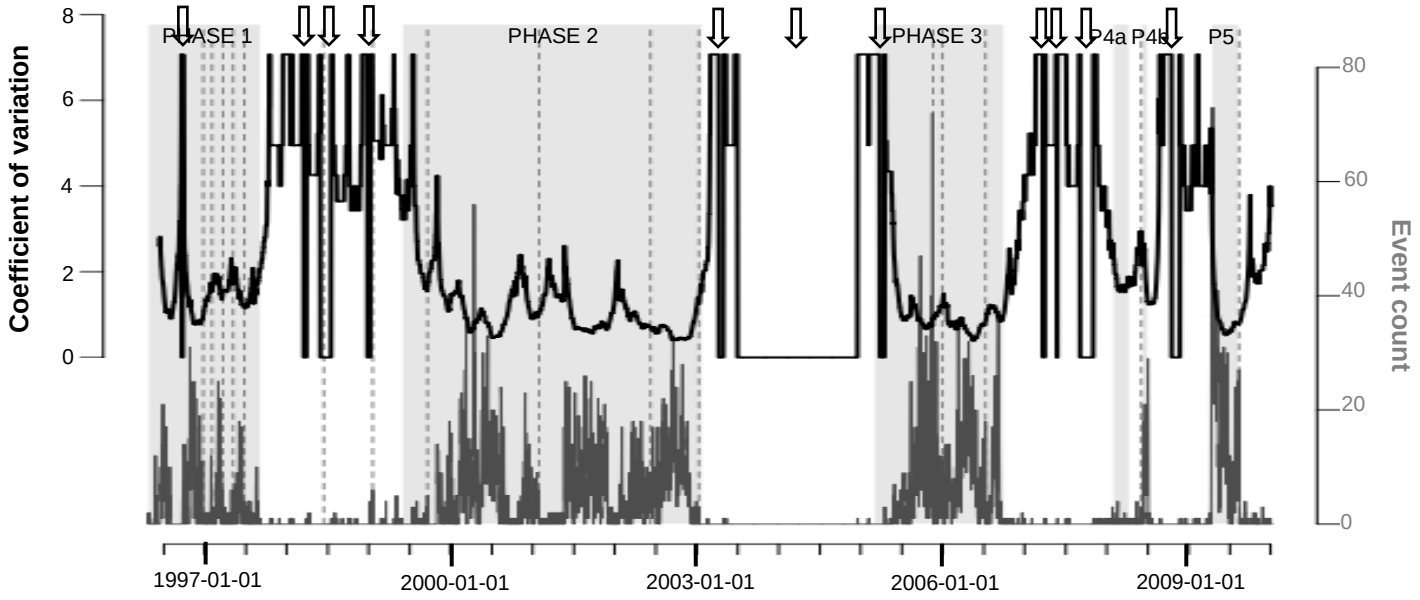

SF3.4 The coefficient of variation (black line) of the daily count of each of the primary volcano-seismic event types at Soufrière Hills Volcano (described in Table 2.2; dark grey line; data from 23 October 1996 to 8 July 2010), calculated for each time-step from a window of the prior 50 days (50 measurements). The shading in each graph indicates phases (labelled) of extrusive and/or explosive activity; the vertical dashed grey lines mark major dome collapse events. The hollow arrows indicate anomalous increases in the coefficient of variation values due to periods of zero counts.

Supplementary File 4.1 List of references in Supplementary Tables 4.1 and 4.2.

[1] Haberle, S.G., Lumley, S.H., 1998. Age and origin of tephras recorded in postglacial lake sediments to the west of the southern Andes, 44°S to 47°S. J. Volcanol. Geotherm. Res. 84, 239–256. doi:10.1016/S0377-0273(98)00037-7

[2] Haberle, S.G., Szeicz, J.M., Bennett, K.D., 2000. Late Holocene vegetation dynamics and lake geochemistry at Laguna Miranda, XI Region, Chile. Rev. Chilena Hist. Nat. 73, 655–669.

[3] Carel, M., Siani, G., Delpech, G., 2011. Tephrostratigraphy of a deep-sea sediment sequence off the south Chilean margin: New insight into the Hudson volcanic activity since the last glacial period. J. Volcanol. Geotherm. Res. 208, 99–111. doi:10.1016/j.jvolgeores.2011.09.011

[4] Siani, G., Colin, C., Michel, E., Carel, M., Richter, T., Kissel, C., Dewilde, F., 2010. Late Glacial to Holocene terrigenous sediment record in the Northern Patagonian margin: Paleoclimate implications. Palaeogeogr., Palaeoclimatol., Palaeoecol. 297, 26–36. doi:10.1016/j.palaeo.2010.07.011

[5] Siani, G., Michel, E., De Pol-Holz, R., DeVries, T., Lamy, F., Carel, M., Isguder, G., Dewilde, F., Lourantou, A., 2013. Carbon isotope records reveal precise timing of enhanced Southern Ocean upwelling during the last deglaciation. Nat Commun 4. doi:10.1038/ncomms3758

[6] Villa-Martinez, R., Moreno, P. I., Valenzuela, M. A., 2011. Deglacial and postglacial vegetation changes on the eastern slopes of the central Patagonian Andes (47 degrees S). Quat. Sci. Rev. 32, 86–99. doi:10.1016/j.quascirev.2011.11.008

[7] Eugenia de Porras, M., Maldonado, A., Abarzúa, A.M., Cárdenas, M.L., Francois, J.P., Martel-Cea, A., Stern, C.R., Méndez, C., Reyes, O., 2012. Postglacial vegetation, fire and climate dynamics at Central Chilean Patagonia (Lake Shaman, 44°S). Quat. Sci. Rev. 50, 71–85. doi:10.1016/j.quascirev.2012.06.015

[8] Stern, C.R., Eugenia de Porras, M., Maldonado, A., 2015. Tephrochronology of the upper Río Cisnes valley (44°S), southern Chile. Andean Geol. 42, 173–189. doi:10.5027/andgeoV42n2-a02

[9] Elbert, J., Wartenburger, R., von Gunten, L., Urrutia, R., Fischer, D., Fujak, M., Hamann, Y., Greber, N.D., Grosjean, M., 2013. Late Holocene air temperature variability reconstructed from the sediments of Laguna Escondida, Patagonia, Chile (45°30'S). Palaeogeogr., Palaeoclimatol., Palaeoecol. 369, 482–492. doi:10.1016/j.palaeo.2012.11.013

[10] Weller, D., Miranda, C.G., Moreno, P.I., Villa-Martínez, R., Stern, C.R., 2014. The large late-glacial Ho eruption of the Hudson volcano, southern Chile. Bull. Volcanol. 76, 831–848. doi:10.1007/s00445-014-0831-9

[11] Markgraf, V., Whitlock, C., Haberle, S., 2007. Vegetation and fire history during the last 18,000 cal yr B.P. in Southern Patagonia: Mallín Pollux, Coyhaique, Province Aisén (45°41′30″ S, 71°50′30″ W, 640 m elevation). Palaeogeog., Palaeoclimatol., Palaeoecol. 254, 492–507. doi:10.1016/j.palaeo.2007.07.008

[12] Markgraf, V., Bradbury, J.P., Schwalb, A., Burns, S.J., Stern, C., Ariztegui, D., Gilli, A., Anselmetti, F.S., Stine, S., Maidana, N., 2003. Holocene palaeoclimates of southern Patagonia: limnological and environmental history of Lago Cardiel, Argentina. The Holocene 13, 581–591. doi:10.1191/0959683603hl648rp

[13] Gilli, A., Ariztegui, D., Anselmetti F.S., McKenzie, J.A., Markgraf, V., Hajdas, I., McCulloch, R.D., 2005. Mid-Holocene strengthening of the Southern Westerlies in South America - Sedimentological evidences from Lago Cardiel, Argentina (49°S). Glob. Planet. Ch. 49, 75–93. doi:10.1016/j.gloplacha.2005.05.004

[14] Holz, A., Haberle, S., Veblen, T.T., De Pol-Holz, R., Southon, J., 2012. Fire history in western Patagonia from paired tree-ring fire-scar and charcoal records. Clim. Past 8, 451–466. doi:10.5194/cp-8-451-2012

[15] Markgraf, V., Huber, U.M., 2010. Late and postglacial vegetation and fire history in Southern Patagonia and Tierra del Fuego. Palaeogeogr., Palaeoclimatol., Palaeoecol. 297, 351–366. doi:10.1016/j.palaeo.2010.08.013

[16] Kilian, R., Hohner, M., Biester, H., Wallrabe-Adams, H.J., Stern, C.R., 2003. Holocene peat and lake sediment tephra record from the southernmost Chilean Andes (53-55°S). Rev. Geol. Chile 30, 23–37. doi:10.4067/S0716-02082003000100002

[17] Heusser, C.J., 1995. Three Late Quaternary pollen diagrams from Southern Patagonia and their palaeoecological implications. Palaeogeog., Palaeoclimatol., Palaeoecol. 118, 1–24. doi:10.1016/0031-0182(94)00138-X

[18] McCulloch, R.D., Davies, S.J., 2001. Late-glacial and Holocene palaeoenvironmental change in the central Strait of Magellan, southern Patagonia. Palaeogeogr. Palaeoclimatol. Palaeoecol. 173, 143–173. doi:10.1016/S0031-0182(01)00316-9

[19] De Vleeschouwer, F., Vanneste, H., Mauquoy, D., Piotrowska, N., Torrejo, F., Roland, T., Stein, A., Le Roux, G., 2014. Emissions from Pre-Hispanic Metallurgy in the South American Atmosphere. PLoS ONE 9, e111315. doi:10.1371/journal.pone.0111315

[20] Laura Benvenuto, M., Fernández Honaine, M., Osterrieth, M., Coronato, A., Rabassa, J., 2013. Silicophytoliths in Holocene peatlands and fossil peat layers from Tierra del Fuego, Argentina, southernmost South America. Quatern. Int. 287, 20–33. doi:10.1016/j.quaint.2011.11.025
[21] Borromei, A.M., 1995. Análisis polínico de una turbera holocénica en el Valle de Andorra, Tierra del Fuego, Argentina. Rev. Ch. Hist. Natural 68, 311–319.
[22] Borromei, A.M., Coronato, A., Franzén, L.G., Ponce, J.F., López Sáez, J.A., Maidana, N., Rabassa, J., Candel, M.S., 2010. Multiproxy record of Holocene paleoenvironmental change, Tierra del Fuego, Argentina. Palaeogeogr., Palaeoclimatol., Palaeoecol. 286, 1–16. doi:10.1016/j.palaeo.2009.11.033
[23] Borromei, A.M., Coronato, A., Quattrocchio, M., Rabassa, J., Grill, S., Roig, C., 2007. Late Pleistocene–Holocene environments in Valle Carbajal, Tierra del Fuego, Argentina. J. South Am. Earth Sci. 23, 321–335. doi:10.1016/j.jsames.2007.02.008
[24] Heusser, C.J., 1990. Late-glacial and Holocene vegetation and climate of Subantarctic South America. Rev. Palaeobot. Palynol. 65, 9–15. doi:10.1016/0034-6667(90)90051-J
[25] Vanneste, H., De Vleeschouwer, F., Martínez-Cortizas, A., von Scheffer, C., Piotrowska, N., Coronato, A., Le Roux, G., 2015. Late-glacial elevated dust deposition linked to westerly wind shifts in southern South America. Sci. Rep. 5, 11670. doi:10.1038/srep11670
[26] Stern, C.R., Moreno, P.I., Henríquez, W.I., Villa-Martínez, R., Sagredo, E., Aravena, J.C., 2013. Tephrochronology in the area around Cochrane, southern Chile. Boll. Geofis. 54 (Suppl. 2), 199–202.
[27] Bertrand, S., Araneda, A., Vargas, P., Jana, P., Fagel, N., Urrutia, R., 2012. Using the N/C ratio to correct bulk radiocarbon ages from lake sediments: Insights from Chilean Patagonia. Quat. Geochron. 12, 23–29. doi:10.1016/j.quageo.2012.06.003
[28] Haberzettl, T., Anselmetti, F.S., Bowen, S.W., Fey, M., Mayr, C., Zolitschka, B., Ariztegui, D., Mauz, B., Ohlendorf, C., Kastner, S., Lücke, A., Schäbitz, F., Wille, M., 2009. Late Pleistocene dust deposition in the Patagonian steppe - extending and refining the paleoenvironmental and tephrochronological record from Laguna Potrok Aike back to 55 ka. Quat. Sci. Rev. 28, 2927–2939. doi:10.1016/j.quascirev.2009.07.021
[29] Hermanns, Y.-M., Biester, H., 2013. A 17,300-year record of mercury accumulation in a pristine lake in southern Chile. J. Paleolimnol. 49, 547–561. doi:10.1007/s10933-012-9668-4
[30] Waldmann, N., Ariztegui, D., Anselmetti, F.S., Austin, J.A., Moy, C.M., Stern, C., Recasens, C., Dunbar, R.B., 2010. Holocene climatic fluctuations and positioning of the Southern Hemisphere westerlies in Tierra del Fuego (54° S), Patagonia. J. Quaternary Sci. 25, 1099–1417. doi:10.1002/jqs.1263
[31] Naranjo, J.A., Stern, C.R., 1998. Holocene explosive activity of Hudson Volcano, southern Andes. Bull. Volcanol. 59, 291–306. doi:10.1007/s004450050193
[32] Lamy, F., Kilian, R., Arz, H.W., Francois, J.-P., Kaiser, J., Prange, M., Steinke, T., 2010. Holocene changes in the position and intensity of the southern westerly wind belt. Nat. Geosci. 3, 695–699. doi:10.1038/ngeo959
[33] Stern, C.R., 2008. Holocene tephrochronology record of large explosive eruptions in the southernmost Patagonian Andes. Bull. Volcanol. 70, 435–454. doi:10.1007/s00445-007-0148-z
[34] Kratzmann, D.J., Carey, S., Scasso, R., Naranjo, J.-A., 2009. Compositional variations and magma mixing in the 1991 eruptions of Hudson volcano, Chile. Bull. Volcanol. 71, 419–439. doi:10.1007/s00445-008-0234-x
[35] Stern, C.R., Moreno, P.I., Henríquez, W.I., Villa-Martínez, R., Sagredo, E., Aravena, J.C., 2013. Tephrochronology in the area around Cochrane, southern Chile. Boll. Geofis. 54 (Suppl. 2), 199–202.
[36] Stern, C.R., 1991. Mid-Holocene tephra on Tierra del Fuego (54°S) derived from the Hudson volcano (46°S): evidence for a large explosive eruption. Revista Geol. de Chile 18, 139–146. doi:10.5027/andgeoV18n2-a04
[37] Stern, C.R., 2008. Holocene tephrochronology record of large explosive eruptions in the southernmost Patagonian Andes. Bull. Volcanol. 70, 435–454. doi:10.1007/s00445-007-0148-z
[38] Orquera, L., Piana, E., 1987. Composicion tipolgica y datos tecnomorfologicos de los distintos conjuntos arqueologicos del sitio Tunel I (Tierra del Fuego). Relac. Soc. Argent. Antropol. 17, 201–239.
[39] Unkel, I., Björck, S., Wohlfarth, B., 2008. Deglacial environmental changes on Isla de los Estados (54.4°S), southeastern Tierra del Fuego. Quatern. Sci. Rev. 27, 1541–1554. doi:10.1016/j.quascirev.2008.05.004
[40] Unkel, I., Fernandez, M., Björck, S., Ljung, K., Wohlfarth, B., 2010. Records of environmental changes during the Holocene from Isla de los Estados (54.4°S), southeastern Tierra del Fuego. Glob. Planet. Change 74, 99–113. doi:10.1016/j.gloplacha.2010.07.003
[41] Björck, S., Rundgren, M., Ljung, K., Unkel, I., Wallin, A., 2012. Multi-proxy analyses of a peat bog on Isla de los Estados, easternmost Tierra del Fuego: a unique record of the variable Southern Hemisphere Westerlies since the last deglaciation. Quatern. Sci. Rev. 42, 1–14. doi:10.1016/j.quascirev.2012.03.015
[42] Miranda, C.G., Moreno, P.I., Vilanova, I., Villa-Martínez, R.P., 2013. Glacial fluctuations in the Coyhaique-Balmaceda sector of central Patagonia (45°S–46°S) during the last glacial termination. Boll. Geofis. 54 (Suppl. 2), 268–271.

[43] Blockley, S., 2012. Developing distal tephrochronology for palaeoenvironmental reconstruction in Patagonia. Quat. Int. 279–280, 54. doi:10.1016/j.quaint.2012.07.239
[44] Kilian, R., Lamy, F., 2012. A review of Glacial and Holocene paleoclimate records from southernmost Patagonia (49–55°S). Quat. Sci. Rev. 53, 1–23. doi:10.1016/j.quascirev.2012.07.017
[45] Markgraf, V., 1980. New data on the Late and Postglacial vegetational history of " La Mission " Tierra del Fuego, Argentina. Proceedings of the IV International Palynological Congress, Lucknow, India (1976 – 77) 3, 68–74.
[46] Narcisi, B., Petit, J.R., Delmonte, B., Basile-Doelsch, I., Maggi, V., 2005. Characteristics and sources of tephra layers in the EPICA-Dome C ice record (East Antarctica): Implications for past atmospheric circulation and ice core stratigraphic correlations. Earth Planet. Sci. Lett. 239, 253–265. doi:10.1016/j.epsl.2005.09.005
[47] Narcisi, B., Petit, J.R., Delmonte, B., Scarchilli, C., Stenni, B., 2012. A 16,000-yr tephra framework for the Antarctic ice sheet: a contribution from the new Talos Dome core. Quat. Sci. Rev. 49, 52–63. doi:10.1016/j.quascirev.2012.06.011
[48] Kurbatov, A.V., Zielinski, G.A., Dunbar, N.W., Mayewski, P.A., Meyerson, E.A., Sneed, S.B., Taylor, K.C., 2006. A 12,000 year record of explosive volcanism in the Siple Dome Ice Core, West Antarctica. J. Geophys. Res. 111, D12307. doi:10.1029/2005JD006072
[49] Naranjo, J.A., Moreno, H., Banks, N.G., 1993b. La erupción del Volcán Hudson en 1991 (46°S), Región XI, Aisén, Chile. Serv. Nac. Geol. Min. Bol. 44, pp. 1–50.
[50] Bitschene, P.R., Fernández, M.I., Arias, N., Arizmendi, A., Griznik, M., Nillni, A., 1993. Volcanology and environmental impact of the August 1991 eruption of the Hudson volcano (Patagonian Andes, Chile). Zbl. Geol. Palaont. Teil. ½, 165–177.
[51] Kratzmann, D.J., Carey, S., Scasso, R., Naranjo, J.-A., 2010. Role of cryptic amphibole crystallization in magma differentiation at Hudson volcano, Southern Volcanic Zone, Chile. Cont. Min. Pet. 159, 237–264. doi:10.1007/s00410-009-0426-1
[52] Ippach, P., 2001. Untersuchung der klimarelevanten Spurengase der Eruption des Cerro Hudson (Sud-Chile) im August 1991. Ph.D. thesis, Christian Albrechts Universität zu Kiel.
[53] Salmi, M., 1941. Die postglazialen Eruptionsschichten Patagoniens und Feuerlands. Annales Academiae Scientiarum Fennicae A3 2, Suomalainen Tiedeakatemia, Helsinki.
[54] Haberzettl, T., Corbella, H., Fey, M., Janssen, S., Lücke, A., Mayr, C., Ohlendorf, C., Schäbitz, F., Schleser, G.H., Wille, M., Wulf, S., Zolitschka, B., 2007. Lateglacial and Holocene wet–dry cycles in southern Patagonia: chronology, sedimentology and geochemistry of a lacustrine record from Laguna Potrok Aike, Argentina. The Holocene 17, 297–310. doi:10.1177/0959683607076437

Supplementary File 4.2 Inter-run comparison of glass secondary standard EMP analyses.

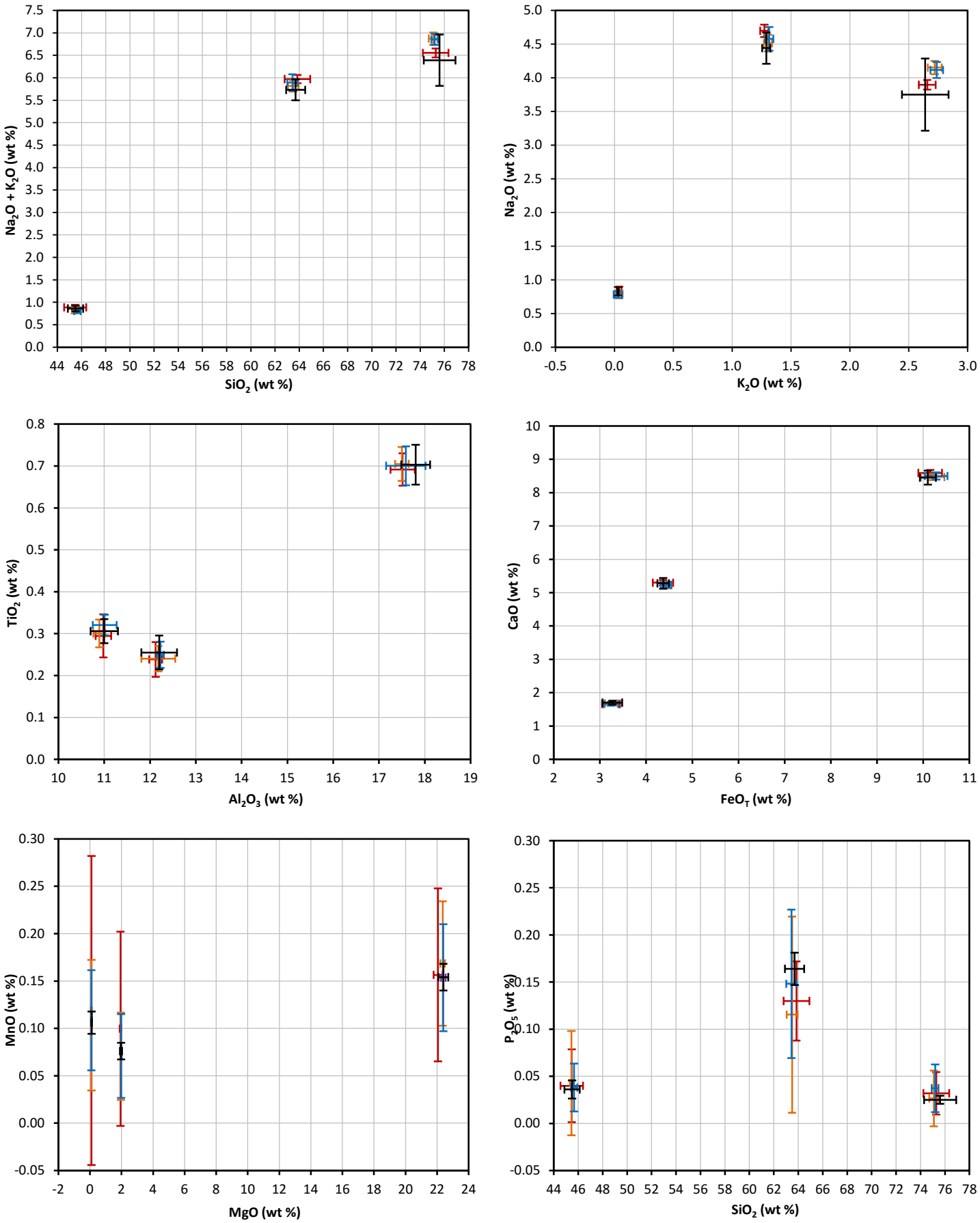

Error bars = 1σ r.s.d. (calculation in Supplementary Table 4.3)

Supplementary File 4.3 Outputs of OxCal Bayesian models applied to radiocarbon date constraints on the age of Volcán Hudson tephras.

(a) Integrated stratigraphy

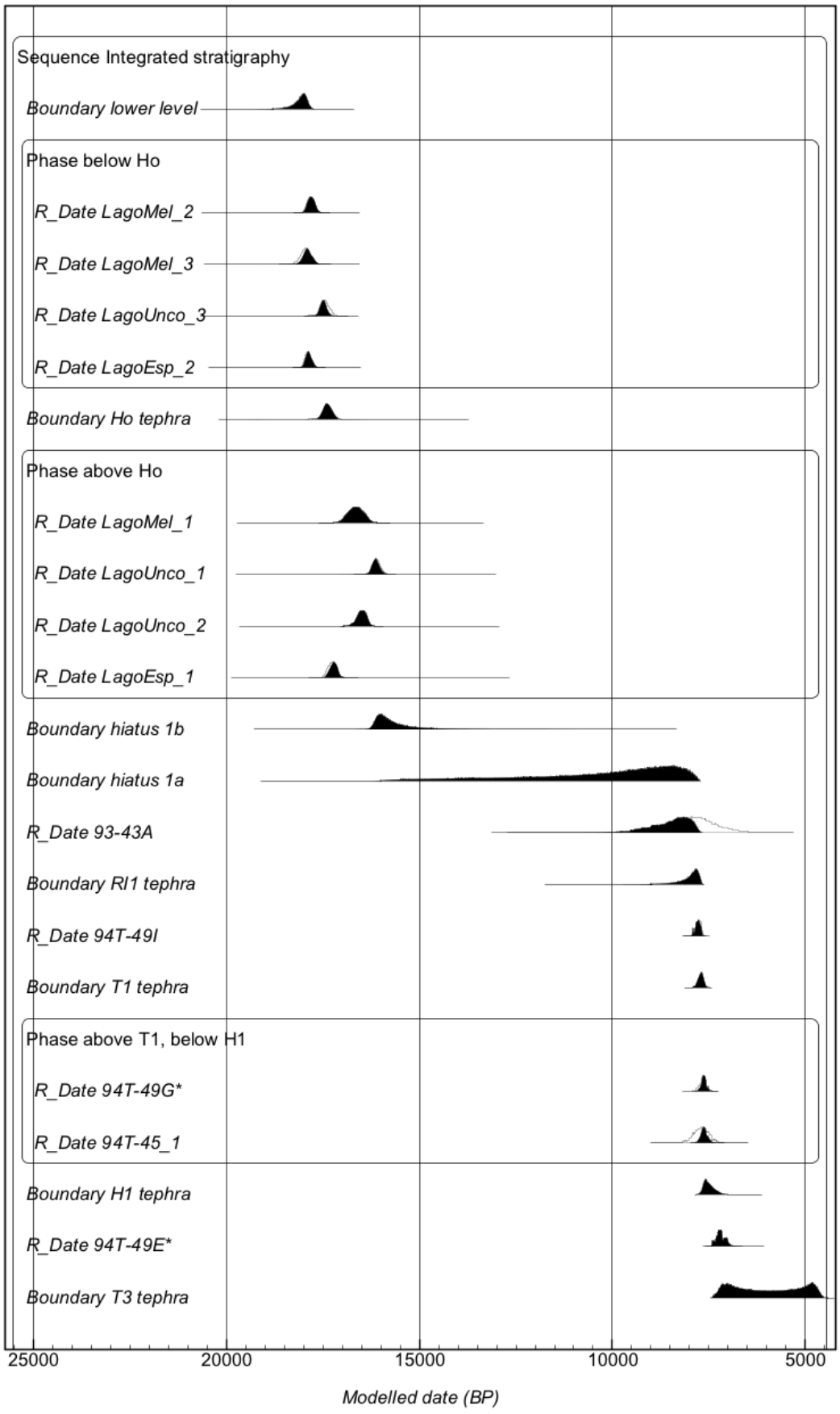

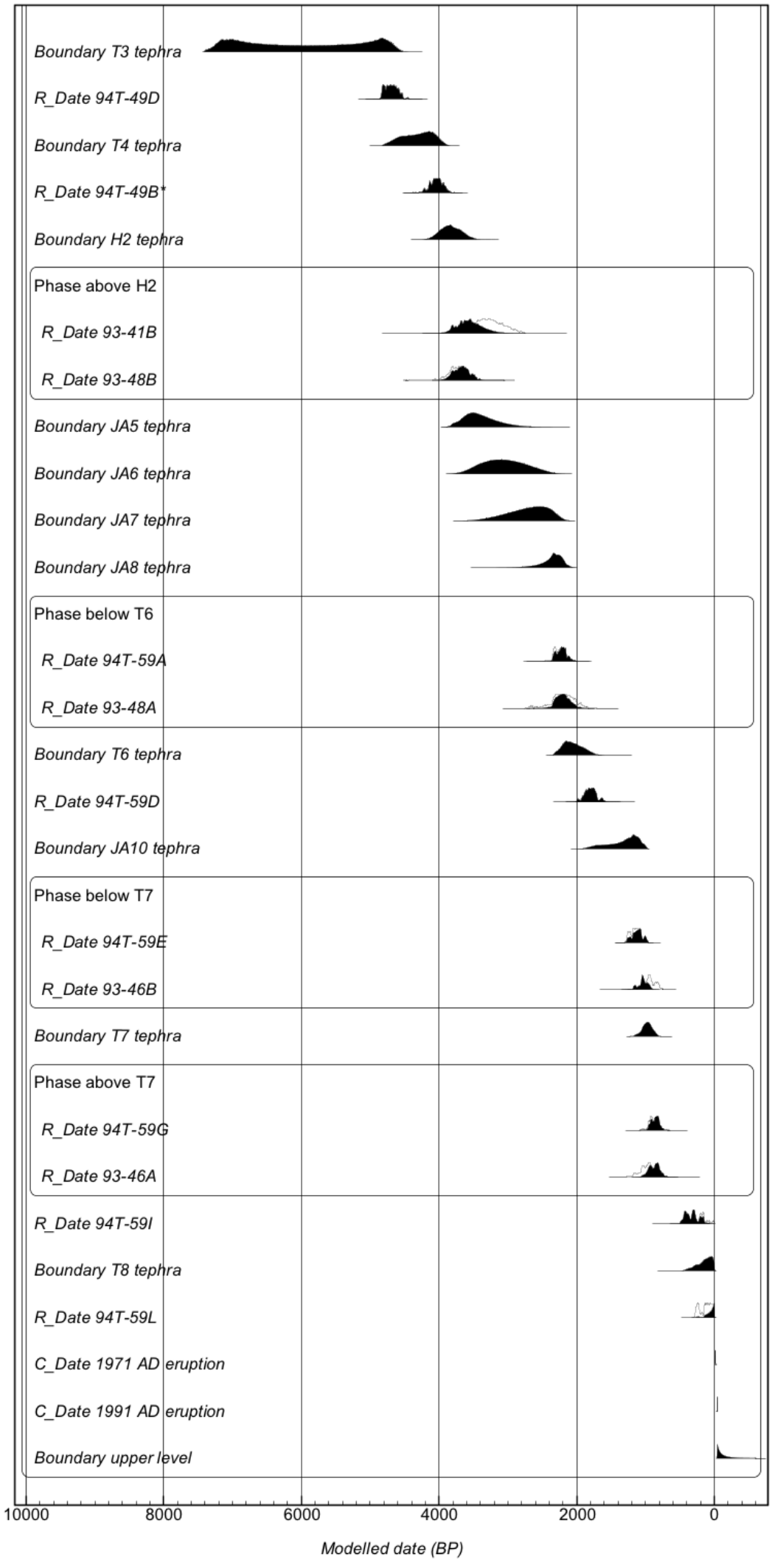
Boundary T3 tephra
R_Date 94T-49D
Boundary T4 tephra
R_Date 94T-49B*
Boundary H2 tephra
Phase above H2
R_Date 93-41B
R_Date 93-48B
Boundary JA5 tephra
Boundary JA6 tephra
Boundary JA7 tephra
Boundary JA8 tephra
Phase below T6
R_Date 94T-59A
R_Date 93-48A
Boundary T6 tephra
R_Date 94T-59D
Boundary JA10 tephra
Phase below T7
R_Date 94T-59E
R_Date 93-46B
Boundary T7 tephra
Phase above T7
R_Date 94T-59G
R_Date 93-46A
R_Date 94T-59I
Boundary T8 tephra
R_Date 94T-59L
C_Date 1971 AD eruption
C_Date 1991 AD eruption
Boundary upper level
10000
8000
6000
4000
2000
0
Modelled date (BP)

(b) Compiled H1 age constraints from Prieto et al. (2013)

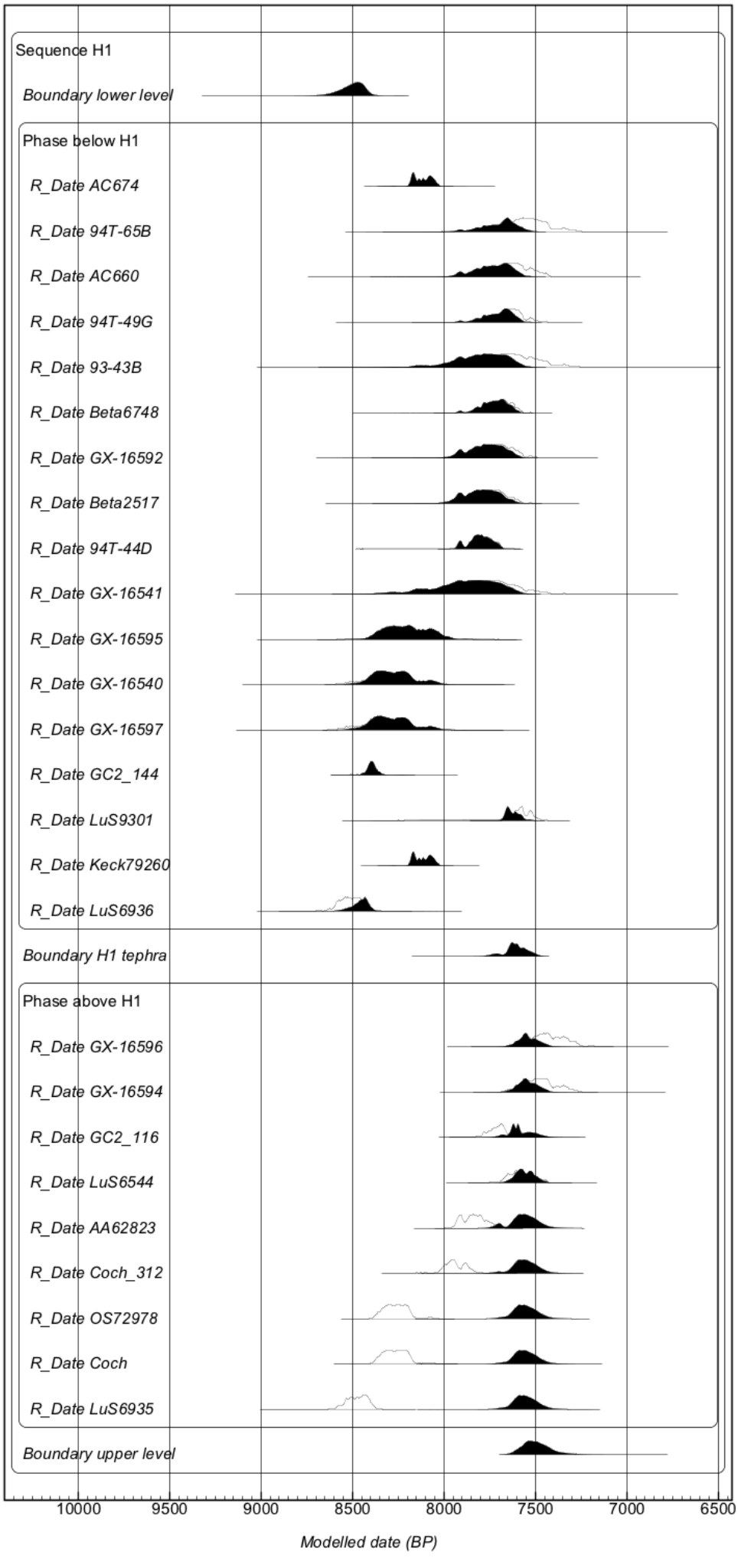

(c) Compiled H2 age constraints (Supplementary Table 4.2)

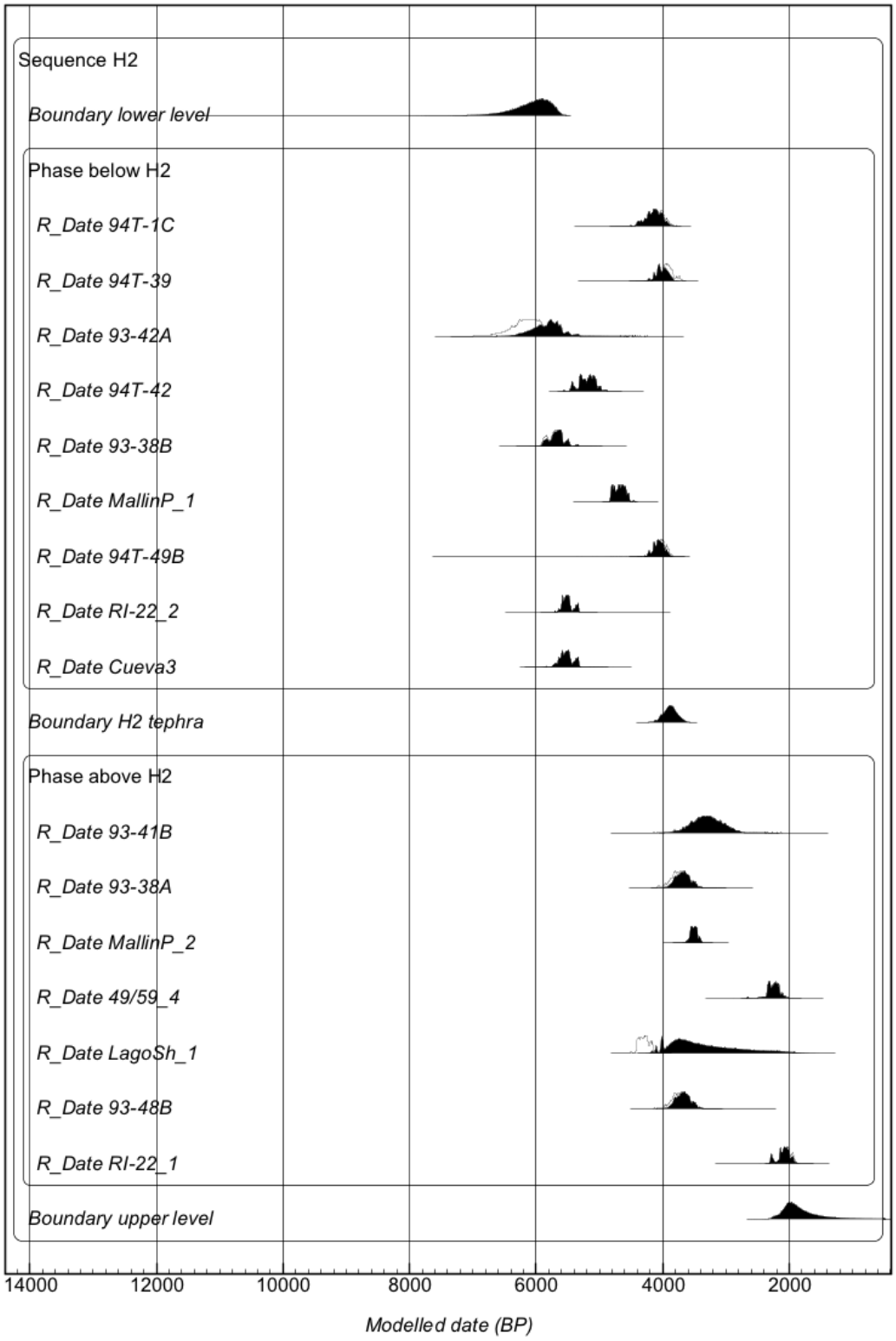

(d) Revised HW (Haberle and Lumley, 1998) eruptions (using only the tephras that are most likely to correlate)

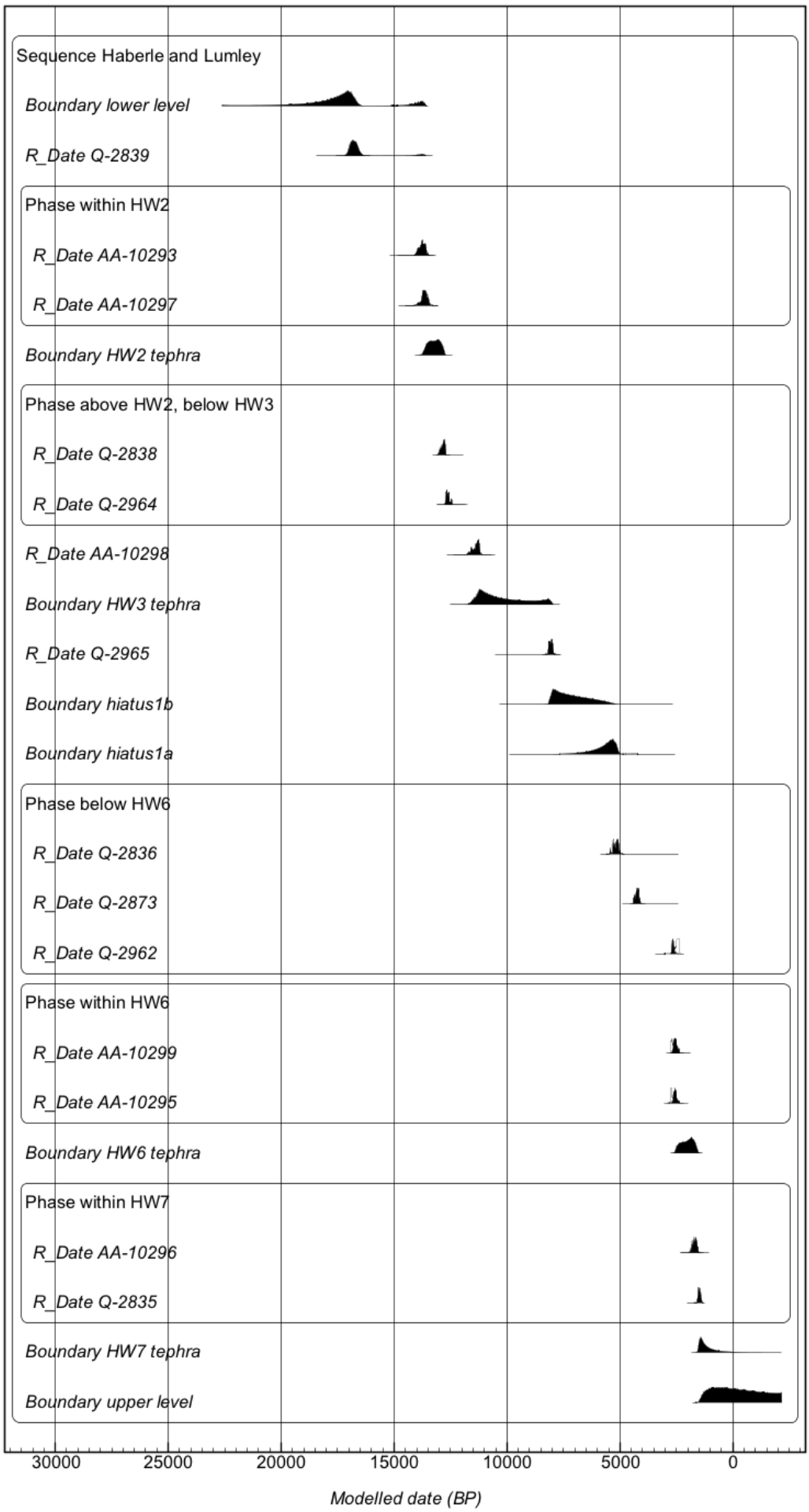

Supplementary File 5.1 List of volcanic centres in southern Chile and Argentina for which there is evidence of post-glacial activity, and the nature of ice cover on these edifices.

Volcano	Subregion[1]	Latitude (°N)	Longitude (°E)	Maximum elevation (m)	GVP number		Activity	Ice[2]
					Former	VNum		
Tupungatito	NSVZ	-33.40	-69.80	6000	1507-01=	357010	Historical	Caldera
San José	NSVZ	-33.78	-69.90	5856	1507-02=	357020	Historical	Glacier
Maipo	NSVZ	-34.16	-69.83	5264	1507-021	357021	Historical	Glacier
Palomo	TSVZ	-34.61	-70.30	4860	1507-022	357022	Holocene	Glacier
Caldera del Atuel	TSVZ	-34.65	-70.05	5189	1507-023	357023	Holocene	
Tinguiririca	TSVZ	-34.81	-70.35	4280	1507-03=	357030	Historical	Glacier
Risco Plateado[a]	TSVZ	-34.93	-70.00	4999	1507-024	357024	*Holocene*	
Infiernillo	TSVZ	-35.14	-69.83	2045	1507-041	357041	Holocene	
Planchón-Peteroa	TSVZ	-35.24	-70.57	4107	1507-04=	357040	Historical	Crater
Calabozos	TSVZ	-35.56	-70.50	3508	1507-042	357042	Holocene	
Descabezado Grande	TSVZ	-35.58	-70.75	3953	1507-05=	357050	Historical	Caldera
Cerro Azul	TSVZ	-35.65	-70.76	3788	1507-06=	357060	Historical	Glacier
San Pedro-Pellado	TSVZ	-35.99	-70.85	3621	1507-062	357062	Holocene	Crater
Laguna del Maule	TSVZ	-36.02	-70.58	3092	1507-061	357061	Holocene	
Nevado de Longaví	TSVZ	-36.19	-71.16	3242	1507-063	357063	Holocene	Glacier
Lomas Blancas	TSVZ	-36.29	-71.01	2268	1507-064	357064	Holocene	
Payún Matru	BA	-36.42	-69.20	3680	1507-066	357066	Holocene	
Resago	TSVZ	-36.45	-70.92	1890	1507-065	357065	Holocene	
Domuyo[a]	TSVZ	-36.58	-70.42	4709	1507-067	357067	*Holocene*	Glacier
Cochiquito Volcanic Group	BA	-36.77	-69.82	1435	1507-071	357071	Holocene	
Nevados de Chillán	TSVZ	-36.86	-71.38	3212	1507-07=	357070	Historical	Crater
Tromen	BA	-37.14	-70.03	3978	1507-072	357072	Historical	Glacier
Antuco	CSVZ	-37.41	-71.35	2979	1507-08=	357080	Historical	Glacier
Puesto Cortaderas[a]	BA	-37.57	-69.62	970	1507-073	357073	*Holocene*	
Trocon[a]	CSVZ	-37.73	-70.90	2500	1507-081	357081	*Holocene*	
Copahue	CSVZ	-37.85	-71.17	2997	1507-09=	357090	Historical	Crater
Callaqui	CSVZ	-37.92	-71.45	3164	1507-091	357091	Historical	Glacier
Laguna Mariñaqui	CSVZ	-38.27	-71.10	2143	1507-092	357092	Holocene	
Tolguaca	CSVZ	-38.31	-71.64	2806	1507-093	357093	Holocene	Glacier
Lonquimay	CSVZ	-38.38	-71.58	2865	1507-10=	357100	Historical	Crater
Tralihue[a]	BA	-38.52	-70.90	2345	1507-101	357101	*Post-glacial*	
Llaima	CSVZ	-38.69	-71.73	3125	1507-11=	357110	Historical	Glacier
Sollipulli	CSVZ	-38.97	-71.52	2282	1507-111	357111	Holocene	Caldera
Laguna Blanca[a]	BA	-39.02	-70.37	1700	1507-102	357102	Holocene	
Caburgua-Huelemolle	CSVZ	-39.25	-71.70	1496	1507-112	357112	Holocene	
Villarrica	CSVZ	-39.42	-71.93	2847	1507-12=	357120	Historical	Glacier
Quetrupillán	CSVZ	-39.50	-71.70	2360	1507-121	357121	Historical	Crater
Lanín	CSVZ	-39.63	-71.50	3747	1507-122	357122	Holocene	Glacier
Huanquihue Group	CSVZ	-39.88	-71.58	2139	1507-123	357123	Historical	
Mocho-Choshuenco	CSVZ	-39.93	-72.03	2422	1507-13=	357130	Historical	Caldera
Carrán-Los Venados	CSVZ	-40.35	-72.07	1114	1507-14=	357140	Historical	
Puyehue-Cordón Caulle	CSVZ	-40.59	-72.12	2236	1507-15=	357150	Historical	Caldera
Cerro Pantoja	CSVZ	-40.77	-71.95	2024	1507-152	357152	Holocene	
Antillanca Group	CSVZ	-40.77	-72.15	1990	1507-153	357153	Holocene	

Puntiagudo-Cordón Cenizos	CSVZ	-40.97	-72.26	2493	1507-16-	357160	Historical	Glacier
Osorno	CSVZ	-41.10	-72.49	2652	1508-01=	358010	Historical	Glacier
Tronador[a]	CSVZ	-41.16	-71.88	3491	1508-011	358011	*Post-glacial*	Glacier
Cayutué-La Viguería	CSVZ	-41.25	-72.27	506	1508-012	358012	Holocene	
Calbuco	CSVZ	-41.33	-72.61	2003	1508-02=	358020	Historical	Crater
Cuernos del Diablo	CSVZ	-41.40	-72.00	1862	1508-021	358021	Holocene	
Yate	SSVZ	-41.75	-72.40	2187	1508-022	358022	Holocene	Glacier
Hornopirén	SSVZ	-41.87	-72.43	1572	1508-023	358023	Holocene	
Apagado	SSVZ	-41.88	-72.58	1210	1508-024	358024	Holocene	
Crater Basalt Volcanic Field	BA	-42.02	-70.18	1359	1508-025	358025	Holocene	
Huequi	SSVZ	-42.38	-72.58	1318	1508-03=	358030	Historical	
Minchinmávida	SSVZ	-42.79	-72.44	2404	1508-04=	358040	Historical	Caldera
Chaitén	SSVZ	-42.83	-72.65	1122	1508-041	358041	Historical	
Corcovado	SSVZ	-43.18	-72.80	2300	1508-05=	358050	Historical	Glacier
Yanteles	SSVZ	-43.50	-72.80	2042	1508-050	358049	Holocene	Glacier
Palena Volcanic Group	SSVZ	-43.78	-72.47	1449	1508-051	358051	Holocene	
Melimoyu	SSVZ	-44.08	-72.88	2400	1508-052	358052	Holocene	Caldera
Puyuhuapi	SSVZ	-44.30	-72.53	524	1508-053	358053	Holocene	
Mentolat	SSVZ	-44.70	-73.08	1660	1508-054	358054	Historical	Caldera
Cay[a]	SSVZ	-45.06	-72.98	2090	1508-055	358055	*Post-glacial*	Glacier
Macá	SSVZ	-45.10	-73.17	2960	1508-056	358056	Holocene	Glacier
Cerro Hudson	SSVZ	-45.90	-72.97	1905	1508-057	358057	Historical	Caldera
Río Murta[a]	SSVZ	-46.17	-72.67	270	1508-058	358058	*Holocene*	
Lautaro	AVZ	-49.02	-73.55	3607	1508-06=	358060	Historical	Crater
Viedma	AVZ	-49.36	-73.28	1500	1508-061	358061	Historical	Caldera
Aguilera	AVZ	-50.33	-73.75	2546	1508-062	358062	Holocene	Glacier
Reclus	AVZ	-50.96	-73.58	1000	1508-063	358063	Historical	Crater
Palei-Aike Volcanic Field	BA	-52.00	-70.00	282	1508-08-	358080	Holocene	
Monte Burney	AVZ	-52.33	-73.40	1758	1508-07=	358070	Historical	Crater
Fueguino	AVZ	-54.95	-70.25	150	1508-09-	358090	Historical	

Unless otherwise stated, data are from Fontijn et al. (2014), after Siebert et al. (2010). VNum refers to the updated index system introduced by the Global Volcanism Program (GVP) online (http:/volcano.si.edu/).

[a] Volcanic centres for which the only evidence of Holocene/post-glacial activity is the presence of morphologically youthful-looking lava domes/flows or pyroclastic cones, for which no/only poor radiometric dates are available.

[1] SVZ = Andean Southern Volcanic Zone (N = North, T = Transitional, C = Central, S = South); AVZ = Andean Austral Volcanic Zone; BA = back-arc volcanoes (Stern, 2004).

[2] Data partly from Siebert et al. (2010) and Rivera and Bown (2013).

Supplementary File 5.2 Supporting data for the Ar-Ar dates obtained from Volcán Sollipulli lava and intrusion samples for this study.

Table SF5.2.1 Summary of $^{40}Ar/^{39}Ar$ incremental heating results for groundmass separates from Volcán Sollipulli lava and intrusion samples, analysed by the Servicio Nacional de Geología y Minería (SERNAGEOMIN) Geochronology Laboratory using the method described by Arancibia et al. (2006).

Samples	Sample number	Sampling location		Age spectrum				Isochron			
		Lat. (°S)	Long. (°W)	Plateau age (ka ± 2σ)[1]	MSWD[2]	Plateau nρ/N [3]	%^{39}Ar released	Inverse isochron age (ka ± 2σ)[1]	Isochron MSWD[2]	Isochron nρ/N [3]	$^{40}Ar/^{36}Ar$ intercept
Dykes in Sharkfin hyaloclastite subseq. truncated at contact with debris flow subseq.	S-210-7	38°58.469'	71°29.918'	350 ± 90	0.13	6/6	100	350 ± 120	0.16	6/6	295.6 ± 0.8
	S-209-12	38°58.878'	71°30.031'	700 ± 140	0.01	5/6	81.3	690 ± 240	0.014	5/6	295.6 ± 1.4
Circum-caldera sequence lava domes/coulées on SE caldera rim	S-218-1	38°59.114'	71°30.238'	26 ± 5	0.37	6/6	100	23 ± 8	0.19	6/6	298 ± 3
	S-225-6	38°58.802'	71°29.977'	68 ± 14	0.36	12/12†	100	61 ± 36	0.67	12/12†	294 ± 3
Isolated lavas on northeast flank (not described in this study)	S-211-12	38°55.036'	71°29.598'	70 ± 50	0.49	6/6	100	40 ± 40	0.67	6/6	297 ± 2
	S-211-7	38°55.428'	71°28.743'	240 ± 40	0.09	6/6	100	250 ± 140	0.11	6/6	290 ± 20

[1] Plateau ages are reported in this study; inverse isochron ages are listed for comparison only.

[2] Mean square weighted deviation. Values close to 1 indicate that scatter in the data is consistent with measurement errors only.

[3] Number of steps.

† Combination of two analyses by incremental heating.

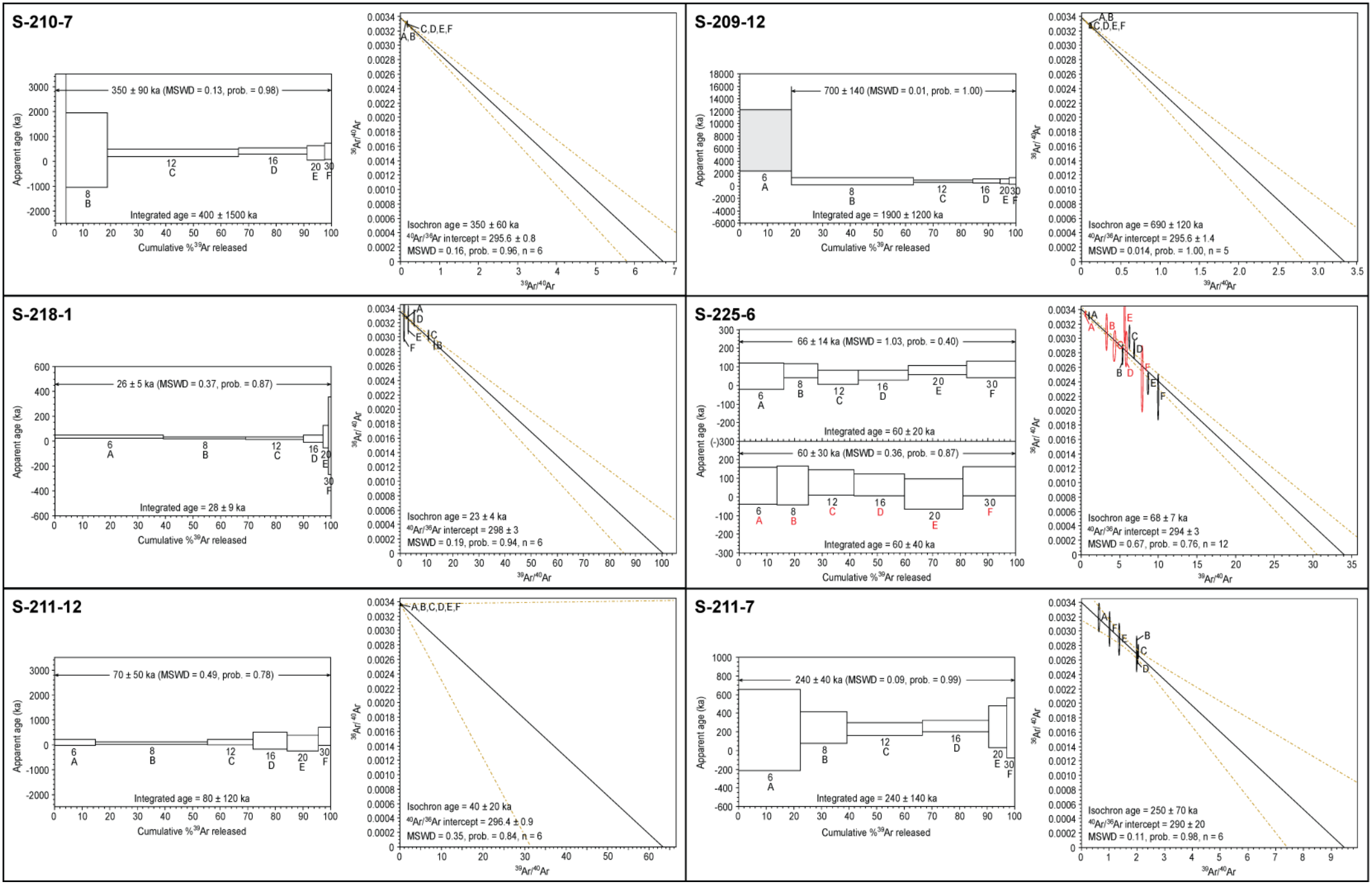

Figure SF5.2.1 $^{40}Ar/^{39}Ar$ incremental heating spectra and isochron plots for the samples listed in Table SF5.2.1. All errors 2σ.

Supplementary File 5.3 Volcán Sollipulli eruption radiocarbon dates and calibration/age models.

Table SF5.3.1 Published radiocarbon dates for Volcán Sollipulli eruption deposits.

Eruption	Sample number	Material dated	Conventional age (yr BP)	Reference
Chufquén	Naranjo93-6	Charred branch beneath lava flow	710 ± 60	Naranjo et al. (1993a)
Alpehué	Naranjo93-3	Charred trunk in PDC deposit	2850 ± 70	Naranjo et al. (1993a)
	Naranjo93-4	Charred branch in PDC deposit	2860 ± 60	Naranjo et al. (1993a)
	Naranjo93-5	Charred trunk in PDC deposit	2900 ± 60	Naranjo et al. (1993a)
	Poz-227	Charcoal below fall deposit	2900 ± 45	De Vleeschouwer (2002)
	SUERC-56148[a]	Charcoal in PDC deposit	2958 ± 35	Fontijn et al. (in review)

[a] from NERC Radiocarbon Facility grant NRCF010001 allocation number 1813.0414

Table SF5.3.2 New AMS radiocarbon dates for Volcán Sollipulli eruption deposits obtained by this study; analysis by Beta Analytic with acid-alkali-acid pre-treatment.

Eruption	Sample numbers		Sampling location		Material dated	d13C (‰)	d14C (‰)	Conventional age (yr BP)
	Study	Beta	Lat. (°S)	Long. (°W)				
Alpehué	S-301-02	297272	51°9.347’	72°5.620’	Charred trunk margin in PDC deposit	-22.9	-305.6 ± 3.5	2930 ± 40
Alpehué	S-306-01/4a	297273	51°21.868’	72°16.875’	Charred trunk margin in PDC deposit	-23.1	-302.2 ± 2.6	2890 ± 30

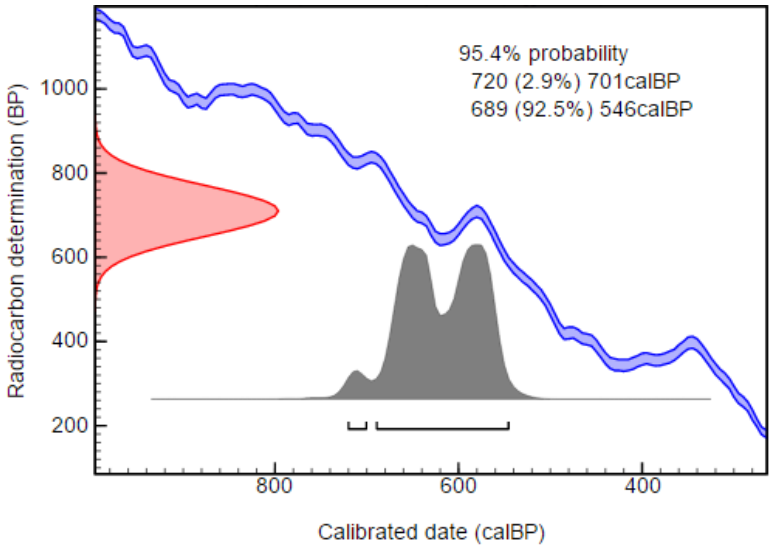

Red = probability density function (pdf) of conventional age;
blue = calibration curve (SHCal13); grey = pdf of calibrated date

Figure SF5.3.1 Calibration of the Chufquén eruption radiocarbon date from Naranjo et al. (1993a) (Table SF3.1) by Bayesian analysis using OxCal v4.2.4 (Bronk Ramsey, 2009) with the SHCal13 atmospheric calibration curve (Hogg et al., 2013).

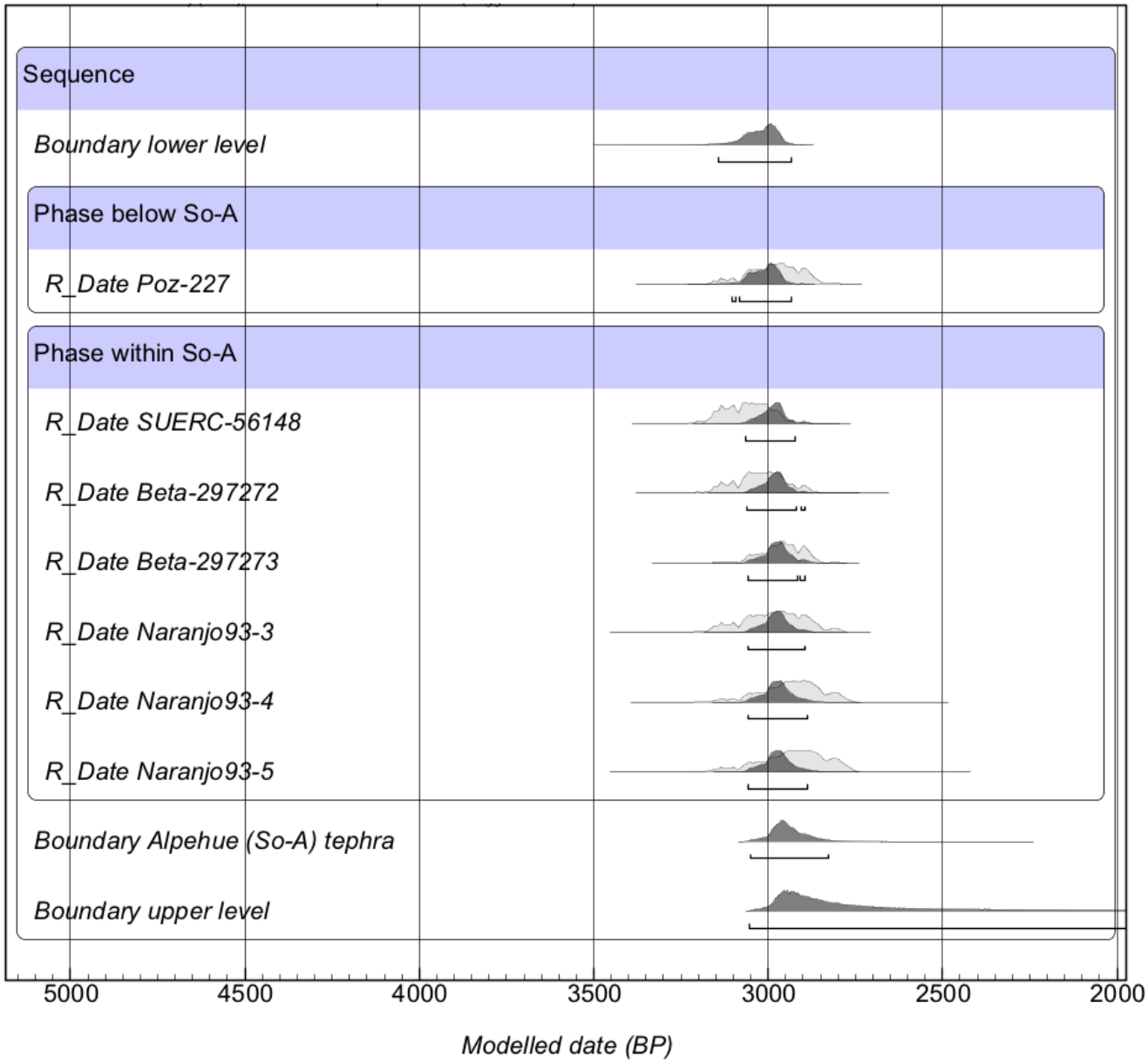

Figure SF5.3.2 Output of a Bayesian model applied to all published radiocarbon dates for the Alpehué eruption (listed in Tables SF5.3.1 and SF5.3.2), computed using OxCal v4.2.4 (Bronk Ramsey, 2009) with the SHCal13 atmospheric calibration curve (Hogg et al., 2013). The pale grey probability distributions are the unmodelled calibrated dates; the overlying dark grey distributions are the modelled equivalent (i.e., the dates resulting from Bayesian analysis considering the stratigraphic constraints). The bars indicate the 2σ confidence interval range for each modelled date. Note that the radiocarbon dates are all in one phase stratigraphically below the Alpehué eruption (Boundary: Alpehue (So-A) tephra), as they are all for carbon incorporated within deposits from the eruption.

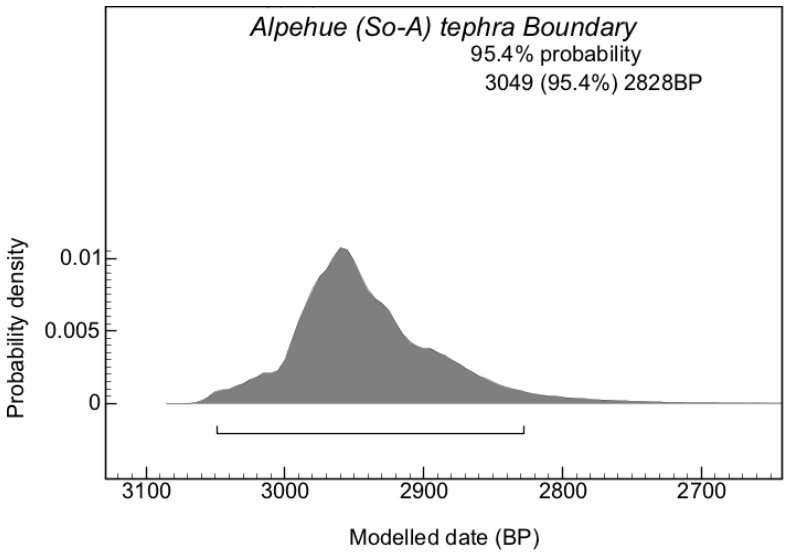

Figure SF5.3.3 Probability distribution for the modelled age of the Alpehué eruption (from Figure SF5.3.2), with 2σ confidence interval.

Supplementary Table 4.1 Occurrences of tephra deposits attributed to Volcán Hudson.

Environment	Location			Core/site			Tephra properties							Age constraints			Inferred eruption		References
	Placename	Latitude (°N)	Longitude (°E)	ID code	Environment	Core type	Tephra ID code	Depth of base from top of core/section (cm)	Thickness (cm)	Colour	Grain size (mm)	Chemical analysis	Composition	Dating method	14C yr BP	Calendar age (cal yr BP)	Original	This study	
Soil/alluvial sections	Río Baguales	*-45.51*	*-72.09*	94T-1			1C			yellow	pumice and ash	bulk XRF	trachydacite	charred wood 14C	<3790 ± 80		H2		31
	Laguna Alta	-45.5369	-72.7047	3, 4			HUD110					glass EPMA	basaltic trachyandesite				1991-P1		34
	Road X-608	-45.6294	-72.1467	47													H2		34
	Road X-659	-45.6347	-71.8989	48													H2		34
	Road X-608	-45.6528	-72.4650	43													H2		34
	Road X-608	-45.6647	-72.3958	44													H2		34
	Road X-608	-45.6658	-72.2042	46													H2		34
	Lago Frio	-45.6731	-71.9639	49													H2		34
	Lago Atravesado	-45.6867	-72.2644	45													H2		34
	Road X-686	-45.7631	-72.1564	14													H2		34
	Route 7	-45.7633	-71.9736	50													H2		34
	Lago Elizalde	-45.7747	-72.1742	13													H2		34
	Road X-674	-45.7800	-72.1169	16													1991-P2 H2		34 34
	Río Paloma	-45.7919	-72.4392	6													1991-P2 H2		34 34
	Laguna Verde (near Elizalde)	-45.7964	-72.2081	12													H2		34
	Lago Caro	-45.7969	-72.4908	5													H2		34
	Lago Elizalde	*-45.80*	*-72.22*	94T-39/66			66B			grey	fine scoria MP=40	bulk XRF	basaltic andesite	charred wood 14C charred wood 14C	<2230 ± 70 <3670 ± 70		T6 H2		31 31
	Road X-684	-45.8183	-72.4200	7													1991-P2 H2		34 34
	Route 7 and 245 junction	-45.8403	-71.8711	51													H2		34
	Road X-686	-45.8442	-72.2644	11													H2		34
	Road X-684	-45.8533	-72.3725	8													H2		34
	Laguna Paloma	-45.8703	-72.0525	15													H2		34
	Road X-686	-45.8836	-72.2861	10													H2		34
	Río Paloma	-45.9108	-72.3172	9													H2		34
	Route 7	-45.9825	-71.9181	52													H2		34
	Cuesta del Diablo	-46.0989	-72.0500	53													H2		34
	Río Ibáñez	-46.1192	-72.5239	32													1991-P2		34
	Río Ibáñez	-46.1228	-72.5600	17	roadcut		HUD141, 143, 149, 155 (units 2A,B,D) HUD203, 204					bulk XRF bulk XRF, glass EPMA	trachyandesite trachydacite				1991-P2 H2 H1		34 34 34
		-46.12	*-72.56*	94T-45	roadcut												1991-P2		31
								150 244	30	yellowish white grey	pumice and coarse ash; MP=75 pumice and ash; MP=40; MAL=~15	bulk XRF, INAA	trachydacite	soil 14C soil 14C	>3155 ± 185; <5360 ± 245 >5360 ± 245; <6865 ± 220		H2 H1		31 31
		-46.1231	-72.5603	RI	roadcut		RI4	12	40	grey	pumice and medium ash; MP=20	bulk XRF/ICP-MS, glass EPMA	trachyandesite; (trachy)dacite glass					1991-P2	This study
							RI3	214	39	yellow-orange	pumice and medium ash; MP=50; ML<10	bulk XRF/ICP-MS, glass EPMA	trachydacite; trachydacite to rhyolite glass					H2	This study
							RI2	345	81	grey to buff	fine ash to pumice; acc. lapilli	bulk XRF/ICP-MS, glass EPMA	trachyandesite; mostly trachydacite glass					H1	This study
							RI1	395	3	yellow	ash	glass EPMA	trachydacite					new	This study
	Cerro Castillo	-46.1256	-72.1933	42													1991-P2 H2		34 34
	Cerro Castillo	-46.1289	-72.1661	41													1991-P2 H1		34 34
	Bosque Muerto	-46.1292	-72.4778	33													1991-P2		34
	Bosque Muerto	-46.1325	-72.4589	34													1991-P2 H2 H1		34 34 34
	Río Ibáñez	-46.1336	-72.4264	36													1991-P2		34
	Route 7	-46.1367	-72.5961	31													1991-P2 H2 H1		34 34 34
	Laguna Verde (near Ibáñez)	-46.1558	-72.3256	38													1991-P2 H2 H1		34 34 34
	Route 7	-46.1569	-72.2581	39													1991-P2 H2 H1		34 34 34
	Río Las Horquetas	-46.1594	-72.3619	37													1991-P2 H2		34 34
	Route 7	-46.1606	-72.6328	30													1991-P2		34
	Lago Verde	-46.16	-72.38	94T-44			44E 44A,B,C					bulk XRF bulk XRF, INAA	trachydacite trachyandesite	charcoal 14C	<7010 ± 140		H2 H1		31 31
	Lago Lapparent			94T-42										charcoal 14C	<4590 ± 70		H2		31
	Río Cajón	-46.1639	-72.6867	29													1991-P2 H2 H1		34 34 34
	Río Cajón	-46.1650	-72.7003	28			HUD207-210 (units 2A-D)					bulk XRF, glass EPMA	trachyandesite				1991-P2		34
	Laguna Cofré	-46.1789	-72.7389	27			HUD206 (unit 2C)					bulk XRF	trachyandesite				1991-P2		34
	Road X-723	-46.1897	-72.1772	40													1991-P2 H2		34 34
	Río Cofré	-46.19	-72.80	94T-47				94	24	yellowish white	pumice and coarse ash; MP=30-48; ML=22; MAL=20						H2		31
								199	95	grey	pumice and ash; MP=45; ML=18						H1		31
	Río Murta	-46.1931	-72.8025	25													1991-P2 H2 H1		34 34 34
	Río Murta	-46.1933	-72.7836	26													H2 H1		34 34
	Río Murta	-46.1942	-72.8039	24													1991-P2 H1		34 34

	Road X-65	-46.1950	-72.0239	54												1991-P2		34
																H2		34
	Río Murta	-46.2628	-72.7981	23												1991-P2		34
																H1		34
	Río Murta	-46.3211	-72.7817	22												1991-P2		34
																H1		34
	Río Murta	-46.4031	-72.7181	21												H1		34
	Bahía Murta	-46.4903	-72.7189	20												1991-P2		34
																H1		34
	Río Jeinimeni	-46.5303	-71.6656	2												1991-P2		34
	Bahía Murta	-46.5383	-72.7167	19												1991-P2		34
	Road X-763 junction	-46.5481	-71.7978	55												1991-P2		34
	Fachinal	-46.56	-71.95	94T-93/38			38		yellow	pumice	bulk XRF	trachydacite	soil 14C	>3495 ± 105; <4980 ± 105		H2		31
	Bahía Murta	-46.5939	-72.6914	18												H1		34
	San Lorenzo	*-47.5?*	*-72.4?*		roadcut			~10	yellow-orange							H1		35
	Altos de Boqueron	-53.28	-70.17		organic soil		90-14G		10				14C	>6575 ± 110; <7550 ± 120		H1		36,37
	Arroyo Catalanes	-54.45	-67.50	Acd-2007	alluvial sediment			134	6							H1?		20
	Túnel 1	-54.87	-67.98		excavation				1				14C	>6300 ± 190; <6680 ± 210; <6830 ± 140; <6900 ± 70; <6980 ± 110		H1		37,38
Peat bog cores or sections	Mallín Pollux	-45.69	-71.84		fen core	piston	*MP-473*	485	25	greenish			sedge 14C	>3320 ± 40; <4180 ± 35		H2		11
							MP-1130	1151	42				sedge/moss 14C	>14100 ± 60; <15250 ± 60		Ho		11
	Juncal Alto	*-46.25*	*-71.94*	49/59	bog section		49K					bulk XRF	trachyandesite			1971 (T9)		31
							59K					bulk XRF	trachyandesite	peat 14C	>140 ± 50; <280 ± 70	T8		31
							59F					bulk XRF	trachydacite	soil 14C	>1030 ± 60; >1090 ± 100; <1085 ± 75; <1270 ± 60	T7		31
							59C					bulk XRF	basaltic andesite	peat 14C	>1910 ± 70; <2235 ± 130; <2290 ± 70	T6		31
							49A		26	yellowish white		bulk XRF	trachydacite	peat 14C	>2290 ± 70; <3740 ± 60	H2 (T5)		31
							49C			grey	ash	bulk XRF	trachydacite	peat 14C	>3740 ± 60; <4200 ± 50	T4		31
										grey	ash			peat 14C	>4200 ± 50; <6330 ± 90	T3		31
							49F			grey	ash	bulk XRF	trachyandesite	peat 14C	>6330 ± 90; <6840 ± 90	H1 (T2)		31
							49H			grey	ash	bulk XRF	trachyandesite	peat 14C	>6840 ± 90; <6980 ± 60	T1		31
		-46.2515	-71.9438	JA	bog section		JA12	6	~4	white	medium lapilli	glass EPMA	(trachy)dacite				1991	This study
							JA11	31	1	white	ash	glass EPMA	trachydacite				T8	This study
							JA10	54	1	buff	ash	glass EPMA	basaltic trachyandesite				new	This study
							JA9	68	12	white	fine ash	glass EPMA	basaltic (trachy)andesite to (trachy)andesite				T6	This study
							JA8c	72	1	buff	medium ash	glass EPMA	trachyandesite				new	This study
							JA8b	73.5	1	pale grey	fine ash	glass EPMA	basaltic (trachy)andesite and (trachy)andesite				new	This study
							JA8a	75	1	grey	coarse ash	glass EPMA	basaltic (trachy)andesite				new	This study
							JA7	92	1	grey	coarse ash	glass EPMA	basaltic trachyandesite				new	This study
							JA6	114	3	grey	medium ash to fine lapilli	glass EPMA	basaltic andesite				new	This study
							JA5	128	2	grey	fine ash	glass EPMA	basaltic trachyandesite				new	This study
							JA4	146	17	yellow to white	fine to medium lapilli	glass EPMA	trachydacite to rhyolite				H2	This study
							JA3	160	6	grey to white	fine ash	glass EPMA	trachydacite				T4	This study
							JA2	174	6	grey to white	fine ash	glass EPMA	trachydacite				T3?	This study
							JA1	202	6	grey	coarse ash to fine lapilli	glass EPMA	basaltic (trachy)andesite to trachydacite				H1	This study
	Cerro Teodoro	*-46.64*	*-72.36*	94T-65			65C		>50	grey	pumice and ash	bulk XRF	trachyandesite	peat 14C	<6720 ± 140			31
	Mallín Casanova	*-47.61*	*-72.94*	MCa	bog/sediment core	piston	*MCa-310*	310	~10					charcoal 14C	<7165 ± 25			14
	Río Rubens	-52.08	-71.52	Río Rubens	bog core		*RR-178*	178						peat 14C	>5310 ± 75; <7480 ± 100			15
	Laguna Blanca	-52.50	-71.35	90-04	bog section				3					14C	>6040 ± 205; <6930 ± 120			36,37
	Canal Gajardo	-52.80	-72.92	GC-2	bog core	Wardenaar, Russian	*GC-2-134*	134	0.1-0.2					peat 14C	>6915 ± 40; <7635 ± 40			16,37
	Route 257	-52.97	-69.42	90-22/90-23	bog section		90-22; 90-23G		15			bulk XRF, glass EPMA	trachydacite	14C	<7015 ± 215; <7535 ± 120			36,37
	Punta Arenas	-53.15	-70.95	PA	bog core		*PA-420*	420	2					peat 14C	>5940 ± 100; <9240 ± 140			17.37
	Reprasa Porvenir	-53.30	-70.33		bog section		93-28G		6									37
	Río San Martin	-53.38	-68.77		bog section		93-16		15									37
	Isla Dawson	-53.50	-70.58	Est. Esmeralda II	bog core	Russian	*EstEsmII-121*	121	2	pale green/brown								18,37
	Río Chico	-53.55	-68.70		bog section		93-21G		20									37
	Puerto del Hambre	-53.60	-70.92	PBr2	bog core	Wardenaar, Russian	*Pbr2-309*	310	2-3			glass EPMA	rhyolite			H1		16.37
				P. del Hambre II	bog core	Russian	*PdHII-507.5*	508	1							H1		18
	Cabo Cameron	-53.68	-69.85		bog section		93-25		6							H1		37
	Río Rushpen	-53.75	-69.25		bog section		90-12		10					14C	>6625 ± 110; <7435 ± 120	H1		36,37
	Karukinka	-53.8600	-69.5764	KAR12-PB01B	bog core	Russian	*KAR12-PB01B-428*	428						bog moss 14C interp.	6850 ± 160	H1		19
	Río Turbio	-54.53	-67.20		bog section											H1?		20
	Valle de Andorra	-54.66	-68.42		bog core		*And-515*	520	10	grey						H1?		21
	Las Cotorras	-54.69	-68.05		bog core	Russian	*LasCot-475*	~475			~0.015	glass EDS	trachydacite	peat 14C	>7043 ± 47	H1?		22
	Valle Carbajal	-54.73	-68.20	Oyarzun bog	bog core		*Oy-350*	360	20					peat 14C	<7640 ± 80	H1?		23
	Isla de los Estados	-54.74	-64.33	Lago Galvarne	bog core	Russian	*LG-540*	~540						peat 14C	<8130 ± 55	H1		39,40
				Galvarne ridge	bog section		*GM-457.5*	458	1					peat 14C	>6490 ± 55	H1		41
	Puerto Haberton	-54.87	-67.88		bog core		*PH1-670*	670						peat 14C	>6390 ± 70; <8350 ± 90	H1?		24
		-54.87	-67.88		bog core		*PH2-560*	~560								H1?		24
		-54.90	-67.17	Haberton	bog core		*Harb-678*	678						peat 14C	>7460 ± 70; <8190 ± 110	H1		15
		-54.9	-67.2	Haberton	bog core	Wardenaar, Russian	*Harb-682.6*	682.6				bulk ICP-OES, ICP-MS				H1		25
Lake sediment cores	Laguna Facil	-44.32	-74.28	Fac	sediment core	piston	Fac-3	~35				glass EPMA	basaltic andesite			Hudson		1
							Fac-2	~470				glass EPMA	basaltic andesite to andesite	14C	10080 ± 100	HW3		1
							Fac-1	~545				glass EPMA	dacite	14C	12480 ± 100	HW1		1
	Laguna Oprasa	-44.35	-73.65	Opr	sediment core	piston	Opr-8	~95				glass EMPA	basaltic andesite			HW7		1
							Opr-7	~160				glass EMPA	basaltic andesite to andesite	14C	<3875 ± 35	HW6		1
							Opr-6	~235				glass EMPA	andesite to dacite			Hudson		1
							Opr-5	~350				glass EMPA	basaltic andesite	14C	<7750 ± 55	H1 (HW4)		1
							Opr-4	~440				glass EMPA	dacite			Hudson		1
							Opr-3	~460				glass EMPA	basaltic andesite to andesite	14C	9830 ± 90	HW3		1
							Opr-2	~480								Hudson		1
							Opr-1	~570				glass EMPA	basaltic andesite	14C	12390 ± 120	HW1		1
	Lago Shaman	-44.43	-71.18	LS0604A	sediment core	piston	LS0604A-v	~708?	2			bulk ICP-MS		14C	>18474 ± 100; <18951 ± 50	Ho		7,8

Laguna Lofel	-44.88	-74.40	Lof	sediment core	piston	Lof-4	~720				glass EMPA	dacite				HW3		1
						Lof-3	~795				glass EMPA	basaltic andesite to dacite				HW2?		1
						Lof-2	~870				glass EMPA	basaltic andesite to dacite				HW2?		1
						Lof-1	~895				glass EMPA	andesite				HW1?		1
Laguna Lincoln	-45.37	-74.07	Lin	sediment core	piston	Lin-4	~20				glass EMPA	basaltic andesite				HW6		1
						Lin-3	~190				glass EMPA	basaltic andesite				HW3		1
						Lin-2	~270				glass EMPA	dacite				HW2		1
						Lin-1	~290				glass EMPA	basaltic andesite				HW1		1
Lago Tranquilo	-45.46	-71.75	PC1203A	sediment core	piston	*PC1203AT5-15*	~510	10								H2		10,42
						PC1203AS9		(9 tephras)								Hudson?		10,42
						PC1203AT12-5	~1240	65		≤20	bulk, glass ICP-MS					Ho		10,42
			PC1203B	sediment core	piston	*PC1203BT4-48*	~444	9								H2		10,42
						PC1203BT11-5	~1135	60		≤20						Ho		10,42
			PC1203C	sediment core	piston	*PC1203CT1-51*	~248	6								H2		10,42
						PC1203CT5-35	~570	70		≤20						Ho		10,42
			PC1203D	sediment core	piston	*PC1203DT2-14*	~218	7								H2		10,42
						PC1203DT6-94	~728	68		≤20						Ho		10,42
Lago El Toro	*-45.53*	*-71.85*	PC1002B	sediment core	piston	*PC1002BT3-5*	~310	10								H2		10,42
						PC1002BS9		(9 tephras)								Hudson?		10,42
						PC1002BT7-20	~745	50		≤20	bulk, glass ICP-MS					Ho		10,42
			PC1002C	sediment core	piston	*PC1002CT3-21*	~325	7								H2		10,42
						PC1002CT5-32	~855	35		≤20						Ho		10,42
Laguna Escondida (Aysén)	-45.53	-71.82	ESC-09-5	sediment core	gravity	ESC-T1	30.5	0.3	black	<2			14C, nuclide		1000	Hudson?		9
						ESC-T2	45	1	dark grey	fine			14C, nuclide		1550	Hudson?		9
						ESC-T3	51	5.5	black	<2	bulk XRF	basalt	14C, nuclide		1790	Hudson?		9
						ESC-T4	53.5	1.5	black	<2	bulk XRF	basaltic andesite	14C, nuclide		1860	Hudson		9
						ESC-T5	56.5	0.2	black	<2			14C, nuclide		2000	Hudson?		9
						ESC-T6	68	2	black	<2	bulk XRF	basaltic andesite	14C, nuclide		2250	T6?		9
Lago Mellizas	*-45.54*	*-71.81*	PC1106A	sediment core	piston	*PC1106AT3-0*	~305	10								H2		10,42
						PC1106AS9		(9 tephras)								Hudson?		10,42
						PC1106AT7-34	~768	68		≤20			organics 14C	>13810 ± 110		Ho		10,42
			PC1106B	sediment core	piston	*PC1106BT2-60*	~265	10								H2		10,42
						PC1106BT6-90	~720	60		≤20			organics 14C	<14670 ± 45; <14800 ± 90		Ho		10,42
Lago Unco	*-45.57*	*-71.72*	PC1103D	sediment core	piston	*PC1103DT3-16*	~322	12								H2		10,42
						PC1103DT8-60	~890	60		≤20						Ho		10,42
			PC1103E	sediment core	piston	*PC1103ET3-63*	~368	10								H2		10,42
						PC1103ES9		(9 tephras)								Hudson?		10,42
						PC1103ET9-8	~938	60		≤20	bulk, glass ICP-MS		organics 14C	>13430 ± 50; >13720 ± 45; <14345 ± 45		Ho		10,42
Lago Castor	-45.60	-71.78	CAS-09-1	sediment core	gravity	CAS-T1	23	0.3	black	<2			14C, nuclide		1150-1350	Hudson?		9
						CAS-T2	29	1	dark grey	fine			14C, nuclide		1550	Hudson?		9
						CAS-T3	34	2	black	<2	bulk XRF	basaltic andesite	14C, nuclide		1790	Hudson?		9
						CAS-T4	37	1.5	black	<2	bulk XRF	basaltic andesite	14C, nuclide		1860	Hudson		9
						CAS-T5	43	0.5	black	<2			14C, nuclide		2000	Hudson?		9
						CAS-T6	49	1	black	<2	bulk XRF	basaltic andesite	14C, nuclide		2259	T6?		9
						CAS-T7	65	0.2	black	<2			14C, nuclide		3650	Hudson?		9
						CAS-T8	70	> 2	grey-white	<2	bulk XRF	dacite	14C, nuclide		3900	H2		9
Lago Thompson	-45.6408	-71.7853	Thompson08-E	sediment core	gravity	*Thompson08E-49*	~49	~1					sedi. 14C (corrected)		>3-148; <109-319		Hudson?	27
						Thompson08E-57	~57	<1					sedi. 14C (corrected)		>3-148; <109-319		Hudson?	27
						Thompson08E-109	~107	~4					sedi. 14C (corrected)		>314-399; <729-934		Hudson?	27
Lago Churrasco	*-45.69*	*-71.82*	PC1201A	sediment core	piston	*PC1201AT2-19*	~228	18								H2		10,42
						PC1201AS9		(9 tephras)								Hudson?		10,42
						PC1201AT6-37	~670	65		≤20	bulk, glass ICP-MS					Ho		10,42
						(additional tephras likely from Hudson in both cores, but no published data)												10,42
			PC1201B	sediment core	piston	*PC1201BT1-59*	~168	18								H2		10,42
						PC1201BT6-90	~720	60		≤20						Ho		10,42
Laguna Burgos	-45.7095	-72.2149	Burgos07	sediment core	gravity	*Burgos07-9*	~9	~1					leaf 14C	<90 ± 30			Hudson?	27
						Burqos07-51	~51	~1					sedi. 14C (corrected)		<0-185		Hudson?	27
						Burgos07-92	~93	~2					sedi. 14C (corrected)		>0-185; <100-255		Hudson?	27
Lago Quijada/Espejo	*-45.71*	*-71.91*	PC1001A	sediment core	piston	*PC1001AT4-34*	~473	78								Ho		10,42
			PC1001B	sediment core	piston	*PC1001BT3-88*	~430	85		≤20						Ho		10,42
						(additional tephras likely from Hudson in all cores, but no published data)												
			PC1001C	sediment core	piston	*PC1001CT2-25*	~235	20								H2		10,42
						PC1001CHo	(deformed)			≤20						Ho		10,42
			PC1001D	sediment core	piston	*PC1001DT2-68*	~278	20								H2		10,42
						PC1001DS9		(9 tephras)								Hudson?		10,42
						PC1001D10-94	~1138	88		≤20			organics 14C	>14220 ± 45		Ho		10,42
			PC1001E	sediment core	piston	*PC1001E-Ho*							organics 14C	<14735 ± 30		Ho		10,42
Lago Élida	*-45.84*	*-71.72*	PC1105B	sediment core	piston	*PC1105BT1-62*	~168	12		≤10						H2		10,42
						PC1105BS9		(9 tephras)								Hudson?		10,42
						PC1105BT7-9	~718	18		≤10	bulk, glass ICP-MS					Ho		10,42
Laguna Miranda	-46.13	-73.43	Mir	sediment core	piston	*Mir-138*	138	0.1					interpolation		1230	Hudson		2
						Mir-139	139	0.3					interpolation		1240	Hudson		2
						Mir-141	141	0.5					interpolation		1270	Hudson		2
						Mir-178	178	0.2					interpolation		1610	Hudson		2
						Mir-180	180	0.2					interpolation		1620	Hudson		2
						Mir-3	189	1.5	olive		glass EPMA	andesite	14C	>1160 ± 30; <2710 ± 35		HW7		1,2
						Mir-223	223	0.1					interpolation		2030	Hudson		2
						Mir-224	224	0.3					interpolation		2040	Hudson		2
						Mir-260	260	0.8					interpolation		2400	Hudson		2
						Mir-307	307	0.3					interpolation		2750	Hudson		2
						Mir-2	311	0.8	olive		glass EPMA	basaltic andesite	14C	>2710 ± 35; <4250 ± 35		HW6		1,2
						Mir-316	316	0.1					interpolation		2900	Hudson		2
						Mir-325	325	0.2					interpolation		3070	Hudson		2
						Mir-342	342	0.6					interpolation		3300	Hudson		2
						Mir-1	389	8	olive grey		glass EPMA	dacite	14C	>2710 ± 35; <4250 ± 35		H2 (HW5)		1,2
						Mir-407	407	0.2					interpolation		4170	Hudson		2
						Mir-423	423	0.5					interpolation		4390	Hudson		2
						Mir-428	428	0.3					interpolation		4480	Hudson		2
						Mir-443.5	444	1.3					interpolation		4680	Hudson		2

							Mir-446.5	447	1					interpolation		4710	Hudson		2
							Mir-450	450	0.1					interpolation		4750	Hudson		2
							Mir-454	454	0.2					interpolation		4810	Hudson		2
							Mir-456	456	0.7					interpolation		4830	Hudson		2
	Laguna Cofre	*-46.18*	*-72.74*		sediment core		(visible tephra and numerous cryptotephra layers, mostly from Hudson)												43
	Laguna Stibnite	-46.42	-74.40	Stb	sediment core	piston	Stb-4	~45				glass EPMA	basaltic andesite to dacite	14C	1830 ± 75		HW7		1
							Stb-3	~75				glass EPMA	basaltic andesite to andesite	14C	2600 ± 60		HW6		1
							Stb-2	~235				glass EPMA	basaltic andesite	14C	9995 ± 85		HW3		1
							Stb-1	~270				glass EPMA	basalt	14C	11965 ± 100		HW2		1
	Laguna Six Minutes	-46.42	-74.33	Six	sediment core	piston	Six-4	~60				glass EPMA	andesite to dacite	14C	1605 ± 55		HW7		1
							Six-3	~85				glass EPMA	basaltic andesite to andesite	14C	2650 ± 55		HW6		1
							Six-2	~200				glass EPMA	basaltic andesite	14C	9930 ± 85		HW3		1
							Six-1	~225				glass EPMA	basaltic andesite	14C	11855 ± 120		HW2		1
	Laguna Marcelo	-46.47	-73.17	Mar	sediment core	piston	Mar-2	~25				glass EPMA	basaltic andesite to dacite				HW7		1
							Mar-1	~45				glass EPMA	basaltic andesite				HW6		1
	Laguna Trapial	-46.7136	-72.7000	Trapial08-F	sediment core	gravity	*Trapial08F-66*	~67	~2					twig remain 14C	2930 ± 30			Hudson?	27
							Trapial08F-88	~88	~1					sedi. 14C (corrected)		>2757-2982; <4362-4772		Hudson?	27
							Trapial08F-97	~98	~2					sedi. 14C (corrected)		>>2757-2982; <4362-4772		Hudson?	27
							Trapial08F-108	~109	~2					sedi. 14C (corrected)		>4362-4772; <5942-6092		Hudson?	27
	Lago Augusta	-47.08	-72.38	PC0604SC1, PC0903A, PC0903B	sediment core	piston	*Aug-271*	275	8			bulk XRF?	andesite	14C	>8625 ± 35; <8890 ± 35		H1		6,35
	Laguna Portazuela	*-47.1?*	*-72.4?*		sediment core		(visible tephra and numerous cryptotephra layers, mostly from Hudson)												43
	Lago Edita	*-47.15*	*-72.37*	PC0902A	sediment core	*piston?*	*PC0902AT3-95*	*~395*	~1			bulk XRF?	dacite				H2		35
							CS-2715	*~738*	~18			bulk XRF?	andesite				H1		35
	Lago Pepa	*-47.15*	*-72.35*	PC0901A	sediment core	*piston?*	CS-3002	*~136*	~14			bulk XRF?	andesite				H1		35
	Lago Maldonado	*-47.26*	*-72.52*	PC0904B	sediment core	*piston?*	CS-1031	*~635*	~10			bulk XRF?	andesite				H1		35
	Lago Cardiel	-48.81	-71.22	CAR-98-2L	sediment core		*CAR98-838.5*	838	1	black		bulk ICP-MS					H1		12
		-48.81	-71.22	CAR-99-2L	sediment core		*CAR99-462.5*	465	5 (dispersed)	black		bulk ICP-MS					H1		12,37
		-48.88	-71.30	CAR-99-7P	sediment core		*CAR-99-7P-369*	372	6			glass EPMA	data not provided				H1		13
		-48.92	-71.28	CAR-99-9P	sediment core		*CAR-99-9P-1071*	1072	2			glass EPMA	data not provided				H1		13
	Laguna Potrok Aike	-51.96	-70.38	PTA03/12-13; 02/4	sediment core	piston	t12-12	1074.5	2					14C interpolation		8100 ± 430	Hudson		28,37
		-51.96	-70.38	PTA03/5	sediment core	piston	t5-1	78						14C interpolation		8100 ± 430	Hudson		28
	Laguna Escondida	-52.50	-71.93	PS-0504D	sediment core		*PS-0504D-518*	520	4								H1		37
	Lago Chandler	-52.82	-72.90	CH-1	sediment core	piston	*CH-1-480*	480	1	light grey to yellow		glass EPMA	rhyolite	14C		>7710 ± 190; <7800 ± 130	H1		16,37
	Lago Hambre	-53.60	-70.95	Hambre	sediment core	piston, gravity	*Hambre-770*	~770						14C	>6425 ± 15; <7370 ± 20		H1		29
	Lago Fagnano	-54.58	-67.50	LF06-PC16	sediment core	piston	*LF06-PC16-482*	484	4.5			bulk ICP-MS					H1		30
		-54.58	-67.87	LF06-PC12	sediment core	piston	*LF06-PC12-142*	144	3.5			bulk ICP-MS					H1		30
	Laguna Cascada	-54.76	-64.34	CAS	sediment core	Russian	CAS-389	390	2.5	greenish grey	fine sand-silt	bulk XRF	data not provided	14C	>7715 ± 60; <7775 ± 60		H1		39.4
Marine sediment cores	Off Taitao Peninsula	-46.07	-75.69	MD07-3088	continental shelf sediment core	piston	TL1	161	cryptotephra	honey and translucent shards		glass EPMA	basaltic andesite to dacite	planktic foram 14C	2510 ± 30		HW7		3
							MD07-3088-279	279	cryptotephra			glass EPMA	basaltic andesite to dacite	planktic foram 14C	4475 ± 30		H2		5
							TL2	610	cryptotephra	honey to colourless shards		glass EPMA	basaltic andesite to dacite	planktic foram 14C	10050 ± 35		Same as Opr-4?		3
							TL3	660	cryptotephra	dark; colourless shards		glass EPMA	basaltic andesite to dacite	planktic foram 14C	10880 ± 35		HW3		3
							TL4	750	cryptotephra	honey shards more than translucent		glass EPMA	basaltic andesite to dacite	planktic foram 14C	12885 ± 40		HW2		3
							TL5	800	cryptotephra	colourless shards		glass EPMA	basaltic andesite to dacite	planktic foram 14C	13755 ± 35		HW1		3
							TL6	870	cryptotephra	majority honey shards		glass EPMA	basaltic andesite to dacite	planktic foram 14C	14970 ± 80		Hudson		3
							TL7	1080	cryptotephra	majority honey shards		glass EPMA	basaltic andesite to dacite	planktic foram 14C	>15755 ± 45; <<16320 ± 45		Hudson		3,5
							TL8	1140	cryptotephra			glass EPMA	basaltic andesite to dacite	planktic foram 14C	>>15755 ± 45; <16320 ± 45		Hudson		3,5
							TL9	1390	cryptotephra			glass EPMA	basaltic andesite to dacite	14C interpolation		19450	Hudson		3
							TL10	1440	cryptotephra	honey and translucent shards		glass EPMA	basaltic andesite to andesite	14C interpolation		19600	Hudson		3
							TL11	1470	cryptotephra	honey to colourless shards		glass EPMA	basaltic andesite to dacite	14C interpolation		19660	Hudson		3
							TL12	1560	cryptotephra			glass EPMA	basaltic andesite to dacite	14C interpolation		19860	Hudson		3
	Estrecho de Magallanes	-52.79	-73.65	PALM-2	fjord sediment core	piston		463									H1		32,44
	La Misión	-53.70	-67.75		*offshore sedi. core?*				6								H1		37,45
Ice cores	Talos Dome (E Antarct.)	-72.82	159.18	TD	ice core		TD193	19225	cryptotephra		≤0.01	glass EDS	trachybasalt	various integrated		2020 ± 70	T6		47
							TD216	21550	cryptotephra		<0.01	glass EDS	rhyolite	various integrated		2360 ± 60	Hudson?		47
	EPICA-Dome C (E Antarct.)	-75.10	123.35	EDC	ice core		*EDC-339.5*	33950	0.2		≤0.5	glass EDS, EPMA	andesite	various integrated		11040 ± 140	HW3?		46,47
	Siple Dome (W Antarct.)	-81.66	-148.81	SDMA	ice core		SDMA-9008	59695.2				glass EMPA	andesite	various integrated		11116	HW3?		48

Supplementary Table 4.2 Published chemical composition data for tephra deposits attributed to Volcán Hudson.

Eruption	Tephra sample			Analysis			Analysis: EPMA/EDS parameters			Major elements (wt. %)											
	Sample ID	Location	Environment	Analyte	Method	n	Current (nA)	Voltage (kV)	Diameter (µm)	SiO2	TiO2	Al2O3	FeO (tot)	Fe2O3 (tot)	FeO	Fe2O3	MnO	MgO	CaO	Na2O	K2O	P2O5	Cl	F
1991	100891 (P1)			tephra	bulk XRF					51.75	2.13	15.88	11.21				0.19	4.32	8.33	4.36	1.36	0.48		
	PC-1 (P1)			tephra	bulk XRF					51.71	2.36	15.85	11.18				0.19	4.28	8.25	4.42	1.35	0.43		
	210192.1D (P1)			tephra	bulk XRF					51.44	2.15	15.79		11.74			0.19	4.21	8.24	4.27	1.22	0.71		
	HUD110 (P1)	3,4		tephra	bulk XRF	5				51.61	2.03	15.96		11.55			0.18	4.14	8.27	4.31	1.23	0.71		
				glass	EPMA	6	9.6-15	15	10	52.55 ± 0.15	2.58 ± 0.03	13.93 ± 0.14	12.16 ± 0.37				0.23 ± 0.08	3.99 ± 0.08	7.72 ± 0.09	4.24 ± 0.16	1.45 ± 0.06	0.88 ± 0.05		
				glass	EPMA	5	9.6-15	15	10	52.52 ± 0.23	2.22 ± 0.08	15.79 ± 0.20	10.72 ± 0.15				0.20 ± 0.07	4.28 ± 0.12	8.20 ± 0.15	4.28 ± 0.23	1.23 ± 0.08	0.70 ± 0.07		
				glass	EPMA	3	9.6-15	15	10	51.68 ± 0.19	2.33 ± 0.03	15.47 ± 0.25	11.33 ± 0.12				0.17 ± 0.01	4.46 ± 0.10	8.41 ± 0.17	3.93 ± 0.07	1.30 ± 0.01	0.93 ± 0.01		
				glass	EPMA	3	9.6-15	15	10	52.27 ± 0.32	2.23 ± 0.16	15.18 ± 0.58	10.88 ± 0.68				0.13 ± 0.03	4.39 ± 0.44	8.27 ± 0.64	4.12 ± 0.14	1.22 ± 0.22	0.78 ± 0.04		
				plg feldspar rim	EPMA		15	15	10	51.27 53.45		31.15 29.00	0.63 0.85						13.87 11.83	3.44 4.41	0.12 0.20				
				plg feldspar core	EPMA		15	15	10	47.41 61.00		33.60 24.84	0.53 0.33						17.16 6.26	1.84 7.36	0.05 0.52				
				orthopyroxene	EPMA		15	15	10	50.60	0.63	0.67	17.64				1.18	24.05	1.68	0.03	0.01			
				clinopyroxene	EPMA		15	15	10	51.53 49.46	0.84 1.13	2.25 3.74	7.71 7.85				0.36 0.21	15.79 15.09	20.37 20.41	0.33 0.36	0.00 0.01			
				olivine	EPMA		15	15	10	36.15	0.05	0.01	27.59				1.02	33.35	0.20	0.01	0.01			
				Fe-Ti oxide pair	EPMA		15	15	10		19.18 49.47	1.54 0.10	71.94 45.25				0.58 0.80	0.75 1.47						
	190891-5 (P2)			tephra	bulk XRF					62.10	1.36	16.38	5.57				0.18	1.74	3.69	6.22	2.49	0.27		
	190392.3a (P2)			tephra	bulk XRF					61.77	1.32	16.44		6.11			0.19	1.69	3.60	6.01	2.44	0.44		
	190392.3f (P2)			tephra	bulk XRF					61.36	1.36	16.39		6.38			0.18	1.72	3.77	5.95	2.40	0.48		
	300192.4a (P2)			tephra	bulk XRF					61.83	1.30	16.43		5.97			0.18	1.70	3.53	6.07	2.45	0.42		
	HUD143 (P2 uA)	17		tephra	bulk XRF					61.40	1.29	16.45		6.02			0.18	2.07	3.65	6.11	2.39	0.44		
	HUD209 (P2 uA)	28		tephra	bulk XRF					61.38	1.29	16.69		6.03			0.18	1.73	3.72	6.16	2.37	0.44		
				glass	EPMA	8	9.6-15	15	10	62.76 ± 0.30	1.22 ± 0.07	16.10 ± 0.18	4.69 ± 0.19				0.18 ± 0.05	1.52 ± 0.02	3.24 ± 0.08	6.70 ± 0.27	2.57 ± 0.13	0.35 ± 0.04		
				glass	EPMA	4	9.6-15	15	10	64.14 ± 0.15	1.04 ± 0.05	16.34 ± 0.08	4.50 ± 0.09				0.19 ± 0.06	1.23 ± 0.06	2.78 ± 0.03	6.80 ± 0.31	2.60 ± 0.09	0.28 ± 0.03		
				glass	EPMA	3	9.6-15	15	10	64.10 ± 1.01	1.09 ± 0.04	16.33 ± 0.03	4.59 ± 0.55				0.21 ± 0.06	1.41 ± 0.20	2.91 ± 0.28	6.68 ± 0.22	2.68 ± 0.06	0.35 ± 0.04		
				plg feldspar rim	EPMA		15	15	10	57.56		26.83	0.54						8.68	5.99	0.32				
				plg feldspar core	EPMA		15	15	10	59.16		25.85	0.44						7.51	6.56	0.39				
				clinopyroxene	EPMA		15	15	10	51.58	0.79	2.08	8.68				0.55	15.44	20.21	0.44	0.01			
				olivine	EPMA		15	15	10	37.32	0.04	0.04	27.72				1.04	33.68	0.17	0.02	0.01			
				Fe-Ti oxide pair	EPMA		15	15	10		15.65 44.8	2.79 0.34	72.41 45.23				0.86 0.93	3.75 5.28						
	HUD141 (P2 uB)	17		tephra	bulk XRF					61.07	1.32	16.66		6.14			0.18	1.74	3.83	6.23	2.37	0.46		
	HUD208 (P2 uB)	28		tephra	bulk XRF					61.05	1.32	16.77		6.12			0.18	1.80	3.81	6.12	2.35	0.46		
				glass	EPMA	5	9.6-15	15	10	62.23 ± 0.35	1.21 ± 0.09	16.18 ± 0.20	4.94 ± 0.16				0.18 ± 0.07	1.58 ± 0.07	3.32 ± 0.17	6.64 ± 0.16	2.40 ± 0.06	0.36 ± 0.06		
				glass	EPMA	3	9.6-15	15	10	63.06 ± 0.46	1.20 ± 0.09	16.20 ± 0.05	4.99 ± 0.10				0.18 ± 0.05	1.45 ± 0.06	3.22 ± 0.26	6.74 ± 0.26	2.62 ± 0.06	0.39 ± 0.02		
				plg feldspar rim	EPMA		15	15	10	57.44		27.16	0.54						8.88	5.95	0.31				
				plg feldspar core	EPMA		15	15	10	57.59		26.58	0.43						8.53	6.09	0.33				
				clinopyroxene	EPMA		15	15	10	51.77	0.74	1.91	8.79				0.62	15.29	20.09	0.46	0			
				olivine	EPMA		15	15	10	37.25	0.02	0.01	27.79				1.09	33.29	0.16	0.01	0.01			
				Fe-Ti oxide pair	EPMA		15	15	10		15.79 45.24	2.89 0.34	72.10 45.25				0.79 0.88	3.80 4.73						
	HUD206 (P2 uC)	27		tephra	bulk XRF					60.99	1.31	16.70		6.20			0.18	1.83	3.94	6.10	2.32	0.44		
	HUD207 (P2 uC)	28		tephra	bulk XRF					60.33	1.38	16.74		6.56			0.18	1.94	4.12	5.96	2.31	0.48		
				glass	EPMA	6	9.6-15	15	10	61.59 ± 0.96	1.31 ± 0.07	16.01 ± 0.08	5.49 ± 0.49				0.23 ± 0.05	1.93 ± 0.24	3.85 ± 0.54	6.31 ± 0.45	2.35 ± 0.11	0.43 ± 0.03		
				plg feldspar rim	EPMA		15	15	10	57.25		27.12	0.56						9.41	5.66	0.30				
				plg feldspar core	EPMA		15	15	10	55.95		28.16	0.53						10.2	5.32	0.25				
				clinopyroxene	EPMA		15	15	10	51.96	0.77	1.91	8.65				0.61	15.29	20.29	0.43	0			
				olivine	EPMA		15	15	10	37.10	0.02	0.02	27.39				1.04	33.36	0.16	0	0.01			
				Fe-Ti oxide pair	EPMA		15	15	10		15.68 45.23	2.79 0.36	72.28 45.23				0.82 0.82	3.75 5.26						
	HUD149 (P2 uD)	17		tephra	bulk XRF					61.23	1.31	16.73		6.18			0.18	1.75	3.72	6.09	2.38	0.44		
	HUD155 (P2 uD)	17		tephra	bulk XRF					61.68	1.29	16.43		6.04			0.18	1.70	3.61	6.20	2.43	0.45		
	HUD210 (P2 uD)	28		tephra	bulk XRF					62.05	1.24	16.39		5.88			0.17	1.70	3.74	5.98	2.43	0.42		
				glass	EPMA	4	9.6-15	15	10	62.42 ± 0.47	1.27 ± 0.06	15.97 ± 0.13	5.23 ± 0.08				0.15 ± 0.05	1.64 ± 0.15	3.41 ± 0.41	6.16 ± 0.23	2.99 ± 0.38	0.42 ± 0.09		
				glass	EPMA	4	9.6-15	15	10	60.84 ± 0.39	1.47 ± 0.02	15.75 ± 0.21	6.18 ± 0.48				0.22 ± 0.03	2.15 ± 0.10	4.50 ± 0.21	6.15 ± 0.08	2.18 ± 0.15	0.58 ± 0.04		
				plg feldspar rim	EPMA		15	15	10	54.97		28.34	0.91						11.15	4.80	0.22				
				plg feldspar core	EPMA		15	15	10	47.46		33.51	0.54						17.01	1.86	0.05				
				clinopyroxene	EPMA		15	15	10	50.71	0.97	2.66	8.79				0.58	15.13	19.79	0.42	0.01			
				olivine	EPMA		15	15	10	37.03	0.04	0.03	27.62				1.05	33.55	0.14	0.02	0.04			
				Fe-Ti oxide pair	EPMA		15	15	10		15.63 45.05	2.74 0.39	72.37 45.21				0.87 0.86	3.79 4.95						
1971 (T9)	49K	94T-59	peat section	tephra	bulk XRF					61.22	1.23	15.92	5.64				0.17	1.73	3.69	5.67	2.41	0.37		
T8	59K	94T-59	peat section	tephra	bulk XRF					60.06	1.51	16.07	5.94				0.17	2.39	4.28	5.11	2.11	0.36		
T7	59F	94T-59	peat section	tephra	bulk XRF					64.26	0.89	15.72	4.04				0.12	1.38	2.16	5.91	2.81	0.26		
Undefined	Fac-3	Lag. Facil	lake sedi. core	glass	EPMA		10	20	10	52.799	1.295	15.162	9.296					5.572	8.223	3.660	0.988		0.059	

										53.137	1.167	15.745	8.930					5.685	8.890	3.169	0.928		0.080	
										53.305	1.178	15.694	8.999					5.712	8.982	3.326	0.888		0.085	
										53.800	1.356	15.008	10.020					5.387	8.546	3.221	0.974		0.087	
										53.432	1.257	15.502	9.709					5.639	8.409	3.240	0.939		0.107	
										53.710	1.175	16.619	8.529					5.081	8.871	3.601	0.833		0.070	
										53.310	1.336	15.009	9.888					5.527	8.265	2.989	1.020		0.092	
										53.288	1.286	16.014	9.832					5.274	9.242	3.129	0.783		0.064	
										53.113	1.294	15.183	9.348					5.356	8.837	3.274	0.942		0.082	
										53.113	1.490	13.186	11.156					5.638	8.474	3.117	0.964		0.085	
										53.650	1.312	15.054	9.109					4.573	8.220	3.495	0.869		0.029	
										53.055	1.495	14.328	10.139					5.066	8.324	3.338	1.033		0.056	
										53.985	1.016	18.317	7.572					3.803	9.266	3.929	0.679		0.049	
										53.373	1.299	14.892	9.368					5.101	8.684	3.240	0.983		0.080	
										53.450	1.280	14.791	9.344					5.677	8.982	2.778	0.861		0.087	
										53.705	1.259	15.243	9.093					5.393	8.799	2.719	0.914		0.045	
HW7	Opr-8	Lag. Oprasa	lake sedi. core	glass	EPMA		10	20	10	54.010	2.474	17.499	7.896					1.360	6.694	4.610	1.653		0.144	
										51.289	2.232	13.453	11.413					7.650	5.482	2.523	2.380		0.096	
										54.051	1.769	16.782	6.374					3.516	9.467	4.372	1.002		0.091	
										52.033	2.813	14.490	11.017					2.276	7.341	4.132	1.903		0.127	
										51.912	2.468	13.275	9.849					4.812	10.951	3.324	1.276		0.135	
										50.204	1.791	14.098	12.471					6.232	6.378	3.706	1.161		0.145	
	Mir-3	Lag. Miranda	lake sedi. core	glass	EPMA		10	20	10	59.320	1.753	16.253	6.650					2.386	4.658	3.813	2.149		0.131	
										55.905	2.354	13.163	10.596					3.351	6.546	3.334	1.862		0.090	
										54.234	1.907	13.299	10.951					5.771	6.076	3.232	1.645		0.114	
										55.151	1.678	16.987	7.949					3.161	7.382	4.060	1.435		0.088	
										55.968	2.436	13.222	10.136					3.059	6.249	3.134	1.889		0.107	
										54.950	2.050	14.548	9.238					3.693	6.804	3.716	1.806		0.124	
										55.473	2.267	13.647	9.930					3.214	6.652	3.280	1.834		0.099	
	Stb-4	Lag. Stibnite	lake sedi. core	glass	EPMA		10	20	10	68.725	0.785	15.282	3.177					0.544	1.506	5.330	3.559	0.104		
										66.562	0.747	15.578	3.566					0.830	1.873	5.195	3.381	0.250		
										65.548	1.199	14.337	5.156					1.163	2.406	3.183	3.514	0.442		
										65.223	1.142	16.094	4.773					1.091	3.133	5.864	2.834	0.386		
										64.528	1.299	15.608	5.122					1.121	2.781	5.035	2.894	0.315		
										64.519	1.159	15.938	4.987					1.328	3.244	3.560	2.611	0.454		
										64.036	1.231	15.513	5.083					1.210	3.130	4.996	2.626	0.254		
										63.989	1.195	15.947	4.752					1.540	3.312	4.743	2.685	0.534		
										63.978	1.244	15.833	5.039					1.334	3.142	5.086	2.759	0.577		
										63.838	1.092	16.742	4.511					0.957	3.498	5.554	2.378	0.478		
										63.730	1.299	15.662	4.828					1.280	3.134	5.011	2.763	0.340		
										63.693	1.191	15.775	4.974					1.518	3.395	4.810	2.508	0.496		
										63.624	1.307	15.101	5.566					1.431	3.080	5.068	2.641	0.497		
										63.576	1.282	15.632	5.047					1.227	2.799	4.947	3.042	0.334		
										63.346	1.156	15.945	4.915					1.291	3.425	4.500	2.668	0.393		
										63.330	1.108	15.816	4.939					1.680	3.438	4.960	2.484	0.460		
										63.223	1.045	17.270	4.115					0.949	3.867	5.683	2.122	0.330		
										61.524	1.551	14.424	6.976					1.604	3.745	3.380	2.920	0.839		
										53.558	2.123	14.326	11.086					3.271	6.660	4.140	1.556	0.666		
	Six-4	Lag. Six Minutes	lake sedi. core	glass	EPMA		10	20	10	65.866	1.072	15.913	4.562					1.045	2.093	4.661	3.081	0.387		
										65.435	1.323	15.566	4.774					0.884	2.732	4.311	2.991	0.508		
										65.021	1.134	15.626	4.465					1.151	2.935	4.238	2.943	0.342		
										64.221	1.058	17.213	4.115					1.134	3.745	5.468	2.329	0.369		
										64.079	1.330	13.990	5.372					1.037	2.359	4.498	3.341	0.550		
										63.869	1.114	15.692	5.028					1.356	3.237	4.034	2.598	0.472		
										62.051	1.173	15.472	4.945					1.380	3.282	4.199	2.551	0.382		
										58.314	1.371	15.866	6.917					2.325	5.290	4.921	2.231	0.438		
										58.073	1.592	16.273	7.571					2.569	5.755	5.091	1.980	0.631		
										56.762	2.843	14.634	9.061					1.773	4.733	4.393	2.422	1.041		
										56.211	1.606	17.698	7.799					1.971	6.962	4.688	1.544	0.633		
										55.498	1.603	16.227	7.328					3.461	8.502	4.991	0.919	0.649		
										54.980	1.292	16.363	7.810					3.561	7.296	4.484	1.462	0.646		
										54.877	1.971	14.377	10.425					3.238	6.271	3.949	1.717	0.819		
										54.665	2.096	15.202	10.620					3.219	7.051	4.312	1.532	0.798		
										54.514	1.816	16.348	8.478					3.049	7.505	4.824	1.582	0.652		
										53.908	1.409	15.977	8.342					3.816	7.430	4.148	1.394	0.610		
										53.567	1.462	15.888	8.358					4.092	7.683	4.300	1.321	0.714		
										53.529	1.494	16.058	8.353					4.041	7.485	4.329	1.320	0.651		
										53.467	1.439	16.169	8.295					4.194	7.728	4.387	1.331	0.632		
	Mar-2	Lag. Marcelo	lake sedi. core	glass	EPMA		10	20	10	65.051	1.095	15.783	4.493					1.233	3.419	6.687	1.214	0.396		
										65.037	1.122	15.621	4.713					1.213	3.021	4.661	2.625	0.404		
										64.025	1.302	14.128	6.134					1.853	2.828	4.592	3.074	0.500		
										64.012	1.066	15.916	5.022					1.602	3.564	5.209	2.572	0.301		
										63.902	1.204	15.698	5.201					1.320	3.153	3.916	2.779	0.504		
										63.816	1.167	16.425	4.381					1.137	3.606	5.077	2.268	0.410		
										63.781	1.245	15.859	4.998					1.408	3.296	4.240	3.085	0.447		
										63.723	0.967	16.558	4.353					1.607	4.311	5.983	2.057	0.337		
										63.622	1.186	15.805	5.154					1.429	2.752	4.779	3.629	0.519		
										63.591	1.080	16.474	4.478					1.057	3.513	4.830	2.348	0.361		
										63.567	1.291	15.305	5.786					1.454	3.192	6.000	2.186	0.457		
										63.564	1.177	16.072	4.630					1.358	3.211	4.719	2.681	0.604		
										63.447	1.169	15.748	5.018					1.400	3.275	4.245	2.643	0.463		
										63.386	1.093	15.226	4.497					1.190	2.792	4.165	4.088	0.246		
										63.134	1.101	16.779	4.589					1.146	3.909	4.761	2.327	0.472		
										62.627	1.501	14.422	6.563					1.364	3.100	5.110	2.880	0.701		
										56.832	1.414	16.241	8.204					3.385	6.604	4.438	1.706	0.650		
										55.594	1.715	13.749	9.091					4.126	6.870	3.764	1.831	0.665		
										55.279	1.478	16.196	8.403					3.943	7.151	4.148	1.515	0.604		

									54.864	1.558	15.801	8.518					4.020	7.235	4.270	1.479	0.554		
									53.162	1.466	16.830	7.586					3.548	7.963	3.937	1.210	0.549		
	TL1	Off Taito Penin.	marine sedi. core	glass	EPMA	10	15	5	54.38	2.28	15.12	10.69				0.16	3.81	7.64	4.11	1.28	0.54		
									54.54	1.77	14.75	11.39				0.12	4.05	8.00	4.02	1.02	0.34		
									54.98	2.69	13.61	10.30				0.17	3.87	7.73	4.03	1.55	1.06		
									55.14	1.55	15.56	8.92				0.09	4.79	8.27	3.96	1.14	0.58		
									55.33	2.12	14.96	10.59				0.25	3.66	7.33	3.84	1.40	0.53		
									55.31	2.68	14.45	10.07				0.22	3.97	7.58	2.88	1.80	1.03		
									55.62	2.04	12.80	12.93				0.19	3.41	7.49	3.84	1.22	0.45		
									55.62	2.11	15.97	8.88				0.19	3.43	7.20	4.59	1.27	0.75		
									57.17	1.98	15.69	8.05				0.18	3.41	6.60	4.30	1.84	0.76		
									60.64	1.31	16.86	6.97				0.18	1.41	5.27	5.42	1.52	0.41		
									62.28	1.40	16.18	5.78				0.26	1.33	5.28	4.48	1.83	1.19		
									65.88	1.38	15.84	4.05				0.26	1.16	2.81	5.40	2.88	0.33		
									66.00	1.06	16.02	4.08				0.09	1.03	2.34	5.77	3.29	0.32		
									66.33	1.06	16.12	5.01				0.24	1.08	2.57	4.37	2.86	0.37		
									66.59	0.97	15.78	4.12				0.11	1.14	2.43	5.30	3.26	0.30		
									66.65	1.27	15.56	4.11				0.08	1.18	2.52	5.39	2.92	0.33		
									68.52	0.80	16.21	2.94				0.15	0.61	1.49	5.71	3.37	0.20		
Undefined	ESC-T3	Lag. Escondida	lake sedi. core	tephra	bulk XRF				49.4	0.8	21.2		6.6			0.1	6.5	9.7	3.8	0.7	0.4		
									50.2	0.8	20.8		6.7			0.1	6.7	10.0	3.1	0.7	0.4		
	CAS-T3	Lag. Castor	lake sedi. core	tephra	bulk XRF				55.3	1.6	17.2		8.2			0.1	3.7	6.6	4.4	1.4	0.7		
									52.1	1.0	19.6		6.9			0.1	5.4	8.7	3.9	0.9	0.5		
Undefined	ESC-T4	Lag. Escondida	lake sedi. core	tephra	bulk XRF				53.3	1.2	19.4		7.2			0.1	4.3	7.9	4.0	1.2	0.5		
									52.9	1.2	19.2		7.2			0.1	4.4	7.8	4.5	1.2	0.5		
	CAS-T4	Lag. Castor	lake sedi. core	tephra	bulk XRF				55.8	1.2	18.4		7.1			0.1	4.0	7.0	3.8	1.4	0.5		
									55.7	1.2	18.4		7.2			0.1	3.8	7.1	4.0	1.3	0.6		
T6	59C	94T-59	peat section	tephra	bulk XRF				53.07	1.87	16.16	10.16				0.16	3.78	6.78	4.32	1.32	0.44		
	66B	94T-66		scoria	bulk XRF				52.85	1.98	16.23	10.26				0.17	3.98	6.89	4.16	1.28	0.41		
	ESC-T6	Lag. Escondida	lake sedi. core	tephra	bulk XRF				55.8	1.5	17.1		8.1			0.1	3.9	6.7	4.2	1.3	0.7		
									55.8	1.5	17.2		7.9			0.1	3.7	6.6	4.4	1.4	0.6		
	CAS-T6	Lag. Castor	lake sedi. core	tephra	bulk XRF				56.3	1.5	17.0		7.9			0.1	3.7	6.5	4.3	1.3	0.7		
									56.2	1.5	17.1		8.0			0.1	3.7	6.5	4.1	1.3	0.7		
	TD193	Talos Dome	ice core	glass	EDS		25		50.6 ± 1.0	2.2 ± 0.5	16.5 ± 0.7	9.9 ± 1.2				0.2 ± 0.1	6.8 ± 1.2	8.2 ± 0.9	4.5 ± 0.5	1.2 ± 0.1			
Undefined	TD216	Talos Dome	ice core	glass	EDS		25		69.6 ± 1.7	0.9 ± 0.7	15.6 ± 0.9	2.4 ± 0.9				0.6 ± 0.5	1.1 ± 0.7	1.1 ± 0.7	5.5 ± 0.7	3.4 ± 0.5			
HW6	Opr-7	Lag. Oprasa	lake sedi. core	glass	EPMA	10	20	10	55.534	2.112	13.262	10.831					3.418	6.622	3.247	1.512		0.135	
									55.159	1.716	15.264	9.699					3.797	7.109	3.772	1.246		0.089	
									51.084	1.633	13.978	12.330					4.347	8.190	3.698	1.118		0.054	
									51.122	1.593	13.763	12.327					4.407	8.230	3.636	1.122		0.036	
									55.126	1.651	15.187	9.633					3.836	6.917	3.667	1.243		0.115	
									54.534	1.683	14.944	9.814					3.723	6.864	4.267	1.271		0.097	
									55.199	1.774	14.752	9.797					3.890	6.908	3.521	1.292		0.106	
									55.250	1.662	15.335	9.626					3.869	6.958	3.459	1.346		0.092	
									56.954	1.547	15.545	8.024					3.015	6.102	3.795	1.534		0.046	
									54.756	1.995	13.907	10.756					3.929	6.732	3.578	1.357		0.124	
									55.636	1.703	16.052	8.934					2.937	7.284	4.534	1.115		0.099	
									55.133	1.873	14.292	10.289					3.906	7.036	3.894	1.169		0.091	
									55.854	1.717	15.102	9.123					3.170	6.662	3.879	1.308		0.087	
									55.710	1.436	17.974	7.705					2.589	7.547	4.413	1.064		0.103	
									54.585	1.763	14.876	9.606					3.741	7.008	3.434	1.265		0.096	
									54.885	1.775	14.481	10.046					3.913	6.834	3.555	1.357		0.102	
									55.167	1.590	16.890	8.650					3.474	7.433	4.170	1.140		0.090	
									59.710	1.796	14.102	8.120					1.690	4.598	3.412	2.235		0.153	
									56.480	1.742	15.292	9.421					3.713	6.683	3.589	1.291		0.060	
									54.824	1.714	15.061	9.690					3.901	7.045	3.812	1.247		0.112	
									55.322	2.045	12.932	10.940					4.444	7.099	3.412	1.290		0.111	
									55.573	1.787	15.969	9.460					3.220	7.210	4.026	1.175		0.084	
									55.295	1.711	15.045	9.613					3.920	6.757	3.527	1.364		0.124	
	Lin-4	Lag. Lincoln	lake sedi. core	glass	EPMA	10	20	10	54.208	1.897	13.502	11.411					3.799	7.939	3.203	1.016		0.073	
									54.460	1.833	13.750	11.241					3.870	8.057	3.196	1.004		0.064	
									54.585	1.780	14.932	10.362					3.664	8.234	3.454	0.879		0.117	
									53.837	1.994	13.232	11.207					3.615	7.656	3.121	1.056		0.092	
									55.228	2.239	12.682	14.086					6.179	6.195	2.835	1.055		0.036	
									59.322	1.747	13.453	9.697					2.674	5.338	3.162	1.625		0.073	
									59.355	1.556	15.179	8.509					2.210	5.601	3.620	1.514		0.050	
									53.930	2.094	12.604	12.023					3.823	8.000	3.258	1.000		0.088	
									57.464	1.468	17.696	8.236					2.878	8.174	4.165	0.792		0.131	
									54.075	1.961	13.548	11.375					4.040	8.089	2.879	1.049		0.113	
									53.422	1.819	12.920	11.989					4.476	7.381	3.263	0.979		0.081	
									54.107	1.901	13.250	11.713					4.092	7.801	3.336	1.087		0.072	
									54.235	1.705	16.554	9.453					3.130	8.384	3.889	0.861		0.059	
	Mir-2	Lag. Miranda	lake sedi. core	glass	EPMA	10	20	10	54.731	1.652	16.096	8.239					4.130	8.157	3.912	1.184		0.097	
									54.038	1.720	15.091	9.043					4.487	7.852	3.348	1.460		0.116	
									54.697	1.747	15.434	8.509					4.788	7.846	3.598	1.344		0.100	
									53.892	1.738	14.451	8.892					5.563	7.876	3.576	1.382		0.087	
									54.148	1.786	14.734	8.968					4.412	7.781	3.487	1.429		0.109	
									56.235	1.550	16.549	8.177					3.934	7.247	3.932	1.490		0.077	
									53.274	1.587	16.190	10.078					5.011	8.441	4.390	1.244		0.072	
									54.031	1.777	15.309	8.699					4.364	7.751	3.494	1.430		0.098	
									54.454	1.933	14.587	9.419					3.982	7.706	3.657	1.548		0.104	
									54.557	1.836	15.010	8.970					4.361	7.640	3.504	1.438		0.094	
	Stb-3	Lag. Stibnite	lake sedi. core	glass	EPMA	10	20	10	58.990	1.773	14.322	7.018					2.166	3.628	3.996	2.559	0.794		
									56.725	2.102	13.857	8.920					2.634	5.307	3.526	2.025	0.929		
									56.138	2.194	15.128	8.221					2.592	6.788	4.540	1.675	0.792		
									55.636	1.879	14.901	8.008					2.486	6.796	4.004	1.607	0.847		
									55.519	2.119	13.975	10.955					3.105	6.621	3.602	1.652	0.873		

										55.514	2.022	14.842	10.056					3.163	6.598	4.503	1.685	0.910		
										55.328	1.951	14.748	10.236					3.413	6.517	4.474	1.730	0.870		
										54.855	2.026	14.900	10.086					3.071	7.081	4.099	1.849	0.800		
										54.835	1.823	16.567	8.714					2.262	7.024	4.502	1.532	0.742		
										54.373	1.828	14.588	9.945					3.694	6.715	4.067	1.554	0.902		
										54.209	1.706	15.251	10.795					3.573	6.961	4.442	1.319	0.747		
										54.075	1.826	15.409	9.501					3.584	7.626	3.660	1.338	0.764		
										54.069	1.696	16.308	8.762					3.060	7.408	4.531	1.366	0.790		
										54.048	1.867	15.387	9.205					2.891	6.924	4.588	1.457	0.747		
										52.600	2.878	14.053	12.225					3.215	6.611	4.351	1.571	0.829		
										52.199	2.171	13.681	11.360					4.315	7.398	3.734	1.391	0.868		
	Six-3	Lag. Six Minutes	lake sedi. core	glass	EPMA		10	20	10	57.817	2.255	13.690	7.802					1.920	4.295	3.691	2.587	0.908		
										56.138	2.194	15.128	8.221					2.592	6.788	4.540	1.675	0.792		
										55.676	1.888	16.842	8.207					2.182	6.816	4.633	1.507	0.819		
										55.382	1.863	17.009	8.610					2.861	7.587	4.400	1.267	0.644		
										55.355	1.732	17.002	8.669					2.472	7.309	4.398	1.415	0.704		
										55.344	2.488	13.895	12.050					2.918	5.956	4.479	1.812	1.078		
										55.316	1.920	15.535	9.254					2.968	7.173	4.262	1.470	0.845		
										55.204	2.220	13.839	10.594					3.225	6.321	3.668	1.874	1.014		
										55.088	2.054	14.069	10.740					3.433	6.477	4.211	1.659	0.894		
										54.848	2.079	14.197	10.139					3.100	6.808	3.983	1.619	1.005		
										54.817	1.835	16.324	8.999					2.631	7.327	4.378	1.544	0.855		
										54.643	1.889	15.836	8.720					2.027	6.841	4.380	1.688	0.816		
										54.574	1.826	14.786	9.319					3.579	7.366	4.399	1.381	0.791		
										54.188	1.501	17.481	7.755					2.370	7.579	4.373	1.170	0.679		
										53.959	1.672	16.014	8.348					2.449	7.314	4.137	1.419	0.660		
										53.950	1.759	15.853	9.298					3.581	7.072	4.186	1.415	0.716		
										52.385	2.128	14.033	10.980					3.947	7.264	4.150	1.345	0.838		
										51.914	1.586	11.097	14.654					10.760	4.772	3.374	1.394	0.878		
	Mar-1	Lag. Marcelo	lake sedi. core	glass	EPMA		10	20	10	56.687	2.005	14.996	8.348					2.774	6.490	4.712	1.880	0.945		
										56.349	2.267	12.940	11.190					3.519	5.791	3.304	1.909	1.003		
										55.854	1.627	16.702	7.783					2.471	7.505	4.555	1.451	0.875		
										55.708	1.760	14.855	10.057					3.317	6.389	4.587	1.888	0.815		
										55.452	2.205	14.387	9.526					3.589	6.716	4.411	1.695	0.860		
										55.371	1.884	16.069	8.814					3.295	7.276	4.543	1.429	0.772		
										55.142	2.228	13.607	10.743					4.183	6.880	3.657	1.749	0.915		
										55.088	1.684	17.033	8.305					2.834	7.458	4.632	1.542	0.775		
										55.017	1.890	14.899	9.565					3.261	7.141	4.223	1.653	0.807		
										54.899	1.704	16.106	9.202					3.183	7.016	4.171	1.473	0.771		
										54.808	2.256	13.823	10.719					3.142	6.501	3.988	1.758	0.948		
										54.510	1.923	16.186	8.703					2.711	7.345	4.010	1.546	0.827		
										54.316	2.146	14.755	9.665					3.404	6.478	4.282	1.740	0.875		
										54.303	1.519	17.528	7.740					2.271	7.791	4.238	1.340	0.629		
										53.350	1.917	16.207	9.631					3.493	7.784	4.344	1.243	0.808		
										52.244	2.823	13.922	11.274					3.556	7.251	3.912	1.598	1.268		
										51.960	2.744	13.721	11.675					3.849	7.282	4.282	1.570	0.963		
Undefined	Opr-6	Lag. Oprasa	lake sedi. core	glass	EPMA		10	20	10	54.446	1.839	14.252	10.121					3.909	6.724	3.479	1.334		0.117	
										63.916	0.995	14.995	6.292					1.175	3.523	3.110	3.075		0.102	
										55.064	1.752	14.834	9.745					3.742	6.967	3.349	1.178		0.144	
										54.803	1.989	14.000	10.194					3.473	6.751	3.287	1.336		0.119	
										64.834	1.241	13.606	6.456					0.842	2.823	2.874	3.818		0.137	
										54.851	1.869	14.272	9.908					3.781	6.606	3.486	1.403		0.125	
										55.121	1.965	14.993	9.503					3.622	6.791	3.526	1.422		0.072	
										54.615	1.643	14.974	9.572					3.866	6.911	3.636	1.267		0.109	
										54.980	1.669	15.005	9.569					3.851	7.018	3.740	1.286		0.096	
										55.451	1.723	15.809	8.995					3.229	7.301	4.055	1.158		0.048	
										54.788	2.459	13.230	10.434					3.370	6.846	2.753	1.959		0.095	
										55.647	2.111	14.789	9.027					2.538	6.510	3.425	1.709		0.089	
H2 (T5, HW5)	44E	94T-44		pumice	bulk XRF					65.02	0.91	15.69	3.48				0.12	1.12	1.92	6.1	3.30	0.25		
	49A	94T-49	peat section	pumice	bulk XRF					64.84	0.85	15.86	3.39				0.12	0.96	1.88	6.19	3.15	0.27		
	38	93-38		pumice	bulk XRF					65.33	0.73	15.79	3.26				0.11	0.91	1.83	6.24	3.21	0.24		
	1C	94T-1		pumice	bulk XRF					65.79	0.77	15.48	3.44				0.11	0.89	2.01	5.96	3.19	0.22		
		94T-45	roadcut	pumice	bulk XRF, INAA					64.30	0.92	15.61			2.40	1.37	0.12	1.02	1.99	5.96	3.21	0.24		
	Layer 3	Cueva 3	cave soil	tephra	bulk wet chem., XRF, INAA					65.12	0.79	15.38			2.20	1.00	0.11	0.88	2.12	6.01	3.36	0.23		
	HUD136 (unit A)	16		tephra	bulk XRF					61.96	0.88	15.56		4.22			0.13	0.96	2.12	5.48	3.10	0.22		
	HUD204 (unit A)	17		tephra	bulk XRF					62.65	0.88	16.23		4.33			0.13	1.17	2.30	5.36	2.93	0.22		
				glass	EPMA	5	9.6-15	15	10	68.49 ± 0.30	0.68 ± 0.02	15.34 ± 0.08	3.05 ± 0.11				0.11 ± 0.04	0.64 ± 0.04	1.67 ± 0.02	6.49 ± 0.12	3.48 ± 0.10	0.12 ± 0.04		
				plg feldspar rim	EPMA		15	15	10	60.00		25.35	0.50						6.82	6.83	0.50			
				plg feldspar core	EPMA		15	15	10	59.83		25.58	0.45						6.98	6.68	0.51			
				orthopyroxene	EPMA		15	15	10	53.36	0.30	0.64	18.61				1.31	23.87	1.50	0.09	0.01	0.004		
				clinopyroxene	EPMA		15	15	10	52.29	0.51	1.45	9.40				0.77	14.94	19.90	0.48	0.03	0.002		
				Fe-Ti oxide pair	EPMA		15	15	10		14.30	2.02	76.01				0.98	2.65						
											44.65	0.24	47.51				1.13	3.81						
	HUD203 (unit B)	17		tephra	bulk XRF					62.26	0.89	16.36		4.16			0.13	0.94	2.21	5.39	2.92	0.22		
				glass	EPMA	6	9.6-15	15	10	67.23 ± 0.39	0.63 ± 0.06	15.11 ± 0.21	3.00 ± 0.28				0.14 ± 0.03	0.62 ± 0.02	1.55 ± 0.05	6.44 ± 0.26	3.43 ± 0.11	0.10 ± 0.02		
				plg feldspar rim	EPMA		15	15	10	60.34		24.57	0.51						6.09	6.94	0.56			
				plg feldspar core	EPMA		15	15	10	59.25		25.32	0.48						7.03	6.61	0.50			
				orthopyroxene	EPMA		15	15	10	53.13	0.31	0.64	18.09				1.24	23.94	1.50	0.02	0.004			
				clinopyroxene	EPMA		15	15	10	51.50	0.65	1.73	8.98				0.67	15.03	19.96	0.40	0.007			
				Fe-Ti oxide pair	EPMA		15	15	10		14.21	2.06	75.52				1.01	2.61						
											44.35	0.31	47.58				1.11	3.88						

	HUD134 (unit C)	16		tephra	bulk XRF					61.07	1.03	16.77		5.08			0.14	1.31	2.85	5.1	2.72	0.29		
	HUD202 (unit C)	17		tephra	bulk XRF					61.49	0.91	16.94		4.31			0.13	0.91	2.18	5.30	2.85	0.22		
				glass	EPMA	4	9.6-15	15	10	67.93 ± 0.38	0.60 ± 0.08	15.14 ± 0.16	3.05 ± 0.23				0.14 ± 0.03	0.64 ± 0.03	1.63 ± 0.08	6.30 ± 0.30	3.48 ± 0.06	0.11 ± 0.04		
				plg feldspar rim	EPMA		15	15	10	60.48		25.49	0.50						6.92	6.74	0.53			
				plg feldspar core	EPMA		15	15	10	59.16		25.80	0.50						7.58	6.37	0.46			
				orthopyroxene	EPMA		15	15	10	53.84	0.31	0.64	18.01				1.22	24.38	1.56	0.05	0.009			
				clinopyroxene	EPMA		15	15	10	51.60	0.66	1.78	9.29				0.74	14.48	20.23	0.46	0.009			
				Fe-Ti oxide pair	EPMA		15	15	10		14.51	2.09	76.06				0.95	2.67						
											45.04	0.26	47.53				1.08	3.97						
	CAS-T8	Lag. Castor	lake sedi. core	tephra	bulk XRF					64.0	0.5	15.7		2.6			0.1	1.2	2.1	4.3	3.1	0.1		
	Mir-1	Lag. Miranda	lake sedi. core	glass	EPMA		10	20	10	64.282	1.182	16.194	4.920					1.477	3.439	2.941	2.675		0.092	
										64.226	1.254	16.013	4.588					1.324	3.263	2.828	2.878		0.108	
										64.232	1.258	16.132	4.624					1.447	3.335	3.062	2.586		0.117	
										65.481	1.129	15.852	4.184					0.968	2.960	3.069	2.794		0.113	
										64.492	1.354	15.502	4.907					1.365	2.857	2.960	2.942		0.119	
										65.664	1.226	16.494	3.805					1.059	3.361	4.952	2.052		0.074	
										64.145	1.182	15.939	4.618					1.445	3.315	3.095	2.678		0.091	
										64.636	1.230	16.131	4.468					1.347	3.258	3.191	2.717		0.071	
										64.040	1.211	16.017	4.822					1.441	3.160	3.438	2.938		0.072	
										64.105	0.886	18.319	3.057					0.744	4.393	4.991	1.861		0.088	
										62.864	1.191	15.752	4.507					1.368	4.874	3.159	2.572		0.130	
										64.108	1.297	16.164	4.861					1.578	3.474	2.882	2.526		0.118	
										64.883	1.247	16.268	4.434					1.379	3.148	2.888	2.693		0.069	
										64.233	1.251	16.001	4.812					1.344	3.337	3.226	2.597		0.069	
										64.591	1.214	16.317	4.822					1.562	3.281	3.042	2.671		0.088	
										64.321	1.246	16.250	4.656					1.527	3.258	2.960	2.665		0.076	
										64.222	1.259	16.217	4.434					1.525	3.336	3.136	2.578		0.105	
										64.022	1.250	15.918	4.425					1.375	3.278	2.913	2.621		0.117	
										64.260	1.207	16.167	4.929					1.544	3.377	3.295	2.672		0.124	
										63.903	1.332	16.072	4.909					1.459	3.468	3.072	2.597		0.121	
										64.676	1.180	16.080	4.431					1.356	3.099	2.977	2.785		0.131	
										63.621	1.212	15.933	4.757					1.467	3.363	3.096	2.580		0.111	
	MD07-3088-279	Off Taito Penin.	marine sedi. core	glass	EPMA		10	15	5	60.10	1.97	18.40	3.43				0.08	1.35	5.97	6.46	1.48	0.67		
										54.06	2.07	14.75	9.78				0.28	4.54	8.33	4.34	1.29	0.56		
										56.43	1.59	16.59	8.10				0.20	3.72	7.29	4.25	1.52	0.32		
										58.72	1.65	16.39	7.24				0.09	2.91	5.61	5.13	1.78	0.48		
										58.78	1.65	16.07	7.96				0.25	2.88	5.80	4.45	1.84	0.32		
										62.10	2.29	13.79	8.16				0.29	1.62	4.02	5.62	1.54	0.57		
										62.38	1.10	18.28	4.55				0.19	0.97	5.90	5.34	0.92	0.37		
										65.26	1.14	16.19	4.34				0.00	1.41	2.83	5.75	2.76	0.31		
T4	49C	94T-49	peat section	tephra	bulk XRF					62.49	1.24	16.16	4.24				0.13	1.75	3.21	5.81	2.69	0.26		
H1 (T2, HW4)	49F	94T-49	peat section	tephra	bulk XRF					61.09	1.50	16.04	5.13				0.17	2.61	4.48	5.52	1.76	0.39		
	44	94T-44		tephra	bulk XRF					60.12	1.67	16.09	5.64				0.18	2.01	3.89	5.49	2.14	0.38		
										60.53	1.56	16.11	5.49				0.17	1.98	3.96	5.54	2.26	0.36		
										60.94	1.50	15.93	5.31				0.17	1.87	3.98	5.63	2.33	0.37		
										60.61	1.59	16.06	5.45				0.17	1.97	4.02	5.57	2.27	0.36		
				pumice	bulk wet chem., XRF, INAA					61.12	1.52	16.00			3.50	2.24	0.18	1.89	3.78	5.61	2.37	0.36		
				glass	EPMA					62.89	1.39	15.61	5.16				0.16	1.81	3.54	5.79	2.81	0.29		
	65C	94T-65		tephra	bulk XRF					60.53	1.48	16.18	5.51				0.18	1.95	3.82	5.69	2.39	0.35		
	HUD174 (unit A)	17		tephra	bulk XRF					55.92	1.38	16.53		6.60			0.17	2.01	3.56	5.09	2.14	0.42		
	HUD187 (unit A)	25		tephra	bulk XRF					57.97	1.34	15.76		5.50			0.16	1.96	4.12	5.79	2.29	0.50		
				glass	EPMA	4	9.6-15	15	10	63.10 ± 0.77	1.35 ± 0.08	15.69 ± 0.18	4.98 ± 0.01				0.22 ± 0.07	1.59 ± 0.02	3.07 ± 0.08	6.34 ± 0.34	2.65 ± 0.06	0.38 ± 0.03		
				plg feldspar rim	EPMA		15	15	10	57.64		26.67	0.56						8.89	5.88	0.31			
				plg feldspar core	EPMA		15	15	10	57.17		26.82	0.50						8.68	5.92	0.34			
				orthopyroxene	EPMA		15	15	10	53.61	0.45	0.89	17.37				1.06	24.65	1.75	0.07	0.002			
				clinopyroxene	EPMA		15	15	10	51.82	0.77	1.80	9.14				0.60	15.49	19.71	0.47	0.003			
				Fe-Ti oxide pair	EPMA		15	15	10		14.73	2.93	72.71				0.72	3.99						
											44.08	0.38	46.75				0.74	4.95						
	HUD186 (unit B)	25		tephra	bulk XRF					57.27	1.37	17.58		6.54			0.16	1.91	3.89	5.23	2.09	0.48		
	HUD205 (unit B)	17		plg feldspar rim	EPMA		15	15	10	59.61		25.48	0.55						7.09	6.79	0.46			
				plg feldspar core	EPMA		15	15	10	59.77		25.47	0.49						7.14	6.64	0.46			
				orthopyroxene	EPMA		15	15	10	53.99	0.36	0.69	16.30				1.00	25.59	1.75	0.06	0.00			
				clinopyroxene	EPMA		15	15	10	51.67	0.79	1.93	9.25				0.60	15.29	19.76	0.45	0.01			
				Fe-Ti oxide pair	EPMA		15	15	10	14.88	2.91	73.71					0.81	3.66						
										43.49	0.40	47.39					0.70	4.82						
	HUD212 (unit B)	29		tephra	bulk XRF					56.56	1.26	15.52		5.15			0.15	1.90	3.90	5.75	2.24	0.46		
				glass	EPMA	3	9.6-15	15	10	64.24 ± 0.43	1.21 ± 0.04	15.29 ± 0.22	4.41 ± 0.19				0.16 ± 0.05	1.20 ± 0.02	2.72 ± 0.06	6.60 ± 0.19	2.84 ± 0.02	0.26 ± 0.02		
				plg feldspar rim	EPMA		15	15	10	47.24		34.27	0.68						17.42	1.57	0.04			
				plg feldspar core	EPMA		15	15	10	46.16		34.71	0.60						18.22	1.25	0.02			
				orthopyroxene	EPMA		15	15	10	53.50	0.40	0.99	16.94				0.87	25.25	1.81	0.04	0.004			
				clinopyroxene	EPMA		15	15	10	52.14	0.72	1.67	8.85				0.61	15.52	19.74	0.43	0.016			
				Fe-Ti oxide pair	EPMA		15	15	10		15.60	2.47	73.27				0.83	3.50						
											44.68	0.34	45.87				0.83	4.81						
	90-12	90-12	peat section	tephra	bulk wet chem., XRF, INAA					61.88	1.42	16.24			3.30	1.60	0.14	1.79	3.84	5.76	2.51	0.30		
										63.04	1.23	16.71	4.66					1.64	3.98	5.89	2.59	0.29		

				glass	EPMA					63.26	1.31	15.96	4.97				0.14	1.66	3.39	5.85	2.91	0.26		
	90-14	90-14	organic soil	tephra	*bulk XRF?*					60.61	1.38	17.14	4.98				0.18	1.57	3.56	5.13	2.26	0.38		
				glass	EPMA					63.85	1.21	15.74	4.74				0.14	1.48	3.14	5.74	2.79	0.24		
	90-23G	90-23	peat section	tephra	*bulk XRF?*					61.76	1.39	16.41	5.15				0.15	1.76	4.01	5.48	2.56	0.32		
										62.58	1.24	16.79	4.55					1.76	4.38	5.78	2.56	0.36		
				glass	EPMA					63.61	1.26	15.55	5.04				0.13	1.61	3.21	5.92	2.88	0.25		
	Opr-5	Lag. Oprasa	lake sedi. core	glass	EPMA		10	20	10	53.684	1.245	15.213	9.264					5.538	8.675	3.071	1.037		0.08	
										53.589	1.166	15.799	8.984					5.501	8.955	3.271	0.835		0.09	
										53.268	1.215	16.009	8.696					5.572	8.984	3.231	0.899		0.06	
										53.300	1.202	15.869	9.032					5.615	8.963	3.411	0.910		0.07	
										54.154	1.329	15.894	9.480					5.763	8.903	3.459	0.844		0.03	
										53.915	1.348	15.327	9.775					5.693	8.429	3.400	0.952		0.07	
										53.323	1.315	14.876	9.365					5.377	8.876	3.235	0.986		0.07	
										53.391	1.302	14.837	9.102					5.154	8.822	3.028	0.925		0.06	
										53.388	1.375	14.569	10.257					5.360	8.448	2.996	0.965		0.08	
										53.384	1.358	14.927	10.076					4.973	8.579	3.298	0.893		0.09	
										53.600	1.280	15.498	9.723					5.489	8.796	3.179	0.986		0.06	
										53.929	1.341	16.160	9.772					5.319	8.754	3.272	0.922		0.04	
										53.376	1.500	13.924	11.197					5.469	8.569	2.747	1.011		0.09	
										53.085	1.506	14.166	10.210					4.970	8.372	3.084	1.031		0.08	
										53.537	1.107	17.847	8.141					3.886	9.527	3.753	0.709		0.07	
										53.386	0.917	18.272	7.001					4.183	9.631	3.423	0.651		0.03	
										53.428	1.254	15.474	9.669					5.097	8.597	3.084	0.948		0.07	
										54.150	1.105	18.247	7.464					3.767	9.211	3.891	0.715		0.05	
										53.049	1.417	13.858	10.562					5.022	8.429	2.993	1.038		0.07	
										53.132	1.226	15.580	9.521					4.477	8.945	3.825	0.866		0.05	
										52.490	1.377	14.387	10.127					5.355	8.419	2.948	0.896		0.05	
										53.068	1.341	14.678	10.067					5.280	8.513	3.211	0.939		0.08	
										53.149	0.983	18.485	7.695					4.497	9.660	3.378	0.696		0.08	
										54.271	1.281	15.708	9.710					5.372	8.754	3.350	0.856		0.05	
										53.377	1.183	15.990	8.704					4.901	9.232	3.259	0.863		0.08	
										53.153	1.269	14.793	9.161					5.193	8.566	3.142	0.973		0.10	
										53.782	1.231	15.341	9.095					5.635	8.613	3.112	1.126		0.08	
	#15 Salmi (1941)			tephra	bulk XRF					59.36	1.79	20.97	5.12				0.11	1.59	3.93	4.34	2.51	0.28		
	Hu-4	Puerto Hambre/ Lago Chandler	peat/lake sedi. core	glass	EPMA		20	15	5-20	76.22	0.19	13.74	1.16				0.02	0.16	1.19	2.94	4.35			
										79.29	0.15	11.82	0.88				0.02	0.18	1.07	2.47	4.12			
										77.51	0.18	13.63	1.10				0.02	0.14	1.19	2.28	3.95			
										78.24	0.16	13.88	1.10				0.00	0.18	1.05	1.76	3.63			
	LF06-PC16-482	Lago Fagnano	lake sedi. core	tephra	bulk ICP-MS																			
	LF06-PC12-142	Lago Fagnano	lake sedi. core	tephra	bulk ICP-MS																			
	LasCot-475	Las Cotorras	peat core	glass	EDS		1	25		65.44	1.64	15.55	5.60				0.31	1.62	3.38	3.46	2.85			
										65.50	1.17	17.51	4.65				0.17	1.54	3.06	3.73	2.43			
										66.00	1.13	17.32	4.06				0.12	1.31	2.99	4.27	2.75			
										65.47	1.20	17.62	3.53				0.14	1.50	2.91	4.92	2.17			
										66.27	1.51	16.59	4.73				0.29	1.27	2.68	3.44	2.79			
										65.95	1.01	17.96	4.04				0.05	1.42	2.66	3.99	1.88			
										67.01	1.30	16.11	4.61				0.14	1.19	2.59	3.05	2.94			
										66.74	1.32	16.64	4.40				0.16	1.41	2.60	3.74	2.74			
										66.10	1.40	16.14	5.38				0.26	1.45	3.07	3.39	2.76			
										66.12	1.31	15.84	4.92				0.19	1.29	2.82	3.49	2.99			
										65.83	1.37	16.39	4.93				0.17	1.59	3.10	3.81	2.73			
										66.28	1.03	16.82	4.16				0.08	1.45	2.60	3.86	2.68			
										62.28	1.22	17.09	5.37				0.22	2.53	4.20	3.86	2.39			
										65.24	1.24	16.55	5.27				0.16	1.49	3.48	3.71	2.82			
										65.38	1.38	16.70	4.47				0.14	1.49	2.96	3.88	2.77			
										66.47	1.26	16.39	4.94				0.08	1.45	2.95	3.49	2.92			
										65.59	1.29	16.28	4.97				0.13	1.32	3.07	4.04	2.86			
										65.52	1.28	16.41	5.26				0.13	1.31	3.28	3.91	2.85			
										65.37	1.35	16.34	5.01				0.06	1.39	3.13	3.52	2.86			
										64.57	1.27	16.08	5.52				0.13	1.88	4.04	3.77	2.69			
										65.11	1.23	16.57	4.44				0.20	1.52	2.82	4.10	2.76			
	PTA-03/12_1090	Potrok-Aike	lake sedi. core	glass	EPMA	19	20	15	15	65.30 ± 0.97	1.23 ± 0.06	16.16 ± 0.09	4.93 ± 0.37				0.16 ± 0.04	1.50 ± 0.26	2.97 ± 0.43	4.47 ± 0.29	2.80 ± 0.12	0.35 ± 0.06	0.13 ± 0.02	
	CAR98-11-124	Lago Cardiel	lake sedi. core	tephra	bulk XRF																			
	CAR98-2L-838.5	Lago Cardiel	lake sedi. core	tephra	bulk XRF																			
	CAR99-2L-462.5	Lago Cardiel	lake sedi. core	tephra	bulk XRF																			
	PCAR-99-7-4-60	Lago Cardiel	lake sedi. core	tephra	bulk XRF																			
	PCAR-99-9-11-370	Lago Cardiel	lake sedi. core	tephra	bulk XRF																			
	CS-3002	Lago Pepa	lake sedi. core	tephra	bulk XRF																			
	CS-2715	Lago Edita	lake sedi. core	tephra	bulk XRF																			
	CS-1031	Lago Maldonado	lake sedi. core	tephra	bulk XRF																			
	Harb-682.6	Haberton	peat core	tephra	bulk ICP-OES, ICP-MS						1.13	13.34						1.23			2.06			
T1	49H	94T-49	peat section	tephra	bulk XRF					58.44	1.93	16.13	6.39				0.16	2.61	4.48	5.52	1.76	0.39		
Undefined	Opr-4	Lag. Oprasa	lake sedi. core	glass	EPMA		10	20	10	62.604	1.587	13.308	7.483					2.008	3.651	3.152	1.799		0.182	
										62.149	1.753	14.415	7.252					1.335	4.008	3.665	1.758		0.166	
										62.507	1.453	15.699	6.473					1.122	4.078	4.364	1.671		0.157	
										61.838	1.562	13.530	7.821					1.836	3.880	4.050	1.948		0.192	
										62.700	1.550	14.265	7.103					1.608	3.801	3.231	1.788		0.211	
										62.972	1.420	15.477	6.711					1.506	4.393	4.314	1.629		0.161	
	TL2	Off Taito Penin.	marine sedi. core	glass	EPMA		10	15	5	55.26	2.00	16.05	9.37				0.19	3.59	6.80	4.64	1.49	0.60		
										55.35	1.79	16.47	9.69				0.23	4.24	8.01	2.10	1.48	0.65		

									55.64	1.74	16.21	9.38				0.18	4.31	7.78	2.58	1.38	0.81		
									56.33	1.61	15.85	10.10				0.19	4.09	7.83	2.02	1.34	0.63		
									57.02	1.59	15.97	8.44				0.13	3.64	6.63	4.21	1.71	0.66		
									57.04	1.96	14.21	10.35				0.22	3.83	7.21	2.54	1.91	0.72		
									57.64	1.71	16.25	8.39				0.21	3.05	6.15	4.41	1.49	0.70		
									59.67	1.60	16.37	7.06				0.15	2.73	5.39	4.46	1.98	0.60		
									59.69	1.70	15.12	9.72				0.23	2.84	6.33	2.07	1.79	0.51		
									60.18	1.58	16.32	8.06				0.22	3.14	6.35	1.83	1.73	0.59		
									60.71	1.50	16.33	7.03				0.17	2.27	4.62	4.48	2.25	0.65		
									64.56	1.52	16.27	6.17				0.15	2.08	4.54	1.88	2.31	0.52		
									64.60	1.29	15.94	5.27				0.16	1.46	2.97	5.28	2.67	0.36		
									66.32	1.22	16.66	4.41				0.21	1.25	2.57	4.14	2.87	0.35		
									69.12	0.65	16.16	3.43				0.16	0.73	1.50	5.04	3.06	0.14		
HW3	Fac-2	Lag. Facil	lake sedi. core	glass	EPMA		10	20	10	54.314	2.133	17.346	9.266					2.400	8.311	3.574	1.282		0.099	
										53.268	1.954	17.728	8.379					1.906	8.285	4.249	1.198		0.042	
										51.606	1.589	16.612	8.558					3.814	7.501	4.278	1.150		0.086	
										53.769	1.863	17.499	8.159					2.224	8.247	4.373	1.135		0.083	
										58.986	1.254	13.459	6.338					2.774	6.795	3.664	2.148		0.002	
										52.997	2.758	13.718	12.519					3.280	6.298	3.872	1.533		0.110	
										54.277	1.911	18.649	6.262					1.484	7.924	3.757	1.181		0.056	
										52.866	1.478	13.280	8.663					6.385	10.417	3.290	0.831		0.043	
										54.211	2.633	14.332	12.009					3.820	6.449	3.689	1.222		0.103	
										52.792	2.209	16.923	10.238					2.022	7.926	4.194	1.378		0.113	
										54.652	2.304	13.290	10.322					3.845	6.944	3.078	2.036		0.062	
										59.983	2.570	12.678	9.800					1.909	2.812	6.448	1.373		0.070	
										60.009	1.772	15.066	7.777					1.908	5.176	3.777	2.323		0.132	
										62.040	1.233	16.698	5.502					0.884	4.551	4.323	2.624		0.075	
										57.523	1.561	16.360	6.765					3.087	5.973	3.455	2.049		0.096	
										59.374	1.836	14.310	8.230					2.129	5.030	3.239	2.415		0.118	
	Opr-3	Lag. Oprasa	lake sedi. core	glass	EPMA		10	20	10	59.340	2.053	14.721	8.592					2.450	4.910	4.012	2.352		0.122	
										56.741	2.597	13.871	11.581					3.847	6.432	3.745	1.866		0.089	
										55.990	2.016	14.935	10.112					3.344	6.479	3.972	1.903		0.089	
										53.643	1.749	14.000	11.047					4.626	8.390	3.330	0.941		0.045	
										55.537	2.196	14.825	10.038					2.550	6.219	4.424	2.141		0.046	
										55.236	1.939	15.715	8.334					2.194	6.569	4.276	1.880		0.088	
										58.691	2.027	15.359	9.522					1.831	3.495	7.781	1.294		0.030	
										57.085	2.813	14.901	11.267					2.447	5.315	3.959	2.063		0.122	
										52.924	0.986	15.46	11.868					9.070	5.879	3.061	1.047		0.054	
										56.532	2.068	18.484	6.965					1.239	6.431	5.397	1.077		0.043	
										54.223	2.197	12.070	11.489					5.563	8.034	3.547	1.392		0.010	
										57.719	1.397	17.595	5.333					1.401	6.727	5.204	1.533		0.067	
										55.205	1.680	16.294	8.427					2.764	7.442	4.268	1.411		0.037	
										53.190	1.530	14.002	10.937					4.578	8.326	2.899	0.869		0.090	
										53.546	1.646	14.107	10.940					4.720	8.171	3.255	0.967		0.090	
										54.085	1.726	14.818	10.119					4.233	7.594	3.532	1.089		0.059	
	Lin-3	Lag. Lincoln	lake sedi. core	glass	EPMA		10	20	10	54.806	2.730	13.901	12.072					3.430	6.926	2.359	1.499		0.142	
										53.165	1.937	13.085	11.372					4.578	8.441	3.067	1.082		0.097	
										55.254	2.850	15.726	10.361					1.925	7.036	4.027	1.455		0.114	
										55.834	2.438	13.900	9.496					3.399	7.858	3.271	1.476		0.120	
										63.276	1.487	14.582	7.032					0.986	4.699	3.758	1.014		0.040	
										54.077	2.593	13.119	11.661					3.618	7.364	2.741	1.389		0.121	
										55.528	2.390	16.006	10.008					2.116	6.963	3.878	1.322		0.119	
										54.614	2.731	12.538	12.474					4.772	7.483	2.385	1.266		0.081	
										54.015	2.374	11.784	13.192					5.534	6.369	3.016	1.475		0.093	
										57.427	1.872	13.285	10.704					3.517	7.601	3.224	1.026		0.066	
										55.959	2.204	14.202	9.075					3.054	6.792	3.537	1.717		0.131	
										54.715	2.234	15.329	10.665					3.524	7.408	3.430	1.156		0.065	
										52.938	1.226	17.358	10.309					4.358	7.388	3.758	0.725		0.094	
										53.328	2.822	13.652	12.081					2.745	5.675	3.698	2.078		0.261	
										54.024	2.764	13.553	10.398					3.113	7.086	3.484	1.788		0.128	
										54.560	2.797	12.072	12.760					4.169	7.938	2.765	1.346		0.104	
										55.219	2.514	14.435	10.727					2.490	6.398	3.326	1.979		0.141	
	Lof-4	Lag. Lofel	lake sedi. core	glass	EPMA		10	20	10	54.541	2.396	14.878	10.360					2.675	7.514	3.314	1.204		0.113	
										54.118	2.822	12.207	13.025					2.755	6.649	2.828	1.892		0.137	
										53.415	2.268	13.382	13.162					5.846	6.109	3.055	1.191		0.100	
										54.364	1.494	18.161	7.664					3.055	9.474	4.793	0.714		0.048	
										54.697	2.953	12.642	11.909					3.832	7.517	2.876	1.113		0.173	
										53.607	1.972	16.852	8.566					2.338	8.425	3.505	1.057		0.069	
										53.303	2.732	13.988	10.766					2.542	6.899	3.539	1.763		0.093	
										52.592	2.566	12.966	11.457					3.499	7.258	3.286	1.716		0.080	
										52.797	1.324	17.772	6.358					4.104	10.000	3.955	0.732		0.069	
										53.382	2.023	17.158	7.013					2.093	8.160	3.985	1.364		0.095	
										53.751	2.963	11.460	14.920					2.998	6.715	2.439	2.196		0.101	
										52.681	2.217	15.111	9.892					3.141	6.999	4.272	1.627		0.029	
										53.657	2.211	16.615	9.407					2.666	8.240	3.077	1.369		0.115	
										56.398	1.585	14.330	9.365					4.031	5.360	4.206	2.324		0.040	
										64.014	0.995	14.559	4.224					1.680	4.261	4.146	2.169		0.124	
										67.073	0.666	14.575	4.196					0.751	2.227	2.952	3.161		0.170	
										67.602	0.635	14.670	4.164					0.588	2.268	3.174	3.253		0.184	
	Stb-2	Lag. Stibnite	lake sedi. core	glass	EPMA		10	20	10	53.247	2.208	15.518	9.711					2.942	7.769	3.684	1.185	0.625		
										52.718	2.437	14.969	9.507					3.459	7.505	3.595	1.691	0.838		
	Six-2	Lag. Six Minutes	lake sedi. core	glass	EPMA		10	20	10	57.710	2.179	14.688	8.932					1.753	5.674	4.455	1.836	1.105		
										55.339	2.414	14.507	11.930					3.710	6.951	3.405	1.212	0.911		
										54.898	2.297	15.644	10.178					2.700	7.785	3.908	1.466	0.745		
										54.773	2.467	14.500	12.490					3.101	7.017	3.622	1.372	0.863		
										54.468	2.248	15.480	10.877					2.609	7.378	3.603	1.340	0.774		

										53.849	2.131	15.763	10.842					3.059	7.610	3.706	1.105	0.695		
										53.836	2.266	15.638	11.015					2.983	7.674	3.540	1.374	0.751		
										53.829	1.960	16.701	9.406					2.466	7.769	4.050	1.276	0.633		
										53.677	2.423	14.174	13.065					3.053	6.455	3.764	1.494	0.763		
										53.628	2.241	14.960	11.794					3.803	7.617	3.329	1.180	0.697		
										53.475	2.076	15.818	10.935					3.562	7.320	3.825	1.241	0.631		
										52.885	2.307	14.056	11.993					4.014	7.292	3.218	1.260	0.721		
										52.613	2.114	13.978	13.541					4.686	6.809	3.481	1.295	0.694		
										52.057	2.297	13.404	12.169					3.760	7.406	3.137	1.098	0.827		
										51.676	1.761	15.197	12.908					5.253	6.389	3.785	1.013	0.604		
	TL3	Off Taito Penin.	marine sedi. core	glass	EPMA		10	15	5	53.83	2.05	16.20	9.42				0.23	3.82	7.62	4.52	1.38	0.93		
										56.57	1.85	16.09	8.68				0.02	3.27	7.18	4.48	1.44	0.42		
										56.67	2.17	15.34	8.30				0.20	3.19	6.05	5.56	1.68	0.84		
										56.92	1.68	16.60	8.20				0.05	3.35	7.21	4.17	1.38	0.43		
										56.97	1.88	16.82	7.99				0.24	2.98	6.55	3.95	1.59	1.04		
										57.69	1.76	16.49	7.06				0.20	3.23	6.23	5.07	1.57	0.69		
										57.93	1.63	16.72	7.25				0.19	2.97	5.93	5.03	1.67	0.69		
										58.09	1.66	16.59	7.22				0.15	3.06	6.05	4.97	1.61	0.61		
										58.95	1.71	16.16	6.95				0.13	2.97	5.70	4.98	1.82	0.63		
										60.70	1.50	16.02	6.64				0.25	2.20	4.90	4.89	2.18	0.72		
										60.70	1.64	16.83	6.13				0.24	2.14	4.67	4.88	2.29	0.49		
										61.08	1.61	16.05	6.21				0.13	2.07	4.48	5.11	2.58	0.69		
										61.20	1.51	16.19	6.15				0.15	2.22	4.50	5.08	2.25	0.77		
										67.14	0.95	16.20	3.33				0.19	0.91	2.11	5.95	2.91	0.31		
										67.42	0.99	16.35	3.64				0.06	0.92	2.04	5.27	3.10	0.22		
										67.48	0.75	15.90	3.45				0.19	0.75	1.47	6.23	3.55	0.23		
										67.61	1.03	16.71	3.61				0.09	0.90	2.73	4.17	2.90	0.25		
										68.56	0.61	16.18	3.27				0.32	0.87	2.21	4.61	3.19	0.18		
	EDC-339.5	EPICA-Dome C	ice core	glass	EPMA		10	15	5-10	57.16 ± 1.01	0.96 ± 0.12	15.59 ± 1.95	11.06 ± 1.56				0.24 ± 0.05	3.49 ± 1.17	7.77 ± 0.45	3.31 ± 0.57	0.43 ± 0.06			
	SDMA-9008	Siple Dome	ice core	glass	EPMA		10	15	10-25	55.31	1.15	12.99	14.06				0.29	3.18	7.37	4.65	0.65	0.23		0.10
										55.69	1.05	15.14	12.96				0.29	2.60	8.94	2.59	0.49	0.18		0.07
										56.29	0.84	13.32	13.07				0.31	6.16	7.33	2.23	0.34	0.07		0.00
										56.42	1.21	16.20	12.05				0.22	2.42	7.32	3.48	0.46	0.13		0.07
										56.48	1.02	15.95	11.10				0.27	2.46	8.53	3.09	0.55	0.15		0.33
										56.61	1.19	14.47	13.11				0.30	2.44	8.30	2.70	0.59	0.17		0.05
										57.50	1.21	13.18	13.12				0.27	2.87	6.92	3.90	0.58	0.20		0.20
										57.61	0.74	17.29	9.22				0.23	2.36	7.59	4.39	0.44	0.10		0.00
										57.81	1.03	15.60	10.81				0.25	2.64	7.42	3.60	0.54	0.15		0.08
										58.24	0.98	14.01	12.41				0.29	3.68	6.88	2.73	0.47	0.17		0.09
										58.49	1.16	14.91	11.92				0.31	2.20	7.00	3.16	0.60	0.21		0.00
										58.92	0.93	15.61	10.83				0.30	2.61	7.01	2.99	0.53	0.11		0.09
										64.18	0.62	14.08	8.65				0.24	2.23	5.74	3.49	0.68	0.09		0.00
HW2	Lof-2	Lag. Lofel	lake sedi. core	glass	EPMA		10	20	10	65.396	1.121	15.427	4.187					0.453	3.493	5.946	1.471		0.021	
										43.974	0.758	11.596	10.205					16.020	10.995	2.415	0.383		0.055	
										68.272	0.545	14.696	5.585					1.555	2.832	4.766	2.809		0.062	
										53.408	1.873	14.698	11.259					4.175	5.818	4.920	2.117		0.097	
	Lof-3	Lag. Lofel	lake sedi. core	glass	EPMA		10	20	10	54.290	2.220	15.047	9.687					3.740	7.224	3.509	1.860		0.117	
										54.654	2.037	14.728	9.331					3.615	7.020	3.460	2.097		0.106	
										54.121	1.942	14.904	9.486					3.828	7.252	3.758	1.790		0.099	
										54.317	2.155	15.041	9.566					3.705	7.106	3.495	1.895		0.110	
										54.401	2.141	15.137	9.283					3.628	6.935	3.545	1.833		0.138	
										54.465	2.001	14.944	9.749					3.567	7.070	3.372	1.945		0.093	
										54.184	2.077	14.985	9.672					3.619	7.097	3.319	1.854		0.129	
										54.025	2.211	14.921	9.609					3.779	7.128	3.547	1.948		0.092	
										65.804	1.004	16.159	3.291					0.979	1.958	3.367	2.940		0.179	
	Lin-2	Lag. Lincoln	lake sedi. core	glass	EPMA		10	20	10	63.189	1.152	16.647	5.206					1.460	3.495	3.116	2.763		0.228	
										61.901	1.222	16.150	5.546					1.616	3.618	3.134	2.680		0.150	
										62.924	1.147	16.364	5.594					1.466	3.618	3.002	2.872		0.168	
										62.753	1.158	16.230	5.641					1.496	3.574	3.321	2.893		0.186	
										63.199	1.568	14.564	6.549					1.183	2.906	2.983	3.296		0.238	
										62.387	1.194	16.157	5.780					1.611	3.463	2.978	2.992		0.203	
										62.674	1.625	14.333	7.213					1.784	3.129	4.161	3.351		0.200	
										63.375	1.157	16.338	5.154					1.333	3.373	3.009	3.030		0.168	
										63.176	1.094	16.883	5.705					1.661	3.620	3.650	2.831		0.197	
										62.988	1.177	16.296	5.288					1.329	3.422	3.515	2.895		0.207	
										62.996	1.343	14.925	6.860					1.544	2.979	3.995	3.537		0.246	
										62.730	1.223	15.532	5.769					1.390	3.846	4.480	2.418		0.167	
										62.014	1.202	16.083	5.412					1.553	3.707	3.467	2.768		0.175	
										62.696	1.269	15.993	5.752					1.652	3.704	3.589	2.830		0.200	
										62.311	1.238	16.637	5.690					1.610	3.773	3.497	2.802		0.166	
										62.587	1.207	16.428	5.562					1.448	3.561	3.149	2.847		0.197	
										62.710	1.247	16.292	5.452					1.509	3.550	2.989	2.890		0.203	
										62.146	1.298	15.509	6.524					1.652	2.956	4.121	3.729		0.224	
										61.429	1.178	15.854	5.952					1.695	3.416	3.412	2.996		0.340	
										63.277	1.093	17.099	4.981					1.348	3.995	5.655	2.166		0.149	
										62.686	1.262	16.380	5.574					1.654	3.773	3.272	2.721		0.178	
										63.234	1.162	16.516	5.310					1.516	3.584	3.289	2.880		0.145	
										61.917	1.207	16.139	6.509					2.593	3.635	3.870	3.584		0.172	
										62.219	1.226	16.360	5.979					1.571	3.696	3.456	2.807		0.184	
										63.123	1.235	16.491	5.553					1.310	3.983	4.143	2.526		0.144	
										62.838	1.124	16.407	5.608					1.409	3.434	3.226	2.872		0.156	
	Stb-1	Lag. Stibnite	lake sedi. core	glass	EPMA		10	20	10	52.451	2.085	16.575	9.631					3.255	8.08	4.08	1.385	1.231		
										52.15	2.288	17.077	9.02					2.471	8.437	4.086	1.747	1.253		
										52.066	1.706	17.298	7.686					2.853	8.941	4.525	1.055	1.013		
										51.693	2.224	16.626	10.141					3.288	8.066	4.504	1.177	1.237		
										51.618	2.415	15.792	9.683					2.762	8.822	4.068	0.931	1.331		

										51.604	2.681	13.968	10.269					3.727	8.316	4.318	1.315	1.232		
										51.601	2.464	15.526	11.256					3.571	7.515	4.234	1.433	1.215		
										51.429	2.468	15.445	10.311					3.651	8.404	4.429	1.408	1.307		
										51.422	2.978	13.203	11.596					3.695	7.658	3.693	2.351	1.694		
										51.406	2.19	14.96	12.146					5.338	7.118	4.493	1.344	1.217		
										51.137	2.698	13.611	11.814					3.832	7.545	3.728	1.607	1.413		
										51.06	2.102	17.38	8.319					3.034	9.011	4.265	0.945	1.181		
										50.967	2.538	14.182	11.405					3.63	7.339	4.399	1.775	1.387		
										50.658	2.476	14.46	12.725					4.512	7.044	4.626	1.406	1.348		
										50.565	2.671	12.85	12.331					4.781	7.278	3.779	1.899	1.518		
										50.376	3.05	12.873	11.709					3.45	8.375	3.777	1.778	1.572		
										49.968	2.855	12.968	11.236					3.443	8.532	4.2	1.101	1.556		
										49.099	2.105	13.165	13.656					7.086	6.197	4.051	1.343	1.191		
	Six-1	Lag. Six Minutes	lake sedi. core	glass	EPMA		10	20	10	54.579	1.997	17.552	9.083					2.978	8.144	5.552	0.906	1.059		
										54.321	2.026	17.706	9.549					3.246	8.226	5.415	0.985	1.044		
										53.626	2.111	17.376	8.86					2.658	8.488	4.793	1.072	1.339		
										53.157	2.201	16.833	9.109					3.467	8.096	4.768	1.862	1.296		
										53.128	2.184	17.184	9.559					3.052	7.238	5.103	1.302	1.116		
										52.431	1.658	17.975	8.955					2.998	7.993	4.888	1.167	1.021		
										52.299	2.662	15.054	10.801					3.405	7.573	4.645	1.631	1.413		
										52.240	2.549	15.870	11.515					3.445	7.411	4.605	1.379	1.523		
										52.124	2.021	16.866	8.860					3.206	8.756	4.537	1.234	1.014		
										52.064	2.153	15.263	11.186					4.156	7.379	4.573	1.552	1.348		
										51.904	2.425	14.268	11.251					4.513	7.948	4.601	1.383	1.524		
										51.886	2.285	15.001	10.306					3.621	8.016	4.372	1.562	1.181		
										51.856	2.580	14.665	10.388					3.439	8.505	4.849	1.377	1.222		
	TL4	Off Taito Penin.	marine sedi. core	glass	EPMA		10	15	5	54.14	1.98	15.21	9.67				0.26	4.51	8.13	4.05	1.43	0.63		
										56.51	1.84	16.21	8.19				0.26	3.29	6.79	4.67	1.57	0.68		
										59.55	1.63	16.33	6.56				0.21	2.74	5.32	4.93	2.07	0.65		
										60.92	1.92	16.44	6.73				0.21	2.77	5.29	2.95	2.02	0.73		
										61.42	1.56	16.43	5.77				0.13	2.23	4.48	5.17	2.27	0.54		
										63.68	1.49	16.22	4.57				0.31	1.49	3.44	5.87	2.46	0.46		
										65.91	1.41	15.64	4.75				0.14	1.31	2.66	5.08	2.69	0.42		
										65.92	1.25	16.28	3.77				0.15	1.07	2.49	5.96	2.78	0.34		
										66.44	1.08	16.47	3.74				0.14	1.12	2.68	5.39	2.67	0.27		
										66.87	1.08	16.74	3.86				0.26	1.15	2.31	4.85	2.62	0.26		
										66.97	0.95	16.09	3.37				0.13	0.97	2.07	6.08	3.14	0.21		
										67.57	0.97	16.02	3.50				0.25	1.02	2.58	4.84	2.99	0.27		
										67.57	1.08	15.70	3.66				0.41	0.89	1.80	5.53	3.12	0.24		
										69.17	0.79	16.09	3.70				0.14	0.91	2.28	3.70	2.96	0.26		
										69.88	0.91	15.65	2.88				0.11	0.64	1.88	4.86	3.04	0.14		
HW1	Fac-1	Lag. Facil	lake sedi. core	glass	EPMA		10	20	10	67.007	1.067	16.485	3.395					0.944	1.797	3.832	3.142		0.111	
										66.021	1.049	15.985	3.381					1.016	1.752	3.441	3.099		0.152	
										65.969	0.979	16.322	3.289					0.954	1.888	3.511	2.985		0.141	
										67.43	1.011	16.694	3.387					0.930	1.994	3.554	2.889		0.140	
										66.925	1.031	16.577	3.322					0.896	1.898	3.613	2.876		0.113	
										63.068	0.521	16.03	5.372					4.949	2.738	6.018	1.581		0.002	
										66.527	0.962	16.454	3.300					0.919	1.935	3.387	2.994		0.082	
										65.902	1.09	16.282	3.729					0.931	2.082	3.823	2.910		0.123	
										66.028	0.977	16.444	3.532					0.983	1.985	3.518	2.943		0.144	
										66.274	0.994	16.335	3.412					0.883	1.948	3.657	2.895		0.125	
										66.569	1.012	16.52	3.273					0.906	1.800	3.601	3.119		0.115	
										65.824	0.974	16.208	3.448					0.947	1.871	3.483	2.979		0.146	
										66.21	1.017	16.438	3.370					1.033	1.834	3.643	2.864		0.131	
										66.99	1.001	15.784	3.388					0.806	1.491	3.170	3.157		0.185	
										66.856	1.019	16.47	3.425					0.983	1.834	3.736	3.014		0.113	
										65.833	1.033	16.341	3.322					0.832	1.940	3.446	2.957		0.116	
										66.615	1.048	16.238	3.373					0.962	1.862	3.629	2.983		0.130	
	Opr-1	Lag. Oprasa	lake sedi. core	glass	EPMA		10	20	10	54.366	1.752	14.784	8.471					3.986	7.927	4.122	1.338		0.094	
										55.152	1.85	15.073	8.070					3.104	8.056	3.693	1.557		0.102	
										58.502	1.322	16.456	5.619					3.756	7.379	4.653	1.246		0.077	
										60.687	1.29	16.221	5.762					2.362	4.792	3.809	2.388		0.127	
										55.189	2.039	14.199	9.289					4.266	6.565	3.691	2.195		0.147	
										57.86	1.961	15.09	8.602					2.864	5.336	3.985	2.324		0.093	
										55.027	1.923	14.215	8.557					3.745	7.293	3.353	1.727		0.088	
										55.11	1.564	15.968	8.000					3.635	7.544	3.907	1.580		0.116	
										56.514	1.209	16.966	5.117					3.307	8.255	3.847	1.524		0.053	
										53.938	1.711	14.54	8.662					4.659	7.518	3.618	1.596		0.073	
										53.554	1.606	15.293	8.162					4.372	7.782	3.561	1.497		0.101	
										54.644	1.551	16.032	7.783					3.795	7.582	3.989	1.568		0.102	
										54.265	1.655	13.204	13.287					4.884	3.160	3.323	2.853		0.101	
										54.704	1.56	15.419	7.604					3.489	6.634	3.690	1.661		0.123	
										53.546	1.734	12.834	9.303					7.276	8.066	2.818	1.327		0.112	
										56.782	1.569	14.963	7.452					3.230	6.527	3.754	1.435		0.103	
	Lof-1	Lag. Lofel	lake sedi. core	glass	EPMA		10	20	10	56.214	1.805	16.405	8.322					3.199	6.594	3.705	1.602		0.116	
										41.794	2.050	11.313	12.654					13.44	11.354	2.441	0.327		0.069	
										41.139	2.259	11.717	12.374					13.34	11.561	2.573	0.306		0.100	
										40.736	0.471	16.075	16.933					8.663	10.745	1.611	0.309		0.042	
										55.796	1.852	14.861	7.511					3.151	4.560	4.566	3.699		0.110	
	Lin-1	Lag. Lincoln	lake sedi. core	glass	EPMA		10	20	10	56.303	2.814	14.245	9.281					3.262	6.150	4.519	1.982		0.088	
										55.437	1.397	16.735	8.258					4.090	9.341	3.271	0.706		0.048	
										55.920	1.640	16.619	8.768					3.380	8.250	4.139	0.931		0.117	
	TL5	Off Taito Penin.	marine sedi. core	glass	EPMA		10	15	5	54.46	1.70	15.92	8.86				0.13	4.86	8.28	3.83	1.25	0.72		
										55.22	2.07	15.25	9.16				0.22	4.21	7.32	4.29	1.26	0.99		
										55.70	2.04	15.97	8.66				0.09	3.79	7.14	4.48	1.37	0.75		
										57.66	1.68	16.36	7.47				0.26	2.93	6.38	4.91	1.60	0.76		

										57.97	2.06	15.93	7.45				0.16	3.02	5.74	4.79	1.78	1.10		
										59.11	1.64	16.26	7.00				0.27	2.81	5.73	4.77	1.65	0.76		
										61.54	1.61	16.16	5.96				0.11	2.14	4.21	5.27	2.42	0.58		
										61.81	1.40	16.78	5.91				0.16	2.33	4.86	4.32	1.92	0.52		
										63.78	1.54	15.90	5.20				0.10	1.55	3.30	5.80	2.40	0.43		
										65.48	1.20	15.74	4.31				0.13	1.27	2.76	5.65	3.05	0.40		
										65.60	1.25	16.13	4.65				0.11	1.54	3.62	4.16	2.54	0.40		
										67.36	1.00	15.97	3.28				0.19	0.79	1.73	6.23	3.26	0.19		
										68.24	0.94	15.79	3.24				0.18	0.94	2.13	5.22	3.09	0.25		
										68.28	0.82	16.19	3.87				0.12	0.88	1.80	4.82	3.03	0.20		
Ho	*PC1201AT6-37*	Lago Churrasco	lake sedi. core	tephra	bulk ICP-MS																			
				dense glass	EPMA, bulk ICP-MS	≤20	15	5-10	54.95	2.03	15.7	9.09				0.18	3.52	6.90	5.30	1.54	0.80		
				olivine	EPMA	20	15	5-10	37.73	0.06	0.02		25.50			0.43	34.92	0.26					
									37.81	0.04	0.00		24.83			0.46	35.85	0.18					
									38.74	0.06	0.01		22.42			0.45	37.76	0.27					
									37.71	0.04	0.03		25.07			0.45	36.68	0.23					
				clinopyroxene	EPMA	20	15	5-10	48.27	1.62	4.16		10.14			0.24	14.4	19.38	0.36				
									48.06	1.84	4.54		11.65			0.39	15.27	16.3	0.38				
									47.06	2.01	4.90		9.60			0.27	13.42	19.79	0.36				
									51.41	0.72	1.63		10.26			0.29	16.29	16.63	0.21				
				plg microlites	EPMA	20	15	5-10	53.02		29.73	0.88					0.11	11.33	4.56	0.18			
									55.7		28.83	0.91					0.11	10.23	5.29	0.23			
									52.68		29.47	0.96					0.15	11.59	4.57	0.17			
									54.65		28.79	0.88					0.11	10.57	5.17	0.21			
									54.25		29.65	0.75					0.11	11.03	4.95	0.21			
									53.51		29.34	0.59					0.08	10.97	4.96	0.18			
	PC1203AT12-5	Lago Tranquilo	lake sedi. core	tephra	bulk ICP-MS																			
				dense glass	bulk ICP-MS																			
	PC1103ET9-8	Lago Unco	lake sedi. core	tephra	bulk ICP-MS																			
	PC1002BT7-20	Lago El Toro	lake sedi. core	tephra	bulk ICP-MS																			
	PC1105BT7-9	Lago Élida	lake sedi. core	tephra	bulk ICP-MS																			
				dense glass	bulk ICP-MS																			
				olivine	EPMA	20	15	5-10	36.67	0.11	0.34		26.35			0.47	33.86	0.48					
									36.25	0.07	0.10		28.64			0.57	32.12	0.28					
				clinopyroxene	EPMA	20	15	5-10	47.73	2.01	4.58		10.92			0.30	13.44	18.09	0.48				
									49.20	1.71	3.68		11.72			0.37	15.67	15.83	0.34				
				plg microlites	EPMA	20	15	5-10	59.41		21.86	0.38					0.04	6.88	6.09	0.43			
									58.79		26.00	0.35					0.03	6.97	7.03	0.42			
									56.31		27.97	0.86					0.09	9.53	5.49	0.30			
	LS0604A-v	Lago Shaman	lake sedi. core	tephra	bulk ICP-MS																			
	PC1106AT7-34	Lago Mellizas	lake sedi. core	dense glass	bulk ICP-MS																			
				dark pumice	EPMA, bulk ICP-MS	≤20	15	5-10	57.66	1.73	15.89	7.99				0.16	2.99	5.87	5.21	1.83	0.67		
				light pumice	EPMA, bulk ICP-MS	≤20	15	5-10	59.30	1.60	15.91	7.10				0.17	2.52	5.24	5.54	2.04	0.59		
				tan pumice	EPMA, bulk ICP-MS	≤20	15	5-10	65.75	0.90	15.48	4.35				0.14	1.08	2.56	6.64	2.90	0.21		
				olivine	EPMA	20	15	5-10	37.91	0.07	0.04		23.94			0.39	36.05	0.35					
				clinopyroxene	EPMA	20	15	5-10	49.93	1.6	4.08		13.48			0.35	15.98	12.36	0.31				
									49.15	1.43	3.9		11.36			0.39	15.43	16.56	0.42				
				orthopyroxene	EPMA	20	15	5-10	51.65	0.19	0.47		23.23			1.32	20.29	1.66					
									51.65	0.17	0.38		23.07			1.31	21.01	1.71					
									53.23	0.30	0.56		22.17			1.22	21.41	1.64					
				plg phenocryst	EPMA	20	15	5-10	54.3		29.69	0.82					0.10	11.13	4.88	0.21			
									54.76		28.74	0.96					0.16	10.73	4.89	0.30			
									58.09		26.03	1.09					0.11	8.00	6.16	0.49			
Undefined	TL6	Off Taito Penin.	marine sedi. core	glass	EPMA	10	15	5	53.27	1.88	16.17	9.64				0.13	4.41	8.22	4.44	1.17	0.66		
									53.92	2.24	15.44	9.86				0.05	3.97	7.24	4.72	1.62	0.93		
									55.77	1.74	16.17	8.06				0.12	4.02	7.83	4.35	1.15	0.80		
									60.07	1.76	16.59	6.46				0.28	2.36	5.13	4.64	2.15	0.55		
									62.05	1.29	16.28	5.68				0.22	2.05	4.35	5.35	2.21	0.54		
									64.92	1.31	16.09	4.57				0.23	1.33	2.72	5.44	3.04	0.33		
									66.85	0.80	16.17	3.93				0.24	1.00	2.60	4.96	3.08	0.37		
									68.03	1.13	15.24	3.69				0.18	0.85	2.32	5.14	3.14	0.26		
									68.24	0.80	16.56	2.79				0.10	0.62	1.38	6.29	3.07	0.14		
Undefined	TL7	Off Taito Penin.	marine sedi. core	glass	EPMA	10	15	5	52.05	2.08	15.40	11.45				0.17	4.50	8.51	4.38	0.97	0.48		
									53.67	1.95	16.71	9.33				0.19	4.86	8.64	2.82	1.08	0.74		
									54.08	1.62	15.28	10.92				0.21	4.63	9.04	2.74	1.18	0.29		
									54.26	1.58	16.18	9.37				0.22	4.91	9.09	2.71	1.26	0.43		
									54.41	1.80	16.27	9.66				0.19	4.61	8.34	2.71	1.38	0.63		
									55.56	1.73	16.85	8.91				0.14	4.49	8.27	2.47	1.16	0.41		
									56.84	1.64	15.26	9.36				0.17	4.16	7.74	2.61	1.73	0.49		
									56.84	1.90	15.99	8.85				0.19	3.14	6.17	4.55	1.69	0.69		
									57.81	1.98	16.33	9.16				0.16	3.26	6.90	2.25	1.56	0.59		
									58.03	1.44	16.46	7.62				0.18	3.33	6.39	4.34	1.67	0.55		
									58.70	1.98	15.14	8.43				0.19	3.00	5.72	4.08	1.82	0.94		
									59.30	1.66	16.96	7.75				0.21	3.12	6.08	2.53	1.79	0.59		
									60.22	1.51	16.34	7.06				0.15	2.45	5.06	4.60	2.12	0.49		
									63.19	1.36	16.37	5.60				0.16	1.83	3.66	4.92	2.42	0.50		
									65.14	1.11	16.27	4.81				0.12	1.33	2.91	5.24	2.73	0.35		
									69.85	0.63	16.43	3.14				0.14	0.68	1.63	4.68	2.68	0.14		
Undefined	TL8	Off Taito Penin.	marine sedi. core	glass	EPMA	10	15	5	53.93	1.95	16.19	9.43				0.16	4.12	7.88	4.24	1.39	0.71		

										54.05	1.58	16.61	8.91				0.24	4.75	8.61	3.80	1.05	0.40		
										56.38	1.92	16.58	9.44				0.18	3.57	7.11	2.30	1.54	0.98		
										56.43	2.02	15.63	10.57				0.19	3.41	6.99	2.32	1.60	0.85		
										56.46	1.80	15.27	9.34				0.18	3.85	7.09	3.88	1.44	0.68		
										58.16	1.76	16.55	7.61				0.17	2.62	5.55	5.00	1.98	0.60		
										58.20	1.55	16.43	7.70				0.17	2.93	5.98	4.58	1.79	0.67		
										61.79	1.74	15.97	7.52				0.12	2.51	5.04	2.51	2.08	0.72		
										62.28	1.65	16.06	8.03				0.21	2.41	5.04	1.42	2.11	0.79		
										63.70	1.37	16.69	5.15				0.17	1.88	3.70	4.67	2.19	0.48		
										67.71	1.38	15.32	4.49				0.16	0.83	2.01	4.57	3.11	0.43		
Undefined	TL9	Off Taito Penin.	marine sedi. core	glass	EPMA		10	15	5	53.63	1.93	16.60	9.73				0.18	4.26	8.94	3.05	1.19	0.51		
										54.74	2.53	14.26	10.78				0.22	3.63	7.63	3.67	1.71	0.83		
										62.25	1.25	15.94	7.98				0.16	2.62	5.48	1.71	2.10	0.51		
										67.92	0.96	16.80	3.86				0.15	0.99	2.59	3.61	2.87	0.23		
										69.51	0.77	16.28	3.11				0.12	0.64	1.59	4.57	3.18	0.22		
Undefined	TL10	Off Taito Penin.	marine sedi. core	glass	EPMA		10	15	5	54.38	1.80	16.66	8.88				0.15	4.10	7.89	4.13	1.38	0.63		
										55.86	2.10	15.36	10.11				0.22	3.49	6.37	3.87	1.73	0.88		
										56.17	1.94	16.03	9.82				0.15	3.83	7.86	2.00	1.56	0.65		
										56.20	1.59	16.14	9.53				0.18	4.32	8.21	2.02	1.29	0.51		
										58.03	1.42	16.55	8.15				0.15	3.19	6.30	3.66	1.79	0.74		
										59.45	1.58	16.29	7.57				0.22	2.98	5.58	3.95	1.89	0.49		
										60.57	1.39	16.30	7.29				0.15	2.66	5.39	3.58	2.10	0.59		
										61.36	1.26	16.43	6.89				0.15	2.42	4.87	3.96	2.22	0.45		
										61.81	1.53	17.61	6.19				0.14	2.47	5.39	2.31	2.00	0.54		
										61.90	1.51	15.91	6.74				0.15	2.30	5.02	3.82	2.23	0.42		
Undefined	TL11	Off Taito Penin.	marine sedi. core	glass	EPMA		10	15	5	54.09	1.77	15.78	8.71				0.12	4.85	6.92	5.32	1.52	0.91		
										54.13	2.05	15.42	10.80				0.15	4.00	7.06	4.20	1.49	0.69		
										54.31	2.08	16.15	9.77				0.18	4.13	7.08	4.05	1.48	0.76		
										55.38	1.53	16.61	9.23				0.16	4.74	8.17	2.24	1.26	0.66		
										57.57	1.74	17.27	8.06				0.16	3.01	6.27	3.66	1.53	0.75		
										57.88	1.87	15.94	9.54				0.12	3.38	6.63	2.33	1.67	0.63		
										65.22	1.36	16.00	5.46				0.16	1.43	4.09	3.43	2.39	0.44		
Undefined	TL12	Off Taito Penin.	marine sedi. core	glass	EPMA		10	15	5	54.97	1.87	16.21	10.05				0.18	4.31	8.22	2.32	1.34	0.53		
										55.54	1.63	16.54	9.15				0.22	4.46	8.11	2.10	1.55	0.70		
										56.15	2.13	15.80	8.69				0.16	3.65	6.76	4.23	1.55	0.88		
										56.45	1.58	15.96	8.23				0.12	3.85	7.49	4.33	1.41	0.58		
										56.69	1.72	16.20	8.64				0.18	3.42	6.55	4.16	1.81	0.63		
										57.40	1.65	16.55	7.94				0.17	3.26	6.52	4.24	1.66	0.62		
										58.99	1.40	16.76	7.08				0.17	2.76	5.52	5.07	1.93	0.33		
										59.61	1.72	15.94	7.62				0.23	2.62	5.28	4.38	2.02	0.58		
										65.17	1.10	16.25	5.22				0.14	1.41	3.35	4.65	2.40	0.31		
										65.92	1.02	16.00	4.67				0.11	1.25	3.07	4.89	2.81	0.25		

				Minor and trace elements (ppm)																																						References
SO2	Cr2O3	LOI	Total	Ti	Mn	S	Rb	Sr	Zr	Nb	Y	Mo	Cs	Ba	Th	U	Pb	Hf	Ta	Sc	La	Ce	Nd	Sm	Eu	Tb	Yb	Lu	V	Cr	Co	Ni	Cu	Zn	Ga	Pr	Gd	Dy	Ho	Er	Tm	
		1.39	100.00																																							34,49
		1.33	100.00																																							34,49
			100.00				27	524	178	5	35	2		371	4	6	9			25	18	49	30	9					322	19	33	12	45	91	19							34,50
		-0.55	100.00				34	546	186	11	38			420	15	22	18				87	65							343	32	30	12	51	120	21							51
			99.72 ± 0.38																																							34
			100.15 ± 0.16																																							34
			99.07 ± 0.01																																							34
			99.47 ± 0.93																																							34
			100.48																																							34
			99.75																																							
			100.59																																							34
			100.30																																							
	0.014		96.23																																							51
	0.001		99.19																																							34
	0.125		98.40																																							
	0.002		98.39																																							34
	0.086		94.07																																							34
	0.008		97.10																																							34
		2.02	100.00																																							34,49
			100.00				60	365	365	18	47	5		691	<4	<6	11			8	40	88	41	8					67	<18	<4	7	<4	103	20							34,50
		0.05	100.00				60	376	353	16	46	4		662	<4	<6	16			11	41	90	36	7					68	<18	15	6	25	107	25							34,50
		0.28	100.00				59	358	355	21	46	<2		685	<4	<6	19			13	28	79	33	<6					59	<18	6	6	15	102	22							34,52
		0.11	100.00			BDL	58.9	348.9	369	18.9	48.9			715.2	0.6		11.4	BDL		BDL	64.4	104.3							65.8	BDL	2.8	3.1	7.5	100.0	22.8							34
		0.09	100.00			192	59.1	369.1	371.2	21.3	49.8			707.4	4.5		11.6	9.0		15.7	54.7	96.1							58.9	18.7	5.5	2.0	5.5	104.1	21.1							34
			99.33 ± 0.32																																							34
			99.63 ± 0.51																																							34
			100.01 ± 0.33																																							34
			99.93																																							34
			99.90																																							34
	0.007		99.78																																							34
	0.020		100.10																																							34
	0.022		95.49																																							34
	0.009		96.59																																							34
		0.18	100.00			BDL	57.1	364.6	359.7	18.5	49.1			703.9	4.5		11.2	BDL		BDL	71.2	99.9							73.1	BDL	4.4	4.0	5.8	98.0	22.5							34
		0.09	100.00			216	59.4	370.2	367.7	20.3	48.5			727.9	5.0		13.1	9.4		15.0	55.7	96.1							69.6	15.9	4.9	1.6	7.4	106.5	21.7							34
			99.04 ± 0.52																																							34
			99.67 ± 0.13																																							34
			100.27																																							34
			99.55																																							34
	0		99.22																																							34
	0		99.63																																							34
	0.025		95.40																																							34
	0.011		96.45																																							34
		0.63	100.00			BDL	57.4	374.1	354.3	18.5	47.9			705.1	6.8	0.1	12.5	BDL		BDL	56.5	99.1							73.3	0.4	10.5	4.5	7.8	101.0	19.9							34
		0.97	100.00			246	56.2	371.3	361.5	20.8	47.4			711.0	1.1		13.9	10.0		18.0	63.5	107.1							87.0	21.4	6.8	2.5	8.7	106.9	21.1							34
			99.13 ± 0.35																																							34
			100.31																																							34
			100.41																																							34
	0.001		99.91																																							34
	0.002		99.09																																							34
	0.020		95.34																																							34
	0.015		96.91																																							34
		0.07	100.00			BDL	58.8	354.3	363.8	18.6	48.5			709.9	0.5		9.6	BDL		BDL	55.8	116.1							71.4	BDL	7.5	3.1	5.1	99.1	21.9							34
		0.08	100.00			BDL	59.4	351.3	367.7	18.9	48.7			692.9	BDL		10.3	BDL		BDL	44.2	91.6							61.5	BDL	1.2	2.4	4.6	98.9	21.3							34
		0.36	100.00			232	60.1	349.5	380.6	20.1	47.1			721.3	4.7		13.1	9.8		18.1	55.7	101.2							73.9	31.8	5.7	1.8	6.6	96.9	21.6							34
			99.25 ± 0.41																																							34
			99.44 ± 0.30																																							34
			100.39																																							34
			100.42																																							34
	0.008		99.07																																							34
	0.014		99.53																																							34
	0.014		95.42																																							34
	0.010		96.47																																							34
			98.05				44	364	307	16	41																																31
			98.00				41	428	271	15	35																																31
			97.55				64	284	374	18	46																																31
			97.27																																							1

			97.90																																							
			98.40																																							
			98.61																																							
			98.53																																							
			98.72																																							
			97.62																																							
			99.07																																							
			97.61																																							
			97.61																																							
			96.48																																							
			96.97																																							
			98.57																																							
			97.20																																							
			97.41																																							
			97.26																																							
			96.51																																						1
			96.82																																							
			97.61																																							
			96.42																																							
			98.28																																							
			96.42																																							
			97.27																																						1
			97.42																																							
			97.53																																							
			98.05																																							
			96.51																																							
			97.21																																							
			96.60																																							
			99.07																																						1
			98.24																																							
			97.09																																							
			100.69																																							
			99.02																																							
			98.06																																							
			98.18																																							
			99.04																																							
			98.99																																							
			99.16																																							
			98.36																																							
			98.54																																							
			98.77																																							
			98.20																																							
			97.82																																							
			98.49																																							
			98.72																																							
			97.36																																							
			97.58																																							
			99.13																																						1
			98.66																																							
			98.15																																							
			99.77																																							
			96.87																																							
			97.71																																							
			95.78																																							
			98.02																																							
			99.66																																							
			98.11																																							
			99.20																																							
			99.32																																							
			98.26																																							
			98.04																																							
			99.91																																							
			98.77																																							
			97.14																																							
			97.63																																							
			97.52																																							
			97.98																																							
			99.64																																						1
			98.81																																							
			98.95																																							
			99.67																																							
			98.00																																							
			98.63																																							
			98.62																																							
			100.05																																							
			99.33																																							
			98.14																																							
			99.53																																							
			98.26																																							
			97.89																																							
			97.16																																							
			98.50																																							
			98.73																																							
			99.87																																							
			97.92																																							
			99.06																																							

			98.55																																							
			96.47																																							
			100																																							3
			100																																							
			100																																							
			100																																							
			100																																							
			100																																							
			100																																							
			100																																							
			100																																							
			100																																							
			100																																							
			100																																							
			100																																							
			100																																							
			100																																							
			100																																							
			100																																							
			99.4																																							9
			99.7																																							
			99.3																																							9
			99.2																																							
			99.3																																							9
			99.2																																							
			99.4																																							9
			99.5																																							
			98.26				26	521	192	12	29																															31
			98.41				25	532	197	10	26																															31
			99.6																																							9
			99.3																																							
			99.4																																							9
			99.3																																							
			97.0 ± 1.3																																							47
			95.5 ± 2.2																																							47
			96.92																																							1
			98.08																																							
			96.75																																							
			96.40																																							
			97.65																																							
			97.44																																							
			97.39																																							
			97.77																																							
			96.63																																							
			97.29																																							
			98.29																																							
			97.85																																							
			97.10																																							
			98.69																																							
			96.58																																							
			97.10																																							
			98.83																																							
			95.96																																							
			98.46																																							
			97.59																																							
			97.94																																							
			98.70																																							
			97.66																																							
			97.27																																							1
			97.71																																							
			98.13																																							
			96.04																																							
			100.84																																							
			97.23																																							
			97.76																																							
			97.01																																							
			101.14																																							
			97.42																																							
			96.60																																							
			97.63																																							
			98.44																																							
			98.34																																							1
			97.37																																							
			98.06																																							
			97.71																																							
			97.08																																							
			99.31																																							
			100.53																																							
			97.16																																							
			97.58																																							
			97.61																																							
			95.59																																							1
			96.49																																							
			98.46																																							
			96.61																																							
			98.82																																							

			99.76																																							
			99.69																																							
			99.11																																							
			98.25																																							
			98.01																																							
			99.40																																							
			98.18																																							
			98.23																																							
			97.50																																							
			98.63																																							
			97.48																																							
			95.45																																							1
			98.46																																							
			98.81																																							
			100.02																																							
			99.29																																							
			100.48																																							
			99.16																																							
			98.27																																							
			99.08																																							
			98.06																																							
			99.16																																							
			97.27																																							
			98.36																																							
			97.33																																							
			96.28																																							
			98.16																																							
			97.40																																							
			100.89																																							
			99.24																																							1
			98.70																																							
			98.92																																							
			99.67																																							
			99.28																																							
			99.73																																							
			99.56																																							
			99.65																																							
			98.90																																							
			98.76																																							
			98.27																																							
			98.15																																							
			98.10																																							
			97.59																																							
			99.16																																							
			98.40																																							
			98.31																																							
			96.38																																							1
			97.30																																							
			97.02																																							
			96.09																																							
			96.79																																							
			96.47																																							
			97.18																																							
			96.80																																							
			97.37																																							
			97.88																																							
			96.14																																							
			96.09																																							
			97.91				76	253	421	19	47																															31
			97.51				68	218	396	18	50																															31
			97.65				80	258	433	18	51																															31
			97.86				74	244	429	20	48																															31
		2.20	99.34				72	227	414	19	50		1.9	1010	9.3			11.9		11.8	51.3	95.0	49.5	9.65	2.19	1.41	5.39	0.79														31
		2.50	99.79				78	243	428	20	49		2.2	1030	9.5			11.9		11.1	49.4	96.3	45.9	8.95	2.25	1.41	5.36	0.77														31,36
		3.80	98.43				79	205	528	23	52			950	4	4	15				79	126							50	>1	2	4	7	77	20							34,51
		3.80	100.00			170	76	217	541	26	54			919			15	14		12	75	143							43	14	BDL	3	9	83	20							34,51
			100.07 ± 0.52																																							34
			100.00																																							51
			100.04																																							51
			99.70																																							51
			99.76																																							51
	0.03		96.00																																							51
	0.02		97.35																																							51
		4.40	99.88			185	74	223	539	26	53			869			10	13		10	60	113							44	12	2	2	8	79	22							34,51
			98.24 ± 0.72																																							34
			99.01																																							51
			99.18																																							51
	0.003		98.87																																							51
	0.003		98.94																																							51
	0.02		95.44																																							51
	0.02		97.25																																							51

		4.80	101.16				71	253	491	22	51			885	BDL	3	11				72	120							77	6	11	5	13	82	21							34,51
		5.10	100.34			198	74	222	547	26	54			879			14	14		13	68	128							47	18	1	3	11	79	21							34,51
			99.01 ± 0.60																																				51
			100.66																																				51
			99.87																																				51
	0.001		100.03																																				51
	0.001		99.25																																				51
	0.03		96.31																																				51
	0.01		97.89																																				51
			93.8																																				9
			97.40																																				1
			96.67																																				
			96.91																																				
			96.71																																				
			96.50																																				
			98.80																																				
			96.63																																				
			97.23																																				
			97.30																																				
			98.44																																				
			96.42																																				
			97.21																																				
			97.12																																				
			97.01																																				
			97.79																																				
			97.15																																				
			97.04																																				
			96.03																																				
			97.73																																				
			97.09																																				
			96.91																																				
			96.14																																				
			100																																				3,5
			100																																				
			100																																				
			100																																				
			100																																				
			100																																				
			100																																				
			100																																				
			97.98				65	335	378	17	44																													31
			97.86				47	396	342	14	37																													31
			97.88				44	412	324	12	36																													31
			97.96				51	362	353	15	39																													31
			97.93				50	374	347	14	41																													31
		1.14	99.21				49	388	345		39																													37
		1.60	99.87				47	382	338	14	38		1.3	797	6.8			10.3		16.5	41.3	85.9	43.1	8.58	2.43	1.25	4.71	0.70											31,37
			100.00																																				37
			98.06				48	341	327	16	41																													31
		3.7	97.52				54	318	432	22	55			773	8	4	14				82	120							93	19	9	14	14	101	23							34,51
		1.4	96.79				54	366	429	21	53			788	15	9	16				88	118							97	0	12	5	11	99	22							34,51
			99.39 ± 0.76																																				51
			99.96																																				51
			99.43																																				51
	0.008		99.86																																				51
	0.006		99.82																																				51
	0.05		95.13																																				51
	0.01		96.92																																				51
		3.2	99.72			289	51	348	479	25	50			817			11	15		22	75	129							89	22	10	4	14	97	23							34,51
			99.98																																				51
			99.98																																				51
	0.003		99.74																																				51
	0.004		99.76																																				51
	0.05		96.03																																				51
	0.01		96.82																																				51
		1.7	94.59				55	351	432	21	52			773	6	3	14				78	126							93	4	7	6	8	98	22							34,51
			98.94 ± 0.54																																				51
			101.22																																				51
			100.95																																				51
	0.014		99.83																																				51
	0.008		99.71																																				51
	0.03		95.71																																				51
	0.01		96.55																																				51
		1.10	99.88				53	369	365	16	42		1.3	852	6.4			9.5		14.3	37.5	78.3	40.9	7.88	2.23	1.17	4.19	0.61											31,37
																																							36

			100.00																																									37
		2.12	99.29				50	392	380		41																																37
			100.00																																									37
		1.05	100.04				52	374	356		37																																37
																																												36
			100.00																																									37
			98.05																																									1
			98.35																																									
			98.05																																									
			98.52																																									
			100.03																																									
			99.13																																									
			97.56																																									
			96.79																																									
			97.68																																									
			97.82																																									
			98.61																																									
			99.59																																									
			98.06																																									
			96.76																																									
			98.75																																									
			97.61																																									
			97.76																																									
			98.77																																									
			96.75																																									
			97.86																																									
			96.24																																									
			97.41																																									
			98.75																																									
			99.53																																									
			97.77																																									
			96.61																																									
			98.16																																									
			100.00																																									37,53
	0.04		100.00																																									16
	0.00		100.00																																									
	0.00		100.00																																									
	0.00		100.00																																									
				8422	1240		49	377	355	16	41		1.3	800	6.5	1.2	12.6	10.0	1.8		39.9	85.2	42.3	8.62	2.41	1.29	4.28	0.61										9.7	10.6	7.53	1.48	4.50	0.58	30
				8649	1323		52	380	361	17	41		1.4	807	6.3	1.2	13.2	9.5	1.5		40.3	81.2	42.7	8.66	2.41	1.26	4.39	0.65										9.7	10.8	7.95	1.43	4.74	0.56	30
			99.85																																									22
			99.76																																									
			99.95																																									
			99.46																																									
			99.57																																									
			98.96																																									
			98.94																																									
			99.75																																									
			99.95																																									
			98.97																																									
			99.92																																									
			98.96																																									
			99.16																																									
			99.96																																									
			99.17																																									
			99.95																																									
			99.55																																									
			99.95																																									
			99.03																																									
			99.95																																									
			98.75																																									
			100.00																																									54
							56	368	328		40																																12
							59	382	319		37																																
							64	346	341		41																																
							51	360	320		42																																12
							48	357	342		41																																
							55	399	363		38																																12
							62	409	330		43																																
							46	391	330		45																																12
							48	378	350		41																																
							60	410	349		45																																12
							47		370	18											41.5						4.46														35
							55		464	21											46.9						5.01														35
							46		313	16											35						3.67														35
							27.71	240.03	367.43				0.74		5.36	1.35	11.35	8.09		13.41	29.08	67.31	35.00	7.31	2.01		3.49	0.55										19.69	8.81	7.00	6.24	1.25	3.67	0.54	25
			97.91				36	489	248	10	33																																31
			95.98																																									1
			96.62																																									
			97.68																																									
			96.90																																									
			96.47																																									
			98.82																																									
			100																																									3
			100																																									

			100 100 100 100 100 100 100 100 100 100 100 100 100																																							
			99.47 97.66 95.99 98.06 97.31 98.07 96.24 97.75 99.46 98.60 97.29 98.48 98.17 97.93 97.06 96.94																																							1
			98.73 100.99 99.01 98.16 98.10 96.38 100.19 100.12 100.59 98.19 98.84 97.10 97.68 96.57 97.65 97.46																																							1
			98.21 97.11 98.92 97.99 96.83 96.92 98.59 98.54 98.08 99.00 96.84 98.71 98.15 96.55 96.58 98.85 97.44																																							1
			97.92 97.81 99.53 99.92 98.79 97.18 96.73 96.35 97.93 96.11 98.38 96.71 98.27 98.06 96.93 95.93 96.69																																							1
			97.21 96.91																																							1
			98.83 100.73 100.09 100.65 99.13																																							1

			99.07																																							
			99.46																																							
			98.53																																							
			99.30																																							
			99.70																																							
			99.17																																							
			98.16																																							
			99.67																																							
			96.62																																							
			98.85																																							
			100																																							3
			100																																							
			100																																							
			100																																							
			100																																							
			100																																							
			100																																							
			100																																							
			100																																							
			100																																							
			100																																							
			100																																							
			100																																							
			100																																							
			100																																							
			100																																							
			100																																							
			100																																							
			100																																							46,47
0.02			100																																							48
0.00			100																																							
0.04			100																																							
0.02			100																																							
0.07			100																																							
0.07			100																																							
0.04			100																																							
0.03			100																																							
0.07			100																																							
0.05			100																																							
0.04			100																																							
0.06			100																																							
0.00			100																																							
			98.09																																							1
			96.70																																							
			101.44																																							
			98.56																																							
			97.86																																							1
			97.23																																							
			97.37																																							
			97.63																																							
			97.30																																							
			97.43																																							
			97.11																																							
			97.51																																							
			95.90																																							
			97.50																																							1
			96.15																																							
			97.28																																							
			97.42																																							
			96.60																																							
			96.93																																							
			98.64																																							
			97.10																																							
			98.98																																							
			97.25																																							
			98.64																																							
			97.76																																							
			96.57																																							
			97.93																																							
			97.91																																							
			97.13																																							
			96.84																																							
			98.40																																							
			96.45																																							
			99.94																																							
			97.75																																							
			97.84																																							
			99.87																																							
			97.68																																							
			98.65																																							
			97.08																																							
			99.06																																							1
			98.83																																							
			97.2																																							
			99.24																																							
			97.53																																							

			97.83 99.12 99.1 98.66 100.48 97.69 97.63 97.9 99.63 98.02 97.26 96.24 98.34																																						
			102.19 102.52 100.32 100.79 100.16 99.43 99.77 100.72 98.62 99.94 99.82 98.61 99.17																																							1
			100 100 100 100 100 100 100 100 100 100 100 100 100 100 100																																							3
			97.98 96.03 96.25 98.23 97.40 100.70 96.81 96.87 96.76 96.74 97.10 96.08 96.69 95.97 97.65 96.03 97.03																																							1
			97.03 96.80 99.16 97.62 97.76 98.31 96.16 97.63 96.96 96.52 96.12 97.18 96.98 95.02 97.17 96.00																																							1
			98.08 95.78 95.52 96.01 96.83																																							1
			98.86 99.44 99.96																																							1
			100 100 100 100																																							3

			100																																							
			100																																							
			100																																							
			100																																							
			100																																							
			100																																							
			100																																							
			100																																							
			100																																							
			100																																							
				8,365	1,182		39	458	203	11	31		1.5	479	4.8	1.1	8.7	5.2			26.4	58.2	31.9	7.21	2.16	1.09	3.03	0.47	240	15	29	18	69	112		7.48	8.26	5.80	1.14	3.45	0.44	10
			100	11,527	1,343		34	525	182	9	32		0.6	456	5.4	1.4	12.1	4.7			35.0	80.7	42.5	9.21	2.68	1.21	2.92	0.46	340	61	27	46	204	133		10.10	10.20	6.42	1.24	3.81	0.41	10
			98.9																																							10
			99.2																																							
			99.7																																							
			100.2																																							
			98.6																																							10
			98.4																																							
			97.4																																							
			97.5																																							
			99.8																																							10
			101.3																																							
			99.6																																							
			100.4																																							
			101.0																																							
			99.6																																							
				8,346	1,157		43	467	222	13	31		1.5	537	5.7	1.2	9.3	6.0			29.4	64.9	34.1	7.57	2.29	1.10	3.14	0.47	212	21	30	21	51	109		8.23	8.61	5.87	1.17	3.5	0.44	10
				8,257	1,091		44	392	228	12	33		1.2	487	5.8	1.2	10.0	5.3			31.7	70.1	34.7	7.62	2.06	1.06	2.75	0.45	215	15	15	21	34	106		8.60	8.4	5.55	1.11	3.33	0.41	10
				7,810	1,097		47	448	275	22	34		1.4	584	8.1	1.3	10.3	6.9			32.7	71.0	36.3	7.76	2.31	1.21	3.34	0.50	175	17	26	13	67	114		8.95	8.89	6.03	1.20	3.61	0.47	10
				8,150	1,161		47	430	261	16	33		1.3	586	6.1	1.5	10	6.5			32.5	70.7	35.3	7.35	2.35	1.05	3.38	0.43	187	13	48	35	30	119		8.55	9.0	6.11	1.16	3.52	0.43	10
				10,508	1,260		27	486	184	10	31		0.7	373	3.7	0.9	5.4	4.4			23.3	53.7	29.9	6.71	2.1	1.02	2.92	0.45	309	34	47	29	68	108		7.01	7.8	5.84	1.11	3.46	0.43	10
				11,121	1,366		22	487	175	8	31			306	3.3	0.6	5.3	3.9			24.3	56.3	30.7	6.58	2.03	1.01	2.65	0.37	328	32	26	34	38	120		7.10	7.3	5.26	1.00	3.13	0.32	10
			98.3																																							10
			98.0																																							
			97.5																																							10
			98.5																																							
			95.1																																							10
			99.6																																							
			100.6																																							
				7,366	890		44	399	213	10	29		1.0	480	4.6	1.3	8.8	6.9			28.0	63.2	31.1	6.49	1.79	0.88	2.97	0.35	–	–	–	–	–	–		7.61	7.37	5.24	0.94	3.12	0.38	8,10
				8995	1173		43	440	263	13	33			502	4.8	1.0	8.1	5.5			34.7	79.2	33.9	7.32	2.13	1.03	2.79	0.40	252	24	14	17	31	133		9.20	7.9	5.41	1.01	3.13	0.27	10
			100	10,311	1,284		45	459	260	13	36		1.1	559	5.5	1.3	9.3	6.2			34.5	76.8	40.8	8.84	2.55	1.28	3.50	0.54	254	15	56	16	42	121		9.7	10.1	7.07	1.31	4.17	0.50	10
			100	8,620	1,181		51	399	287	15	36		1.3	604	6.0	1.4	10.5	7.2			34.9	78.1	41.6	9.14	2.58	1.31	3.80	0.56	195	12	75	17	39	114		10.0	10.4	7.03	1.39	4.41	0.52	10
			100	5,940	1,017		64	290	362	18	38		1.7	720	7.3	1.8	13.4	8.6			40.7	90.1	43.4	9.50	2.50	1.35	4.05	0.64	104	13	30	16	30	111		10.7	11.1	7.18	1.48	4.38	0.60	10
			98.8																																							10
			98.1																																							10
			98.7																																							
			98.8																																							10
			99.3																																							
			100.6																																							
			101.1																																							
			100.5																																							
			100.0																																							
			100																																							3
			100																																							
			100																																							
			100																																							
			100																																							
			100																																							
			100																																							
			100																																							
			100																																							
			100																																							3
			100																																							
			100																																							
			100																																							
			100																																							
			100																																							
			100																																							
			100																																							
			100																																							
			100																																							
			100																																							
			100																																							
			100																																							
			100																																							
			100																																							
			100																																							
			100																																							3

			100																																							
			100																																							
			100																																							
			100																																							
			100																																							
			100																																							
			100																																							
			100																																							
			100																																							
			100																																							
			100																																							3
			100																																							
			100																																							
			100																																							
			100																																							
			100																																							3
			100																																							
			100																																							
			100																																							
			100																																							
			100																																							
			100																																							
			100																																							
			100																																							
			100																																							
			100																																							3
			100																																							
			100																																							
			100																																							
			100																																							
			100																																							
			100																																							
			100																																							3
			100																																							
			100																																							
			100																																							
			100																																							
			100																																							
			100																																							
			100																																							
			100																																							
			100																																							

Supplementary Table 4.3 Chemical composition data for secondary standards and blanks analysed for this study.

a)

GOR132-G (basalt)	Composition (unnormalised wt %)										
	Na_2O	MgO	Al_2O3	SiO_2	K_2O	CaO	TiO_2	MnO	FeO_T	P_2O_5	Total
Preferred value	0.83	22.4	11.0	45.5	0.0308	8.45	0.306	0.154	10.1	0.036	98.83
0.5(95% CI)	0.04	0.2	0.2	0.4	0.003	0.12	0.013	0.007	0.1	0.012	
N (analyses)	12	12	11	12	13	14	21	18	14	5	
1σ s.d.	0.06	0.31	0.30	0.63	0.01	0.21	0.03	0.01	0.17	0.01	
Begbroke EPMA	0.83	22.05	10.83	45.44	0.04	8.67	0.26	0.09	10.39	0.06	98.67
	0.86	21.64	10.71	44.64	0.05	8.41	0.24	0.16	10.15	0.03	96.90
	0.92	21.51	10.67	43.51	0.06	8.47	0.29	0.08	10.48	0.04	96.04
	0.78	21.77	10.77	45.28	0.05	8.52	0.17	0.12	10.22	0.07	97.76
	0.85	21.85	10.83	44.38	0.05	8.61	0.30	0.14	9.89	0.03	96.91
	0.88	22.00	11.06	44.91	0.05	8.55	0.24	0.27	9.94	0.02	97.93
	0.81	22.24	11.21	44.33	0.02	8.70	0.31	0.18	10.33	0.04	98.17
	0.79	21.87	11.13	45.61	0.05	8.56	0.31	0.13	10.08	0.02	98.55
	0.84	21.64	10.76	44.42	0.04	8.64	0.29	0.19	10.19	0.03	97.02
	0.77	21.93	11.07	45.84	0.02	8.47	0.31	0.27	9.93	0.03	98.62
	0.92	22.03	11.25	46.49	0.01	8.66	0.33	0.11	10.11	0.05	99.95
	0.87	22.04	10.98	46.59	0.05	8.62	0.31	0.16	10.20	0.02	99.85
	0.79	22.14	11.08	46.76	0.04	8.48	0.32	0.12	9.65	0.07	99.44
	0.87	22.22	11.05	46.63	0.03	8.49	0.35	0.11	10.47	0.04	100.26
	0.89	22.27	11.05	46.34	0.03	8.66	0.35	0.18	10.50	0.04	100.31
	0.88	22.51	11.11	45.95	0.04	8.69	0.26	0.17	9.89	0.02	99.51
	0.86	22.39	10.99	46.33	0.03	8.58	0.29	0.19	10.33	0.02	100.01
	0.93	22.41	10.89	45.47	0.06	8.52	0.31	0.19	9.84	0.05	98.67
	0.78	22.35	11.17	44.90	0.02	8.72	0.30	0.19	10.51	0.08	99.02
	0.81	22.34	11.02	45.59	0.05	8.73	0.35	0.09	9.91	0.03	98.94
Mean	0.85	22.06	10.98	45.47	0.04	8.59	0.29	0.16	10.15	0.04	98.63
1σ r.s.d. of max.	0.05	0.28	0.17	0.92	0.02	0.09	0.05	0.09	0.26	0.04	
RLAHA 1 EPMA	0.82	22.70	11.16	45.94	0.02	8.39	0.36	0.17	10.55	0.10	100.21
	0.85	22.11	10.91	45.94	0.04	8.54	0.33	0.18	10.07	0.02	98.99
	0.86	22.45	11.06	45.44	0.03	8.41	0.26	0.22	10.31	0.06	99.10
	0.73	22.19	10.84	45.15	0.05	8.54	0.29	0.19	9.61	0.06	97.66
	0.73	22.26	10.97	45.75	-	8.38	0.29	0.16	10.17	-	98.72
	0.78	22.48	11.09	45.33	0.06	8.60	0.31	0.25	9.99	0.02	98.91
	0.83	22.49	10.86	45.19	0.02	8.55	0.29	0.13	10.21	0.03	98.62
	0.85	22.55	10.66	45.18	0.04	8.44	0.25	0.10	10.51	0.01	98.61
	0.70	22.25	10.77	45.63	0.03	8.33	0.26	0.21	10.52	0.04	98.74
	0.68	22.24	10.79	45.25	0.01	8.39	0.32	0.20	9.99	0.03	97.91
	0.80	22.28	10.82	45.36	0.05	8.37	0.30	0.13	10.01	0.05	98.16
	0.82	22.39	10.92	45.35	0.07	8.50	0.32	0.16	10.20	0.01	98.74
	0.79	22.29	10.85	45.54	0.02	8.57	0.31	0.10	10.15	0.04	98.66
	0.78	22.36	10.83	45.41	0.05	8.42	0.30	0.20	10.22	0.06	98.62
	0.77	22.31	10.86	45.17	0.05	8.56	0.30	0.11	10.51	0.07	98.72
Mean	0.79	22.36	10.89	45.44	0.04	8.47	0.30	0.17	10.20	0.04	98.69
1σ r.s.d. of max.	0.06	0.15	0.13	0.26	0.03	0.09	0.03	0.07	0.26	0.06	
RLAHA 2 EPMA	0.86	22.31	10.99	45.21	0.01	8.58	0.33	0.15	10.57	0.05	99.05
	0.82	22.42	10.95	45.83	0.02	8.39	0.34	0.18	10.24	0.05	99.25
	0.82	22.67	11.13	45.77	0.04	8.64	0.31	0.16	10.24	0.03	99.80
	0.76	22.42	11.03	45.62	0.04	8.42	0.34	0.13	10.03	0.02	98.82
	0.74	22.09	10.93	45.32	0.03	8.47	0.33	0.13	10.17	0.04	98.23
	0.78	22.36	11.01	45.52	0.06	8.41	0.31	0.13	10.29	0.03	98.88
	0.82	22.38	11.03	45.32	0.01	8.36	0.31	0.09	10.12	0.03	98.47

	0.74	22.35	10.99	45.60	0.02	8.35	0.28	0.13	10.62	0.04	99.11
	0.79	22.54	11.01	45.60	0.05	8.72	0.32	0.22	10.46	0.03	99.73
	0.72	22.54	10.75	45.81	0.03	8.52	0.31	0.08	10.17	0.03	98.96
	0.73	22.33	11.10	46.00	0.01	8.54	0.28	0.21	9.94	0.04	99.18
	0.78	22.42	11.05	46.03	0.05	8.48	0.37	0.19	10.17	0.04	99.58
	0.84	22.48	11.05	45.70	-	8.52	0.34	0.15	10.81	0.08	99.97
	0.73	22.49	11.20	46.09	0.02	8.60	0.32	0.17	10.35	-	99.95
	0.81	22.13	10.94	45.48	0.01	8.49	0.32	0.19	10.07	-	98.45
Mean	0.78	22.40	11.01	45.66	0.03	8.50	0.32	0.15	10.28	0.04	99.16
1σ r.s.d. of max.	0.05	0.15	0.10	0.26	0.04	0.11	0.02	0.06	0.24	0.03	
Mean	**0.81**	**22.25**	**10.96**	**45.52**	**0.04**	**8.52**	**0.30**	**0.16**	**10.21**	**0.04**	**98.81**
1σ r.s.d. of max.	**0.07**	**0.27**	**0.15**	**0.62**	**0.03**	**0.11**	**0.04**	**0.08**	**0.26**	**0.05**	

StHs6/80-G (dacite)	Composition (unnormalised wt %)										
	Na_2O	MgO	Al_2O3	SiO_2	K_2O	CaO	TiO_2	MnO	FeO_T	P_2O_5	Total
Preferred value	**4.44**	**1.97**	**17.8**	**63.7**	**1.29**	**5.28**	**0.703**	**0.076**	**4.37**	**0.164**	**99.82**
0.5(95% CI)	**0.14**	**0.04**	**0.2**	**0.5**	**0.02**	**0.09**	**0.021**	**0.004**	**0.07**	**0.018**	
N (analyses)	**13**	**13**	**12**	**12**	**14**	**15**	**22**	**21**	**15**	**6**	
1σ s.d.	**0.23**	**0.07**	**0.31**	**0.79**	**0.03**	**0.16**	**0.05**	**0.01**	**0.13**	**0.02**	
Begbroke EPMA	4.62	1.92	17.24	62.50	1.23	5.33	0.74	0.03	4.43	0.16	98.20
	4.63	1.84	16.96	61.73	1.33	5.22	0.66	0.10	4.26	0.10	96.82
	4.74	1.99	17.01	62.21	1.30	5.33	0.74	0.20	4.66	0.15	98.33
	4.68	1.90	17.24	63.21	1.24	5.16	0.72	0.05	4.76	0.13	99.08
	4.69	1.97	17.39	63.43	1.22	5.17	0.69	0.08	4.25	0.13	99.00
	4.63	1.84	17.90	64.53	1.22	5.33	0.72	0.12	4.43	0.10	100.82
	4.75	1.95	17.51	63.43	1.27	5.29	0.69	0.05	4.07	0.08	99.08
	4.74	1.97	17.71	63.64	1.31	5.50	0.68	0.10	4.48	0.17	100.29
	4.63	2.00	17.40	63.92	1.27	5.24	0.68	0.20	4.23	0.11	99.69
	4.73	1.96	17.57	63.19	1.30	5.27	0.65	-	4.55	0.15	99.35
	4.70	1.96	17.41	64.28	1.29	5.26	0.69	0.09	4.05	0.08	99.79
	4.72	1.94	17.49	64.50	1.26	5.34	0.68	0.06	4.45	0.15	100.58
	4.59	1.99	17.74	65.16	1.32	5.33	0.75	-	4.20	0.16	101.24
	4.91	1.93	17.83	65.68	1.26	5.38	0.75	0.08	4.56	0.15	102.54
	4.73	1.88	17.91	65.69	1.24	5.30	0.69	0.09	4.50	0.15	102.18
	4.85	1.97	17.60	64.32	1.31	5.33	0.71	-	4.26	0.12	100.46
	4.57	1.89	17.54	63.22	1.29	5.35	0.66	0.07	4.24	0.14	98.97
	4.63	1.90	17.52	64.12	1.27	5.20	0.61	0.20	4.24	0.06	99.73
	4.58	1.93	17.58	63.68	1.30	5.29	0.67	0.13	4.63	0.14	99.93
	4.84	1.95	17.77	64.56	1.23	5.39	0.67	0.05	4.08	0.16	100.70
Mean	4.70	1.93	17.51	63.85	1.27	5.30	0.69	0.10	4.37	0.13	99.84
1σ r.s.d. of max.	0.09	0.05	0.26	1.05	0.03	0.08	0.04	0.10	0.22	0.04	
RLAHA 1 EPMA	4.56	1.94	17.34	63.63	1.30	5.13	0.73	0.06	4.42	0.08	99.20
	4.61	1.98	17.35	63.57	1.30	5.24	0.68	0.11	4.45	0.03	99.33
	4.26	1.90	17.64	63.78	1.32	5.20	0.61	0.10	4.57	0.05	99.43
	4.54	1.95	17.41	63.85	1.34	5.17	0.72	0.11	4.49	0.09	99.68
	4.56	1.99	17.66	64.01	1.33	5.33	0.64	-	4.42	0.04	99.98
	4.54	1.87	17.81	64.40	1.34	5.09	0.70	0.02	4.42	0.05	100.24
	4.52	1.92	17.36	63.43	1.25	5.09	0.71	0.07	4.39	0.08	98.82
	4.47	1.97	17.33	63.07	1.29	5.13	0.69	0.05	4.38	0.10	98.47
	4.70	1.97	17.45	63.33	1.32	5.21	0.71	0.08	4.49	0.16	99.41
	4.45	1.99	17.57	62.97	1.30	5.29	0.73	0.02	4.56	0.20	99.08
	4.35	2.01	17.34	62.75	1.29	5.41	0.69	0.09	4.51	0.16	98.59
	4.49	1.95	17.51	62.89	1.23	5.36	0.72	0.08	4.47	0.20	98.88
	4.40	2.01	17.45	63.45	1.35	5.31	0.75	0.07	4.51	0.19	99.49
	4.52	1.99	17.59	63.65	1.33	5.27	0.75	0.06	4.58	0.16	99.89
	4.74	1.95	17.67	63.62	1.29	5.25	0.75	0.08	4.58	0.14	100.07
Mean	4.51	1.96	17.50	63.49	1.30	5.23	0.70	0.07	4.48	0.12	99.37
1σ r.s.d. of max.	0.12	0.04	0.15	0.44	0.03	0.10	0.04	0.05	0.07	0.10	

RLAHA 2 EPMA	4.58	1.93	17.30	62.96	1.35	5.21	0.68	0.08	4.42	0.19	98.71
	4.64	2.00	17.58	63.81	1.35	5.27	0.62	0.03	4.25	0.16	99.70
	4.55	1.97	17.56	63.70	1.27	5.03	0.66	0.06	4.40	0.19	99.40
	4.46	2.03	17.72	63.55	1.32	5.29	0.73	0.06	4.51	0.20	99.86
	4.85	1.95	17.86	63.34	1.27	5.23	0.75	0.08	4.57	0.20	100.11
	4.35	1.99	17.87	63.84	1.32	5.25	0.66	0.03	4.53	0.17	100.00
	4.43	1.98	17.63	63.42	1.36	5.32	0.64	0.04	4.43	0.17	99.43
	4.89	2.01	17.62	62.10	1.37	5.37	0.73	0.11	4.40	0.20	98.81
	4.63	1.97	17.52	63.20	1.32	5.29	0.72	0.09	4.48	0.19	99.41
	4.35	1.99	17.30	63.69	1.29	5.15	0.78	0.12	4.57	0.02	99.27
	4.72	1.98	17.49	63.56	1.28	5.25	0.69	0.05	4.34	0.04	99.40
	4.73	1.94	17.58	63.77	1.34	5.20	0.71	0.06	4.50	0.07	99.89
	4.55	1.94	17.58	63.72	1.27	5.16	0.73	0.10	4.43	0.10	99.57
	4.55	1.99	17.63	63.46	1.35	5.16	0.68	0.06	4.45	0.18	99.50
	4.37	1.97	17.57	63.50	1.27	5.27	0.72	0.09	4.16	0.14	99.07
Mean	4.58	1.98	17.59	63.44	1.31	5.23	0.70	0.07	4.43	0.15	99.47
1σ r.s.d. of max.	0.18	0.03	0.16	0.43	0.04	0.08	0.05	0.04	0.11	0.08	
Mean	4.61	1.95	17.53	63.62	1.30	5.26	0.70	0.08	4.42	0.13	99.59
1σ r.s.d. of max.	0.16	0.04	0.21	0.78	0.04	0.09	0.04	0.10	0.16	0.08	

ATHO-G (rhyolite)	Composition (unnormalised wt %)										
	Na_2O	MgO	Al_2O3	SiO_2	K_2O	CaO	TiO_2	MnO	FeO_T	P_2O_5	Total
Preferred value	3.75	0.103	12.2	75.6	2.64	1.70	0.255	0.106	3.27	0.025	99.66
0.5(95% CI)	0.31	0.010	0.2	0.7	0.09	0.03	0.016	0.005	0.10	0.004	
N (analyses)	14	16	17	16	21	17	27	24	20	7	
1σ s.d.	0.54	0.02	0.39	1.31	0.20	0.06	0.04	0.01	0.21	0.00	
Begbroke EPMA	3.85	0.12	11.90	73.38	2.60	1.66	0.23	0.06	3.20	-	97.01
	3.91	0.08	11.81	73.56	2.60	1.75	0.22	-	3.30	0.02	97.26
	3.89	0.08	11.95	73.42	2.61	1.62	0.28	0.13	3.68	0.04	97.69
	3.99	0.12	12.02	75.37	2.83	1.69	0.22	0.10	3.32	0.01	99.67
	3.79	0.09	12.14	76.00	2.65	1.59	0.22	0.12	3.39	0.02	100.02
	3.81	0.10	12.08	74.23	2.71	1.62	0.27	-	2.95	0.04	97.80
	3.89	0.10	12.22	74.44	2.62	1.68	0.24	0.06	3.25	0.04	98.53
	3.95	0.09	12.31	74.15	2.72	1.68	0.28	0.23	3.38	0.02	98.80
	3.85	0.08	12.10	75.34	2.62	1.65	0.24	0.05	3.08	0.01	99.02
	3.91	0.10	12.25	75.90	2.75	1.72	0.24	0.11	3.18	-	100.15
	3.87	0.08	12.08	76.72	2.62	1.66	0.21	0.06	3.49	0.04	100.84
	3.97	0.11	12.21	75.74	2.59	1.61	0.18	0.03	3.31	-	99.74
	3.84	0.08	12.11	76.20	2.77	1.66	0.32	0.15	3.35	0.01	100.49
	3.84	0.11	11.92	75.64	2.71	1.63	0.22	0.12	3.23	0.04	99.46
	3.85	0.08	12.24	75.96	2.58	1.59	0.28	0.19	3.22	-	99.98
	4.03	0.10	12.28	75.12	2.64	1.63	0.24	0.11	3.20	-	99.36
	3.89	0.08	12.17	75.95	2.63	1.70	0.22	0.12	3.05	0.05	99.84
	3.89	0.07	12.21	75.65	2.59	1.73	0.24	0.30	3.17	0.06	99.90
	3.86	0.10	12.14	76.07	2.68	1.68	0.23	0.13	2.90	-	99.79
	4.05	0.07	12.32	76.85	2.61	1.68	0.22	0.09	3.20	0.04	101.13
Mean	3.90	0.09	12.12	75.28	2.66	1.66	0.24	0.12	3.24	0.03	99.32
1σ r.s.d. of max.	0.07	0.02	0.14	1.06	0.07	0.05	0.04	0.16	0.19	0.02	
RLAHA 1 EPMA	4.13	0.07	12.40	74.91	2.75	1.70	0.25	0.06	3.31	0.02	99.61
	4.25	0.11	12.37	75.50	2.83	1.71	0.27	0.06	3.16	0.02	100.27
	4.25	0.10	12.32	76.06	2.77	1.66	0.22	0.06	3.38	-	100.82
	4.17	0.11	12.05	75.19	2.74	1.73	0.25	0.10	3.19	0.05	99.58
	4.09	0.10	11.99	74.60	2.80	1.67	0.23	0.11	3.17	0.01	98.78
	4.16	0.11	12.21	74.74	2.73	1.68	0.21	0.08	3.22	0.01	99.15
	4.23	0.08	12.15	75.15	2.69	1.59	0.27	0.11	3.26	0.01	99.55
	4.23	0.09	12.34	75.39	2.73	1.70	0.25	0.17	3.12	0.03	100.04
	4.25	0.09	12.07	74.66	2.70	1.79	0.19	0.07	3.56	0.03	99.41
	4.11	0.09	12.20	74.89	2.67	1.61	0.21	0.12	3.31	-	99.21

	4.29	0.10	12.31	75.27	2.73	1.70	0.27	0.12	3.37	0.04	100.22
	4.02	0.11	12.03	74.89	2.58	1.70	0.25	0.08	3.20	0.01	98.88
	4.10	0.10	11.99	74.82	2.67	1.61	0.21	0.08	3.14	0.03	98.74
	4.04	0.08	12.09	74.98	2.69	1.65	0.27	0.19	3.16	0.02	99.16
	3.95	0.12	12.18	75.26	2.73	1.71	0.26	0.13	3.11	0.05	99.49
Mean	4.15	0.10	12.18	75.09	2.72	1.68	0.24	0.10	3.24	0.03	99.53
1σ r.s.d. of max.	0.10	0.02	0.14	0.37	0.06	0.05	0.03	0.07	0.13	0.03	
RLAHA 2 EPMA	4.16	0.08	12.11	74.76	2.69	1.70	0.25	0.08	3.40	0.03	99.25
	4.15	0.13	12.15	75.08	2.79	1.69	0.21	0.13	3.32	0.05	99.70
	4.16	0.11	12.32	75.34	2.80	1.68	0.23	0.18	3.42	0.06	100.28
	4.00	0.11	12.41	75.64	2.77	1.64	0.27	0.13	3.29	0.04	100.30
	4.15	0.05	12.25	75.16	2.82	1.60	0.22	0.11	3.03	0.06	99.44
	4.16	0.09	12.24	74.92	2.79	1.64	0.27	0.09	3.30	0.04	99.54
	4.18	0.10	12.28	75.73	2.73	1.67	0.24	0.08	3.46	0.04	100.50
	3.92	0.07	12.18	75.49	2.76	1.77	0.27	0.09	3.03	0.03	99.60
	4.15	0.10	12.17	74.95	2.68	1.62	0.22	0.08	3.28	0.03	99.29
	4.24	0.10	12.13	74.84	2.68	1.57	0.25	0.11	3.31	0.02	99.24
	4.15	0.07	12.27	75.24	2.72	1.64	0.24	0.09	3.26	-	99.70
	4.16	0.07	12.28	75.40	2.78	1.62	0.29	0.17	3.30	0.01	100.08
	4.23	0.08	12.21	75.31	2.72	1.70	0.27	0.10	3.30	-	99.91
	4.11	0.10	12.22	75.05	2.63	1.71	0.30	0.07	3.00	0.02	99.21
	3.80	0.10	12.20	75.10	2.73	1.64	0.22	0.15	2.99	0.05	98.97
Mean	4.12	0.09	12.23	75.20	2.74	1.66	0.25	0.11	3.25	0.04	99.67
1σ r.s.d. of max.	0.12	0.03	0.08	0.28	0.05	0.05	0.03	0.05	0.16	0.03	
Mean	**4.04**	**0.09**	**12.17**	**75.20**	**2.70**	**1.67**	**0.24**	**0.11**	**3.24**	**0.03**	**99.49**
1σ r.s.d. of max.	**0.16**	**0.02**	**0.13**	**0.72**	**0.07**	**0.05**	**0.04**	**0.13**	**0.17**	**0.03**	

b)

	Whole rock composition (ppm)																
Element	Sc	V	Cr	Co	Ni	Cu	Zn	Ga	Rb	Sr	Y	Zr	Nb	Mo	Cs	Ba	La
Blank sample analyses	<LDL	<LDL	<LDL	<LDL	<LDL	1.16	<LDL	<LDL	<LDL	0.92	<LDL	<LDL	<LDL	<LDL	<LDL	<LDL	0.001
	<LDL	<LDL	<LDL	<LDL	<LDL	1.75	0.15	0.002	<LDL	<LDL	<LDL	0.05	<LDL	<LDL	<LDL	<LDL	0.003
	<LDL	<LDL	<LDL	<LDL	<LDL	1.84	0.14	<LDL	<LDL	<LDL	0.006	<LDL	<LDL	<LDL	<LDL	<LDL	<LDL
Pub. BHVO-2 mean	32	317	280	45	119	127	103	21.7	9.8	389	26	172	18	-	-	130	15
Pub. BHVO-2 1σ s.d.	1	11	19	3	7	7	6	0.9	1.0	23	2	11	2	-	-	13	1
Sample analyses	30.10	353.80	318.17	42.90	131.35	142.22	110.41	20.06	9.48	426.18	22.70	172.61	18.94	4.36	0.10	142.79	14.92
	29.29	368.62	335.18	42.06	135.94	148.05	115.04	19.41	9.90	445.64	21.65	180.25	18.89	6.17	0.10	152.07	14.71
Pub. AGV-2 mean	13	120	17	16	19	53	86	20	68.6	658	20	230	15	-	1.16	1140	38
Pub. AGV-2 1σ s.d.	1	5	2	1	3	4	8	1	2.3	17	1	4	1	-	0.08	32	1
Sample analyses	9.95	135.40	17.59	12.03	<LDL	60.09	102.97	15.42	74.57	721.88	13.51	251.37	13.29	1.72	0.97	>UDL	29.31
	12.42	136.29	18.11	15.49	<LDL	61.85	103.71	20.28	75.52	725.00	17.71	259.92	14.27	2.04	1.20	>UDL	37.69

	Whole rock composition (ppm)																
Element	Ce	Pr	Nd	Sm	Eu	Gd	Tb	Dy	Ho	Er	Tm	Yb	Lu	Hf	Ta	Pb	Th	U
Blank sample analyses	<LDL	0.0004	0.0019	<LDL	<LDL	<LDL	<LDL	<LDL	<LDL	0.0004	<LDL	0.0003	<LDL	<LDL	<LDL	0.06	0.003	0.0006
	<LDL	0.0013	0.0022	0.0007	<LDL	<LDL	<LDL	0.001	<LDL	<LDL	<LDL	<LDL	<LDL	<LDL	<LDL	0.02	<LDL	0.0004
	<LDL	<LDL	0.0009	<LDL	<LDL	<LDL	<LDL	<LDL	<LDL	<LDL	<LDL	<LDL	<LDL	<LDL	<LDL	0.02	<LDL	<LDL
Pub. BHVO-2 mean	38	-	25.0	6.2	-	6.3	0.9	-	1.04	-	-	2.0	0.28	4.1	1.4	-	1.2	-
Pub. BHVO-2 1σ s.d.	2	-	1.8	0.4	-	0.2	-	-	0.04	-	-	0.2	0.01	0.3	-	-	0.3	-
Sample analyses	40.04	5.19	23.29	5.83	1.95	5.88	0.88	5.01	0.93	2.40	0.31	1.88	0.26	4.47	1.19	2.33	1.27	0.46
	41.98	5.00	22.39	5.52	1.92	5.62	0.82	4.89	0.87	2.29	0.29	1.78	0.24	4.36	1.19	1.81	1.23	0.43
Pub. AGV-2 mean	68	8.3	30	5.7	1.54	4.69	0.64	3.6	0.71	1.79	0.26	1.6	0.25	5.08	0.89	13	6.1	1.88
Pub. AGV-2 1σ s.d.	3	0.6	2	0.3	0.10	0.26	0.04	0.2	0.08	0.11	0.02	0.2	0.01	0.20	0.08	1	0.6	0.16
Sample analyses	76.57	6.31	25.23	4.48	1.22	3.66	0.49	2.82	0.54	1.44	0.20	1.30	0.19	4.82	0.86	13.59	5.14	1.64
	76.52	7.93	32.07	5.85	1.58	4.87	0.63	3.71	0.70	1.95	0.26	1.73	0.25	5.67	0.92	15.59	6.44	2.04

LDL = lower detection limit
UDL = upper detection limit

Supplementary Table 4.4 Complete unnormalised composition dataset for Volcán Hudson matrix glass samples.

Eruption	Tephra code	Composition (unnormalised wt. %)										
		Na_2O	MgO	Al_2O_3	SiO_2	K_2O	CaO	TiO_2	MnO	FeO_T	P_2O_5	Total
1991	JA12	5.92	1.46	15.64	61.13	2.61	3.21	1.17	0.04	4.99	0.40	96.57
		5.94	1.37	16.12	61.85	2.65	3.01	1.20	0.18	4.97	0.36	97.66
		3.21	1.40	16.14	62.99	2.54	3.01	1.18	0.15	4.76	0.40	95.79
		6.03	1.44	16.21	63.70	2.57	3.12	1.14	0.18	4.94	0.38	99.70
		5.41	1.46	16.18	63.02	2.56	3.03	1.19	0.18	4.86	0.37	98.25
		3.49	1.40	16.40	64.49	2.64	3.14	1.25	0.17	4.90	0.41	98.28
		4.26	1.40	15.87	61.21	2.54	2.99	1.14	0.12	5.32	0.40	95.25
		5.74	1.33	15.98	60.79	2.62	2.99	1.15	0.15	5.02	0.33	96.09
		5.98	1.22	16.05	63.66	2.64	2.69	1.03	0.22	4.23	0.23	97.96
		5.67	1.41	15.98	60.30	2.52	2.98	1.26	0.19	5.06	0.40	95.75
		4.26	1.40	16.42	63.02	2.60	2.95	1.16	0.22	5.16	0.34	97.54
		6.45	1.32	15.86	63.13	2.96	2.61	1.16	0.09	4.61	0.35	98.52
		5.99	1.37	16.19	62.85	2.63	2.96	1.16	0.11	4.74	0.30	98.31
		5.82	1.41	16.05	60.51	2.54	3.24	1.19	0.24	5.02	0.36	96.39
		5.48	1.34	16.48	63.68	2.77	2.78	1.11	0.18	4.81	0.30	98.92
		5.87	1.36	16.30	63.16	2.63	2.86	1.21	0.19	4.70	0.36	98.64
		5.82	1.37	16.48	63.08	2.69	2.92	1.18	0.23	4.97	0.40	99.14
		5.78	1.36	16.16	62.71	2.66	2.98	1.24	0.10	4.86	0.44	98.29
		6.05	1.50	16.45	62.64	2.66	3.09	1.24	0.21	4.84	0.37	99.06
		5.76	1.38	16.44	63.03	2.67	3.14	1.20	0.22	4.94	0.40	99.17
		5.83	1.49	16.49	62.92	2.58	3.04	1.19	0.20	4.95	0.42	99.09
		5.52	1.46	16.71	63.03	2.64	3.14	1.30	0.12	5.10	0.45	99.46
		5.72	1.44	15.93	61.86	2.64	2.93	1.23	0.22	4.66	0.43	97.06
		3.37	1.42	16.54	64.02	2.72	3.04	1.30	0.16	4.90	0.41	97.88
	RI4g	5.40	1.55	16.35	62.13	2.42	3.54	1.20	0.24	5.44	0.40	98.67
		6.08	1.55	16.28	62.51	2.50	3.50	1.23	0.13	4.85	0.39	99.02
		5.51	1.49	16.13	62.32	2.60	3.25	1.30	0.14	5.08	0.42	98.25
		5.63	1.51	16.19	62.25	2.64	3.14	1.23	0.13	4.95	0.35	98.03
		5.83	1.82	16.01	60.94	2.37	3.75	1.35	0.21	6.03	0.42	98.73
		5.56	1.54	15.95	61.10	2.45	3.49	1.29	0.16	4.97	0.39	96.90
		5.50	1.65	16.12	61.54	2.56	3.38	1.21	0.26	4.97	0.43	97.61
		5.43	1.60	15.94	59.52	2.40	3.50	1.25	0.19	5.49	0.42	95.73
		5.76	1.50	16.25	60.64	2.49	3.32	1.23	0.20	5.30	0.44	97.13
		5.96	1.61	16.01	61.41	2.45	3.59	1.36	0.13	5.25	0.46	98.23
		5.73	1.44	16.56	62.00	2.54	3.14	1.20	0.14	4.91	0.40	98.06
		5.72	1.50	16.26	62.39	2.53	3.22	1.21	0.11	5.01	0.40	98.34
		5.66	1.52	16.26	62.04	2.58	3.31	1.21	0.24	5.36	0.38	98.56
		6.22	1.54	16.69	63.37	2.54	3.11	1.29	0.22	5.07	0.49	100.53
		5.87	1.47	16.07	62.68	2.60	3.09	1.22	0.19	5.27	0.44	98.89
		5.98	1.44	16.21	63.05	2.67	2.92	1.25	0.09	4.73	0.42	98.77
		5.95	1.73	16.44	61.92	2.55	3.50	1.28	0.18	5.29	0.49	99.33
		5.81	1.43	16.20	62.44	2.60	2.91	1.30	0.17	5.22	0.42	98.50
		6.18	1.44	16.13	62.50	2.64	3.04	1.19	0.21	4.92	0.37	98.61
		5.70	1.57	16.49	62.80	2.53	3.19	1.24	0.17	5.36	0.43	99.48
		5.96	1.72	16.55	62.25	2.47	3.38	1.30	0.13	5.51	0.48	99.76

		5.97	1.46	16.27	62.60	2.58	3.21	1.21	0.19	5.01	0.38	98.89
		5.78	1.55	16.46	63.26	2.56	3.20	1.28	0.21	5.25	0.42	99.97
		5.88	1.48	16.36	62.67	2.61	3.15	1.19	0.21	5.01	0.42	98.99
T8?	JA11	6.03	1.24	16.34	66.17	2.70	2.80	1.09	0.20	4.35	0.29	101.19
		5.95	1.27	16.52	63.33	2.64	2.77	1.10	0.10	4.74	0.29	98.72
		6.16	1.27	16.36	63.95	2.62	2.77	1.13	0.14	4.67	0.31	99.38
		6.09	1.20	16.14	64.04	2.64	2.73	0.99	0.12	4.59	0.33	98.86
		5.72	1.33	16.25	62.55	2.55	3.04	1.14	0.16	4.84	0.31	97.88
		5.91	1.25	16.45	63.25	2.63	2.64	1.06	0.19	4.59	0.28	98.27
		6.02	1.28	16.32	62.54	2.70	2.90	0.99	0.09	4.47	0.29	97.61
		6.15	1.20	16.45	63.61	2.57	2.82	0.99	0.16	4.54	0.34	98.82
		5.67	1.23	16.32	62.27	2.61	2.71	1.03	0.16	4.74	0.31	97.05
		6.20	1.17	16.24	64.41	2.70	2.70	1.10	0.07	4.68	0.32	99.58
		5.98	1.24	16.50	65.19	2.62	2.79	1.11	0.11	4.73	0.28	100.54
		6.12	1.35	16.12	63.23	2.54	2.93	1.16	0.03	4.32	0.30	98.10
		6.01	1.09	16.05	60.37	2.74	2.66	1.04	0.18	4.56	0.28	94.98
		5.99	1.27	16.49	63.93	2.66	2.99	1.12	0.24	4.97	0.34	99.99
		5.76	1.35	16.19	62.86	2.63	2.76	1.13	0.21	4.97	0.38	98.25
		5.85	1.43	16.17	62.52	2.64	2.94	1.13	0.16	4.78	0.38	98.01
		6.12	1.31	16.25	63.23	2.65	2.71	1.01	0.20	4.73	0.37	98.59
		5.87	1.32	16.25	63.36	2.70	2.72	1.15	0.08	4.91	0.38	98.75
		5.98	1.39	16.14	62.88	2.63	2.94	1.07	0.18	4.56	0.33	98.11
		6.02	1.35	16.39	62.57	2.69	2.78	1.12	0.17	4.78	0.38	98.26
		6.01	1.29	16.20	62.93	2.59	2.82	1.10	0.14	4.76	0.38	98.22
		5.99	1.29	16.57	63.82	2.79	2.85	1.16	0.19	4.39	0.33	99.37
		6.06	1.21	16.15	62.95	2.58	2.50	1.05	0.23	4.41	0.35	97.50
		5.83	1.31	16.27	62.86	2.66	2.72	1.13	0.20	4.53	0.32	97.82
?	JA10	4.52	4.45	15.49	51.50	1.18	8.23	2.26	0.20	10.26	0.68	98.76
		4.59	4.31	15.58	51.35	1.29	8.13	2.27	0.18	10.25	0.71	98.65
		4.47	4.22	15.66	51.34	1.19	8.18	2.16	0.09	10.71	0.73	98.75
		4.60	4.24	15.45	49.48	1.22	8.15	2.30	0.26	9.80	0.71	96.19
		4.79	4.11	14.48	50.01	1.43	7.78	2.70	0.30	10.77	0.99	97.36
		4.44	4.51	15.41	50.09	1.28	8.03	2.24	0.22	10.31	0.76	97.28
		4.48	4.28	15.76	51.45	1.17	8.32	2.11	0.19	10.25	0.65	98.65
		4.57	4.27	15.80	51.08	1.21	8.03	2.17	0.14	9.78	0.70	97.76
		4.62	4.27	15.31	50.19	1.24	8.13	2.22	0.22	9.78	0.67	96.65
		4.38	4.12	15.55	48.78	1.15	8.11	2.29	0.17	10.45	0.72	95.73
		4.60	4.47	14.77	49.68	1.32	7.93	2.32	0.28	10.78	0.73	96.87
		4.57	4.25	15.80	52.15	1.25	8.14	2.27	0.23	9.80	0.64	99.09
		4.55	4.39	15.67	52.43	1.20	8.29	2.19	0.16	9.92	0.68	99.47
		4.53	4.21	15.62	51.35	1.21	8.12	2.21	0.18	10.55	0.73	98.69
		4.12	4.40	15.47	52.96	1.20	8.11	2.38	0.13	10.34	0.71	99.81
		4.30	4.26	15.26	51.25	1.26	8.09	2.40	0.13	10.42	0.83	98.19
		4.27	4.39	14.93	50.85	1.26	7.93	2.34	0.22	10.50	0.84	97.52
		4.48	4.46	15.11	51.24	1.29	7.82	2.24	0.22	10.20	0.83	97.89
		4.64	4.36	15.59	51.35	1.30	8.01	2.20	0.22	10.38	0.79	98.86
		4.01	4.35	15.20	51.18	1.27	8.02	2.32	0.18	10.29	0.87	97.70
		4.19	4.47	15.02	51.60	1.31	7.99	2.32	0.18	10.55	0.86	98.50
		4.28	4.27	15.46	51.52	1.30	8.13	2.24	0.20	9.73	0.78	97.92
		4.23	4.38	15.31	51.33	1.22	8.19	2.24	0.20	10.48	0.82	98.40

T6?	JA9	5.03	2.40	14.67	58.91	2.21	4.97	1.84	0.25	7.92	0.74	98.94
		3.65	3.71	14.79	55.02	1.51	6.95	1.86	0.11	9.22	0.75	97.56
		4.23	4.05	14.62	53.21	1.26	7.63	1.79	0.19	9.73	0.66	97.37
		4.07	4.37	14.68	51.50	1.29	7.85	1.80	0.15	10.05	0.68	96.43
		3.91	3.01	15.00	57.16	2.05	5.51	1.81	0.25	7.99	0.71	97.40
		4.08	2.92	15.94	57.07	1.83	6.02	1.60	0.11	8.08	0.61	98.25
		3.74	2.84	15.67	57.57	1.89	5.94	1.71	0.21	8.00	0.60	98.17
		3.81	2.84	15.79	57.96	1.81	6.04	1.61	0.18	8.30	0.59	98.93
		4.39	2.56	13.63	54.59	2.24	5.54	1.96	0.18	9.50	0.86	95.45
		4.00	4.74	15.98	50.84	1.13	8.86	1.39	0.20	8.46	0.51	96.10
		4.07	4.43	14.59	53.77	1.33	7.86	1.78	0.15	9.85	0.72	98.54
		4.79	2.57	15.99	55.42	1.78	5.72	1.49	0.12	7.51	0.67	96.07
		3.77	3.97	14.32	52.66	1.39	7.94	1.83	0.14	9.58	0.76	96.34
		3.85	4.55	15.90	53.73	1.34	8.12	1.41	0.15	8.29	0.45	97.78
		4.18	3.78	14.61	53.74	1.31	7.50	1.81	0.22	9.59	0.74	97.48
		4.71	3.04	15.82	56.39	1.74	6.00	1.60	0.16	8.33	0.75	98.54
		4.56	3.03	15.56	56.56	1.79	5.96	1.60	0.16	8.33	0.72	98.26
		4.14	4.69	16.04	53.58	1.19	8.38	1.38	0.29	8.73	0.60	99.02
		4.65	2.97	15.99	56.67	1.81	5.75	1.57	0.17	8.11	0.77	98.45
		4.26	3.32	15.65	55.87	1.75	6.42	1.55	0.26	7.92	0.65	97.66
		4.65	2.34	15.69	59.17	2.20	4.82	1.61	0.15	6.90	0.65	98.17
		4.19	3.55	15.70	55.24	1.55	6.65	1.55	0.13	8.15	0.63	97.36
		4.58	2.93	15.99	57.00	1.78	5.95	1.68	0.17	8.28	0.68	99.03
		4.63	2.81	16.06	56.65	1.80	5.89	1.50	0.17	7.86	0.73	98.11
?	JA8c	5.08	1.95	15.71	58.72	2.14	4.30	1.45	0.11	6.09	0.51	96.06
		4.28	2.05	15.99	60.12	2.26	4.38	1.40	0.17	5.91	0.56	97.13
		4.59	2.33	15.76	59.72	2.13	4.82	1.44	0.24	6.43	0.60	98.04
		4.97	2.35	15.49	57.89	2.02	4.65	1.35	0.11	6.79	0.61	96.23
		4.93	2.34	15.63	57.69	2.09	4.85	1.47	0.19	5.93	0.60	95.73
		4.98	2.24	15.78	57.71	2.07	4.83	1.49	0.12	6.83	0.58	96.64
		5.22	2.16	15.74	59.08	2.18	4.50	1.38	0.12	5.59	0.50	96.47
		4.94	2.35	15.67	58.09	2.00	4.75	1.45	0.15	6.44	0.57	96.42
		5.13	2.34	16.14	59.80	2.06	4.89	1.46	0.21	6.77	0.56	99.37
		5.04	2.25	15.84	59.61	2.21	4.73	1.52	0.22	6.66	0.57	98.64
		3.56	2.21	15.60	60.72	2.75	4.26	1.51	0.12	7.15	0.56	98.44
		4.91	2.21	15.92	59.39	2.25	4.51	1.48	0.02	6.38	0.66	97.74
		5.40	2.01	15.88	59.93	2.27	4.29	1.34	0.17	6.08	0.62	97.98
		5.20	2.30	15.96	58.96	2.13	4.91	1.49	0.16	6.63	0.64	98.40
		4.88	2.28	16.06	59.12	2.22	4.79	1.54	0.19	6.78	0.64	98.49
		4.69	2.26	15.75	58.76	2.12	4.59	1.47	0.20	6.16	0.58	96.58
		4.59	2.24	16.02	59.66	2.21	4.72	1.50	0.14	6.63	0.67	98.40
		4.93	2.03	14.97	60.65	2.51	4.27	1.74	0.15	7.36	0.77	99.37
		4.91	2.26	16.05	60.04	2.16	4.70	1.46	0.20	6.80	0.69	99.27
		4.94	2.38	16.05	59.20	2.07	4.88	1.52	0.07	6.70	0.59	98.38
	JA8b	4.82	2.25	15.88	58.84	2.03	4.92	1.31	0.15	6.28	0.55	97.02
		4.60	2.28	16.05	58.59	2.07	4.95	1.45	0.15	6.31	0.53	96.98
		4.67	2.28	15.99	58.65	2.08	4.91	1.46	0.13	6.32	0.58	97.08
		3.87	4.16	15.13	52.41	1.39	7.66	1.51	0.20	9.08	0.56	95.97
		4.42	3.78	15.98	54.93	1.34	7.58	1.52	0.09	8.40	0.51	98.55
		4.85	2.29	15.83	58.60	2.08	4.75	1.33	0.17	6.78	0.61	97.27

		3.91	3.51	13.77	54.51	1.64	7.16	1.89	0.29	9.73	0.72	97.13
		3.93	3.64	13.87	54.28	1.69	6.95	2.04	0.22	10.06	0.76	97.43
		3.80	3.47	13.58	53.69	1.68	6.95	2.03	0.21	10.73	0.78	96.91
		4.08	3.66	13.75	53.79	1.68	7.30	1.98	0.15	10.74	0.77	97.91
		3.87	3.66	13.99	55.53	1.74	7.29	1.97	0.15	10.29	0.71	99.19
		3.95	3.65	14.21	56.15	1.52	7.12	2.01	0.17	10.29	0.70	99.76
		5.03	2.34	15.96	57.89	2.02	4.78	1.40	0.09	6.57	0.60	96.68
		5.19	2.07	15.79	58.97	2.28	4.45	1.40	0.16	5.83	0.58	96.71
		4.82	2.30	16.04	58.68	2.10	4.82	1.47	0.11	6.87	0.68	97.88
		5.19	2.13	16.10	59.45	2.14	4.46	1.42	0.24	5.93	0.64	97.70
		5.20	2.07	16.19	59.87	2.25	4.40	1.42	0.16	6.51	0.62	98.70
		3.90	3.35	15.28	54.26	1.52	7.33	1.78	0.14	9.42	0.83	97.82
		4.83	2.43	15.90	58.36	2.18	4.95	1.44	0.12	6.72	0.64	97.57
		3.97	3.31	14.90	54.73	1.67	7.34	1.87	0.23	9.92	0.81	98.75
		4.24	3.46	13.10	53.86	1.82	6.55	2.07	0.24	9.86	0.90	96.12
		4.97	2.21	15.54	58.34	2.24	4.72	1.49	0.15	6.54	0.64	96.83
		4.87	2.47	16.16	59.07	2.16	5.03	1.47	0.16	6.75	0.65	98.80
	JA8a	4.19	4.08	13.66	52.71	1.48	7.91	1.84	0.18	10.49	0.68	97.22
		3.39	3.72	13.47	52.59	1.56	7.65	1.91	0.24	9.85	0.72	95.09
		4.14	3.84	13.59	53.47	1.45	7.60	1.91	0.19	10.18	0.70	97.05
		4.08	4.29	14.40	53.11	1.32	8.66	1.66	0.21	9.66	0.48	97.85
		3.94	3.81	13.29	52.77	1.51	7.48	2.05	0.14	10.54	0.82	96.35
		3.59	3.95	13.44	53.13	1.46	7.87	2.04	0.19	10.63	0.73	97.01
		3.78	3.88	14.02	53.21	1.36	7.90	1.87	0.07	9.96	0.66	96.73
		3.83	3.54	14.16	52.75	1.51	7.02	2.20	0.23	10.56	0.62	96.40
		3.76	5.12	14.86	52.29	1.20	8.14	1.58	0.15	9.14	0.56	96.78
		3.89	4.55	15.28	52.59	1.27	8.05	1.67	0.18	9.55	0.67	97.69
		3.78	3.96	14.20	54.05	1.43	7.88	1.96	0.18	10.40	0.76	98.60
		3.86	3.86	14.67	53.36	1.35	8.09	1.94	0.23	9.86	0.74	97.96
		3.78	3.87	14.71	53.08	1.40	8.09	1.84	0.24	10.05	0.77	97.83
		3.91	4.16	15.66	52.58	1.23	8.03	1.60	0.22	9.06	0.65	97.09
		4.07	4.35	15.24	51.51	1.22	7.92	1.70	0.19	9.49	0.66	96.36
		3.51	4.03	14.17	54.02	1.47	7.63	1.93	0.15	10.44	0.79	98.14
		3.66	4.38	14.54	52.15	1.26	8.63	1.77	0.24	9.59	0.49	96.72
		3.53	3.97	14.03	53.18	1.43	7.71	1.97	0.21	10.07	0.81	96.91
		3.87	4.71	15.06	52.27	1.34	7.87	1.64	0.17	9.52	0.69	97.15
		3.59	4.08	14.21	53.74	1.38	7.83	1.95	0.30	10.38	0.76	98.22
?	JA7	4.42	3.79	13.37	49.72	1.52	7.77	2.59	0.14	12.39	0.79	96.51
		3.69	4.45	14.01	49.88	1.29	8.41	2.27	0.22	11.19	0.71	96.12
		4.32	3.45	13.61	51.22	1.58	7.54	2.83	0.25	12.02	0.85	97.67
		4.59	4.01	14.01	52.07	1.42	8.04	2.49	0.22	11.89	0.79	99.52
		4.48	3.81	13.45	49.68	1.46	7.83	2.51	0.22	12.43	0.86	96.74
		4.27	3.58	13.84	52.98	1.46	7.97	2.74	0.18	12.16	0.79	99.97
		4.31	3.57	13.78	52.36	1.56	7.61	2.54	0.21	11.47	0.81	98.23
		4.21	3.37	13.44	52.61	1.66	7.63	2.93	0.20	12.59	0.91	99.54
		4.17	4.31	13.97	51.20	1.36	8.17	2.31	0.24	11.16	0.69	97.59
		4.12	3.57	13.40	50.37	1.60	8.18	2.80	0.19	12.15	0.82	97.20
		4.26	4.24	13.71	50.01	1.36	8.34	2.34	0.27	11.32	0.67	96.52
		4.20	3.90	13.77	51.37	1.52	7.90	2.46	0.29	11.63	0.76	97.79
		3.92	3.71	13.57	50.92	1.58	7.55	2.77	0.17	12.56	0.83	97.57

		4.19	3.63	13.67	50.79	1.59	7.59	2.53	0.21	11.44	0.75	96.39
		4.00	3.87	14.61	52.00	1.36	8.26	2.31	0.24	11.22	0.74	98.61
		3.97	4.70	12.72	49.62	1.40	7.64	2.49	0.21	12.39	0.78	95.92
		4.04	4.14	14.49	51.90	1.32	8.11	2.39	0.22	11.12	0.75	98.48
		3.70	3.29	14.07	51.88	1.77	7.41	2.77	0.13	11.89	0.89	97.79
		4.14	3.74	13.65	51.82	1.53	7.80	2.70	0.23	12.00	0.89	98.51
		4.04	3.75	13.73	52.20	1.62	7.76	2.68	0.23	12.00	0.89	98.91
?	JA6	3.97	5.06	14.97	53.09	1.07	8.82	1.77	0.26	10.16	0.64	99.80
		4.08	4.84	15.05	51.45	1.02	8.76	1.61	0.23	9.66	0.54	97.24
		3.92	4.61	14.35	51.69	1.07	8.98	1.67	0.15	10.20	0.57	97.19
		3.64	5.17	14.90	51.49	1.14	9.27	1.60	0.18	9.50	0.48	97.37
		4.00	4.94	14.78	51.36	1.05	8.75	1.70	0.20	9.56	0.66	97.00
		4.05	4.85	15.44	52.70	1.19	9.15	1.69	0.10	9.62	0.40	99.20
		3.86	4.77	15.20	51.70	1.02	8.80	1.57	0.14	9.89	0.56	97.49
		3.85	4.74	14.66	51.30	1.01	8.76	1.59	0.06	9.30	0.60	95.87
		3.76	4.92	14.87	52.76	1.06	8.72	1.60	0.21	9.67	0.62	98.18
		4.15	4.62	15.44	53.31	1.05	8.78	1.68	0.16	9.75	0.63	99.56
		3.90	4.68	15.72	53.67	1.37	8.93	1.57	0.21	9.01	0.40	99.46
		4.11	4.83	14.74	54.93	1.09	8.59	1.69	0.21	10.30	0.66	101.16
		3.94	4.79	15.67	55.35	1.22	8.92	1.58	0.23	8.86	0.37	100.94
		3.91	4.76	14.97	54.31	1.01	8.86	1.51	0.12	10.21	0.59	100.25
		3.66	4.90	14.83	52.42	1.09	8.65	1.68	0.18	9.86	0.67	97.92
		3.31	4.45	14.35	53.27	1.15	8.49	1.87	0.14	9.87	0.72	97.62
		3.66	4.70	15.12	52.41	1.12	8.71	1.67	0.17	10.13	0.73	98.42
		3.53	4.81	14.82	52.08	1.08	8.55	1.64	0.12	9.79	0.72	97.15
		3.45	5.05	14.99	51.63	1.13	9.09	1.59	0.16	9.32	0.43	96.83
		3.50	5.05	15.70	51.75	1.14	9.00	1.48	0.23	9.34	0.42	97.62
		3.69	4.93	15.22	51.99	1.18	8.76	1.50	0.21	9.71	0.51	97.70
		3.45	4.90	15.45	52.48	1.24	8.96	1.65	0.17	9.45	0.50	98.25
		3.57	4.90	15.20	52.51	1.01	8.75	1.65	0.24	9.38	0.66	97.87
		3.30	4.67	15.13	50.51	1.43	8.68	1.58	0.20	9.34	0.41	95.25
?	JA5	3.71	4.84	15.00	49.79	1.33	9.35	1.56	0.10	9.75	0.42	95.84
		4.00	4.83	15.12	51.83	1.38	9.17	1.54	0.14	9.56	0.42	97.99
		3.92	5.15	14.49	49.07	1.55	8.69	1.61	0.21	9.95	0.45	95.07
		3.68	4.79	15.30	50.26	1.40	9.04	1.55	0.34	9.22	0.41	96.00
		4.03	4.46	14.33	50.79	1.66	8.74	1.88	0.12	10.04	0.51	96.55
		3.87	4.97	15.67	51.94	1.30	9.32	1.57	0.16	8.85	0.39	98.04
		3.76	4.88	15.22	49.96	1.43	8.93	1.51	0.14	9.71	0.40	95.94
		3.94	4.07	13.88	51.69	1.73	8.42	1.84	0.27	10.57	0.51	96.92
		5.88	0.58	14.98	66.60	3.58	1.67	0.65	0.20	2.93	0.11	97.17
		5.43	1.73	15.85	62.55	2.47	3.72	1.22	0.11	5.33	0.46	98.88
		5.48	0.60	14.55	65.41	3.45	1.53	0.74	0.05	3.03	0.11	94.94
		3.77	5.16	14.79	52.13	1.48	9.05	1.59	0.16	9.54	0.41	98.07
		3.78	4.82	15.58	50.44	1.34	9.09	1.40	0.11	9.43	0.40	96.38
		3.90	5.17	16.18	53.92	1.29	9.38	1.55	0.05	8.51	0.40	100.34
		3.38	4.33	14.37	52.92	1.61	8.73	1.87	0.28	10.17	0.48	98.15
		3.59	4.44	14.38	52.66	1.73	8.47	1.78	0.21	10.27	0.56	98.07
		3.22	5.01	15.54	51.81	1.30	9.23	1.60	0.10	9.50	0.46	97.77
		5.19	0.53	14.85	66.65	3.58	1.45	0.66	0.00	2.86	0.11	95.87
		5.45	0.62	15.19	68.39	3.73	1.52	0.73	0.13	2.96	0.12	98.84

		3.67	5.13	15.44	51.93	1.40	8.97	1.69	0.19	9.05	0.45	97.91
		5.34	0.57	14.83	65.89	3.56	1.56	0.66	0.07	3.11	0.12	95.71
		5.07	1.74	15.74	60.12	2.50	3.77	1.36	0.06	5.24	0.55	96.16
		3.43	5.07	15.77	51.93	1.35	9.15	1.42	0.22	9.42	0.41	98.17
H2 (T5)	JA4d	5.40	0.62	15.32	69.14	3.47	1.53	0.68	0.21	2.88	0.12	99.37
		5.18	0.58	15.06	65.88	3.40	1.52	0.69	0.16	3.17	0.10	95.73
		5.47	0.59	14.91	65.33	3.51	1.57	0.67	0.19	2.93	0.10	95.28
		5.25	0.60	14.96	65.83	3.50	1.44	0.65	0.09	2.57	0.10	95.00
		5.37	0.59	15.08	66.12	3.47	1.58	0.64	0.18	2.70	0.11	95.84
		5.75	0.58	15.24	66.62	3.43	1.52	0.66	0.09	2.84	0.12	96.85
		5.22	0.63	15.03	66.30	3.44	1.59	0.70	0.03	2.99	0.10	96.02
		5.35	0.59	15.20	67.88	3.38	1.60	0.66	0.05	3.20	0.11	98.03
		5.28	0.62	15.25	67.42	3.37	1.58	0.71	0.12	3.03	0.09	97.46
		5.37	0.55	15.04	66.46	3.54	1.53	0.66	0.03	3.21	0.15	96.53
		5.56	0.59	15.11	68.01	3.44	1.59	0.59	0.14	2.99	0.11	98.13
		5.42	0.58	15.08	66.66	3.52	1.54	0.65	0.02	2.78	0.12	96.36
		5.37	0.60	15.24	66.99	3.49	1.55	0.59	0.06	2.81	0.11	96.81
		5.30	0.61	15.10	67.43	3.54	1.47	0.66	0.08	2.89	0.11	97.19
		5.33	0.58	15.04	67.29	3.57	1.49	0.65	0.04	2.94	0.14	97.08
		5.60	0.60	15.51	68.55	3.59	1.55	0.74	0.14	2.90	0.17	99.35
		5.67	0.59	15.28	68.02	3.42	1.51	0.68	0.14	2.77	0.14	98.22
		5.64	0.57	14.79	66.63	3.47	1.46	0.64	0.16	2.88	0.11	96.34
		5.55	0.64	15.13	67.50	3.50	1.53	0.77	0.12	2.99	0.14	97.88
		5.66	0.58	15.08	66.75	3.48	1.58	0.65	0.08	2.72	0.13	96.69
		5.57	0.55	15.15	67.70	3.53	1.49	0.77	0.07	2.99	0.13	97.95
		5.32	0.59	15.14	67.33	3.48	1.58	0.65	0.05	2.86	0.14	97.13
		5.92	0.56	14.93	67.29	3.53	1.58	0.70	0.10	2.86	0.11	97.58
	JA4a	5.60	0.60	15.24	68.45	3.43	1.45	0.62	0.10	2.77	0.10	98.36
		4.88	1.14	15.62	63.80	2.93	2.94	1.06	0.18	4.73	0.32	97.59
		5.26	0.63	15.17	66.08	3.40	1.63	0.76	0.23	2.98	0.12	96.25
		5.35	0.63	15.10	66.54	3.52	1.53	0.63	0.11	2.96	0.12	96.51
		5.54	0.59	15.24	66.29	3.59	1.54	0.63	0.07	3.18	0.12	96.79
		5.50	0.53	15.29	67.64	3.52	1.48	0.68	0.22	3.05	0.13	98.05
		5.34	0.62	15.26	68.73	3.37	1.58	0.71	0.11	2.71	0.12	98.55
		5.53	0.58	15.28	68.23	3.51	1.59	0.76	0.11	3.09	0.14	98.81
		5.62	0.64	15.42	68.68	3.46	1.58	0.72	0.07	3.02	0.12	99.33
		5.35	0.56	15.36	66.79	3.45	1.56	0.56	0.13	2.77	0.14	96.66
		4.97	1.28	15.38	63.96	3.00	3.12	1.07	0.19	4.75	0.25	97.98
		5.24	0.54	14.94	68.29	3.45	1.57	0.67	0.09	2.95	0.10	97.83
		5.29	0.58	14.64	66.30	3.45	1.42	0.66	0.20	2.78	0.14	95.44
		5.12	1.19	15.50	65.10	3.06	2.69	0.90	0.16	4.24	0.26	98.22
		5.54	0.64	15.20	67.80	3.51	1.65	0.57	0.12	2.84	0.20	98.07
		5.44	0.80	15.21	66.16	3.43	1.94	0.81	0.10	3.49	0.15	97.53
		5.34	0.59	14.90	67.31	3.58	1.53	0.68	0.12	3.04	0.11	97.20
		5.51	0.62	15.24	68.22	3.47	1.44	0.62	0.11	2.84	0.11	98.19
		5.59	0.62	15.19	67.67	3.66	1.53	0.72	0.11	2.90	0.13	98.12
		5.64	0.91	15.63	66.43	3.29	2.42	0.83	0.09	3.56	0.15	98.96
		5.34	0.96	15.83	64.25	3.04	2.91	0.90	0.15	3.94	0.26	97.57
		5.39	1.35	15.62	64.27	3.01	3.08	1.06	0.16	5.02	0.33	99.27
		5.49	0.57	15.36	68.54	3.60	1.58	0.72	0.15	2.94	0.13	99.08

		5.34	0.60	15.06	67.70	3.51	1.52	0.70	0.11	2.95	0.14	97.62
	RI3a	5.48	0.44	15.12	66.69	3.54	1.26	0.61	0.14	2.56	0.09	95.92
		5.21	0.61	15.22	68.07	3.51	1.54	0.69	0.04	2.92	0.17	97.97
		5.34	0.64	15.59	68.31	3.46	1.52	0.69	0.05	2.68	0.13	98.40
		5.12	0.64	15.36	68.96	3.44	1.62	0.77	0.10	3.13	0.13	99.27
		5.01	0.55	15.08	65.92	3.41	1.54	0.73	0.13	2.81	0.09	95.27
		5.06	0.59	15.35	68.11	3.50	1.66	0.68	0.09	2.92	0.15	98.12
		4.99	0.48	15.25	69.32	3.63	1.31	0.60	0.11	2.41	0.08	98.19
		5.36	0.60	15.04	69.48	3.49	1.53	0.69	0.05	2.76	0.08	99.07
		5.83	0.56	15.49	69.10	3.42	1.48	0.74	0.11	2.88	0.11	99.73
		4.06	0.56	15.26	66.00	3.58	1.52	0.71	0.17	3.09	0.13	95.09
		5.38	0.62	15.23	67.09	3.46	1.48	0.67	0.12	2.73	0.11	96.89
		5.69	0.62	15.21	68.24	3.53	1.48	0.76	0.09	2.99	0.12	98.72
		5.65	0.67	15.55	68.48	3.58	1.57	0.70	0.05	3.14	0.18	99.56
		5.97	0.64	15.58	68.84	3.57	1.67	0.64	0.16	2.92	0.11	100.10
		5.35	0.65	15.11	67.85	3.63	1.57	0.68	0.15	2.96	0.13	98.08
		5.82	0.60	15.68	68.88	3.61	1.52	0.67	0.04	2.89	0.12	99.84
		5.53	0.49	15.13	69.62	3.68	1.24	0.56	0.13	2.41	0.08	98.88
		5.64	0.64	15.51	69.01	3.51	1.52	0.69	0.11	2.79	0.11	99.53
		5.88	0.45	15.24	69.76	3.76	1.26	0.51	0.10	2.39	0.12	99.49
		5.68	0.60	15.42	68.77	3.55	1.45	0.66	0.17	2.80	0.12	99.20
		5.79	0.60	15.15	67.87	3.50	1.50	0.75	0.00	2.87	0.16	98.18
		5.70	0.62	15.60	68.77	3.55	1.45	0.70	0.09	2.91	0.13	99.53
		5.77	0.59	15.29	68.40	3.60	1.65	0.67	0.09	2.95	0.16	99.17
		5.91	0.44	14.88	69.09	3.78	1.28	0.56	0.15	2.64	0.10	98.84
T4?	JA3	5.51	0.82	15.19	65.66	3.28	1.95	0.87	0.12	3.37	0.18	96.94
		5.59	0.84	15.23	65.41	3.29	1.87	0.83	0.18	3.55	0.13	96.92
		5.52	0.88	15.48	66.56	3.24	2.07	0.73	0.09	3.34	0.20	98.12
		5.44	0.80	15.18	68.02	3.29	1.93	0.89	0.09	3.24	0.13	99.01
		4.42	0.79	15.46	67.07	3.43	1.99	1.00	0.18	3.30	0.17	97.81
		5.67	0.77	15.25	66.52	3.29	1.83	0.83	0.05	3.35	0.21	97.76
		5.34	0.88	15.46	66.40	3.35	2.14	0.92	0.16	3.48	0.17	98.30
		6.11	0.77	15.13	65.56	3.12	2.02	0.90	0.09	3.45	0.17	97.32
		4.44	0.81	15.35	65.11	3.23	1.91	0.89	0.24	3.40	0.18	95.56
		5.55	0.85	15.15	64.57	3.43	1.89	0.84	0.09	3.30	0.18	95.83
		5.67	0.88	15.60	67.16	3.18	2.16	0.90	0.22	3.44	0.16	99.37
		5.41	0.78	15.11	64.94	3.28	2.03	0.82	0.01	3.41	0.15	95.94
		5.50	0.82	15.29	67.18	3.20	2.06	0.87	0.10	3.38	0.16	98.57
		5.54	0.79	15.42	67.16	3.33	1.81	0.85	0.10	3.55	0.20	98.75
		5.26	0.92	15.68	66.42	3.21	2.10	0.87	0.10	3.57	0.22	98.35
		5.20	0.81	15.50	67.21	3.47	1.84	0.86	0.07	3.45	0.20	98.60
		5.47	0.73	15.38	67.84	3.46	1.82	0.94	0.19	3.43	0.22	99.48
		5.26	0.84	15.53	66.74	3.36	1.92	0.88	0.12	3.31	0.19	98.15
		5.42	0.76	15.55	67.26	3.43	1.86	0.91	0.11	3.36	0.21	98.89
		5.62	0.81	15.89	67.51	3.60	1.97	0.90	0.11	3.43	0.21	100.04
		5.53	0.81	15.47	67.08	3.47	1.87	0.81	0.13	3.44	0.22	98.82
		5.72	0.69	15.64	67.27	3.39	1.81	0.80	0.18	3.32	0.20	99.00
		5.44	0.82	15.44	67.30	3.45	1.86	0.77	0.07	3.52	0.16	98.83
		5.15	0.81	15.10	65.95	3.43	1.89	0.86	0.10	3.50	0.21	97.00
		5.61	0.90	15.35	67.03	3.44	1.90	0.87	0.16	3.74	0.20	99.21

T3??	JA2b	5.14	1.27	16.26	62.31	2.71	2.59	1.15	0.10	4.26	0.30	96.08
		4.81	1.17	15.27	63.63	3.05	2.66	1.14	0.08	4.87	0.32	96.98
		5.37	1.17	15.57	64.01	3.00	2.43	1.07	0.20	3.99	0.30	97.11
		5.41	1.22	15.48	62.68	2.85	2.44	1.16	0.15	4.52	0.32	96.23
		5.30	2.14	15.78	62.54	2.53	4.05	1.19	0.13	5.55	0.34	99.53
		4.64	1.16	15.47	63.30	2.96	2.40	1.15	0.13	4.64	0.33	96.20
		5.36	1.10	15.80	64.51	3.03	2.21	0.97	0.11	3.86	0.29	97.23
		5.46	1.44	15.63	62.61	2.85	2.93	1.31	0.05	5.10	0.39	97.76
		4.46	1.06	15.75	63.82	3.00	2.46	1.02	0.17	4.61	0.28	96.64
		5.37	1.16	15.42	63.85	3.06	2.58	1.18	0.04	4.53	0.39	97.56
		6.09	1.22	16.73	63.83	2.88	2.56	1.13	0.13	4.25	0.37	99.18
		5.83	1.18	15.75	64.79	3.01	2.48	1.22	0.19	4.44	0.31	99.20
		6.06	0.95	16.36	65.48	2.96	2.03	0.94	0.16	3.30	0.26	98.51
		5.36	1.21	15.76	65.01	2.93	2.50	1.06	0.18	4.53	0.31	98.84
		5.55	1.09	16.04	65.54	2.99	2.32	1.13	0.20	4.22	0.26	99.35
		4.98	1.70	15.91	63.16	2.60	3.80	1.32	0.06	5.47	0.45	99.43
		5.78	1.49	16.04	64.04	2.80	2.91	1.28	0.19	4.71	0.48	99.72
		5.51	1.22	15.06	62.28	2.80	2.65	1.13	0.08	4.58	0.38	95.68
		5.51	1.66	15.96	63.16	2.65	3.23	1.14	0.17	5.18	0.36	99.01
		5.59	1.08	15.56	64.61	2.98	2.23	1.13	0.09	4.20	0.33	97.81
		5.72	1.10	15.49	63.99	2.94	2.38	1.10	0.10	4.37	0.30	97.50
		5.77	1.17	16.13	65.35	3.05	2.38	1.06	0.18	4.22	0.28	99.61
	JA2a	5.75	0.87	15.70	68.48	3.16	2.04	0.89	0.17	3.51	0.17	100.73
		5.96	1.31	15.83	65.78	2.78	2.74	1.22	0.22	4.83	0.35	101.01
		5.97	0.63	15.49	68.52	3.73	1.37	0.79	0.03	3.13	0.12	99.78
		5.42	1.12	16.06	66.20	2.85	2.44	1.04	0.15	4.40	0.25	99.93
		5.43	0.80	15.72	63.97	3.30	1.94	0.79	0.15	3.44	0.17	95.70
		5.24	1.42	16.27	65.98	2.73	2.92	1.20	0.07	4.81	0.30	100.94
		5.85	0.62	14.93	67.64	3.63	1.44	0.78	0.13	3.13	0.14	98.29
		5.92	0.62	15.11	67.72	3.63	1.47	0.79	0.15	3.39	0.16	98.96
		5.75	0.71	15.02	67.81	3.65	1.54	0.79	0.09	3.34	0.17	98.87
		5.70	1.25	15.02	63.05	2.90	2.70	1.22	0.12	5.02	0.33	97.31
		5.64	1.23	15.50	64.82	2.92	2.42	1.15	0.26	4.48	0.29	98.71
		5.96	0.63	15.06	68.01	3.59	1.50	0.82	0.15	3.49	0.16	99.37
		5.77	1.28	15.61	64.05	2.74	2.92	1.16	0.18	4.85	0.36	98.92
		5.48	0.97	15.70	63.27	3.09	2.09	0.91	0.28	3.67	0.24	95.70
		5.31	0.79	15.01	64.86	3.16	1.82	0.86	0.10	3.46	0.18	95.55
		5.27	0.96	15.06	64.29	3.07	2.25	0.99	0.16	4.14	0.28	96.47
		5.70	1.37	15.83	61.50	2.57	2.92	1.15	0.12	4.85	0.36	96.37
		5.84	1.44	15.96	64.50	2.88	2.86	1.24	0.19	4.87	0.36	100.14
		5.65	1.38	16.33	64.27	2.89	2.87	1.20	0.18	4.89	0.39	100.06
		5.91	0.89	15.62	68.39	3.40	2.01	0.84	0.09	3.20	0.21	100.56
		6.07	1.58	16.06	63.12	2.66	3.47	1.27	0.15	5.32	0.48	100.18
		5.83	1.22	15.95	65.35	2.90	2.61	1.20	0.19	4.90	0.33	100.49
H1 (T2)	JA1	5.57	1.06	15.57	66.46	2.98	2.37	1.11	0.01	4.20	0.25	99.58
		4.83	2.83	15.60	59.54	2.04	5.48	1.72	0.16	7.25	0.54	99.99
		4.31	4.07	15.77	55.03	1.49	7.52	1.62	0.28	8.68	0.54	99.31
		4.34	4.02	15.78	57.26	1.59	7.39	1.77	0.21	8.77	0.58	101.70
		4.07	4.07	15.58	56.28	1.52	7.60	1.67	0.25	8.48	0.58	100.10
		5.03	1.28	15.70	65.97	2.81	2.68	1.09	0.20	4.60	0.29	99.62

		5.52	1.40	15.92	64.63	2.74	3.17	1.19	0.13	4.69	0.35	99.74
		5.42	1.33	15.78	64.10	2.83	2.97	1.25	0.27	4.54	0.35	98.83
		6.10	1.27	15.49	64.62	2.89	2.75	1.11	0.16	4.50	0.34	99.22
		5.67	1.52	16.24	64.70	2.65	3.13	1.21	0.20	5.06	0.40	100.78
		5.35	1.31	15.64	62.27	2.79	2.90	1.07	0.26	4.99	0.29	96.85
		5.75	1.40	15.94	64.43	2.71	3.19	1.24	0.00	5.53	0.37	100.55
		5.67	1.22	15.87	65.24	2.98	2.53	1.15	0.12	4.37	0.35	99.50
		5.81	1.36	15.76	63.70	2.81	2.98	1.16	0.14	5.03	0.39	99.13
		5.57	1.31	15.90	64.75	2.90	2.71	1.28	0.15	4.67	0.32	99.56
		5.62	1.40	15.77	64.21	2.88	2.99	1.14	0.06	5.16	0.33	99.55
		5.49	1.48	15.56	62.04	2.66	2.95	1.27	0.21	5.04	0.46	97.15
		5.79	1.39	16.00	62.55	2.85	3.02	1.23	0.18	4.74	0.37	98.13
		5.65	1.25	15.93	65.13	3.06	2.87	1.19	0.16	4.80	0.39	100.42
		4.89	2.41	15.12	59.87	2.28	4.74	1.59	0.15	6.91	0.61	98.58
		4.36	1.37	15.94	64.87	2.94	2.71	1.24	0.08	4.73	0.42	98.66
		5.59	1.60	15.91	62.46	2.62	3.06	1.23	0.13	4.88	0.41	97.90
		5.67	1.32	15.79	65.10	2.90	2.84	1.20	0.18	4.82	0.37	100.19
	RI2e	5.62	1.50	16.10	65.98	2.74	3.06	1.25	0.15	4.79	0.32	101.50
		5.76	1.32	16.10	65.88	2.78	2.89	1.18	0.14	4.56	0.33	100.94
		5.26	1.48	16.07	65.30	2.70	3.01	1.18	0.15	5.08	0.35	100.58
		5.79	1.38	16.32	65.42	2.77	2.99	1.24	0.19	4.89	0.37	101.36
		5.71	1.48	16.02	65.19	2.70	3.03	1.26	0.20	4.77	0.36	100.72
		5.66	1.51	16.07	64.54	2.71	2.99	1.24	0.09	4.68	0.32	99.79
		5.94	1.36	16.39	64.84	2.78	2.96	1.15	0.14	4.55	0.37	100.48
		5.11	1.45	16.30	64.51	2.69	2.99	1.19	0.15	5.21	0.35	99.94
		5.31	1.44	16.13	63.50	2.74	2.94	1.15	0.13	4.72	0.33	98.40
		5.56	1.33	15.85	66.71	2.87	2.71	1.16	0.28	4.86	0.29	101.62
		5.40	1.20	16.21	66.96	2.96	2.70	1.21	0.18	4.43	0.30	101.53
		5.04	1.38	16.04	60.80	2.65	3.18	1.25	0.21	5.06	0.37	95.96
		5.78	1.38	16.08	64.19	2.84	2.97	1.15	0.20	5.06	0.32	99.97
		5.72	1.35	16.17	65.18	2.88	2.86	1.21	0.14	4.63	0.40	100.54
		5.81	1.40	15.95	64.35	2.86	2.94	1.24	0.11	4.91	0.35	99.92
		5.66	1.27	15.83	65.01	2.92	2.59	1.27	0.18	4.38	0.33	99.45
		5.90	1.41	16.01	64.51	2.76	2.68	1.12	0.10	4.71	0.36	99.54
		5.61	1.42	15.93	64.67	2.81	2.94	1.29	0.19	4.72	0.33	99.93
		5.68	1.25	15.12	61.50	2.80	2.85	1.17	0.13	4.54	0.37	95.41
		5.96	1.43	15.95	64.84	2.81	2.98	1.19	0.21	4.81	0.38	100.58
		5.97	1.44	16.42	64.03	2.76	3.31	1.12	0.15	4.68	0.38	100.26
		5.91	1.38	16.04	64.02	2.81	2.85	1.24	0.10	4.83	0.34	99.53
		5.53	1.34	16.13	64.98	2.87	2.83	1.17	0.10	4.71	0.32	99.99
		5.84	1.34	15.60	63.48	2.84	2.77	1.10	0.17	4.45	0.37	97.97
		5.51	1.44	16.06	64.67	2.88	3.01	1.19	0.23	4.99	0.36	100.34
	90-22	6.23	1.30	15.32	63.39	3.05	2.46	1.08	0.14	4.85	0.31	98.13
		6.34	1.60	15.43	62.10	2.84	3.00	1.24	0.11	5.09	0.43	98.18
		5.69	1.74	15.80	62.14	2.69	3.37	1.20	0.19	5.08	0.35	98.24
		5.77	1.53	15.61	61.87	2.87	3.16	1.28	0.16	5.16	0.39	97.81
		6.42	1.47	15.62	63.36	2.82	2.97	1.19	0.16	4.94	0.35	99.30
		5.52	1.94	15.07	59.27	2.32	4.71	1.34	0.14	6.61	0.41	97.34
		5.42	1.89	15.46	61.07	2.61	4.13	1.29	0.13	5.34	0.40	97.74
		5.82	1.56	15.61	62.72	2.83	3.04	1.20	0.17	4.94	0.39	98.27

		6.40	1.11	15.23	64.29	3.01	2.53	0.97	0.12	4.21	0.25	98.12
		6.31	1.19	15.49	64.28	3.18	2.56	1.07	0.16	4.66	0.36	99.26
		5.74	1.48	15.62	62.13	2.72	3.12	1.17	0.08	5.23	0.45	97.74
		5.77	1.63	15.54	61.72	2.56	3.16	1.26	0.19	5.27	0.42	97.53
		5.59	1.48	15.43	63.49	3.00	3.20	1.23	0.13	5.06	0.37	98.97
		6.32	1.25	15.45	63.01	2.95	2.64	1.14	0.14	4.86	0.34	98.10
		6.28	1.33	15.36	63.04	2.86	2.67	1.18	0.22	4.75	0.35	98.03
		6.31	1.16	15.20	64.72	2.96	2.40	1.02	0.14	4.40	0.27	98.58
		6.13	1.36	15.79	63.98	2.80	2.53	1.24	0.10	4.48	0.36	98.76
		6.11	1.31	15.82	63.26	2.84	2.78	1.14	0.12	4.71	0.41	98.50
		5.87	1.10	15.40	63.52	2.95	2.39	1.13	0.21	4.65	0.28	97.49
		5.74	1.55	15.66	63.17	2.89	2.75	1.26	0.20	4.81	0.44	98.48
		6.46	1.36	15.57	63.12	2.77	2.92	1.15	0.20	4.91	0.37	98.83
		6.08	1.35	15.44	62.57	2.86	2.83	1.18	0.19	4.69	0.35	97.55
		5.95	1.40	15.69	63.93	2.86	2.81	1.23	0.19	4.89	0.36	99.31
		5.97	1.26	15.77	63.83	2.94	2.59	1.21	0.15	4.56	0.32	98.61
		6.13	1.63	15.58	62.41	2.74	3.05	1.24	0.15	5.00	0.44	98.38
		6.27	1.32	15.42	63.00	2.97	2.75	1.21	0.11	4.72	0.35	98.11
		5.57	1.35	15.68	64.45	2.99	2.52	1.15	0.15	4.74	0.31	98.91
		6.39	1.22	15.60	63.00	2.88	2.81	1.14	0.23	4.70	0.33	98.30
?	RI1	6.49	1.07	16.65	65.74	3.00	2.11	0.97	0.19	3.85	0.21	100.28
		6.55	1.00	16.82	66.50	2.78	2.13	0.97	0.13	3.72	0.26	100.87
		6.22	1.06	16.91	66.35	2.97	2.10	0.96	0.11	3.71	0.23	100.61
		6.40	0.98	16.55	66.18	3.03	2.14	0.98	0.19	3.74	0.22	100.42
		6.44	1.05	16.32	64.69	2.86	2.02	1.04	0.23	3.78	0.25	98.68
		6.11	1.13	16.65	65.14	2.85	2.24	0.97	0.17	4.15	0.27	99.68
		6.50	1.01	16.51	65.56	2.90	2.05	0.94	0.12	3.79	0.22	99.60
		6.27	1.12	16.67	65.29	2.84	2.32	1.08	0.11	4.03	0.29	100.02
		6.37	1.09	16.84	66.20	2.90	2.29	0.97	0.21	4.19	0.21	101.27
		6.21	1.33	16.32	64.01	2.71	2.62	1.20	0.19	4.05	0.31	98.96
		6.35	1.09	16.27	65.05	2.82	2.20	1.02	0.16	4.04	0.26	99.26
		6.19	0.96	16.59	65.74	2.89	2.06	0.93	0.24	3.56	0.24	99.40
		6.60	1.04	16.87	65.98	2.94	2.11	1.02	0.23	3.61	0.25	100.65
		5.93	1.03	16.31	64.53	2.89	2.08	0.94	0.14	3.45	0.26	97.56
		6.42	1.23	16.88	65.59	2.82	2.15	1.02	0.20	3.81	0.29	100.41
		6.39	1.01	16.97	65.50	3.03	2.11	1.03	0.16	3.56	0.24	99.98
		6.41	1.08	16.07	63.69	2.95	2.00	0.94	0.25	3.66	0.25	97.30
		6.51	1.21	16.66	64.57	2.78	2.34	1.05	0.09	3.88	0.29	99.37
		6.28	1.08	16.31	65.07	2.93	2.17	0.98	0.20	3.53	0.26	98.83

Supplementary Table 5.1 Whole rock composition data for samples of Volcán Sollipulli eruption deposits.

Unit		Chufquén cone			Alpehué					Redondo cone		Circum-caldera lavas	
Sample		Scoria	Lava		Pumice			Lithic	Ignim.	Scoria			
Code		211/03	305/07	305/08	211/10	214/02	224/01	227/03	301/03	206/01	211/09	208/01	214/04
Whole rock composition (wt %), by XRF	SiO_2	52.22	52.76	53.65	58.76	67.81	67.37	54.20	66.78	51.96	47.98	66.74	61.79
	TiO_2	0.831	1.254	1.284	0.570	0.442	0.459	0.980	0.510	0.955	1.455	0.643	0.984
	Al_2O_3	18.46	17.40	17.62	18.95	15.49	15.18	17.91	15.67	17.82	20.45	15.78	16.34
	$Fe_2O_{3\,T}$	8.75	9.79	9.99	5.90	3.25	3.34	8.83	3.75	9.47	11.47	4.58	6.53
	MnO	0.153	0.162	0.166	0.154	0.075	0.077	0.148	0.086	0.156	0.161	0.098	0.131
	MgO	5.61	4.86	4.31	0.46	0.74	0.77	4.98	0.93	5.86	4.11	1.21	2.28
	CaO	10.26	8.70	8.00	1.96	2.52	2.42	8.21	2.64	9.33	7.12	3.19	4.85
	Na_2O	3.07	3.77	4.00	4.66	5.02	5.00	3.82	4.86	3.10	3.04	5.23	4.94
	K_2O	0.699	0.982	1.091	1.218	3.108	3.146	1.080	2.922	0.628	0.579	2.658	1.997
	P_2O_5	0.158	0.306	0.367	0.146	0.122	0.119	0.195	0.131	0.171	0.403	0.137	0.265
	SO_3	<0.002	<0.002	<0.002	0.006	0.004	0.004	0.041	0.003	0.011	<0.002	<0.002	<0.002
	LOI	-0.25*	-0.01*	-0.01*	6.16	1.90	2.30	0.33	2.29	1.11	3.00	0.04	0.04
	Total	99.95	99.97	100.46	98.95	100.48	100.17	100.71	100.58	100.58	99.77	100.30	100.14
Whole rock composition (ppm), by solution ICP-MS	Sc	25.38	26.03	23.81		6.07	6.03	21.36		24.85		11.91	15.65
	Cr	109.70	76.50	15.15		<LDL	<LDL	70.36		108.54		5.03	3.39
	Co	25.08	39.15	23.39		3.57	3.73	24.40		26.92		13.99	11.63
	Cu	96.27	66.82	57.25		14.68	19.56	59.61		108.56		33.30	36.86
	Zn	80.97	88.06	98.44		44.52	49.57	83.02		90.23		70.02	84.88
	Ga	14.43	15.68	16.07		14.09	14.76	14.92		14.16		16.99	15.28
	Rb	15.31	23.04	25.95		83.12	92.43	26.75		16.07		70.24	48.51
	Sr	640.31	602.00	620.22		240.43	239.97	556.94		523.13		331.73	479.08
	Y	11.92	18.54	19.30		18.81	20.41	15.70		13.66		25.06	21.62
	Nb	2.35	5.13	5.87		7.68	7.97	3.82		2.11		7.38	6.28
	Mo	0.48	0.68	1.09		1.99	2.14	0.70		0.44		1.67	1.19
	Cs	1.13	0.95	1.23		4.60	4.79	1.41		0.92		3.56	2.39
	Ba	237.11	337.53	422.02		679.24	733.79	345.08		228.22		681.46	574.58
	La	8.25	14.04	16.35		21.11	22.87	11.46		6.66		23.12	19.57
	Ce	24.66	39.89	46.64		51.40	56.30	32.71		20.77		57.88	56.52
	Pr	2.44	4.10	4.66		5.11	5.43	3.31		2.00		6.18	5.42
	Nd	11.30	18.73	20.12		19.10	20.00	13.53		9.76		23.41	21.69
	Sm	2.57	4.34	4.29		3.75	3.88	3.04		2.45		4.81	4.55
	Eu	0.85	1.29	1.33		0.80	0.83	0.93		0.83		1.12	1.22
	Gd	2.50	4.08	4.08		3.16	3.39	3.04		2.72		4.54	4.22
	Tb	0.37	0.60	0.61		0.51	0.55	0.46		0.43		0.71	0.66
	Dy	2.48	3.71	3.81		3.23	3.46	2.93		2.83		4.38	3.96
	Ho	0.52	0.78	0.75		0.68	0.71	0.60		0.56		0.89	0.82
	Er	1.49	2.21	2.20		2.10	2.23	1.77		1.61		2.71	2.39
	Tm	0.21	0.30	0.31		0.32	0.34	0.24		0.24		0.40	0.35
	Yb	1.33	2.02	2.10		2.28	2.41	1.65		1.52		2.73	2.37
	Lu	0.20	0.32	0.31		0.35	0.37	0.25		0.23		0.43	0.37
	Hf	1.87	3.08	3.31		5.45	5.80	2.59		1.84		5.84	4.50
	Ta	0.16	0.32	0.35		0.52	0.54	0.24		0.14		0.55	0.39
	Pb	9.60	9.14	10.51		23.86	25.22	9.49		7.15		23.87	18.63
	Th	2.85	2.58	2.53		8.60	9.44	2.79		1.35		7.69	5.87
	U	0.90	0.74	0.79		2.50	2.70	0.84		0.46		2.26	1.64

LDL = lower detection limit

* Excluded from calculation of total

Unit		Circum-caldera lavas			Chufquén Valley lavas			Sharkfin sequence						
Sample								Lava subsequence						
Code		218/01	210/10	216/07	213/02	213/04	213/05	209/03	209/06	209/09	210/03	210/04	225/03	209/05
Whole rock composition (wt %), by XRF	SiO_2	63.41	60.66	63.34	55.16	54.75	55.41	50.31	50.47	50.27	50.16	51.04	49.71	49.31
	TiO_2	0.772	0.933	0.988	0.752	0.676	0.672	0.845	0.842	0.871	1.020	1.040	0.855	0.730
	Al_2O_3	16.47	16.35	15.66	18.49	18.56	18.85	21.35	21.18	21.31	20.19	19.83	20.90	21.48
	$Fe_2O_{3\,T}$	5.93	6.70	6.01	7.38	7.29	7.40	7.58	7.79	7.72	8.47	8.61	7.91	6.95
	MnO	0.113	0.131	0.126	0.131	0.127	0.129	0.113	0.119	0.115	0.126	0.135	0.128	0.111
	MgO	2.12	2.21	1.62	5.23	5.28	5.42	4.20	4.24	4.32	4.57	5.13	4.04	4.18
	CaO	4.71	4.96	3.65	8.93	9.09	9.23	11.24	11.10	11.32	10.77	10.55	11.08	10.33
	Na_2O	4.84	4.82	5.17	3.38	3.22	3.23	2.77	2.87	2.88	3.05	3.22	2.79	1.96
	K_2O	2.071	2.047	2.734	1.007	0.983	0.973	0.478	0.473	0.377	0.466	0.656	0.496	0.863
	P_2O_5	0.165	0.264	0.312	0.173	0.151	0.153	0.161	0.161	0.166	0.189	0.210	0.161	0.152
	SO_3	<0.002	0.005	0.004	<0.002	<0.002	<0.002	<0.002	<0.002	<0.002	<0.002	<0.002	<0.002	<0.002
	LOI	-0.03*	0.23	0.35	0.30	0.40	0.35	0.93	0.76	0.88	0.89	0.85	0.76	2.35
	Total	100.58	99.31	99.97	100.93	100.53	101.82	99.97	100.01	100.24	99.90	101.27	98.84	98.40
Whole rock composition (ppm), by solution ICP-MS	Sc	16.76	15.58	11.78	21.99	18.72	20.82	20.08		19.55	21.75	23.07		
	Cr	7.72	6.20	<LDL	58.11	61.43	60.85	97.22		93.85	131.86	127.80		
	Co	12.83	11.75	7.69	22.62	18.87	21.75	20.03		18.75	21.71	22.39		
	Cu	61.95	33.01	14.05	87.30	87.69	82.71	85.40		85.18	89.75	88.15		
	Zn	75.06	81.53	85.74	73.29	71.91	72.25	69.81		71.99	74.27	71.41		
	Ga	18.52	15.58	14.32	15.73	12.54	14.52	14.58		13.40	13.47	14.24		
	Rb	54.58	53.57	75.11	21.62	21.45	21.20	9.22		3.29	9.31	10.74		
	Sr	469.51	466.41	370.30	694.01	707.83	705.39	710.42		714.38	704.93	658.95		
	Y	24.15	22.97	23.86	13.27	9.91	11.45	11.50		10.78	12.13	13.37		
	Nb	6.16	7.42	8.19	2.91	2.64	2.69	2.15		2.17	3.62	3.77		
	Mo	1.08	1.33	1.70	0.68	0.61	0.63	0.29		0.22	0.23	0.36		
	Cs	1.76	2.64	3.16	1.22	1.02	1.09	0.47		0.08	0.64	0.58		
	Ba	582.25	576.28	728.75	311.30	307.10	306.58	202.41		234.37	272.97	286.78		
	La	21.95	19.88	21.81	10.79	9.03	10.31	7.61		7.33	8.66	9.43		
	Ce	49.89	54.43	65.20	29.71	28.75	28.94	23.52		24.12	27.89	27.48		
	Pr	5.77	5.54	5.83	3.05	2.45	2.74	2.24		2.17	2.56	2.80		
	Nd	23.07	22.16	23.53	12.90	10.25	10.96	10.86		10.66	11.84	13.12		
	Sm	4.87	4.73	4.93	2.88	2.20	2.49	2.47		2.40	2.71	3.03		
	Eu	1.25	1.26	1.19	0.88	0.69	0.74	0.85		0.83	0.91	1.01		
	Gd	4.61	4.56	4.64	2.70	2.03	2.27	2.57		2.46	2.69	2.97		
	Tb	0.71	0.68	0.70	0.42	0.31	0.34	0.38		0.38	0.39	0.44		
	Dy	4.50	4.27	4.52	2.44	1.93	2.15	2.38		2.33	2.58	2.76		
	Ho	0.90	0.86	0.91	0.50	0.38	0.42	0.48		0.47	0.50	0.55		
	Er	2.72	2.49	2.67	1.47	1.15	1.23	1.39		1.33	1.42	1.58		
	Tm	0.40	0.36	0.40	0.21	0.16	0.17	0.21		0.19	0.20	0.22		
	Yb	2.77	2.49	2.64	1.46	1.13	1.20	1.29		1.25	1.28	1.48		
	Lu	0.42	0.37	0.39	0.21	0.16	0.18	0.19		0.18	0.18	0.22		
	Hf	5.25	4.80	5.81	2.28	1.97	1.98	1.82		1.81	1.96	2.06		
	Ta	0.40	0.45	0.55	0.18	0.16	0.16	0.14		0.14	0.23	0.23		
	Pb	20.95	17.16	19.89	12.69	10.89	11.46	7.00		6.81	6.86	7.31		
	Th	7.15	5.21	6.82	3.80	3.43	3.72	1.59		1.50	1.62	1.73		
	U	2.21	1.56	2.15	1.17	1.00	1.09	0.55		0.42	0.45	0.58		

Unit		Sharkfin sequence											
Sample		Intrusions											
Code		209/07	209/12	210/05	210/07	210/13	216/03	216/05	216/06	216/08	223/01	223/03	305/02
Whole rock composition (wt %), by XRF	SiO_2	50.55	52.85	52.72	49.82	51.37	52.87	52.66	51.57	53.35	54.56	51.94	52.45
	TiO_2	1.020	1.225	1.234	1.030	0.863	0.948	0.809	1.021	0.791	1.020	1.000	0.959
	Al_2O_3	21.11	17.62	17.63	18.41	17.79	17.53	17.53	18.92	18.23	18.34	18.45	18.16
	$Fe_2O_{3\,T}$	8.53	10.32	9.44	8.69	9.16	8.11	7.80	8.85	8.21	8.17	8.48	8.34
	MnO	0.124	0.165	0.154	0.132	0.146	0.148	0.134	0.142	0.141	0.134	0.138	0.147
	MgO	3.63	4.37	4.77	5.99	7.53	4.84	6.15	5.71	5.30	4.66	5.12	5.51
	CaO	10.79	8.70	8.75	9.36	9.17	9.32	9.21	8.76	9.53	7.82	8.89	9.21
	Na_2O	3.16	3.90	3.60	3.39	2.91	3.49	3.31	3.72	3.28	3.97	3.52	3.52
	K_2O	0.650	0.926	1.090	0.917	0.739	1.105	1.038	1.032	0.790	1.372	0.827	0.995
	P_2O_5	0.210	0.243	0.278	0.278	0.194	0.211	0.191	0.297	0.163	0.306	0.308	0.246
	SO_3	<0.002	<0.002	0.041	<0.002	<0.002	0.002	<0.002	0.012	<0.002	0.002	<0.002	<0.002
	LOI	0.44	0.62	0.65	0.39	0.69	1.17	0.66	0.21	0.23	0.16	0.82	0.96
	Total	100.21	100.93	100.37	98.41	100.56	99.74	99.49	100.24	100.01	100.51	99.48	100.49
Whole rock composition (ppm), by solution ICP-MS	Sc	19.89	26.21	25.79	21.93	22.30	19.13	19.95	20.08	19.91	17.00	17.07	
	Cr	36.09	29.85	83.46	159.02	201.81	102.76	159.61	95.78	55.27	59.00	65.28	
	Co	18.81	23.20	24.83	25.35	32.35	19.34	22.42	25.32	19.93	19.62	21.79	
	Cu	102.85	104.34	102.56	102.95	81.30	84.51	86.16	53.95	88.12	73.74	72.27	
	Zn	75.92	95.37	88.88	82.55	81.81	78.70	82.48	86.97	78.40	82.23	85.82	
	Ga	14.58	15.87	16.32	14.07	14.23	12.23	13.53	14.98	12.04	14.39	13.61	
	Rb	12.90	18.35	27.37	22.56	19.07	22.81	17.98	18.77	14.90	27.10	13.65	
	Sr	720.68	570.24	626.55	668.41	540.88	744.24	825.46	896.32	693.24	775.75	824.01	
	Y	11.70	17.14	18.76	14.31	14.08	12.91	12.97	15.13	9.64	16.11	14.07	
	Nb	3.29	4.18	4.66	5.93	3.13	3.68	3.65	4.82	2.22	5.42	4.83	
	Mo	0.39	0.56	0.70	0.63	0.46	0.69	0.48	0.26	0.42	0.72	0.49	
	Cs	0.38	0.42	1.27	0.43	0.91	0.87	0.56	0.49	0.63	0.52	0.63	
	Ba	248.53	289.76	378.68	394.25	274.14	365.69	365.01	394.65	255.74	448.62	382.26	
	La	8.60	9.88	12.95	11.36	9.70	11.99	13.25	16.53	8.19	17.71	15.19	
	Ce	27.49	30.02	39.28	35.61	28.08	42.15	41.91	49.12	27.11	52.72	48.36	
	Pr	2.53	3.02	3.95	3.30	2.85	3.29	3.49	4.60	2.27	4.83	4.28	
	Nd	11.13	14.80	18.56	14.55	13.14	14.28	16.09	20.24	9.77	19.31	19.27	
	Sm	2.52	3.63	4.43	3.29	3.02	3.01	3.17	4.12	2.16	3.85	3.93	
	Eu	0.84	1.19	1.27	1.03	0.93	0.93	0.93	1.22	0.69	1.10	1.13	
	Gd	2.51	3.55	4.10	3.20	3.08	2.91	2.93	3.57	2.04	3.36	3.45	
	Tb	0.38	0.55	0.61	0.46	0.44	0.42	0.41	0.51	0.30	0.47	0.49	
	Dy	2.34	3.46	3.85	2.79	2.81	2.58	2.69	3.18	1.89	2.95	2.97	
	Ho	0.48	0.73	0.78	0.57	0.58	0.54	0.54	0.62	0.39	0.61	0.61	
	Er	1.40	2.10	2.30	1.65	1.71	1.56	1.56	1.82	1.09	1.74	1.73	
	Tm	0.19	0.30	0.32	0.24	0.24	0.22	0.21	0.25	0.16	0.25	0.25	
	Yb	1.25	1.92	2.10	1.50	1.56	1.43	1.49	1.64	1.03	1.70	1.55	
	Lu	0.19	0.29	0.31	0.22	0.23	0.22	0.22	0.25	0.16	0.25	0.24	
	Hf	1.87	2.60	3.10	2.34	2.39	2.65	2.66	2.88	1.79	3.14	3.02	
	Ta	0.20	0.27	0.29	0.38	0.20	0.24	0.23	0.28	0.14	0.31	0.29	
	Pb	5.66	7.00	10.32	7.33	7.69	10.72	17.26	11.22	7.98	7.86	9.31	
	Th	1.41	1.81	2.87	1.78	1.94	4.47	4.45	3.57	2.86	4.37	3.05	
	U	0.42	0.58	0.93	0.62	0.62	1.25	1.19	0.95	0.73	1.21	0.85	

Unit		Sharkfin sequence									
Sample		Hyaloclastite subsequence								Scoria	
Code		209/10	209/11	209/17	210/06	210/09	210/12	305/03	305/04	223/04	305/06
Whole rock composition (wt %), by XRF	SiO_2	50.03	51.49	49.33	53.46	51.64	52.47	53.02	55.33	54.41	51.74
	TiO_2	0.913	1.065	0.747	0.769	0.742	1.239	1.329	1.233	0.782	0.780
	Al_2O_3	19.49	19.08	17.44	18.34	17.99	17.58	17.85	17.96	17.10	18.38
	$Fe_2O_{3\,T}$	8.60	8.90	7.79	7.38	7.51	9.37	10.04	8.27	7.49	8.77
	MnO	0.135	0.143	0.127	0.120	0.120	0.149	0.139	0.141	0.131	0.141
	MgO	5.33	5.03	7.63	5.34	6.61	4.62	2.81	2.60	5.73	5.50
	CaO	9.04	9.79	10.18	8.92	8.81	8.60	8.16	7.58	8.03	10.41
	Na_2O	1.88	3.25	2.14	3.07	2.44	3.60	3.56	3.79	3.67	2.77
	K_2O	1.260	0.672	0.692	1.017	1.084	1.042	1.128	1.508	1.264	0.662
	P_2O_5	0.178	0.213	0.186	0.173	0.175	0.277	0.327	0.307	0.180	0.154
	SO_3	<0.002	<0.002	0.004	0.004	0.025	<0.002	<0.002	<0.002	<0.002	<0.002
	LOI	3.40	0.68	3.53	1.52	2.17	0.87	1.51	1.30	0.58	0.64
	Total	100.26	100.31	99.81	100.11	99.33	99.81	99.87	100.02	99.37	99.95
Whole rock composition (ppm), by solution ICP-MS	Sc	20.51	24.04	20.06		17.78	23.04			19.16	21.44
	Cr	103.69	121.28	145.45		148.67	84.52			138.17	117.57
	Co	24.66	24.41	28.62		24.98	22.60			22.70	23.97
	Cu	90.86	100.91	84.32		61.13	102.90			74.71	61.93
	Zn	72.66	79.11	73.24		74.29	88.87			75.20	77.05
	Ga	12.94	15.07	13.25		13.62	14.47			14.94	12.84
	Rb	32.40	14.12	11.51		24.21	25.80			30.43	16.32
	Sr	547.51	645.77	831.33		719.92	617.42			715.32	643.19
	Y	11.95	15.04	10.60		12.67	17.40			16.09	10.38
	Nb	2.68	3.28	2.50		3.56	4.75			4.70	2.51
	Mo	0.08	0.49	0.25		0.30	0.64			0.90	0.42
	Cs	1.36	0.87	0.53		1.15	1.26			1.69	0.98
	Ba	273.07	290.50	292.08		323.84	387.27			414.66	241.58
	La	8.21	10.01	12.94		12.65	12.90			16.51	7.34
	Ce	25.25	29.50	35.74		34.85	39.28			43.00	23.29
	Pr	2.44	3.02	3.48		3.36	3.75			4.22	2.19
	Nd	11.44	14.03	15.45		14.96	17.13			17.58	10.10
	Sm	2.66	3.42	3.00		3.13	4.02			3.55	2.36
	Eu	0.88	1.05	0.93		0.88	1.15			1.01	0.76
	Gd	2.69	3.29	2.68		2.89	3.77			3.27	2.32
	Tb	0.39	0.48	0.37		0.41	0.55			0.49	0.34
	Dy	2.51	3.08	2.29		2.66	3.53			3.21	2.16
	Ho	0.51	0.63	0.45		0.52	0.72			0.63	0.46
	Er	1.49	1.80	1.24		1.56	2.01			1.83	1.27
	Tm	0.20	0.25	0.18		0.22	0.28			0.26	0.18
	Yb	1.32	1.68	1.14		1.45	1.89			1.78	1.21
	Lu	0.20	0.25	0.17		0.23	0.28			0.26	0.18
	Hf	1.94	2.33	1.91		2.73	2.98			3.39	1.87
	Ta	0.17	0.20	0.14		0.23	0.30			0.28	0.17
	Pb	7.53	8.98	7.33		10.77	10.64			13.24	9.54
	Th	1.66	2.10	3.60		3.96	2.68			5.91	2.29
	U	0.55	0.71	0.91		0.98	0.87			1.67	0.82